AGSO JOURNAL
OF AUSTRALIAN GEOLOGY & GEOPHYSICS

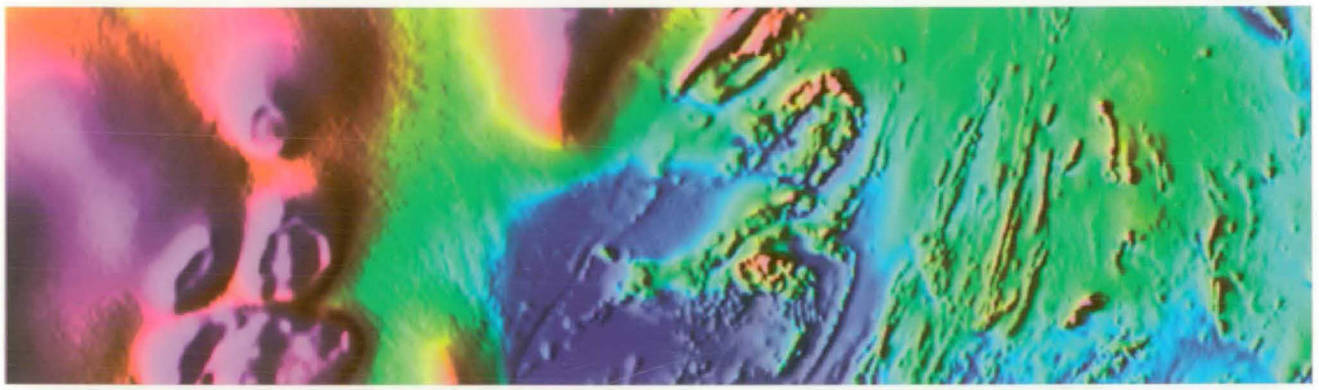

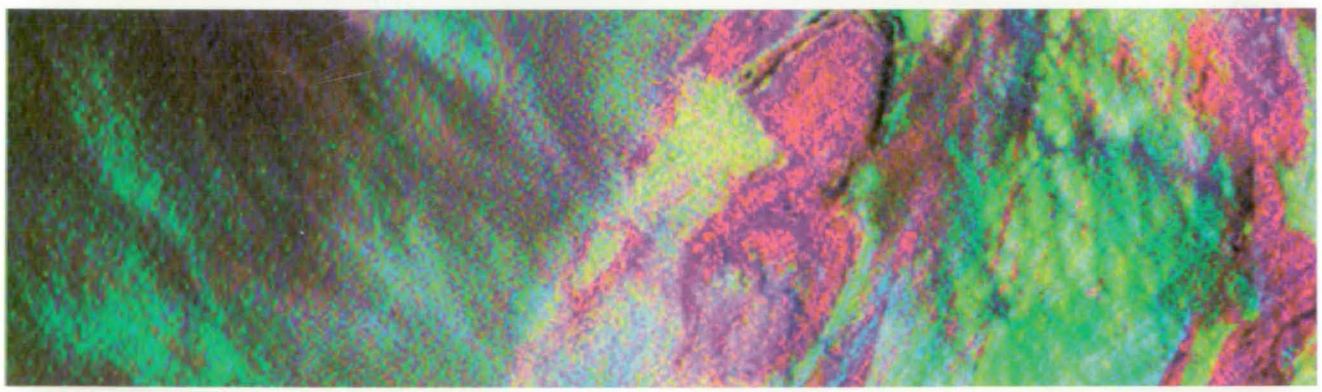

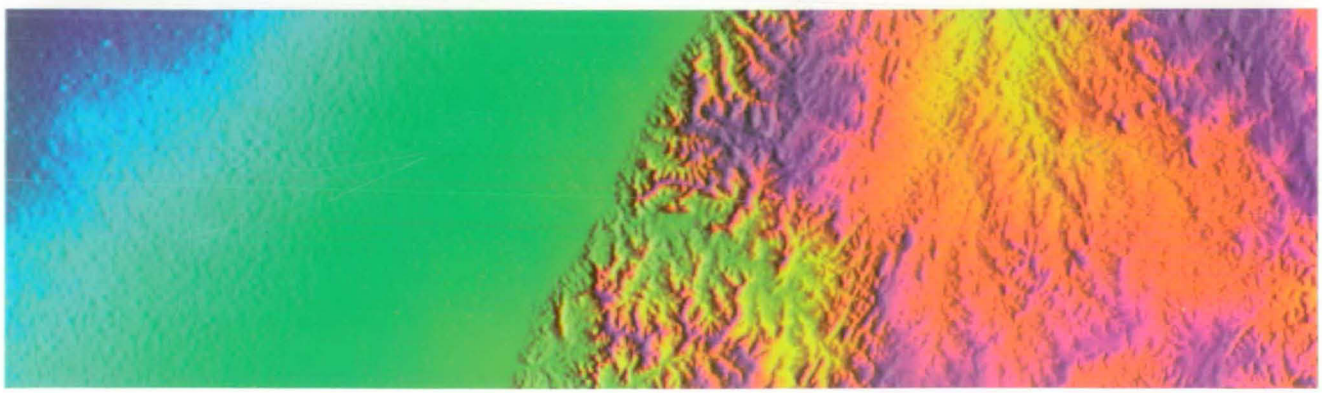

AIRBORNE MAGNETIC AND RADIOMETRIC SURVEYS

VOLUME 17, NUMBER 2

AUSTRALIA

AGSO JOURNAL

OF AUSTRALIAN GEOLOGY & GEOPHYSICS

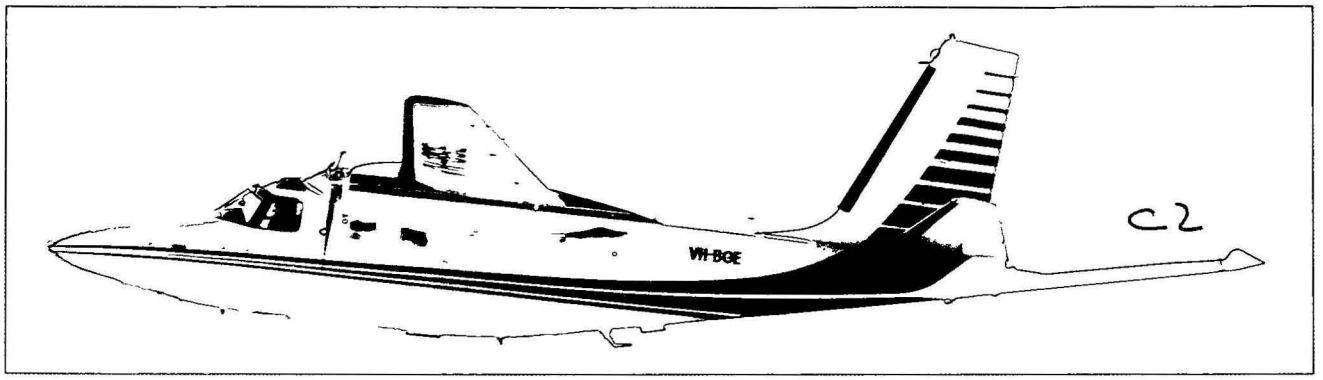

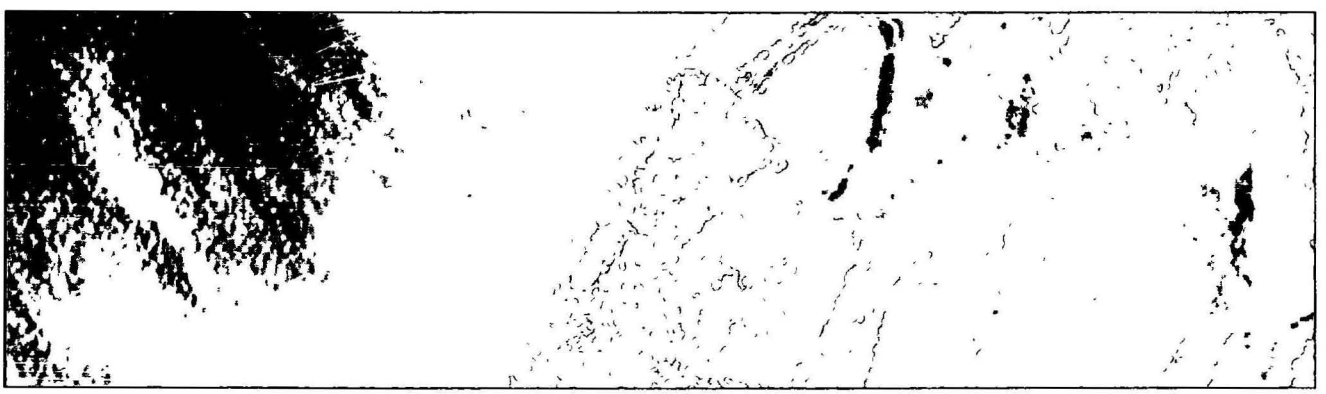

AIRBORNE MAGNETIC AND RADIOMETRIC SURVEYS

VOLUME 17, NUMBER 2

AGSO Journal of Australian Geology & Geophysics

Editor: Ian Hodgson, Corporate Publications, Australian Geological Survey Organisation

Information for contributors

From the end of volume 17, the *AGSO Journal of Australian Geology & Geophysics* will merge with the *Australian Journal of Earth Sciences* (*AJES*). The *AJES* is published by Blackwell Science for the Geological Society of Australia Inc. The editorial board of the *AGSO Journal of Australian Geology & Geophysics* is confident that the new combined journal, part of Blackwell's internationally recognised stable of quality scientific journals, will be well placed to keep Australian research at the leading edge of international geoscience.

As volume 17 is a series of special thematic issues, which are all fully committed, the Editor is unable to accept further unsolicited contributions. However, the Editor of the *Australian Journal of Earth Sciences* will be pleased to consider manuscripts for publication. Contributions should be sent to A.E. Cockbain, PO Box 8114, Angelo Street, South Perth, WA 6151, Australia (tel. and fax 09 367 7037; email: tcockbai@cyllene.uwa.edu.au).

AGSO JOURNAL

OF AUSTRALIAN GEOLOGY & GEOPHYSICS

VOLUME 17, NUMBER 2, 1997

Thematic issue: Airborne magnetic and radiometric surveys
Guest associate editor: Peter Gunn

ISSN 1320–1271

Copies of the AGSO Journal can be purchased from the Australian Geological Survey Organisation (GPO Box 378, Canberra ACT 2601; tel. 06 249 9642, fax 06 249 9982).

Other matters concerning the Journal should be sent to the Editor, AGSO Journal

Editor, AGSO Journal: Ian Hodgson
Cover design and figures prepared by AGSO Cartographic Services Unit unless otherwise indicated
Prepared for publication by Lin Kay

Printed in Australia by National Capital Printing, Fyshwick, A.C.T. 2609

AUSTRALIAN GOVERNMENT PUBLISHING SERVICE CANBERRA 1997

Month of issue, February 1997

***Front-cover illustration*:**

The AGSO Aero Commander geophysical survey aircraft, VH-BGE, and airborne geophysical data acquired along east–west flight lines, 100 metres apart and 60 metres above the ground, over an area immediately north of Broken Hill in New South Wales. The data are *(from top to bottom)* total magnetic intensity, ternary gamma-ray spectrometry and digital elevation.

AGSO Journal of Australian Geology & Geophysics, 17(2), 1–1

Airborne magnetic and radiometric surveys

Preface

When I first started using airborne magnetic and radiometric survey data I was frustrated that no practical textbook existed to explain how the data were collected and processed and how they should be interpreted. At the time of writing this editorial no such textbook has yet appeared, despite the enormous advances in these fields and the logarithmic increase in the amount of airborne magnetic and radiometric data acquired each year. The collection of papers in this issue of the AGSO Journal of Australian Geology & Geophysics does not pretend to be the required textbook. Our purpose is to present the methodologies and ideas of various specialists who are active in the disciplines that contribute to the acquisition, processing, presentation and evaluation of airborne magnetic and radiometric data. We are confident in our products; however, we do not claim that our approaches and ideas are necessarily the best. They are continually evolving and it is possible that we will have modified our ideas by the time this volume appears. We offer the volume as a snapshot of our opinions and activities in mid 1996. The contents of this issue have been structured to provide both introductory material and review material. We hope it will fill some of the documentary black holes until the necessary textbook appears.

Peter Gunn
December 1996

AGSO Journal of Australian Geology & Geophysics, 17(2), 3–9

Airborne geophysics in Australia: the government contribution

David Denham[1]

Airborne geophysical data sets provide important cost-effective information for resource exploration and land management. Improved techniques, developed recently, now enable high-resolution aeromagnetic and gamma-ray surveys to be used extensively by the resource industries to improve the cost effectiveness of exploration and by governments to encourage resource development and sustainable management of natural resources. Although airborne geophysical techniques have been used extensively and are now used almost routinely by mineral explorers, it is only in the last few years that governments have been involved as major players in the acquisition of data. The exploration industry pioneered the imaging of high-resolution airborne geophysical data sets in the early 1980s and, at the same time, the Northern Territory Government started a modest program of flying the Northern Territory, at 500 m flight-line spacing, to attract mineral exploration. After the start of the National Geoscience Mapping Accord in 1990, the then BMR and its State/Territory counterparts used the new high-resolution data as an essential ingredient to underpin mapping programs. These new data sets proved so valuable that, starting in 1992/93, the annual expenditure by the Commonwealth and the States/Northern Territory increased from roughly $2m per year to a massive $10m per year. The South Australian Exploration Initiative, which started in 1992, was the first major State initiative. It was followed by similar programs in Victoria, New South Wales and Queensland. These investments by governments, although unlikely to be permanently sustainable, have been made to encourage and expand exploration activity by providing new high-quality data sets to industry at very low cost. There are now approximately 11 million line-km of airborne geophysical data available in databases held by the Commonwealth, States and Northern Territory. The results so far have seen a significant increase in exploration activity in States that have embarked on this course (e.g. South Australia and Victoria), and the information provided from these surveys is proving crucial to understanding the geology of the continent and for land management issues.

Introduction

The prosperity of Australia and the rest of the world depends almost entirely on the natural resources of the Earth, which provides almost all the basic ingredients essential for sustaining our standard of living. For example:

- elements such as iron, aluminium, copper, zinc, tin, tungsten, etc. are essential for the manufacture of automobiles, aircraft, computers, refrigerators, telephones, televisions, etc., not to mention the 'essential' luxuries of life that are made from gold, diamonds, silver, opals and the like;
- oil, gas and coal provide energy for heating, cooling, lighting, transport and electrical power;
- clay, limestone, granite, and sand and gravel, provide the building materials for our cities, towns and roads;
- soils are needed for crops, pastures, and trees; and
- groundwater is required for irrigation and urban water supplies.

All these resources are derived directly from the Earth, and so that we can properly manage them in a sustainable way, it is essential that we understand the Earth.

In the early part of this century, sustainability and the management of natural resources was not an important issue in Australia. There was enough land to go round, water resources were not a major problem and dry-land salinity and land degradation were problems of the future. The situation has now changed enormously, and the sustainabilty of our agricultural and pastoral industries is of serious concern. Furthermore, the supply of minerals and petroleum products, while not presently under threat, may become a serious issue in the future because of the increasing difficulty of finding new deposits and competition for land use (AMIC 1990).

If we focus on the mineral industry, we can see that Australia is well endowed with mineral resources and has developed a world-class mining and (to a lesser extent) mineral processing industry. It is amongst the world's leading producers of bauxite, diamonds, gold, iron ore, silver/lead/zinc ores and mineral sands and has the potential to further develop these industries in the future (BRS 1995).

Many early discoveries were made where prospectors were able to directly sample rock outcrops or where the ore was very close to the surface. However, new discoveries are proving harder to make and several of the old mines are nearing the end of their economic lives. For example, the Broken Hill silver/lead/zinc deposit, which was found because the ore cropped out, has yielded approximately $50 billion worth of metal (1995 dollars) since its discovery in 1883 (Pasminco 1994). However, the ore-body is rapidly reaching the end of its economic life. Existing reserves are declining and unless new deposits are found in the next few years the viability of both Broken Hill and Port Pirie, where the ore is smelted, will be in doubt. Any new finds in that region will undoubtedly come from areas where the prospective rocks are covered and, in fact, this situation will probably apply for most future discoveries in Australia.

One of the main impediments to new discoveries is the regolith. This comprises a mantle of residual and/or transported material overlying deeply weathered, and potentially prospective, bedrock. The regolith is significant in two ways:

- it conceals more than 85 per cent of the Australian continent, making the task of exploring for minerals within fresh bedrock difficult (Fig. 1); and
- the geological processes that have taken place in the surficial zone above fresh bedrock, namely the regolith, have resulted in the formation of several major ore deposit types, e.g. bauxite, clays, opal, gold and iron ore.

The challenge is therefore to develop methods to map and 'see through' the regolith to reduce the risk associated with exploration strategies. Furthermore, these new methods must be environmentally friendly so that minimal change is made to the surface of the Earth.

The situation in the petroleum exploration industry is very similar. The obvious onshore exploration targets, based on well-defined structures that may host petroleum deposits, have probably been discovered and tested (BMR 1992). The task of finding the more subtle targets is getting harder and more expensive. High resolution aeromagnetic surveys are now providing valuable information for petroleum exploration. Improvements in data acquisition, processing and interpretation techniques have enabled not only the gross basin architecture to be determined, but also the more subtle intra-basin features (Gunn 1996).

In the last five years or so, the use of high-quality airborne geophysical data sets has proved extremely valuable, not only for penetrating the regolith to map the bedrock geology, but also to map the regolith itself. Furthermore these data sets can be used, not only for mineral exploration, but for petroleum exploration and land-use management. The increased use of airborne geophysics has been primarily a result of improvements

[1] Australian Geological Survey Organisation, GPO Box 378, Canberra, ACT, 2601, Australia

in techniques to acquire, process and image aeromagnetic and gamma-ray data sets.

Acquisition of airborne geophysical data sets—the national coverage

The first systematic surveys of the continent were carried out by BMR (AGSO's predecessor) in the 1950s (Milligan et al. 1994). These surveys were restricted to recording aeromagnetic anomalies and were primarily designed to delineate sedimentary basins for petroleum exploration. The aircraft flew at 150 m elevation and the flight-line spacings were at least 1500 m. In due course, the surveys were extended to cover the whole continent for both mineral and petroleum exploration as well as key information for understanding the geology of Australia. By 1990, most of the continent had been covered by these reconnaissance surveys and, with improvements in instrumentation described above, more detailed surveys were being flown over priority areas of the continent.

Before 1990, in the context of publicly funded surveys, only the Northern Territory government had used more detailed regional surveys. In the Northern Territory, 500 m line spacings were flown as early as 1981, with the Barrow Creek survey (Milligan et al. 1994), and since then a continual program of data acquisition has been supported. The data are sold at ~20c/km, compared to an acquisition cost of ~$10/km (1995 dollars). By the end of 1995, the Northern Territory government will have funded approximately 800 000 km of 500 m high-resolution airborne geophysical data. This amounts to approximately $8m in 1995 dollars and coverage of over one quarter of the Territory.

Large regional surveys with flight-line spacing of 500 m or less were not flown in other parts of Australia by governments until the National Geoscience Mapping Accord (NGMA) started in 1990. The NGMA is a joint Commonwealth/State and Northern Territory initiative to assist in developing an integrated approach to sustainable development and, in particular, to help maximise the benefits to the community from the nation's petroleum, mineral, land and water resources. The objectives of the NGMA include

- optimising the environment for mineral and fuel exploration through the provision of geoscientific data, maps and reports,
- providing a reliable base for the assessment of undiscovered mineral and fuel resources, and

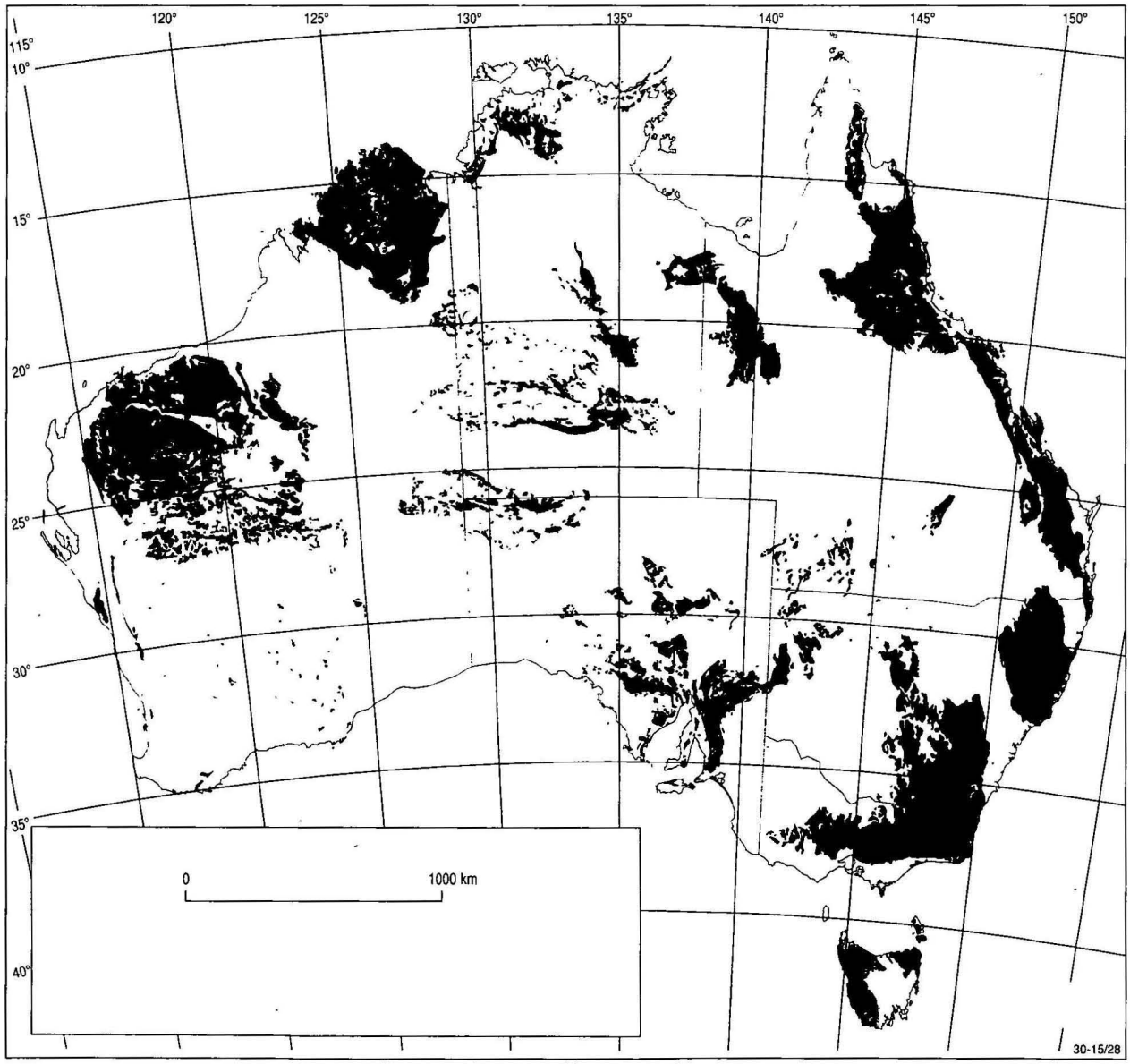

Figure 1. Favourable areas for bedrock mapping using remote sensing (in black). Actual outcrop occupies only a portion of the black shaded areas.

- strengthening the geoscientific base to provide a basis for sound environmental management (BMR 1990).

The NGMA arose out of the 1988 Woods Review (Woods 1988). This Review was tasked to undertake a comprehensive review of the role and functions of the then Bureau of Mineral Resources, Geology and Geophysics (BMR) in the context of Australia's national needs in the area of geoscientific and related activities.

That review considered that 'Geoscientific maps and data sets, supported where appropriate by published reports, should be regarded as the most important products of the geoscientific research and related studies undertaken by BMR'. Consequently, as a matter of priority it recommended that the BMR and the State/Northern Territory geological surveys, through the Chief Government Geologists' Conference, and in consultation with industry and the academic community, develop a national geoscience mapping strategy.

Airborne geophysical surveys were seen as essential to the preparation of new maps and data sets. Starting in 1990, with flying of the Ebagoola 1:250 000 Sheet area as part of the North Queensland NGMA project and the Bathurst Sheet area in New South Wales as part of the Lachlan NGMA project, the equivalent of 113 of the 500 or so map sheet areas covering the onshore part of the continent will have been flown in Australia as a result of government programs by the end of 1996.

The table below shows the expected situation by the end of 1996.

State	*Map sheet areas (1:250 000)*	*number covered at ≤ 500 m*	*percentage of State/Territory*
Tas	6	~1	20
Vic	18	10.5	58
NSW	51	18.5	36
SA	66	29	44
NT	83	25	30
WA	163	19	12
Qld	113	10	9
Total	***500***	***113***	***22***

These numbers are only approximate because not all surveys correspond to map sheet boundaries, but they represent the level of investment provided by the States, Northern Territory and the Commonwealth. Figure 2 shows the locations of these map sheet areas. The flight-line spacing is somewhat variable, ranging from 100 m over the Broken Hill 1:250 000 Sheet area to 500 m over most of the Northern Territory. If the data

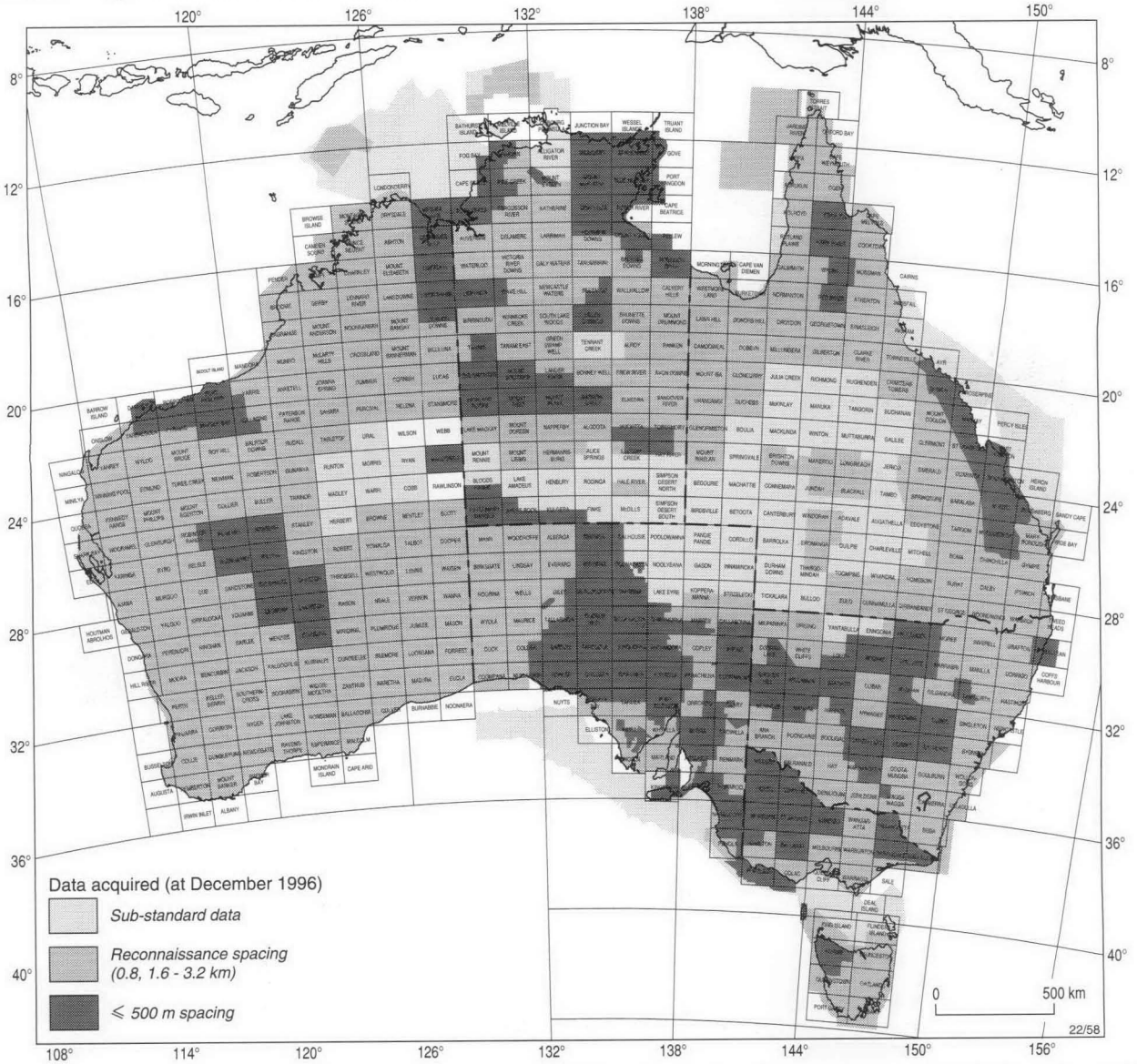

Figure 2. Aeromagnetic data acquired by the Commonwealth and States over the Australian continent (end 1996). Over 20 per cent of the continent has now been covered by high-quality airborne geophysical surveys at line spacing of 500 m.

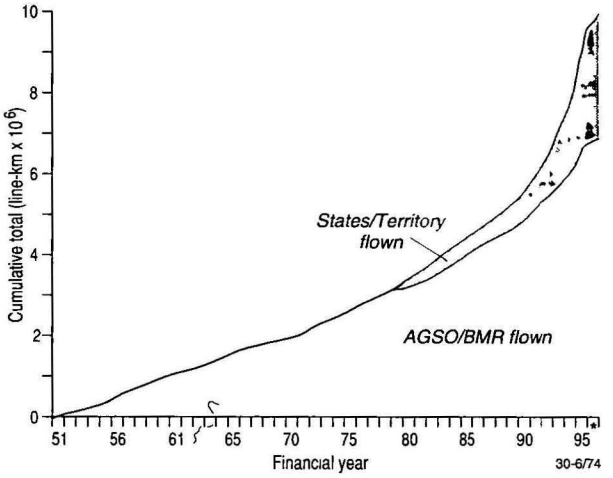

Figure 3. Rate of acquisition of aeromagnetic data by the States, Northern Territory and the Commonwealth.

acquired at spacings of 500 m or less are added to AGSO's reconnaissance data set (line spacing 800 m), it turns out that approximately 11 million line-km of airborne geophysical data are available from the States/Northern Territory and Commonwealth databases. This would cost approximately $100m to re-fly at 1996 prices. Figure 3 shows the rate of acquisition of these data sets.

Commonwealth, State and Northern Territory programs

Commonwealth Government

BMR and AGSO have been acquiring airborne geophysical data sets since the early 1950s. In the period 1990–1995 approximately $2m per year was invested in data acquisition programs. Approximately $1.2m per year was allocated to operate AGSO's aircraft, which acquires 200 000–250 000 km per year, and to generate standard products. The remainder was invested in contract flying (Hone et al. 1997).

AGSO's data base contains about 5.4 million line-km of aeromagnetic data acquired by AGSO's aircraft and 1.8 million line-km either flown under contract to AGSO or purchased from industry. These data sets form a crucial part of the national information database. If these data sets had to be reflown today the cost would be approximately $65m—a huge investment.

Northern Territory

The Northern Territory Geological Survey was the first to invest in high-quality regional surveys on a systematic basis, starting with the Barrow Creek survey, which was flown at a 500 m line spacing in 1981. Since then it has gradually acquired, under contract, data over an average of one and a half 1:250 000 map sheet areas every year, and as of mid-1995 nearly 30 per cent of the Territory has been covered.

South Australia

In July 1992, the South Australian Government announced details of the $11m South Australian Exploration Initiative (this was subsequently expanded to ~$25m). The initiative was described by Ministers Arnold and Klunder (Arnold & Klunder 1992) as a 'dramatic affirmation of the importance which the Government attaches to the long term expansion of the State's mineral and petroleum industries.' The government hoped that this investment would generate up to $18m of output, in terms of exploration activity as well as the wealth that would be generated if new mines and petroleum fields were developed.

A large part of the initial $11m and subsequent funding went into the acquisition of high-quality aeromagnetic data sets, and the result has been the release, at nominal prices (~3c/km), of data sets covering over 40 per cent of the State. These data sets were acquired at flying heights of 80 m and line spacings of 400 m. By the end of 1996 approximately 1 million line-km of new data will have been acquired over the State and made available in the public domain under the auspices of the SAEI.

Victoria

The Victorian Initiative for Minerals and Petroleum was announced by the Minister for Energy and Minerals, Mr Jim Plowman, in April 1994 (Plowman 1994). It comprises a $16.5m initiative over three years, to encourage mineral and petroleum exploration in Victoria. A large part of these funds has been allocated to airborne geophysics.

The two target areas are the northwest of the State, where 140 000 line-km of new data have been acquired, and the Eastern Highlands, where 90 000 line-km of helicopter data have been acquired. In addition, high-quality company data sets of 200 m line spacing have been incorporated into the publicly available database. At present, nearly 60 per cent of the State is covered by data owned by the State. The price for newly flown data is approximately 2c/km.

New South Wales

New South Wales' *Discovery 2000* was announced in September 1994 (Fahey & Causley 1994). The Fahey Government committed $40m over 6 years to promote the minerals and petroleum industries in New South Wales and the Carr Government reaffirmed its commitment to this initiative (Martin 1995). A large part of these funds will be invested in airborne geophysical datasets and by the end of 1996 the equivalent of 18 map sheet areas (~820 000 line-km) will have been acquired under the auspices of this program. The eventual plan will be to cover as much of the State as possible with the available funding.

The flight-line spacing for the surveys is 250–400 m, depending on the type and depth of the target rocks.

Queensland

In the northern part of the State, 4 map sheet areas have been acquired under the NGMA North Queensland project, which is being followed by a State initiative entitled *Geomap 2005*, which started in October 1993 (McGrady 1994). This is a 12 year program, involving a whole range of mapping activities. The airborne geophysical program focuses on the Yarrol Province. To date, approximately six 1:250 000 map sheet areas have been surveyed.

Tasmania

Although no specific exploration initiative has been undertaken in Tasmania, there has been an overall policy of improving the coverage of airborne geophysics over the entire State. By the end of 1996 approximately 20 per cent of the State will have been covered at line spacings closer than 500 m.

Western Australia

In 1993, the Western Australian Government made available $5m over 4 years towards initiatives to assist and encourage mineral exploration in that State. A major portion of these additional funds has been provided for airborne geophysical data sets over the Eastern Goldfields and Pilbarra regions. AGSO supplemented these efforts and, at present, approximately 14 map sheet areas have been covered in these regions. By the end of 1996, only 12 per cent of the State will have been covered by publicly acquired data sets.

Data acquisition systems

The recent large expansion in the data acquisition programs has been possible because of the improvements in the data acquisition, processing and imaging capabilities. Essentially, four main advances have combined to form one of the most cost-effective multi-use data acquisition systems currently available (Horsfall 1997).

The use of GPS for navigation, flight-path recovery and digital elevation models

One of the most labour-intensive parts of pre-1980 airborne surveying was the flight-path recovery process. Photographs or video taken from the aircraft were used to identify, with the help of controlled aerial photographs, where the plane had flown. In featureless country this was often very difficult, and accuracies in position were seldom better than 50 m. However, in the 1950–1970s the flight-lines were typically as much as 1500 m apart and often up to 3 km. The aircraft flew at 150 m ground clearance, so the positioning errors were not as crucial as they are now.

Nowadays, with real-time differential GPS techniques and pre-programmed flight lines to assist pilot navigation, the positional accuracy is down to 2–3 m. This improvement has made a huge difference to the data quality and ensures that the anomalies observed in the aircraft can be accurately ground-truthed. It is also possible to combine navigational data from the GPS observations with the aircraft terrain clearance from the radar altimeter to produce a digital elevation model of the ground being surveyed. The GPS data are converted to AGD84 and adjusted for the height of the aircraft above the ground to produce raw elevation data. These data are then corrected for the geoid-ellipsoid separation and the height difference between the radar altimeter and the GPS antennas. For surveys of 400 m line spacing, the data are gridded to an 80 m cell size, and tests have shown that grids are accurate to about 2–3 m (Fig 4).

Better magnetometers

Caesium or helium vapour magnetometers commonly used in standard aeromagnetic surveys have a resolution 0.01 nT or better and can cycle every 0.1 s. This corresponds to approximately one sample every 6–7 m on the ground and enables the magnetic data to be used for high-precision ground truthing. No longer are the accuracy of the magnetometer and its cycling limiting parameters in aeromagnetic data quality.

Better gamma-ray spectrometers

Modern spectrometers usually provide a 33 litre crystal detector with energy partitions covering 256 channels. The crystals and their detector systems are usually fully balanced and calibrated so that valid and statistically meaningful data sets can be acquired. The spectrometers normally sample every second because of the difficulty in observing the low energies involved. This corresponds to a ground sample interval of 70 m and a swath width of approximately 150 m at a flying height of 60 m.

More powerful computers

The increasing speed and capacity of digital acquisition systems has enabled very large data sets to be acquired in real-time. At present an average flight of approximately 1000 km will acquire about 50 Mb of data and, because of the capabilities of modern computers, the raw size of the data set is not a restriction.

Computers are becoming more and more powerful, and continued miniaturisation of the components that comprise the complete data acquisition system has led to a decrease in the weight and size of the recording instruments. This has enabled survey aircraft to carry larger crystals to record the gamma radiation and more fuel, allowing longer flights.

This raft of improvements has enabled the development of an extremely cost-effective acquisition package that can be used for a wide range of tasks. At present, AGSO's aircraft (an Aero Commander Shrike), which represents a leading-edge industry standard, measures the following physical parameters when flying at 240 km/hour.

Parameter	*Sample time (s)*	*Interval distance (m)*	*Storage space (bytes real)*
Total magnetic intensity	0.1	6.7	8
256-channel gamma-ray spectrometer	1.0	67	4 x 256
Radar altimeter	1.0	67	4
x,y,z position above the ellipsoid by GPS	1.0	67	8 x 3
Barometric pressure	10.0	670	4
Temperature	10.0	670	4
VLF total field & vertical quad. comp.	1.0	67	4 x 2
Doppler position (along track & across track)	1.0	67	4 x 2
Video (colour) of ground vertically below aircraft	continuous		

For example, the AGSO 1:250 000 Sir Samuel Sheet area survey consisted of 47 075 km of data (lines plus ties), with lines spaced at 400 m, and ties spaced at 4 000 m. Thus, the total number of measurements obtained for this survey was approximately 191 000 000 for the first seven parameters listed above (the last two are for backup purposes). This amounts to approximately 801 000 000 bytes, i.e. nearly 1 Gb.

These system improvements have led to changes in the specifications for airborne geophysical surveys, a boost in the total kilometres flown throughout the whole of Australia and an enormous increase in the quality of the results.

Improvements in data processing and imaging

Hand in hand with the progress in data acquisition techniques has been a corresponding improvement in processing and imaging of the new data sets, which because of their size has involved a new approach to their handling (Luyendyk 1997; Milligan & Gunn 1997). The processing involves eight major steps in two phases:

Phase 1: Preprocessing

- Verifying and editing the raw data; and
- Locating the data in x and y coordinates.

Phase 2: Processing

- Parallax corrections for aircraft and sensor geometrics;
- Removing diurnals from the geomagnetic field;
- Removing large-scale regional field effects;
- Levelling the data by minimising navigation and loop closure errors;
- Levelling to remove any residual levelling errors; and
- Gridding so that the data sets can be imaged and contoured.

The use of small (~80m) grids and colour graphics has been a key factor in determining the quality of the imaging processes.

The Australian mineral exploration industry first began to use image processing techniques in the early 1980s, as a result of advances made by CSIRO in the ERTS and LANDSAT programs (Williams 1993). Typically, a 400 m survey will provide an 80 m grid, which corresponds to an equivalent pixel size on any images produced. Spatial features of the magnetic anomalies inherent in these grids can be emphasised by the judicious use of various processing and filtering techniques, image enhancement and display mechanisms.

AGSO uses the INTREPID software package for grid

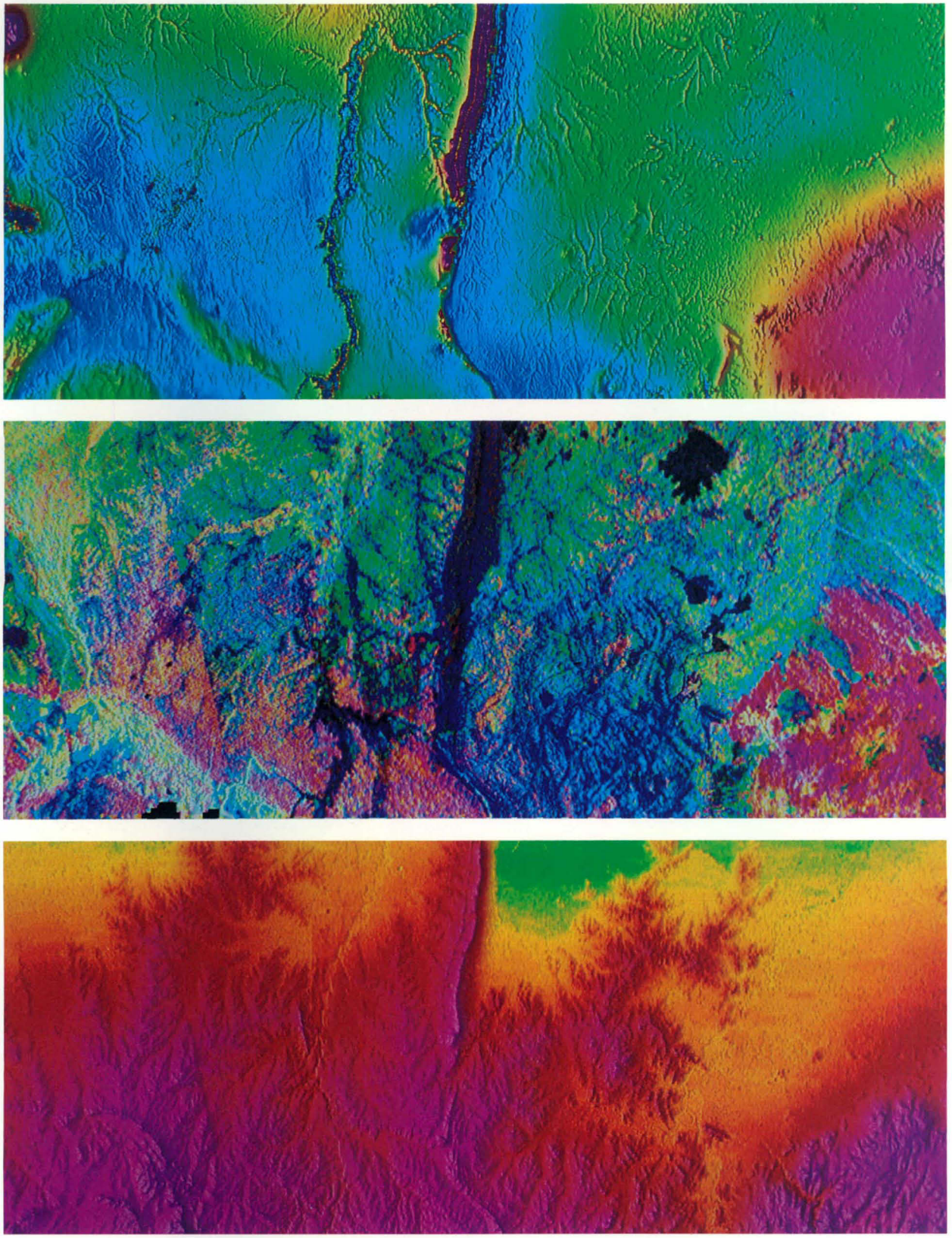

Figure 4. Pixel images of part of the Bendigo 1:250 000 Sheet area (scale 1:900 000). Notice how the three data sets each make significantly different contributions to the understanding of the land surface and the rocks beneath. Top—Total magnetic intensity reduced to the pole, westerly illumination; centre—Gamma-ray spectrometry, potassium (red), thorium (green), uranium (blue); bottom—Digital elevation model, westerly illumination.

post-processing coupled with ER MAPPER for displaying images and producing hard copy maps. The following routines are available and commonly used:

- Reduction to the pole (RTP), which transforms the data to represent the induced anomaly field if the inclination of the field was vertical.
- Derivatives (vertical and horizontal), usually first vertical or second vertical derivative filters are used; these emphasise the high-frequency components in the anomaly patterns.
- Upward and downward continuation to correct the surveys flown at different ground clearances.
- Frequency filters to select frequency ranges.
- Euler deconvolution to calculate the source locations and depths.

The images can be produced with a range of colour, sun angle, hue, intensity, wetness and so on.

AGSO's standard products for each map sheet area are Total Magnetic Intensity with RTP and appropriate sun-angle illumination; a three-band composite gamma-ray spectrometric image (potassium, red; thorium, green; and uranium, blue) and a digital elevation model, with appropriate sun-angle illumination (Fig. 4). More detailed surveys at 100 m line spacing and 60 m elevation provide even more information, but the standard 400 m spaced survey is proving to be a useful standard.

Conclusions

The main use of the airborne geophysical data sets thus far has been focused on aeromagnetic information. In future, as land management issues become more important, radiometric and digital elevation information will become more significant. These data sets provide crucial information on such things as soil types and drainage models (Dickson & Scott 1996). The 1995 Liverpool Plains survey by AGSO is a good example of this application, where 200 m spaced data sets have been acquired to map soil types in the context of dry-land salinity problems

The big challenge is to ensure that these continent-wide information-rich resources are maintained and continually upgraded in a readily accessible format so that the whole nation can take full advantage of the databases, for a whole range of issues.

Acknowledgements

I thank Terry Crabb, Ian Hone and Neil Williams for reviewing this paper and helping to improve the final product.

References

AMIC, 1990. Shrinking Australia: Australia's economic future: access to land. Australian Mining Industry Council, Special Publication, Canberra, p.15.

Arnold, L. & Klunder, J., 1992. Mineral exploration programme detailed. News release of 22 July 1992 by The Hon. John Klunder M.P., Minister of Emergency Services, Mines and Energy, and Forests, Adelaide.

BMR, 1990. A national strategy for geoscience mapping (August 1990). BMR internal document adopted by Chief Government Geologists' Conference 1990 (unpublished).

BMR, 1992. Oil and gas resources of Australia. Petroleum Resource Assessment Branch, Bureau of Mineral Resources, Canberra.

BRS, 1995. Australia's identified mineral resources, 1994. Bureau of Resource Sciences, Canberra.

Dickson, B.L. & Scott, K.M., 1996. Interpretation of aerial gamma-ray surveys. AGSO Journal of Australian Geology & Geophysics, 17 (this issue).

Fahey, J. & Causley, I., 1994. Discovering New South Wales mineral and petroleum wealth—Discovery 2000. News releases from Department of Mineral Resources, Sydney, 1994.

Gunn, P.J., 1997. Regional magnetic and gravity responses of extensional sedimentary Basins. AGSO Journal of Australian Geology & Geophysics, 17(2)—this issue.

Hone,I., Milligan, P.R., Mitchell, J.N. & Horsfall, K., 1997. Regional airborne magnetic and gamma-ray databases in Australia. AGSO Journal of Australian Geology & Geophysics, 17(2)—this issue.

Horsfall, K., 1997. Airborne magnetic and gamma-ray data acquisition. AGSO Journal of Australian Geology & Geophysics, 17(2)—this issue.

Luyendyk, A., 1997. Processing of airborne magnetic data. AGSO Journal of Australian Geology & Geophysics, 17(2)—this issue.

McGrady, A., 1994. Leading the way, in the leading state. A Queensland Government statement on minerals and energy initiatives in Queensland, May 1994, Brisbane, Queensland Government Publication.

Martin, R., 1995. Government to spend $8 million on search for minerals and petroleum. News release of 22 August 1995 by the Hon. Bob Martin, M.P., Minister for Mineral Resources, Sydney.

Milligan, P.R. & Gunn, P.J., 1997. Enhancement and presentation of airborne geophysical data. AGSO Journal of Australian Geology & Geophysics, 17(2)—this issue.

Milligan, P., Mitchell, J., Collins, D., Wyatt, B., Souter, D., Reitsma, R., Simonis, F., Sampath, N., Rickardsson, L. & Davidson, D., 1994. Index of airborne geophysical surveys. Australian Geological Survey Organisation, Record 1994/44.

Pasminco, 1994. Broken Hill operation—geological overview, 1994. Pasminco, Broken Hill (unpublished report).

Plowman, S.J., 1994. The Victorian Initiative for Minerals & Petroleum. Mining boom creating wealth and jobs for Victoria, and Major mining boost for regional Victoria. News releases of 13 and 20 April 1994, by the Hon. S.J. Plowman, Minister for Energy and Minerals, Melbourne.

Williams, N., 1993. Image processing—the quiet revolution in Australian geoscience. Chairman's address to ACT Territories Division of the Geological Society of Australia.

Woods, A.J., 1988. Review of the Bureau of Mineral Resources, Geology and Geophysics., A report to the Minister for Resources by Mr. A.J. Woods, AO, December 1988, Canberra.

AGSO Journal of Australian Geology & Geophysics, 17(2), 11–21

Australian national airborne geophysical databases

I.G. Hone[1], P.R. Milligan[1], J.N. Mitchell[1], K.R.Horsfall[1]

The Australian Geological Survey Organisation maintains national databases of aeromagnetic, radiometric and digital elevation data, which have been progressively collected since the 1950s and are still being added to. The quality of the information collected in recent years is such that a case can be made for re-flying large parts of Australia, over which only old, poor-quality data are available.

Introduction

The major, publicly available, Australia-wide databases of airborne geophysical data are those operated by the Australian Geological Survey Organisation (AGSO). State government departments hold sets of data relating to their particular State and some private companies maintain proprietary databases.

The national airborne geophysical databases held in AGSO contain data covering 99 per cent of onshore Australia, and substantial areas offshore, encompassing over 9 000 000 km^2 in total. The data have been collected continually since 1951 and have a wide range of specifications, resulting from changes in technology, procedures, and specific requirements over this period. Data types have expanded from just magnetic, to include gamma-ray spectrometry data and, since 1992, digital elevation data. The databases, which are being continually upgraded, are a valuable resource for Australia.

At the end of 1996, the databases held 11 000 000 km of magnetic data, 8 000 000 km of gamma-ray data, and 1600 000 km of digital elevation data. The areal percentage coverage of onshore Australia is:

Type	*Total coverage*	*Acceptable broad reconnaissance (3200 m line spacing)*	*Acceptable regional (500 m line spacing)*
Magnetic	99%	85%	23%
Gamma-ray	50%	50%	23%
Elevation	6%	6%	6%

The data in AGSO's national airborne geophysical databases provide a strategic framework necessary for both Government, industry and other researchers to assess resource potential, determine land use and environmental management policies, and plan detailed exploration activities. They form an integral basis for establishing the geological framework of Australia and maintaining Australia's international exploration competitiveness.

AGSO (formerly the Bureau of Mineral Resources, Geology & Geophysics—BMR) commenced airborne geophysical surveying in Australia with a survey in the Gippsland area of Victoria in 1951. Since then, AGSO has been acquiring data from surveys it has flown itself, and from surveys flown for it under contract. The data have been catalogued and stored and form the basis of the national airborne geophysical databases. These data have been added to by data from State surveys and companies, and by data which came available through the Petroleum Search Subsidy Acts (PSSA).

The State government databases of airborne geophysical data can be divided into two types, based on how they were acquired. The first contains data acquired by private companies as part of their exploration programs and provided to the State government as part of the legal requirements for the issuing of exploration tenements. Most of the data sets in these databases arise from surveys over small areas, and thus are not regional. Data sets over large areas will be incorporated into regional databases. Some of the company data are held confidentially. The second type contains data which have usually been acquired under contract for the State government. Most data in the latter databases have been incorporated into AGSO's national airborne geophysical databases.

Databases held by private companies contain data the companies have acquired from government or other agencies and data they have had flown for themselves. The companies do not usually make data available from their databases. However, some geophysical contractors hold data which they will sell on a multi-client basis, and brokerage services exist which have the rights to sell some private company data.

This paper describes AGSO's databases, which hold the widest coverage of publicly available regional data. An earlier review of the airborne magnetic surveys in these databases was given by Tucker et al. (1988).

Rate of accumulation of data

AGSO acquires, on average, approximately 250 000 line km of geophysical data annually with its own aircraft and up to 300 000 line km by contract (Figs 1, 2). The AGSO program is long-term and ensures a steady stream of data to the latest quality standards.

In recent times, increased airborne geophysical activity by State governments has markedly increased the growth rate of the databases. Recent data acquisition is summarised in Table 1. Of the formal State exploration initiatives, the South Australian

Table 1. Summary of recent airborne geophysical data acquisition by State government.

State	*Period*	*Amount (km)*	*Comments*
New South Wales	1994 – 1996	800 000	Discovery 2000. Additional 180 000 km in joint projects with AGSO.
Northern Territory	–1996	930 000	Long-term program.
Queensland	1994 – 1996	290 000	Mainly Airdata—part of Geomap 2005.
South Australia	1993 – 1995	930 000	South Australian Exploration Initiative. Additional 70 000 km in joint projects with AGSO.
Tasmania		70 000	
Victoria	1994 – 1997	360 000	Victorian Initiative for Minerals and Petroleum. Additional 200 00 km in joint projects with AGSO.
Western Australia	1994, 1995	120 000	Additional 170 000 km in joint projects with AGSO.

[1] Australian Geological Survey Organisation, GPO Box 378, Canberra, ACT 2601

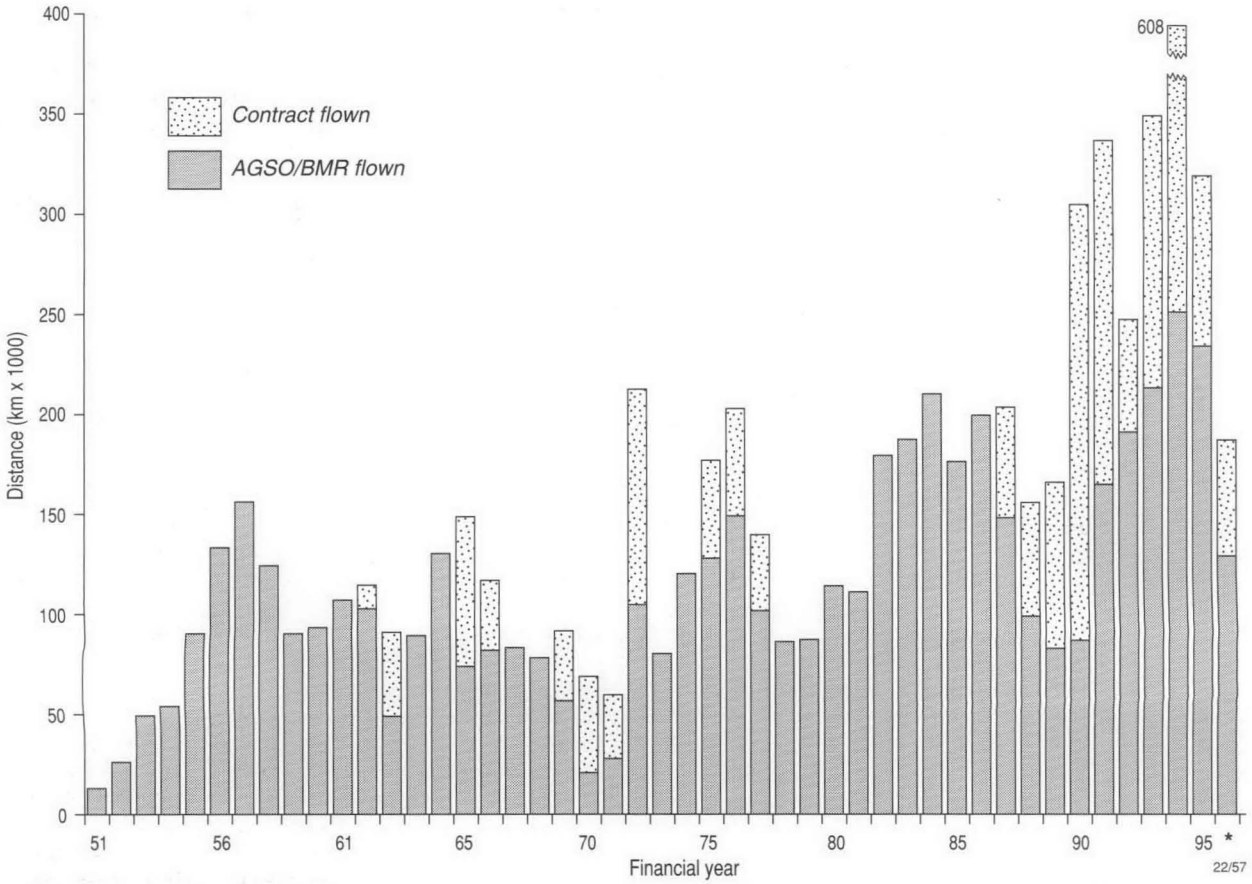

Figure 1. Accumulation of AGSO data into national airborne geophysical databases—frequency distribution up to December 1996.

Exploration Initiative has just been completed, and data acquisition in the Victorian, New South Wales, and Queensland initiatives is programmed to finish in 1997, 2000, and 2000, respectively.

Survey cover

Airborne magnetic surveying and, more recently, gamma-ray spectrometric surveying, in Australia have been conducted in a systematic manner for the past 40 years. The Australian continent is topographically mapped into regular mapping areas, the standard mapping unit for Australia-wide reconnaissance airborne surveys being the 1:250 000 map sheet. Each sheet is 1.5° longitude by 1.0° latitude, equating to approximately 150 km by 100 km (depending on latitude).

Approximately 99 per cent of onshore Australia has coverage of magnetic data (Fig. 3). The only areas with no coverage are Rawlinson, Wilson, and Webb 1:250 000 Sheet areas in central Australia. Although completion of first pass coverage was aimed for by 1989, it is now unlikely that complete coverage will be obtained until 1997 or later.

Gamma-ray data which can be presented as maps cover about 50 per cent of onshore Australia (Fig. 4). Many of the early gamma-ray data were acquired and processed in such a way that the best form of presentation was as locations of the most significant anomalies; these data are not considered as part of the coverage in the maps in this paper, although the results are still available from the database.

Digital elevation data cover about 6 per cent of onshore Australia (Fig. 5).

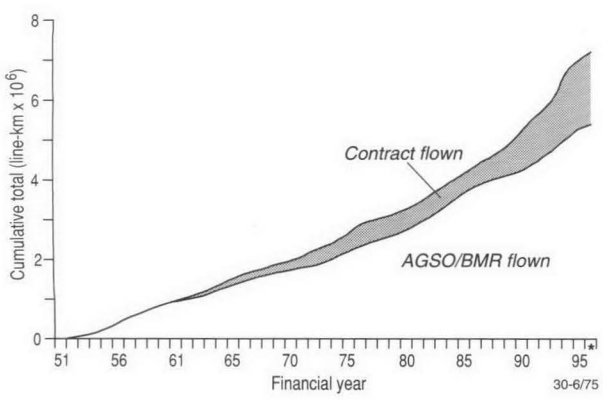

Figure 2. Accumulation of AGSO data into national airborne geophysical databases—cumulative distribution.

Line spacing

Figures 3, 4 & 5 show line spacing of data coverage over Australia for magnetic, gamma-ray and digital elevation data. For areas surveyed more than once, the line spacing of the latest survey has been used.

The line spacing of aeromagnetic data in the coverage of Australia has a wide range and is an important consideration when discussing coverage. Until the 1980s, 1500–1600 m was considered satisfactory as a first pass reconnaissance standard for hardrock areas, and 3200 m for sedimentary basins. AGSO surveys, which were the major contributors to the databases, reflected this. Data acquired at wider line spacings were considered substandard, but adequate for first pass reconnaissance coverage. A few areas where 1600 m spaced lines were parallel to strike, or where there were large noise envelopes on data, were also considered substandard.

The early acceptance of 1500–3200 m line spacing was strongly motivated by a desire to achieve airborne magnetic coverage over all of onshore Australia as soon as possible.

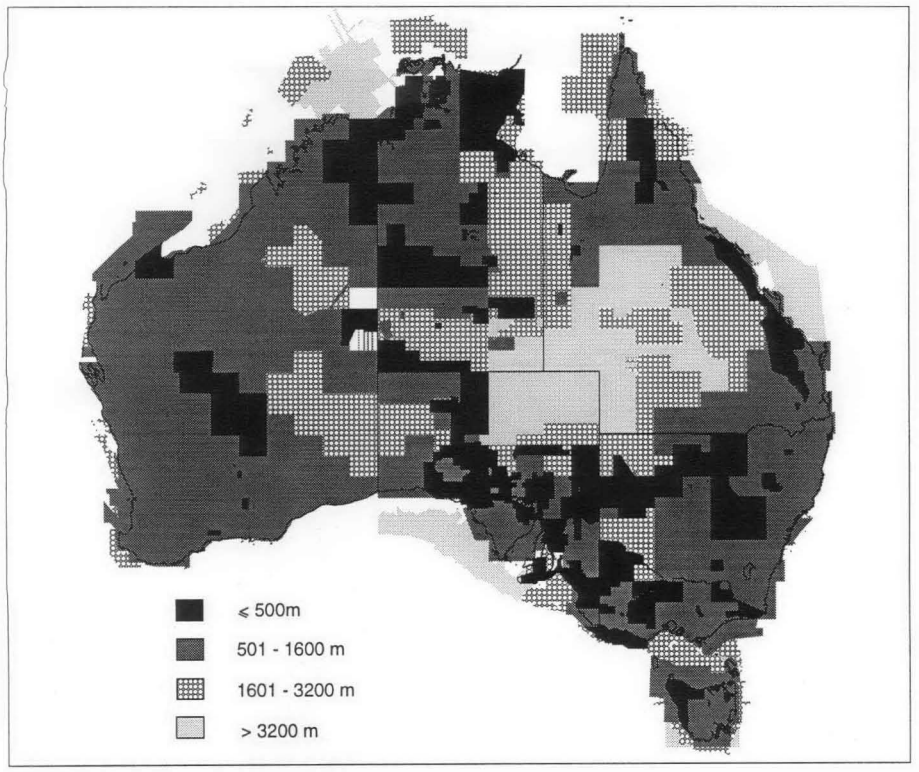

Figure 3. Airborne magnetic coverage of Australia—line spacing.

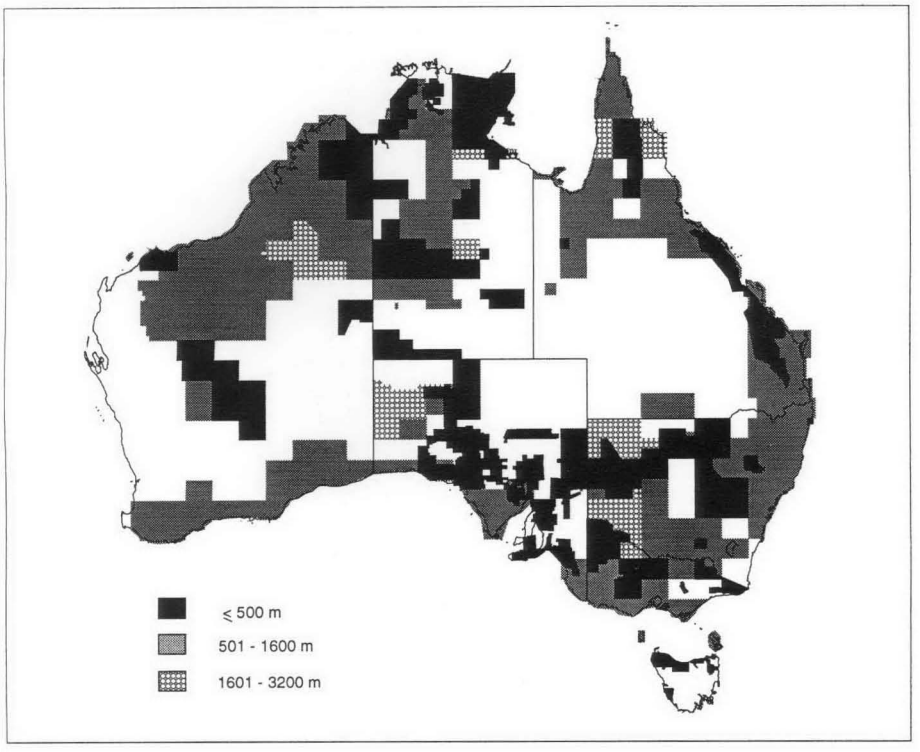

Figure 4. Airborne gamma-ray coverage of Australia—line spacing.

As closer line spacing slows down the rate of coverage, a trade-off was made for a moderate amount of information over large areas in preference to a large amount of information over small areas.

Despite the tendency to survey with 1500–3200 m line spacing, and closer in recent years, there is still almost 15 per cent of onshore Australia where line spacing is more than 3200 m. For most of this area digital line data are not available. Digital gridded data with a basic cell size of 2 km, which were generated for the 1976 Magnetic Map of Australia (BMR 1976), are the only digital data available.

Less than 25 per cent of onshore Australia is covered with aeromagnetic data acquired along flight lines spaced at 500 m or less. Spacing of 400–500 m is now considered the standard for onshore regional surveys with appropriate line direction, and for most future regional surveys it will be no more than 400 m.

Figure 6 illustrates the effects of line spacing on the resolution of magnetic pixel image maps and the usefulness of data, particularly for geological mapping. The data are from a small portion of the Broken Hill 1:100 000 Sheet area and were acquired with a line spacing of 100 m and a flying height of 60 m above ground surface. They form part of the data set acquired by AGSO for the Broken Hill Exploration Initiative, a collaborative program between the governments of New South Wales, South Australia and the Australian Federal Government.

The four colour images (Fig. 6 a–d), display histogram-equalised TMI data at 1:100 000 scale for line spacing of 100, 200, 400 and 800 m, with grid intervals of one-fifth of the line spacing—20, 40, 80 and 160 m, respectively. Note that the calculated grid cells have not been interpolated to a smaller grid cell size, which would give smoother looking images, but would not increase the amount of information. Whereas the 100 m and 200 m line-spaced data show good resolution, there is some degradation when the line spacing increases to 400 m. Resolution of anomalies is poor for the data at 800 m spacing.

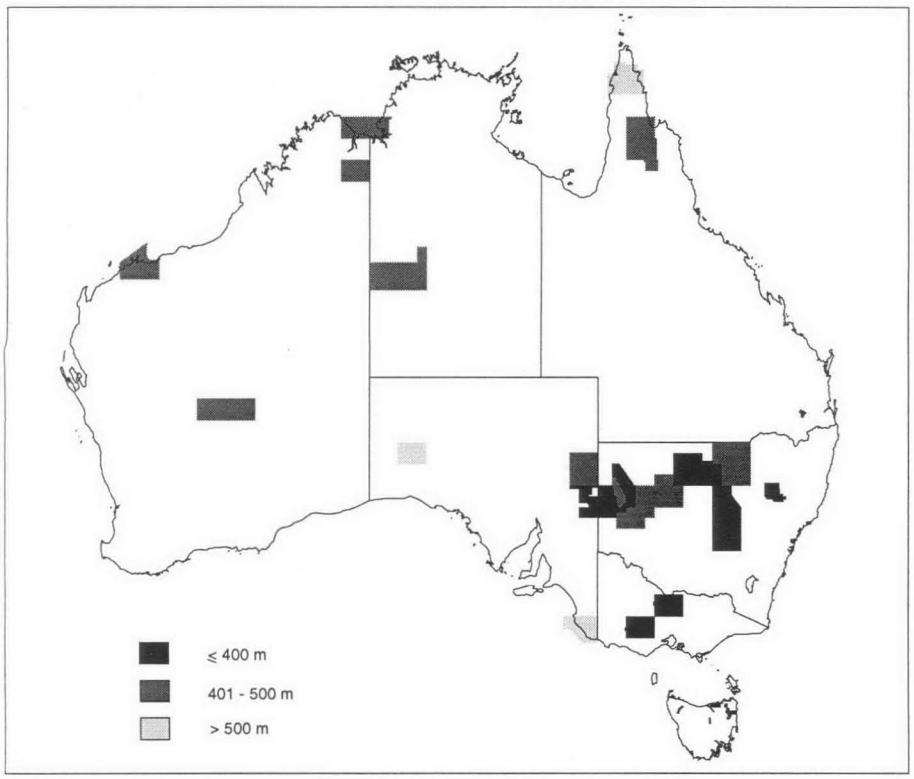

Figure 5. Coverage of Australia by digital elevation models derived from airborne geophysical surveys—line spacing.

The four grey-scale images (Fig. 6 e–h) further illustrate the concept and show how manipulations of data require close line spacing. Grid data used to generate these images have been reduced to the geomagnetic pole and the first vertical derivative calculated. This is a technique which emphasises high frequencies, and with the addition of a sun angle (from the west for these images) is capable of revealing very subtle information in the data. This technique is frequently used in exploration and geological mapping. For detailed mapping, these images illustrate that data from the 400 m line spacing break down under the first vertical derivative, and that even the 200 m line-spaced data do not give full resolution. 100 m line-spaced data are required for the first vertical derivative transformation in this instance.

Recent experience in using airborne magnetic data in regional geological mapping, such as described above, and analysis of large areas of airborne magnetic data acquired at 400/500 m flight-line spacing vis à vis 800 m and 1500/1600 m spacing, indicate that 400 m is the acceptable standard for regional airborne surveys (see Fig. 4 and later).

As with magnetic data, reassessment of data coverage has redefined what is an acceptable standard for coverage of gamma-ray data. At present, to be acceptable, gamma-ray data from areas of hard-rock outcrop should be acquired with 400/500 m flight-line spacing. In other areas, spacing of 1600 m may be acceptable, but closer is desirable, and mandatory in many instances.

Flying height

Figures 7 and 8 show the flying height of data coverage over Australia for magnetic and gamma-ray surveys. Most regional airborne geophysical data over Australia have been acquired on surveys flown at a nominal constant terrain clearance. Some early surveys in hydrocarbon-related projects and surveys in very mountainous areas maintained a constant height above sea-level. These surveys could have a large range of terrain clearance.

Most coverage of magnetic and gamma-ray data is at 150 m flying height, and is generally from surveys conducted before 1989. Specifications set at the start of the National Geoscience Mapping Accord (NGMA) require a flying height of 100 m. In some areas of Australia this has been lowered in practice to enable a better match with surveys organised by States or to enable the data to better solve specific geological problems. In general, exploration surveys have been flown at a lower height than surveys for regional geological mapping.

Accuracy of data

The data in the national geophysical databases show there has been a large range of instrumentation and survey specifications used over the years of acquisition. Changes have resulted from the quest for improvement in data quality and efficiency of acquisition and processing. Some of the major changes that have occurred and their effect on data quality are given in Table 2.

Data in the databases have been generated by a large range of instrumentation, as illustrated in the Appendix, which provides details of the acquisition systems employed by AGSO since 1951.

Magnetic data acquired by AGSO since 1975 have had the International Geomagnetic Reference Field (IGRF) for the appropriate year removed. Data from some earlier AGSO surveys also had the IGRF removed, but, for many surveys, an arbitrary regional was removed, which was not always documented.

Table 2. AGSO airborne survey instrumentation and specifications, 1951–1996.

Years	Navigation and flight path recovery	*Effect on data quality*
1951–1980	Photographs alone	Overall improvement in accuracy of locations—accuracies range from
1971–1991	Photographs and Doppler	200 m to better than 5 m.
1955–1965	Early radio-navigation (e.g. requiring flying in arcs)	Departures from the desired track range from over 2 km to less than
1980–1992	Later radio-navigation	20 m.
1988–	GPS, differential GPS (and real-time differential GPS navigation)	
	Magnetometry	
1951–1983	Fluxgate magnetometers	Reduction in rates of drift:
1963–1989	Proton precession magnetometers	up to 50 nT/hr for fluxgates (particularly in early stages of a flight);
1985–	Alkali-vapour magnetometers	almost zero for proton precession and alkali vapour.
		More accurate digital recording—proton precession and alkali vapour.
		Changes in noise level of magnetometers: fluxgate, 0.1–0.5 nT; proton precession, 5 nT (very early magnetometers)–0.1 nT; alkali vapour, 0.1 nT–better than 0.01 nT. Changes in sample interval: fluxgate, continuous analogue recording, records digitised usually at 1 s intervals; proton precession, 0.2–1 s (60–70 m at normal survey speeds)—note that noise level increased as the sample interval decreased for any instrument; alkali vapour, 0.1–0.3 s (6–7 m to 18–21 m at normal survey speeds).
	Gamma-ray spectrometry	
1952–1968	Scintillometers	Increase of channels from 1 (i.e. total count) to 256—note that some
1969–	Spectrometers	spectrometers have 1024 channels.
	Size of crystals	
1952–1981	0.4–< 17 L	Decrease in noise of acquired data.
1979–1991	17 L	Approximate decrease in relative noise by 1.4 when crystal size is doubled.
1985–	33 L	
1984–	Removal of effects of atmospheric radon by use of upward-looking crystals	
1989–	by analysis of the spectrum	Improvement in quality and integrity of processed gamma-ray data.
	Data acquisition systems	
1951–1974	Analogue recording and processing systems	
1968–	Digital recording and processing systems	Enables better processing of digital data.

Datums

Following recommendations by the Intergovernmental Committee on Surveying and Mapping (ICSM) in 1994 that the Australian geodetic reference system should be based on a geocentric datum, airborne geophysical data since October 1994 have been located using the WGS84 datum. At present, these data sets are the only ones in the national airborne geophysical databases using this datum.

Most location data older than 1966 are referenced to the Clarke 1858 ellipsoid. The Australian Geodetic Datum was adopted in 1965 as the official datum for Australia. However, for some surveys conducted after 1965, the maps used for flight-path recovery were still in the previous datum and, thus, the geophysical data were still referenced to the earlier datum.

Fluxgate magnetometers provide field values to an arbitrary datum. Proton precession and alkali-vapour magnetometers give absolute readings of the magnetic field. AGSO data recorded with these instruments have had 5000 nT added following removal of the IGRF. This is not usually the case for data acquired from other sources

The height datum used in the digital elevation models is the Australian Height Datum (AHD)

Contents of database

The data holdings in the national airborne geophysical databases consist of analogue and digital data and include original material gathered in the field as well as processed data.

Digital data

The digital data are stored in survey units. For ease of access and indexing, most AGSO surveys correspond to regular areas, such as one or more full 1:250 000 Sheet areas or 1:100 000 Sheet areas. Three sets of digital data are normally archived:

- raw field data,
- checked and edited (but otherwise unprocessed) data, and
- final, processed data—both point-located and gridded data.

Three copies of each set are archived: one copy is kept at AGSO, two are stored off-site.

Until 1994, all digital data were archived on archive-quality 9-track magnetic tapes. Because of the large volumes of data being generated from recent surveys (0.1 s sampling intervals for magnetic data, 256 channels of gamma-ray data recorded each second), compared to the capacity of a 9-track tape, since 1994 data have been archived on 5 Gb Exabyte tapes, using two different brands per set. A fourth copy of the processed digital data is now also archived on magneto-optical

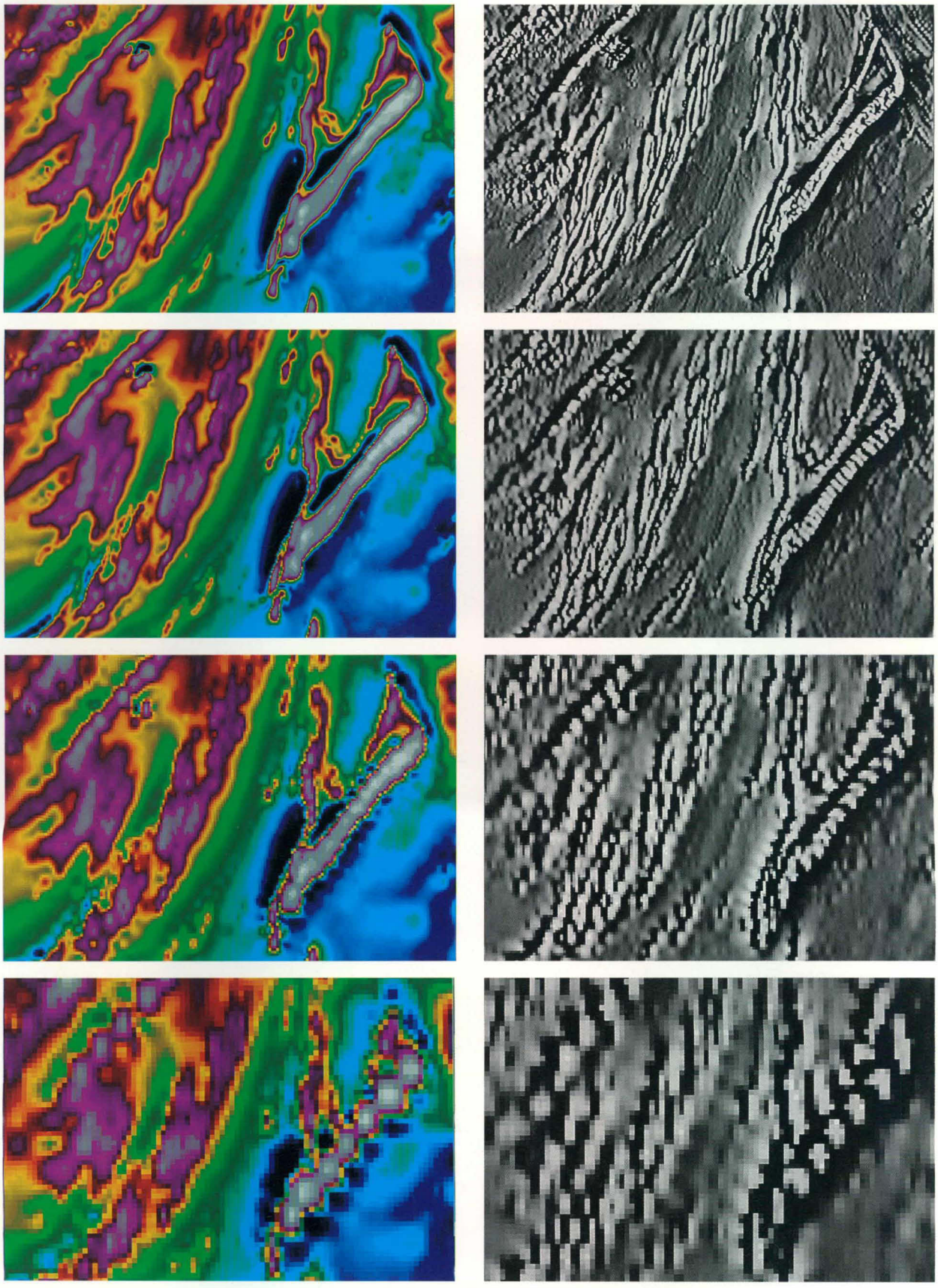

Figure 6. Effect of line spacing on resolution of airborne magnetic surveys. From top to bottom, left-hand column—total magnetic intensity: (a) 100 m, (b) 200 m, (c) 400 m, (d) 800 m; right-hand column—first vertical derivative: (e) 100 m, (f) 200 m, (g) 400 m, (n) 800 m. Survey flown 60 m above ground level.

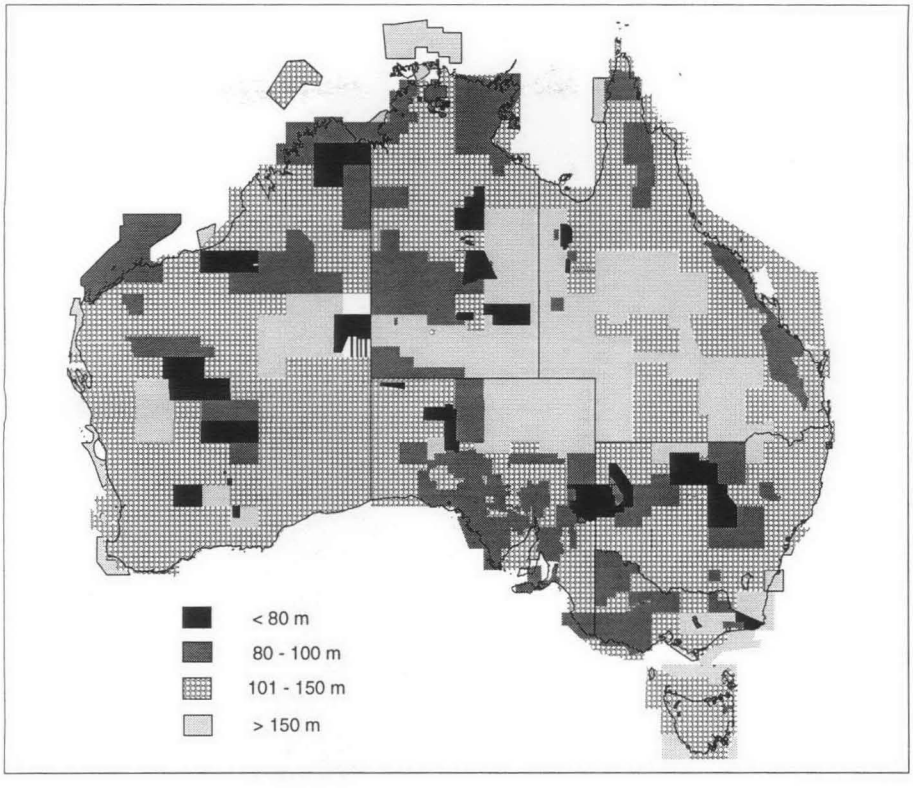

Figure 7. Flying height—magnetic data.

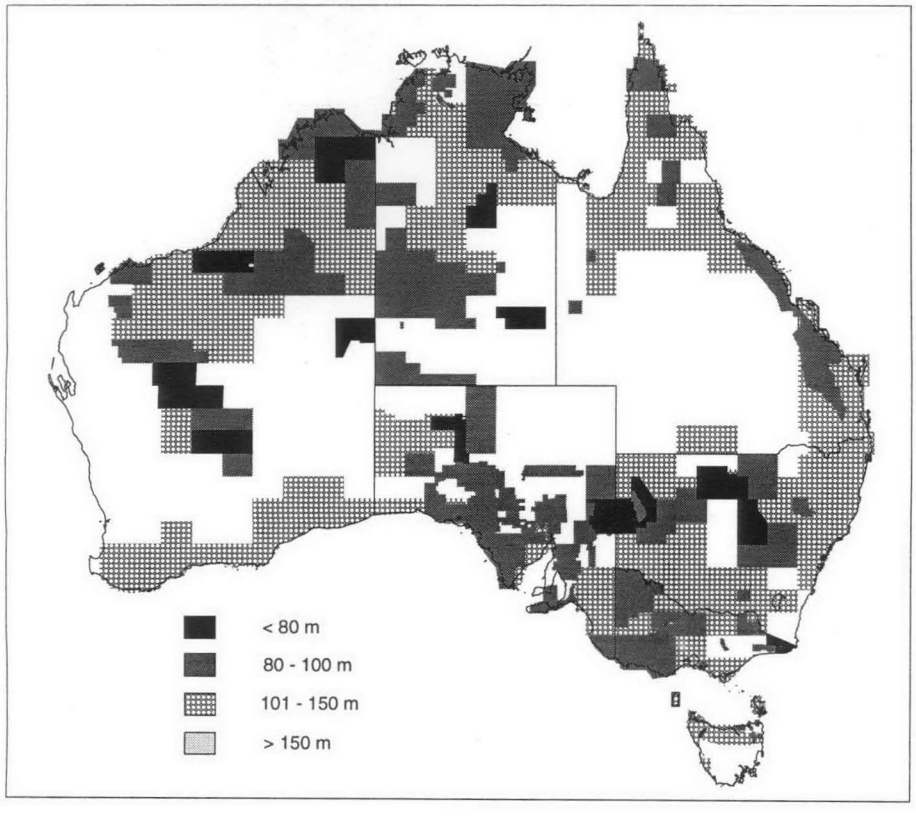

Figure 8. Flying height—gamma-ray data.

disk to facilitate copying for distribution. In 1996, archiving commenced on CD-ROM.

Analogue data

For surveys using analogue data acquisition, the original data and their presentation are archived. For surveys using digital data acquisition, any analogue charts and material which duplicate digital information are temporarily archived for a minimum of two years after processing and public release of the final data.

Original survey data which are archived include:

- analogue charts of magnetic data,
- four-channel gamma-ray data,
- radio-altimeter observations,
- survey documentation, such as information on calibrations, test flights and flight logs.

For surveys carried out before digital recording of magnetic base-station data, the base-station charts are archived. For surveys in which flight-path recovery was calculated using photographs, the final material in the flight-path recovery process, such as base maps and compilation maps, has been archived. Video film is temporarily archived for at least two years after release of the final processed geophysical data.

All presentations of publicly released data are archived. These include contour, profile, and flight-path maps, and pixel image maps.

Product availability

A wide range of products is made available to the public from the national airborne geophysical databases. Most data are available at a low cost from AGSO. Data owned solely by State governments are obtainable from the particular State department. A small number of data are available from airborne survey operators for a fixed period before being available from AGSO. A very small number of data in the databases have been supplied to AGSO on condition that they are not released to the public or that public release only occurs after a specified date.

Digital data

Point-located (profile) digital data and gridded digital data are available.

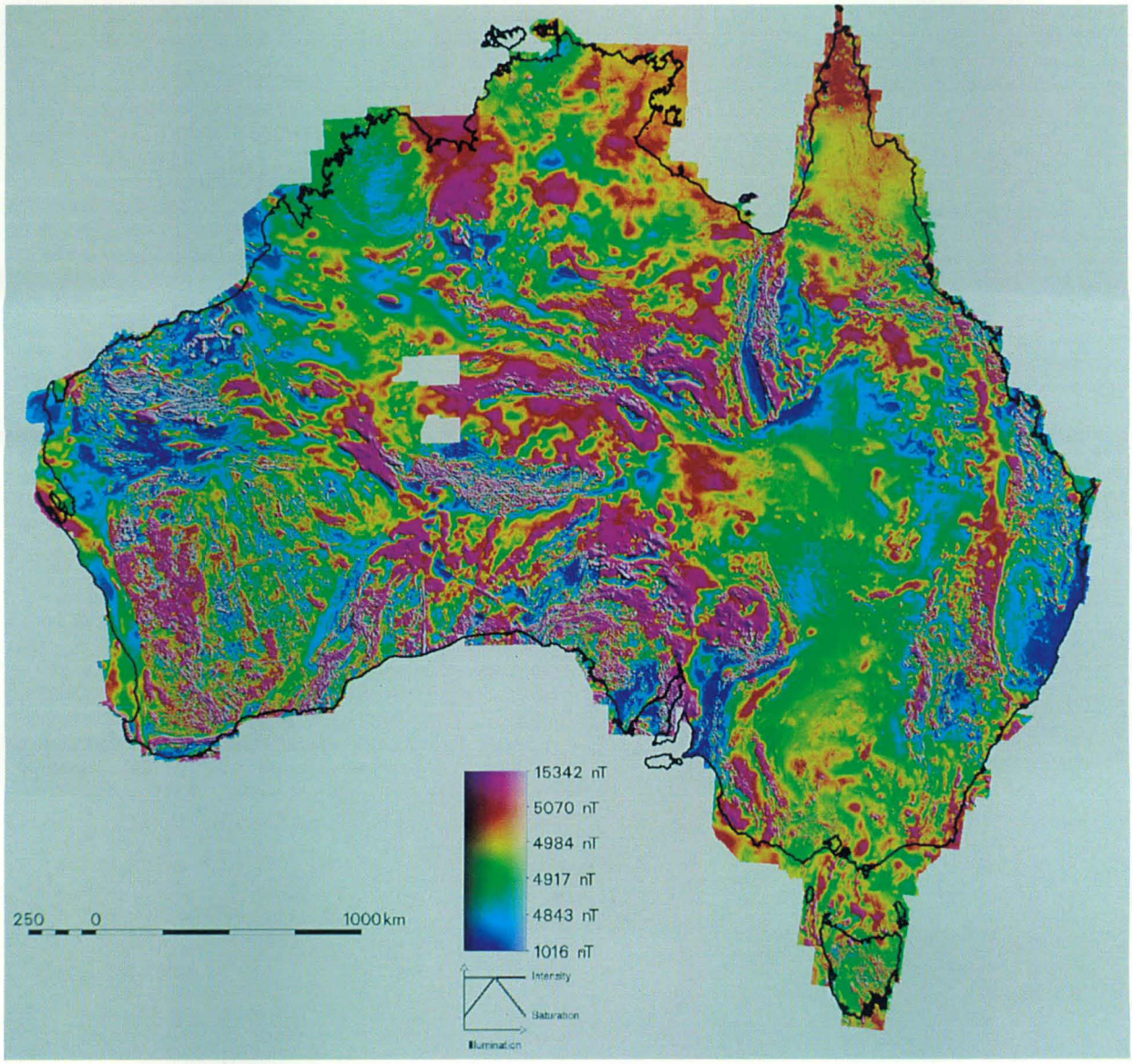

Figure 9. Magnetic anomaly map of Australia.

The point-located magnetic and gamma-ray data for surveys with flight-line spacing of 1500 m or more are available in units of 1:250 000 Sheet areas. For surveys with flight lines of 500 m or less, they are available in units of 7.5′ x 7.5′ for 1:25 000 Sheet areas.

The gridded magnetic data for surveys with flight-line spacing of 1500 m or more are included in compilations of 1:1 000 000 Sheet areas, which are released as part of the Magnetic Map of Australia grid. For surveys with flight lines of 500 m or less, magnetic and gamma-ray data are available in units of 1:100 000 Sheet areas. For some surveys with flight-line spacing of 200 m, grids are also available in units of 1:50 000 Sheet areas. Grids of magnetic and gamma-ray data are available for parts of the Broken Hill area in 15′ x 7.5′ units.

Digital elevation data are available in units of 1:250 000 Sheet areas. For data acquired on flight lines with 100 m spacing, they are available in units of 1:100 000 Sheet areas.

Analogue data

For surveys with flight-line spacings of 1500 m or more, the following basic maps at 1:250 000 are available:

- magnetic data—contours and profiles of residual total magnetic intensity;
- gamma-ray data—contours of total-count channel; profiles of potassium, uranium, thorium, and total-count channels;
- radio-altimeter—profiles;
- flight line map.

For semi-detailed surveys acquired after 1989, the following basic magnetic and gamma-ray maps are available:

1:250 000	*1:100 000*
contours of total magnetic intensity	contours of total magnetic intensity
contours of total-count channel	contours of total-count channel
	profiles of total magnetic intensity
	flight-line map.

For data at 200 m flight-line spacing, the abovementioned maps at 1:100 000 are also available at 1:50 000. For data at 100 m flight-line spacing, the maps are also available at 1:25 000.

Contour maps of digital elevation models are available at

1:250 000 and 1:100 000, depending on the flight-line spacing.

Pixel image maps are available for most data sets acquired after 1989 at flight-line spacings of 500 m or less. They are:

- colour and greyscale magnetic,
- colour gamma-ray composite, and
- colour or greyscale digital elevation model.

These are at 1:250 000 except when the data have been acquired on 100 m flight-line spacing, when they are at 1:100 000.

Compilations at various scales are also available.

Magnetic map of Australia

Several magnetic maps of Australia have been issued by AGSO. The first, which included offshore as well as onshore areas, was released in 1976 as a 1:2 500 000 scale map and a 2 km grid (BMR 1976). A compilation of photo-reduced contour maps from onshore Australia was released in 1984 (Tucker & Hone 1984). Tarlowski et al. (1993) made a major advance in presentation and resolution when they released colour pixel image maps at 1:5 000 000, 1:10 000 000, and 1:25 000 000, which accompanied a grid with 400 m cell size. The second edition map (Fig. 9) and associated grid,which was released in 1996, has additional data and additional processing (Tarlowski et al., 1996).

The magnetic maps of Australia provide a good summary of the status of acquisition of magnetic data over Australia. Because the largest scale of the latest map is 1:5 000 000, the benefits of the 400/500 m flight-line surveys are not shown as well as they would be in larger scale presentations. However, the lack of detail in areas of substandard data at first pass reconnaissance standard is indicated even at the 1:5 000 000 scale.

Conclusions

The national airborne geophysical databases provide data over most of onshore Australia and parts of offshore Australia. Although 99 per cent of onshore Australia is covered by aeromagnetic data, there are substantial areas where the data quality needs upgrading. Offshore, large areas are deficient of data.

The early definitions of standard and substandard data were strongly controlled by a desire to achieve airborne magnetic coverage over all of onshore Australia as soon as possible. Later thinking on what should be considered as the standard for continent-wide coverage has changed for the following reasons:

- first pass coverage is almost complete,
- increasing importance of airborne geophysics in mapping and exploration, and
- increasing demands on quality of data by post-processing, analysis and interpretation.

Over the last ten years, enormous advances have been made in the quality of data, and improvements will continue. Accordingly, as the data age, they become further removed from the latest quality standards. Also, the older data are, the more they are used and more of the information they contain is extracted, until no significantly new information remains to be extracted. However, new data acquired later and of a better quality will reveal new information useful for mapping, exploration, and other purposes. Data more than twenty years old can usually be significantly upgraded, and can be thought of as previous generation. Constant replenishment of the databases is required so that geological mapping and knowledge are upgraded, new mineral discoveries made, and other applications to which the data can be put are more effective.

To ensure that onshore Australia, which occupies the equivalent of about 470 standard 1:250 000 map sheet areas, is covered by data less than twenty years old ('present generation'), new data will have to be acquired at the rate of more than twenty sheet areas a year. The present state of technology demands that flight-line spacing must be 400–500 m for data coverage to be considered satisfactory. This and the other criteria for acceptable standards will become tighter with time. Recent initiatives by State governments have provided an increase in data acquisition in the short term. However long-term programs of data acquisition must be continued to enable a supply of new data to the latest standards.

References

BMR, 1976. Magnetic map of Australia. Residuals of total intensity 1:2 500 000 scale. Bureau of Mineral Resources, Canberra.

Tarlowski, C., Milligan, P. & Simonis, F., 1993. Magnetic anomaly map of Australia, scale 1:5 000 000. Australian Geological Survey Organisation, Canberra.

Tarlowski, C., Milligan, P. & Simonis, F., 1993. Magnetic anomaly map of Australia, scale 1:10 000 000. Australian Geological Survey Organisation, Canberra.

Tarlowski, C., Milligan, P. & Simonis, F., 1993. Magnetic anomaly map of Australia, scale 1:25 000 000. Australian Geological Survey Organisation, Canberra.

Tarlowski, C.Z., McEwin, A., Reeves, C.R. & Barton, C.E, 1996. De-warping the composite aeromagnetic anomaly map of Australia using control traverses and base stations. Geophysics, 61, 696–705.

Tucker, D.H. & Hone, I.G, 1984. Magnetic map of onshore Australia. Contours of residuals of total intensity, BMR airborne database 1984. 1:2 500 000 scale. Bureau of Mineral Resources, Canberra.

Tucker, D.H., Hone, I.G., Downie, D.N., Luyendyk, A.P.J., Horsfall, K.R. & Anfiloff, V., 1988. Aeromagnetic regional survey of onshore Australia. Geophysics, 53(2), 254–265.

Appendix: Summary of AGSO airborne systems used for airborne geophysical surveys

(Modified from Tucker et al 1988)

Year	*Aircraft*	*Magnetometer*	*Gamma-ray instrumentation*		*Recording*	*Aircraft*	*Magnetometer*	*Gamma*	*Recording*	
		(B) Bird (S) Stinger	Crystal volume (litres)	Channels	(A) Analogue (D) Digital		(B) Bird (S) Stinger	Crystal volume (litres)	Channels	
1951	DC3 VH-BUR	Flux AN-ASQ-1 (S)	–	–	A					
1952	DC3 VH-BUR	Flux AN-ASQ-1 (S)	0.4	1	A					
1953	DC3 VH-BUR	Flux AN-ASQ-1 (S)	0.4	1	A					
1954	DC3 VH-BUR	Flux AN-ASQ-1 (S)	0 4	1	A	DC3 VH-MIN		0.4	1	A
1955	DC3 VH-BUR	Flux AN-ASQ-1 (S)	0.4	1	A	DC3 VH-MIN		0.4	1	A
1956	DC3 VH-BUR	Flux AN-ASQ-1 (S)	0.4	1	A	DC3 VH-MIN	Flux AN-ASQ-1 (S)	0 4	1	A
1957	DC3 VH-BUR	Flux AN-ASQ-1 (S)	0.4	1	A	DC3 VH-MIN	Flux AN-ASQ-1 (S)	0.4	1	A
1958	DC3 VH-BUR	Flux AN-ASQ-8 (S)	0 4 (I), 1.2 (O)	1	A	DC3 VH-MIN	Flux AN-ASQ-1 (S)	0.4	1	A
1959	Aircraft sold					DC3 VH-MIN	Flux AN-ASQ-8 (S)	0 4 (I); 1.2 (O)	1	A
1960	Cessna 180 VH-GEO	–	0 5	1	A	DC3 VH-MIN	Flux AN-ASQ-8 (S)	0 4 (I), 1.2 (O)	1	A/PT
1961	Cessna 180 VH-GEO	–	0.5	1	A	DC3 VH-MIN	Fluxgate MFS4 (S)	0 4 (I), 1.2 (O)	1	A/PT
1962	Cessna 180 VH-GEO	–	0.5	1	A	DC3 VH-MIN	Fluxgate MFS5 (S)	0 4 (I), 1 2 (O)	1	A/PT
1963	Cessna 180 VH-GEO	Proton MNS1 (B)	–	–	A	DC3 VH-MIN	Fluxgate MFS5 (S)	0.4 (I), 1 2 (O)	1	A/PT
1964	Cessna 180 VH-GEO	Proton MNS1 (B)	–	–	A	DC3 VH-MIN	Fluxgate MFS5 (S)	0 4 (I); 1.2 (O)	1	A/PT
1965	Cessna 180 VH-GEO	Proton MNS1 (B)	–	–	A	DC3 VH-MIN	Fluxgate MFS5 (S)	0 4 (I); 1 2 (O)	1	A/PT
1966	Cessna 180 VH-GEO	Proton MNS1 (B)	–	–	A	DC3 VH-MIN	Fluxgate MFS5 (S)	0.4 (I), 1.2 (O)	1	A/PT
1967	Cessna 180 VH-GEO	Proton MNS1 (B)	0.5	–	A	DC3 VH-MIN	Fluxgate MFS5 (S)	0 4 (I); 1.2 (O)	1	A/PT
1968	Aircraft sold	Proton MNS1 (B)	–	–	A	DC3 VH-MIN	Fluxgate MFS5 (S)	0 4 (I); 1 2 (O)	1	A/PT
1969	Aero Commander VH-BMR	Proton MNS1 (B)	3.7	4**	A	DC3 VH-MIN	Fluxgate MFS5 (S)	3.7	2*	A/PT
1970	Aero Commander VH-BMR	Proton MNS1 (B)	3 7	4**	A	DC3 VH-MIN	Fluxgate MFS5 (S)	3 7	2*	A/PT
1971	Aero Commander VH-BMR	Proton MNS1 (B)	3.7	4**	A	Twin Otter VH-BMG	Fluxgate MFS7 (S)	3.7	4**	D
1972	Aero Commander VH-BMR	Proton MNS2 (B)	3.7	4**	A	Twin Otter VH-BMG	Fluxgate MFS7 (S)	3.7	4**	D
1973	Aero Commander VH-BMR	Proton MNS2 (B)	3.7	4**	A	Twin Otter VH-BMG	Fluxgate MFS7 (S)	3.7	4**	D
1974	Aero Commander VH-BMR	Proton MNS2 (B)	3 7	4**	A	Twin Otter VH-BMG	Fluxgate MFS7 (S)	3.7	4**	D
1975	Aero Commander VH-BMR	Fluxgate MFS7 (S)	7.4	4**	D	Twin Otter VH-BMG	Fluxgate MFS7 (S)	3.7	4**	D
1976	Aero Commander VH-BMR	Fluxgate MFS7 (S)	5.5	4**	D	Twin Otter VH-BMG	Fluxgate MFS7 (S)	5 5	4**	D
1977	Aero Commander VH-BMR	Fluxgate MFS7 (S)	5.5	4**	D	Twin Otter VH-BMG	Fluxgate MFS7 (S)	5.5	4**	D
1978	Aero Commander VH-BMR	Proton G803 (S)	5.5	4**	D	Twin Otter VH-BMG	Fluxgate MFS7 (S)	5.5	4**	D

Year	*Aircraft*	*Magnetometer*	*Gamma*		*Recording*	*Aircraft*	*Magnetometer*	*Gamma*		*Recording*
1979	Aero Commander VH-BMR	Proton G803 (S)	5.5	4**	D	Twin Otter VH-BMG	Fluxgate MFS7 (S)	16.8	4**	D
1980	Aero Commander VH-BMR	Proton G803 (S)	5.5	4**	D	Twin Otter VH-BMG	Fluxgate MFS7 (S)	16.8	4**	D
1981	Aero Commander VH-BMR	Proton G803 (S)	7.4	4**	D	Twin Otter VH-BMG	Fluxgate MFS7 (S)	16.8	4**	D
1982	Aero Commander VH-BMR	Proton G803 (S)	16.8	4***	D	Twin Otter VH-BMG	Fluxgate MFS7 (S)	16.8	4***	D
1983	Aero Commander VH-BMR	Proton G803 (S)	16.8	4***	D	Twin Otter VH-BMG	Fluxgate MFS7 (S)	16.8	4***	D
1984	Aero Commander VH-BMR	Proton G813 (S)	16.8 (D) 4.2 (U)	4***	D	Twin Otter VH-BMG	Proton G803	16.8 (D) 4.2 (U)	4***	D
1985	Aero Commander VH-BMR	Proton G813 (S)	16.8 (D) 4.2 (U)	4***	D	Twin Otter VH-BMG	Proton G803	16.8 (D) 4.2 (U)	4***	D
1986	Aero Commander VH-BMR	Proton G813 (S)	16.8 (D) 4.2 (U)	4***	D	Twin Otter VH-BMG	Proton G803	16.8 (D) 4 2 (U)	4***	D
1987	Aero Commander VH-BMR	Proton G813 (S)	16.8 (D) 4.2 (U)	4***	D					
1988	Aero Commander VH-BMR	Proton G813 (S)	16 8 (D) 4.2 (U)	4***	D					
1989	Aero Commander VH-BMR	Proton G813 (S)	16.8 (D) 4.2 (U)	4***	D					
1990	Aero Commander VH-BGE	Helium G833 (S)	33 6 (D) 8.4 (U)	4***	D					
1991	Aero Commander VH-BGE	Helium G833 (S)	33.6	4***	D					
1992	Aero Commander VH-BGE	Helium G833 (S)	33.6	4***	D					
1993	Aero Commander VH-BGE	Helium G833 (S)	33.6	256	D					
1994	Aero Commander VH-BGE	Helium G833 (S)	33.6	256	D					
1995	Aero Commander VH-BGE	Helium G833 (S)	33.6	256	D					
1996	Aero Commander VH-BGE	Helium G833 (S)	33 6	256	D					

* 0 2–3.0 MeV and 1.6–3.0 MeV

** 0 84–3.0, 1.3–1.6, 1.6–1.9, 2.4–2.8 MeV

*** 0.4–3.0, 1.35–1 57, 1.63–1.89, 2.42–2.82 MeV

AGSO Journal of Australian Geology & Geophysics, 17(2), 23–30

Airborne magnetic and gamma-ray data acquisition

K.R. Horsfall[1]

Current aeromagnetic data acquisition has benefited from improvements in measurement precision and compensation systems for removing the magnetic effects of survey aircraft. GPS positioning enables flying with closer line spacing than previously, and this has stimulated a demand for lower survey altitudes with flight heights of the order of 60–80 m now common. Radiometric recording of 256 channels of gamma-ray data is now virtually standard and in-flight stabilisation of these systems has improved markedly. Digital acquisition systems are now designed to facilitate both in-flight and post-flight verification of the data.

Introduction

The first airborne magnetic survey in Australia was flown in 1947 by Oscar Weiss, Consulting Geophysicist (Doyle 1987). Four years later, in 1951, systematic airborne geophysical surveys were begun by the Bureau of Mineral Resources, Geology and Geophysics (BMR), the predecessor of the current Australian Geological Survey Organisation (AGSO). Since then there has been an ongoing program of acquisition of airborne magnetic and gamma-ray data by government agencies to assist the State and Commonwealth Governments and the wider community in developing strategies for resource development and environmental management. Airborne surveys are also used extensively by private companies for a variety of more specific mapping purposes, such as mineral and hydrocarbon exploration.

This document briefly outlines the history of the acquisition equipment used in the earlier surveys and details the current state-of-the-art technology and methodology used in airborne magnetic and gamma-ray surveys.

Figure 1. The AGSO Aero Commander survey aircraft.

Methodology

Airborne survey design

Airborne surveys are normally flown along a series of equally spaced parallel flight lines. For general reconnaissance mapping purposes the flight line direction is usually oriented north–south or east–west, depending on the predominant strike of the known geology. For more specific surveys, such as the definition of mineral exploration targets, the flight-line direction will be oriented across strike to maximise the magnetic signature.

To level the data to a common base level and to assist in removing any errors in the data a set of tie lines is flown at right angles to the main set of flight lines. Further information on tie-line levelling is given by Luyendyk (1997). In general the tie-line spacing is set at a ratio of 10 x flight-line spacing (i.e. for a survey with a flight-line spacing of 1 km, the tie-line spacing would be 10 km). However, for some petroleum exploration surveys, where tighter control is required, the ratio may be as low as 3.

Line spacing. Flight-line spacing is determined by the degree of detail required in the final mapping or the size of exploration target. It is also limited by the financial resources available for the survey. In the past, 3000 m was considered adequate for surveys over sedimentary basins. This generally defined the broad magnetic basement and formed a basis for further seismic exploration. With the availability of more sensitive magnetometers, there has been greater interest in the more subtle magnetic features which may be present in the sedimentary section above basement, and surveys over sedimentary basins are now commonly flown with line spacing of the order of 500 m.

Reconnaissance surveying in hard-rock areas was previously limited to flight-line spacing of 1500 m. This provided generalised details of magnetic features and was considered adequate for mapping at a scale of 1:250 000. Much of Australia is covered by surveys flown at this flight-line spacing.

More recently, there has been emphasis on providing geophysical data sets to underpin semi-detailed geological mapping at 1:100 000 scale. To support this new generation mapping over hard-rock areas, airborne surveys are flown routinely at line spacings of 400–500 m and in some areas, where even greater detail is required, flight-line spacing is reduced to 200 m.

Surveys flown specifically for mineral exploration have line spacing usually less than 200 m and maybe as close as 50 m.

Survey flying height. The magnetic field decreases approximately as the inverse of the square of the distance from the magnetic source, and the gamma-ray signal from radioactive sources decreases exponentially with distance, owing to attenuation of gamma-rays in the air column. Therefore, to record small variations in these fields, surveys must be flown close to the ground.

The first reconnaissance surveys were generally flown at a constant ground clearance of 150 m. More recently, a flying height of 100 m has been adopted for surveys with 400 m line spacing. Surveys with 200 m line spacing are typically flown 80 m above ground, while surveys with 100 m line spacing may be flown at 60 m above ground. Flying height has a bearing on the strip of terrain sampled by the spectrometer on each flight line. For example, at a height of 60 m, 75 per cent of the counts recorded from the ground are produced from a strip 240 m wide; whereas at 100 m flying height, the same percentage of counts originates from a strip 300 m wide. The counts recorded for each one second sample period are all the counts received from a strip on the ground, the width of which depends on flying height and the length, on flying height and aircraft speed over the ground. Flying heights and

[1] Australian Geological Survey Organisation, GPO Box 378, Canberra, ACT 2601

line spacings given above result in a good compromise between overall coverage and sensitivity to point sources.

Owing to terrain, safety and government restrictions it is not always possible to fly surveys at the ideal height. Aircraft performance is the main factor in maintaining constant ground clearance, and in undulating to mountainous terrain it is preferable for surveys to be flown by helicopter rather than fixed-wing aircraft. However, the cost of helicopter surveys often precludes this option.

Survey aircraft. Equipment for airborne geophysical surveys has reduced physically to the point where it can be fitted into small fixed-wing aircraft and helicopters. Normally, all the electronic equipment, except sensors, can fit into one standard rack.

Ideally, the aircraft for airborne magnetic and gamma-ray surveys should have the following features:

- Efficient operating speed of less than 250 km/h.
- Twin engines for perceived added safety.
- Preferably, piston engines for economical, low-altitude operations.
- High-wings for better visibility and stability at low speeds.
- Endurance, with full operational load (250 kg of equipment plus operator), of at least 6 hours, plus reserve.
- Short take-off and landing (STOL) performance with good angle of climb, and safe single engine performance.

In the past, a variety of fixed-wing aircraft has been used used for airborne geophysical surveying in Australia. At present, the most common, and currently used by AGSO for its airborne survey operations, is the Aero Commander (Fig. 1). This aircraft is a compromise between good endurance and economical operation, but has fairly poor climb performance. Other aircraft which are or have been used are the Cessna 206, Cessna 210, Cessna 404 and Cessna Caravan, Douglas DC3, Twin Otter, Nomad, and Britten Norman Islander.

In rugged terrain where it is not possible to use a fixed-wing aircraft helicopters are used. The most common of these are the Jet Ranger 206 and Squirrel. For surveys requiring magnetometer data only, the small Bell 47 helicopters are sometimes used.

Data acquisition systems

The basic function of any data acquisition system (DAS) for airborne geophysical surveying is to digitally record all geophysical, navigation, altitude, temperature and pressure data.

Computer hardware and software

Acquisition systems are normally based on a personal computer with proprietary software written in a high-level language such as C. Some systems are basically data loggers and rely on peripheral equipment to provide navigation information for the aircraft guidance, while others are more complete and perform much of the data checking, navigation, and graphics displays in the central computer.

Time synchronisation

Sampling of all geophysical and navigation equipment must be synchronised by a master timer. These days, the aircraft global positioning system (GPS) provides very accurate time, which is synchronised with the geophysical data and recorded on the data acquisition system. Accurate time synchronisation is essential for removal of the daily magnetic variations recorded at the magnetic base station.

Graphics

Most airborne acquisition systems incorporate a real-time display of outputs from geophysical and navigation instruments. The display is commonly in the form of analog records of the magnetometer, 4 channels of the gamma-ray spectrometer, ground clearance from the radar altimeter, and along-track and across-track positioning data. Industry uses a variety of graphics devices, ranging from sophisticated computer-controlled recorders to simple graphics printers.

There is a trend for some operators to dispense with hard-copy displays in the aircraft and rely on screen displays of data. Hard copies, which simulate analog records from an aircraft, may be produced post-flight from a plotter in the field survey office. Dispensing with the aircraft recorder has a weight saving benefit, which may be significant in a small aircraft or helicopter.

Flight-path tracking camera

Flight-path tracking cameras (either 35 mm or video) were an essential part of all airborne geophysical survey systems prior to the introduction of radio navigation, and more recently GPS, for survey aircraft navigation and flight-path recovery. The cameras were time synchronised to the geophysical data via the timer and used to accurately position the geophysical data with respect to the ground. Some survey aircraft were also fitted with Doppler navigation systems which were used to provide infill navigation information between the ground fixes provided from the camera. With the universal use of GPS navigation there is no need to visually recover the flight path of the aircraft and the camera flight-path tracking function is secondary. The flight path is now recorded on video and is only used to check for cultural effects which may be reflected in the geophysical data and to plot the start and ends of spectrometer test lines. The video is also used to check the accuracy of navigation and system parallax. A typical flight-path recording system consists of a colour video camera, video cassette recorder, and liquid crystal display monitor.

Data recording

Recording of the geophysical and navigation data in digital form is accomplished on various media—internal fixed hard disks, portable hard disks, floppy disks, cartridge tapes, nine-track tapes and removable hard disks. Data recorded to an internal hard disk is copied to a tape after the flight for transfer to the field or office computer.

Data sampling rates

Survey aircraft are generally flown at 220–280 km/h. The Aero Commanders, by far the most common survey aircraft in Australia, are flown at about 240 km/hr (67 m/s). Some of the smaller single-engine aircraft, and STOL aircraft (Twin Otter, Nomad) are able to fly at the slower speeds. The flying speed of the survey platform is not so critical now, because airborne magnetometers are capable of fast sampling and gamma-ray spectrometers use large volume crystal detectors, which increase count rates and improve counting statistics.

All modern magnetometers are capable of being sampled 10 times per second and this equates to 'pixels' of 6–8 m on the ground. In general, spectrometer systems are sampled every 1 s, which is a compromise between longer sampling time, with a larger number of counts, and the ability to define smaller sources. The sampling time of 1 s equates to a 60–80 m 'pixel' on the ground. Navigation and ground clearance data (radar altimeter), temperature and atmospheric pressure are sampled every 1 s.

Current commercial DAS

Two commercial DAS are readily available.

Picodas PDAS 1000. This is an integrated PC-based DAS, which usually incorporates real-time magnetic compensation, gamma-ray spectrometer processing and data logging. Data are usually recorded on the computer's hard disc and backed up onto a removable data tape. An RMS GR33A graphics recorder is normally used to display analog traces for in-flight data checking.

RMS Instruments DAS-8. The DAS-8 system is basically a data-logging device connected to various external devices to handle magnetic compensation, gamma-ray spectrometer processing, and navigation. The data are normally stored on an RMS HDS60 tape cartridge and fixed hard disc with an RMS GR33A graphic recorder used for analog display.

Neither of these systems has any real-time digital data quality-checking capabilities. Data quality is checked mainly through the examination of analog charts; post-flight data are checked by computer.

AGSO DAS

The current AGSO airborne DAS (Fig. 2) has evolved over the last 20 years and is based on Hewlett Packard (HP) A-400 computer hardware, RTE-A operating system with the software written by AGSO personnel in HP Assembler. This has functioned well and has been progressively upgraded to its present standard. It is one of the most flexible systems in use today. Data are recorded on floppy disks and a portable hard disk.

In addition to the basic recording functions, the system developed by AGSO has the additional features of:

- Data checking (spikes, noise, validity) and reporting on all data.
- Pilot navigation information defined by a predetermined flight path.
- Real-time display of all data of interest for operator viewing.

Facilities for the operator to dump data, store spectra, report on the positions of diagnostic spectra peaks, and check the gain of the gamma-ray spectrometer system.

AGSO is currently developing a replacement system, based on PC hardware, using QNX, and a real-time UNIX-like operating system, with software written in C. This will be less expensive, because of the availability of cheap PC hardware, and much easier to maintain. The data will be recorded on a removable hard disc.

Navigation systems

Aircraft navigation systems are vital for high-quality geophysical survey results. They must provide the pilot with information for aircraft guidance along a predetermined flight path, and provide accurate flight-path positioning information to the data acquisition system.

Previous methods

Visual navigation. There have been great advances in airborne survey navigation in the last 10 to 15 years. Previously, most surveys were navigated visually, with the pilot or navigator following a line drawn on an aerial photograph. In many cases, the photography was old and features on the ground bore little resemblance to the image on the photograph. This led to lines being flown in the wrong place, and costly repeat lines. Some aircraft were fitted with Doppler navigation systems, which gave the relative position and aircraft ground speed and drift. The flight path was recovered manually by comparing images recorded on the aircraft's flight-path tracking camera (35 mm strip or video film) with the aerial photographs used for the survey navigation. If Doppler navigation was available, this was used to give flight-path information between the recovered fixes. Errors in the recovered position of the final flight path for reconnaissance scale surveys (1500–3000 m line spacing) plotted onto 1:80 000 scale photography were 50 m or greater, depending on the quality of the base mapping.

Radio navigation systems. Radio navigation systems, such as the Shoran systems developed during World War 2, were quite successfully adapted for airborne geophysical survey aircraft in the early 1960s. However, the ground radio-transmitter equipment was large and required permanent manning with 240 volt or generator power. The aircraft equipment was also large and had to be constantly manually adjusted to provide guidance information to the pilot. Flight-path recovery was by camera photo recovery.

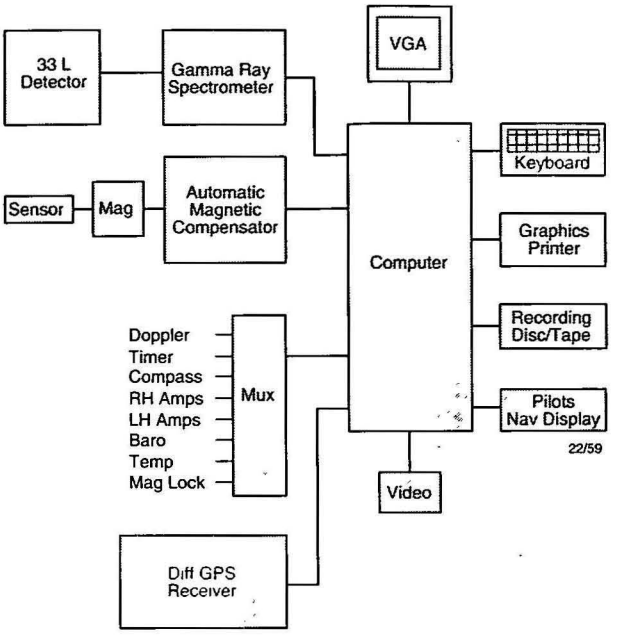

Figure 2. Block diagram of the AGSO digital acquisition system used for airborne surveys.

Survey navigation methods advanced in the 1980s, when modern radio-navigation systems were introduced, providing the accuracy needed to fly detailed surveys. These new systems (eg Syledis, Maxiran) used low-power UHF radio transmitters, which had been primarily designed for marine use. However, they were expensive, and required considerable set up time. Each radio beacon had to be located at a known survey point (trig) and, because the method relied on triangulation to determine position, three beacons had to be always within range of the aircraft's receiver. As UHF transmissions are effectively line-of-sight (about 60 km in ideal conditions), the limited range presented problems in mountainous terrain and over large survey areas. The accuracy of the final positional data relied on the accuracy of the location of the beacon sites and the calibration of the system. However, a well-maintained system established on accurate position sites would provide final positions to within 5 m.

Current methods

Global positioning system (GPS). GPS has become the industry standard for airborne geophysical survey navigation. It uses the US-established GPS satellite network, which comprises 24 NAVSTAR GPS satellites (21 operational and 3 spare) orbiting the Earth every 12 hours at a height of about 20 000 km (Boyd 1992). The exact altitude, position and speed of the satellites are measured precisely as they come into view of the system control and monitoring stations established on Earth. Corrections to the satellite's positional information (ephemeris corrections) and its atomic clock are transmitted to the satellite and incorporated in data messages transmitted by the satellite.

A GPS receiver, taking signals from four satellites, computes its position by triangulation. The position is usually relative to the World Geodetic System (WGS) reference ellipsoid, giving latitude, longitude and height, but numerous different reference ellipsoids have been adopted by individual countries and coordinates of positions may vary by several hundred metres, depending on the reference ellipsoid used. In 1991, the US introduced selective availability (SA), by dithering

ephemeris and satellite clock corrections, and effectively downgraded the positional accuracy available to civilian operators of single GPS receivers from about ±15 m up to ±100 m (for 95% of the time) (Boyd 1992). AGSO's experience has shown that the error is generally less than 50 m. The errors in satellite information, introduced under selective availability, vary with time and prevent any method of correcting for the error using one receiver.

Differential GPS. To overcome the errors in single receiver GPS positioning, differential GPS systems were developed. Differential GPS uses a second GPS receiver, at a fixed reference location, to log the range data to the satellites and determine errors in the range data. Using post-processing software, errors in the range data recorded from satellites common to the base GPS and the airborne GPS can be largely eliminated. The final positional accuracy is better than 5 m.

In practice, the base GPS receiver is set up in the field survey office and, before a survey commences, the position of the base GPS receiver is surveyed from a nearby trig site, using the two GPS receivers in differential mode. One hour GPS records are made simultaneously at several sites. The data are then processed using differential GPS post-processing software, the results averaged, and the base station position is established to within 2–3 m. In the future, when dual frequency GPS receivers are used for airborne survey navigation, the time to survey the base station will be reduced to about 5 minutes, and the error in calculated position will only a few centimetres.

A typical differential GPS navigation system incorporates two identical 12-channel, single-frequency, C/A code navigation receivers, such as the Ashtech 'Ranger' Each receiver computes a position every 0.5 s to an accuracy as discussed earlier and stores the raw satellite range data internally for post processing. Single-frequency GPS receivers perform the task adequately at present; however, in the future, when there is greater emphasis on producing digital elevation models at higher accuracy, superior dual-frequency GPS equipment will be needed to improve the accuracy of the reference height information of the survey aircraft. The main impediment to using dual-frequency GPS at present is the cost of each receiver, which may be $50 000 compared with $30 000 for a single-frequency unit.

GPS navigation may be done in several modes, depending on the survey line spacing.

- ***Post-processed differential GPS.*** For surveys with 400 m line spacing or greater, the pilot's aircraft-guidance information from a stand-alone GPS receiver in the aircraft is acceptable to keep the aircraft within 80 m (or ±20% of the line spacing) of the desired track. The raw GPS data stored by the aircraft receiver and the base receiver are differentially processed after the flight to reduce the error in the actual flight path positioning of the aircraft to less than 5 m.

- ***Real-time differential GPS.*** For more closely spaced survey lines (100 m or 200 m line spacing), where deviations from the desired flight path are more critical, the pilot must have the most accurate information available. This is achieved with real-time differential navigation, which requires corrections to the range data, measured at the GPS base station, to be transmitted to the aircraft to correct errors measured in the aircraft's GPS receiver. UHF radio has been commonly used for this purpose. As UHF is line of site communication (60 km) it is usually necessary to install repeater transceivers on high points within the area. These low-power repeaters are portable and powered by lead–acid batteries, which are recharged by solar panels. Real-time differential navigation information is accurate to within 5 m.

- ***Wide-area differential GPS.*** Recently, commercial services have been introduced to provide real-time GPS navigation in Australia and surrounding waters, using base stations established around Australia (Featherstone 1995). The system uses the corrections from multiple base stations to give a better solution to that obtained from a single base station, and is commonly known as *wide-area differential* GPS. The GPS real-time differential corrections are transmitted to the aircraft through the Optus satellite communications link. The accuracy of the system is claimed to be comparable with ground based systems.

- ***Specialised real-time GPS.*** The Australian Survey and Land Information Group (AUSLIG) is in the process of establishing localised real-time differential systems to service populated areas and specialist clients. At present, the service has been set up in some Australian capital cities and at least one country area. The service provided in the Narrabri area of New South Wales is being used by contractors during aerial spraying of cotton crops. The GPS real-time corrections are broadcast on the sub-carrier of the local FM radio station signal. The coverage of the FM transmissions is limited in range; however, for a survey near the transmitter, there is no reason why it would not be suitable for airborne geophysical surveying.

Aircraft altimeters

Radar

Airborne geophysical surveys are normally specified to be flown at a constant ground clearance. For this reason, all survey aircraft are fitted with radar altimeters, which provide the pilot with the height of the aircraft above the ground. The aircraft ground-clearance data are also used in conjunction with the aircraft GPS height information to produce a digital elevation model of the area being flown.

The radar altimeter system includes an analog pilot display and a digital output for the DAS. Data are normally recorded at least every 1 s. The equipment is maintained at the manufacturers claimed accuracy of ± 2% through regular bench calibrations. Its performance should be checked in the field at the start of each major survey by flying at selected ground clearances over a flat area and comparing the data from the aircraft's radar altimeter, barometric altimeter and GPS.

Barometer

The atmospheric pressure is recorded in the aircraft and used in the corrections applied to the gamma-ray spectrometer data.

Airborne magnetics

Airborne magnetic surveys are a quick and cost-effective method of mapping the Earth's magnetic field. Magnetic anomalies in the Earth's magnetic field are caused by magnetic minerals in the rocks, and maps and images of these anomalies can be interpreted in terms of the geology.

Aircraft magnetometers

Previous magnetometers. Fluxgate magnetometers, first applied to airborne surveying in 1947 (Doyle 1987), were used for many years. They were not absolute reading and had serious instrument drift problems. Drift rates of up to 10 nT/hr were common; the drift being removed by using a series of tie lines. The output from the fluxgate sensor was a continuous signal proportional to the Earth's magnetic field, which was sampled at up to 0.2 s to a resolution of 1 nT with a noise envelope of 2 nT.

Proton precession magnetometers were also used in survey aircraft. These measured the absolute magnetic field, but to obtain an acceptable resolution of 0.1 nT, with a noise envelope of 1 nT or less, the sampling interval was limited to a minimum of 1 s. Overhauser effect magnetometers were a further

development of the proton magnetometers, but polarisation was by radiofrequency rather than direct current. This resulted in higher signals with lower power requirements and smaller sensors. The resolution was 0.01 nT at a sampling frequency of 0.2 s. It is not known whether Overhauser magnetometers were used in airborne applications.

Optically pumped potassium magnetometers have recently become available for airborne surveys. They have a resolution of 0.001 nT, and a noise envelope of ±0.005 nT at a sampling interval of 10 readings per second.

Current magnetometers. Optically pumped caesium and helium magnetometers are the current industry standard airborne magnetometers. Scintrex Pty Ltd has been producing its current CS-2 caesium sensor for several years and, more recently, GeoMetrics Inc. released its G-822 caesium sensor.

The caesium magnetometer sensor comprises a miniature atomic absorption unit, from which a signal proportional to the intensity of the ambient magnetic field is derived. An external counter converts this signal (called the Larmor signal) into magnetic field strength in nT. The constant of proportionality, which relates the Larmor signal to the intensity of the magnetic field, is called the 'gyromagnetic ratio of electrons'. There are 3 main elements of the CS-2 caesium sensor—a caesium lamp, an absorption cell containing caesium vapour, and a photosensitive diode, all mounted on a common optical axis within a cylinder.

GeoMetrics Inc. has been marketing its Helium G-833 sensor since the late 1980s. This sensor employs a metastable helium-resonance system operating as a control element in a frequency-tracking loop. The frequency of the loop varies directly with the external magnetic field at the sensor, yielding precise measurements of the external magnetic field. The G-833 consists of 3 modules—the sensor, the lamp oscillator, and the loop electronics. Outside this system is the frequency counter, which measures the Larmor frequency output from the loop electronics.

Both common types of optically pumped magnetometers may be sampled at 0.1 s. Their manufacturers quote a resolution of 0.001 nT and, in an ideal environment (completely shielded from any external effects), these magnetometers have a noise envelope of less than 0.01 nT.

Magnetometer counters

The output from caesium and helium magnetometer sensors, described above, is a frequency proportional to the total magnetic field. This must be counted and converted into a digital format for recording by the DAS. It is industry practice now to do this in the aircraft magnetometer compensation system.

Automatic aeromagnetic digital compensation systems (AADC)

The magnetic signature of the aircraft comprises three components:

- its permanent or remanent magnetisation;
- its induced magnetisation, produced by the Earth's field and the motion of the aircraft through the Earth's magnetic field; and
- a component due to the flow of random electrical currents within the aircraft and other effects unrelated to the aircraft orientation.

To produce reliable magnetic data it is essential to minimise these non-geological effects on the magnetometer data recorded in the aircraft. This function is performed by an *automatic aeromagnetic digital compensation system* (AADC). Present-day AADCs are capable of minimising, to a large extent, the effects of permanent and induced magnetisation of the aircraft. The minimisation of effects associated with varying currents requires strict adherence to procedures and vigilance on the part of the pilot, observer and data-quality analyst.

Function. An AADC unit consists of:

- an input counter and signal processor circuitry, which will accept signals from various magnetometer types—caesium, helium, proton;
- a main microcomputer, real-time clock, digital output circuitry, software package; and
- a three-component orthogonal fluxgate vector magnetometer.

The counter records the Larmor frequency from the magnetometer sensor and the fluxgate, which is rigidly mounted in a magnetically quiet part of the aircraft to provide the aircraft orientation. By correlating the magnetometer response produced during the compensator-calibration manoeuvres with the orientation information from the fluxgate, the compensator computer derives a set of terms to define this response. In normal survey mode the AADC corrects the incoming magnetometer data for the effects of the aircraft in real time.

The residual magnetic manoeuvre noise of the aircraft after compensation is usually less than ±0.15 nT for manoeuvres of ± 10° of roll, ± 5° of pitch and ± 5° of yaw. The heading error due to the aircraft is reduced to less than ± 0.25 nT.

Instruments. There are two industry standard AADCs used in Australia; the RMS Instruments AADC2 and Picodas compensation system. Each manufacturers equipment comprises the same fundamental components. However, the RMS unit is a stand-alone unit, whereas the Picodas system is more likely to be integrated into the Picodas PDAS system. The one main difference between the two is that the Picodas data can be processed, whereas RMS does not offer this facility.

Base station magnetometer

The Earth's magnetic field, at any particular location, varies with time. Several classes of variation can occur, with periods of a few seconds to days (Parasnis 1983). The long-period daily variation (diurnal) of the field varies fairly smoothly, with the amplitude dependent on magnetic latitude and increasing towards the magnetic poles. In Australia, the average magnetic diurnal variation is about 40 nT. In contrast, there are severe magnetic disturbances, called magnetic storms, during which the magnetic field may change by several hundred nT and be affected for several days. Short-wavelength magnetic disturbances, known as geomagnetic pulsations or micropulsations, occur randomly and may have periods of less than 1 second to more than 2 minutes, with amplitudes of 0.1 nT for those with highest frequency to about 5 nT for those with the longer periods. In general, only pulsations with periods of 18–40 s, classed as P3 pulsations, with amplitude of <1–3 nT, occur during daylight hours.

The variation of the magnetic field due to non-geological sources presents a problem for magnetic surveying. Almost all airborne surveys are flown during daylight hours, with the rare exception being offshore surveys, which may be flown at night for logistic reasons. Therefore, the main magnetic variations of concern are the daily diurnal effects and the P3 geomagnetic pulsations. Magnetic surveys must not be flown during magnetic storms

To reliably map the magnetic anomalies due to geological sources it is necessary to monitor the non-geological effects outlined above. This monitoring is accomplished by using a base-station magnetometer as close as possible to the survey area, in an area of low magnetic gradient and away from the influences of cultural effects.

The adopted practice has been to subtract the variations recorded at the base station from the data recorded by the magnetometer in the aircraft. However, studies in the Bendigo region (Milligan 1995) have revealed that the amplitude of pulsations, and the longer period diurnal effects, recorded simultaneously at several base stations separated by up to

100 km, are not always the same. Milligan (1995) concluded that these non-geological variations cannot be adequately removed by recordings made at a single base station and suggested that multiple base stations should be used. Tie-line levelling has been adopted for removing the smoothly varying diurnal effects.

The most common base-station magnetometer used in magnetic surveying is the GeoMetrics G856 proton-precession magnetometer. This instrument is completely portable, has internal data-logging capacity, and is usually powered by a 12 volt lead–acid battery. The resolution of the magnetometer is 0.1 nT, and at a sampling interval of 5 s, an acceptable noise envelope of 0.2 nT peak to peak is achieved. Faster sampling rates result in a larger noise envelope. The disadvantage of this type of instruments is that it is not possible to easily examine past readings while the instrument is in operation.

GeoMetrics produced the G866 proton-precession magnetometer as a base-station magnetometer. It is a variation on the G856, but has an inbuilt chart recorder, which makes it easy to check diurnal history before and during the flight. There is no inbuilt data recording available in this model, but a data stream of time and magnetic values is available on a serial port.

AGSO uses a high-sensitivity helium base station, which records the magnetic field at a 0.1 s interval to a resolution of 0.01 nT. A GPS receiver in the system enables accurate timing for synchronisation with the aircraft's magnetic data. The higher resolution and faster sampling rate of this magnetometer also provides information for research into high-frequency micropulsation magnetic variations.

Airborne gamma-ray spectrometry

Gamma-rays (of different energies) are emitted during the decay of some naturally occurring elements in the Earth. The most diagnostically useful of these for geological mapping correspond to potassium (1.46 MeV), bismuth-214 (1.765 MeV) from the uranium-238 decay series, and thallium-232 (2.614 MeV) from the thorium-232 decay series. The instrument used to record these gamma-rays is the gamma-ray spectrometer, which may be calibrated to selectively record 'windows' corresponding to the energy levels of interest.

The International Atomic Energy Agency's (IAEA) recommended windows for geophysical surveying are (Grasty et al, 1991):

Window	*Lower MeV*	*Upper MeV*	*Peak MeV*	*Radio-nuclide*
Total Count	0.41	2.81		
Potassium	1.37	1.57	1.46	K-40
Uranium	1.66	1.86	1.765	Bi-214
Thorium	2.41	2.81	2.614	Tl-208
Cosmic	3.0	and higher		

The data recorded in the non-geological cosmic channel are used in the data processing.

Instrumentation

The gamma-ray detection system consists of:

- the gamma-ray detector, and
- the detector controller/spectrometer.

The gamma-ray detector. Gamma-ray detectors rely on various types of reactions of gamma radiation with matter. For the measurement of low-intensity gamma radiation, as required for airborne surveying, scintillation detectors are used almost exclusively. These measure the fluorescence produced in the detector material from its excitation by gamma-rays. The fluorescent photons (scintillations) are reflected onto a photomultiplier tube (PMT) cemented to one end of the detector, where the charge they produce at the photocathode of the PMT is amplified by 10^6. The amplitude of each pulse is proportional to the energy of the gamma-ray in the detector.

Scintillation detectors used for airborne surveys are made of sodium iodide treated with thallium in the form of single crystals up to 4 L in volume. The sides of the crystals are coated with light reflecting magnesium oxide. The detectors are insulated to reduce drift in the crystals and PMT and, until recent technological advances, the packs included a heating blanket, which was used to maintain the pack at a constant temperature. The normal practice for airborne gamma-ray spectrometric surveying is to use two detector packages, each containing four individual crystal detectors, giving a total detector volume of 33 L. The crystal packs, which weigh about 80 kg each, are usually mounted close to each other in the aircraft to allow simultaneous ground calibration of the system.

Plastic scintillation detectors have not been adopted for airborne surveying because of their poorer resolution and larger bulk than the equivalent NaI detector.

Spectrum controller/spectrometer. Up until a few years ago the calibration of the gamma-ray spectrometers was a tedious process. The system calibration required the crystal packs, including the PMTs, to be maintained at a constant temperature and to achieve thermal stability. Each crystal pack assembly incorporated an internal heating blanket and temperature monitoring circuitry which required power to be attached at all times. Owing to the thermal inertia of the crystals, more than 24 hours was required before their temperature stabilised. The system required regular manual calibration and comprehensive system monitored, using various sources, at the start and end of each day.

Today most geophysical survey operators use self-calibrating spectrometers. The most widely used units being the Exploranium GR-820 and the Picodas PGAM 1000. These state-of-the-art spectrometers are a great advance on previous equipment, where drift in the photomultipliers and electronics often led to a decrease in the resolution of the final data.

The current units continuously analyse the spectrum from each crystal and adjust the system gain to ensure that the chosen calibration peak is in the correct channel. In particular, the GR-820 equipment can display the spectrum from each crystal on the console to verify operation. It also calculates and reports the resolution of each crystal after each calibration (normal accumulation time is 20 minutes) and logs and outputs the system dead time for inclusion in the data processing. The operator has flexibility to define up to eight regions of interest (windows) for special applications, e.g. environmental studies where the normal geophysical parameters may not be applicable.

A typical survey aircraft, such as that operated by AGSO, is fitted with an Exploranium GR-820, with two 16.5 L gamma-ray detectors and, as well as recording the four windows corresponding to total count, potassium, uranium and thorium, the DAS records the total 256-channel data every second. The four-channel data are mainly used for in-flight data monitoring. Data processing has been developed to further enhance quality through the use of 256-channel data.

Equipment calibration and field data quality checking

Magnetic-compensation procedures

Magnetic compensation must be undertaken at the start of a survey and after any modification or maintenance has been performed on the aircraft or system. An appropriate standard set of procedures must be developed and complied with to achieve the best compensation. AGSO has been using an RMS AADC since 1990 and has adopted the following procedures

relating to aircraft magnetic compensation.

The AGSO magnetic-compensation procedure is as follows:

- aircraft must be in normal operational mode;
- all equipment operating;
- all equipment for survey on board;
- for efficiency, the area where the compensation is to be performed should be close to the survey area;
- perform the compensation at an altitude of 2500 m a.g.l. in an area of low magnetic gradient;
- operate the AADC in calibration mode and perform a series of aircraft manoeuvres; (± 10° of roll, ± 5° of pitch and ± 5° of yaw) for each of the cardinal headings;
- after completing the calibration, operate the AADC in compensated mode and verify the data quality by flying check manoeuvres;
- make a final check of the data on the field data processing system.

Spectrometer checks

Annual spectrometer calibrations. There are several gamma-ray spectrometer calibrations which must be performed at least once a year (Grasty & Minty 1995):

- ***Cosmic calibrations.*** The count rates in any window contain a component due to high-energy cosmic-ray particles, which increases with height Grasty & Minty (1995) have described a procedure to relate the count rates in the cosmic channel and each other channel and to remove the cosmic component during data processing. The basic data are acquired by flying over the sea at heights of 250 m and 2250 m.

- ***Radon calibrations.*** The removal of the radon background component in the potassium, uranium and thorium windows is an essential part of the calibration process to convert airborne count rates to ground-level concentrations of potassium, uranium and thorium. Methods such as the use of upward-looking crystals or spectral-ratio method (Minty, 1992) are described by Grasty & Minty (1995).

- ***Pad calibrations.*** The energy-stripping coefficients for the spectrometer system are calculated from data recorded with the aircraft positioned on the ground over a set of specially constructed calibration pads. The calibration requires four pads, made from a uniform mixture of concrete, which have been doped with potassium, uranium, thorium and one blank. As stripping coefficients vary with distance from the source, the effect of the air column is simulated by placing various sheets of plywood between the calibration pad and the detector.

- ***Sensitivity and height attenuation calibrations.*** The aircraft must be flown at a several different heights over a spectrometer calibration range (Grasty & Minty 1995) to determine the aircraft system sensitivity and height attenuation coefficients.

Survey spectrometer checks

- ***Stringent thorium-source test.*** Before a survey commences, a stringent thorium-source test must be carried out to demonstrate that the sensitivity of the equipment has not changed since the last calibration. The corrected thorium results must be within 3% of previous thorium calibration tests.

- ***Daily thorium-source test.*** Thorium-source checks are conducted before and after each days flying. The background-corrected count rates in the thorium window serve to verify that the system has remained the same during the survey. The variation in the source tests must not be more than 5%.

- ***Daily system resolution checks.*** The spectrometer system resolution, based on the thorium 2.615 keV photopeak, must be calculated before and after each day's flying. The resolution of a spectrum photopeak (background subtracted) is defined as the width of the peak at half the maximum amplitude divided by the energy of the photopeak and expressed as a percentage. Grasty & Minty (1995) have specified that the overall system resolution, calculated using the thallium 208 peak at 2.615 MeV, must be better than 7%.

- ***Daily spectrum stability checks.*** The stability of the system, calculated using the thallium 208 peak at 2.615 MeV, must be within ±1 channel for a 256-channel system. System stability is checked from the thorium-source check data at the start and end of each day.

- ***Daily test line check.*** Operators of airborne gamma-ray spectrometer surveys are required to select a test line in the vicinity of the survey area to verify the operation of their equipment in the air. This line is to be flown at the start and end of each day. A suitable test line is one which has uniform radioactivity along its length, is easily identified from the air to assist in navigation, and is at least 5 km long. The counts in the thorium channel are background corrected to give the actual radiation contribution from the ground. The flight to flight variation in the average thorium background-corrected counts along the test line should be less than ±10% . Deviations beyond 10% may indicate an equipment problem, the introduction of some radioactive material into the aircraft, or rain-affected ground surface along the test line.

In-flight data checking

Magnetometer, gamma-ray spectrometer, radar altimeter, and navigation data are displayed on the graphics printer output in the aircraft and should reveal any major in-flight problems with the data. In addition, some DAS, such as that developed by AGSO, monitor the data for noise, spikes, and validity. Errors are reported on a printer. In addition to these checks, the gamma-ray spectrometer has facilities by which the operator may verify the operation. The magnetometer data plotted as total field and fourth differences indicate data quality.

Post-flight data checking

Most clients require contractors to have an in-field data processing system to check, process and display data. Each contractor has their own software tailored to their needs. AGSO field surveys operate from a mobile office set up at the survey base. The office is used by the party leader and technical personnel for the day-to-day survey management, data quality checking and equipment maintenance. It is equipped with a UNIX-based computer running Intrepid, the airborne geophysical data-processing system written by Desmond Fitzgerald & Associates Pty Ltd in association with AGSO. This software is the same as that used at AGSO's headquarters in Canberra. In the field office, the data are gridded and imaged.

The following are carried out:

- Checking data profiles for noise and spikes and making appropriate edits.
- Differential post-processing of GPS data.
- Plotting of flight path to check compliance with specifications.
- Merging of navigational and geophysical data.
- Draft processing of magnetic data, including removal of magnetic diurnal variations and the International Geomagnetic Reference Field (AGRF). Tie-line levelling is not attempted until the survey has been completed.
- Gridding and imaging of magnetic data with enhancements, such as across-line illumination, to emphasise line-to-line level shifts. These shifts would normally be removed later with tie-line levelling. Contours of magnetic data may be plotted on the field plotter.
- The 256-channel gamma-ray spectrometer data are spectrum equalised to remove any drift. The 4-channel data are then corrected for system dead time, background, Compton scattering (stripped), and height (ground clearance variation).

- The total count, potassium, uranium, and thorium channels are gridded and imaged to check for flight-to-flight consistency.
- Digital elevation model data, produced from the GPS height and radar altimeter data, are gridded and imaged to verify data quality.

The examination of data in profiles and images, immediately it is available from the aircraft, is the only way to ensure the quality of data and minimise the need for costly repeat flying.

Conclusion

The methodology and instrumentation for airborne magnetic and gamma-ray spectrometric surveys have progressed greatly over the last 45 years. Industry now collects high-resolution magnetic data at a sample interval of about 7 m and from as low as 40 m above ground. Safety and operational factors limit lower flying height for conventional fixed wing aircraft, but the recently promoted concept of using unmanned aircraft for magnetic surveying may provide a way of overcoming this limitation and a cost-effective solution.

Gamma-ray spectrometry equipment has advanced recently with the introduction of self-calibrating spectrometers. Some manufacturers have introduced 1024-channel recording of data from each crystal with the aim of providing the raw data for energy calibration of individual crystals. In addition, there is ongoing research and cooperation within the industry into the standardisation of calibration, collection and processing of gamma-ray data, which will result in higher quality and more consistent data sets. Research into comparative methods of determining non-geological background is expected to result in a more appropriate method for calculating radon background.

GPS has become the industry standard navigation system for airborne geophysical surveying. The typical errors for differentially processed GPS positioning are less than 5 m in the horizontal and up to 10 m in height. The introduction of dual-frequency GPS receivers into airborne data acquisition is expected to reduce errors in position to about 1 m in the horizontal and about 3 m in height GPS height and aircraft radar altimeter data have led to the routine production of digital elevation maps to accompany the geophysical maps. The airborne survey industry is currently adopting the commercially available wide-area differential GPS service, which will improve the accuracy of all surveys and make it possible to infill to a higher resolution at a later date.

Appendix: Summary of AGSO equipment

The following is a summary of the equipment used by AGSO to carry out airborne geophysical surveys.

Data acquisition

- ***Data acquisition system:*** HP A400 computer, Timer, HP9122C 720 Kb disc drive, Compaq Notebook and portable hard disc.
- ***Aircraft magnetometer:*** GeoMetrics G833 Helium magnetometer (0.01 nT resolution), RMS AADC-2 Compensator
- ***Gamma-ray spectrometer:*** Exploranium Spectrum processor (GR 820), and 33600 cm^3 crystal detector
- ***Radar Altimeter:*** Collins ALT-50
- ***Navigation Systems:*** Ashtech real-time differential satellite navigation system consisting of two GPS Ranger receivers; one in aircraft and the other used as a base station, and associated radiolinks.

Racal (Decca) Doppler antenna unit (80561 CAD) and Sperry C14 D compass

- ***Flight path camera:*** National colour video camera (WV CL 302E), VCR (NV180) and LCD TV (TCL 3A)
- ***Graphics Display:*** HP Think Jet printer
- ***Thermometer:*** Digital thermometer (AGSO built- RS sensor)
- ***Barometer:*** Digital barometer (AGSO built- Setra sensor)
- ***Base Station Magnetometers:*** GeoMetrics G833 helium sensor high resolution base station with digital recording (0.1 s sampling at 0.01 resolution). GeoMetrics G866 base station magnetometer (storm monitoring) with remote digital data recording (5 s sampling at 0.1 resolution) and field display monitoring via a Philip's telemetry system and a Toshiba T1600 lap-top computer

The total weight of the survey equipment in the aircraft is approximately 260 kg.

Field data processing equipment

The field-survey office caravan is fitted with the following data processing equipment.

- ***UNIX Workstation:*** SUN Sparkstation IPX and Exabyte tape backup
- ***Plotter:*** Calcomp drum plotter
- ***PC:*** Compaq SLT386s/20 Laptop Computer (networked to SUN), Compaq VGA Colour Monitor, Oki Printer

References:

Boyd, T.J., 1992. An annotated outline of GPS. Preview, 40, 15–26.

Doyle, H.A., 1987. Geophysics in Australia. Earth Sciences History, 6(2), 178–204.

Featherstone, W.E., 1995. The global positioning system (GPS) and its use in geophysical exploration. Exploration Geophysics, 26, 1–18.

Grasty, R.L., Melender, H. & Parker, M., 1991. Airborne gamma-ray spectrometer surveying. International Atomic Energy Agency, Vienna; Technical Reports Series, No. 323.

Grasty, R.L. & Minty, B.R.S., 1995. A guide to the technical specifications for airborne gamma-ray surveys. Australian Geological Survey Organisation, Record 1995/60.

Luyendyk, A., 1997. Processing of airborne magnetic data. AGSO Journal of Australian Geology & Geophysics, 17(2)—this issue).

Milligan, P.R., 1995. Short-period geomagnetic variations recorded concurrently with an aeromagnetic survey across the Bendigo area, Victoria. Exploration Geophysics, 26, 173–178.

Minty, B.R.S., 1992. Airborne gamma-ray spectrometric background estimation using full spectrum analysis. Geophysics, 57, 279–287.

Parasnis, W.D., 1983. Introduction to geomagnetism. Scottish Academic Press, Edinburgh and London.

AGSO Journal of Australian Geology & Geophysics, 17(2), 31–38

Processing of airborne magnetic data

A.P.J. Luyendyk[1]

The processing of aeromagnetic data collected along survey flight lines to a grid of values ready for the application of enhancement techniques and interpretation involves the sequential processes of editing, correction for diurnal effects, removal of the Earth's background magnetic field, the levelling of all data to a common base and, finally, the application of a gridding routine.

Introduction

The aim of this document is to give an overview of the processing of airborne magnetic data, referring to examples of methodologies used by the Australian Geological Survey Organisation (AGSO).

While the general procedures are well defined, it is still not practicable to make all the measurements needed to unambiguously process airborne data. A skilled analyst is still needed to make judgements in the levelling and micro-levelling processing procedures, which can have a significant effect on the overall result. The current industry aim is to level magnetic data to better than 1 nT. Whether or not this has been achieved is often difficult to assess. The measure of quality usually used is that enhanced images of levelled data should reveal a minimum of artefacts attributable to the data gathering or reduction processes. It is still not possible to guarantee that an image without appreciable artefacts can be produced without seriously affecting the integrity of the data. The most likely sources of errors are discussed.

Processing of aeromagnetic survey data

The overall processing of aeromagnetic data involves eight major steps in two phases:

Phase 1—Pre-processing

- verifying and editing the raw data;
- locating the data in x and y.

Phase 2—Processing

- parallax corrections;
- removing diurnals;
- removing the component attributable to the Earth's regional field;
- levelling the data;
- micro-levelling—removal of any residual levelling errors;
- gridding and contouring.

A variety of software packages is available for processing and presenting aeromagnetic data. They vary in the features and methodologies they provide, their style of user interface, which ranges from command line through to menu driven, fully fledged graphical user interfaces, and the level of user feedback. User feedback is often ignored in software assessment, but it can be critical in the production of high-quality processed magnetic data, as some of the major processing phases, such as levelling, rely heavily on the skill of the operator, whose job is made much easier with interactive visual feedback.

No attempt is made here to assess or provide an exhaustive list of available software packages. Some of those available and their developers are listed below.

- ARGUS — Australian Geological Survey Organisation.
- ECS — Software Engineering Computer Services, Bowral, New South Wales.
- GIPSI — Paterson, Grant & Watson, Ontario, Canada.
- TerraTools — TerraSense Inc., California, USA.
- Intrepid — Desmond Fitzgerald & Associates, Brighton, Victoria.

The algorithms and techniques described here have been implemented in a software package called Intrepid, jointly developed by Desmond Fitzgerald & Associates, AGSO and a consortium of Australian mining companies, including BHP Minerals, Pasminco and Stockdale (Fitzgerald & Associates 1996).

The reference level

For aeromagnetics, since we are only interested in magnetic perturbations due to the Earth's crust, the ideal data set is a 'snap-shot' of the magnetic field at all required locations at the same instant of time, but with the Earth's regional magnetic field removed. This ideal data set is the reference surface to which the data are to be reduced.

Sources of errors

Magnetometers

Modern magnetometers give an absolute measurement of high sensitivity, with virtually no drift and for all intents and purposes can be regarded as giving an exact reading. Typical 'noise envelopes' are ± 0.1 nT.

The same cannot be said of the fluxgate magnetometers used as little as 10 years ago. They were not absolute and had to be manually calibrated, had high rates of drift and were sensitive to about ± 1 nT. Drift curves varied exponentially with time and, even allowing for standard operating procedures, such as turning them on well before the commencement of a day's flying, drift rates up to 10 nT per hour were common.

Aircraft effects

The magnetic signature of the aircraft consists of three components. Its permanent magnetisation, magnetisation induced by the motion of the aircraft through the Earth's magnetic field, and a component due to the flow of electrical currents within the aircraft. These currents fluctuate as the pilot varies any aircraft controls, such as changing the engine speed, adjusting ailerons, etc.

The permanent magnetisation of the aircraft leads to the familiar *heading error* caused by the vector addition of the Earth's field with that of the aircraft, resulting in a base-level shift between lines flown in opposite directions. Higher frequency errors are introduced by aircraft manoeuvring and are referred to as *manoeuvre noise*. The general procedure for removing these effects is called *compensation*.

Modern survey aircraft are compensated in real time by sophisticated modelling packages, which have the aircraft orientation as their input. The normal procedure is to establish the various model parameters by flying the aircraft around a square at high altitude, over a region of low magnetic relief, while executing several roll, pitch and yaw manoeuvres. These are then used to eliminate any induced magnetic effects. There is no direct control on the flow of electrical currents, but the aircraft is always operated in a 'steady state' to minimise any effects. Routine tests are carried out during the survey to

[1] Australian Geological Survey Organisation, GPO Box 378, Canberra, ACT 2601

ensure the compensation has not deteriorated. With these procedures heading error is reduced to ± 0.25 nT and manoeuvre noise to ± 0.15 nT.

Older surveys were not flown with such sophisticated techniques. The 'compensator' consisted of an array of three orthogonal electrical coils acting as magnets. By varying the current through each coil the permanent magnetisation of the aircraft could be effectively neutralised. The standard procedure involved rotating the aircraft on the ground over a fixed spot and varying the currents until a constant reading was obtained. Time-varying effects were not compensated for, and the procedure was prone to error, as it was basically a manual operation. Heading errors of ± 5.0 nT were common.

Navigational effects

The advent of global positioning systems (GPS) in the late eighties has greatly improved the quality of navigational data. Positional accuracies of about ± 5 m are now routine (Boyd 1992). When comparing data between lines, and especially line/tie intersection points, the effect of navigational errors is obviously related to the gradient of the local field and will have a varying effect. It should be remembered that the GPS data include X, Y and Z data. The Z values, the height above the ellipsoid, can be put to good use when processing aeromagnetic data, specifically, when transforming the positional data between datums, in the calculation of the Geomagnetic Reference Field (GRF), and in combination with ground clearance data to produce digital elevation models.

In most systems the primary navigation data are adjusted to reflect the location of the most position-sensitive recording instrument—invariably the magnetometer. If this adjustment is not made, parallax errors result with readings from adjacent lines being offset by twice the distance between the magnetometer and the actual navigation reference point along the axis of the aircraft. The distance between the navigation and magnetometer recording instruments is referred to as the *cable length.*

Before the advent of GPS, radio-beacons were often used for navigation. More commonly, the location of the aircraft was determined by comparing strip film or video recordings made of the ground during flight with aerial photography and topographic maps. In the latter case, an optimistic accuracy of the order of ± 50 m was claimed for each of these *fixes.* Three to four fixes were determined at the start and end of each line and then at regular intervals along it, usually chosen to coincide with tie crossover points. Intermediate points were infilled with additional navigational aids. At AGSO, Doppler infill was used. Where such facilities were not available, extra fixes were needed and the flight path was approximated by straight line segments between neighbouring fixes. Variations in ellipsoidal height were ignored, the mean height of the survey region above sea level being used whenever such values were required.

In regions with few distinguishable topographic features, such as deserts, errors of the order of 500 m were often detected during processing. Clearly, in many cases the navigation was not very precise and was considered the greatest source of levelling errors before the introduction of GPS.

Time variation in the magnetic field

The Earth's magnetic field varies with time (Table 1). The variations can be random or cyclic, varying from the 11 year cycle of sunspot activity down to geomagnetic pulsations with periods of the order of seconds (Parkinson 1983). Some relate to local time, for example diurnals, but others, such as magnetic storms, relate to universal time and can be considered synchronised to less than a minute worldwide. Not only can these variations be out of phase, but their amplitude can also vary significantly with position. Typically, for a 1:250 000 map sheet area, the average variation peak to peak along a line is of the order 3 nT, and the total variation over the whole survey is about 30 nT.

Table 1. Time variations in the Earth's magnetic field.

Class	*Description*
Pulsations	Period 1–300 s; magnitude generally below 10 nT with the amplitude of pulsations decreasing with frequency; occur at random.
Magnetic storms	Sudden onset with decay lasting from hours to weeks; magnitude up to tens of nanoteslas; caused by solar flares leading to a rapid change in the flux of cosmic rays interacting with the atmosphere.
Diurnal	Period of 24 hours; magnitude up to 50 nT; due to the rotation of the Earth relative to the sun.
Lunar	Period of 27 days; due to the orbit of the moon about the sun
Solar	Period of 1 year; due to the orbit of the Earth about the sun.
Secular	Gradual change with a variable rate across Australia within the range of –20 to 30 nT per year.

Ground clearance variation

The amplitude of local magnetic anomalies varies with distance from the recording instrument, i.e. with respect to the ground clearance of the aircraft. The rate of change increases as the wavelength of the anomaly decreases. This is most noticeable where the plane flies across an escarpment, since it needs to climb gradually as it approaches it from one direction, but may descend much more rapidly in the other. A typical herringbone pattern can be observed in a grid of the magnetic data, attributable to the variations in ground clearance between adjacent lines. For example, AGSO's Aero Commander has a survey speed of 70 m/s and a climb rate at this speed of 50 m/km. To clear a 50 m obstacle climbing must commence about 20 s beforehand to give a margin for safety. Ground clearance variation can be expected to cause errors of tens of nanoteslas over a typical survey area.

Altitude variation

The Earth's magnetic field varies with height above the ellipsoid. Typically, the rate of change with height is 0.025 nT/m. Since rapid changes in altitude are usually associated with changes in ground clearance, these effects are usually masked by ground clearance variations.

Wave noise

Over large bodies of water, surface waves can produce detectable variation in the magnetic field Waves represent a conductor moving through the Earth's magnetic field resulting in a secondary induced magnetic field (Weaver 1965; Ochadlick 1989). Wave noise from ocean swells of 1.5 nT has been detected by AGSO's survey aircraft at a flying height of 80 m.

Pre-processing

Verifying and editing raw data

Raw data must be visually inspected for spikes, gaps, instrument noise or any other irregularities in the data. This is most easily performed via an interactive editor where the data are displayed as a continuous trace as a function of time. Automatic procedures to detect spikes are well documented, including fourth difference analysis and Naudy filtering (Naudy & Dreyer 1968) to extract any short-wavelength noise.

As a rule of thumb, the depth to the source of a narrow magnetic anomaly is given by the width of the anomaly at half its amplitude. With this in mind, any data with a wavelength

less than that of the flying height of the survey aircraft can be regarded as noise and removed via low-pass filtering. Such filtering is only applied in limited cases, such as when high-frequency wave noise is apparent.

Ideally, this verification phase should be carried out in the field so that any errors attributable to data acquisition can be corrected in the survey aircraft as quickly as possible.

Locating data in X and Y

Once the navigation data have been checked and edited they can be merged with the magnetic data in order to locate the magnetic data.

Processing

Parallax correction

The distance between the navigation reference point along the axis of the aircraft and the magnetometer recording instrument is referred to as the *cable length*. If the cable length is not zero a parallax correction must be applied to synchronise the magnetic and navigational data. Since the navigation data vary smoothly and are not the primary data set, they should be interpolated to coincide with the location of the recording instrument rather than interpolating the data to coincide with the navigation. A parallax correction is applied by calculating the velocity of the aircraft at each x,y point from the navigation data. This velocity is then used to adjust the navigation data to allow for the cable length.

Diurnal variation corrections. It is common practice to collectively refer to all the time variations of the Earth's magnetic field by the misnomer *diurnals*. This practice is continued here. The diurnal variation is monitored by a base station at a fixed location on the ground. It serves two purposes.

- It is used to monitor the short-term rate of change of the field. Flying should be curtailed if the rate of change exceeds a specified cut-off, typically 2 nT per minute. The main purpose is thus to identify periods of magnetic storms, but the readings can also indicate periods of high pulsation activity.
- The base station data are time-synchronised with the aircraft data, and can be subtracted to give a residual which is a function of position only. This assumes that base station variations are fully representative of temporal variations over the whole survey area. This is not strictly true. Significant variations in phase and amplitude are known to occur over distances of 50 km or more. There is a risk of introducing high-frequency errors that cannot be removed by subsequent levelling procedures.

Applying diurnal corrections introduces an arbitrary base-level shift into the magnetic data. In general, this is of no consequence as we are only interested in local anomalies and not the absolute value of the magnetic field. A constant representative of the mean magnetic field value over the survey area can be added to the survey data. Moving the base station or the use of more than one base station will lead to different base-level shifts which are automatically removed by the standard levelling procedures, described below. In addition, the noise envelope of the base station magnetometer is added to that of the aircraft, but this is insignificant for modern magnetometers in comparison to other errors.

If base station data are not subtracted, diurnals with a period less than twice the flying time between ties cannot be removed by subsequent levelling procedures. A typical survey aircraft speed would be 70 m/s, giving a flying time of 70 s between ties separated by 5 km. The base station magnetometer should obviously be sampled at a rate high enough to effectively monitor the temporal variations—typically 1 s or less—with interpolation being used for intermediate values. (Note that low sampling rates would render the high-frequency micropulsations invisible.)

The debate is continuing on the usefulness of subtracting diurnals (Barton & Johnson 1988). At AGSO it is standard practice to apply this correction after filtering the diurnals to remove all wavelengths with a period of less than 10 s. Experiments are currently being conducted, using a high-precision base station magnetometer, sampling at 0.1 s and accurately synchronised to Universal Time, to try to resolve the problem.

GRF—removing the Earth's regional magnetic field

This processing step merely involves subtracting a well-defined model of the Earth's regional field, the so-called Geomagnetic Reference Field (GRF), from the data. Standard models of the Earth's regional field are based on satellite and ground observations. They provide estimates of the field as a function of position, including height above the ellipsoid, and time. The secular variation is very slow and is ignored with a mean date for the survey being used to calculate the GRF.

GPS navigation provides the (X,Y,Z) data that should be used to calculate the GRF as a function of position. It is standard practice to replace the Z value with the mean height of the aircraft above sea level for a particular survey. The errors introduced by this approximation are small, as the rate of change of the Earth's magnetic field with height is of the order of 0.025 nT/m. These errors can be eliminated altogether by using the GPS Z data when available.

The field varies slowly with position, the change being insignificant over the sample interval of the magnetometer. To speed up calculation of the GRF, it is normal practice within the industry to calculate values at an interval within the range 100–500 m, with intermediate values being interpolated from their neighbours. As this operation only has to be applied once, the additional overheads to calculate the field for every point are insignificant.

For the Australian continent there is a choice of two GRF models, the International Geomagnetic Reference Field (IGRF) and the Australian Geomagnetic Reference Field (AGRF) (IAGA 1991; Barton 1988). Both are satisfactory, although the AGRF, which applies to the Australian region only, does reflect the long-wavelength field over Australia more accurately. For our purposes, with survey areas of only 100–200 km, the choice is academic. As applicable AGRF models were not available until 1985, and the IGRF is widely recognised, AGSO has always used the IGRF. It should be emphasised that the reference model and input parameters used should be recorded so that in the future it is possible to adjust the data to another GRF model.

Levelling

Aeromagnetic surveys are flown in a particular pattern, or grid, designed to give duplicate measurements at so called *crossover points*. The magnetic reference to which the magnetic data are levelled is time invariant and, therefore, any discrepancy at a crossover point represents an error. A typical flight path consists of *lines*, which give the primary coverage for the survey, and *ties*, which are flown at right angles to the lines and are used for control. The intersections of the ties with the lines give the crossover points.

Levelling is the procedure by which the discrepancies between the readings at each crossover point, the *intersection errors*, are reduced by systematically proportioning them between the ties and the lines. Several methods are in common use (Green 1983; Yarger et al. 1978; Foster et al. 1970). They can be grouped into three categories.

Minimising intersection errors by adjusting navigation data. If an estimate of the accuracy of the navigation data is known, then this can be used to define a circle about each intersection point in which the intersection point can be freely

moved. Since the gradient of the magnetic field is known at an intersection point, its true position within this circle is assumed to be the one that minimises the intersection error. This procedure is repeated at each crossover point, giving a set of corrections to the navigation data which can be interpolated to all the navigation data.

This type of methodology can be applied with various levels of sophistication, generally aimed at determining that proportion of the intersection error to be attributed to errors in the navigation. Thus Green (1983) considered the eight immediate neighbours of an intersection point and deemed the error attributable to the navigation to be that which minimises the closure errors of the loops formed with these neighbouring points.

The main objection to adjusting intersection points by such methods is that it treats each intersection point in isolation, or only considers some effect from immediate neighbours, and will always reduce the errors at every intersection point. In general it is only used in combination with other levelling procedures.

Loop closure methods. The grid of intersection points of lines and ties can be considered a network of closed loops and standard procedures for network adjustment in geodetic surveying can be applied. For a more detailed analysis see Green (1983). Though mathematically attractive, in that an immediate solution is available with no manual intervention, it has been found to work well only in regions of low magnetic gradient where the range of intersection errors is small. Because of this, it is standard practice to apply navigational adjustment, as described above, to minimise intersection errors before applying this method.

Polynomial Levelling. In its simplest form, this method involves fitting a polynomial to the intersection errors along a flight, line or tie as a function of elapsed time, by the method of least squares. These polynomials are then subtracted from the original data, reducing the intersection errors. Various implementations of this method have been described (Yarger et al. 1978; Foster et al. 1970). The main disadvantages of the polynomial levelling method are:

- Problems can occur at the end of lines where the polynomial may not be well controlled and it diverges from what would be regarded as an acceptable fit to the data.
- A skilled operator is required to get the best results, it being necessary to judiciously select the degree of the polynomials fitted to the data. To this end, it is essential that interactive visual feedback be provided so that the operator can rapidly check the fitted polynomials and adjust them accordingly.
- When the intersection errors are irregular the simple polynomial fits may not follow the variations well enough. In such instances a series of localised polynomials is required to get good results.

Since this type of levelling is the one chosen by AGSO, the implementation devised by AGSO is described in some detail in Appendix 1.

Micro-levelling

Micro-levelling is a general term that refers to the removal of any apparent residual errors in airborne geophysical data after standard processing and the application of the more rigorous levelling techniques described above. Micro-levelling adjustments are necessary because quite minor data errors become clearly visible when grids of data are displayed as enhanced images. Not only does this make the image unattractive, but subtle features may be masked.

Geophysical exploration companies regard their own micro-levelling techniques as proprietary and little information is available on particular processes. In general, automated methods involve filtering a grid of data to detect residual errors. These errors are then subtracted from the original point-located data. Data are also manually edited, but this can be very time consuming. It involves correlating errors from images or grids of data with flight-path information to estimate the magnitude of any observable errors. These errors are then subtracted from the original point-located data.

AGSO currently uses a grid filtering technique for micro-levelling, the details of which are described in Appendix 2.

Gridding and contouring

Gridding point-located data is the first step in AGSO's micro-levelling method and provides the best method of data quality control via their display as enhanced images. It is essential that a grid honours the original point-located data and also provides a smooth continuous surface.

The gridding technique used by AGSO is an algorithm developed by Briggs (1974), as implemented by the software package Intrepid. It takes the randomly distributed survey data and interpolates it onto a regular grid. The method represents the surface locally with splines, whose total curvature is minimised. If a grid point has an original observation falling within half a grid cell size of it, the surface is further constrained to pass through that point. A direct solution is not available and the final solution is obtained iteratively from initial values determined for each grid point by interpolating from the three closest original observations.

Though producing an excellent result, the technique converges very slowly to the final solution, the rate of convergence for a given grid cell decreasing the further it is from an original data point. To obtain a visually acceptable grid, this effectively restricts the cell size of the grid to a minimum of about one-fifth of the line separation.

Because the data sampling interval along the flight-line direction is typically hundreds of times greater than the line spacing, aliasing problems are often present in gridded aeromagnetic data. To alleviate the problem, the line data should be low pass filtered so the frequency content of the data in the flight-line direction is comparable to that perpendicular to the flight-line. Likewise, typical grid cell sizes are an order of magnitude greater than the data sampling interval along the line. Data with a wavelength less than twice the grid cell size can only be regarded as noise and, again, should be removed before being sampled for input to a grid. In general, because the end users of gridded data want the highest frequency content possible, line data are not filtered before being gridded. Once a grid has been produced it can be displayed as an image or a contour map.

Conclusions

The methodology and rationale for the processing of aeromagnetic data has been reviewed, with the techniques used by AGSO for levelling and micro-levelling being given in some detail in Appendixes 1 and 2.

The data cannot, as yet, be unambiguously processed, the results especially depending on the levelling and micro-levelling techniques employed and the judgement of the analyst using them. Research is still needed to develop non-invasive, effective micro-levelling techniques, as the current options remove a significant proportion of the true signal.

Diurnal removal is another contentious issue. On the one hand, tie-line spacings generally used in surveying are insufficient to allow high-frequency diurnal variations to be removed, while, on the other, current techniques used to monitor the Earth's field, using base stations, are inadequate.

Ground clearance variations are generally ignored and a standard methodology for their removal needs to be developed.

Appendix 1. AGSO polynomial levelling

Aeromagnetic surveys are flown in a particular pattern, or grid, designed to give duplicate measurements at so-called *crossover points*. The magnetic reference to which the magnetic data are levelled is time invariant and, therefore, any discrepancy at a crossover point represents an error. A typical flight-path pattern consists of *lines*, which give the primary coverage for the survey, and *ties*, which are flown at right angles to the lines and used for control. The intersections of the ties with the lines are referred to as crossover points, and the difference between the magnetic measurement made along the tie and that along the line at the crossover point is known as the *intersection error*.

The basic assumption underlying the method is that the errors in the magnetic readings associated with each line or tie vary slowly and can be well approximated by a set of local polynomials as a function of time. These polynomials are referred to as *drift curves* and the task is to reconstruct them from the observed intersection errors. The intersection error at a given crossover point will be made up of two components, one from the line and one from the tie. The method attempts to separate the errors into those due to the lines and those due to the ties. Any errors due to navigation are regarded as noise.

Note that flights typically consist of several lines. Lines recorded in the same flight can normally be related to each other by time and, therefore, drift curves that apply to a flight can also be considered.

There are four basic procedures. These are listed below in the sequence they should be applied.

- Level the ties: calculating the tie drift curves.
- Drift the lines by flight to the ties: calculating the drift curves for individual flights of lines.
- Drift the lines individually to the ties: calculating drift curves for individual lines.
- Drift the ties individually to the lines: calculating residual errors for individual ties.

Principal tie

The first problem is that an absolute reference is required. No such reference is available and an arbitrary tie from the survey is chosen as the absolute reference, the so called *principal* tie, which is assumed to have zero drift. Obviously the principal tie should be chosen carefully. To enhance the reliability of the principal tie, it should be one that was flown during a period of quiet diurnal activity, be located over a region of low magnetic relief, and be located approximately at the centre of the survey area.

Levelling ties

Here, the task is to calculate the drift curves for each tie, effectively levelling them to each other. Firstly, a tie is selected to be the principal tie. It acts as the absolute reference to which the whole survey is levelled. Ties are classified as either *levelled* or *unlevelled*. In the first instance, the levelled set of ties consists of the principal tie only. Each tie in the survey is levelled in turn by adjusting it to the current set of levelled ties.

At this stage, each intersection error involving the unlevelled ties consists of a component from the tie and one from the line at the corresponding crossover point. The first task is to estimate the drift, or error in the magnetic reading, attributable to a line at its crossover with the tie being levelled. Once it is known, it can be subtracted from the corresponding intersection error, giving the error at the crossover point due to the tie alone.

The estimate of the drift of a line is determined by inspecting its intersection errors with the current set of levelled ties. Since the drift for the levelled ties is assumed to be zero, the intersection errors between them and a line consist of the component due to the line alone. In actual practice, a better estimate of the drift curve of a line can be obtained by considering the whole flight containing the line. Since there are more crossover points along a flight compared to those for a single line, a higher degree polynomial can be fitted to the intersection errors, giving a better estimate of the drift curve.

The actual levelling of an unlevelled tie proceeds as follows (note that all the other unlevelled ties are ignored at this stage). Each flight of lines is considered in turn. A polynomial is fitted to its intersection errors with the set of levelled ties, as a function of time along the flight, giving an estimate of the drift for the flight. (In the case of the first tie being levelled, the only control is where a particular flight crosses the principal tie. As the procedure progresses, the pool of levelled ties becomes larger, improving the control for the estimate of a flight's drift curve.)

The tie to be levelled is now inspected. At each of its crossover points with the current flight, the component of the error due to the line at the crossover is calculated from the estimate of the drift curve for the flight. This is a simple matter, since the flight time at the crossover point along the line is known. Subtracting it from the current intersection error gives an estimate of that part of the intersection error attributable to only the unlevelled tie at that crossover point. These components of the intersection errors due to the unlevelled tie are saved.

Once all the flights have been processed, a complete set exists of estimates of the component of the intersection errors attributable to the unlevelled tie, to which a polynomial is fitted as a function of time along the tie. This polynomial gives the required drift curve for the unlevelled tie. The drift curve is used to update the magnetic value at each crossover point along the unlevelled tie, which is then considered to be levelled and added to the set of levelled ties. The procedure is then repeated for the next tie to be levelled, ultimately giving a complete set of levelled ties.

Drifting lines by flight

Once the ties are considered levelled to each other, their drift is assumed to be zero and any remaining discrepancies at the crossover points are attributed to errors along the lines alone. Thus, the recalculated intersection errors can be used directly to give an estimate of the drift that occurred during each flight.

Lines are processed in flights at this stage to give the widest continuous time base available. Longer period trends in the intersection errors can, therefore, be detected than if the lines were processed individually.

Each flight is considered in turn and its drift curve estimated by fitting a polynomial to its intersection errors. This estimated drift curve is then used to update the magnetic value at each crossover point for each line in the flight.

Drifting individual lines

The procedure is identical to that for drifting lines by flight, except the individual drift curves are calculated for each line and used to update the corresponding magnetic values. This will remove effects that are line specific, such as heading error.

Drifting individual ties

Once the ties have been levelled and the lines drifted by both *flight* and *line*, the survey is essentially levelled. Any residual errors in the ties can be removed by drifting them to the lines. Several iterations of drifting lines and drifting ties can be performed, effectively 'shaking down' the survey, but have little if any effect after the first iteration.

Applying corrections to the full data set

At this stage only the magnetic values at each crossover point have been adjusted. It is a simple matter to calculate the corrections applied by subtracting the original values from the levelled ones. These corrections are interpolated along each line or tie by the local polynomial procedure described by Akima (1970) and subtracted from the original magnetic values, producing a levelled survey.

Polynomial fitting

All drift curves are approximated by polynomials fitted to the underlying data by the method of least squares. The success of the AGSO polynomial levelling method is critically dependent on the quality of these fits. Polynomials are used since the data being fitted can be well approximated by polynomials as a function of time over a localised region.

Least squares techniques are used to fit polynomials to the data to allow for random noise. That is, the intersection errors will always have a noise component due to navigational errors and any temporal variations with a wavelength less than twice the spacing between the ties and lines. The least squares technique minimises the discrepancies between the function being fitted and the actual data, but it does not require that the data be exactly honoured. In addition, data points can be weighted in proportion to their gradient, thereby recognising the fact that errors in navigation will have greater effect in areas of high gradient.

There are several problems associated with fitting polynomials to noisy data by the least squares technique.

- The degree of the polynomial should be small in comparison to the number of data points being fitted.
- The fit may be poor at the ends of lines/ties, since there is no constraint on the polynomial beyond the limits of the data and they may diverge from the expected result. The problem becomes more severe as the degree of the polynomial is increased.
- Data points should be evenly spread along the data interval being fitted, to ensure that the polynomial is well behaved between the data points. Irregular groupings of data points can lead to the polynomial diverging markedly from the 'expected' result between the groups of data points.
- Data points that are in error may have an undue influence on the result of the fit.

To force some control over the first problem, restrictions are automatically applied on the maximum degree of the fitted polynomial in comparison to the number of data points. For example, at least 3 points are required to fit a degree 1 polynomial, 5 for a degree 2, and so on.

The fourth problem is minimised by fitting the polynomials in a two-step process. An initial polynomial is fitted and 'rogue' points lying outside a few standard deviations of the resultant fit are rejected. The final polynomial is then calculated from the remaining points.

It is necessary to use high-order polynomials to fit the data well, but this exacerbates the problems associated with their use. To minimise these problems the concept of *piecewise* polynomials was introduced in an attempt to limit the degree of the polynomial, but at the same time achieving a close fit to the data. Instead of fitting a single polynomial over the entire data set to obtain an interpolated value at point N, a subset of the M closest points to point N is used. M is called the *window width*. A single polynomial is fitted to the M points, from which the interpolated value for point N is calculated. To obtain an interpolated value at point N+1 the window is moved along by 1 point and the procedure repeated. By reducing the window width, the data can be honoured as closely as required since, in the degenerate case of M=1, the data will be honoured exactly. Conversely, if the window width is chosen to be the entire data set, normal polynomial fitting results.

One disadvantage of the use of piecewise polynomials is that the resultant set of interpolated points will not necessarily vary as smoothly as required. This results because the polynomials fitted to successive subsets may be very different, even though successive subsets differ by only two points. Consequently, the interpolated points are filtered to smooth out this high frequency 'noise'. Another disadvantage is that interpolated values can only be directly derived for positions that coincide with the original data set. This necessitates another level of interpolation for intermediate points—a software consideration only.

For the polynomial fitting procedure to be fully effective, it is critical that the software in use allows the user to vary the parameters defining the piecewise polynomials and provides interactive visual feedback of the resultant fit. The user can then iteratively vary these parameters until a visually satisfactory fit is obtained at each step of the levelling process.

Tie sequencing when levelling ties

The success of levelling the ties is dependent on the sequence in which the ties are used. The earlier a tie is used, the greater effect it has on the overall result. This is because only the current set of levelled ties is used to predict the drift along a flight (see section ***Levelling ties***). Early on in the process there are not many crossover points being used, they may be poorly distributed along the flight, and any that are inaccurate may have a marked effect on the predicted drift. To minimise this effect, the ties should be sequenced according to the following factors:

- Ties should extend as close as possible across the full width of the survey area. Note that only those flights that intersect both the currently selected set of ties and the next tie in the list can be used. This may lead to regions of the unlevelled tie being uncontrolled if their geographical extent is beyond that of the currently levelled ties.
- To minimise the effects of navigation errors, preference should be given to ties over areas of low magnetic gradient.
- Preference should be given to ties flown during periods of quiet diurnal activity.
- The ties should be sequenced in such a way as to best define the drift curves for each flight in the tie levelling process. The wider the spread of points in time along the drift curve, the better. Thus, the first tie should be chosen as close to the centre of the survey as possible, the second towards one boundary of the survey, and the third close to the other boundary. Subsequent ties should be sequenced to lie as close as possible at the centre of the gaps across the survey area formed by the previously selected ties.

Appendix 2. AGSO micro-levelling

The AGSO micro-levelling tool is based on the procedure developed by Minty (1991). The technique is based on the assumption that residual errors in the data are characterised by being elongated along the flight-line direction and confined to individual lines. That is, visually, they would appear as streaks in a grid of data which can be theoretically detected and removed from the grid by the application of directional filters. The filtered grid can then be used to correct the original point-located data. The other constraint on the residual errors, especially for aeromagnetic data, is that they are expected to have a small dynamic range about zero.

The micro-levelling method is not rigorous, and cannot distinguish between levelling errors and real elongate anomalies parallel to the flight-line direction. Likewise, neighbouring lines may have errors of similar magnitude and it will only be the difference between the errors that can be detected.

The AGSO procedure for micro-levelling is as follows. If a grid of data is produced, then the residual errors will be

evident as spurious elongate anomalies characterised by the following:

- a wavelength in the flight-line direction greater than the tie-line spacing;
- a wavelength perpendicular to the flight-line direction of precisely twice the flight-line spacing;
- a relatively small dynamic range.

If one grid axis is parallel to the flight-line, then the spurious elongate anomalies can be removed from the grid by applying one-dimensional filters in turn to the rows and columns of the grid. The procedure is as follows:

- Create a grid from the original point located data, say grid A.
- Apply a high-pass filter to grid A in the direction perpendicular to the flight-line and store the result in grid B.
- Inspect grid B to restrict its dynamic range by setting all values that fall outside two user defined-limits to those limits.
- Apply a low-pass filter to grid B in the flight-line direction and store the result in grid C. Grid C should now contain only the elongate anomalies we wish to remove.
- Inspect grid C to restrict its dynamic range by setting all values that fall outside two user-defined limits to those limits. Grid C now contains the required residual errors or corrections to be applied to the survey data.
- Subtract grid C from the original grid, A, to get the final grid with all spurious elongate anomalies removed.
- Once a visually well-levelled grid is obtained, the corresponding grid of residual errors from step 5 is subtracted from the actual point-located data, thus completing the micro-levelling process.

Though conceptually simple, the implementation is difficult, owing to the mathematical limitations of digital filters and the subtle nature of errors compared with the large dynamic range of the data. The filters must detect all the residual errors, but at the same time exclude as many real anomalies as possible and introduce no artefacts, that is they must be designed to correspond with real anomalies as little as possible—they must be long and narrow. Therefore, the object of the exercise is to extract residual errors with the longest possible wavelength along the line; the shortest possible wavelength perpendicular to the lines; and the smallest dynamic range such that the procedure still produces a visually well-levelled grid. This is achieved by trial and error by varying the cut-off wavelengths and the allowed dynamic range of the various filtered grids.

Typically, good results are achieved with the following parameters:

- a long wavelength of the order of 1–3 times the tie spacing;
- a short wavelength of 2 times the line spacing;
- limits to the dynamic range of 5–10 nT.

To give some idea of the numbers involved, micro-levelling in a recent survey adjusted 30 per cent of the data by amounts of 1–10 nT and only 23 per cent of points by less than 0.1 nT, i.e. very significant adjustments were made.

Although the micro-levelling technique is conceptually simple, the design of adequate filters to implement it is not. Various filtering techniques have been investigated with the following combination producing the best results:

- Naudy non-linear filter (Naudy & Dreyer 1968) for high-pass filtering;
- Fuller band pass convolution filter (Fraser et al. 1966) for low-pass filtering.

The Naudy filter is not a true frequency filter, but operates by detecting anomalies of wavelength shorter than the defined cut-off. Such anomalies are then replaced by extrapolation from neighbouring data points. It is particularly effective as a high-pass filter, normally being used to detect high-frequency noise. Points to note are:

- it is designed to completely remove all anomalies of width less than a given cut-off, while those above the cut-off retain their original shape;
- the anomaly-detecting algorithm is not foolproof and some anomalies may not be removed;
- the interpolation algorithm will leave some data of wavelength shorter than the intended cut-off.

The convolution technique of Fuller is less than perfect: the response of the filter at the cut-off wavelength is not abrupt; for low-pass filters it acts as a smoothing operator where the area under the profile remains constant; and data extrapolation is required to allow filtered values to be determined up to the data boundaries. Therefore:

- leakage occurs around anomalies whose wavelength is comparable to the cut-off wavelength of the low-pass filter;
- when a high-amplitude, short-wavelength anomaly occurs, the base level of the filtered data about this anomaly is raised, producing an artefact similar to the residual errors that are to be removed.

For both types of filters, the data must be extrapolated beyond the edge of the grid to allow filtered values to be determined up to the grid boundary. These extrapolation techniques often lead to unwanted edge effects, especially where large anomalies occur along the grid boundary.

References

Akima, H., 1970. A new method of interpolating and smooth curve fitting based on local procedures. Journal of the Association of Computing Machinery, 17(4), 589–602.

Barton, C.E., 1988. Global and regional geomagnetic reference fields. Exploration Geophysics, 19, 401–416.

Barton, C.E. & Johnson, B D , 1988. Workshop report and discussion paper: geomagnetic reference fields; base-level and diurnal corrections to aeromagnetic data. Exploration Geophysics, 19, 447–452.

Boyd, T.J., 1992. An annotated outline of GPS. ASEG Preview, 15–26.

Briggs, I.C., 1974 Machine contouring using minimum curvature. Geophysics, 39(1), 39–48.

Fitzgerald & Associates, 1996. INTREPID geophysical processing system and visualisation tools. Desmond Fitzgerald & Associates, Unit 2, 1 Male Street, Brighton, Melbourne, Victoria 3186, Australia.

Foster, M.R., Jines, W.R. & Van Der Weg, K., 1970. Statistical estimation of systematic errors at intersections of lines of aeromagnetic survey data. Journal of Geophysical Research, 75(8), 1507–1511.

Fraser, D.C., Fuller, B.D. & Ward, S.H., 1966. Some numerical techniques for application in mining exploration. Geophysics, 31(6), 1066–1077.

Green, A.A., 1983, A comparison of adjustment procedures for levelling aeromagnetic survey data. Geophysics, 48(6), 743–753.

IAGA, 1991. International Association of Geomagnetism and Aeronomy, Division V, Working Group 8, International Geomagnetic Reference Field, 1991 Revision. Journal of Geomagnetism and Geoelectricity, 43, 1007–1012.

Minty, B.R.S., 1991. Simple micro-levelling for aeromagnetic data. Exploration Geophysics, 22, 591–592.

Naudy, H. & Dreyer, H., 1968. Non-linear filtering applied to aeromagnetic profiles. Geophysical Prospecting, 16(2), 171–178.

Ochadlick, A.R.Jr, 1989. Measurements of the magnetic fluctuations associated with ocean swell compared with Weaver's theory. Journal of Geophysical Research, 94(C11), 16,237–16,242.

Parkinson, W.D., 1983. Introduction to geomagnetism. Scottish Academic Press, Edinburgh.
Weaver, J.T., 1965. Magnetic variations associated with ocean waves and swell. Journal Of Geophysical Research, 70(8), 1921–1929.
Yarger, H.L., Robertson, R.R. & Wentland, R.L., 1978. Diurnal drift removal from aeromagnetic data using least squares. Geophysics, 43, 1148–1156.

AGSO Journal of Australian Geology & Geophysics, 17(2), 39–50

Fundamentals of airborne gamma-ray spectrometry

B.R.S. Minty[1]

The interpretation of gamma-ray spectrometric data requires an understanding of the underlying physics of the method, and an insight into the data acquisition, system calibration, and data processing and presentation procedures. The shape and intensity of a measured airborne gamma-ray spectrum is a complex function of many variables. Source thickness, source diameter, the detector response, and the distance between the source and the detector all affect the measured spectrum. The approach taken to calibration, therefore, is empirical. The source and detector are viewed as a single system, and the response of this system to changes in aircraft height (to obtain attenuation coefficients) and sources of known geometry and concentration (to obtain sensitivity coefficients) is measured. These empirically determined constants are, however, only valid for the source and source–detector geometry used in the calibration process.

Introduction

Airborne gamma-ray spectrometry requires consideration of many variables. For example, in addition to the geometry and physical property contrasts of the radioactive sources, the measured gamma radiation is a function of the size, efficiency and speed of the detector. It is also dependent on environmental and other effects, such as soil moisture, rainfall, vegetation, non-radioactive overburden, and the movement of airborne sources of radiation in the lower atmosphere. Interpretation of gamma-ray spectrometric data requires an understanding of the underlying physics of the method, and an insight into the data acquisition, system calibration, and data processing and presentation procedures. Effective interpretation also needs consideration of disequilibrium conditions in the uranium decay series, and an insight into the chemistry of potassium (K), uranium (U), and thorium (Th) in the natural environment.

The purpose of this paper is to review the fundamentals of airborne gamma-ray spectrometry. Basic radioactivity and the sources of gamma radiation are reviewed. This is followed by discussion on the interaction of gamma rays with matter, the response of an airborne detector system, and the properties of measured airborne gamma-ray spectra—including factors that affect the shape of measured spectra. The use of mathematical models of the gamma-ray field for survey design, data processing and interpretation are then briefly reviewed. The paper concludes with a discussion of the application of the method, including the corrections that must be applied to field data.

The review is intended to provide an insight into the theoretical and practical aspects of airborne gamma-ray spectrometry needed for an understanding of calibration and data-processing procedures.

Basic radioactivity

Some isotopes are unstable and change to more stable nuclei by the emission of energetic ionising radiation. These isotopes are called radioactive isotopes or radioisotopes. Each radioisotope has a characteristic probability associated with the radioactive disintegration of its nuclei. This is the so-called 'half-life' of the isotope and is the time taken for half the nuclei to decay. Thus after one half-life, half the original radioactive isotopes remain, and after two half-lives, one quarter of the original radioactive isotopes remain, and so on.

The three main types of radiation arising from radioactive decay are alpha, beta, and gamma rays. Alpha rays (or alpha particles) are fragments of the original nuclei and consist of 2 protons and 2 neutrons. They have a discrete energy, and the emitting isotope can be identified by this energy. Since alpha particles have both a charge and mass, they are easily absorbed by a few centimetres of air Beta particles are identical to electrons and carry a unit negative charge. They do not have a characteristic energy. Beta particles are less easily absorbed than alpha particles and can travel up to a metre in air.

The emission of an alpha or beta particle usually leaves the new nucleus in an excited state and the surplus energy is radiated as gamma rays. These are quanta or photons of energy which are very penetrating because they possess neither charge nor mass. Gamma rays can penetrate up to 30 cm of rock and several hundred metres of air, and are the only choice available for the remote sensing of terrestrial radioactivity. Each gamma-ray photon has a discrete energy, and this energy is characteristic of the source isotope. This forms the basis of gamma-ray spectrometry, i.e. the measurement of gamma-ray photon energy allows the source of the radiation to be diagnosed. Energies of geological interest lie between 0.2 and 3 MeV, which corresponds to electromagnetic wavelengths of about 3×10^{-12} m and a frequency of about 3×10^{19} Hz.

The radioactivity decay law

While it is impossible to predict the exact moment at which a particular atom will decay, each radioisotope has a characteristic rate of disintegration, which is proportional to the number of nuclei present. Thus the number of nuclei (dN) which decay during a short time (dt) is proportional to the number of nuclei present (N). i.e.

$$\frac{dN}{dt} = -\lambda N \tag{1}$$

or

$$N = N_0 e^{-\lambda t} \tag{2}$$

where λ is the decay constant, N_0 is the number of radionuclides present at time $t = 0$, and N is the number of nuclides present after a time t. A related constant is the previously mentioned 'half-life'. When $N = \frac{1}{2} N_0$ we have

$$t_{\frac{1}{2}} = \frac{0.693}{\lambda} \tag{3}$$

Usually, the activity of the source (number of disintegrations per unit time) is measured, and the activity also decreases exponentially over time with the same half-life as that used in equation 2.

Multiple decay and chain disintegration

Some radionuclides have more than one mode of decay. For example, 64 per cent of ^{212}Bi disintegrations are by alpha particle emission to ^{212}Po, and 34 per cent are by beta particle emission to ^{208}Th. But irrespective of the type of radiation we are measuring, the observed half-life is always the same.

Radioactive decay often occurs in a series (or chain) with a number of daughter products, which are also radioactive, and terminates in a stable isotope. In this case, the net rate at which a daughter changes is the difference between the rate at which it is produced and the rate at which it decays. The growth of a radioactive daughter from its radioactive parent is thus controlled by the half-lives of both isotopes.

[1] Australian Geological Survey Organisation, GPO Box 378, Canberra, ACT 2601

Sources of gamma-radiation

The sources of natural gamma-radiation can be conveniently divided into 3 groups, according to their origin (Kogan et al. 1969). The first group includes ^{40}K, ^{238}U, ^{235}U and ^{232}Th, which are believed to have been synthesised during the creation of the universe and have half-lives of the same order as the age of the earth (5×10^9 years). The second group comprises radioactive isotopes that are daughter products from the decay of isotopes in the first group. These have half-lives ranging from small fractions of a second to 10^4–10^5 years. The third group would include isotopes created by external causes, such as the interaction of cosmic rays with the Earth and its atmosphere.

Natural sources of radiation

Potassium, U, and Th are the only naturally occurring elements with radioisotopes that produce gamma rays of sufficient energy and intensity to be measured at airborne survey heights. Average crustal abundances are K—2%, U—2.7ppm, Th—8.5ppm. These elements have been decaying continually since their creation, and their concentration in the Earth is, therefore, continually decreasing. But these isotopes have very long half-lives and, therefore, are still relatively abundant. The decay of these radioisotopes and their daughters is sometimes accompanied by gamma-ray emissions.

^{40}K is the only radioactive isotope of K, and occurs as 0.012 per cent of natural K. Eighty-nine per cent of ^{40}K nuclei decay by electron emission (i.e. beta particle) to ^{40}Ca, while the remaining 11 per cent decay by electron capture to ^{40}Ar. This is followed by the emission of a single gamma-ray photon with energy 1.46 MeV. Since ^{40}K occurs as a fixed proportion of K in the natural environment, the gamma-ray flux from ^{40}K can, therefore, be used to estimate the total amount of K present. K is a much weaker source of radiation than the U or Th series, but because it is so abundant (2%), it is found to be an equal contributor to U and Th in the natural radiation flux.

Uranium occurs naturally as the radioisotopes ^{238}U and ^{235}U, which give rise to decay series that terminate in the stable isotopes ^{206}Pb and ^{207}Pb, respectively (Tables 1, 2). ^{238}U has a half-life of 4.47×10^9 years. The half-life of ^{235}U is 7.13×10^8 years. Since these half-lives are not the same, it follows that the ratio $^{235}U/^{238}U$ is changing very slowly with time. ^{235}U forms only 0.72 per cent of naturally occurring U and the gamma-ray energies in its decay series are too low to be diagnostic in airborne gamma-ray surveying.

Thorium occurs naturally as the radioisotope ^{232}Th, which gives rise to a decay series that terminates in the stable isotope ^{208}Pb (Table 3).

Note that neither ^{238}U nor ^{232}Th emit gamma rays, and we thus rely on the gamma-ray emissions from their radioactive daughter products to estimate their concentrations.

Disequilibrium

Disequilibrium in the U decay series is a serious source of error in gamma-ray spectrometric surveying. When radioactive decay results in an unstable daughter product with a half-life shorter than that of the parent, a situation will eventually be reached where the daughter product is decaying as rapidly as it is being produced. If this is true for all the daughters in a decay series, then the series is said to be in secular equilibrium, and the total activity decreases at the same rate as that of the original parent. Note that equal activity under equilibrium conditions does not imply equal concentration, since the relevant half-lives must be considered when calculating the relative concentration of members of a decay series.

Disequilibrium occurs when one or more decay products are completely or partially removed or added to the system, and it may take days, weeks or even millions of years to restore equilibrium, depending on the half-lives of the radioisotopes involved. Thorium rarely occurs out of equilibrium in nature, and there are no disequilibrium problems with K, since it only exhibits a single photo-peak. However, in the U decay series, disequilibrium is common in the natural environment. Fractionation can be due to both physical and chemical mechanisms. For example, the nuclear recoil from an atomic disintegration can result in an isotope being moved from its original position in a crystal lattice into a position more accessible to oxidising solutions, such as within microfractures. Examples of chemical mechanisms are coprecipitation (Ra preferentially scavenged from solution by hydroxides of Fe), adsorption (Ra preferentially adsorbed onto the surface of clays), and biological uptake (Ra more readily absorbed into plant tissues than U). Disequilibrium can result from fractionation at (at least) 5 positions in the ^{238}U decay series:

- ^{238}U can be selectively leached relative to ^{234}U, particularly in a clay matrix;
- ^{234}U can be selectively leached relative to ^{238}U;
- ^{230}Th can be selectively leached relative to the other isotopes in the chain;
- ^{226}Ra fractionation; and
- ^{222}Rn (radon gas) is very mobile and can escape into the atmosphere from soil and rock fissures.

Both U and Ra are soluble and, thus, transportable. In an oxidising environment, U is preferentially leached relative to Ra, and in a reducing environment Ra may be preferentially leached relative to U.

If ^{222}Rn escapes, the short-lived nuclides ^{214}Bi and ^{214}Pb, which occur below ^{222}Rn in the U decay series and are the major gamma-ray emitters in this series, will decay to insignificant activities within hours. The time taken for equilibrium to be re-established in this case is about 38 days, as the time needed to restore 99.9 per cent equilibrium for a disturbed member of a series is about 10 times the half-life of the disturbed member. Where there has been preferential leaching of ^{238}U and ^{234}U relative to Ra, it can take up to a million years to re-establish equilibrium. In this case the ^{214}Bi and ^{214}Pb concentrations will remain high for a very long time—even though ^{238}U and ^{234}U may have been completely removed. This is due to the long half-life of ^{230}Th, which intervenes between ^{234}U and $^{214}Bi/^{214}Pb$ in the U decay series (Table 1).

Note that isotopes of Rn also occur in the ^{235}U decay series (^{219}Rn—emanation Actinon) and in the ^{232}Th decay series (^{220}Rn—emanation Thoron). These are not sources of disequilibrium, since their half-lives are very short.

Accurate estimates of U from gamma-ray spectrometry, where we rely on the abundance of isotopes such as ^{214}Bi and ^{214}Pb, which occur far down in the radioactive decay chain, require equilibrium conditions that are frequently not present. These estimates are, therefore, usually reported as 'equivalent uranium' (eU), reminding us that the accuracy of these is dependent on the presence of equilibrium conditions. Thorium is also usually reported as 'equivalent thorium' (eTh), although the Th decay series is almost always in equilibrium.

Background radiation

Any radiation not originating from the ground is regarded as 'background', since it is of no geological significance and needs to be removed from the observed data. There are four sources of background radiation flux—atmospheric radon, cosmic background, aircraft background, and fallout products from atomic explosions and nuclear accidents.

Atmospheric ^{222}Rn and its daughter products, specifically ^{214}Bi and ^{214}Pb, are the major contributors to the background. ^{222}Rn (radon gas) is very mobile and can escape into the atmosphere from soil and rock fissures in response to the 'pumping' action of changing temperature and pressure. Its

Table 1. ^{238}U decay series (simplified after Radiological Health Handbook 1970, and Ivanovich & Harmon 1982).

Nuclide	*Half-life*	*Major radiation energy (MeV) and intensity**					
		α		β		γ	
^{238}U	4.468×10^9 y.	4.15 4.19	(23%) (77%)	–		–	
^{234}Th	24.1 d.	–		~0.103 0.191	(19%) (81%)	0 063 0.093	(3.5%) (4%)
^{234}Pa	1.18 m	–		2.29	(98%)	0.765 1.001	(0.30%) (0.60%)
99 86% / 0 14%							
^{234}Pa	6.7 h	–		0.53 1.13	(66%) (13%)	0 10 0.70 0.90	(50%) (24%) (70%)
^{234}U	2.48×10^5 y.	4.72 4.77	(28%) (72%)	–		0.053	(0.2%)
^{230}Th	7.52×10^4 y	4.62 4.68	(24%) (76%)	–		0.068 0.142	(0.6%) (0.07%)
^{226}Ra	1602 y.	4.60 4.78	(5 5%) (94 5%)	–		0.186	(4%)
^{222}Rn	3.825 d	5.49	(~100%)	–		0.510	(0.07%)
^{218}Po	3.05 m	6 11	(100%)	0 33	(100%)	–	
99 98% / 0 02%							
^{214}Pb	26 8 m	–		1 03	(6%)	0.295 0 352	(19%) (36%)
^{218}At	2 s	6.65 6.70	(6%) (94%)	0.67	(94%)	–	
^{214}Bi	19.7 m	5 61	(100%)	3.26	(100%)	0.609 1.120 1 764	(47%) (17%) (17%)
99.96% / 0 04%							
^{214}Po	164 μs	7.83	(100%)	–		0 799	(0.014%)
^{210}Tl	1.32 m	–		2 3	(100%)	0.296 0.795 1 31	(80%) (100%) (21%)
^{210}Pb	~22 y.	3 7	(1.8×10^{-8}%)	0.017 0.064	(85%) (15%)	0 047	(4%)
^{210}Bi	5.02 d.	4.93 4.89 4.59	(60%) (34%) (5%)	1.155	(100%)	–	
~100% / ~.00001%							
^{210}Po	138.3 d	5 30	(100%)	–		0 803	(0.0011%)
^{206}Tl	4 19 m	–		1.520	(100%)	–	
^{206}Pb	Stable	–		–		–	

* Intensity refers to percentage of disintegrations of the nuclide itself, not to the original parent of the series

daughter products ^{214}Bi and ^{214}Pb attach to airborne aerosols and dust particles and their distribution is thus a function of air movements and wind patterns. Foote (1969) showed that atmospheric background first increased and then decreased during the course of a day, and attributed this to the rise of the near-surface temperature inversion layer and its subsequent break-up in the afternoon. During warm settled weather it is common for atmospheric ^{214}Bi and ^{214}Pb to be at a maximum close to the ground early in the morning and to decrease during the day as increasing air turbulence mixes the lower atmosphere. Temperature inversion layers over topographic depressions and lakes often trap Rn close to the ground and under still air conditions there can be measurable differences in atmospheric radioactivity at sites only a few kilometres apart (Darnley & Grasty 1971).

Primary cosmic radiation from outside our solar system and from the sun reacts with atoms and molecules in the upper atmosphere and generates a complex secondary radiation. This radiation reacts with the air, aircraft and detector to produce the measured 'cosmic' gamma-ray background. In the lower atmosphere, this radiation has a constant energy distribution, but it decreases in amplitude with decreasing altitude (Aviv & Vulcan 1983). The effect of cosmic interaction with rocks is small (Gregory 1960), and variations in cosmic

Table 2. ^{235}U decay series (simplified after Radiological Health Handbook 1970, and Ivanovich & Harmon 1982).

Nuclide	*Half-life*	*Major radiation energy (MeV) and intensity**					
		α		β		γ	
^{235}U	7.13×10^8 y.	4.36	(18%)	–		0.143	(11%)
		4.39	(57%)			0.185	(54%)
		4.1-4.6	(8%)			0.204	(5%)
^{231}Th	25 64 h	–		0 300	(~100%)	0.026	(2%)
						0 084	(10%)
^{231}Pa	3.43×10^4 y.	5.01	(<20 %)	–		0.027	(6%)
		4.99	(25 4%)			0.29	(6%)
		4.94	(22.8%)				
^{227}Ac	22 y.	4.95	(48 7%)	0.046	(100%)	0.070	(0 08%)
		4.94	(36 1%)				
98 8% 1 2%		4.87	(6 9%)				
^{227}Th	18 17 d	5.76	(21%)	–		0.050	(8%)
		5.98	(24%)			0.237	(15%)
		6 04	(23%)			0 31	(8%)
^{223}Fr	21 m	5.34	(005%)	1.15	(100%)	0 050	(40%)
						0.080	(13%)
						0.234	(4%)
^{223}Ra	11.68 d.	5 61	(26%)	–		0.149	(10%)
		5.71	(53.7%)			0 270	(10%)
		5 75	(9.1%)			0.33	(6%)
^{219}Rn	3.92 s	6 42	(8%)	–		0.272	(9%)
		6.55	(11%)			0.401	(5%)
		6 82	(81%)				
^{215}Po	1.83 ms	7.38	(100%)	–		–	
^{211}Pb	36 1 m	–		0.95	(1 4%)	0 405	(3.4%)
				0 53	(5.5%)	0 427	(1.8%)
				1.36	(92.4%)	0.832	(3 4%)
^{211}Bi	2.16 m	6.28	(17%)	0.60	(0 28%)	0.351	(14%)
0 32% 98 68%		6 62	(83%)				
^{211}Po	0 52 s	7 43	(99%)	–		0 570	(0.5%)
						0 90	(0.5%)
^{207}Tl	4.79 m	–		1.44	(100%)	0 897	(0.16%)
^{207}Pb	Stable	–		–		–	

* Intensity refers to percentage of disintegrations of the nuclide itself, not to the original parent of the series

background on a day-to-day basis due to changes in atmospheric pressure are minor (Grasty & Carson 1982).

Aircraft background refers to radiation due to trace amounts of K, U and Th in the aircraft and equipment, as well as the detector itself. This component of background is constant.

The main fallout from nuclear explosions and accidents that affects airborne gamma-ray spectrometry is ^{137}Cs. This exhibits a single photopeak at 0.662 MeV and has a half-life of about 30 years.

Interaction of gamma rays with matter

There are three principal processes by which gamma rays interact with matter—the photoelectric effect, Compton scattering, and pair production.

The ***photoelectric effect*** results in all the energy of the photon being absorbed by the bound electron of an atom (as kinetic energy). This is the predominant absorption process at low energy levels.

Compton scattering is the process whereby an incident

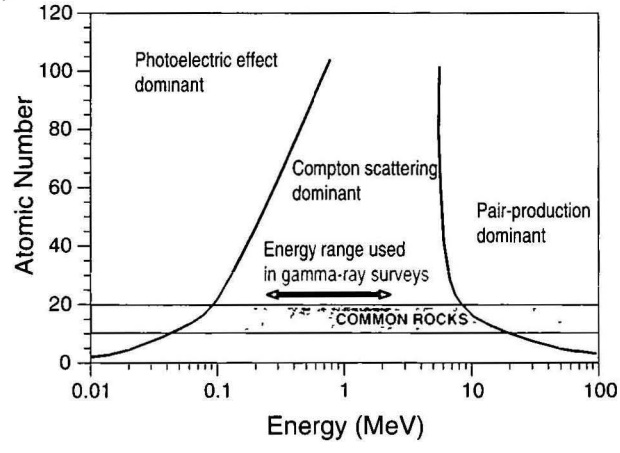

Figure 1. The interaction of gamma rays with matter.

Table 3 ^{232}Th decay series (simplified after Radiological Health Handbook 1970, and Ivanovich & Harmon 1982).

Nuclide	*Half-life*	*Major radiation energy (MeV) and intensity**					
		α		β		γ	
^{232}Th	1.39×10^{10} y.	3.95	(24%)	–		–	
		4.01	(76%)				
^{228}Ra	5.75 y.	–		0.055	(100%)	–	
^{228}Ac	6.13 h	–		2.11	(100%)	0.34	(15%)
						0.908	(25%)
						0.96	(20%)
^{228}Th	1.913 y.	5.34	(28%)	–		0.084	(1.6%)
		5.42	(71%)			0 214	(0.3%)
^{224}Ra	3.64 d.	5.45	(5.5%)	–		0.241	(3.7%)
		5.68	(94.5%)				
^{220}Rn	55.6 s	6 30	(~100%)	–		0.55	(0.07%)
^{216}Po	0.145 s	6.78	(100%)	–		–	
^{212}Pb	10.64 h	–		0.580		0 239	(47%)
						0.300	(3.2%)
^{212}Bi	60.5 m	6 05	(70%)	2 25	(100%)	0.040	(2%)
		6.09	(30%)			0.727	(7%)
						1.620	(1 8%)
64.0% → ^{212}Po	304 ns	8.78	(100%)	–		–	
36 0% → ^{208}Tl	3.1 m	–		1 80	(100%)	0.511	(23%)
						0.583	(86%)
						0.860	(12%)
						2 614	(100%)
^{208}Pb	Stable	–		–		–	

* Intensity refers to percentage of disintegrations of the nuclide itself, not to the original parent of the series

photon loses part of its energy to an electron, and is 'scattered' at an angle to its original direction. The energy lost by the gamma ray is transferred as kinetic energy to the electron. This is the predominant process for moderate energy levels.

Pair production is the process whereby an incident photon is completely absorbed. This results in the creation of an electron-positron pair in the electrostatic field of a nucleus and with a total energies equal to that of the original photon. This can occur at energy greater than 1.02 MeV and predominates at very high energy and particularly in materials of high atomic number. The life expectancy of the positron is very short. The positron annihilates with an electron producing two 0.511 MeV gamma rays.

Figure 1 illustrates the relationship between these processes, the gamma-ray energy of the incident photon, and the atomic number of the absorbing medium. From this it is clear that Compton scattering is the predominant process for the range of energy and absorbing media encountered in airborne gamma-ray surveying. The gamma-ray photons lose energy through successive Compton scattering events, until eventually the resulting low-energy photons are completely absorbed through the photoelectric effect. Typically, gamma-ray photons in the energy range 0.7–3.0 MeV lose (on average) slightly more than half of their energy during each scattering event. Gamma-ray photons that have been scattered twice will have their energies reduced (on average) to about one-fifth of their original energy (Bailey 1986). Thus, most gamma-ray photons detected in this energy range have either been scattered only once or not at all.

Both Compton scattering and the photoelectric effect are electron collision processes, and the attenuation of gamma rays in most materials encountered in airborne gamma-ray surveying is thus proportional to the electron density of the material. Wood, for example, can be used to shield the detectors from radioactive sources during experiments on the ground, and thus simulate the attenuation of gamma rays by hundreds of metres of air.

Properties of airborne gamma-ray spectra

K and the U and Th equilibrium series each have a characteristic theoretical line spectrum (Figs 2, 3, 4). These line spectra represent the energy distribution of emitted photons at the source. But the energy of these original photons is degraded by Compton scattering in the source, in matter between the source and the detector, and in the detector itself. Figures 5–7 show the simulated gamma-ray flux due to K, U, and Th at 300 m height (Kirkegaard & Lovborg 1974). Each radioelement generates a sharp peak representing the energy of directly transmitted photons. This is superimposed on the spectrum of Compton scattered photons, which show a continuum of energy up to the maximum of the photons emitted by the isotope (e.g. Fig. 5). This continuum is due to single and multiple scattering events between the source and the detector. The gamma-ray flux distributions shown in Figures 6 and 7 are then the sum of the flux spectra for each of the radioelements in the respective decay series. The relative contribution of scattered and unscattered photons to the gamma-ray flux at airborne altitude depends on the source geometry (thickness

and lateral extent) and on the amount of attenuating material between the source and the detector.

The shape of the gamma-ray flux spectrum at airborne heights is thus a function of the concentration of radioelements in the source, the source geometry, the thickness of any non-radioactive overburden, and the height of the detector above the ground. In practice, it is impossible to record the gamma-ray flux spectra shown in Figures 5–7. This is because the shape of the measured spectrum, in addition to the factors mentioned above, is also a function of the detector response. These are discussed below:

The detector response

Tl-doped NaI scintillation crystals are universally used in airborne gamma-ray spectrometry to detect gamma rays. The effect of the scattering and absorption of an incident gamma-ray photon within the detector crystal is the production of one or more highly energetic electrons. NaI(Tl) scintillation crystals have the special property of converting the energy transferred to the electrons into a flash of light. The physical processes

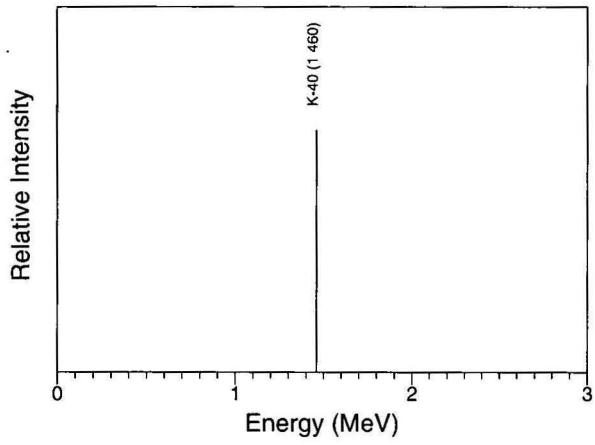

Figure 2. Potassium line spectrum.

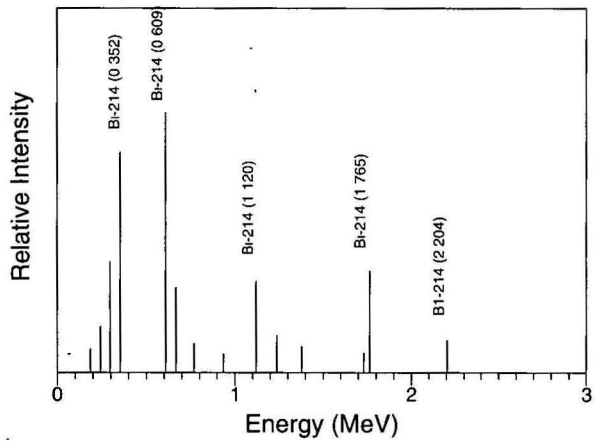

Figure 3. Uranium line spectrum.

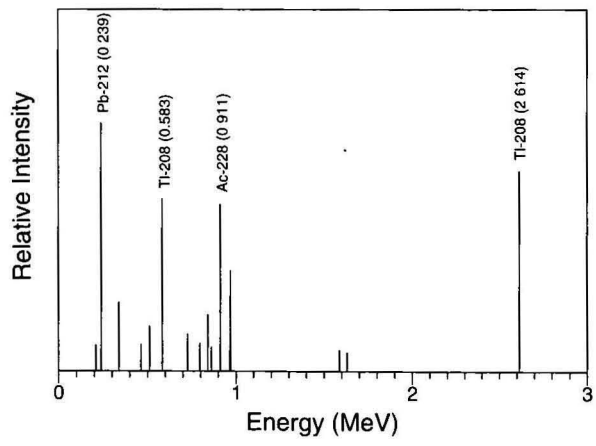

Figure 4. Thorium line spectrum.

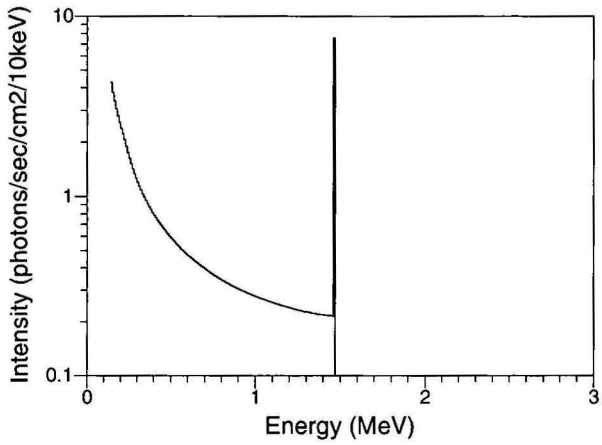

Figure 5. Simulated potassium gamma-ray flux at 300 m altitude.

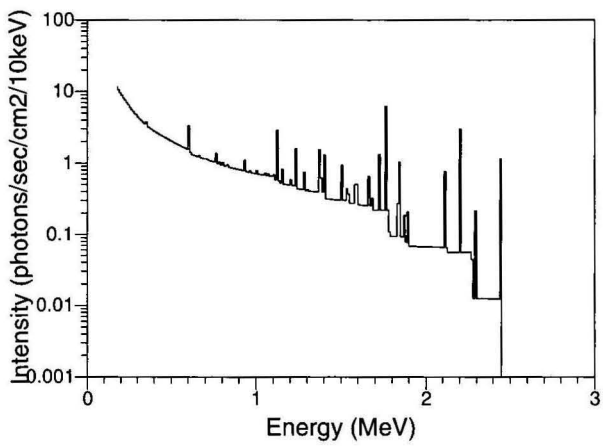

Figure 6. Simulated uranium decay series gamma-ray flux at 300 m

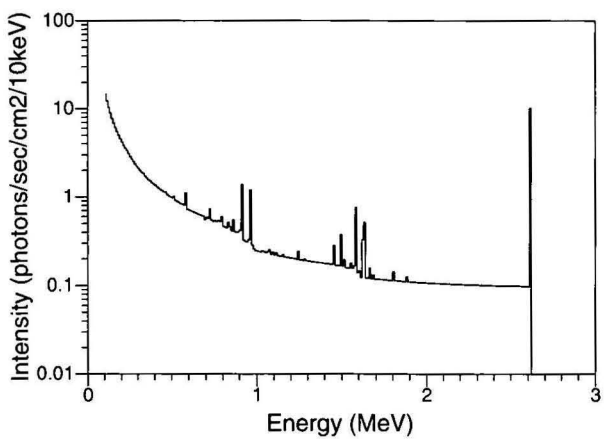

Figure 7. Simulated thorium decay series gamma-ray flux at 300 m altitude.

involved in the scintillation effect are quite complex, and will not be discussed here. Typically, an incident photon might suffer several Compton scattering events within the crystal before being absorbed by the photoelectric effect. The sum of all the photons of visible light released by the process is proportional to the gamma-ray energy of the incident gamma ray.

A photomultiplier tube is attached to the end of each scintillation crystal. Photons of visible light produced in the body of the crystal liberate electrons from the photomultiplier's photocathode. The electrons are multiplied and converted to electrical signals. The amplitude of output pulses from the photomultiplier tubes is proportional to the energy of the original gamma-ray photons.

The airborne gamma-ray detector modifies the spectrum considerably. The main aspects of the detector response are: detector efficiency as a function of energy; directional sensitivity; resolution; dead time; and factors contributing to the shape of the actual pulse height spectrum measured by spectrometers.

Detector efficiency can be considered as a measure of the probability that a photon emitted from the source will interact in the detector with the loss of a finite amount of energy. NaI(Tl) detectors are far more efficient at absorbing low-energy photons than high-energy photons. This is one reason for the higher count rates in the lower-energy channels. Also, slab crystals laid side by side present a greater cross-sectional area to photons approaching from below the aircraft than from the side, and this gives the detector a directional sensitivity.

Detector resolution is a measure of a detector's ability to distinguish between two gamma rays of only slightly different energy. In airborne gamma-ray spectrometry, this is usually defined as the width of a photopeak at half the maximum amplitude divided by the photopeak energy. Typical resolutions are 10% for ^{137}Cs at 0.662 MeV and 7% for ^{208}Tl at 2.615 MeV.

Dead time refers to the finite time required for the spectrometer to process individual photons. This should be as small as possible, since the total counting time available is reduced by the time taken to process all photons detected.

Heath (1964) gave a good summary of ***factors affecting the shape of the pulse amplitude spectrum***, such as escape events, accidental summing, and the characteristic 'Compton edge', representing maximum energy transfer between the photon and a recoil electron. Some photons may escape the detector after being only partially absorbed, and their interaction would result in a measured energy somewhat lower than that of the incident photon ('Compton scatter escape'). In each 'pair-production' event, two 0.51 MeV gamma rays are produced by the annihilation of the positron. Escape of either or both of these photons results in recorded pulses with energy 0.51 MeV and 1.02 MeV less, respectively, than that of the incident photon ('pair-production escape'). This effect can lead to recognisable 'escape peaks' in the spectrum, with energy either 0.51 MeV or 1.02 MeV lower than prominent photopeaks. A similar effect occurs when the 28 keV X-ray given off during the photoelectric process escapes the crystal without further interaction ('x-ray escape'). Also, pair production outside the crystals can result in either or both of the 0.51 MeV photons being detected, to produce 'annihilation radiation peaks'.

Note that the photopeaks in a typical spectrum are essentially Gaussian in shape. This is mainly due to statistical processes and electronic noise in the detector, which contribute to the detector's energy resolution. It is also partly due to energy degradation from scattering, together with absorption on the low-energy side of the peak, and the effect of 'accidental summing' on the high-energy side of the peak. The latter effect is due to the accidental time-coincidence between events in the detector. Backscattering from metals and other absorbers close to the detector also contribute to the observed spectrum.

Source–detector geometry

Both source thickness and source type (i.e. point, line, or broad) affect the shape of the observed spectrum. Gregory & Horwood (1961) showed that with increasing source thickness there is a greater build-up of the Compton continuum. The photopeaks—which are the distinguishing characteristic of all spectra—are reduced relative to the Compton background. This effect is most severe in the low-energy region of the spectrum, since low-energy photons are more easily attenuated than high-energy photons. Also, the build-up due to Compton scattering is greatest in the low-energy region of the spectrum. A similar change in spectrum shape is seen between spectra from point and broad sources; i.e. with broad sources, greater Compton scattering in the sources themselves results in a build-up of the Compton continuum.

Radiation from the ground is attenuated by material between the source and the detector, as well as within the source itself (e.g. barren regolith, vegetation, moisture, and air) Again, with increasing attenuation the photopeaks diminish relative to the energy continuum because of scattered radiation. However, the attenuation of low-energy radiation is greater than that of high-energy radiation, with the result that even with increased energy degradation due to scattering, the total flux at all energy levels is reduced for increasing source–detector distances or increasing cover. Mass-attenuation coefficients and half-thicknesses for various gamma-ray energy levels in air, water, and concrete are given in Table 4 (Grasty 1979). The effect of detector height on total flux is also important. For example, a 10 per cent change in height at 100 m will cause an 8 per cent change in the measured total-count count rate.

Measured spectra are thus complex functions of many variables. In addition to the concentration and geometry of the source, the spectra are also functions of the height of the detector above the ground, the thickness of any non-radioactive overburden, and the response function of the detector. Typical examples of K U, and Th spectra that would be recorded at airborne height with a long integration time are shown in Figures 8, 9, & 10. These were recorded on the ground using specially constructed radioactive sources. Wood was used to shield the detectors from the sources, thus simulating the attenuation of the gamma rays by air. The measured spectra are continuous functions of energy. A comparison with the simulated fluxes (Figs 5, 6, 7—note log scale on ordinates) illustrates the large effect the detector response has on the measured data. Obviously, the detector response must be considered in the calibration of airborne spectrometers and processing of data.

Environmental effects

Environmental factors that can influence gamma-ray spectrometry include non-radioactive overburden, air temperature and pressure, precipitation, temperature-inversion layers and air movements in the lower atmosphere, and soil moisture.

Barren overburden, because of its high density, can dramatically reduce the radiation output from the Earth's surface. Just 2 cm of cover can reduce it by 35 per cent. In some areas, dense vegetation may have the same capacity to shield the source of radiation as 50 m of air. The trunks of trees in dense forest will have a collimating effect on radiation from the ground. Changing temperature and pressure can lead to a change in air density by up to 30 per cent. This translates into a corresponding change in height correction factors. The effect of Rn trapped in temperature-inversion layers close to the ground under early morning still-air conditions was mentioned earlier. This can adversely affect estimates of background and, ideally, flying should only commence once thermal activity has thoroughly mixed the radon through the lower atmosphere.

Table 4. Mass attenuation coefficient and half-thickness for various gamma-ray energies in air, water, and concrete (after Grasty 1979).

	Mass-attenuation coefficient (cm^2/g)			*Half-thickness*[a]		
Photon energy (MeV)	*Air*[b]	*Water*	*Concrete*[c]	*Air*[d] *(m)*	*Water (cm)*	*Concrete (cm)*
0.01	4.82	4 99	26.5	1.11	0.139	0.01
0.10	0 151	0 168	0.171	35.5	4.13	1.62
0.15	0.134	0.149	0.140	40.0	4 65	1.98
0 20	0.123	0.136	0.125	43.6	5.10	2.22
0.30	0.106	0 118	0 107	50.6	5.87	2.59
0.40	0.0954	0 106	0.0957	56.2	6.54	2.90
0.50	0 0868	0.0966	0 0873	61.8	7.18	3 18
0.60	0.0804	0.0894	0.0807	66.7	7.75	3 43
0.80	0.0706	0.0785	0.0708	75.9	8.83	3 92
1.0	0 0635	0 0706	0.0637	84.4	9.82	4.35
1.46	0 0526	0.0585	0 0528	102	11.8	5.25
1 5	0 0517	0.0572	0.0519	104	12.1	5 34
1.76	0.0479	0.0532	0 0482	112	13 0	5.75
2.0	0.0444	0.0493	0.0447	121	14.1	6.20
2.62	0 0391	0.0433	0.0396	137	16.0	7.00
3 0	0.0358	0.0396	0.0365	150	17 5	7 60

[a] Thickness of material that reduces the intensity of the beam to half its initial value

[b] 75.5% N, 23 2% O, 1.3% Ar by weight.

[c] For compositions of typical concrete see Hubbel & Berger (1968). Density of concrete is 2 5 g/cm^3.

[d] For air at 0°C and 76 cm of Hg with a density of 0.001293 g/cm^3.

The effect of rainfall is complicated. In general, a 10 per cent increase in soil moisture will decrease the radiation flux from the surface by about the same amount. But for U estimation, the effect of rainfall is one of competing effects. The daughter products of airborne Rn attach themselves to dust particles in the atmosphere. The radioactive precipitation of these particles by rain can lead to apparent increases of more than 2000 per cent in U ground concentration (Charbonneau & Darnley 1970). Surveying should thus cease in areas of recent rainfall until anomalous surface activity has had a chance to decay (about 3 hours). However, Rn escapes more freely from dry soil than from wet soil. High moisture content can actually lead to an increase in the radiation output due to U, because of a build-up of Rn in the soil.

Basic models

The mathematical modelling of gamma-ray fields provides an insight into the physics of the airborne gamma-ray spectrometric method. This insight is important because it provides the necessary tools for effective survey design and an understanding of the physics required for data processing and interpretation.

Physical models

Perhaps the simplest approach to the modelling of gamma-ray fields is a semi-empirical one based on monoenergetic (i.e. unscattered) radiation. A radiation intensity law for an ele-

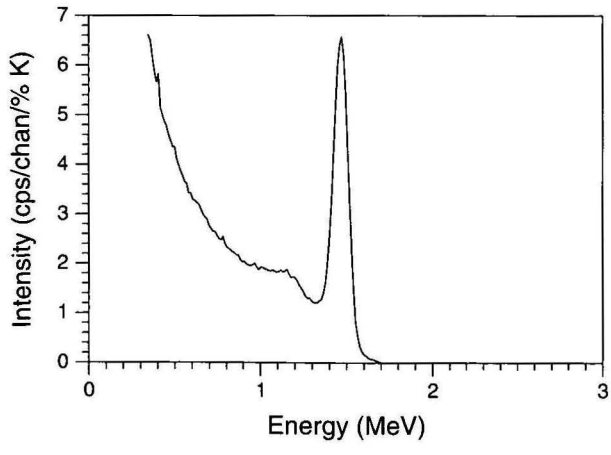

Figure 8. Simulated potassium spectrum at 100 m altitude with a large integration time.

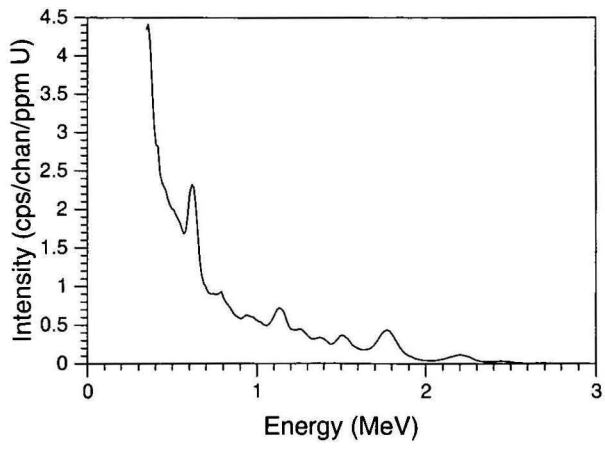

Figure 9. Simulated uranium spectrum at 100 m altitude with a large integration time.

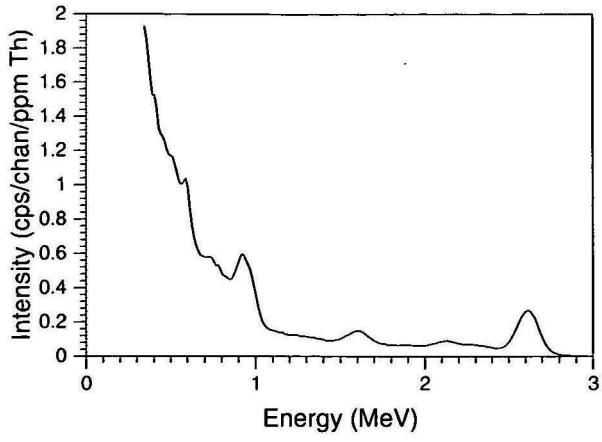

Figure 10. Simulated thorium spectrum at 100 m altitude with a large integration time.

mentary point source is either assumed or determined by laboratory experiment. This expression is then integrated over various geometries to obtain the intensities due to the required sources. For a collimated beam of radiation intensity, I, the amount of radiation, dI, absorbed by an absorber of thickness dx is proportional to both I and dx (Grasty 1979). Thus

$$dI = -\mu I dx \tag{4}$$

where μ is called the linear attenuation coefficient and is characteristic of the absorbing medium and the energy of the radiation. If $I=I_0$ for no absorber present (x=0), then

$$I = I_0 e^{-\mu x} \tag{5}$$

which is the classical law of absorption. This relationship has been verified experimentally (Fano 1953).

However, gamma rays are also subject to the inverse-square law of attenuation for point sources of electromagnetic radiation. Thus, for monoenergetic radiation from an isotropic point source at a distance r, from the detector, we have

$$I \propto \frac{e^{-\mu r}}{r^2} \tag{6}$$

Consider now a two-layer model with the Earth as an infinite half-space with a constant density and radioelement concentration overlain by non-radioactive air of constant density (Figure 11). Assume, also, that the detector at point P presents an equal cross-sectional area in all directions and has an efficiency which is not directionally dependent. Then, the monoenergetic radiation intensity, dI, due to a photopeak of intensity E_0 from gamma-ray emissions by a volume element dV within the Earth is given by (Clark et al. 1972)

$$dI = \frac{A\varepsilon}{4\pi R^2} e^{-\mu_e r_e} e^{-\mu_a r_a} N dV \tag{7}$$

where A = effective cross-sectional area of the detector

ε = photopeak efficiency of the detector for gamma rays of energy E_0

μ_e, μ_a = linear attenuation coefficients for the Earth and air respectively

r_e, r_a = the distances through the Earth and air that the gamma rays travel ($R=r_a+r_e$)

Equation 7 can then be integrated over various geometries to obtain the photopeak response due to a range of source types. For example, the radiation due to a thick circular source expressed as a percentage of the radiation due to an infinite source is given by (Grasty 1987)

$$P = 100\left(\frac{E_2(\mu h) - \cos\varphi E_2\left(\frac{\mu h}{\cos\varphi}\right)}{E_2(\mu h)}\right) \tag{8}$$

where h is the detector height above ground level, μ is the linear attenuation coefficient of gamma rays in air, E_2 is the exponential integral of the second kind, and the circular source subtends an angle of 2φ at the detector.

This type of formulation has been used in several 'fields of view' type investigations, where an insight into the response of the detector system to sources of various geometry is sought (e.g. Duval et al. 1971; Grasty et al. 1979; Tewari & Raghuwanshi 1987). Figure 12 shows the percentage of the infinite source yield for Th gamma rays (^{208}Tl) at 2.61 MeV as a function of source radius. A linear attenuation coefficient for air of 0.00505 m^{-1} and detector height of 100 m have been used. This shows that at 100 m height, less than 40 per cent of the infinite source yield originates from a source with a radius of 100 m, and over 20 per cent of the measured photons for an infinite source originate at lateral distances greater than 300 m. The 'field of view' represented by a typical airborne sample is thus much larger than the 60 m interval over which samples are typically acquired.

As a second example, the radiation due to a broad source of thickness D expressed as a percentage of the radiation due to a broad source of infinite thickness is given by (Grasty 1987)

$$P = 100\,(1 - E_2(\mu D)) \tag{9}$$

where μ is the linear attenuation coefficient of the source material, and the detector is at ground level. This relationship is illustrated in Figure 13 for Th gamma rays (^{208}Tl) at 2.61 MeV. A source density of 2.2 gm/cm^3 and a mass attenuation coefficient of 0.0396 cm^2/gm (ie. μ=0.0871 cm^{-1}) was used. This shows that over 98 per cent of the radiation comes from the top 35 cm of the Earth's crust. Airborne gamma-ray spectrometry can, therefore, only map the concentration of radioelements in a thin layer at the Earth's surface.

More sophisticated derivations of equations 8 and 9 are available. Grasty et al. (1979) included the effect of the angular sensitivities of cylindrical detectors into the analysis. Tewari & Raghuwanshi (1987) repeated this work using the measured angular sensitivity of the more modern rectangular slab detectors. Models that incorporate both scattered and unscattered radiation are also available. In the latter case , a 'build-up' factor is used to accommodate the component due to scattered radiation (e.g. Gregory 1960; Davis & Reinhardt 1962).

The most comprehensive form of modelling in airborne gamma-ray spectrometry is the simulation of gamma-ray transport. Kirkegaard (1972) developed a numerical method to solve Boltzmann's equation for a two-layer model and, hence, simulate the gamma-ray flux distributions at airborne height (Figs 5, 6 & 7). The main limitation to this type of modelling is the detector response. This is a complicated

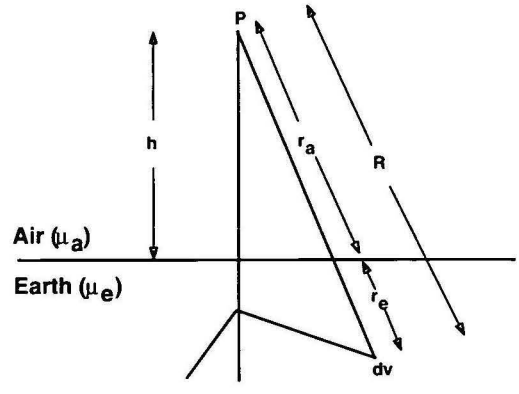

Figure 11. Source detector geometry for the two-layer Earth model. The detector is at point P relative to a source element dV within the Earth.

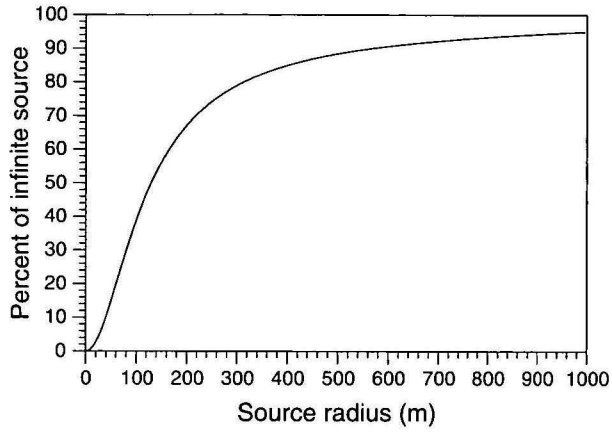

Figure 12. Percentage of the infinite source radiation detected from thick circular sources of varying radius for thorium gamma rays of energy 2.62 MeV and a detector height of 100 m. The angular sensitivity of rectangular slab detectors was included in the analysis.

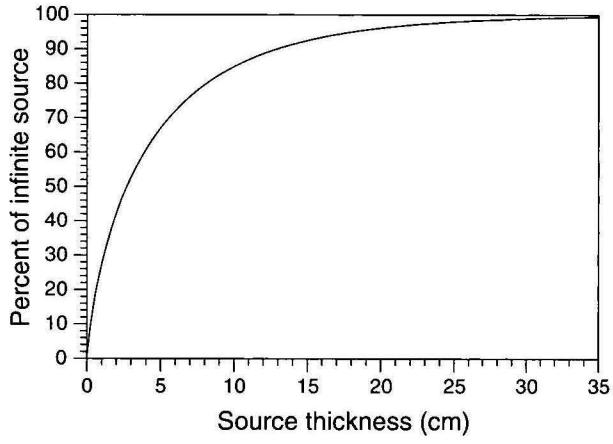

Figure 13. Percentage of the infinite source radiation detected from broad sources of varying thickness for thorium gamma rays of energy 2.62 MeV and a source density of 2.2 gm.cm^{-3}.

function, particularly for airborne spectrometers, where a large proportion of the measured count rates result from scattered radiation, and the effects of partial outscatter, escape peaks, and so on have to be considered. A very large number of Monte Carlo type calculations are required to simulate a response function of adequate detail. Grasty (1979) has suggested that detector response can only be satisfactorily determined through a combination of experiment and Monte Carlo simulations.

Statistical models

Each atomic disintegration during radioactive decay occurs completely independently of every other decay event. This means that the frequency of the radioactive decay, or the frequency of the measured gamma rays associated with the decay, follow a Poisson statistical distribution, ie.

$$P(x) = \frac{\psi^x e^{-\psi}}{x!} \qquad (x = 0,1,2,3,...) \qquad (10)$$

where ψ is a given constant.

A special property of the Poisson distribution often used in gamma-ray spectrometry is that the standard deviation is equal to the square root of the mean count rate:

$$\sigma = \sqrt{n} \qquad (11)$$

where n is the mean count rate. Also, the variance of a distribution is the mean square deviation, equivalent to the square of the standard deviation:

$$v = \sigma^2 = n \qquad (12)$$

The fractional deviation is given by

$$\frac{\sqrt{n}}{n} = \frac{1}{\sqrt{n}} \qquad (13)$$

These relationships give us a convenient means for estimating errors in gamma-ray spectrometry. In other areas of science, errors are usually estimated by repeating the experiment or observation a number of times. In gamma-ray spectrometry, we usually assume that all errors are due to the random nature of radioactive decay, and the variance is taken to be approximately equal to the number of counts observed. For large count rates, the Poisson distribution becomes more normal and, for mean count rates greater than 20, the Poisson and normal distributions are almost identical (Dickson 1980). Under these circumstances it is appropriate to use the weighted least-squares method for the inversion of over-determined systems in gamma-ray spectrometry.

Airborne surveying

Typically, a regional airborne geophysical survey would be flown with 400 m line spacing and at a flying height of between 80 and 100 m. Both gamma-ray spectrometric and magnetic data are usually recorded on these surveys. The line spacing is a compromise between the desired resolution of the data, and the cost of the survey. The flying height is usually related to the line spacing, but is limited by safety considerations. The speed of the aircraft is usually about 50–60 m/s for fixed-wing surveys, but can be appreciably slower for helicopter surveys. There is obviously a trade-off in data acquisition between the measured count rates and, hence, the accuracy of the measurements, sampling time, aircraft speed, and spatial resolution of the data. 'Fields of view' type calculations, using equations such as number 8 above, can be used to estimate the effective coverage for various flying heights. The field of view of the spectrometer is wider at greater heights, but the quality of the gamma-ray spectrometric data improves dramatically as the elevation of the detector decreases, since the fall-off in intensity of radiation with height is roughly exponential. But the survey parameters are almost always optimised for the acquisition of magnetic data, which have traditionally been viewed as the primary exploration and mapping tool.

Modern airborne gamma-ray spectrometric data acquisition systems for regional mapping would comprise a multichannel spectrometer capable of measuring at least 256 channels of data in the energy range 0–3 MeV, and a detector volume of not less than 33 litres of NaI (Tl) crystal. Even with this volume of crystal, multichannel count rates are low. A typical spectrum from one of these regional surveys is shown in Figure 14. The conventional approach to the acquisition and processing of airborne gamma-ray spectrometric data is to monitor four relatively broad spectral windows (Table 5). Windows centred on the 1.46 MeV (K), 1.76 MeV (U) and 2.62 MeV (Th) photopeaks (Fig. 15) have been generally accepted as the most suitable for the measurement of K, U and Th. The total-count window gives a measure of total radioactivity.

The K, U and Th windows are centred on the highest energy diagnostic photopeak for each of the three radioelements. This is significant, since only high-energy photons are able to penetrate in significant numbers to airborne heights, and they are also less susceptible to variations in source geometry or the height of the detector than lower energy photons.

Multichannel data were once used only for monitoring equipment performance, but are now, increasingly, being used for energy calibration of data during processing and for

Table 5. Standard windows for natural radioelement mapping (IAEA 1991). The energy of the photopeak being monitored is shown in brackets after each nuclide.

Window	*Nuclide*	*Energy range (MeV)*
Total Count	–	0.4–2.81
Potassium	^{40}K (1.460 MeV)	1.370–1.570
Uranium	^{214}Bi (1.765 MeV)	1.660–1.860
Thorium	^{208}Tl (2.614 MeV)	2.410–2.810

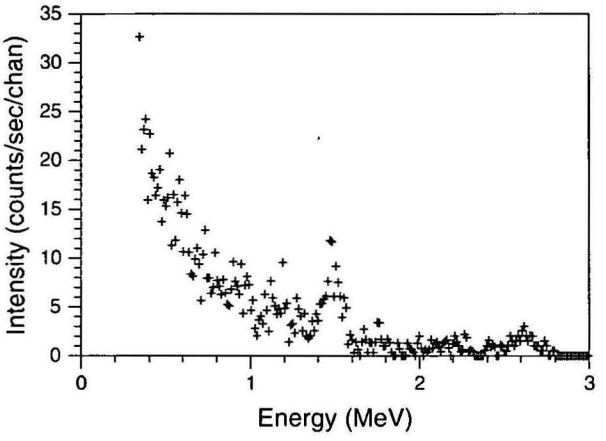

Figure 14. A typical gamma-ray spectrum recorded at 100 m altitude with a 1 s integration time. There are 256 channels between 0 and 3 MeV, giving a channel width of about 11.7 keV.

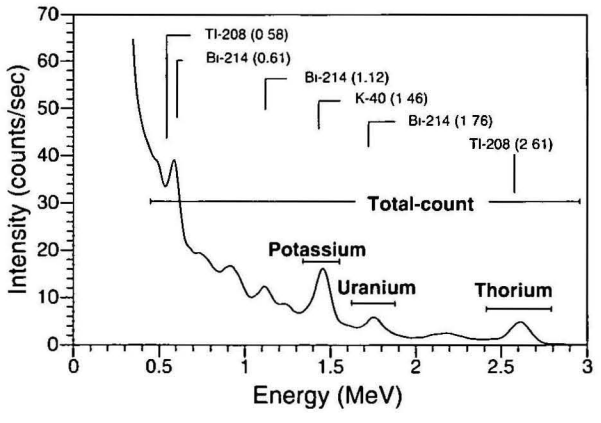

Figure 15. A typical gamma-ray spectrum recorded at 100 m altitude with a large integration time, showing prominent photopeaks and the positions of the conventional 3-channel windows.

estimation of gamma-ray background. The observed spectrum can be considered as the sum of three terrestrial and three background components as follows:

$$I_{obs} = I_K + I_U + I_{Th} + I_{air} + I_{cos} + I_{rad} \quad (14)$$

where I_K, I_U and I_{Th} are the spectra of K and the U and Th decay series, and I_{air}, I_{cos} and I_{rad} are, respectively, the aircraft, cosmic and atmospheric radon background components.

Calibration and data processing for airborne gamma-ray spectrometry are described by Minty et al. (1997). Briefly, the data are processed as follows. The measured spectra are corrected for equipment dead time and then energy calibrated to correct for energy drift in the spectrometer. The background components are then estimated and removed. At this point, the spectra are summed over the conventional windows for further processing. Each elemental window count rate (Fig. 15) is corrected for counts due to the other radioelements (channel interaction correction or 'stripping'). These background-corrected and stripped count rates are then corrected for variations in the height of the detector (height correction) and reduced to elemental concentrations on the ground. For many of the corrections, the approach taken to calibration is empirical. We view the source and detector as a single system and measure its response, for example, to changes in aircraft height (to obtain height attenuation coefficients) and sources of known geometry and concentration (to obtain sensitivity coefficients). It is important to realise, however, that these empirically determined constants are only valid for the source and source–detector geometry used in the calibration process.

Conclusion

The purpose of this paper has been to review the fundamentals of airborne gamma-ray spectrometry. A knowledge of these is essential for an understanding of the calibration of airborne gamma-ray spectrometers and the processing and interpretation of airborne gamma-ray spectrometric data, which are covered elsewhere in this volume (Minty, et al. 1997; Dickson & Scott 1997).

The paper has reviewed basic radioactivity and the source of gamma-radiation, and discussed the interaction of gamma rays with matter, the response of an airborne detector system, and the properties of airborne gamma-ray spectra. The discussions have illustrated that the measured spectrum is a complex function of many variables. The approach taken to calibration, therefore, is empirical, i.e. the response of the source–detector system to sources of known concentration and geometry is measured.

References

Aviv, R. & Vulcan, U., 1983. Airborne gamma-ray survey over Israel: the methodology of the calibration of the airborne system. Israel Atomic Energy Commission, Report No. Z.D. 58/82.

Bailey, R.C., 1986. The altitude dependence of terrestrial gamma-ray spectra: A simple model. Geophysics, 51(11), 2108–2116.

Charbonneau, B.W. & Darnley, A.G., 1970. Radioactive precipitation and its significance to high sensitivity gamma-ray spectrometer surveys. Geological Survey of Canada, Paper 70–1, part B, 32–36.

Clark, R.B., Duval, J.S. Jr. & Adams, J.A.S., 1972. Computer simulation of an airborne gamma-ray spectrometer. Journal of Geophysical Research, 77(17), 3021–3031.

Darnley, A.G. & Grasty, R.L., 1971. Mapping from the air by gamma-ray spectrometry. In: Geochemical exploration. Canadian Institute of Mining & Metallurgy, Special Volume 11, 485–500.

Davis, F.J. & Reinhardt, P.W., 1962. Radiation measurements over simulated plane sources. Health Physics, 8, 233–243.

Dickson, B.L. & Scott, K.M., 1997. Interpretation of aerial gamma-ray surveys. AGSO Journal of Australian Geology & Geophysics, 17(2)—this issue.

Dickson, B.H., 1980. Analytic methods for multichannel airborne radiometrics. MSc. thesis, University of Toronto.

Duval, J.S., Cook, B. & Adams J.A.S., 1971. Circle of investigation of an airborne gamma-ray spectrometer. Journal of Geophysical Research, 76, 8466–8470.

Fano, U., 1953. Gamma-ray attenuation, Part I, Basic processes. Nucleonics, 11(8), 8–12.

Foote, R.S., 1969. Improvements in airborne gamma-radiation data analyses for anomalous radiation by removal of environmental and pedologic radiation changes. In: Nuclear techniques and mineral resources. I.A.E.A., Proceedings Series, 187–196.

Grasty, R.L., 1979. Gamma-ray spectrometric methods in uranium exploration—theory and operational procedures. In: Geophysics and geochemistry in the search for metallic ores. Geological Survey of Canada, Economic Geology Report 31, Paper 10B.

Grasty, R.L., 1987. The design, construction and application of airborne gamma-ray spectrometer calibration pads—Thailand. Geological Survey of Canada, Paper 87-10.

Grasty, R.L. & Carson, J. M., 1982. Discussion on 'Inversion of gamma-ray data for element abundances' (Crossley, D.J. & Reid, A.B.). Geophysics, 47, 1737–1738.

Grasty, R.L., Kosanke, K.L. & Foote, R.S., 1979. Fields of view of airborne gamma-ray detectors. Geophysics, 44(8), 1447–1457.

Gregory, A.F., 1960. Geological interpretation of aeroradiometric data. Geological Survey of Canada, Bulletin 66.

Gregory, A.F. & Horwood, J.L., 1961. A laboratory study of gamma-ray spectra at the surface of rocks. Department of Energy, Mines & Resources, Ottawa, Mines Branch Research Report R85.

Heath, R.L., 1964. Scintillation spectrometry. Gamma-ray spectrum catalogue, 2nd Edition, Volumes 1 and 2: U.S.A.E.C. Research and Development Report IDO–16880–1, Physics T.I.D.–4500 (31st edition).

Hubbell, J.H. & Berger, M.J., 1968. Attenuation coefficients, energy absorption coefficients, and related quantities. Engineering Compendium on Radiological Shielding, v. 1. Springer Verlag, Berlin.

IAEA, 1991. Airborne gamma ray spectrometer surveying. International Atomic Energy Agency, Technical Report Series, No. 323.

Ivanovich, M. Harmon, R.S. (editors), 1982. Uranium series disequilibrium: applications to environmental problems. Clarendon Press, Oxford.

Kirkegaard, P., 1972. Double P1 calculation of gamma-ray transport in semi-infinite media. Danish Atomic Energy Commission, Research Establishment Riso, Report Riso-*M-1460.*

Kirkegaard, P. & Lovborg, L. , 1974. Computer modelling of terrestrial gamma-radiation fields. Riso Report No. 303.

Kogan, R.M., Nazarov, I.M. & Fridman, Sh.D., 1969. Gamma spectrometry of natural environments and formations. Translation 1971 by Israel Program for Scientific Translations Ltd. No. 5778, available from the U.S. Dept. of Commerce, Nat. Tech. Inf. Ser., Springfield, Va., 22151, 337 p.

Minty, B.R.S., Luyendyk, A.P.J. & Brodie, R.C., 1997. Calibration and data processing for airborne gamma-ray spectrometry. AGSO Journal of Australian Geology & Geophysics, 17(2)—this issue..

Tewari, S.G. & Raghuwanshi, S.S., 1987. Some problems on the range of investigation in airborne gamma-ray spectrometry. Uranium, 4(1), 67–82.

AGSO Journal of Australian Geology & Geophysics, 17(2), 51–62

Calibration and data processing for airborne gamma-ray spectrometry

B.R.S. Minty[1], A.P.J. Luyendyk[1] & R.C. Brodie[1]

The shape and intensity of multichannel airborne gamma-ray spectra are influenced by many variables. The role of data processing is to correct the data for those influences not related to the geology, and to transform the observed spectra to equivalent concentrations of radioelements in the ground. The data need to be corrected for dead time, energy drift, and background radiation before being inverted to elemental count rates. The elemental count rates are then corrected for variations in the terrain clearance of the detector and reduced to elemental concentrations in the ground. Statistical errors in the raw data are propagated by the data processing procedures. The removal of background radiation increases the fractional errors for each of the potassium, uranium and thorium window count rates. The fractional errors in the potassium and uranium window count rates are also amplified by the stripping procedure. Large errors can be introduced into the data through the height correction procedure if radon background is not adequately removed. Radon background can be adequately removed using a spectral-ratio method.

Introduction

Modern multichannel airborne gamma-ray spectrometers used for regional mapping use detector volumes of not less than 33 litres of NaI (Tl) crystals, and sample integration times of one second. Even with this volume of crystals, multichannel count rates at typical survey heights of 80–100 m are low. A typical spectrum is shown in Figure 1. The conventional approach to the acquisition and processing of airborne gamma-ray spectrometric data is to monitor four relatively broad spectral windows (Fig. 2). The potassium (K), uranium (U), and thorium (Th) windows (Table 1) are centred on the 1.46 MeV (K), 1.76 MeV (U) and 2.61 MeV (Th) photopeaks, and are generally accepted as the most suitable for the measurement of K, U and Th. The total count window gives a measure of total radioactivity.

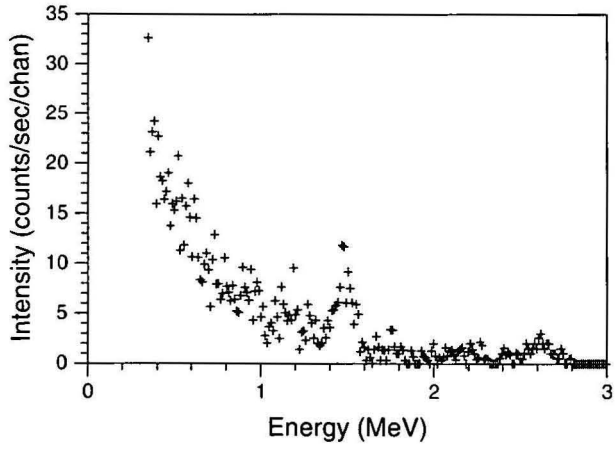

Figure 1. A typical gamma-ray spectrum recorded at 100 m height with a 1 s integration time. There are 256 channels between 0 and 3 MeV, giving a channel width of about 11.7 keV.

The shape and amplitude of airborne multichannel gamma-ray spectra are influenced by many variables. The role of data processing is to correct the observed data for those influences not related to the geology, and to transform the observed spectra to equivalent concentrations of radioelements in the ground. The purpose of this paper is to describe current methodology for calibrating multichannel airborne gamma-ray spectrometers and processing data collected by them. Wherever possible, we take a 'full-spectrum' approach to calibration, since this tends to give a clearer insight into the physics of the method. Calibration constants for the conventional 4-window method are then derived directly from the calibration spectra.

[1] Australian Geological Survey Organisation, GPO Box 378, Canberra, ACT, 2601

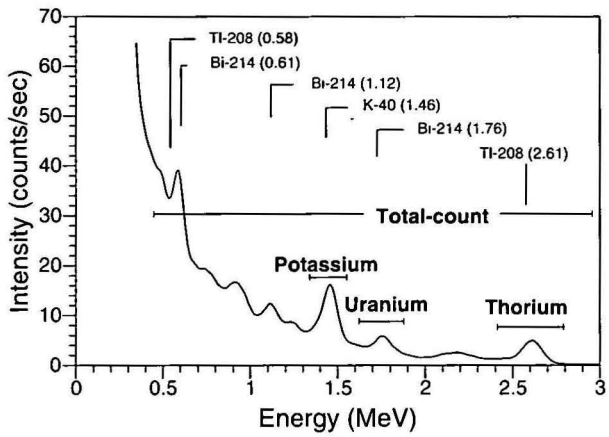

Figure 2. A typical gamma-ray spectrum recorded at 100 m height with a large integration time and showing prominent photopeaks and the positions of the conventional 4-channel windows.

Table 1. IAEA recommended windows for conventional 3-channel airborne gamma-ray spectrometry (IAEA 1991).

Element analysed	*Isotope used*	*Gamma ray energy MeV*	*Energy window MeV*
Potassium	^{40}K	1.46	1.370–1.570
Uranium	^{214}Bi	1.76	1.660–1.860
Thorium	^{208}Tl	2.61	2.410–2.810

This paper reviews each correction that needs to be applied to airborne gamma-ray spectrometric data. They are described below in the order in which they must be applied. The calibration requirements for each correction are also described. We conclude by investigating the source of errors in airborne gamma-ray spectrometry, and their propagation by the data processing procedures.

Dead time correction

Spectrometers require a finite time to process each pulse from the detector. Any pulse that arrives while another is being processed is automatically rejected, and the total counting time available is thus reduced by the time taken to process all pulses detected. A typical dead time would be of the order of 5–15 μs/pulse, and can be corrected for as follows:

$$N = \frac{n}{1-t} \qquad (1)$$

where N = corrected count rate (counts/sec);
n = observed count rate (counts/sec);
t = the total dead time (in seconds) for this one-second sample interval.

The dead time correction is usually very small, but can be significant in areas of high radioactivity or during some calibration procedures.

Dead time can be measured experimentally (IAEA 1991) by connecting the spectrometer to two identical detector packages. The total count rate is measured first with each detector package connected to the spectrometer separately and then with both packages connected to the spectrometer simultaneously. Clearly, the difference between the count rate measured with both packages connected and the sum of the count rates for the individual packages gives an indirect measure of the equipment dead time. Usually, the individual detector packages will give approximately the same count rate, in which case the dead time is given by (IAEA 1991)

$$t = \frac{2N - N_T}{NN_T} \quad (2)$$

where N = average total count rate from the individual detector packages (counts/sec);
N_T = total count rate measured with both detector packages connected (counts/sec);
t = dead time per pulse (seconds).

This calibration procedure is based on the assumption that the total dead time is nt, where n is the total number of counts recorded. This is not necessarily the case, and users should refer to the manufacturer's specifications for individual spectrometers. The Exploranium GR820, for example, has a very small dead time per pulse, but has a system dead time overhead of 10 ms per integration interval. In this case the calibration procedure, as described above, cannot be used to calculate dead time. Most modern spectrometers automatically record the system dead time, which is output with the data stream for later processing.

Energy calibration

All spectrometers are affected by energy drift in the measured spectra. This is mainly due to changes in the gain of the photomultiplier tubes because of drift in the high-voltage supply and changes in temperature. Lovborg (1984) simulated the effect of drift on the stripping ratios for a portable spectrometer. Using synthetic spectra, he showed that a gain drift of just 2 per cent (4.5 channels for the Th photopeak at 2.61 MeV) changes the stripping ratios by several per cent, thus introducing a systematic error into the processed data.

It is not unusual for older airborne spectrometers to drift up to 2–3 channels during the course of a day (1 channel =11.7 keV), and spectrometer drift is thus a significant source of error with these instruments. Modern spectrometers have built-in self-stabilising features and the total drift with these instruments is less than one channel. Multichannel airborne spectrometer data can be corrected for energy drift as long as all the crystal/photomultiplier assemblages in the detector drift sympathetically.

Estimation of photopeak positions for energy calibration requires good-quality spectra. One approach is to sum the spectra along each line over at least 600 s and determine the peak positions from this total spectrum. These are then used to calibrate the energy of each individual 1 s spectrum used in the summation. A simple method of calibrating multichannel spectra is that used by the Geological Survey of Canada (R.L. Grasty personal communication). The energy of at least two prominent photopeaks is determined as the maximum value of a quadratic fitted in the vicinity of each photopeak. A linear function is then fitted to the photopeak positions (channel number vs energy) to obtain the energy at channel 1 and the gain (keV per channel). These parameters are then used to correct each 1 s spectrum within the integration period by resampling each channel to its correct energy range.

Aircraft and cosmic background correction

The aircraft background spectrum is due to the radioactivity of the aircraft and its contents and is a constant. The cosmic background component arises from the reaction of primary cosmic radiation with atoms and molecules in the upper atmosphere. This generates a complex secondary radiation, which reacts with the air, aircraft, and the detector to produce the measured cosmic spectrum. The procedure for removing aircraft and cosmic background uses the fact that in the lower atmosphere the cosmic spectrum has a near constant shape, but its amplitude decreases with reducing altitude. Also, at energies greater than 3 MeV, all radiation is cosmic in origin, and airborne spectrometers routinely monitor a cosmic window (typically 3–6 MeV) to estimate cosmic background. The cosmic contribution in any channel is, thus, proportional to the cosmic window count rate, and if the shape of the cosmic spectrum for a particular installation is known, then the cosmic window count rate can be used to calculate the cosmic contribution in any particular channel.

Aircraft and cosmic background spectra are estimated as follows:

$$N_i = a_i + b_i N_{\cos} \quad (3)$$

where N_i = aircraft+cosmic background count rate in the ith channel;
$N_{\cos}$ = cosmic window count rate;
a_i = aircraft background in the ith channel;
b_i = cosmic background in the ith channel normalised to unit counts in the cosmic window.

The a_i and b_i have to be determined by suitable calibration. The cosmic window count rate can be lightly filtered before estimating the correction. The aircraft and cosmic background spectra are subtracted from the dead-time corrected and energy-calibrated observed spectra.

The calibration strategy for aircraft and cosmic background correction requires the acquisition of gamma-ray spectra over water at a number of different heights (say 1.0, 1.5, 2.0, ... 4.0 km) in an area where atmospheric radon (Rn) is at a minimum. These data would typically be acquired offshore, where the prevailing winds are landwards, after a high-pressure front arrives, or after general precipitation in the calibration area, since these tend to reduce atmospheric radioactivity to low levels (Fritzsche 1982). The measured spectra are each the sum of the aircraft component (constant) and the cosmic

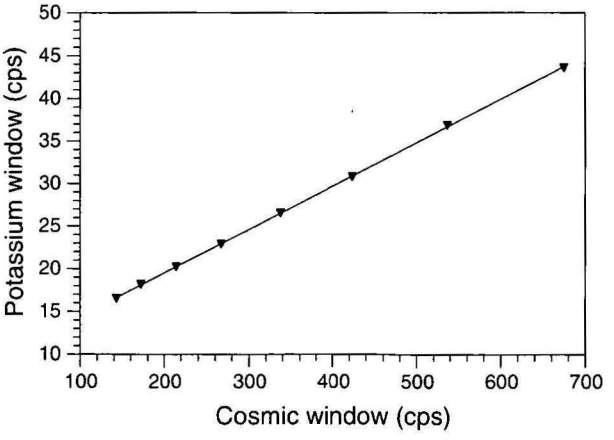

Figure 3. High-altitude regression plot for aircraft and cosmic background in the potassium window.

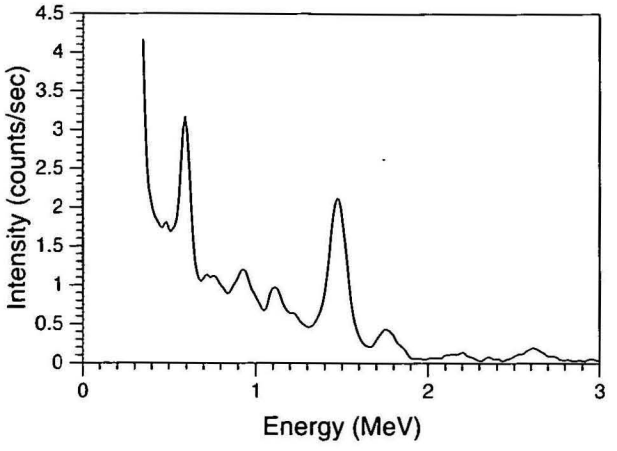

Figure 4. The aircraft gamma-energy spectrum.

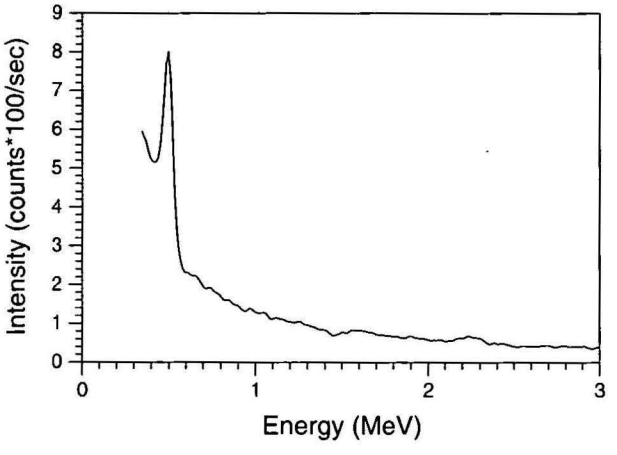

Figure 5. The normalised cosmic gamma-energy spectrum.

component. Also, the count rate in the 3–6 MeV cosmic window is linearly related to the count rate in the *i*th energy channel by equation 3. Thus, a linear regression of the cosmic window count rate on any other particular channel gives the cosmic sensitivity (slope of regression line) and aircraft background (zero intercept) for that channel. Any deviation from a linear relationship is a clear indication of the presence of Rn.

This type of analysis can also be applied to 4-channel window data. A typical regression is shown in Figure 3. Aircraft and cosmic spectra are shown in Figures 4 and 5.

Radon background correction

Radon gas (^{222}Rn) is very mobile and can escape into the atmosphere from soils and rock fissures in response to the pumping action of changing temperature and pressure. The Rn component of background is due to atmospheric ^{222}Rn and its daughters. This is a major contributor to background radiation. Up to 50 per cent of the U window count rate can arise from Rn daughter products in the atmosphere. A serious problem associated with the removal of Rn background is that it is not evenly distributed through the lower atmosphere. For example, under early morning still-air conditions Rn and its daughters can be trapped close to the ground in temperature inversion layers. The spectrum of airborne Rn and its daughters has a very similar shape to that of U and its daughter products in the ground. This is because the most prominent gamma-ray emitter (^{214}Bi) occurs below ^{222}Rn in the ^{238}U decay chain, and only the relative height of photopeaks distinguishes the two spectra.

There are two procedures that can be used for removing Rn background. The first is a spectral-ratio method, where the relative height of U series photopeaks is used to determine the contributions to the spectrum of U in the ground and Rn in the air. The second approach is through the use of upward-looking detectors. The spectral-ratio method requires multichannel spectra that have been dead-time corrected, energy calibrated, and have had aircraft and cosmic background components removed. The upward-looking detector method only requires window data. In this case, the 1 s spectra can be integrated over the conventional 4-channel windows after energy calibration, and a 4-channel aircraft and cosmic background calibration and removal would be sufficient. The two methods for estimating Rn are described below.

Radon removal (spectral-ratio method)

The method described here is a variation of that described by Minty (1992). The method derives from the observation that the low energy ^{214}Bi photopeak at 0.609 MeV from atmospheric Rn suffers far less attenuation relative to the ^{214}Bi peak at 1.76 MeV than is the case for radiation from the ground. So the ratio of the counts in each of these photopeaks is diagnostic of the relative contributions of atmospheric Rn and in-ground U to the observed spectrum.

A heuristic calibration procedure can be used to calibrate the spectral ratio method by considering the contributions of atmospheric Rn and terrestrial sources of K, U and Th to the spectral regions of interest (Minty 1996). But the data requirements for this calibration are stringent. Fortunately, a simple two-component model based on an atmospheric Rn spectrum and a composite K, U and Th ground spectrum can be used to estimate Rn background almost as well as the complete four-component model. This two-component model works well in areas of relatively constant Th/U concentrations. It is also easily calibrated using normal survey data.

Figure 6 shows the Rn spectrum and an average ground spectrum relative to a low-energy (0.54–0.68 MeV) window centred on the ^{214}Bi 0.609 MeV photopeak and the conventional U window centred on the 1.76 MeV photopeak. The cosmic and aircraft spectra are first removed from the observed spectrum, since they can be independently calculated. The important feature of the low-energy window at 0.609 MeV is that the majority of counts above the Compton continuum are due to either U or Rn, with perhaps a lesser contribution from Th. These counts (the 'peak' counts) are estimated by integrating under the photopeak, but above the exponential used to approximate the Compton continuum (Fig. 6).

The method calls for the monitoring of two windows which we denote by L (low energy) and H (high energy). L represents counts above the Compton continuum in the 0.609 MeV photopeak and H represents counts in the conventional U window (1.66–1.86 MeV).

Let L_{ob} and H_{ob} be the observed count rates in the low and high-energy windows, respectively, after correcting the spectrum for aircraft and cosmic background. Let L_r and H_r be the Rn contributions to the low and high-energy windows, and let L_g and H_g be the corresponding contribution to these windows from radiation from the ground. Then

$$L_{ob} = L_r + L_g \tag{4}$$

and

$$H_{ob} = H_r + H_g \tag{5}$$

Also, since the shape of the Rn spectrum can be assumed constant for a particular height, and U and Th concentrations correlate well over most lithological units, we have

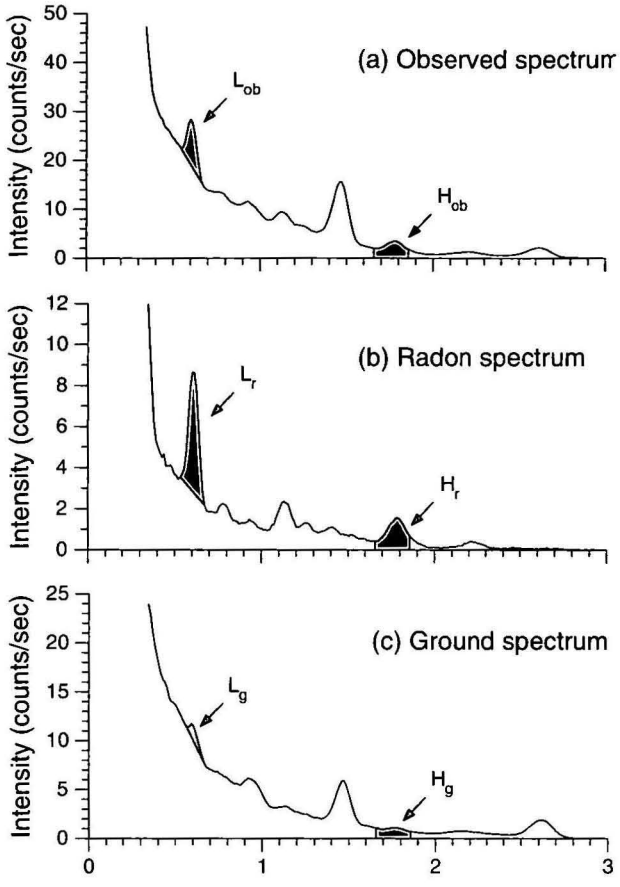

Figure 6. The radon and ground spectra relative to the 2 windows used by the spectral-ratio background estimation method. The 'observed spectrum' has been corrected for aircraft and cosmic background.

$$L_r = c_1 H_r \tag{6}$$

and

$$L_g = c_2 H_g \tag{7}$$

where c_1 and c_2 are constants that have to be determined. These quantities are shown graphically in Figure 6. Solving equations 4 to 7 gives

$$L_r = \frac{(L_{ob} - c_2 H_{ob})}{(1 - c_2 / c_1)} \tag{8}$$

The Rn contribution in the conventional U window is then calculated from equation 6.

Equations similar to equation 6 can be used to determine the Rn contribution to the conventional K and Th windows. At this stage of the processing, the multichannel spectra may be summed over the conventional windows to obtain 4-channel count rates. The Rn contribution to each window is then subtracted.

The Rn spectrum can be derived from calibration flights at survey height over water and in the presence of Rn. The aircraft and cosmic contributions are subtracted from the observed spectrum to give the Rn spectrum. Constant c_1 is measured directly from the Rn spectrum. The factors required to calculate the Rn contribution to the K and Th windows for a fixed number of Rn counts in the U window are also determined directly from the Rn spectrum.

Constant c_2 is derived from a pure 'ground' spectrum. The ground spectrum can be calculated directly from survey data by using a differencing procedure to remove all background components (Minty 1996).

An example of the application of the spectral-ratio method is shown in Figure 7—(a) shows a gradient-enhanced image of the U channel over the Lissadel 1:250 000 sheet area (Western Australia) before the removal of background radiation; (b) shows the same data after background removal. An integration time of 200 s was used to sum spectra for estimating Rn background. The Rn removal procedure has significantly reduced the amount of streaking in the image due to variations in atmospheric Rn levels during the course of the survey. The residual short-wavelength streaking shown in Figure 7(b) is probably due to variations in the height of the detector and the influence of this on the background estimation. Variation in the detector height on this survey was severe.

The effect on the data of Rn removal is demonstrated by the line averages of the data before and after Rn has been removed. Figure 8 shows line averages for the Th channel plotted as a function of latitude. Since this channel is virtually unaffected by Rn, variation in these average count rates with latitude reflects changes in the geology traversed by each line. Similar plots for the U channel before and after Rn removal are shown in Figures 9 and 10. The significant scatter in the line averages shown in Figure 9 is largely due to the presence of Rn. This scatter is less evident after Rn removal (Fig. 10), and the background-corrected U line averages show similar variation with latitude to those seen in the Th channel. This is expected, as U and Th are highly correlated in most rock types.

Note that the spectral-ratio method cannot be used where ^{137}Cs contamination from atomic weapons fallout or nuclear accident is significant This is because the ^{137}Cs photopeak at 0.662 Mev will significantly corrupt measurement of the U and Rn contributions to the 0.609 MeV peak count rates.

Radon removal (upward-looking detector method)

In most survey aircraft it is possible to have an 'upward-looking' detector to monitor the background level of radiation continuously (Grasty et al. 1988). An additional crystal pack is partially shielded from radiation from below to give the system a directional sensitivity and the ability to discriminate between radiation from the atmosphere and from the ground. As with the spectral-ratio method, the Rn is estimated by summing the window count rates over large time intervals—typically 600 s in the case of the upward-looking detector method.

The Rn contribution to the U window of the main detector package (i.e. the 'downward' U window) is given by (IAEA 1991)

$$U_r = \frac{u - a_1 U - a_2 T + a_2 b_t - b_u}{a_u - a_1 - a_2 a_t} \tag{11}$$

where U_r = Rn background in the downward U window
u = count rate in the upward U window
U = count rate in the downward U window
T = count rate in the downward Th window

and a_1, a_2, a_u, a_t, b_u and b_t are constants derived by suitable calibration.

Grasty (1975) showed that the total count and K backgrounds are linearly related to the U background and can be derived from the U channel background by suitable calibration.

The calibration requirements for the upward-looking detector method are comprehensively described in IAEA (1991). The constants a_u, a_t, b_u and b_t are regression coefficients that relate Rn background in the upward and downward U windows ($u_r = a_u U_r + b_u$), and Rn background in the downward Th and U windows ($T_r = a_t U_r + b_t$). These are determined by subtracting aircraft and cosmic background from flights over water showing a range of Rn concentrations. Linear regressions yield the calibration coefficients a_u, a_t, b_u and b_t. Similar regressions

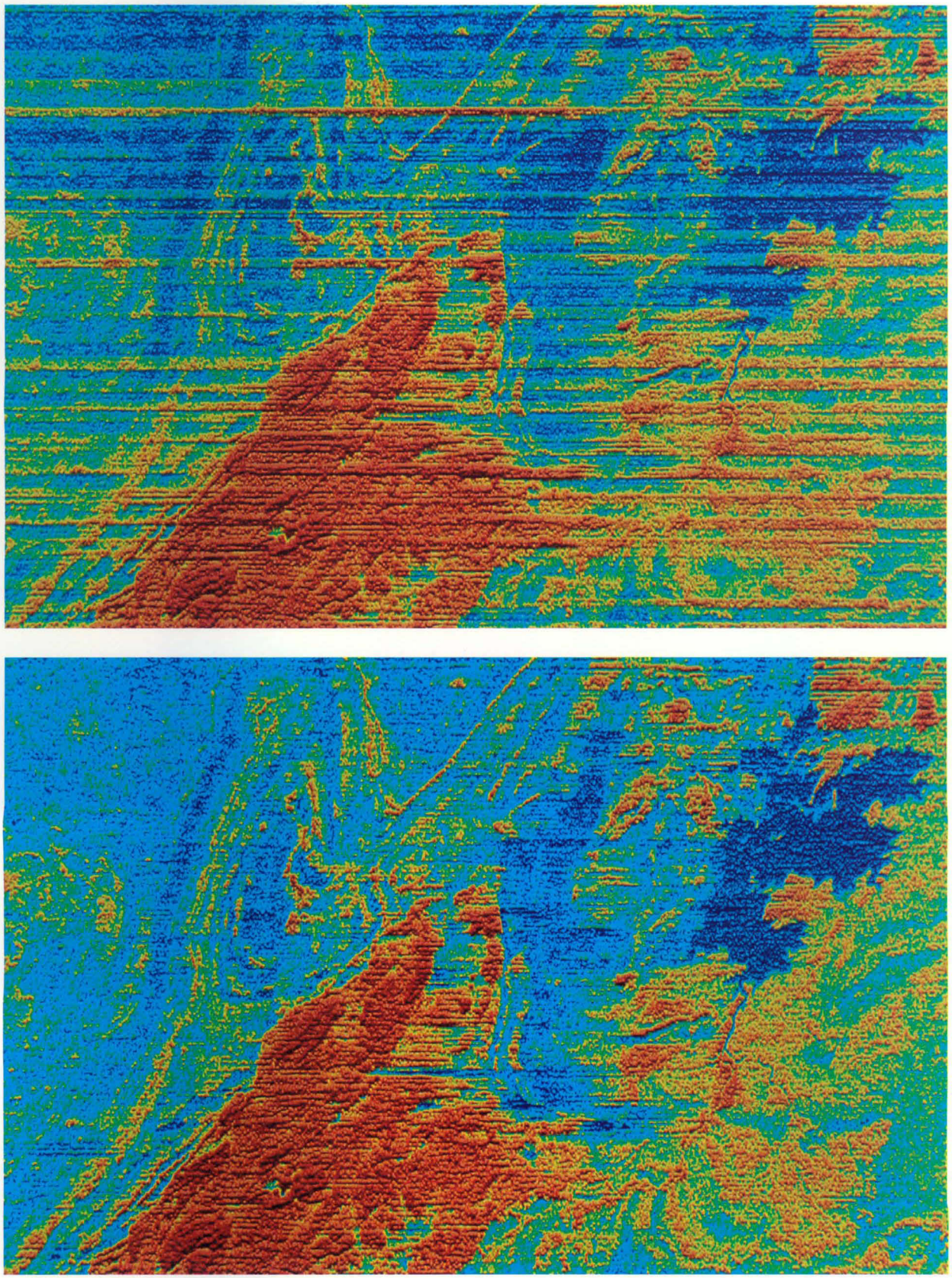

Figure 7. Gradient enhanced pseudocolour image of the uranium window count rates for the Lissadel map sheet area, Western Australia. (a—upper) The window count rates without radon background removed. Variations in atmospheric radon concentrations during the course of the survey result in significant streaking in the image. (b—lower) The window count rates with radon background removed, resulting in a marked improvement to the quality of the processed data.

on these data give the constants required for determining the Rn contribution to the total count and K windows from the Rn background in the U window.

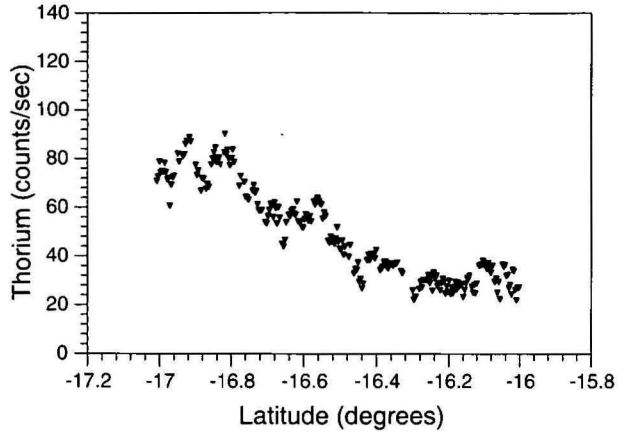

Figure 8. Thorium window line averages for the Lissadel map sheet area, Western Australia, after removing background.

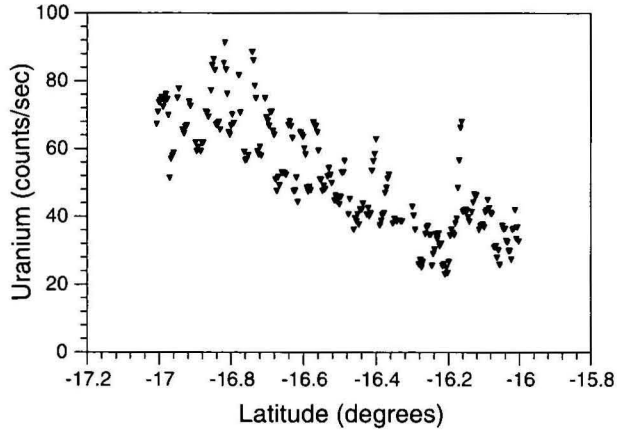

Figure 9. Uranium window line averages for the Lissadel map sheet area, Western Australia, after removing aircraft and cosmic background only. The significant scatter in the averages is due to variations in radon background during the course of the survey.

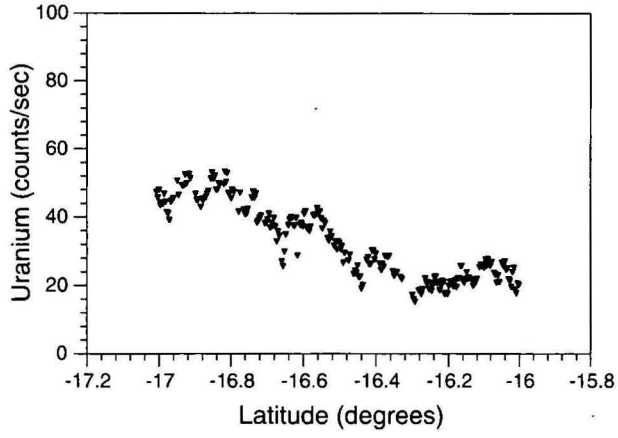

Figure 10. Uranium window line averages for the Lissadel map sheet area, Western Australia, after removing aircraft cosmic and radon background. The scatter seen in Figure 9 is no longer evident, and the line averages more closely reflect the geological signal evident in the thorium averages (Figure 8).

The second stage of the calibration is to relate measured count rates in the upward U window to those in the downward U window for radiation due to U in the ground. These components are related by the equation

$$u_g = a_1 U_g + a_2 T_g \tag{12}$$

where u_g, U_g and T_g are the ground components, and a_1 and a_2 are the calibration coefficients required. The easiest way to determine a_1 and a_2 is from background-corrected data acquired from lines that both traverse and are adjacent to a large body of water. The over-water sections of the lines are used to remove the total background to give a number of estimates of u_g, U_g, and T_g over a range of source concentrations. Estimates of a_1 and a_2 are obtained by solving the simultaneous equations (IAEA 1991)

$$a_1 \sum (U_g)^2 + a_2 \sum U_g T_g = \sum u_g U_g \tag{13}$$

$$a_1 \sum U_g T_g + a_2 \sum (T_g)^2 = \sum u_g T_g \tag{14}$$

Stripping

This correction, also known as the channel interaction correction, is used to correct K, U and Th window count rates for gamma rays not originating from the radioelement or decay series being monitored. For example, Th series gamma rays appear in both the U and K windows, and U series gamma rays appear in the K window. The corrections are applied as follows:

$$\begin{aligned} N_{Th(corr)} &= N_{Th} \\ N_{U(corr)} &= N_U - \alpha N_{Th(corr)} \\ N_{K(corr)} &= N_K - \beta N_{Th(corr)} - \gamma N_{U(corr)} \end{aligned} \tag{15}$$

where α is the counts in the U window per unit count in the Th window, β is the counts in the K window per unit count in the Th window, and γ is the counts in the K window per unit count in the U window. These quantities are shown graphically in Figure 11.

The stripping ratio a (U into Th) is small and often neglected during processing. If this stripping ratio is included, then equation 15 becomes

$$\begin{aligned} N_{Th(corr)} &= \frac{N_{Th} - a N_U}{1 - a\alpha} \\ N_{U(corr)} &= \frac{N_U - \alpha N_{Th}}{1 - a\alpha} \\ N_{K(corr)} &= N_K - \beta N_{Th(corr)} - \gamma N_{U(corr)} \end{aligned} \tag{16}$$

The stripping ratios α, β and γ can be calculated directly from pure U and Th spectra. The shape of airborne spectra is a function of source diameter and detector height, and since thick broad sources (infinite diameter) are the most common in the geological environment, we should simulate pure spectra due to this source type. But source diameter does not appreciably affect the shape of the spectrum in the vicinity of the K, U and Th windows, and finite sources can be used for the calibration. Changes in spectral shape with height, however, are significant, and calibration spectra should be simulated for a range of heights. Minty et al. (1990) built a set of portable cylindrical calibration sources and used these to simulate the response of an airborne spectrometer to semi-infinite sources over a range of simulated heights. The experiment resulted in K, U, and Th model spectra at five simulated heights between 0 and 200m.

Alternatively, specially constructed concrete slabs can be used for calibration and for determining pure spectra for each of the radioelements. Grasty et al. (1991) originally constructed sets of transportable concrete slabs for the calibration of portable gamma-ray spectrometers. These consist of four 1m x 1m x 30cm slabs, each weighing about 700 kg. Three of the slabs have elevated concentrations of either K, U, or

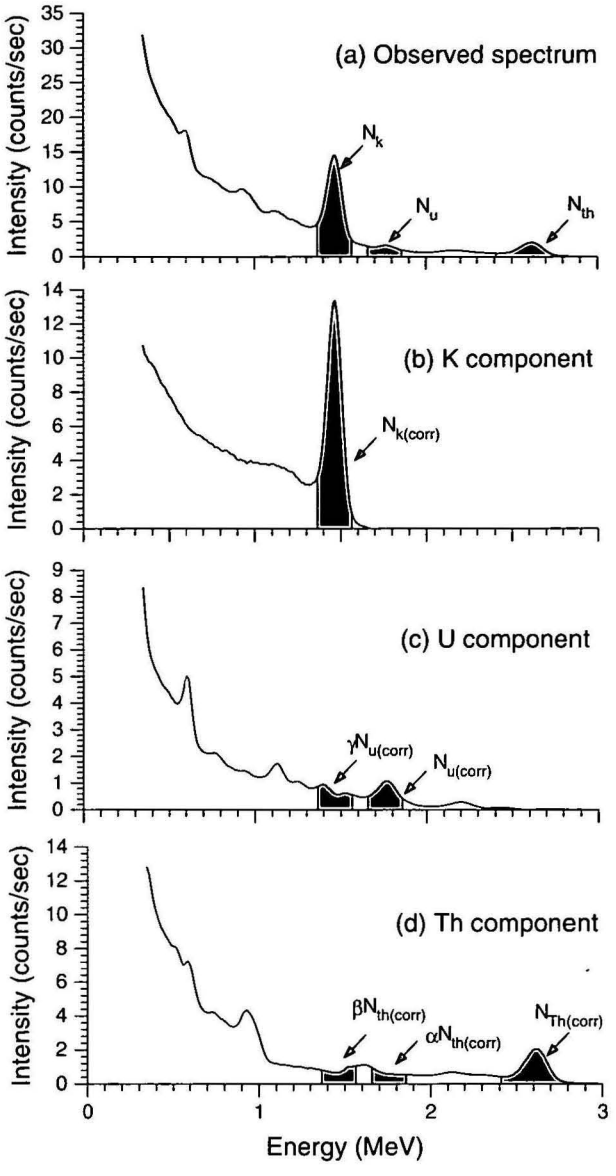

Figure 11. The potassium, uranium and thorium spectra at a simulated altitude of 100 m, showing the positions of the conventional K, U, and Th windows and the parameters used for stripping.

Th, respectively. The fourth slab is doped to have concentrations of the radioelements as near as possible to that of the impurities in the other 3 slabs, and serves as a background slab. Grasty et al. (1991) showed that the 3-channel stripping ratios derived from the slabs were not significantly different from those derived from larger airport calibration pads—thus demonstrating that the changes in spectral shape due to source diameter at these energies is not significant. Spectra derived from these slab sources can, therefore, be used to calibrate 3-channel airborne spectrometer systems.

Multichannel spectra are acquired over each of the slabs in turn, and sheets of wood are used to shield the detectors from radiation emanating from the slabs. Since Compton scattering is an electron collision process and wood has the same number of electrons per gram as air, the wood can be used to simulate the attenuation of the gamma rays by air. The measured spectra are corrected for dead time and energy drift. Spectra acquired over the fourth slab are used as background, and these are subtracted from the observed spectra for each simulated height. The final processing step is to reduce the measured spectra to pure spectra from each of the three radioelements. For a single source and n channels, the channel count rates are related to the radioelement concentration of the source as follows:

$$R_i = \sum_{j=1}^{3} a_{ij} x_j \qquad i=1,2,...,n, \quad n \geq 3 \qquad (17)$$

where R_i = count rate in the ith channel,
x_j = source concentration of the jth element (ie. K, U, or Th), and
a_{ij} = proportion of the counts appearing in the ith channel for a given concentration of the jth element.

For three sources, this can be expressed in matrix notation as

$$\mathbf{R} = \mathbf{AX} \qquad (18)$$

$$\mathbf{A} = \mathbf{RX}^{-1} \qquad (19)$$

The elements of **A** are the channel count rates per unit concentration of K, U and Th, and the measured spectra have thus been reduced to pure spectra from each of the three radioelements.

Examples of K, U, and Th spectra acquired at various simulated heights are given in Figures 12–14. Stripping ratios as functions of height can be derived directly from the spectra at each simulated height (e.g. Fig. 15). Alternatively, stripping ratios can be determined at ground level only, and a correction applied to the stripping ratios for the survey height (IAEA 1991). Correction factors are given in Table 2. This is the preferred method, as these published increases in stripping

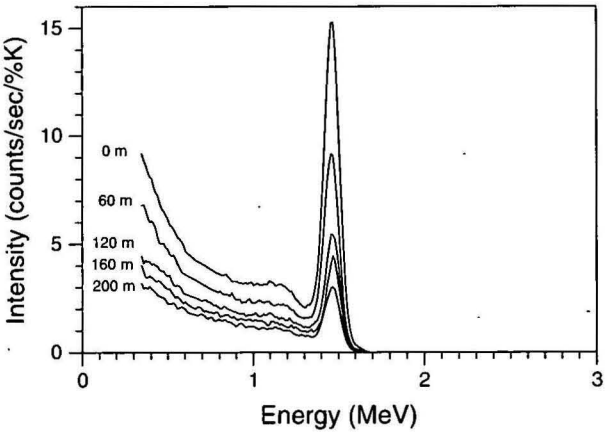

Figure 12. Potassium spectra at various simulated heights.

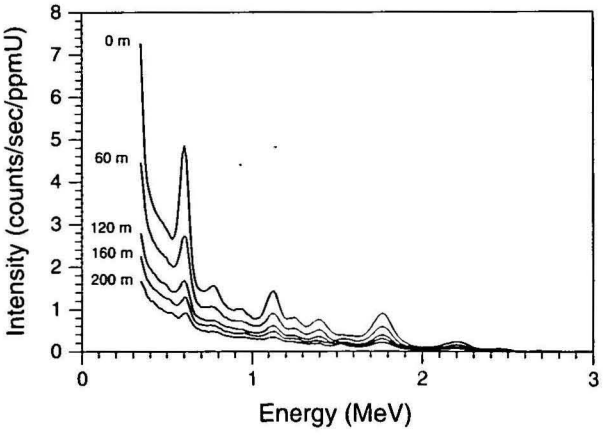

Figure 13. Uranium spectra at various simulated heights.

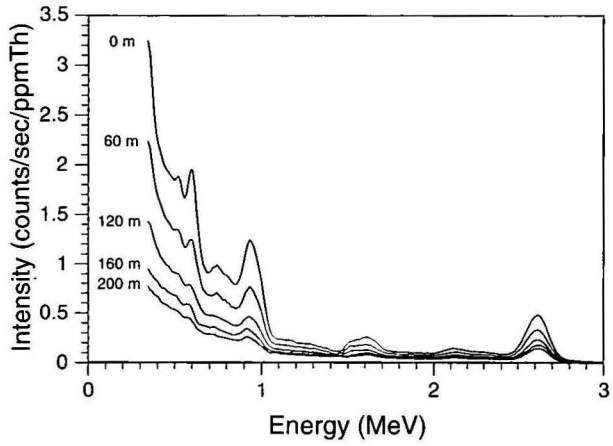

Figure 14. Thorium spectra at various simulated heights.

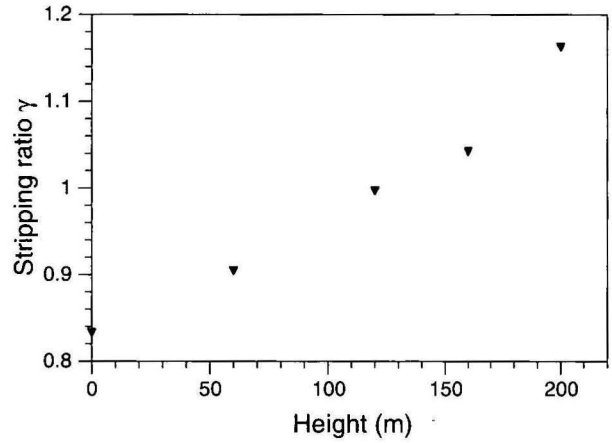

Figure 15. The stripping ratio γ as a function of simulated height.

Table 2. Increase in stripping ratios with height (after IAEA 1991).

Stripping ratio	Increase per metre
α	0.00049
β	0.00065
γ	0.00069

ratios with height were derived through a combination of both theory and experiment. Note that STP height (height at standard temperature and pressure—see following section) should be used to calculate the stripping ratio correction factors. Height correction for the stripping ratio a is small and usually neglected.

Height correction

Airborne gamma-ray spectrometric data need to be corrected to a nominal survey height to remove the effect of variation in the height of the detector. The attenuation of gamma rays with elevation above the ground depends on the geometry of the source as well as the energy of the radiation. Thus, radiation from narrow sources attenuates more rapidly with distance than that from broad sources, and low-energy radiation falls off more rapidly with distance than high-energy radiation.

A gross correction for height can be obtained by considering an exponential fall-off of radiation as a function of the instantaneous height of the detector:

$$N = N_0 e^{-\mu (H-h)} \quad (20)$$

where μ = the empirically derived height attenuation coefficient for any particular energy interval and a particular source type;
N_0 = the observed count rate at the STP height, h, and
N = the corrected count rate for the nominal survey height H.

This algorithm is adequate for subdued topography and heights in the range 50–250 m. Attenuation coefficients for broad sources are universally used as this is the most common source type in the geological environment. More accurate algorithms are available. Schwarz et al. (1992), for example, modelled the terrain in both 2 and 3 dimensions to develop an improved method for handling height corrections in areas of rugged topography.

Note that the height used in equation 20 must be corrected for the ambient temperature and pressure, since both affect the density and, thus, the attenuating properties of the air. The equivalent height at standard temperature (273.15 K) and pressure (101.325 kPa), i.e. the STP height, is given by (IAEA 1991)

$$h_{STP} = \frac{273.15 \times P \times h_{obs}}{(T + 273.15) \times (101.325)} \quad (21)$$

where h_{obs} = observed height above ground level (metres);
h_{STP} = equivalent height at STP (metres);
T = air temperature (°C);
P = barometric pressure (kPa).

The temperature, pressure and radio altimeter data can be lightly filtered before application of the height correction. Height attenuation coefficients for each window are calculated from data acquired over a calibration range. This is an easily navigated strip of land with uniform concentrations of the radioelements—thus approximating an infinite source.

The calibration range is flown at several heights, and attenuation coefficients are derived from an exponential regression of each background-corrected and stripped channel count rate against height (e.g. Fig. 16).

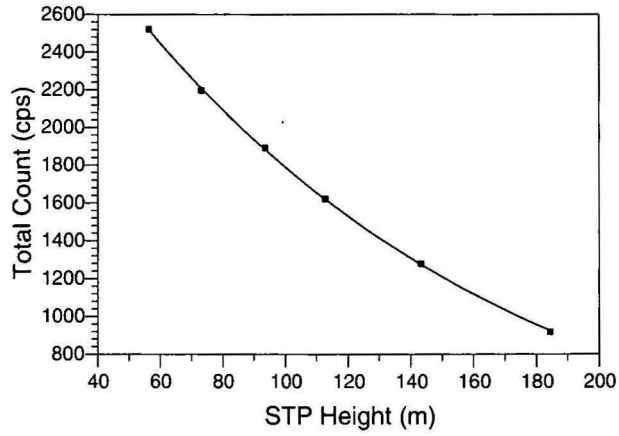

Figure 16. Height attenuation regression plot for the total-count window.

Reduction to elemental concentrations

Gamma-ray spectrometric data are often presented in counts per unit time (count rates). This is undesirable because the count rates are dependent not only on the ground radioelement concentrations, but also on the equipment used and the nominal height of the particular survey. Crystal volume, detector

efficiency, and window widths all affect the observed count rate and make it difficult to compare results from two different surveys. Measuring units should have a direct geological significance and be independent of instrument and survey parameters. Airborne count rates should, therefore, be converted to mean-ground-level abundances of the radioelements.

The conversion is usually performed by dividing each of the corrected three channel count rates by a 'sensitivity' coefficient. This depends on source type and detector height, and as with height attenuation coefficients, is measured for each energy window from data acquired over the effectively infinite source provided by the calibration range. The concentration of radioelements along the calibration range is measured using a well-calibrated portable spectrometer at the same time as the airborne data are acquired. This allows changing radiation output from the ground due to soil-moisture content and other environmental factors to be accommodated.

The sensitivity coefficient for each window is calculated by simply dividing the average background-corrected and stripped window count rate at each height by the appropriate average ground concentration for the calibration range, i.e.

$$S = \frac{N}{C} \tag{22}$$

where N = average background-corrected and stripped count rate at the nominal survey height;
C = average ground concentration;
S = sensitivity coefficient.

Levelling the data

Changes in soil moisture, vegetation thickness and Rn content of rocks and soils during the course of an airborne survey cause variations in the radiation output of the Earth and result in unwanted changes in the measured radiation both along and between lines. The effect is particularly severe for radiation from U. Also, all the data-correction procedures involve assumptions about source geometry that may not always be valid. These, combined with the errors in the calibration constants, can result in long-wavelength 'level shift' errors in the processed data. One or more of three methods are usually used to correct the data.

Conventional levelling using crossover ties

Tie lines are usually flown perpendicular to the flight lines and spaced at about 10 times the line spacing. These can be used to level the data by warping each line and tie (using low-order polynomials, for example) to minimise differences at their intersection points.

Between-channel correlation information

Green (1987) developed a procedure for removing residual background estimation errors for the U window, using between-channel correlation information. The method is based on the assumption that, for background-corrected data, the U flight-line means are a linear function of the K and Th flight-line means, and the correction is constant for the length of each line. Obviously, the K and Th window data need to be level for the method to work successfully.

Microlevelling

Minty(1991) described a simple method for removing residual levelling errors from located aeromagnetic data, which is just as applicable to airborne gamma-ray spectrometric data. The errors are removed from a grid of the data by a directional grid filtering technique, and the filtered grid is then used to correct the located data. The method must be used selectively, since it is not rigorous, and real elongate anomalies in the flight-line direction are removed just as easily as levelling errors.

The levelling of the data concludes the data processing. In the following section we discuss the source of errors in airborne gamma-ray spectrometry and show how errors are amplified by data processing procedures.

Error propagation

Statistical counting errors in gamma-ray spectrometry follow a Poisson distribution. A special property of this distribution is that the standard deviation is equal to the square root of the mean count rate:

$$\sigma = \sqrt{n} \tag{23}$$

where n is the mean count rate. Also, the variance of a distribution is the mean square deviation and is, thus, equivalent to the square of the standard deviation:

$$v = \sigma^2 = n \tag{24}$$

'Percentage standard deviation' is often used to quote errors. This is the fractional deviation expressed as a percentage of the mean count rate:

$$\frac{\sqrt{n}}{n} \times 100 = \frac{100}{\sqrt{n}} \tag{25}$$

These relationships provide a convenient means for estimating errors in gamma-ray spectrometry. If all errors are assumed to be due to the random nature of radioactive decay, then the variance in observed count rates is approximately equal to the number of counts observed. Also, for a function of two variables, $f(x,y)$ with known standard deviations (σ_x and σ_y, say) associated with the variables x and y, the standard deviation in $f(x,y)$ is given by:

$$\sigma_f = \sqrt{\left(\frac{\partial f}{\partial x}\right)^2 \left(\sigma_x\right)^2 + \left(\frac{\partial f}{\partial y}\right)^2 \left(\sigma_y\right)^2} \tag{26}$$

Equation 26 can be used to trace the propagation of statistical errors through the data processing stream to obtain an insight into the magnitude of statistical errors and how these errors are amplified by the data processing.

Table 3 shows the window count-rate contributions from both background and terrestrial sources for typical crustal material (2% K, 2.5 ppm eU, 9 ppm eTh) at 100 m height, under conditions of low and high atmospheric Rn concentration. For 'high Rn', 45 per cent of counts in the U channel are due to atmospheric Rn; and for 'low Rn', 20 per cent. These data have been used to simulate the propagation of statistical errors by the data processing procedures. Tables 4 and 5 show how the background correction and stripping affect both the absolute and fractional standard deviations.

Table 3. Window count rate contributions over typical crustal material (2% K, 2.5 ppm eU, 9 ppm eTh) at 100 m height and under conditions of both low and high atmospheric Rn concentrations.

	Window count rates Low Rn			*Window count rates High Rn*		
Source	K	U	Th	K	U	Th
Ground	212.1	30.3	45.5	212.1	30.3	45.5
Background	25.2	17.0	6.3	41.6	36.0	8.0
Observed	237.3	47.3	51.8	253.7	66.3	53.5

Since the purpose of this simulation is to illustrate how the error envelope on data is affected by the data processing, we have assumed that there are no errors associated with the background estimates. Background is usually calculated every 200–400 s, and since the same background is subtracted from

Table 4. Propagation of statistical errors by the data processing procedures for airborne count rates over typical crustal material (2% K, 2.5 ppm eU, 9 ppm eTh) at 100 m height and under conditions of high atmospheric Rn concentration. The fractional errors are shown in brackets and are the standard deviations expressed as percentages of the count rates.

	Window count rates and fractional errors		
	K	U	Th
Observed	253.7 ± 15.9 (6.3)	66.3 ± 8.1 (12.3)	53.5 ± 7.3 (13.7)
Background adjusted	212.1 ± 15.9 (7.5)	30.3 ± 8.1 (26.9)	45.5 ± 7.3 (16.1)
Stripped	175.9 ± 18.3 (10.4)	14.7 ± 8.5 (58.0)	45.5 ± 7.3 (16.1)

Table 5. Propagation of statistical errors by the data processing procedures for airborne count rates over typical crustal material (2% K, 2.5 ppm eU, 9 ppm eTh) at 100 m height and under conditions of low atmospheric Rn concentration. The fractional errors are shown in brackets and are the standard deviations expressed as percentages of the count rates.

	Window count rates and fractional errors		
	K	U	Th
Observed	237.3 ± 15.4 (6.5)	47.3 ± 6.9 (14.5)	51.8 ± 7.2 (13.9)
Background adjusted	212.1 ± 15.4 (7.3)	30.3 ± 6.9 (22.7)	45.5 ± 7.2 (15.8)
Stripped	175.9 ± 17.3 (9.8)	14.7 ± 7.3 (49.8)	45.5 ± 7.2 (15.8)

successive samples, this procedure does not increase the absolute size of the error envelope. However, the background correction increases the fractional errors in all channels, since the count rates are reduced in all channels.

We assume that the data are adequately stripped using just three stripping ratios—α, β and γ. The stripping correction results in an increase in the absolute error in both the K and U channels, since Th statistical errors are propagated into the U channel, and both Th and U statistical errors are propagated into the K channel.

The error analysis summarised in Tables 4 & 5 has only been concerned with the noise envelope. The height correction procedure has not been included in this analysis, since the process scales both signal and noise by the same factor and the fractional errors thus remain the same. But for significant variations from the nominal height of the survey, the factors by which the height correction procedure scales the data are large (Table 6). At 300 m height, for example, U channel data are scaled by 9.97 to reduce these data to a nominal height of 100 m (Table 6) and the noise envelope is amplified to the same degree. Table 7 illustrates the propagation of errors for data acquired at various heights. The errors increase rapidly for data acquired at heights above about 250 m; consequently, the height used for height correction is usually restricted to about 250 m for actual heights above this limit.

It is not commonly recognised that the height correction procedure can also introduce large errors if the data have not been adequately background corrected. This is because the amplitude of the background radiation components (particularly Rn) is largely unaffected by detector height. But the amplitude of the height correction imposed by equation 20 depends on both the deviation of the detector height from the nominal survey height and the background-corrected count rate N_0. If N_0 includes a background component, then large errors can be introduced into the data. Specifically, if $N_0=N_1+N_{bgd}$ is the observed count rate at height h, where N_1 is the terrestrial component and N_{bgd} is an uncorrected background component, then equation 20 can be rewritten as

$$N_0 = \left(N_1 + N_{bgd}\right) e^{-\mu (H-h)}$$
$$= N_1 e^{-\mu (H-h)} + N_{bgd} e^{-\mu (H-h)} \quad (27)$$

and the uncorrected background term is amplified by the factor $e^{-\mu (H-h)}$.

An example of this is shown in Figure 17, in which the profiles show the detector height and the stripped and height-corrected U window count rates for a profile where all components of background have been removed, and for a second profile, where only the aircraft and cosmic background have been removed. The data are clearly over-corrected for height effects on the profile where Rn background has not been removed. This is an extreme example, as the variations in height along this profile are large, but it demonstrates the point well. The larger noise envelope associated with the greater heights is also visible.

Table 6. Height correction factors for a range of heights and a nominal survey height of 100 m.

	Height correction factor		
Height	K (μ = 0.00943 m^{-1})	U (μ = 0.01150 m^{-1})	Th (μ = 0.00747 m^{-1})
110	1.09	1.12	1.07
150	1.60	1.77	1.45
200	2.56	3.15	2.11
300	6.59	9.97	4.45

Conclusion

The calibration of airborne gamma-ray spectrometer systems and the methodology for the processing of airborne gamma-ray spectrometric data have been reviewed. Wherever possible we have taken a 'full spectrum' approach to the description of the calibration procedures, since this gives a clearer insight into the physics of the method.

A variation on the spectral-ratio method for estimating Rn background has been described. The method appears to work well under Australian conditions. We have shown how the error envelope due to statistical errors in the observed data is affected by the data processing procedures. Errors in U count rates are due to a combination of large background and stripping corrections. Large errors can be introduced into the

Table 7. Propagation of U statistical errors by the data processing procedures for airborne count rates over typical crustal material (2% K, 2.5 ppm eU, 9 ppm eTh) at various heights and under conditions of high atmospheric Rn concentration. The count rates are height corrected to a nominal survey height of 100 m. The fractional errors are shown in brackets and are the standard deviations expressed as percentages of the count rates.

	U window count rates and fractional errors for data acquired at 100, 200 and 300 m height		
	100 m	200 m	300 m
Observed	66.3 ± 8.1 (12.3)	48.9 ± 7.0 (14.3)	41.8 ± 6.5 (15.5)
Background adjusted	30.3 ± 8.1 (26.9)	12.9 ± 7.0 (54.3)	5.8 ± 6.5 (112.0)
Stripped	14.7 ± 8.5 (58.0)	4.6 ± 7.3 (156.9)	1.5 ± 6.7 (455.7)
Height corrected (to 100 m)	14.7 ± 8.5 (58.0)	14.7 ± 22 (156.9)	14.7 ± 66 (455.7)

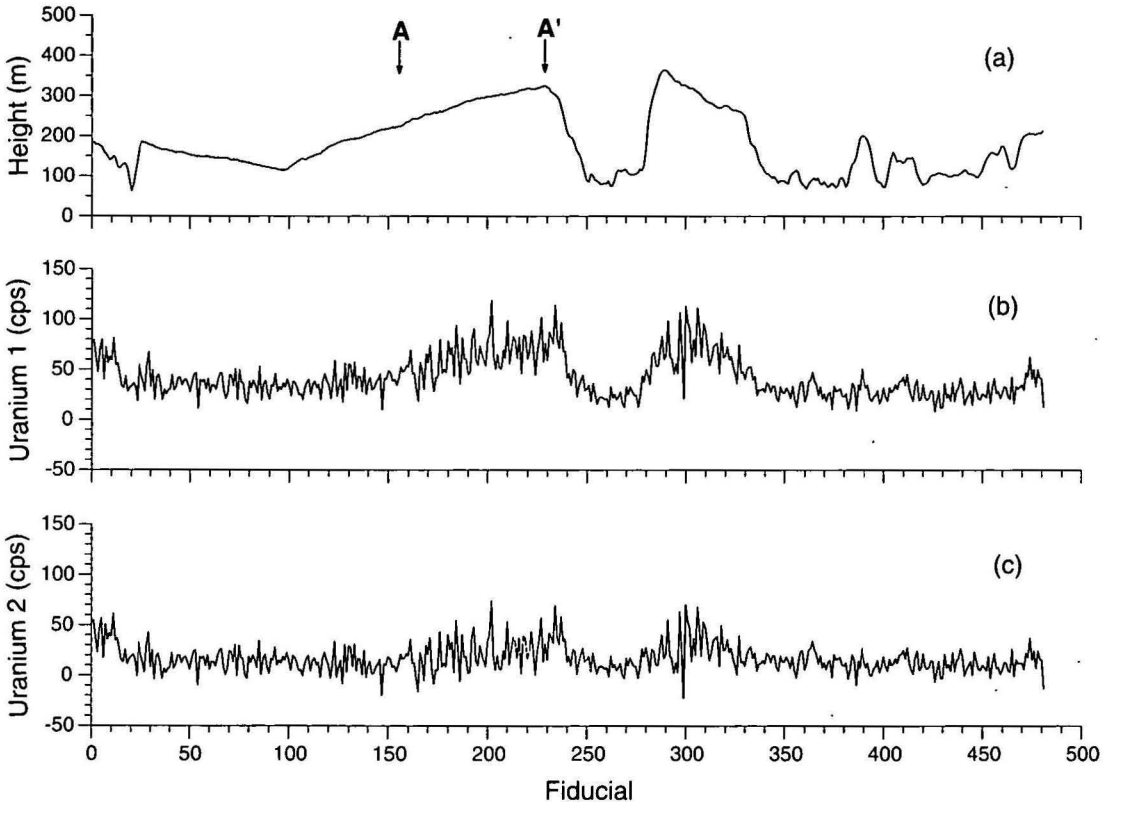

Figure 17. Profiles from the Lissadel map sheet area, Western Australia, showing (a) instantaneous height, (b) stripped and height-corrected uranium window profile where only the aircraft and cosmic background have been removed, and (c) a second uranium window profile showing the stripped and height-corrected data where all components of background have been removed. Profile (b) is clearly over-corrected for height effects in the region A–A, for example.

data through the height correction procedure if the background radiation is not adequately removed.

References

Fritzsche, A.E., 1982. The National Weather Service gamma snow system—physics calibration. Report by GeoMetrics to National Oceanic & Atmospheric Administration/National Weather Service, by contract with the United States Department of Energy.

Grasty, R.L., 1975. Uranium measurements by airborne gamma-ray spectrometry. Geophysics, 40(3), 503–519.

Grasty, R.L., Wilkes, P.G. & Kooyman, R., 1988. Background measurements in gamma-ray surveys. Geological Survey of Canada, Paper 88-11.

Grasty, R.L., Holman, P.B. & Blanchard, Y.B., 1991. Transportable calibration pads for ground and airborne gamma-ray spectrometers. Geological Survey of Canada, Paper No. 90-23, 25pp.

Green, A.A., 1987. Levelling airborne gamma-radiation data using between-channel correlation information. Geophysics, 52(11), 1557–1562.

IAEA, 1991. Airborne gamma ray spectrometer surveying. International Atomic Energy Agency, Technical Report Series, No. 323.

Lovborg, L., 1984. The calibration of portable and airborne gamma-ray spectrometers—theory, problems, and facilities. Riso National Laboratory, DK-4000 Roskilde, Denmark, Report Riso-M-2456.

Minty, B.R.S., 1991. Simple micro-levelling for aeromagnetic data. Exploration Geophysics, 22, 591–592.
Minty, B.R.S., 1992. Airborne gamma-ray spectrometric background estimation using full spectrum analysis. Geophysics, 57(2), 279–287.
Minty, B.R.S., 1996. The analysis of multichannel airborne gamma-ray spectra. PhD Thesis, Australian National University.
Minty, B.R.S., Morse, M.P. & Richardson, L.M., 1990. Portable calibration sources for airborne gamma-ray spectrometers. Exploration Geophysics, 21, 187–195.
Schwarz, G.F., Klingele, E.E. & Rybach, L., 1992. How to handle rugged topography in airborne gamma-ray spectrometry surveys. First Break, 10(1), 11–17.

AGSO Journal of Australian Geology & Geophysics, 17(2), 63–75

Enhancement and presentation of airborne geophysical data

P.R. Milligan[1] & P.J. Gunn[1]

Airborne geophysical data can be enhanced by a range of linear and non-linear filtering algorithms which selectively enhance the anomalies due to one group of geological sources relative to anomalies due to other groups of geological sources. Mathematical enhancement techniques are complemented by a range of imaging routines which can be specified to visually enhance the effects of selected geological sources.

Enhancement of airborne data

After the recording of airborne magnetic and gamma-ray spectrometric data, several corrections are applied to the data to produce located profile and grid versions of 'processed' total magnetic intensity, total radiometric count rate, and count rates for the potassium, thorium and uranium energy windows. These values are normally displayed as profiles, contours and images; however, in many cases it is possible to apply various filtering and transformation processes prior to the display of these data sets to produce secondary products with an obviously improved information content.

The following discussion describes these enhancement techniques. Note that most of the methods described have been developed in the context of processing aeromagnetic data, and, consequently, the discussion is mainly on aeromagnetic applications. Adaptations of the techniques to enhancing gamma-ray data are described where appropriate. Emphasis is on the principles behind the enhancements and on the usefulness of the enhancements in the interpretation of data. The mathematics behind the various routines has been kept to a minimum, with sufficient references provided for readers to obtain greater detail if required.

Linear transformations (filters)

A linear filtering process changes, in a predetermined way, the amplitude and/or phase relationships of the assemblage of sine waves that constitutes every profile or grid data set. It can be done by multiplying the Fourier transform of the data set in the frequency domain to obtain the desired amplitude and phase alterations, and then transforming the spectrum of the modified data set back into the space domain. Alternatively, the same transformation can be done by convolving the data set in the space domain with a set of filter coefficients whose frequency response (i.e. Fourier transform) is the same as the desired amplitude and phase changes. These processes are well-known mathematical techniques and will not be elaborated upon here. Readers requiring more detail are referred to basic texts such as Fuller (1967) and Gonzalez & Woods (1992). It is important, however, to be aware (in the context of processing airborne geophysical data) of the transformations that can be achieved by linear filtering processes, and the significance and utility of these transformations. Transformation processes may conveniently be subdivided into:

- those which, in effect, convert fields representing physically measurable parameters into other fields representing different physically measurable parameters, and
- those which enhance data sets by selectively removing certain unwanted frequency (wavelength) components.

Transformation processes

The generalised spectral representation of magnetic fields (Gunn 1975) provides an appreciation of many of the transformations possible with magnetic fields. This generalised expression is:

$$M_f(u,v,o) = 2\pi.D_1(u,v).D_2(u,v).I(u,v).m_s(u,v,h).H(u,v,h)$$

where

2π is a scaling factor

$D_1 = [jLu + jMv + N(u^2 + v^2)^{1/2}]$ is a factor for direction of magnetisation,

$D_2 = [jlu + jmv + n(u^2 + v^2)^{1/2}]$ is a factor for direction of measurement,

$H = e^{-h(u2 + v2)^{1/2}}$ is a depth factor,

$m_s = m_s(u,v,h)$ is an equivalent layer factor (which incorporates source body shapes),

and,

$I = \dfrac{1}{(u^2+v^2)^{1/2}}$ is an extra factor distinguishing magnetic from gravity fields.

The important point illustrated by this equation is that, in the frequency domain, magnetic intensity is defined by simple multiplications of factors related to the depth of the sources, source body shapes, direction of magnetisation and magnetic latitude. These factors can be altered by linear filtering processes which result in the magnetic intensity being transformed into another representation. For example, multiplication of the spectrum of a field by a factor $H = e^{-h(u^2+v^2)^{1/2}}$ converts it into the spectrum of the field measured at a distance h above the plane of observation of the original field. A reverse Fourier transformation back to the space domain gives the actual field at the higher level. This is equivalent to convolving the field in the space domain by an operator (or filter) whose frequency response is equivalent to $e^{-h(u^2+v^2)^{1/2}}$. All linear transformations of magnetic fields work in this way.

Gunn (1975) described the transformations possible by the alteration of these factors. They are:

Upward and downward continuation. Computation of fields at higher or lower levels is called upward or downward continuation. As described above, the process has a frequency response of $e^{-h(u^2+v^2)^{1/2}}$. This means that upward continuation smooths out high-frequency anomalies relative to low-frequency anomalies. The process can be useful for suppressing the effects of shallow anomalies when detail on deeper anomalies is required. Downward continuation sharpens the effects of anomalies (enhances high frequencies) by bringing them closer to the plane of observation—it simulates flying the survey closer to the ground. In practice, high-frequency noise is enhanced as well as the geological anomalies, and it is normally difficult to continue a field downward very far. The practical limits depend on the sample interval and the quality of the data set.

It is also theoretically possible to continue airborne radiometric measurements upward or downward. Gunn (1978) developed an analytic expression for the frequency response of this process, which has been calculated numerically by Craig (1993).

Figure 1B is an example of TMI data from Tasmania that have been upward continued to 1000 m. The original data are shown in Figure 1A.

[1] Australian Geological Survey Organisation, GPO Box 378, Canberra, ACT 2601

Reduction to the pole or to any other magnetic latitude. Reduction to the pole is the process of converting the magnetic field from a magnetic latitude where the Earth's field is inclined, to the field at a magnetic pole, where the inducing field is vertical. When the Earth's field is inclined, magnetic anomalies due to induction have forms that are asymmetrically related to their sources, but when the inducing field is vertical, the induced anomalies are directly over their sources. The same process can be used to convert magnetic fields between any two magnetic latitudes. Reduction to the pole greatly simplifies the interpretation of magnetic data, because at magnetic latitudes less than 50° the relationship of anomaly form to source geometry is often not obvious (e.g. Vacquier et al. 1951).

As discussed by Macleod et al. (1994), problems can arise in the reduction to the pole process at magnetic latitudes less than 15°, as the Fourier domain transformation process becomes unstable, owing to the need to divide the spectrum by a very small term. Some workers avoid this problem by limiting their transformations to greater than 15° and accepting the results. Others approximate the process by doing two transformations for smaller amounts, where the sum of the angles involved in the transformations equals the difference between the survey latitude and the pole. Some workers avoid the issue altogether by performing a reduction to the equator. This does indeed produce anomalies that are symmetrically related to their sources; however, such anomalies have elongations and subsidiary peaks that do not occur in polar anomalies and

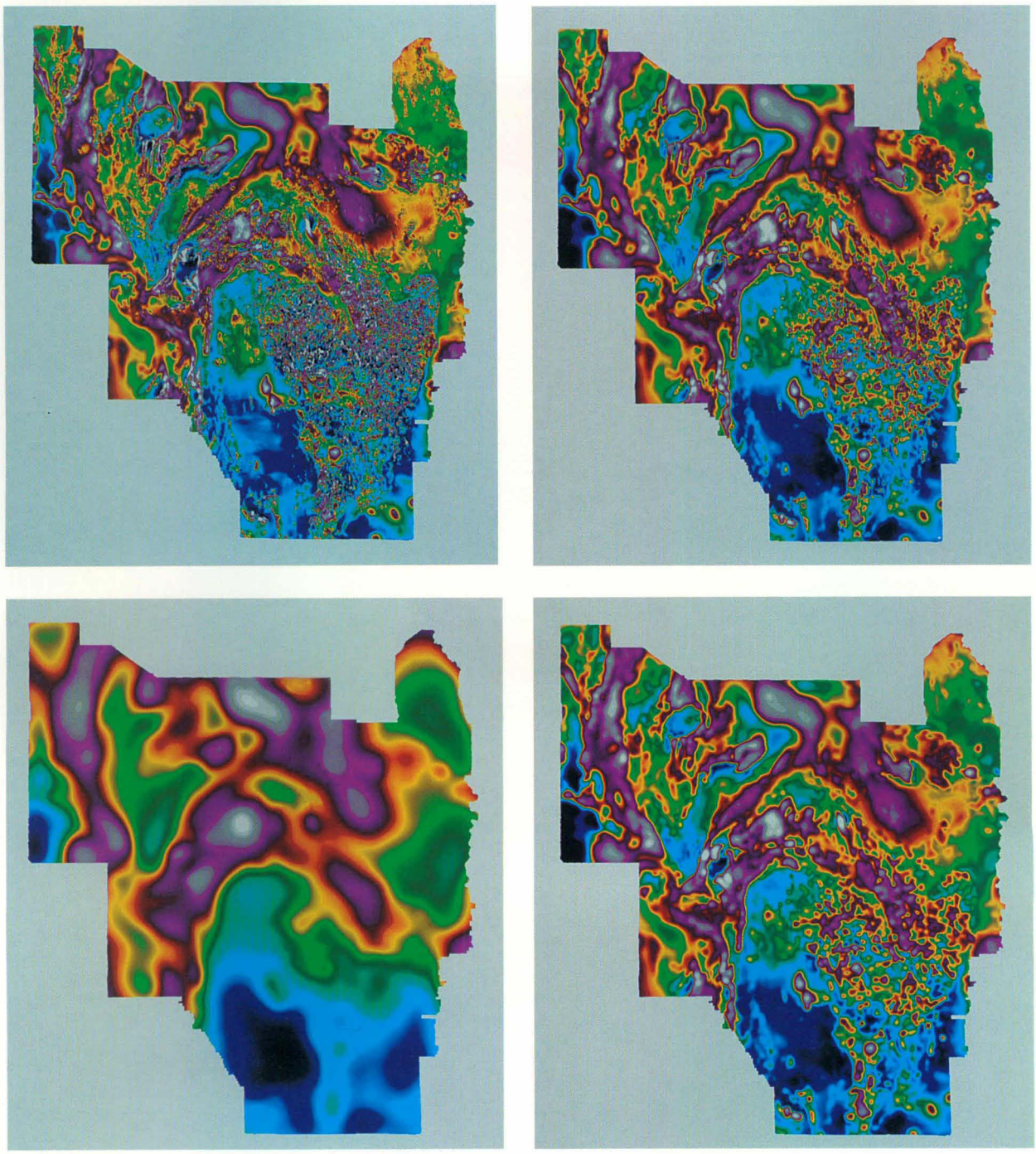

Figure 1. Examples of various filters applied to the Tasmanian total magnetic intensity (TMI) data. (A, upper left) Reduced to the pole; (B, upper right) Upward continued to 1000 m; (C, lower left) Matched filtered; (D, lower right) Low-pass filtered, removing wavelengths less than 5000 m. 'Comtal' LUT.

they are, consequently, more difficult to interpret. Gunn & Almond (1977) have demonstrated a space domain solution to the problem of transformations at low latitudes.

A basic assumption of the reduction to the pole process is that all bodies are magnetised by induction. Macleod et al. (1994) have demonstrated that smearings of anomalies can occur in transformed maps when significant remanent magnetism is present. In the authors' experience, significant remanence appears to be relatively rare and its possibility should not inhibit the use of reduction to the pole. The analytic signal (described below) can provide a check on the presence of remanence because computed analytic signal peaks, which occur above source bodies regardless of the direction of magnetisation, can be correlated with the peaks of reduction to the pole data to check for consistency.

Figures 2A and 2C are examples of TMI data from the Medusa Banks 1:250 000 map sheet area, before and after reduction to the pole.

Computation of vertical derivatives. Various vertical derivatives of the magnetic field can be computed by multiplying the amplitude spectra of the field by a factor of the form:

$$\frac{1}{n}\left[\left(u^2+v^2\right)^{1/2}\right]^n$$

where n is the order of the vertical derivative. The first vertical derivative (or vertical gradient) is physically equivalent to measuring the magnetic field simultaneously at two points vertically above each other, subtracting the data and dividing the result by the vertical spatial separation of the measurement points. The second vertical derivative is the vertical gradient of the first vertical derivative and so on. The formula for the frequency response of these operations shows that the process enhances high frequencies relative to low frequencies, and this property is the basis for the application of the derivative process which eliminates long-wavelength regional effects and resolves the effects of adjacent anomalies. First vertical derivative data have become almost a basic necessity in magnetic interpretation projects. The second vertical derivative has even more resolving power than the first vertical derivative, but its application requires high quality data as its greater enhancement of high frequencies results in greater enhancement of noise. Higher orders of derivatives are virtually never used to produce interpretation products. In principle, a derivative product could be produced where n is not an integer in the above equation. For example, a 1.5th vertical derivative could be produced as a compromise between the first and second vertical derivatives.

Figure 4 provides several examples of derivative enhancements of TMI data for the 1:25 000 map sheet area of Mount Gipps, near Broken Hill. These are very high-resolution data, collected as part of the Broken Hill Exploration Initiative, a cooperative venture between the Australian Federal Government and the State Governments of New South Wales and South Australia.

Horizontal derivatives. The filter responses to calculate the nth horizontal derivatives in the x or y directions are $(ju)^n$ and $(jv)^n$. It can be seen that this process involves a phase transformation as well as an enhancement of high frequencies. The phase transformation generally has the result of producing anomaly peaks approximately located over the edges of wide bodies and the enhancement of the high frequencies sharpens these peaks to increase the definition of the body edges. Some interpreters use this quality of the horizontal derivatives to map body outlines. The process becomes extremely ambiguous for narrow bodies, however, and it is difficult to see what advantage horizontal derivatives have over vertical derivatives, which give peaks over the tops of sources and indicate source outlines by steep gradients and inflections.

Converting magnetic fields into equivalent gravity fields. It is possible to transform magnetic fields into pseudo-gravity fields in which the anomalies due to the magnetic bodies have the character of gravity anomalies. This transformation can be useful for relating magnetic and gravity survey data. In practice, gravity and magnetic anomalies often arise from different sources, so the application of such a process is limited to special situations.

Converting one component of measurement into another. While it is possible to convert one component of measurement of a magnetic field into another—for example, total magnetic intensity could, with some assumptions, be converted into vertical intensity—this does not appear to enhance the interpretability of the data and the option does not appear to be used.

Magnetisation and susceptibility mapping. If the magnetic anomalies in an area all arise from vertically sided blocks with the same depth to their tops and the same depth extent, and if all these blocks have the same known magnetisation, it is possible to transform the magnetic data into an areal distribution of the magnetisation causing the anomalies. The amplitude of this magnetisation mapping gives the amplitude of magnetisation of the blocks causing the anomalies. By processing the magnetic data using small sample intervals, the irregular outlines of bodies can be mapped. If the magnetisation is due to induction, the susceptibility of the rock units can be determined by dividing the magnetisation by the intensity of the Earth's field at the survey location. The technique has not been widely used because the necessary assumptions are rarely applicable and, when it is used, the fact that the transformation involves a downward continuation to the tops of the sources normally requires that severe additional smoothing be applied to the results to suppress noise enhancement. Such smoothings degrade the utility of the results. Gunn (1972) demonstrated theoretical and field examples of magnetisation mapping (Fig. 3).

Analytic signal. The analytic signal (Roest et al. 1992) is a function related to magnetic fields by the derivatives, i.e.

$$\text{analytic signal: } |A(x,y)| = \left(\left(\frac{\partial m}{\partial x}\right)^2+\left(\frac{\partial m}{\partial y}\right)^2+\left(\frac{\partial m}{\partial z}\right)^2\right)$$

where m = magnetic anomaly

While this function is not a measurable parameter, it is extremely interesting in the context of interpretation, as it is completely independent of the direction of magnetisation and the direction of the Earth's field. This means that all bodies with the same geometry have the same analytic signal. Furthermore, as the peaks of analytic signal functions are symmetrical and occur directly over the edges of wide bodies and directly over the centres of narrow bodies, interpretation of analytic signal maps and images should, in principle, provide simple, easily understood indications of magnetic source geometry. The analytic function certainly appears to be a worthwhile interpretation tool, but more case history details are required before its general applicability can be assumed. The authors have been involved in several projects where the analytic signal was calculated. In general, sharp anomaly peaks were not obtained over anomaly edges and, instead, diffuse peaks were obtained with outlines less clear than the original total magnetic intensity. This has been ascribed mainly to the fact that source geometry was more complicated than vertical contacts. The difficulty of accurately computing horizontal derivatives for small anomalies trending perpendicular to flight-line directions may, however, have influenced the results.

Analytic signal maps and images are useful as a type of reduction to the pole, as they are not subject to the instability that occurs in transformations of magnetic fields from low magnetic latitudes (MacLeod et al. 1993); they also define

source positions regardless of any remanence in the sources.

Figure 2D shows the analytic signal computed for TMI data from the Medusa Banks 1:250 000 map sheet area.

Anomaly separation using linear filtering

In addition to the transformation processes described above, which all produce parametric representations related to measurable properties, a range of mathematically based linear filtering processes exists, the purpose of which is to remove anomalies with certain characteristics from the data. The products of these mathematically based anomaly removal processes visually enhance the data by making features easier to recognise; however, they all distort the results from being true magnetic or gamma-ray measurements, and this distortion must be appreciated before interpretation of such data is attempted.

All linear filtering processes used to remove magnetic anomalies from data sets are based on differences in the average frequency content of the 'noise' anomalies being removed and the 'signal' anomalies being retained. The fact that anomalies from shallow sources contain higher frequencies than anomalies from deeper sources often allows such a process to provide a satisfactory resolution of magnetic effects arising from different depths. Similarly, acquisition noise can be suppressed on the basis that it typically contains much higher frequencies than anomalies due to geological sources. It is important to appreciate, however, that the frequency content of magnetic anomalies covers a very wide spectrum. Frequencies may overlap between shallow and deep sources and linear filtering is not always able to completely remove the effects of noise anomalies from a data set without also removing a significant proportion of the signal anomalies.

Mathematical linear filtering processes that have been applied to aeromagnetic data to separate anomalies with different frequency characteristics are as follows. Low-pass, averaging and Wiener filters can all be used to smooth statistical and noise variations from gamma-ray spectrometric data.

High-pass, low-pass and band-pass filters. Frequencies in a range can be removed from data by simply eliminating the frequency range from the spectrum of the data (Fuller 1967). For example, if a magnetic data set contains a series of high-frequency anomalies with shallow sources and these high-frequency anomalies are obscuring a series of deep anomalies of special interest, then, in principle, it is possible to remove the high-frequency anomalies by a low-pass process which eliminates anomaly wavelengths shorter than a specified value. The effectiveness of this technique depends on the difference in frequency content of the deeper anomalies relative to the shallower anomalies. Meaningful results can be obtained in cases where the frequency content of the signal and noise is vastly different; however, severe distortion can occur with straight frequency cutting to the extent that the results are misleading.

The first problem is that unless a ramp is used in the frequency cutting, a ripple is introduced into the data, owing to an effect known as 'Gibb's phenomenon'. The types of ramp that should be used and their effects are never obvious. The second problem is that as more and more frequencies are removed from the data the results look less and less like magnetic anomalies and become more difficult to interpret meaningfully. An extreme case, for example, would occur when only a very narrow band of frequencies was preserved, and the output would approximate a simple sine wave. These types of filters should be used with great caution.

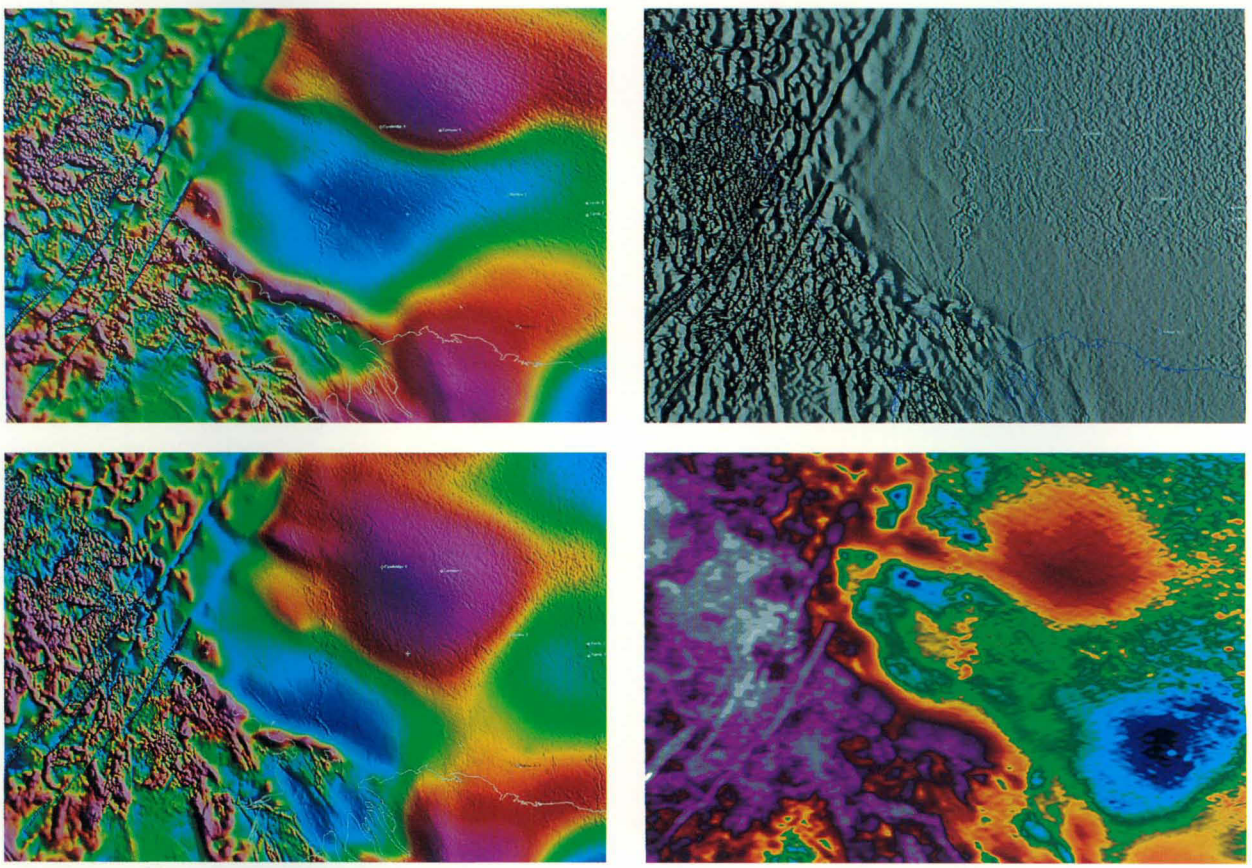

Figure 2. Various filters and enhancements of AGSO TMI data from the Medusa Banks 1:250 000 map sheet area. (A, upper left) TMI with 'rainbow' pseudo-colour with gradient enhancement using a sun-angle routine with azimuth from the northeast; (B, upper right) Bandpass-filtered TMI with illumination from the east; (C, lower left) TMI reduced to the pole with 'rainbow' pseudo-colour and illumination from the northeast; (D, lower right) Analytic signal of the TMI with 'Comtal' pseudo-colour.

An example of band-pass filtering for the Medusa Banks TMI data is shown in Figure 2B, and Figure 1D is an example of low-pass filtering applied to Tasmanian TMI data.

Matched filters. Spector & Parker (1979) described a process they call 'matched filtering', which uses a study of the spectrum of the field to be filtered to design a linear filter to optimise separation of magnetic anomalies arising from different depths. The filter design is facilitated by the fact that 'ensembles' of anomalies with approximately the same depth manifest themselves as straight line segments on a radially averaged logarithmic representation of the energy spectrum of the magnetic field. The filters have tapered cutoffs. The authors' experience is that the process can produce useful results and that the problems associated with straight frequency cuts are avoided. Cowan & Cowan (1993) compared the process with other types of filtering.

Figure 1C is an example of matched filtering applied to Tasmanian TMI data.

Averages. Running averages of adjacent field values can help smooth out minor noise in the data. The exact frequency response of each averaging process varies according to the number of points used in the averaging and the geometrical relationship of the points sampled. Such averages should only ever be used if the frequency of the noise to be averaged out is very high compared to the dominant frequencies of the magnetic anomalies due to geology. The number of coefficients used should also be kept to a minimum to avoid complicated frequency responses and excessive distortion of the geological signal.

Wiener filters. Filters can be designed to give outputs such that the sum of the squares between a desired and an actual output is a minimum. Gunn (1974) showed that such filters, known as Wiener filters, can remove certain types of noise from magnetic fields where average characteristics such as the anomalies of interest and the typical form of a noise anomaly are known. Gunn demonstrated good results with this process in suppressing white noise (i.e. a random distribution of spikes) in a downward continuation process. Wiener filters are not commonly applied to the processing of magnetic data.

Strike filters. It is possible to design filters that suppress frequencies in one direction relative to those in other directions (Fuller 1967). The application of such filters, which can enhance anomalies trending in one direction relative to anomalies trending in other directions, is called strike filtering or trend enhancement. Such filters should be used with extreme caution, as they can introduce apparent trends that do not really exist.

General comments concerning the use of linear filters

Several properties of linear filters and problems associated with their application must be appreciated to avoid pitfalls in understanding their results.

Inputs to a linear filtering process can be applied in any order and the same result will be obtained. This is called the 'principle of superposition'. For example, the same result will be obtained whether a particular smoothing operation is applied to the data before or after a particular transformation.

If an input to a linear filtering process is multiplied by a constant the output will be multiplied by the same constant. This is the 'principle of homogeneity'.

The highest frequency in a sampled data set is the Nyquist frequency, which is equal to the reciprocal of twice the sample interval. This means it is not possible to exactly create rectangular output functions. Processes such as magnetisation mapping and downward continuation to levels near the anomaly source often show ripples due to the lack of these high frequencies. This ripple effect, which is often confused with the effects of noise enhancement, is termed 'Gibb's phenomenon'. The side lobes on the output of the filter illustrated in Figure 3 are due to Gibb's phenomenon.

All linear filtering, regardless of whether it is in the space domain or the frequency domain, uses an array of values of

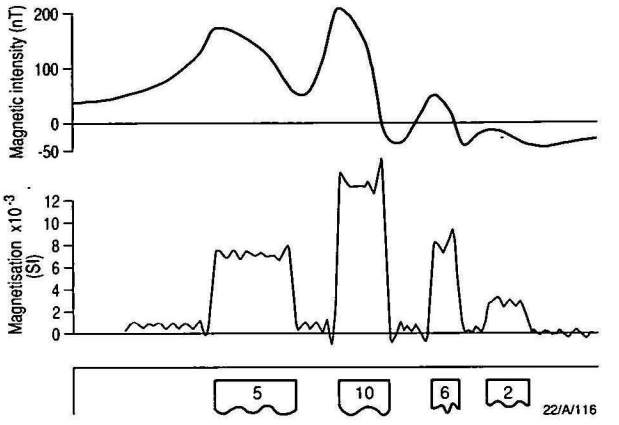

Figure 3. Calculating the magnetisation of a series of vertical dykes magnetised in a field dipping 65° downwards in the direction of the profile. The bottom profile outlines the dykes and the amplitudes correspond to the magnetisations of the dykes. The numbers in the dykes correspond to their magnetisation x 10^{-4} (taken from Gunn 1972, fig. 4).

the original field centred on the point for which the transformation is being calculated. Normally, some form of extrapolation is applied to data sets to allow the calculation of transformed values near the edge of the data set. Obviously, the reality of transformed values near the edge will depend upon the validity of the extrapolation process used. Interpreters should be wary of spurious results associated with this problem. With multiple transformations it is better to combine them into one operation so that only one extrapolation is involved.

Aeromagnetic data are commonly sampled at intervals of about 7.5 m along profiles and when grids of the data are produced, the data on the profiles are resampled at an interval about one fifth of the flight-line spacing. This creates two problems. Firstly, unless an anti-alias filter is applied to the data before the resampling to remove all frequencies higher than the Nyquist frequency of the new grid, fictitious anomalies may be created. The simplest example of this is to consider two spikes that just happen to occur on two adjacent sample points. This will create the impression of an anomaly at least two sample intervals wide when in fact no such anomaly exists. Secondly, the resampling will result in an apparent smoothing of the data, because the creation of grids of aeromagnetic data results in the discarding of much valuable detail. It is important to realise this and to inspect profile data when such detail is important to a particular interpretation problem.

All filtering processes are performed on finite length data sets with what are effectively finite length filters. The net effect of this reality is that most of the transformation type filtering processes only produce approximations to the desired result. For example, reduced to the pole results of model anomalies normally have slightly smaller amplitudes than is expected from theory. This is thought to be due to the fact that the anomaly 'tails' extend off the sample being processed, and as a result become unavailable to the processing. Normally, such effects are not important in visual qualitative interpretations of transformed data; however they can be extremely important if quantitative modelling is attempted with transformed data. For accurate modelling of transformed data, the correct procedure is to calculate the model for magnetic

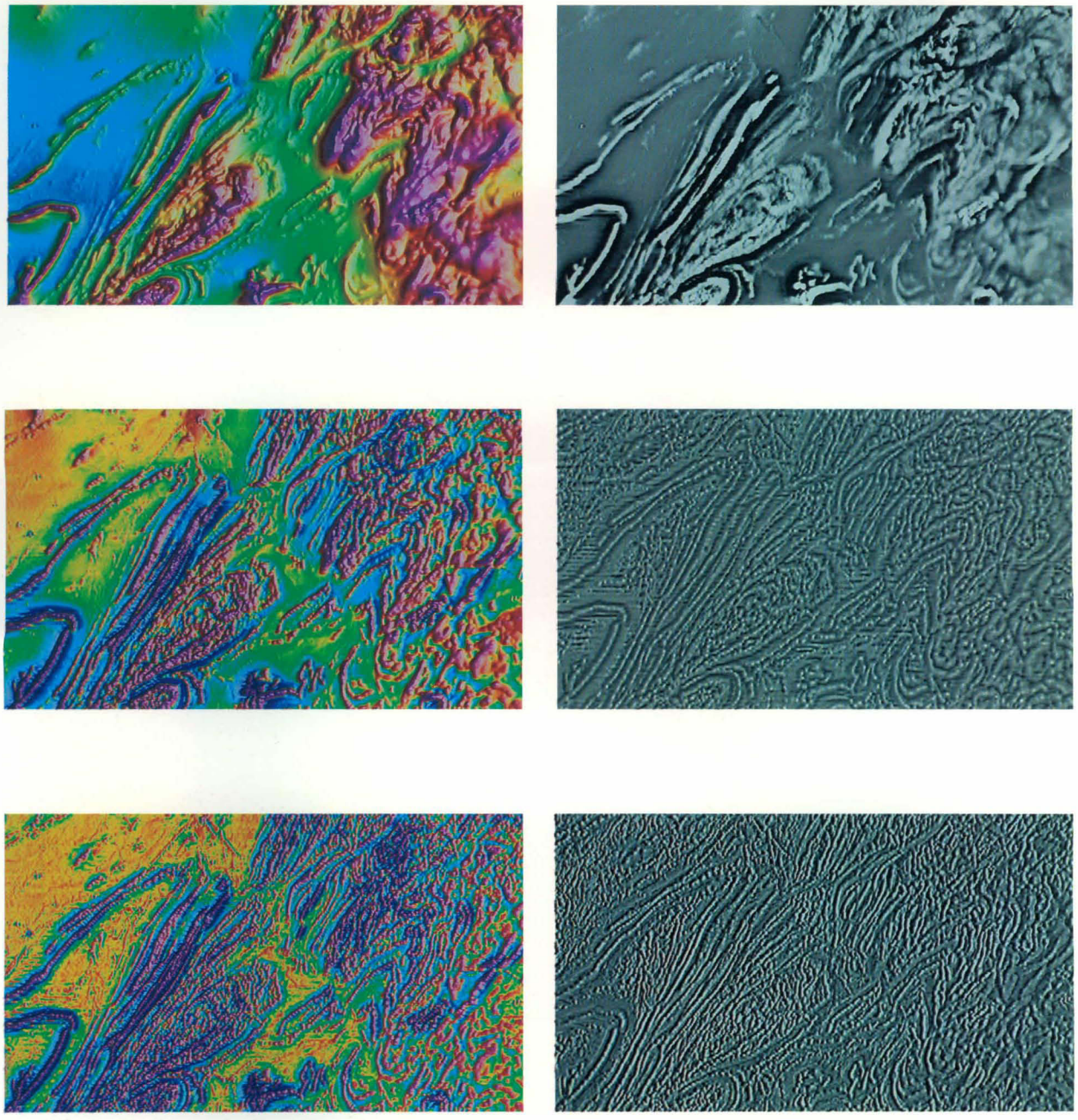

Figure 4. Various TMI filters / enhancements of TMI data for the Mount Gipps 1:25 000 map sheet area. These data were acquired by AGSO as part of the Broken Hill Exploration Initiative. (A, top left) Reduced to the pole with easterly illumination; (B, top right) TMI RP VD1 greyscale; (C, centre left) TMI RP VD1 with 'Comtal' pseudo-colour; (D, centre right) TMI RP VD1 with automatic gain control (AGC); (E, bottom left) TMI RP VD2 with 'Comtal' pseudo-colour; (F, bottom right) TMI RP VD1 AGC with east–west gradient.

intensity with the same location and elevation as that where the data were acquired. Then transform the computed magnetic intensity with the same linear filter process as applied to the transformed product that is the objective of the modelling. The matching should then be made using the transformed model anomaly, which will have exactly the same deviations from the ideal situation as the transformed data set.

Non-linear filters

Outputs of linear filters are predictive in the sense that the amplitude and phase relationships of the signal before and after the filtering process are defined by the frequency response of the filter. The results of non-linear filters cannot be defined in this way; the filters do not necessarily obey the principles of superposition and homogeneity.

Naudy non-linear filtering. Naudy (1967) designed a non-linear filter to remove all or none of an anomaly. The routine works on profile data and successively applies a series of test criteria to determine if an anomaly exists and, if so, whether it can be considered as a single peak or a peak flanked by lows. Depending on the form of the anomaly, the routine fits a background regional to what it regards as the non-anomalous field and thereby enables the removal of the anomaly. The results are dependent on the sampling interval used. In practice, the method does not work realistically with anomalies arising from geological sources, but it can be very useful for removing

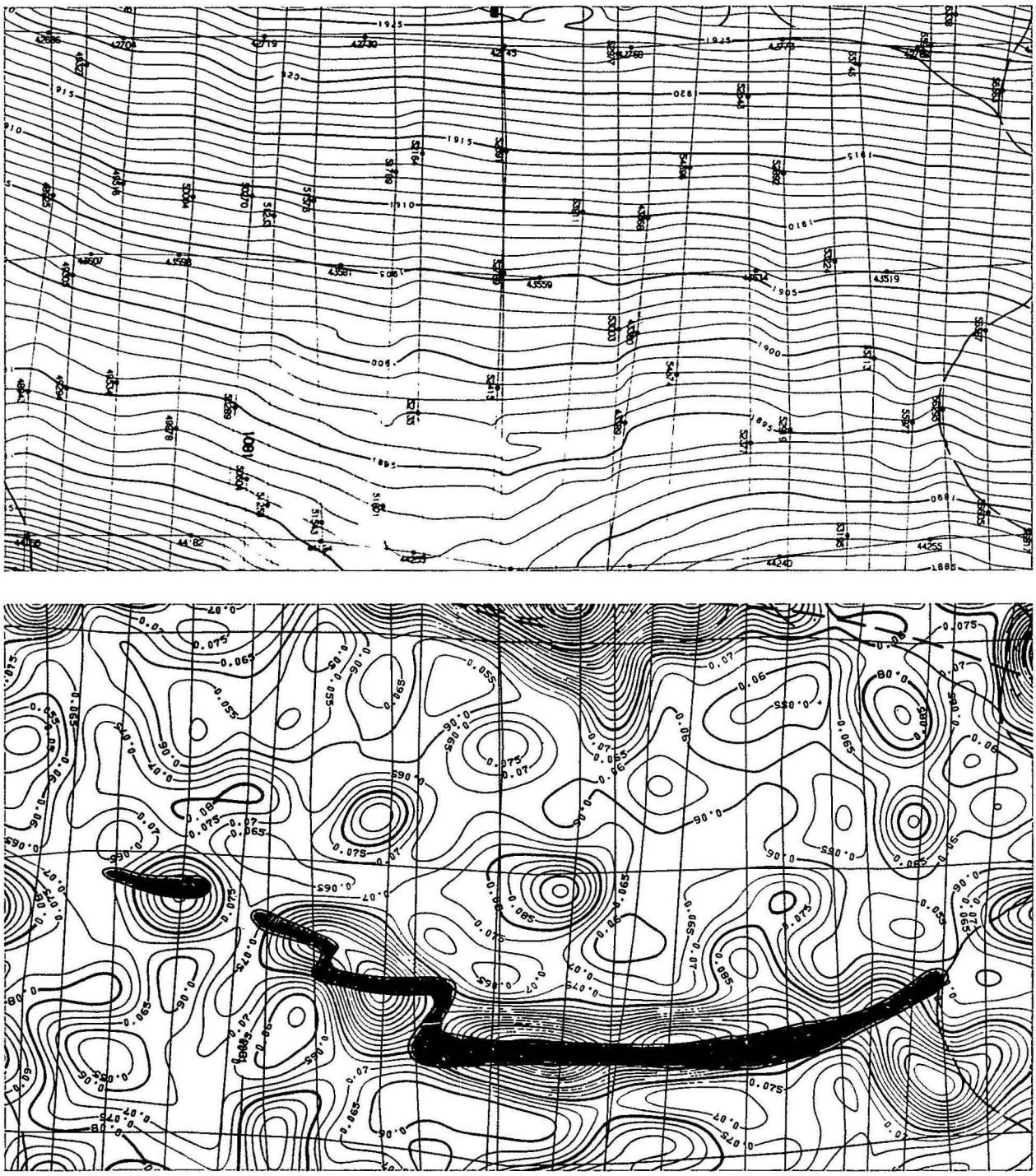

Figure 5. (A) Magnetic intensity; (B) An example of the 'Pitt' filter. This filter map features in the regolith. Shaded feature is a shale unit.

spurious narrow 'spike-type' noise from data.

Automatic gain control. Automatic gain control (AGC) converts waveforms of variable amplitude into waveforms of semi-constant amplitude. The net result is the removal of amplitude information from data sets, producing a representation of the data that gives an equal emphasis to signals with both low and high amplitudes. AGC stacked profiles (Rajagopalan 1987; Mudge 1991) and images (Rajagopalan & Milligan 1995) are extremely useful for structural mapping because they tend to show coherent alignments not apparent in true amplitude data. An example presented by Rajagopalan & Milligan illustrates a situation where part of a magnetic data set appears characterless in both total magnetic intensity and vertical gradient images, but shows coherent assemblages of anomalies in AGC images. AGC routines can be applied either to profile data, and then contoured, or directly to grid data. The successful application of AGC requires the data set to have a zero average base-level. As this is generally easier to approximate with gradient data than total magnetic intensity data, and as the anomaly forms in gradient data are sharper than in total intensity data, it is generally better to calculate AGC results using gradient data.

Figures 4D and F show examples of AGC applied to TMI data from the Mount Gipps 1:25 000 map sheet area.

Median filters. A median filter replaces the central value of a kernel operator with the median of the neighbouring values within the kernel. It is very useful for removing noise spikes from data without smoothing out sharp detail (Gonzalez &

Woods 1992). It is successfully applied in the removal of statistical high-frequency noise from gamma-ray spectrometric data, particularly in the U channel, which usually has the lowest count-rates of the three channels.

Pitt filter. Figure 5A shows total magnetic intensity data contoured at an interval of 1 nT. No discrete anomalies are apparent in these data. Figure 5B, which covers the same area, shows an obvious anomaly that correlates almost exactly with a mapped shale unit. The parameter being contoured is a representation of the high-frequency 'noise' in the data. An extreme high-cut filter has been applied to remove small bumps in the profile data with widths of the order of a few metres. The amplitude of this subtracted noise has then been squared to make it positive, and the logarithmic value computed to narrow the amplitude range. Finally, an areal averaging process has been applied to allow realistic contouring of the data. The values contoured in Figure 5B are, in effect, a non-linear representation of the noise in the data that appears to be related to some characteristic of the regolith associated with the shale unit.

This previously unpublished work was compiled by John Pitt of Pitt Research Pty Ltd in 1981 for one of the authors of this paper (PJG). John has since died. It appears appropriate to refer to the process as a 'Pitt filter'.

Presentation of airborne data

Overview

Display options for airborne data include traditional methods such as line profile and contour maps, and now, more commonly, pixel-image maps, with the raster image being generated by an image processing system.

Contour maps and stacked profiles are still essential components of the display process. Contours provide better definition of gradients necessary for depth and dip estimates and often give a clearer representation of absolute and relative amplitudes than images do. Coloured contours combine some of the visual advantages of images with all the advantages of contours. Profiles can show fine detail lost in gridding routines necessary for the display of data as contours or images. Because most users of airborne data are familiar with the production of profile and contour maps, the following discussion concentrates on the production of images from grid data.

There is a variety of grid data types and formats, and this paper does not aim to comprehensively discuss their relative merits. Format mainly depends on the software employed in the processing, and the most efficient systems use software packages with compatible grid formats, so that conversion between formats is not necessary—for example, Intrepid geophysical processing software and ER Mapper image processing software use the same grid format specifications. Grid data can also be stored in a number of 'bands'—for example, the potassium, thorium and uranium channels of gamma-ray spectrometric data may be stored in one file as three bands—which is often very convenient for image processing.

Most geophysical software packages support a variety of data types, such as single and double-precision real data, integer data and byte data. It is important that sufficient precision is maintained during the various manipulations of the data to ensure that information is not lost. This usually requires grid data to be stored with a minimum precision of 4-byte real. Only in the final display stage must the information be quantised into single byte data.

The initial grid data to be presented is usually obtained in projected form, now using the WGS84 datum and, usually, the Universal Transverse Mercator Projection (depending upon the choice of final map scale). Older grids for Australia were mainly in the AGD66 datum, with projection into the Transverse Mercator Australian Map Grid (TMAMG) system (Steed 1995).

An important part of map-making is the quantity and quality of the annotation. For interpretation purposes, different map products must be able to be overlaid exactly on top of each other with grid references in either projected units or geodetic coordinates. High-quality vector annotation on top of raster images may be composed in the more sophisticated image processing packages; the combined final raster image and vector data are most conveniently output in postscript format. This can then be translated into a variety of machine formats, depending upon the final method of reproduction.

The following sections describe how enhanced pixel-image maps are generated in the Australian Geological Survey Organisation. Only the basic products are described in detail—the variety of image processing that can be done on different data sets to highlight specific features is virtually unlimited.

Image processing

Colour models. Colour VDU raster displays of image information use an additive combination of the red, green, and blue (RGB) primary colours (in a cartesian coordinate system). Although this is convenient for the display of colours on a VDU screen, a more intuitive model in terms of colour variation perceived by the human eye is the *hue*, *saturation*, and *value* model (HSV), using a cylindrical coordinate system. For printing images, a subtractive model is used based on the primary colours cyan, magenta and yellow (CMY). These three models are mathematically related and 3-band image data may be converted from one model to the other.

In the HSV model, hue refers to combinations of red, green, and blue primary additives, value is the intensity (or energy) of the colour, and saturation is the relative lack of white in the colour (or the spectral purity). With reference to Figure 6(A), hue is measured around the vertical axis from 0° (red) to 360°, saturation varies from 0 on the vertical axis to 1 on the triangular surfaces of the hex-cone, and value varies from 0 (black) through shades of grey along the central axis to 1 (white) at the top. Thus, for a colour of constant hue and saturation, if its value is decreased it darkens towards black. For a colour of constant hue and value, if the saturation is decreased it becomes whiter.

These variations in value and saturation are perceived by the human eye in, for example, naturally sunlit scenes. Areas in strong direct sunlight are undersaturated, with excess white light reflected, and thus appear 'washed out', whereas areas in shadow are low in value, with less intense reflected light, and hence appear to be darker. However, the fundamental hues of the scene remain the same. We apply this principle to images of pseudo-coloured geophysical data, with the variations in value and saturation usually being derived from an artificial sun-angle routine (Horn 1981; Pelton 1987). The resulting image is thus 'gradient enhanced' (Milligan et al. 1992).

Colour look-up tables (LUTs). If data of only one band are to be displayed in either colour or grey-scale on a VDU, then ranges of the data must be assigned to different colours or shades of grey. AGSO displays of airborne geophysical data mainly use two different colour look-up tables—the 'Rainbow' table, comprising the primary saturated hues with blue representing low values and magenta representing high values of the data, and the 'Comtal' look-up table (Fig. 6B).

The Comtal table, by inclusion of lower intensity colours than the Rainbow table, is divided into more visually discrete bands. This provides better definition of displayed data if they are not gradient enhanced (Fig. 7 also illustrates this concept). If the same data are to be displayed with a gradient enhancement, then the Rainbow table is used. Figure 6 also illustrates how the gradient information changes the Rainbow colours as it

modulates either the saturation or the value.

Image processing of airborne TMI data. The final grid obtained from the processes described earlier consists of data in 4-byte binary real format, and retains the precision of the originally sampled TMI data. This cannot be displayed on a VDU and is converted to 1-byte integer format during the final stage of imaging. Hence, most of the image processing operations manipulate data with the original precision.

For the production of AGSO standard gradient-enhanced pixel image colour maps for sale, the following procedures apply (Fig. 8). There are also many one-off maps produced in-house, for interpretation and display, which do not necessarily follow these procedures.

Two new grids are generated from a real data input file—a shaded-relief (or gradient) image, usually using a sun-angle routine that artificially illuminates the grid surface in a direction perpendicular to the primary geological structures (Horn 1981; Pelton 1987), and a scaled histogram-equalised (HE) grid of the original TMI values. The HE grid is converted into a 3-band pseudo-coloured image, using the Rainbow colour look-up table, in which the colours are each fully saturated and at maximum value according to the HSV model.

Grid values for both the sun-angle image and the HE image are scaled to be within the range 0–255. HE assigns equal quantities of grid values to each of the 256 levels available—hence, when displayed as pseudo-coloured images, equal areas of each colour will result, enhancing the colour resolution available for densely populated pixel intensity levels.

Another common non-linear histogram manipulation is histogram normalisation (HN). This converts the data into an approximate Gaussian distribution, with the result that there are more levels of pixel population for the mid-ranges of the data than for HE. The overall result, if viewed in grey-scale, is to provide less 'contrast' than for HE data. Figure 7 shows examples of how the histograms of a data set may be 'stretched' from an initial raw histogram to give different levels of spatial resolution of the data, with the two colour look-up tables applied to the data for comparison.

The shaded relief is combined into the 3-band image data as follows:

- the contrast of the sun-angle data is enhanced by scaling, after visual inspection on the VDU to determine the amount needed for optimum visual effect;
- from a visual inspection of the sun-angle histogram, the data are divided into two groups—values less than and greater than the histogram peak (respectively, dark and light areas of the hill-shade image);
- these two parts are scaled again, if necessary, and then used to modulate the value and saturation of the HSV colour model by direct substitution.

The resulting image, when converted back to RGB values and displayed on a VDU, provides the long-wavelength information as primary colours (the hue), and the short-wavelength information as shaded-relief. Hence, on slopes of anomalies facing the 'sun' the colours tend towards white (undersaturated), and on the opposite slopes the intensity of the colours is reduced (they tend towards black). Thus a 'natural' effect is produced as if sunlight is shining on a topographic surface. AGSO also produces pixel-image maps of digital elevation models (DEMs), which represent actual topographic information—these are a by-product of the acquisition radio-altimeter and the satellite global positioning system (GPS).

Images which have had artificial illumination applied should be interpreted cautiously, as the divide between shadow and illumination at the crest of an anomaly may not be exactly at the maximum value. Its position will depend upon the elevation of the illumination source.

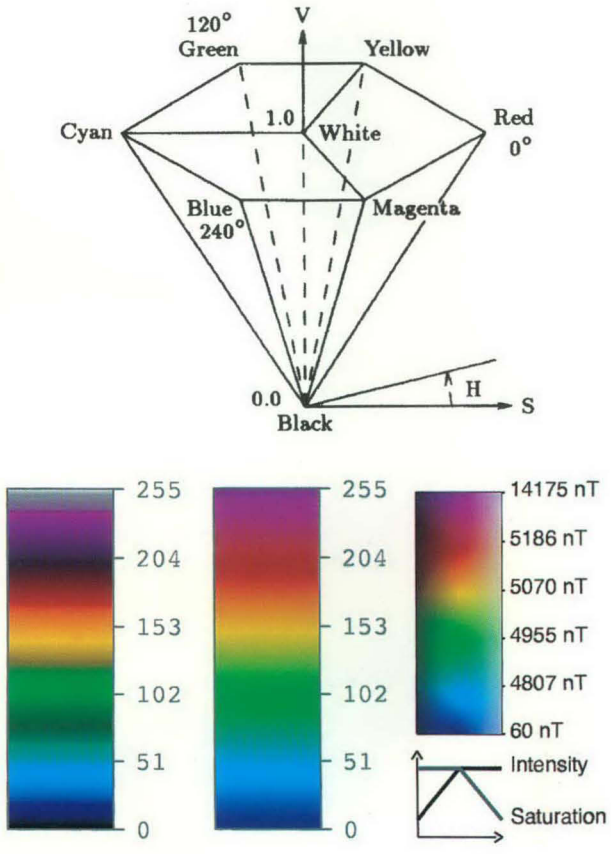

Figure 6. (A) The HSV colour model—H, S, and V represent hue, saturation, and value of colour intensity, respectively; (B) Examples of the LUTs used by AGSO in image processing. Left, 'Comtal'; centre, 'rainbow'; right, 'rainbow' with gradient enhancement.

Image processing of airborne gamma-ray spectrometry data. Four final grid products are produced from processed spectrometer data—total count (TC), potassium (K), uranium (U) and thorium (Th) grids, which represent different combinations of energy windows of the recorded 256-channel gamma-ray spectrum.

There are two basic ways in which AGSO displays these data at present.

The contrast of each can be individually enhanced by manipulation of their histograms and then displayed in pseudo-colour, using an appropriate look-up table (a gradient could be added, and an image produced such as described for the TMI data). This allows observation of the spatial variations of the data within the individual bands and it is commonly used to display TC data. At the top of Figure 9 examples of potassium, thorium and uranium grids are shown displayed in this way.

The three bands of K, U and Th can be assigned to the red, green, and blue components of the RGB colour model. The resulting image, when displayed, comprises colours generated from the relative intensities of the three components—it shows subtle variations in the ratios of the three bands, and is much more useful for interpretation purposes. Such images are sometimes referred to as 'ternary'.

In practice, both types of images are generated. For the three-band images, it is usual to assign K to red, Th to green and U to blue. The U channel usually contains the poorest signal-to-noise ratio, and assigning it to blue tends to reduce its prominence in the final image. Before combination of the three bands, their individual histograms are contrast enhanced,

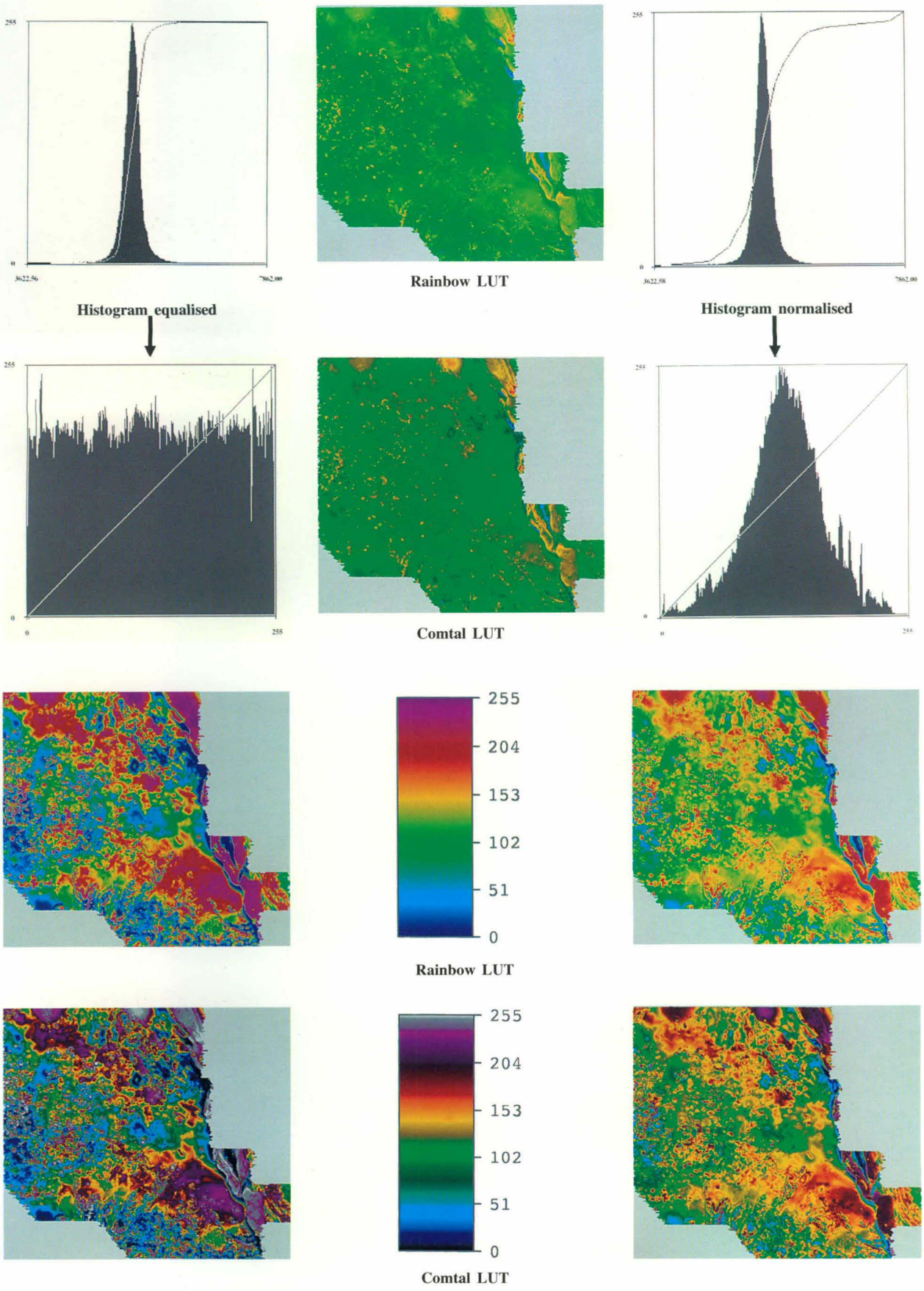

Figure 7. Examples of different histogram and look-up table (LUT) manipulations. The original TMI data are shown at the centre top, using the two LUTs (upper top—'Rainbow', lower—'Comtal') and only a linear transform to quantise them into 255 levels. The left-hand column shows the histogram equalisation transformation, and the right-hand column the histogram normalisation transformation.

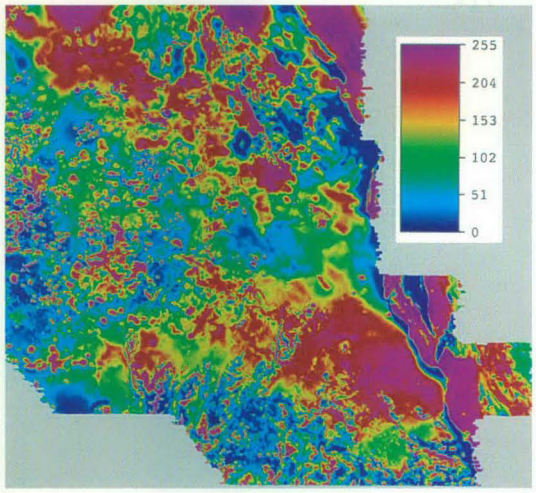

TMI 'rainbow' pseudocolour

+

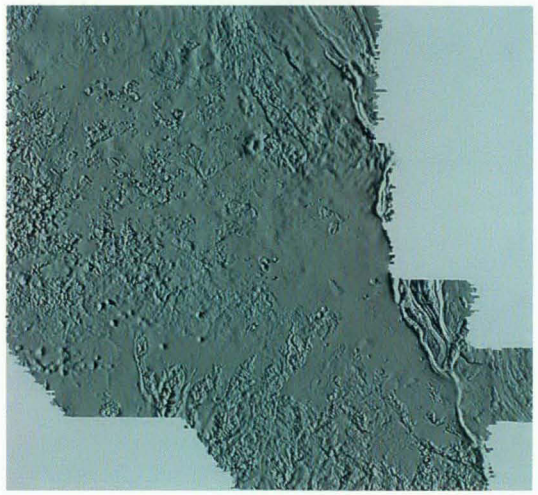

E–W illumination of TMI

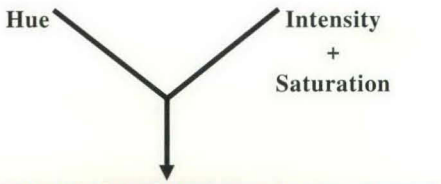

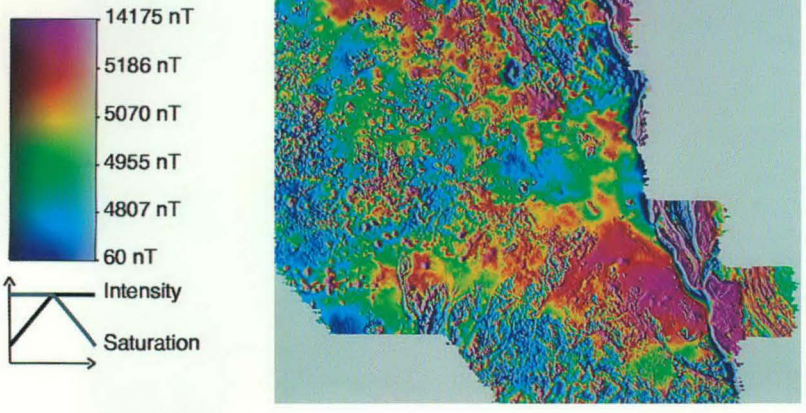

Gradient-enhanced TMI

Figure 8. The production of gradient-enhanced images, using the HSV colour model. The TMI 'rainbow' pseudo-coloured data are transformed into the HSV model from the RGB model. The S and V are then replaced with data from the greyscale gradient image, and the result transformed back to the RGB model for display. Data from AGSO Liverpool Plains survey.

usually by histogram equalisation or histogram normalisation, to give the best colour variations after they are combined. Often, as mentioned previously, the data are median filtered to reduce statistical noise.

The three-band image may be further enhanced by transforming it to the HSV colour model. If there are dark areas, where the intensity of all three bands is low, the value may be increased to brighten them and so allow more detail to be seen. Similarly, if there are areas with a white, 'washed-out' appearance, where the bands all have high values and the colours have become unsaturated, the saturation may be increased in an attempt to increase the colour variation in these areas.

Figure 9 shows the steps involved in this production. As with the TMI images, a percentage of the gradient of total count can also be added to value and saturation to improve the definition of high-frequency information, but care is needed to ensure the original colour balance from the combination of the three radioelements is not significantly altered.

Printed map production

Final pixel-image maps must satisfy the following criteria:

- the images are enhanced to clearly display both long and short-wavelength information on hard-copy output;
- the colours are as true as possible to those ideally chosen using the HSV colour model (if applicable) and faithfully reproduce from VDU to hardcopy;
- the image data are accurately projected, with an appropriately annotated graticule;
- resolution of the map legend and graticule is high enough for individual pixels not to be visible.

With the output devices available at present, it is not easy to satisfy all of these requirements. Most image development is undertaken using VDU devices, with some intermediate test hard-copy from either colour laser printers or A0 'paint-jet' type printers.

Map legends and graticules (vector data) are added to the image once the final raster has been developed in the image processing system. Vector and raster data are then converted into a postscript file, either for printing on a paper hard-copy device or for sending to a commercial printer. The vector information is 'burnt in' to the image during conversion from postscript to the final print medium.

The final highest-quality hard-copy maps published by AGSO are reproduced by a photographic process in which a 20 x 20 cm colour negative is made commercially, and enlarged prints made from that.

This process gives a high-quality product in terms of a photographic image at full scale, but the colours can vary significantly from those expected, and may also vary from one print to another. It is also dificult to maintain an accurate scale, as all photographically enlarged images suffer from varying degrees of distortion.

An alternative printing method, which is much more expensive than photographic reproduction, is to print the maps using a commercial digital graphic-art process. Image data are then used to produce four printing separates (for a colour print) in the CMYK colour model (CMY with the addition of black). Proof prints can be inspected by thermally combining etched film in these four colours (printers' dots are now used instead of pixels), and the final maps are produced on a standard colour printing press.

The colours on printed maps are superior to the photographic process, and the image is printed exactly to scale. While production of the plates is not cheap, this is to some extent compensated for by cheaper printing costs. Thus, if many copies are to be produced the cost of the printed map is comparable to that of the photographic process.

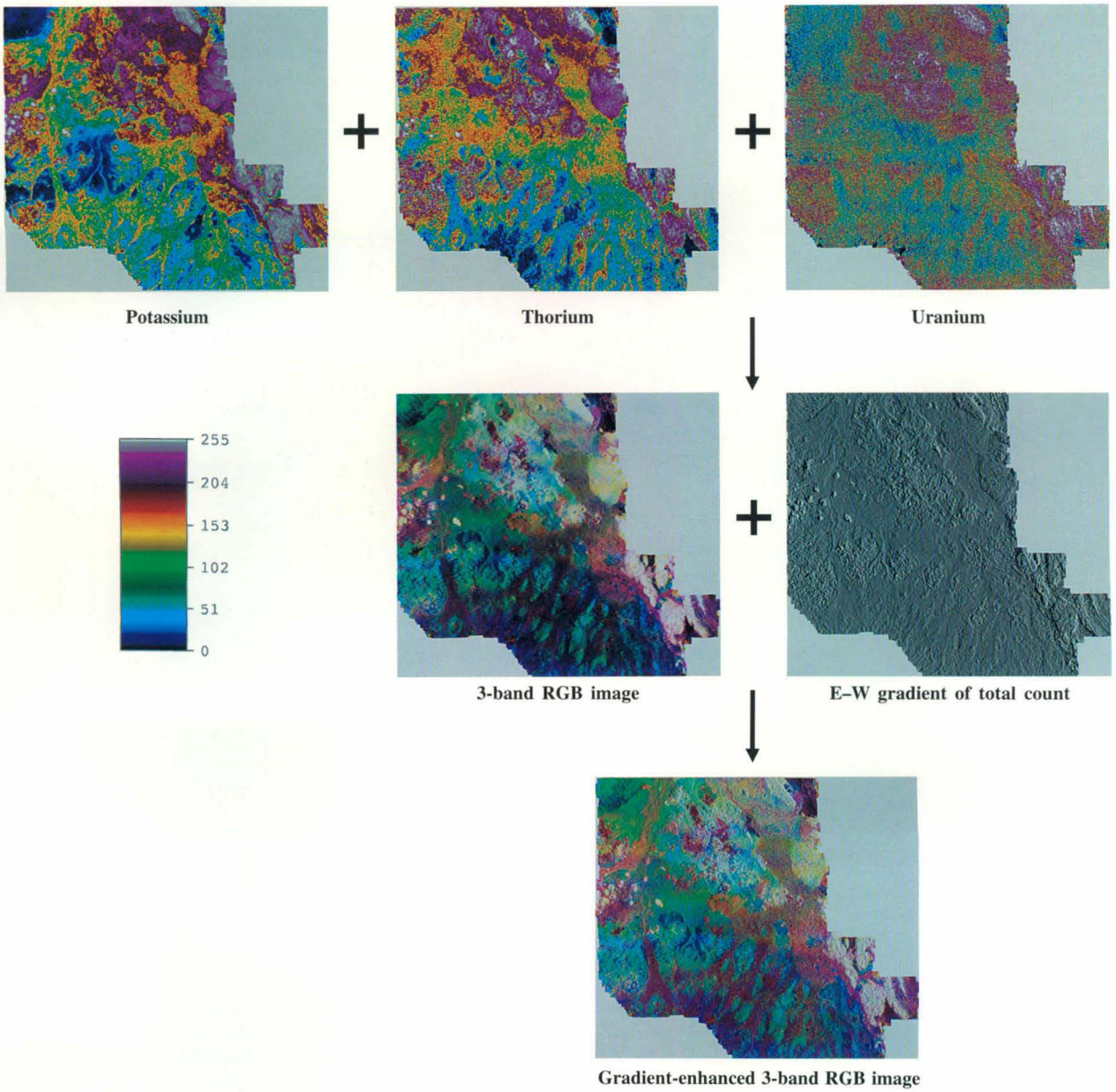

Figure 9. Production of gradient-enhanced 3-band gamma-ray spectrometric images. The K, Th and U grids are initially histogram-equalised and combined into a RGB image. This can be enhanced in the HSV model in a similar way to the TMI data described in Figure 7.

Conclusion

There are many filtering and transformation operations that can be applied to line and grid geophysical data, in both the spatial and frequency domains, to highlight information useful for geological interpretation.

Image processing of grid data produced by these operations complements the data manipulation, to highlight the enhanced information visually, using either VDU or hard-copy outputs. Also, different grid data can be combined, particularly as described for gamma-ray spectrometric data, to show subtle ratio differences—apparent as colour variations—not visible in any one enhanced grid.

References

Cowan, D.R. & Cowan, S., 1993. Separation filtering applied to aeromagnetic data. Exploration Geophysics, 24, 429–436.

Craig, M., 1993. The point spread function for airborne radiometry. Mathematical Geology, 25, 1003–1013.

Fuller, B.D., 1967. Two-dimensional frequency analysis and design of grid operators. In: Mining geophysics, Society of Exploration Geophysicists, Tulsa, 658–708.

Gonzalez, R.C. & Woods, R.E., 1992. Digital image processing. Addison-Wesley Publishing Company.

Gunn, P.J., 1972. Application of Wiener filters to transformations of gravity and magnetic fields. Geophysical Prospecting, 10, 860–871.

Gunn, P.J., 1974. Applications of Wiener filters to remove autocorrelated noise from magnetic fields. Australian Society of Exploration Geophysicists, Bulletin, 5, 127–130.

Gunn, P.J., 1975. Linear transformations of gravity and magnetic fields, Geophysical Prospecting, 23, 300–312.

Gunn, P.J., 1978. Inversion of airborne radiometric data. Geophysics, 43, 133–143.

Gunn, P.J. & Almond, R. 1997. A method for calculating equivalent layers corresponding to large aeromagnetic and radiometric grids. Exploration Geophysics (in press).

Horn, B.P.K., 1981. Hill shading and the reflectance map. Proceedings of the IEEE, 69, 14–47.

MacLeod, I.N., Jones, K. & Ting Fan Dai, 1993. 3-D analytic signal in the interpretation of total magnetic field data at low magnetic latitudes. Exploration Geophysics, 24, 679–688.

Milligan, P.R., Morse, M.P. & Rajagopalan, S., 1992. Pixel map preparation using the HSV colour model. Exploration Geophysics, 23, 219–224.

Mudge, S.T., 1991. New developments in resolving detail in aeromagnetic data. Exploration Geophysics, 22, 277–284.

Naudy, H., 1967. Essai de filtrage non-lineare applique aux profils aeromagnetiques. Geophysical Prospecting, 16, 171–178.

Pelton, C., 1987. A computer program for hill-shading digital topographic data sets. Computers and Geosciences, 13, 545–548.

Rajagopalan, S., 1987. The use of "automatic gain control" to display vertical magnetic gradient data. Exploration Geophysics, 18, 166–169.

Rajagopalan, S. & Milligan, P., 1995. Image enhancement of aeromagnetic data using automatic gain control. Exploration Geophysics, 25, 173–178.

Roest W.R., Verhoef, V. & Pilkington, M., 1992. Magnetic interpretation using the 3-D analytic signal. Geophysics, 57, 116–125.

Spector, A. & Grant, F.S., 1970. Statistical methods for interpreting aeromagnetic data. Geophysics, 35, 293–302.

Spector, A. & Parker, W., 1979. Computer compilation and interpretation of geophysical data. In: Geophysics and geochemistry in the search for metallic ores. Geological Survey of Canada, Economic Geology Report 31, 527–544.

Steed, J., 1995. The geocentric datum of Australia. Surveying World, 4, 14–17.

Thompson, D.T., 1982. A new technique for making computer-assisted depth estimates from magnetic data. Geophysics, 47, 31–37.

Vacquier, V., Steenland, N.C., Henderson, R.G. & Zeitz, 1951. Interpretation of aeromagnetic maps. Geological Society of America Memoir 47.

AGSO Journal of Australian Geology & Geophysics, 17(2), 77–82

Enhancements of the magnetic map of Australia

C. Tarlowski[1], P.J. Gunn[1] & T. Mackey[1]

A new version of the Magnetic Anomaly Map of Australia has been produced which has a more complete coverage than earlier versions. Long-period warps have been minimised in by using data from special control flights. The information content of the map has been enhanced by a vertical gradient transformation, which increases fine detail in the data, upward continuation transformations, which suppress the effects of shallow sources relative to deeper larger sources, and a reduction-to-the-pole process, which has removed anomaly asymmetry due to induction effects.

Introduction

The first Australia-wide compilation of a digital grid merging *all significant* publicly available aeromagnetic surveys was prepared by the Australian Geological Survey Organisation (AGSO) (Tarlowski et al. 1992), which subsequently published a 1:5 000 000 colour image of this compilation (Tarlowski et al. 1993). The digital grid of these data and the image have found widespread usage by government bodies, research organisations and exploration companies. The purpose of this paper is to present the second edition of the map, as published by AGSO (Tarlowski et al. 1995). As well as including significant new data, the new version has been corrected for a long-wavelength warp, introduced into the original map during the merging of its various constituent surveys. The paper also presents the results of various transformation

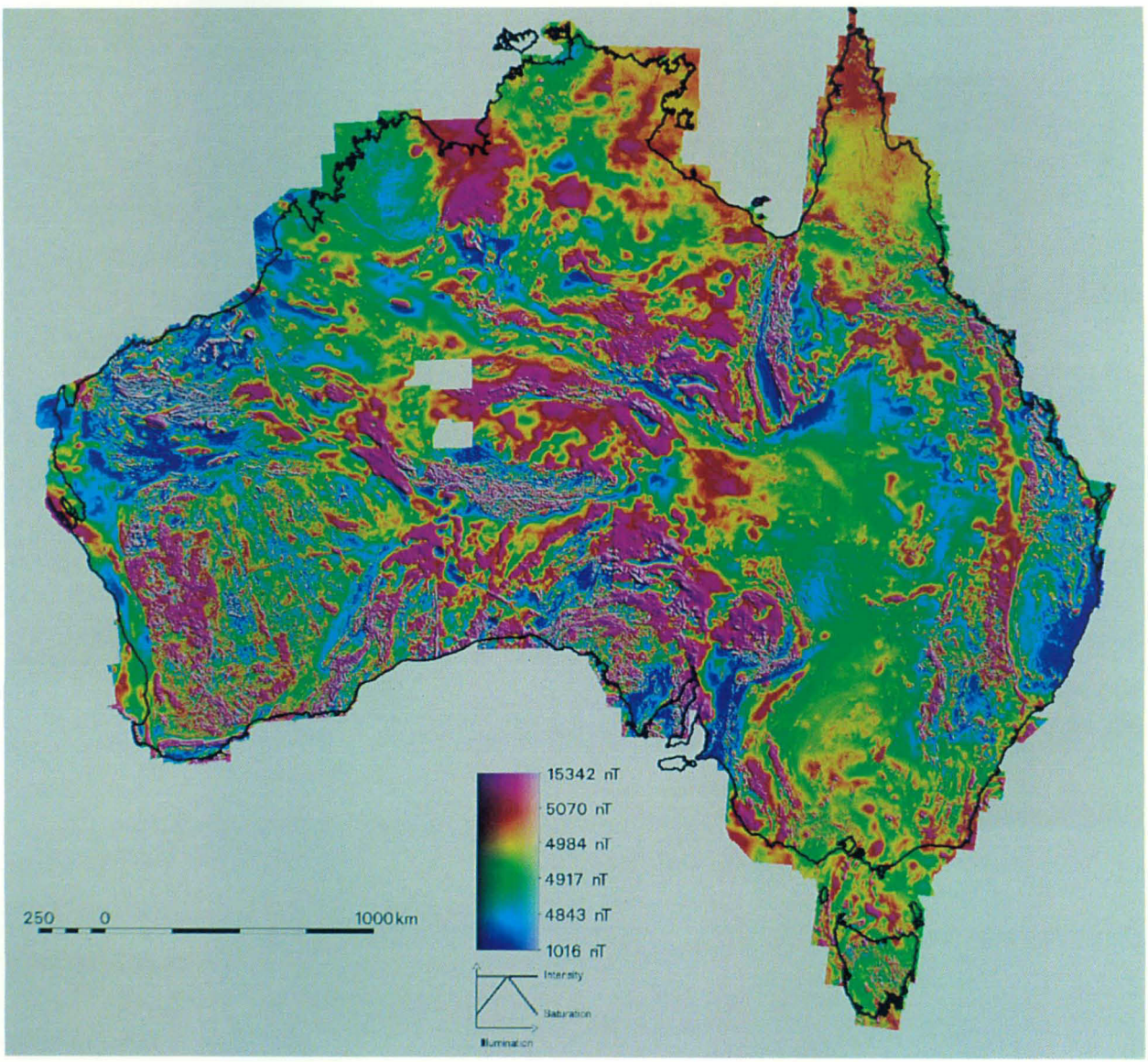

Figure 1. Image of the Magnetic Anomaly Map of Australia with northeast illumination. Histogram equalised, blue low, magenta high.

[1] Australian Geological Survey Organisation, GPO Box 378, Canberra, ACT 2601

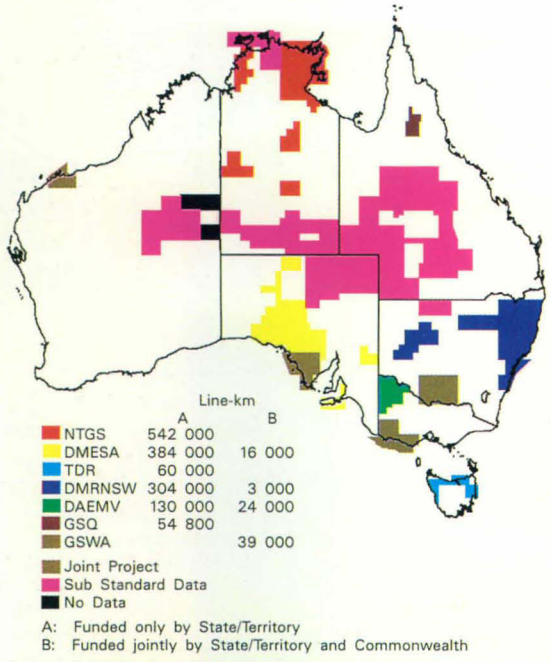

Figure 2. Sources and quality of magnetic data used to compile the magnetic map of Australia.

processes applied to the new data set, which reveal features not obvious in the total magnetic image.

Details of the second edition of the Magnetic Anomaly Map of Australia

The second edition of the Magnetic Anomaly Map of Australia (Tarlowski et al. 1995) is shown in Figure 1. The image is derived from approximately 6 million kilometres of total magnetic intensity data held in the national airborne geophysical database by the Australian Geological Survey Organisation (AGSO) (Hone et al. 1997). Most surveys (4.5 million km) were flown by AGSO (formerly the Bureau of Mineral Resources, Geology and Geophysics–BMR), using its own aircraft, as part of the airborne geophysical reconnaissance of Australia, which commenced in 1951. Some were carried out by companies operating under contract to AGSO and the State and Northern Territory geological surveys, either separately or as joint projects. A number of other surveys, carried out for the private sector, have also been acquired by AGSO. In total, the equivalent of 528 1:250 000 map sheet areas has been incorporated into this map.

The AGSO surveys flown before 1990 were acquired mainly at an altitude of 150 m above terrain, with lines oriented either north–south or east–west and spaced between 1.5 and 3.2 km apart. Since 1990, AGSO surveys have been acquired mainly with line spacings of 400 m or less at altitudes of 100 m or less.

The data supplied by the Northern Territory Geological Survey (NTGS), Minerals and Energy South Australia (MESA), Tasmania Development and Resources (TDR), New South Wales Department of Mineral Resources (DMRNSW) and the Department of Agriculture, Energy and Minerals (DAEM), Victoria; (Fig. 2) were acquired at a nominal ground clearance

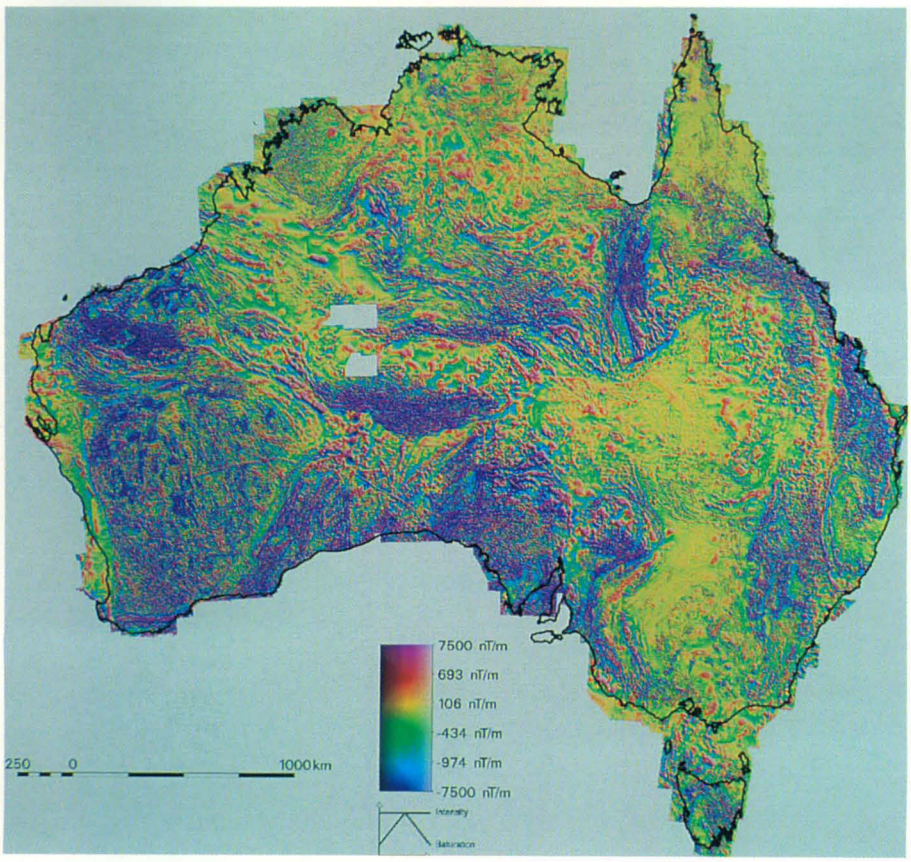

Figure 3. Colour vertical gradient image of total magnetic intensity with northeast illumination.

of 100 m or less above terrain, along lines spaced 500 m apart or less.

Many of the earlier surveys were acquired at line spacings greater than 3.2 km—data from these are sub-standard by current criteria in terms of line spacing and location accuracy (Fig. 2).

Profile data for about one-third of the surveys, acquired in the earlier years of the program, were recorded in analogue form and have since been digitised. Other sub-standard analogue data cover 14 per cent of the land area—mainly sedimentary basins. Coverage for these areas was obtained from the grid of the Magnetic Map of Australia (BMR 1976), digitised from contour maps. The original cell size of 0.02° has been interpolated to 15 seconds of arc.

The International Geomagnetic Reference Field (IGRF) for an appropriate epoch has been removed from each survey, and a grid created with cell size of 15 seconds of arc (about 400 m), using the minimum curvature method of Briggs (1974). In some cases the grids were subjected to 'micro-levelling' (Minty 1991).

The majority of individual surveys are approximately delineated by boundaries coincident with 1:250 000 map sheet areas, with a margin of overlap. By gridding according to geographical coordinates, surveys of adjacent sheets have coincident locations of marginal grid rows and columns in the overlap zones. The gridded data for pairs of 1:250 000 map sheets were registered and levelled together by minimising (in a least squares sense) the discrepancies between grid values along their common rows or columns. To do this, low-order polynomials were fitted to the differences between values along grid rows and columns, and one grid was then adjusted to match the other grid by using the polynomial. The remaining high-frequency errors were smoothed out (Teskey et al. 1982).

In cases where survey boundaries have complex and irregular shapes, Intrepid software, supplied by Desmond FitzGerald and Associates Pty Ltd, has been used for merging separate areas.

The composite grid across the Australian mainland has been corrected for spurious warps introduced during the compilation process by using two special control-lines flown continuously around Australia early in 1990 (Tarlowski et al. 1996). This project involved the accurate subtraction of diurnal variations by means of base station recordings on a continent-wide magnetometer array. A third control loop, flown in late 1994, across Bass Strait tied the Tasmanian data to the mainland data. The geodetically based grid was finally reprojected to a cell size of 800 m, using a simple conic projection with standard parallels of 18° and 36° S and a central meridian of 132° E.

The image (Fig. 1) was generated from the natural colour palette (magenta high, blue low), using histogram equalisation to maximise the use of the colour range. Over 80 per cent of the grid point values fall within 500 nT of the average value. To emphasise the expression of anomalies attributable to near-surface geology, a Sobel filter (Gonzalez & Woods 1992) was used to produce an artificial sun-angle illumination. The output of the filter was used to modulate the colour intensity and saturation of the initial colour image after transformation to the hue, saturation, value (HSV) colour space (Milligan et al. 1992).

The original grid data with a cell size of 15 seconds of arc (about 400 m) used for the preparation of the image are available from AGSO in digital form for the whole continent, and for individual 1:1 000 000 sheets.

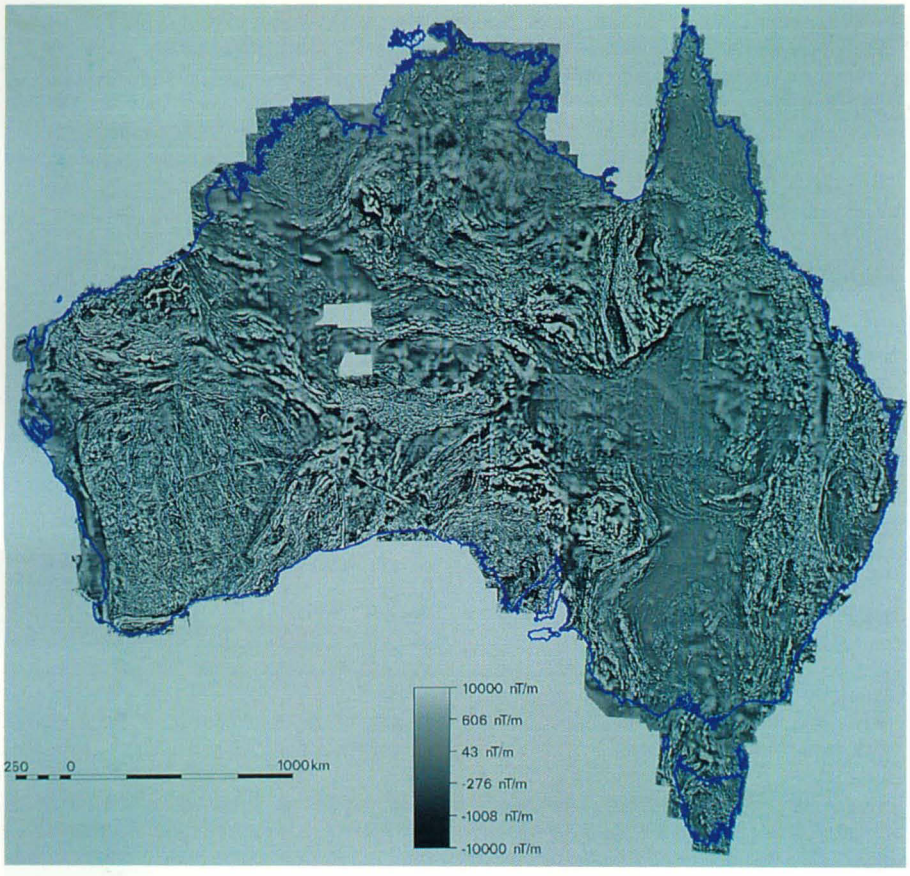

Figure 4. Greyscale vertical gradient image of total magnetic intensity. Histogram equalised, black low, white high.

Enhancements of the total magnetic intensity image

While the total magnetic intensity image (Fig. 1) can be interpreted to provide valuable insights into the regional geology of Australia, it is also possible to apply various mathematical transformations, which are, in effect, filtering operations, to make different facets of the datasets more obvious to interpreters. Several such transformations are described below. Milligan & Gunn (1997) have reviewed the techniques and background to the various enhancements, and it should be appreciated from their review that the examples presented here are a small subset of the many enhancement techniques available.

Vertical gradient

Vertical gradient (first vertical derivative) images enhance fine detail by suppressing long-wavelength components and by resolving interfering effects of adjacent anomalies. The colour and greyscale vertical gradient images of the total magnetic intensity (Figs 3 & 4) have worked well in these respects and show significant structural and lithologic detail not obvious in Figure 1. Note that the colour and greyscale images complement each other: while in some respects the greyscale image allows recognition of finer detail, the colour image gives a better indication of amplitude.

Several apparent defects are obvious in the vertical gradient images, which reflect the variable quality of the datasets used in the compilation of the TMI image (Fig. 1). These are:

- linear features at the junction of surveys flown at different altitudes and with different regional effects removed: the vertical gradient process enhances any steps in magnetic field values, which were smoothed at such junctions by the survey 'stitching' process;
- streaks, reflecting widely spaced, poorly levelled flightline data; and
- fuzzy areas of ill-defined semi-random anomalies: these areas are particularly obvious in central eastern Australia, where the survey line spacings are so wide that considerable aliasing of magnetic patterns has occurred, resulting in spurious anomaly patterns.

Upward continuation

Figures 5 and 6 show versions of the total magnetic image continued up to distances of 800 m and 4500 m, respectively; i.e. they show images of the total magnetic intensity data that would be produced if the data were collected at heights of 800 m and 4500 m higher than the surveys of the original compilation. The upward continuation process smoothes the data according to a precise relationship. In physical terms, as the continuation distance is increased, the effects of smaller, narrower and thinner magnetic bodies progressively disappear relative to the effects of larger magnetic bodies of considerable depth extent. As a result, upward-continuation maps can give indications of the main tectonic and crustal blocks in an area.

Upward continuation total magnetic intensity maps (Figs 5 & 6) are providing new insights into crustal structure in, for example, the extensive Archaean shield areas of Western Australia. There, the upward continuation images indicate large crustal blocks of markedly different magnetic composition, while the total magnetic intensity and vertical gradient images suggest large areas of similar composition.

Reduction to the pole

Rock units in the Earth's continental crust are magnetised by induction in the Earth's magnetic field. Consequently, a body that causes an anomaly directly over itself at the Earth's magnetic poles, where the Earth's field is vertical, causes

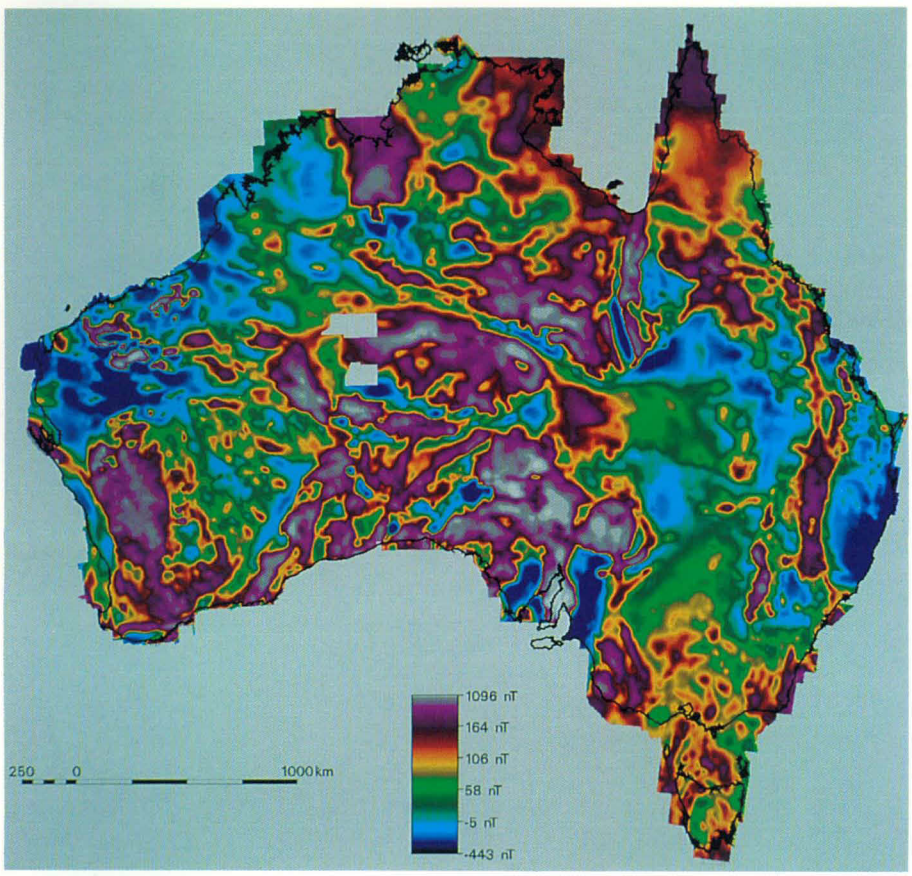

Figure 5. Total magnetic intensity 'continued upwards' 800 m. Histogram equalised, black low, white high.

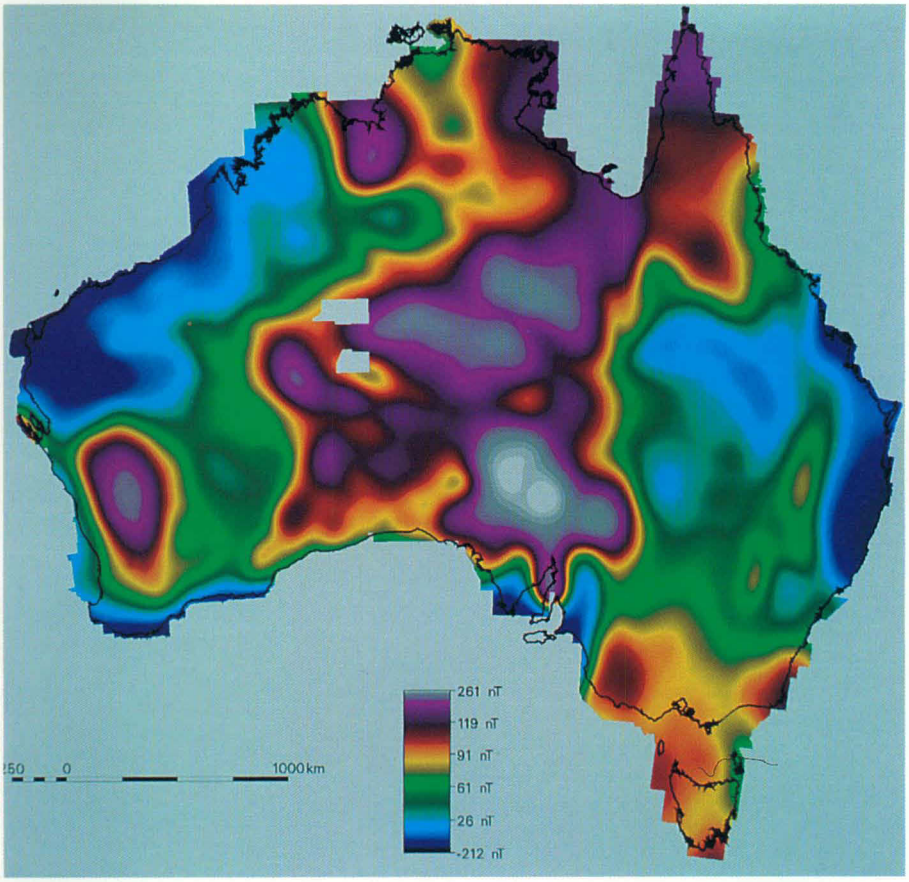

Figure 6. Total magnetic intensity 'continued upwards' 4500 m. Histogram equalised, black low, white high.

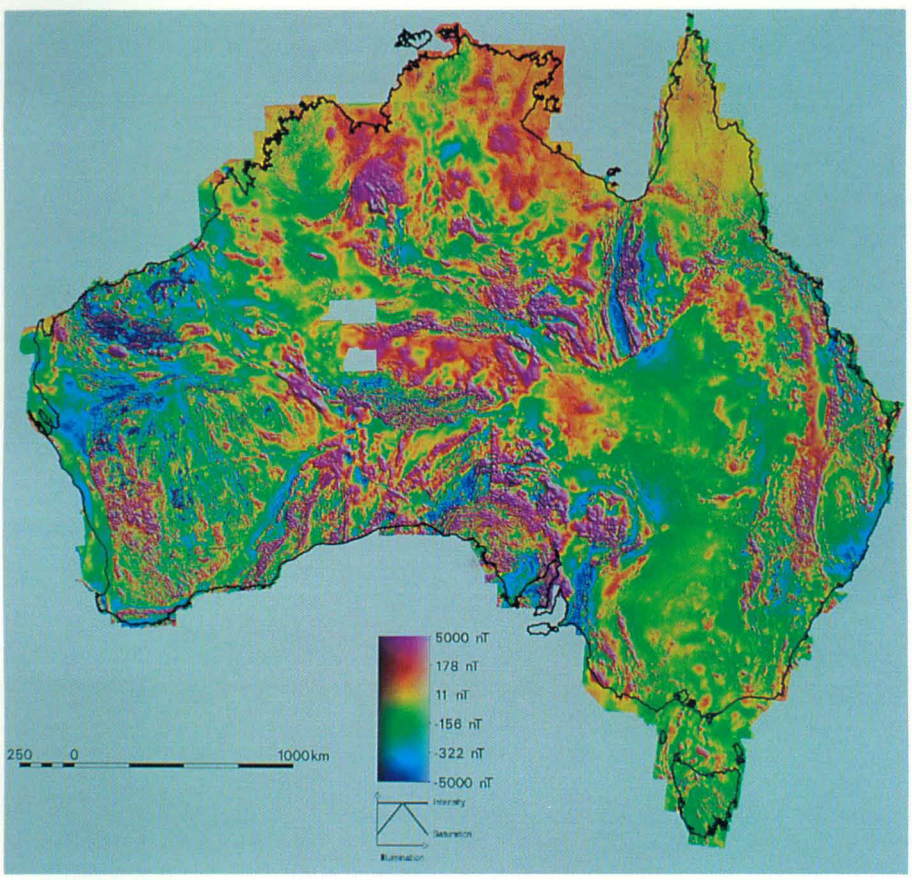

Figure 7. Total magnetic intensity reduced to the pole with northeast illumination. Histogram equalised, blue low, magenta high.

progressively more asymmetric anomalies as the inclination of the Earth's magnetic field approaches 45 degrees. This is the approximate inclination of the Earth's field over much of northern Australia. As asymmetric anomalies are difficult to relate to source geometry, 'reduction to the pole' is often used to transform anomalies observed in areas of low magnetic latitude to their forms at the magnetic pole (Fig. 7). Such transformations are valid provided no anomalies are caused by remanent magnetisation with a direction significantly different to the Earth's ambient magnetic field. If such is the case, it is often apparent in 'reduced to the pole' maps and images as unrealistic smearing of the results.

The inclination of the Earth's magnetic field varies from 73° over the southern regions of Tasmania to 40° over the northern limits of Australia. While anomalies in southern Australia consist of simple peaks closely approximating the outlines of their sources, many in northern Australia are combinations of positive peaks and negative troughs, where the actual source underlies the inflection between the positive and negative anomalies. Reduction to the pole of the total magnetic intensity data will facilitate the interpretation of the data.

Because no simple algorithm exists for reduction to the pole where a significant range of inclinations is involved in the transformation process, it has been necessary to adapt existing software for the purpose. The approach used to produce Figure 7 was to process the data in strips covering 6° of latitude, using the value of the field inclination at the centre of the strip for the transformation. Adjacent strips were processed with 1° overlaps, and a ramp-type averaging process was used to merge the results of adjacent strips. A single declination value, corresponding to the value of the declination in the centre of Australia (5° E), was used in all transformations. As the declination over Australia ranges from 2° W to 12° E, this approximation is unlikely to cause significant errors.

The transformation process appears to have worked successfully. Many north Australian anomalies originally associated with significant lows consist of simple peaks with no associated lows after the transformation process. Reduction to the pole appears to have clarified the position of many magnetic sources.

Conclusion

Despite the impression given by the images in this paper that Australia is virtually covered by aeromagnetic surveys, it should be appreciated that surveys over large portions of the country were flown with line spacing in the order of several kilometres and at altitudes in the order of several hundred metres. These older surveys were also flown with inaccurate navigation systems and low-sensitivity recording systems. Much more flying is needed to completely cover Australia with modern recording systems at the currently accepted minimum standards for reconnaissance surveys—line spacing of 400 m and survey altitude of 100 m or less. It would then be possible to produce a grid of data across the country on a 100 m mesh instead of the current 400 m interval.

Although this paper has not attempted to incorporate any significant interpretation of the various images, it is obvious that the second edition of the Magnetic Anomaly Map of Australia reveals significantly more geological and tectonic detail than the first edition Furthermore, the various transformed versions of the original total magnetic intensity grid show significant detail not obvious in the original. Such transformed products are indispensable to any regional analysis of the Australia's magnetic field.

Acknowledgments

Permission of the Northern Territory Geological Survey, Minerals and Energy South Australia, Tasmania Development and Resources, New South Wales Department of Mineral Resources, and Department of Agriculture, Energy and Minerals Victoria for the incorporation of their data into the magnetic compilation is gratefully acknowledged.

We also acknowledge all staff of the Airborne Geophysics Section for their contributions to the national airborne geophysical database, and help with the map compilation by P. Milligan, I. Hone, F. Simonis, and Desmond FitzGerald & Associates Pty Ltd.

References

BMR, 1976. Magnetic map of Australia, residuals of total intensity, scale 1:2 500 000, Bureau of Mineral Resources, Geology and Geophysics, Canberra.

Briggs, I.C., 1974. Machine contouring using minimum curvature. Geophysics, 39, 39–48.

Gonzalez, R.C. & Woods, R.E., 1992. Digital image processing. Addison-Wesley Publishing Company, New York, 716 pp

Hone, I.G., Milligan, P.R., Mitchell, J.N. & Horsfall, K.R., 1997. Regional airborne magnetic and gamma-ray databases in Australia. AGSO Journal of Australian Geology & Geophysics 17(2)—this issue.

Milligan, P.R. & Gunn, P.J. 1997. Enhancements and presentation of airborne geophysical data. AGSO Journal of Australian Geology & Geophysics 17(2)—this issue.

Milligan, P.R., Morse, M.P. & Rajagopalan, S., 1992. Pixel map preparation using the HSV colour model, Exploration Geophysics, 23, 219–224.

Minty, B.R.S., 1991. Simple micro-levelling for aeromagnetic data. Exploration Geophysics, 22, 591–592.

Tarlowski, C., Simonis, F., Whitaker, A. & Milligan, P., 1992. The magnetic anomaly map of Australia. Exploration Geophysics, 23, 339–342.

Tarlowski, C., Simonis, F., & Milligan, P., 1993. Magnetic anomaly map of Australia, scale 1:5 000 000. Australian Geological Survey Organisation, Canberra.

Tarlowski, C., Milligan, P.R. & Mackey, T., 1995. Magnetic anomaly map of Australia (2nd edition), scale 1:5 000 000. Australian Geological Survey Organisation, Canberra.

Tarlowski, C., McEwin, A.J., Reeves, C.V., & Barton, C.E., 1996. De-warping the composite aeromagnetic anomaly map of Australia using control traverses and base stations. Geophysics, 61(3), 696–705.

Teskey, D.J., Dodds, S.D., & Hood, P.J., 1982. Compilation techniques for 1:1 000 000 magnetic anomaly maps series. Current Research, Part A, Geological Survey of Canada, Paper 82-1A, 351–358.

AGSO Journal of Australian Geology & Geophysics, 17(2), 83–103

Magnetic petrophysics and magnetic petrology: aids to geological interpretation of magnetic surveys

D.A. Clark[1]

The present capability to acquire, process and display very large sets of high-quality magnetic survey data has far outstripped the capacity to extract all the geological information from the data. Interpretation of magnetics has lagged behind, largely because of a lack of information on magnetic properties within the survey areas and because the geological factors and processes that determine magnetic signatures are often poorly understood. In the absence of magnetic property measurements, simplistic rules-of-thumb concerning magnetic properties of different rock types can be deceptive. Furthermore, empirical correlations between mapped geology and magnetics in one area cannot necessarily be extrapolated to other areas of poor exposure if changes in depositional environment, metamorphic grade or structural setting are ignored. Magnetic modelling is afflicted by the inherent non-uniqueness of source geometry. Information on magnetic properties in the area of interest is important for constraining interpretation in order to resolve this ambiguity. Magnetic petrology integrates rock magnetism and conventional petrology in order to define the processes that create, alter and destroy magnetic minerals in rocks. By relating magnetic mineralogy, bulk magnetic properties, petrology and geochemistry to observed magnetic anomalies an understanding of the geological factors that control magnetic signatures is obtained, which can be used to improve *geological* interpretation of magnetic surveys.

Introduction

Although the magnetic method has been widely used in mineral exploration for decades, recent improvements in magnetic data acquisition, processing and presentation, and reduced airborne acquisition costs have increased the utility and importance of magnetic surveys, particularly high-resolution aeromagnetic surveys. Increasingly, high-quality surveys of large areas are available at reasonable cost. This has led to increasing emphasis on magnetics in area selection and regional mapping, as well as prospect-scale mapping and drill targetting.

We have now reached a stage where the ability to acquire, process and present magnetic survey data far outstrips the capacity to interpret the surveys. There is often far more geological information in these very large data sets than can presently be extracted in the time available for interpretation. Better understanding of the relationships between magnetic signatures and geology can facilitate the interpretation process and produce more reliable geological interpretations.

Magnetic anomalies arise from sources at all depths within the crust and, therefore, magnetic surveys provide 3D geological information. Unlike other airborne geophysical mapping tools, which detect properties of superficial layers (radiometrics, remote sensing) or have limited depth penetration (EM), magnetics have the ability, in principle, to see to great depths. This aspect of magnetic survey data is not yet fully exploited, because of the lack of adequate 3D modelling tools and automated interpretation techniques for large data sets. With the increased affordability of computing power, the opportunity exists to develop software aimed at extracting true three-dimensional pictures of the Earth from magnetics. By constraining such models with other geodata, fully integrated interpretations of multiple data sets will be achievable.

A crucial limitation of 3D interpretations of magnetic surveys arises from the fundamental non-uniqueness of potential field source distributions. This ambiguity in source geometry can only be addressed by constraining models. The most important control on the reliability of magnetic models is information on magnetic properties. Understanding of the factors that determine magnetisation intensities and directions for the geological units within the survey area is essential for resolving geological ambiguity in order to produce a reliable interpretation of subsurface geology.

Induced, remanent and viscous magnetisation

Magnetised matter contains a distribution of microscopic magnetic moments. Unpaired electron spins are the most important sources of magnetic moment. Magnetisation **J** is defined as the magnetic dipole moment per unit volume of the material. *Induced magnetisation* $\mathbf{J_I}$ is the component of magnetisation produced in response to an applied field. The induced magnetisation varies sympathetically with changes in the applied field and vanishes when the field is removed. *Remanent magnetisation* or *remanence* $\mathbf{J_R}$ is the 'permanent' magnetisation that remains when the applied field is removed, and is essentially unaffected by weak fields.

The total magnetisation is the vector sum of the induced and remanent magnetisations:

$$\mathbf{J} = \mathbf{J_I} + \mathbf{J_R}$$

For sufficiently weak fields, such as the geomagnetic field, the induced magnetisation is approximately proportional to the applied field. The constant of proportionality is known as the *susceptibility*, k. Thus if the applied field is **F**, the induced and total magnetisations are given by:

$$\mathbf{J_I} = k\mathbf{F} \; ; \; \mathbf{J} = k\mathbf{F} + \mathbf{J_R}$$

For most rocks, the induced magnetisation is essentially parallel to the applied field, irrespective of the field direction. In this case the susceptibility is a scalar quantity, i.e. it is characterised simply by its magnitude and is isotropic. The case of anisotropic susceptibility is discussed below. The *Koenigsberger ratio* (Q) is a convenient parameter for expressing the relative importance of remanent and induced magnetisations. It is given by:

$$Q = J_R / J_I = J_R / kF.$$

Thus Q>1 indicates that remanence dominates induced magnetisation, whereas Q<1 implies that induced magnetisation is dominant.

The distinction between induced and remanent magnetisations is not completely clear-cut because, strictly speaking, remanent magnetisation is metastable, not permanent. A wide range of time constants characterises the equilibration of magnetisation in many magnetic materials. Thus, magnetisation responds over time to changes in the applied field. The time-varying part of the remanence is called *viscous remanent magnetisation*. Figure 1 illustrates the distinction between induced magnetisation, viscous remanence and stable remanence. Figure 1a shows the changes in magnetisation of an initially demagnetised sample in response to an applied field, which is switched on and off as shown in Figure 1b. Small applied fields, comparable in strength to the geomagnetic field, produce small, reversible changes in magnetisation when they are applied briefly, i.e. the magnetisation vanishes on removal of the field. This induced magnetisation is approximately

[1] CSIRO Exploration & Mining, PO Box 136, North Ryde, NSW 2113

proportional to the strength of the applied field. Thus, the susceptibility, which is defined as the induced magnetisation divided by the applied field, is approximately independent of the field. If a larger field is applied and then removed an irreversible change in magnetisation occurs—an *isothermal remanent magnetisation* J_{IRM} has been imparted to the sample. This magnetisation can be regarded as permanent on the experimental time scale. Figure 1c illustrates this behaviour in terms of the hysteresis loop, plotting magnetisation J versus applied field H. The initial portion of the J–H curve is approximately linear and is traversed reversibly when a small field is applied and removed. When the larger field is applied and instantaneously removed, the sample follows the trajectory abc. At point b, the total magnetisation is the sum of the induced magnetisation, which by definition is the component that vanishes when the field is removed, and the isothermal remanence.

If the field is again switched on, the magnetisation follows the path cd and returns initially to its former value (J_{IRM} + J_{IND}). If the applied field remains on, however, the total magnetisation increases gradually with time, from d to e. After an initial period, which depends on the grain size distribution, the increase in magnetisation is usually found to be approximately proportional to the logarithm of time, over several

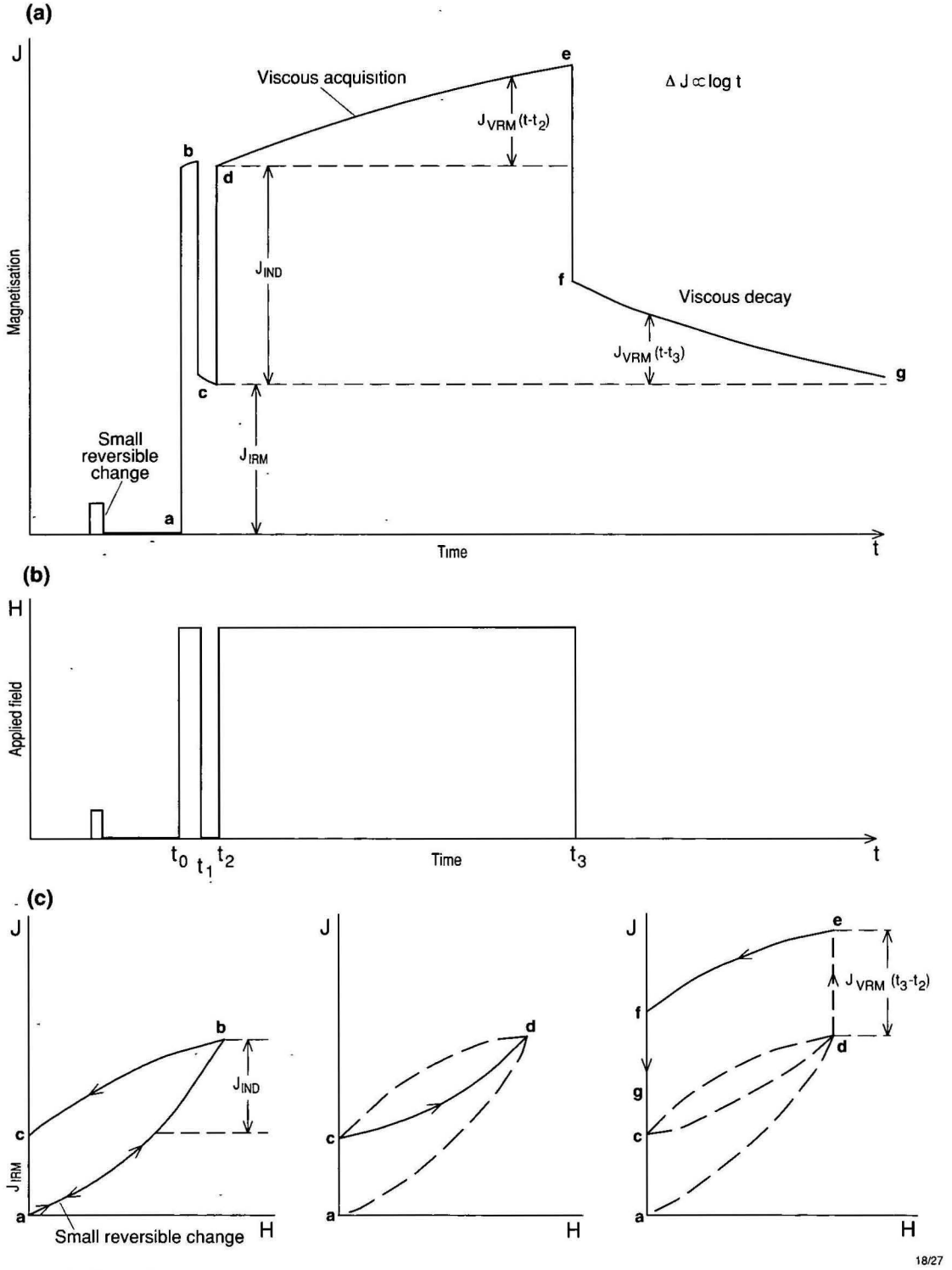

Figure 1. Distinction between induced, viscous and remanent magnetisations (see text).

decades of t. When the field is removed, this excess magnetisation, the viscous remanent magnetisation (VRM), remains and augments the isothermal remanence, but decays at a rate comparable to the acquisition rate. After sufficient time in zero field, the VRM has decayed completely and only the stable IRM remains. Thus, viscous remanence is a temporary magnetisation that is intermediate in character between induced magnetisation and more stable forms of remanence. The separation of magnetisation into induced, viscous and stable components is not exact, because the distinction depends on the time scale under consideration.

In general, the sample may not be initially in a demagnetised state. If the sample carries a stable remanence component initially, the magnetisation plots in Figures 1a and 1c are simply shifted upwards.

Types of remanent magnetisation

The natural remanent magnetisation (NRM) of a rock reflects its history and the ambient field. Some rock samples carry isothermal remanent magnetisation as a result of exposure to magnetic fields. In this case, the NRM is not representative of the remanence carried by the bulk of the rock unit. Lightning-affected samples often carry intense NRM, characterised by anomalously high Q and directions that are scattered for samples separated by a few metres or more. NRM measurements from surface exposures should, therefore, be regarded with caution. Drilling, logging with pencil magnets, mining activities and exposure to fields during or after collection can contaminate sample NRMs with IRM components of no geological significance. Standard palaeomagnetic cleaning techniques are strongly recommended to detect and preferentially remove these sources of palaeomagnetic noise.

During initial cooling of an igneous rock, magnetic mineral grains make the transition from paramagnetism to ferromagnetism as they cool through their Curie points. A spontaneous magnetisation appears that is initially in equilibrium with the applied field, but becomes 'frozen in' or blocked at a somewhat lower temperature, called the blocking temperature, when the relaxation time of the grain's magnetic moment increases prodigiously. Below the blocking temperature, the magnetisation is a stable remanence, which is known as *thermoremanent magnetisation* (TRM). Chemical changes to these ferromagnetic minerals at elevated temperature, but below the Curie temperature, produce *thermochemical remanent magnetisation* (TCRM).

Detrital magnetic mineral grains align their magnetic moments with the ambient field as they settle through water. As a result, sediments acquire detrital remanent magnetisation (DRM), which is subparallel to, but slightly shallower than, the ambient field. Subsequent rotation of grains within pore spaces produces a *post-depositional remanent magnetisation* (pDRM) which more closely reflects the ambient field. Crystallisation of new magnetic minerals or physico-chemical changes to existing magnetic minerals during diagenesis produces *chemical remanent magnetisation* (CRM) in many sedimentary rocks. Neglecting anisotropy, TRM and CRM are acquired parallel to the ambient field at the time of acquisition. For each of these types of remanence the remanent intensity is approximately proportional to the magnitude of the field, for typical geomagnetic field strengths.

The NRM of a rock may consist of components, carried by different subpopulations of magnetic minerals, acquired at different times. For example low-grade or medium-grade metamorphism may overprint a primary remanence with a partial TRM. Alteration or weathering may superimpose a CRM on an earlier remanence.

Magnetic minerals in rocks

Diamagnetism, paramagnetism and ferromagnetism

Diamagnetism arises from the response of orbiting electrons in atoms to a magnetic field. The orbital motions adjust to oppose the applied field, i.e. diamagnetism is characterised by a negative susceptibility. Diamagnetism is present in all materials, but is very weak and is overwhelmed by paramagnetism when permanent magnetic dipoles, usually due to unpaired electron spins, are present. Diamagnetic minerals (e.g. calcite and quartz) have very weak, negative susceptibilities (about -10^{-6} G/Oe or -10^{-5} SI) and can usually be regarded as nonmagnetic for geophysical purposes. Minerals that contain iron, manganese or a number of other transition metal and rare-earth ions are paramagnetic, provided that the electron spins of adjacent ions are weakly correlated. Paramagnetic minerals (e.g. olivines, pyroxenes and pure ilmenite) have weak positive susceptibilities (maximum $\sim 10^{-3}$ G/Oe $\approx 10^{-2}$ SI; generally less than 10^{-4} G/Oe $\approx 10^{-3}$ SI) and do not carry remanence. They were, therefore, normally unimportant for magnetic interpretation, given that most rocks only contain a few per cent of these minerals. In recent times, however, the enhanced sensitivity of magnetometers and improved resolution of magnetic surveys permit detection of susceptibility contrasts between rocks of differing paramagnetic mineral contents.

Antiferromagnetism occurs when magnetic moments are parallel within a sublattice, but antiparallel on different sublattices, such that the nett moment is zero, in the absence of an applied field. The susceptibility of antiferromagnetic minerals is low, similar to that of paramagnetic substances, and they do not acquire remanence. Magnetically ordered phases that possess spontaneous magnetisation can be ferromagnetic sensu stricto (e.g. iron) or ferrimagnetic (e.g. magnetite). Ferromagnetism occurs when exchange interactions tend to align electron spins. Ferrimagnetism occurs when there is antiferromagnetic coupling, but the moments of the two magnetic sublattices are unequal. For simplicity, all these strongly magnetic minerals will be referred to hereafter as ferromagnetic. Ferromagnetic minerals lose their spontaneous magnetisation at a characteristic temperature, the Curie point (T_C), which is a function only of composition and which can, therefore, be used to detect particular ferromagnetic phases. Below its Curie temperature, a ferromagnetic mineral has high susceptibility and can carry remanence. Above T_C the mineral becomes paramagnetic, with low susceptibility and no remanence. Paramagnetic minerals have greater susceptibility at low temperatures, reflecting a $\sim 1/T$ dependence, and may become magnetically ordered, i.e. ferromagnetic or antiferromagnetic, below a transition temperature (the Curie point or the Néel point, respectively) which is composition dependent and can be used to determine the presence of particular paramagnetic minerals. Table 1 gives susceptibilities of common diamagnetic and paramagnetic minerals. The properties of ferromagnetic minerals are discussed below. Readers are referred to O'Reilly (1984) for detailed discussion of the atomic basis of magnetism and the properties of natural minerals.

Intrinsic magnetic properties of spinel group minerals

Banerjee (1991) has recently reviewed the magnetic properties of Fe–Ti oxide minerals. Bleil & Petersen (1982) compiled extensive data on magnetic properties of natural minerals, including spinels. Figure 2a shows the compositions of the Fe–Ti oxide minerals that play a major role in rock magnetism. Many cations other than titanium can substitute into magnetite, with important effects on magnetic properties. Spontaneous magnetisation at room temperature (J_S) and Curie temperature

(T_C), which are intrinsic properties dependent only on composition, are given in Table 2 for a number of minerals, including some end-member spinel phases. Titanomagnetites with less than ~80 mole% ulvospinel are ferromagnetic at room temperature. Although the spontaneous magnetisation and Curie temperature of titanomagnetites decrease steadily with increasing titanium content (Fig. 2b, c), the susceptibility and specific remanent intensity of TRM are not strongly dependent on composition for the ferromagnetic phases. Thus, moderate titanium content in magnetite does not generally produce weaker magnetic properties, contrary to popular opinion. In fact, grain size is a more important factor influencing magnetisation of titanomagnetite-bearing rocks (Fig. 2d, e).

Note that the Curie point of maghaemite cannot be observed directly, because maghaemite inverts to haematite below its Curie temperature, at temperatures as low as ~300°C, depending on impurities. The Curie temperature of magnetite-bearing spinel minerals varies systematically with magnetite content To a first approximation, the Curie point of a particular spinel composition can be estimated by linear interpolation between the T_C of the constituent end members. Diamagnetic minerals can be assigned a nominal T_C of absolute zero (–273°C) for this purpose. For the titanomagnetite series, a more accurate expression relating Curie temperature to mole fraction of ulvospinel (x) is:

$Fe_{3-x}Ti_xO_4$: T_C (°C) = 578 – 580x – 150x^2.

Table 1. Common diamagnetic and paramagnetic minerals (data from Bleil & Petersen 1982).

Mineral	*Type of magnetism*	*Susceptibility (G/Oe)*	*Susceptibility (SI)*
Quartz*	Diamagnetic	-1.2×10^{-6}	-1.5×10^{-5}
Orthoclase*	Diamagnetic	-1.1×10^{-6}	-1.4×10^{-5}
Forsterite*	Diamagnetic	-1.0×10^{-6}	-1.3×10^{-5}
Calcite*	Diamagnetic	-1.0×10^{-6}	-1.3×10^{-5}
Gypsum*	Diamagnetic	-2.3×10^{-6}	-2.9×10^{-5}
Anhydrite*	Diamagnetic	-4.7×10^{-6}	-5.9×10^{-5}
Halite*	Diamagnetic	-0.8×10^{-6}	-1.0×10^{-5}
Galena*	Diamagnetic	-2.6×10^{-6}	-3.3×10^{-5}
Sphalerite*	Diamagnetic	-1.0×10^{-6}	-1.3×10^{-5}
Apatite*	Diamagnetic	-0.85×10^{-6}	-1.1×10^{-5}
Fayalite*	Paramagnetic	390×10^{-6}	490×10^{-5}
Ferrosilite*	Paramagnetic	260×10^{-6}	330×10^{-5}
Hedenbergite*	Paramagnetic	220×10^{-6}	270×10^{-5}
Olivine	Paramagnetic	$10...430 \times 10^{-6}$	$12...540 \times 10^{-5}$
Orthopyroxene	Paramagnetic	$10...260 \times 10^{-6}$	$12...330 \times 10^{-5}$
Clinopyroxene	Paramagnetic	$50...220 \times 10^{-6}$	$60..280 \times 10^{-5}$
Actinolite	Paramagnetic	40×10^{-6}	50×10^{-5}
Hornblende	Paramagnetic	$60...110 \times 10^{-6}$	$75...130 \times 10^{-5}$
Sodic amphiboles	Paramagnetic	270×10^{-6}	340×10^{-5}
Pyrope	Paramagnetic	40×10^{-6}	50×10^{-5}
Almandine	Paramagnetic	$210...530 \times 10^{-6}$	$260...660 \times 10^{-5}$
Spessartine	Paramagnetic	540×10^{-6}	680×10^{-5}
Andradite	Paramagnetic	$180...350 \times 10^{-6}$	$230...440 \times 10^{-5}$
Biotite	Paramagnetic	$70...260 \times 10^{-6}$	$90...330 \times 10^{-5}$
Phlogopite	Paramagnetic	$15...25 \times 10^{-6}$	$20...30 \times 10^{-5}$
Muscovite	Paramagnetic	$3...60 \times 10^{-6}$	$4...75 \times 10^{-5}$
Cordierite	Paramagnetic	$15...90 \times 10^{-6}$	$20...110 \times 10^{-5}$
Epidote	Paramagnetic	80×10^{-6}	100×10^{-5}
Sphene	Paramagnetic	20×10^{-6}	30×10^{-5}
Psilomelane	Paramagnetic	270×10^{-6}	340×10^{-6}
Ilmenite	Paramagnetic	150×10^{-6}	190×10^{-5}
Hausmannite	Paramagnetic	60×10^{-6}	75×10^{-5}
Chromite	Paramagnetic	$225\ 580 \times 10^{-6}$	$280...730 \times 10^{-6}$
Spinel	Paramagnetic	2×10^{-6}	3×10^{-5}
Siderite	Paramagnetic	$210...810 \times 10^{-6}$	$260....1020 \times 10^{-5}$
Magnesite	Paramagnetic	5×10^{-6}	6×10^{-5}
Dolomite	Paramagnetic	1×10^{-6}	1.2×10^{-5}
Rhodochrosite	Paramagnetic	380×10^{-6}	480×10^{-5}
Pyrite	Paramagnetic	3.4×10^{-6}	4.3×10^{-5}
Marcasite	Paramagnetic	$5...20 \times 10^{-6}$	$6...25 \times 10^{-5}$
Sphalerite	Paramagnetic	$0...160 \times 10^{-6}$	$0...200 \times 10^{-5}$
Chalcopyrite	Paramagnetic	$25...35 \times 10^{-6}$	$30...40 \times 10^{-5}$
Bornite	Paramagnetic	$45...70 \times 10^{-6}$	$55...90 \times 10^{-5}$
Arsenopyrite	Paramagnetic	$3...50 \times 10^{-6}$	$4...60 \times 10^{-5}$

* pure phases

Table 2. Intrinsic magnetic properties of ferromagnetic minerals.

Mineral	*Chemical formula*	*Spontaneous magnetisation (G)*	*Curie temperature (°C)*
Iron	Fe	1710	770
Awaruite	Ni_3Fe	950	620
Magnetite	Fe_3O_4	480	578
Ulvospinel	Fe_2TiO_4	0	–153
Titanomagnetite	$Fe_{3-x}Ti_xO_4$	~480–600x (x<0.8);0 (x ≥0.8)	~578–580x –150x^2
Maghaemite	γFe_2O_3	440	>>300 (750?)
Kenomagnetite (cation-deficient magnetite)	$Fe_{3-y}O_4$ (0 <y <1.3)	~460	~600...630
Titanomaghaemite	$Fe_{(3-x)R}Ti_{xR}O_4$ (0.89< R < 1)	10...70 (not monotonic)	150...450 (common range)
Magnesioferrite	$MgFe_2O_4$	≤220 (function of cation dist)	≤420 (function of cation dist)
Chromite	$FeCr_2O_4$	0	–185
Ferrichromite/ Cr-magnetite	$Fe_{3-x}Cr_xO_4$ $0 \le x \le 1.2$	ferromag for	–185...578
	e.g Fe_2CrO_4	250	200
Hercynite	$FeAl_2O_4$	0	–265
Magnesian ulvospinel	Mg_2TiO_4	0	diamagnetic
Picrochromite	$MgCr_2O_4$	0	–258
Spinel	$MgAl_2O_4$	0	diamagnetic
Jacobsite	$MnFe_2O_4$	397	300
Jacobsite/ Mn-magnetite	$Fe_{3-x}Mn_xO_4$	ferromag for $0 \le x \le 2.5$	
Trevorite	$NiFe_2O_4$	330	595
Coulsonite	FeV_2O_4	0	–164
Haematite	αFe_2O_3	2	680
Ilmenite	$FeTiO_3$	0	–205
Titanohaematite	$Fe_{2-x}Ti_xO_3$	$0 \le x <0.5$: antiferro $0.5 \le x \le 0.8$: ferro $0.8 < x \le 1$: para	~680–885x
Monoclinic pyrrhotite	Fe_7S_8	90	320
Hexagonal pyrrhotite	$Fe_9S_{10}...Fe_{11}S_{12}$	0	270...210
Smythite	Fe_9S_{11}	~50	>300 (~400?)
Greigite	Fe_3S_4	~30	~350

1 G = 1 kAm^{-1} (SI)

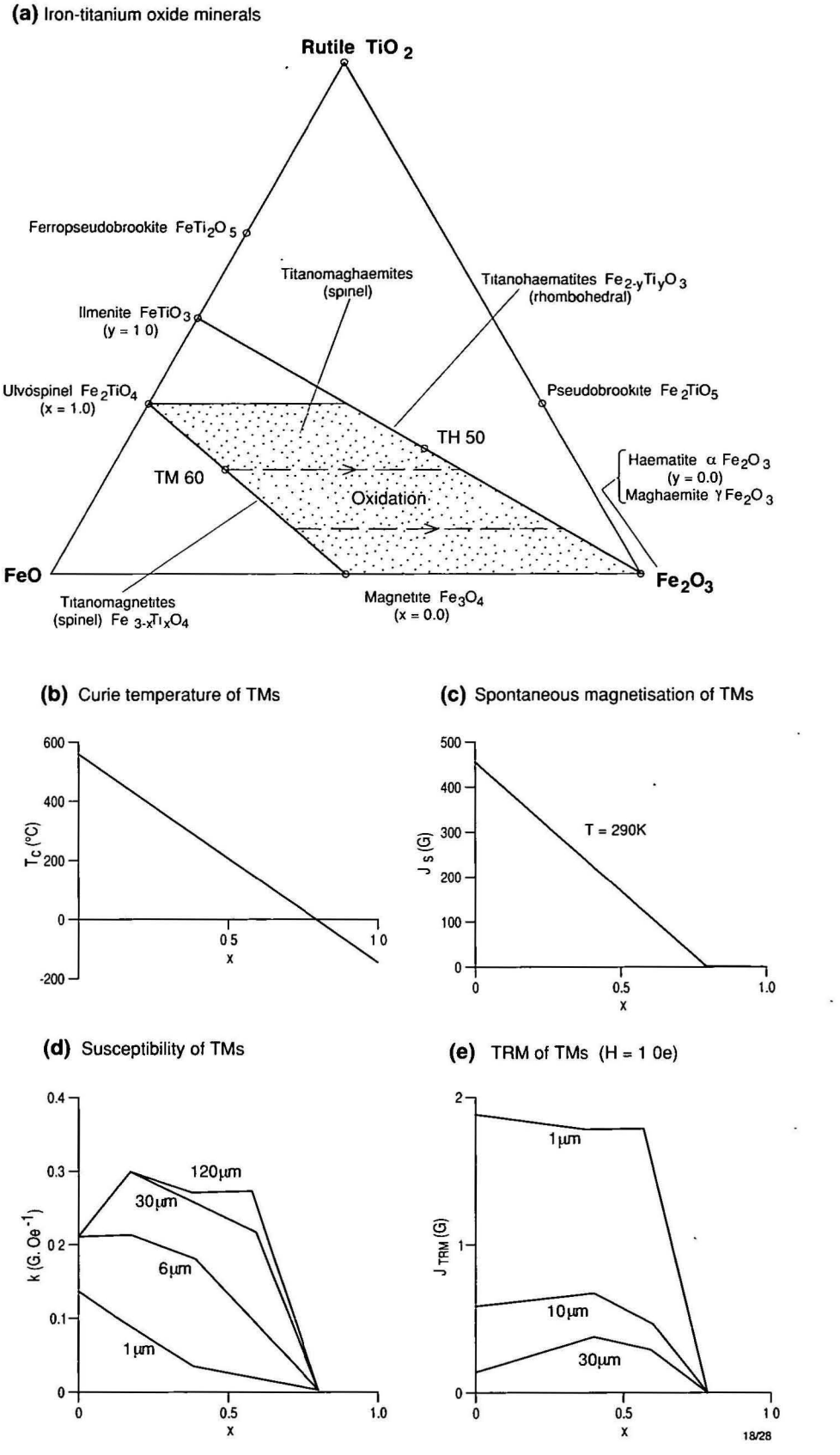

Figure 2. (a) Composition of the Fe–Ti oxide minerals that play a major role in rock magnetism. Composition dependence of: (b) Curie temperature, (c) spontaneous magnetisation, (d) susceptibility and (e) specific remanent intensity of TRM for titanomagnetites. Note the grain-size dependence of susceptibility and TRM intensity.

The effect on T_C of substitution of Cr, Al and V into magnetite is broadly similar to that of Ti substitution. Substitution of Ni increases the Curie point slightly, as does cation deficiency. Thus cation-deficient magnetites ('kenomagnetite'), representing compositions intermediate between stoichiometric magnetite and maghaemite, can have T_C above 600°C. Magnesioferrite is the only important spinel end member, other than magnetite, that is ferromagnetic at room temperature. The magnetic properties of magnesioferrite depend strongly on the cation distribution, which reflects thermal history. The Curie point of magnesioferrite is given by:

$MgFe_2O_4$: $T_C(°C) = 417 - 490f$,

where f is the fraction of Mg^{2+} ions on tetrahedral sites. Because of the elevated T_C and high spontaneous magnetisation, magnesioferrite-rich spinels and Mg-magnetites are strongly magnetic and can be important contributors to the magnetic properties of rocks (e.g. some kimberlites) in which they occur.

A note of caution needs to be sounded concerning the magnetic properties of spinels. Although a number of three-component solid-solution series have been studied, in most cases the composition is restricted to the edges of the spinel prisms. Large portions of the interiors have not been systematically investigated. Although there is some theoretical basis for predicting the properties of complex spinel compositions, unusual behaviour has been found in special cases and it is conceivable that some of the exotic spinels found in some mafic and ultramafic rocks may have unexpected behaviour.

Intrinsic magnetic properties of titanohaematites and picroilmenites

The rhombohedral titanohaematites are second in importance only to the titanomagnetites. The magnetic phase diagram of the titanohaematite series is complex and the magnetic properties of the compositions that are ferromagnetic at room temperature are influenced by thermal history. $FeTiO_3$–Fe_2O_3 solid solutions have been thoroughly studied. The Curie temperature decreases approximately linearly with increasing ilmenite content. Titanohaematites containing between 50 mole% and 80 mole% ilmenite are strongly magnetic and are efficient carriers of remanence. An interesting property of titanohaematites that contain between 50 mole% and 73 mole% ilmenite is that they can acquire self-reversed thermoremanent magnetisation. Although full self-reversal of remanence is a rare phenomenon in rocks, the majority of well-documented cases are attributable to titanohaematites within this composition range. Compositions closer to ilmenite are paramagnetic at room temperature and haematite-rich compositions are only weakly magnetic.

Pure haematite has a diagnostic magnetic transition (the Morin transition) at –20°C. Below this temperature, atomic magnetic moments are aligned with the crystallographic c-axis and haematite is antiferromagnetic. Above the transition the moments lie in the basal plane, but are slightly canted out of antiparallelism, giving rise to weak ferromagnetism and an increased susceptibility. The Morin transition can also be exploited for diagnosis of well-crystallised haematite by the effect of low temperature demagnetisation on remanence. As well as the intrinsic weak ferromagnetism due to spin-canting, haematite has an additional ferromagnetism associated with crystal defects. This defect moment is dependent on grain size, crystallinity and stress history, but is not affected by the Morin transition.

The magnetic properties of picroilmenites (solid solutions between ilmenite, haematite and geikielite, $MgTiO_3$) have not been systematically studied outside the former Soviet Union. Most of the data have been gathered from kimberlitic ilmenite megacrysts, but the Russian literature on this subject is often difficult to interpret, even in translation, and some inconsistencies between different studies are evident.

Results reported by Frantsesson (1970), Garanin et al. (1978) and Yakubovskaya & Ilyupin (1982) indicate that kimberlitic picroilmenites from particular pipes or clusters tend to have an inverse relationship between haematite and geikelite contents, with ilmenite approximately constant. The Curie temperature increases monotonically with haematite content. The picroilmenites in each case had somewhat different compositions. These studies found that the investigated picroilmenites became ferromagnetic at room temperature when the haematite content exceeded ~10 mole% (ilmenite ~68 mole%), ~15 mole% (ilmenite ~50 mole%) and ~20 mole% (ilmenite ~60 mole%) respectively. In all cases picroilmenites with less than 20 mole% haematite were found to have low T_C, below 200°C. The maximum Curie temperatures reported for the most haematite-rich picroilmenites were 230°C, 240°C and 220°C for these three studies respectively. Approximate Curie temperature for picroilmenites with ~15 mole% haematite was found to be, respectively, 95°C, 0°C and –110°C. It seems established, therefore, that kimberlitic picroilmenites with 10 mole% haematite are paramagnetic and those with >20 mole% haematite are ferromagnetic at room temperature, but have relatively low Curie temperatures. The properties of intermediate compositions require further study.

Magnetic properties of iron sulphide minerals

The crystallography and mineralogy of the pyrrhotite group have been reviewed by Ward (1970), Ribbe (1974), Power & Fine (1976), Vaughn & Craig (1978) and Vaughn & Lennie (1991). The general formula of pyrrhotites is $Fe_{1-x}S$, with $0 \le x \le 0.13$. Crystal structures in the pyrrhotite group are all superstructures of the NiAs structure. At elevated temperatures, above 300°C, Fe vacancies in the structure are disordered and the $Fe_{1-x}S$ solid solution adopts the hexagonal NiAs structure, which is denoted 1C. At lower temperatures the random distribution of vacancies gives way to various vacancy ordering schemes (depending on composition and thermal history) accompanied by formation of superstructures, usually with a lowering of crystal symmetry.

The only common pyrrhotite type that is ferrimagnetic at ambient temperatures is monoclinic pyrrhotite with 4C superstructure and approximate composition Fe_7S_8. The ferrimagnetism of monoclinic pyrrhotite arises from the ordering of Fe vacancies onto alternate, antiferromagnetically coupled, layers of Fe atoms. The spontaneous magnetisation of monoclinic pyrrhotite is ~90 G (90 kA/m) and its Curie temperature is ~320°C. The spontaneous magnetisation is confined to the basal plane, except at cryogenic temperatures, by strong magnetocrystalline anisotropy. Within the basal plane there is also substantial intrinsic anisotropy, which controls magnetic domain structure and structure-dependent properties, such as susceptibility, remanence intensity and stability of remanence. Other common types, such as 5C pyrrhotite with composition ~Fe_9S_{10} and 6C pyrrhotite (~$Fe_{11}S_{12}$), are antiferromagnetic at room temperature. The temperature dependence of the crystal structure of pyrrhotite is very sensitive to composition. The variation of magnetic properties with temperature is, therefore, diagnostic of composition. Thermomagnetic analysis of pyrrhotites has been discussed at length by Schwarz & Vaughn (1972).

Monoclinic pyrrhotite with composition ~Fe_7S_8 is a relatively common ferromagnetic mineral, particularly in areas with sulphide mineralisation. The magnetic susceptibility of monoclinic pyrrhotite is less than that of magnetite, but is nevertheless substantial and strongly dependent on grain size. The susceptibility of monoclinic pyrrhotite decreases monotonically with decreasing grain size from ~0.1 G/Oe (1.3 SI) for very coarse (≥1 mm) grains, ~0.025 G/Oe (0.31 SI) for ~80 μm grains, 0.01 G/Oe (0.13 SI) for ~10 μm grains, to ~0.004 G/Oe (0.05 SI) for single domain (≤ 2 μm) grains

(Clark 1983b). The grain-size dependence of magnetic hysteresis properties of natural pyrrhotites has been studied by Clark (1983b, 1984) and Dekkers (1988, 1989).

Rocks and ores containing monoclinic pyrrhotite often carry relatively intense remanent magnetisation, characterised by Koenigsberger ratios greater than unity (Kropacek 1971; Kropacek & Krs 1971; Schwarz 1974; Clark 1983b; Thomson et al. 1991; Clark & Tonkin 1994). Clark (1983b) has shown that strong specific remanent intensities, high coercivity and high Koenigsberger ratios are predictable consequences of the intrinsic properties of monoclinic pyrrhotite, in particular the moderately high spontaneous magnetisation and the strong magnetocrystalline anisotropy. Theoretical, experimental and petrophysical studies have demonstrated that remanence carried by monoclinic pyrrhotite, particularly by fine grains, is magnetically hard and can be stable for geologically long periods at low temperatures (Clark 1983b). Remanence carried by monoclinic pyrrhotite is easily thermally reset, however, because of the low Curie temperature and the instability of the monoclinic phase with respect to antiferromagnetic pyrrhotite phases + pyrite above ~250°C. It is quite common, therefore, for pyrrhotite-bearing rocks to have a magnetisation dominated by an ancient remanence, which dates from the last significant thermal event or events experienced by the rocks and which may be highly oblique to the present field. Temperatures as low as ~100°C can superimpose an overprint remanence on an older magnetisation carried by monoclinic pyrrhotite (Clark 1983b). Interpretation of magnetic anomalies associated with such rocks may be seriously in error if the effects of remanence are ignored.

Because of the high intrinsic anisotropy of monoclinic pyrrhotite, any preferred orientation of pyrrhotite grains produces substantial susceptibility anisotropy of the rock or ore within which the pyrrhotite occurs. The effect of anisotropy on the magnitude and direction of induced and remanent magnetisations may also be significant for magnetic interpretation, particularly when the pyrrhotite is coarse-grained (Clark 1983b; Thomson et al. 1991).

Monoclinic pyrrhotite exhibits significant field-dependence of susceptibility (Worm 1991). Therefore, susceptibilities of pyrrhotite-bearing rocks should be measured in fields that are comparable in intensity to the geomagnetic field. In addition, the susceptibility of massive sulphide ores with pyrrhotite, but not disseminated pyrrhotite-bearing rocks, is dependent on measurement frequency, owing to eddy currents induced in the specimens (Worm et al. 1993). Thus, susceptibility of sulphide ores should be measured at the lowest practicable frequency. Frequencies of ~1 kHz or less are acceptable.

Greigite is iron thiospinel, Fe_3S_4, the sulphur analogue of magnetite. The spontaneous magnetisation and inferred Curie temperature of greigite are similar to those of monoclinic pyrrhotite. In recent times it has been realised that greigite is a common magnetic sulphide mineral in young sediments and in sedimentary rocks from a variety of environments (Snowball 1991; Krs et al. 1990, 1992; Roberts & Turner 1993; Reynolds et al. 1994). The magnetic properties of greigite have been characterised by Snowball (1991) and Hoffman (1992).

Smythite, which has approximate composition $(Fe, Ni)_9S_{11}$, is a relatively rare ferromagnetic mineral associated with some magmatic ores and is also present in some sedimentary rocks. The magnetic properties of smythite probably resemble those of monoclinic pyrrhotite. Krs et al. (1993) have studied magnetic properties of smythite from organic-rich Lower Miocene claystones of Bohemia.

Domain structure

The bulk magnetic properties of rocks reflect the modal proportions, composition and microstructure of the magnetic mineral grains, which are usually present in only minor amounts. Microstructure includes, inter alia, grain size and shape, degree of crystallinity and textural relationships, and strongly influences the magnetic domain state of the grains. The most important control on domain structure is the effective grain size, which is equivalent to the actual grain size in a homogeneous grain, but is related to lamella size in grains with exsolution lamellae and the size of the ferromagnetic zone in a zoned grain.

Sufficiently small grains are uniformly magnetised, i.e. they have single domain (SD) structure. Ultrafine SD grains (<0.03 μm for equant magnetite) are sufficiently perturbed by thermal fluctuations that the orientation of the spontaneous magnetisation flips rapidly between two or more easy directions. Such grains cannot retain a stable remanence and their magnetisation tends to relax rapidly towards any applied field, leading to a very high susceptibility. This behaviour is called superparamagnetism, and the grains are termed superparamagnetic (SPM). Rocks and soils that contain substantial quantities of SPM grains exhibit substantial frequency-dependence of susceptibility, often greater than 10 per cent and up to 24 per cent decrease in susceptibility per decade of frequency (Thompson & Oldfield 1986). Lateritic soils that contain SPM grains of cation-deficient magnetite or maghaemite are responsible for anomalous decays in coincident-loop TEM surveys (Buselli 1982).

The relaxation time for superparamagnetism increases exponentially with grain volume. Thus, slightly larger grains have very long relaxation times, even on a geological time scale, and can retain remanent magnetisation indefinitely. These stable SD grains, typically in the submicron size range, are important carriers of remanent magnetisation in many rocks. Acicular grain shape, or elongated lamellar shape, favours SD behaviour and extends the maximum size for SD behaviour to the micron range.

With increasing size it becomes energetically favourable for the grain to subdivide into a number of magnetic domains with differently oriented magnetisations. These multidomain (MD) grains have susceptibilities, controlled by self-demagnetisation, which in the case of strongly magnetic minerals, such as magnetite, are comparable to the susceptibilities of SD grains with similar composition. The remanence of MD grains is more easily demagnetised ('softer') than that carried by SD grains and is of lower specific intensity. The case of magnetite will be considered in some detail, but other magnetic minerals exhibit qualitatively similar behaviour. Magnetite grains larger than ~20 m exhibit true MD behaviour. The coercivity, which is a measure of the ease of demagnetisation, and the remanent intensity decrease steadily with increasing grain size until they level out for grain sizes greater than ~100 μm.

Grains smaller than ~20 μm have properties intermediate between those of SD and true MD grains and are called pseudosingle domain (PSD). Small PSD grains, a few microns in size, are relatively hard and carry relatively intense remanence. For this reason, small PSD grains are the most important remanence carriers in many rocks, in spite of the fact that they constitute a minor proportion of the magnetic mineral assemblage and even though relatively large MD grains may dominate the susceptibility of the rocks.

The behaviour of some important magnetic properties with increasing grain size (above the SPM threshold size) can be summarised as: remanence, coercivity and Koenigsberger ratio (remanent/induced magnetisation) decrease; susceptibility increases slightly. Typical values of susceptibility, remanent intensity and Koenigsberger ratio of various domain states for a number of magnetic minerals are summarised in Fig. 3 (from Clark 1983a). The theoretical maximum size for superparamagnetic and single domain behaviour for equant grains of a number of magnetic minerals are summarised in Table 3.

It has become apparent in recent years that magnetic grains frequently occupy metastable domain states of anomalously low domain multiplicity. The above values for the critical SD size assume equilibrium, i.e. that the grain is in the absolute energy minimum state. In fact, grains an order of magnitude larger than the theoretical size can remain in a metastable SD state, because formation of a domain wall requires an energy barrier to be overcome. Thus the effective upper limit for SD

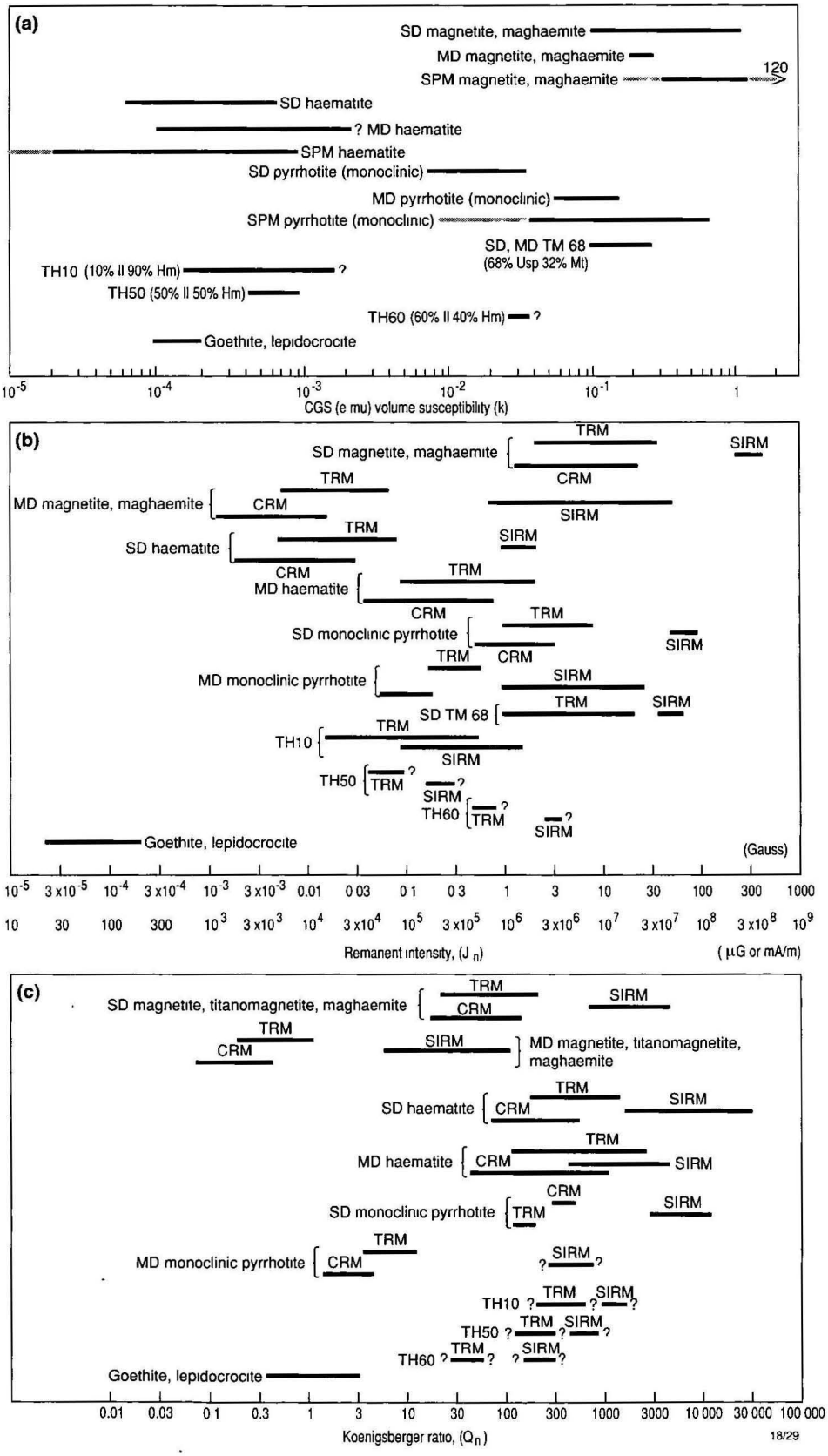

Figure 3. Typical values of (a) susceptibility, (b) remanent intensity and (c) Koenigsberger ratio of various domain states for common magnetic minerals. SIRM = saturation IRM. (from Clark 1983).

Table 3. Superparamagnetic threshold and critical single domain sizes.

Mineral	*SPM threshold size (μm)*	*Critical SD size (μm)*
Iron	<0.008	0.023
Magnetite	0.03	0.06
Maghaemaite	0.02	0.06
Titanomagnetite (60% usp)	0.08	0.4
Haematite	0.03	15
Monoclinic pyrrhotite	0.018	1.6
Greigite	~0.04	~0.8

Table 4. Domain state size ranges and coercivities for magnetite.

Domain state	*Size (μm)*	*Coercivity (Oe)*
SPM	<0.05	0
(Acicular) SD	0.05–1	>600
PSD	~1–20	100–600
MD	>20	100

1 Oe = 0 1 mT (SI)

behaviour has been extended to ~1 μm for magnetite and by a similar factor for other minerals. The threshold sizes are also larger for elongated grains than for equant grains. The domain structure transition sizes for titanomagnetites and other spinel phases with lower spontaneous magnetisations are larger than for magnetite. Thus the single domain/two domain transition, the upper limit of the PSD size range etc. occur at larger grain sizes for spinels with decreasing magnetite contents.

Taking metastable behaviour into account, the approximate size ranges and coercivities for SPM, (stable) SD, PSD and MD behaviour for magnetite are listed in Table 4.

Palaeomagnetic cleaning techniques

Collinson (1983) and Butler (1992) described demagnetisation techniques routinely used for resolving palaeomagnetic components and for characterising magnetic mineralogy. Alternating field (AF) demagnetisation is similar to degaussing of permanent magnetisation of ships or tape recorder heads. The sample is subjected to an alternating magnetic field that is gradually reduced to zero, thereby randomising the moments of all grains with coercivity less than the initial AF amplitude. This procedure is repeated at successively higher fields, demagnetising successively harder fractions of the magnetic mineral assemblage and isolating the most stable component of remanence. AF demagnetisation is particularly effective at removing isothermal remanent magnetisation (IRM) acquired by exposure to strong magnetic fields, such as those produced by mining equipment or lightning strikes etc. AF demagnetisation is sometimes effective in selectively removing VRM.

Thermal demagnetisation involves heating the sample and recooling to room temperature, in zero magnetic field. This randomises the magnetic moments of all grains with unblocking temperatures less than the heating temperature. The procedure is repeated at successively higher temperatures, thereby demagnetising successively higher unblocking-temperature fractions Thermal demagnetisation is particularly effective at unravelling the thermal history of the rock, for instance by resolving primary TRM from a later metamorphic overprint. Thermal demagnetisation is especially useful for removing VRM components acquired at low temperatures, but is not so effective against IRM noise.

Low-temperature demagnetisation involves cooling the sample to very low temperatures (e.g. the boiling point of liquid nitrogen) and rewarming to room temperature, in zero field. This technique exploits low-temperature magnetic transitions of particular magnetic minerals, to isolate remanence components carried by different minerals or by different grain-size fractions of magnetite, for example. The effect of low-temperature demagnetisation can be characterised by the parameter R_K, which is the ratio of the remanence remaining at room temperature, after cooling to –196°C in zero field, to the original remanence.

Because different remanence components are carried by subpopulations of grains with different characteristics, they can usually be distinguished by their different responses to various demagnetisation techniques. Palaeomagnetic cleaning techniques have three main applications, which can be termed palaeomagnetic, petrophysical and rock magnetic, respectively:

- Resolution of remanence components acquired at different times, allowing estimation of palaeofield directions and palaeopole positions at the time of formation, at the time of metamorphism etc.,
- Removal of palaeomagnetic noise components, which are not representative of the bulk in-situ properties, allowing characteristic NRMs of the rock to be determined,
- Identification of magnetic minerals by their demagnetisation characteristics. Information on compositions, domain states and grain sizes of the magnetic minerals can be obtained.

When two or more components of remanence are present in a rock unit, the NRM direction and intensity of individual samples can be very variable, depending on the relative proportion of each component in the sample. Estimating the effective remanence of a large volume of rock from NRM measurements alone is difficult in these circumstances. Statistical techniques for estimating average vectors and errors in these circumstances are in their infancy. However, if the NRM of each sample is resolved into discrete components, a well-grouped set of directions and moderate range of intensities can be determined for each generation of remanence. Standard statistical techniques can then be used to estimate an average remanence vector, and its uncertainty, for each component. The estimated remanence vector for the rock unit can then be reconstructed from the components.

The difference in AF demagnetisation behaviour of acicular SD, small PSD and large MD magnetite is shown in Figure 4. The remanence being demagnetised is an artificially imparted saturation IRM (SIRM), produced by placing the samples in a very strong field. The plot shows remanent intensity, normalised to the initial value before AF treatment, versus AF field. The corresponding coercivity spectra can be obtained from the demagnetisation curves by differentiation, as the coercivity spectrum is the magnitude of the slope of the demagnetisation curve. Thus, the coercivity spectrum of the large MD grains peaks at low fields (less than 5 mT), the spectrum for the small PSD grains peaks at ~15 mT and that of the SD grains peaks above 40 mT. The Lowrie–Fuller test exploits the differences between AF demagnetisation behaviour of small and large grains. For SD and PSD grains, weak field remanence, such as TRM, is more resistant to demagnetisation than strong field remanence, particularly SIRM. For true MD grains the relative stability of weak and strong field remanence is reversed.

Demagnetisation behaviour can be used to detect the presence of other magnetic minerals. For example, haematite is very hard (coercivity >>1000 Oe) and does not thermally demagnetise until close to 670°C. Goethite has even greater coercivity than haematite, but has a Curie temperature of ~120°C, and is, therefore, very easily thermally demagnetised.

Thermomagnetic analysis of magnetic mineralogy

The variation of magnetic properties of magnetic minerals with temperature depends on composition and, in some cases, on domain state and microstructure. This variation can, therefore, be used for analysis of magnetic minerals and for optimising thermal demagnetisation steps (Schmidt 1993). The variation of susceptibility with temperature is particularly useful, because of the rapid change in susceptibility close to T_C, which enables well-defined Curie points to be determined, and because of the sensitivity of susceptibility to domain state and microstructure.

The characteristic susceptibility (k) versus temperature (T) behaviour of different magnetic minerals is shown in Figure 5. The k–T curve for paramagnetic minerals is hyperbolic, reflecting the 1/T dependence of paramagnetic susceptibility. The k–T curve of magnetite with MD structure, including PSD grains as well as true MD grains, is very diagnostic. There is a prominent peak at –155°C, which corresponds to the isotropic point of magnetite. Below this temperature, the easy magnetisation directions are along the <100> cubic axes, whereas above it the easy directions lie along <111> body diagonals of the cubic unit cell. At the isotropic point, the magnetisation rotates freely to align with an applied field, giving rise to an increase in susceptibility. The susceptibility of MD grains is limited by self-demagnetisation, and the observed susceptibility remains almost constant until just below the Curie temperature, when it plummets to paramagnetic values. The isotropic point is very sensitive to composition, and substitution of cations other than iron or departures from stoichiometry tend to lower the isotropic point. Titanomagnetites containing more than ~10 mole% ulvospinel have isotropic points below liquid-nitrogen temperature. Thus the presence of a well-defined peak around –155°C is diagnostic of the presence of nearly pure PSD and/or MD magnetite.

The titanomagnetite for which the k–T curve is shown has a Curie point of ~200°C and contains ~60 mole% ulvospinel. The k–T curve is irreversible on cooling from high temperature (not shown), owing to exsolution of more magnetite-rich and magnetite-poor titanomagnetites than the original composition. Thus two Curie points, one above 500°C and the other shifted somewhat lower than the original T_C, would be seen in the cooling curve.

The k–T curve for SD magnetite does not exhibit a peak at the isotropic point, because the properties of SD grains are controlled largely by shape anisotropy, rather than by magnetocrystalline anisotropy. The susceptibility is almost constant at low temperatures, but increases as the Curie temperature is approached. This increase in k reflects unblocking of fine grains below T_C.

The susceptibility of grains increases sharply at the unblocking temperature, because the relaxation time suddenly decreases, allowing the magnetic moments of the grains to equilibrate rapidly with the applied field. Above the unblocking temperature, the superparamagnetic susceptibility of grains of specified volume is proportional to J_s^2/T and is much higher than the room temperature susceptibility, until the Curie temperature is approached (at which point $J_s \rightarrow 0$, so $k \rightarrow 0$). Thus, the presence of significant unblocking of remanence well below the Curie temperature may indicate that this portion of the remanence is carried by very fine (submicron) single domain grains.

Even smaller grains unblock at much lower temperatures and exhibit superparamagnetism at room temperature. The k–T curve shown for SPM grains is idealised for an assemblage of identical grains. In rocks, there is always a distribution of grain sizes, and the superposition of unblocking peaks over a wide range of temperature leads to a steady increase in susceptibility from below room temperature up to the maximum unblocking temperature of the ultrafine SPM + SD assemblage.

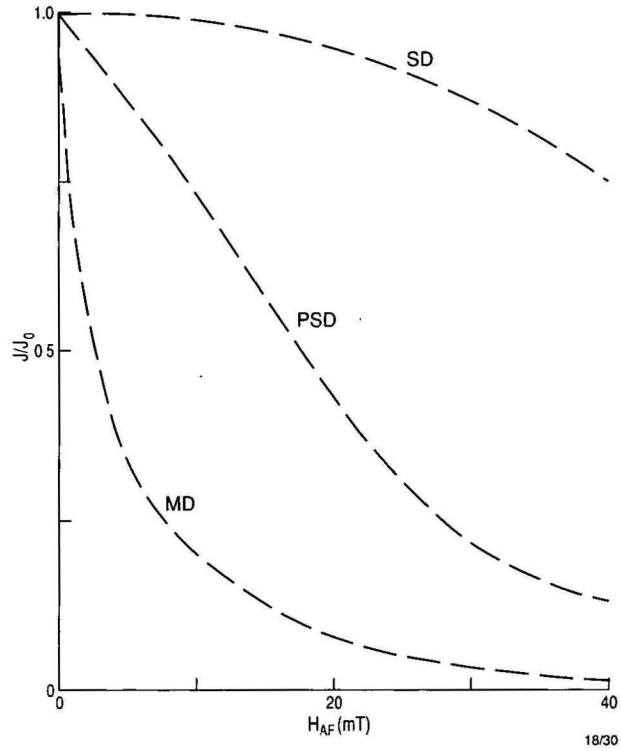

Figure 4. Characteristic AF demagnetisation behaviour of acicular SD, small PSD and large MD magnetite. 1mt = 10 Oe.

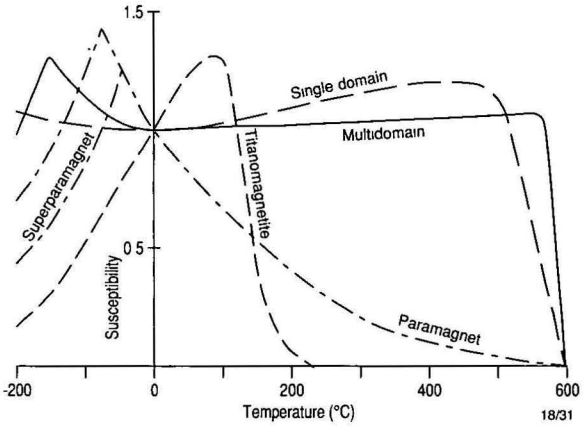

Figure 5. The characteristic susceptibility (k) versus temperature (T) behaviour of different magnetic minerals (after Thompson & Oldfield 1986).

This behaviour is commonly seen in soil samples, particularly lateritic soils.

Large multidomain grains also exhibit substantial unblocking below the Curie temperature, owing to rearrangements of domain structure with changes in temperature. The component unblocked below the Curie temperature has much lower coercivity if it is carried by MD grains than by SD grains. The unblocking behaviour of partial TRMs is quite diagnostic of SD versus MD carriers. For SD grains the maximum unblocking temperature for a PTRM acquired at a given temperature below the Curie point is approximately the maximum temperature of acquisition. For MD grains, on the other hand, unblocking occurs from low temperatures right up to the Curie point.

As the Curie temperature of a magnetic mineral is approached, there is a rapid decrease in spontaneous magnetisation and an even more rapid decrease in magnetocrystalline anisotropy. As a consequence, the remanence of even the most

stable grains unblocks, but without an increase in k. In fact, the susceptibility plummets until it attains paramagnetic values at T_C.

Thermal demagnetisation of remanence provides another analytical technique. MD grains exhibit a spectrum of unblocking temperatures right up to T_C, whereas the unblocking-temperature spectrum of SD grains cuts off below the Curie point. However, given that the grain-size range of a particular mineral extends at least to the upper end of the SD range, the maximum unblocking temperature lies just below T_C. Thus, Curie points can also be estimated from thermal demagnetisation data. Prominent inflexions in the demagnetisation curve, corresponding to a sharp peak in the blocking-temperature spectrum, indicate the approximate Curie temperature of a particular phase. Comparison of the blocking-temperature spectra with k–T curves enables phases originally present in samples to be distinguished from phases created during heating. Low-temperature demagnetisation also allows magnetic transitions characteristic of magnetite and haematite to be detected. Judicious application of a variety of rock magnetic techniques, including thermomagnetic analysis, allows the relative contributions to susceptibility and remanence of different compositions and grain-size ranges to be estimated. Lowrie (1990) has presented an elegant technique for identifying magnetic minerals, even in trace amounts, which exploits differences in Curie temperature and coercivity for different minerals.

Magnetic susceptibility of minerals and rocks

Figure 3a plots susceptibility *for dilute dispersions* of common ferromagnetic minerals, in various domain states, normalised to 100 per cent by volume. That is, if the specific volume susceptibility indicated is χ and the volume fraction of the mineral is f, the contribution of that mineral to the susceptibility of the rock is $\sim\chi f$, *provided* $f << 1$. For strongly magnetic minerals, such as magnetite, the susceptibility versus volume fraction relationship departs substantially from linearity for $f > 0.1$. This is because the effective susceptibility of isolated strongly magnetic grains is mainly controlled by self-demagnetisation and depends only weakly on the intrinsic susceptibility of the grain material. Thus the microstructure and size of the grains does not greatly affect the observed susceptibility of sparsely dispersed magnetite particles. At high concentrations, however, susceptibility is influenced by interactions between grains and increases faster than the extrapolated linear relationship applying for low concentrations. On the other hand, for weakly magnetic minerals, such as haematite, the contribution to the susceptibility is essentially proportional to the volume content, for all f.

A simple model of grain interactions adequately accounts for the concentration-dependence of susceptibility for magnetite-bearing rocks. Each magnetite grain can be regarded as residing in a cavity within a magnetised medium (see Fig. 6). The environment of each grain is a magnetic 'plum pudding' of randomly dispersed magnetic grains, of average magnetisation J, within a non-magnetic matrix. Replacing the actual environment with a continuous medium that has the same volume-averaged magnetisation, viz. fJ, the nett magnetic field within each grain is:

$$H' = H - NJ + NfJ,$$

where H′ is the internal field of the grain, H is the applied field, and N is the self-demagnetising factor of the grain. The second term on the RHS is the self-demagnetising field and the third term is the Lorentz field term, which corrects for the grain interactions.

Thus, the induced magnetisation of each grain obeys:

$$J = \chi H' = \chi[H - N(1 - f)J],$$

$$\therefore J = \chi H/[1 + (1 - f)N\chi].$$

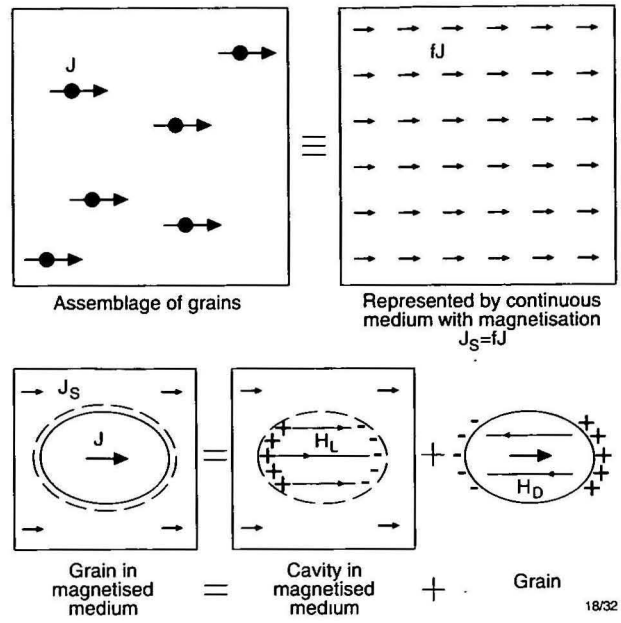

Figure 6. Simple model of effect of grain interactions on susceptibility of ferromagnetic mineral-rich rocks. The self-demagnetising field of each grain is opposed by the Lorentz field of the cavity occupied by the grain.

The magnetisation of the *rock* is fJ, which implies that the observed susceptibility of the rock is:

$$k = fJ/H = f\chi/[1 + (1 - f)N\chi].$$

For low concentrations of magnetite, this reduces to:

$$k = f\chi/[1 + N\chi]. \qquad (f < 1)$$

For MD magnetite, the intrinsic susceptibility depends on microstructure, but is always high ($\chi \geq 1$ G/Oe = 13 SI), and N is of the order of 3–4 Oe/G (0.25–0.3 SI). Therefore $N\chi >> 1$ and the susceptibility of the rock is almost independent of χ at low concentrations of magnetite:

$$k \approx f/N. \qquad (f << 1)$$

Thus, the susceptibility of a rock containing low to moderate amounts of MD magnetite is approximately proportional to magnetite content, irrespective of the magnetite grain size or microstructure. Conversely, the susceptibility can be used to infer the magnetite content for moderately magnetic magnetite-bearing rocks. According to Puranen (1989), a reasonable average empirical relationship between susceptibility and magnetite content for magnetite contents up to a few per cent is:

$k \approx 0.276f$ G/Oe = $2760v$ μG/Oe = $3.47f$ SI = $3470v \times 10^{-5}$ SI,

where v = 100f is the volume per cent magnetite content.

Significant departures from the linear k–f relationship occur for magnetite content greater than about 10 per cent. In the limit of 100 per cent magnetite, the susceptibility of the ore is simply the intrinsic susceptibility of the magnetite crystals, which depends on average grain size, crystallinity, dislocation density etc. The susceptibility of pure magnetite ore approaches χ, which ranges from ~1 G/Oe (13 SI) for fine-grained, poorly crystalline, inhomogeneous or stressed grains to ~10 G/Oe (130 SI) for very coarse, well-crystallised magnetite. Parry (1980) estimated the average effective demagnetising factor, N, for MD magnetite grains to be 3 Oe/G (0.24 SI). Puranen's relationship is consistent with the theoretical relationship if a typical value of intrinsic susceptibility of natural magnetite grains in rocks is ~1.6 G/Oe (20 SI), which agrees well with Stacey & Banejee's (1974) estimates of intrinsic susceptibility

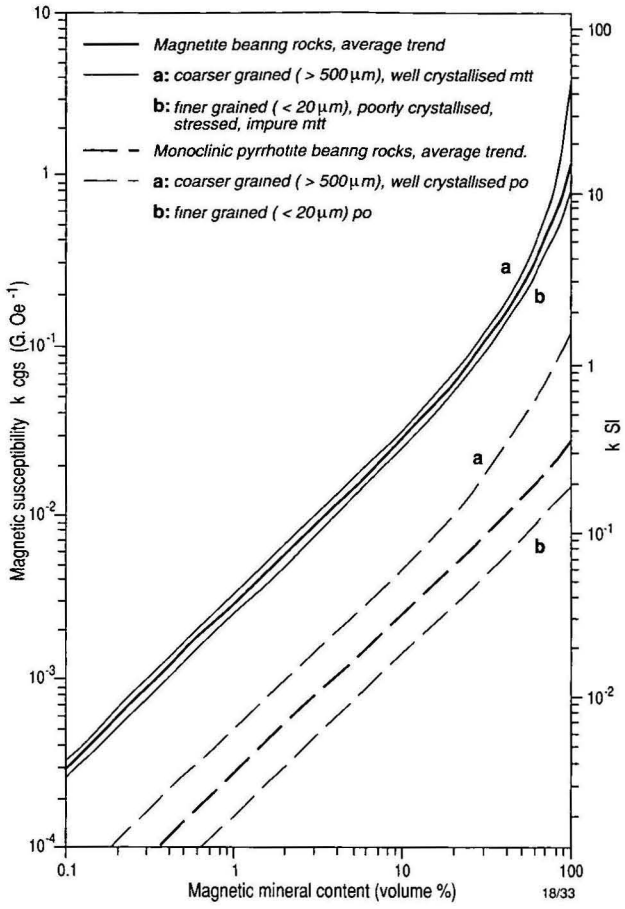

Figure 7 Susceptibility versus magnetic mineral content for magnetite and monoclinic pyrrhotite.

of large multidomain magnetite grains. Figure 7 shows curves of susceptibility versus magnetic mineral content for magnetite and monoclinic pyrrhotite, based on the theory presented above and confirmatory experimental data.

The paramagnetic susceptibility of rocks containing no ferromagnetic minerals can usually be estimated simply and reasonably accurately from their total iron content (Puranen 1989). In this case,

$k_{SI} \approx 2.86 \times 10^{-8} \times$ wt% Fe $\times$ density (kg/m^3) $= 2.22 \times 10^{-8} \times$ wt% $FeO^T \times$ density (kg/m^3)

k (G/Oe) $\approx 2.27 \times 10^{-6} \times$ wt% Fe $\times$ density (g/cm^3) $= 1.77 \times 10^{-6} \times$ wt% $FeO^T \times$ density (g/cm^3).

As examples, a paramagnetic granite with 2 wt% total iron as FeO and a density of 2.65 g/cm^3 = 2650 kg/m^3 has a susceptibility of 9 μG/Oe = 12×10^{-5} SI, whereas a paramagnetic gabbro with 12 wt% total iron as FeO and a density of 3.0 g/cm^3 = 3000 kg/m^3 has a susceptibility of 64 μG/Oe = 80×10^{-5} SI (Clark & Emerson 1991). The maximum anomaly that could be associated with a contact between rock units with these susceptibilities is ~20 nT. Susceptibility contrast between paramagnetic rock units with differing total iron contents is certainly easily detectable, if the background variation due to ferromagnetic rocks in the area is sufficiently subdued.

Figure 8 plots observed susceptibility ranges and common susceptibility ranges for various rock types. The implications of these data will be discussed below in the section on magnetic petrology.

Remanent magnetisation of minerals and rocks

The susceptibility of most rocks primarily reflects their magnetite content. Remanence intensity, while also correlated with modal magnetite, is sensitive to other factors, particularly grain size and microstructure of magnetic minerals and geological history. The natural remanent magnetisation of rocks is often multicomponent in character, i.e. it represents the sum of remanence components, each carried by a different subpopulation of magnetic grains, acquired at different times and, therefore, generally with differing directions. Variation in the relative proportions of remanence components throughout a rock unit produces scatter in the remanence direction, as well as variation in intensity. Specific remanent intensity is highest for acicular submicron magnetite grains in the single domain size range. Pseudosingle domain (titano)magnetite grains, up to ~20 μm diameter, also carry relatively intense remanence and are the dominant remanence carriers in many rocks. Larger magnetite grains have relatively weaker remanence, corresponding to Q values less than unity.

Remanence carried by haematite and monoclinic pyrrhotite is characterised by high Q values, but haematite is only weakly magnetic and, therefore, haematite-rich rocks are rarely responsible for substantial anomalies, unless the haematite is associated with magnetite and/or maghaemite. In cases where minor amounts of magnetite or maghaemite are intimately intergrown with haematite a relatively intense remanence, characterised by exceptionally high Q, may be present.

Pyrrhotite-bearing rocks often carry a relatively intense remanence, which may be ancient and quite oblique to the present field. Greigite also seems to be associated with high Q values (Reynolds et al. 1990b). The remanence carried by magnetically soft multidomain magnetite, which is the dominant magnetic phase in many rocks, is dominated by viscous magnetisation. This remanence is subparallel to the present field and, therefore, augments the induced magnetisation, enhancing the effective susceptibility. Thus, most anomalies can be interpreted in terms of magnetisation by induction, even when typical Koenigsberger ratios are comparable to unity. However, for a given source geometry, the anomaly amplitudes may be larger than measured susceptibilities indicate, owing to the viscous remanent magnetisation. Neglect of remanence may, therefore, mislead quantitative interpretation, even though the anomaly form is consistent with magnetisation parallel to the present field.

Koenigsberger ratios for viscous remanence carried by multidomain magnetite have an upper limit of about unity, but are typically much lower, averaging ~0.2. Rocks containing predominantly somewhat harder multidomain magnetite grains may carry a stable ancient remanence, characterised by a larger Q value. The Koenigsberger ratio of thermoremanence carried by an igneous rock containing predominantly such multidomain grains is typically ~0.5. In this case, the remanence direction records the geomagnetic field direction at the time of initial cooling. This direction can be of either normal or reversed polarity and may be highly oblique to the present field, depending on the age of the rock. Figure 3c summarises Koenigsberger ratios for various types of magnetisation carried by the major magnetic minerals, as a function of domain state. Figure 9 shows ranges of Koenigsberger ratio found for a variety of rock types.

Estimation of the bulk remanent magnetisation of a rock unit is not straightforward. The scatter of direction must be taken into account, as well as the distribution of intensity. Remanence makes a greater contribution to the anomaly associated with a unit showing consistent remanence direction and moderate Koenigsberger ratios than a unit with highly scattered remanence directions on a mesoscopic scale, even though the samples may all have high Q values. Measurements of raw NRMs can also be quite misleading. Surface samples are often affected by lightning, which imparts unrepresentatively high remanent intensities and Q values. Drill-core samples may carry spurious remanence imparted by drilling. Estimation

of representative remanence vectors requires palaeomagnetic cleaning of samples to remove spurious components and to identify the components that correspond to bulk in-situ properties. The remanent magnetisation identified in this way should then be analysed statistically as *vectors*, rather than as directions and scalar intensities, separately.

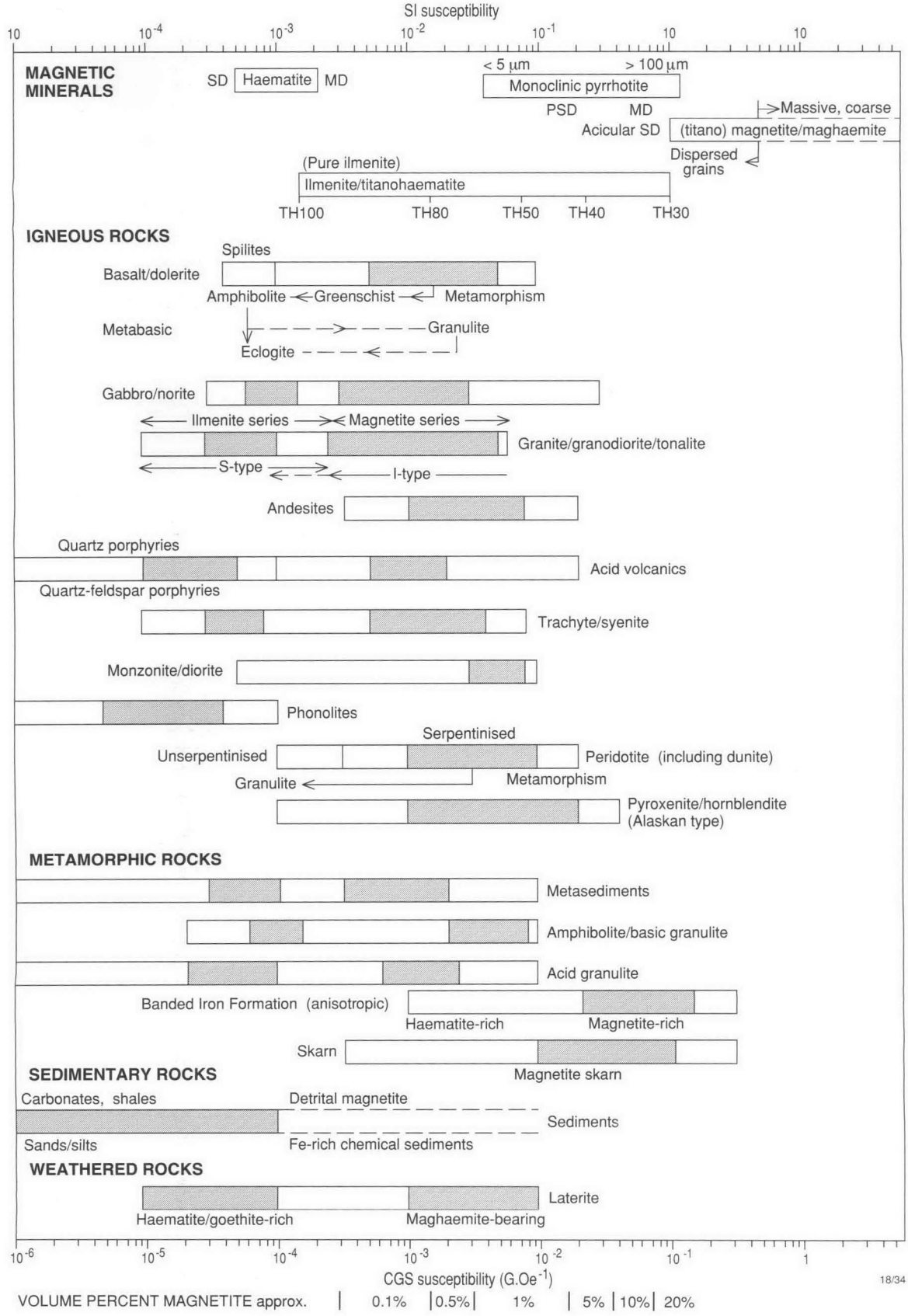

Figure 8. Observed and common susceptibility ranges for various rock types.

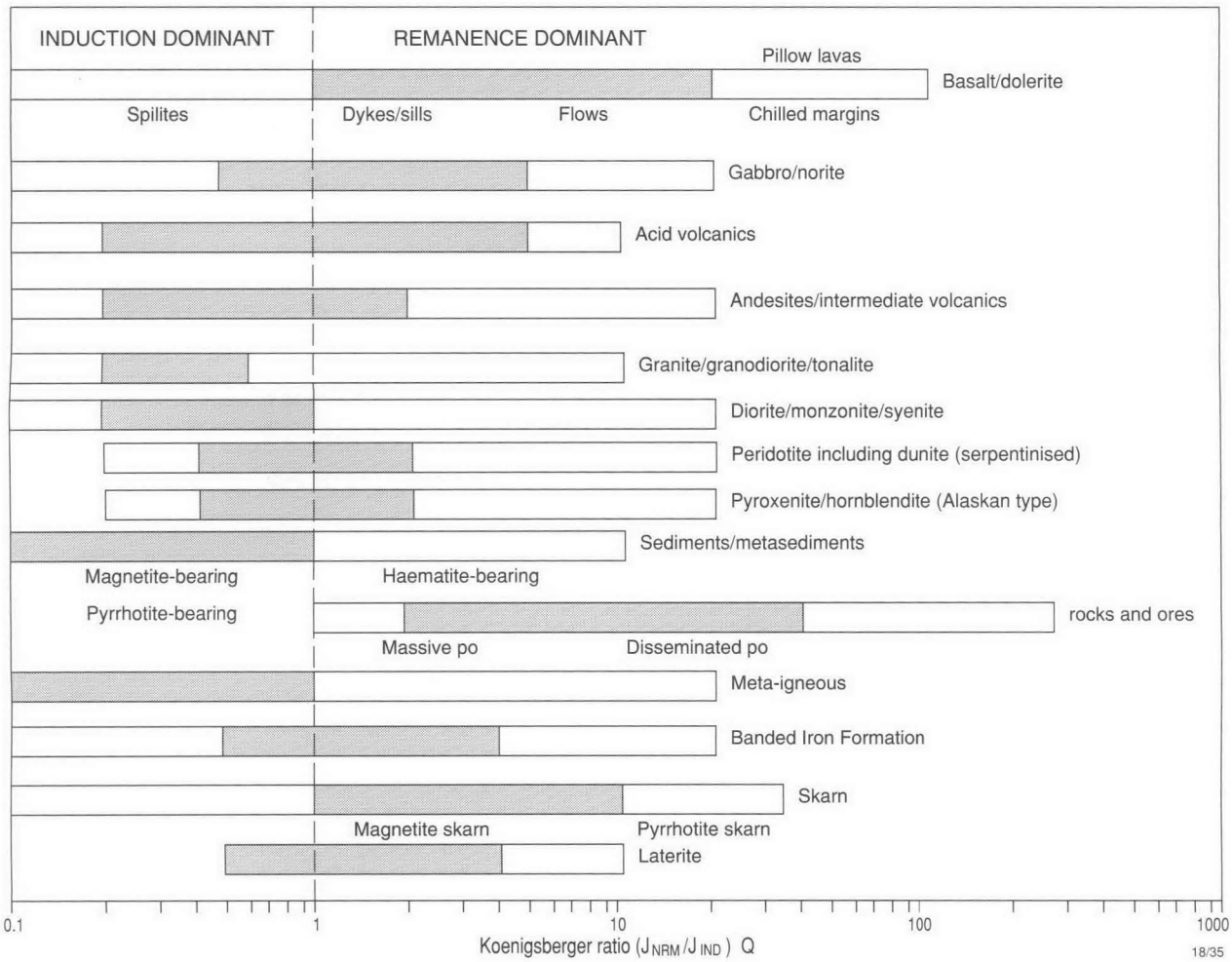

Figure 9. Observed and common ranges for Koenigsberger ratios of various rock types.

Magnetic anisotropy of minerals and rocks

Anisotropic susceptibility cannot be described by a scalar quantity, but takes the form of a symmetric second-order tensor. For any crystal and, similarly, for any homogeneous but anisotropic rock, three mutually orthogonal axes can be defined, along which the susceptibility has maximum, intermediate and minimum values. These principal axes (the *major*, *intermediate*, and *minor axes*, respectively) define an ellipsoid, the *susceptibility ellipsoid* (Nye 1957), which describes the behaviour of the susceptibility and induced magnetisation uniquely and also characterises the *magnetic fabric* of the rock. The *magnetic foliation* is the plane containing the major and intermediate susceptibility axes. It reflects planar structures in the rock. The *magnetic lineation* coincides with the major susceptibility axis and reflects linear structures. Figure 10 illustrates the concept of the susceptibility ellipsoid.

The susceptibility of paramagnetic and diamagnetic minerals can differ along different crystallographic directions, depending on crystal symmetry (Nye 1957). Cubic minerals have isotropic susceptibility, whereas that of minerals with lower crystallographic symmmetry is anisotropic. The anisotropy can be characterised by the parameter A, which is the ratio of the major susceptibility to the minor susceptibility. Common paramagnetic minerals for which anisotropy has been measured have A ranging from ~1.1 to ~1.8. In highly deformed rocks, for which paramagnetic phases, such as mica, dominate the susceptibility, the high degree of preferred orientation of mica can produce substantial anisotropy of the rock. The orientation of major susceptibility axes reflects, and can be used to infer, the planar and linear petrofabric elements in such rocks.

Ferromagnetic minerals of low crystal symmetry, such as haematite and monoclinic pyrrhotite show very strong susceptibility anisotropy. For both these minerals, susceptibility in the basal plane is orders of magnitude greater than along the c-axis. Therefore, even a slight preferred crystallographic orientation of haematite or monoclinic pyrrhotite can produce substantial anisotropy for the rock.

The susceptibility anisotropy of (titano)magnetite-bearing rocks arises from self-demagnetisation. In the case of dispersed grains, the effective susceptibility is greatest along the long axis of the grain and least along the short axis, because the grain demagnetising factor is least along the long axis and greatest along the short axis. Preferred dimensional orientation of magnetite grains, therefore, leads to anisotropic susceptibility of the rock, with maximum susceptibility parallel to the preferred alignment of long axes. When magnetite grains are inhomogeneously distributed, self-demagnetisation of the magnetite aggregates can produce strong anisotropy. The classic case is banded iron formations with magnetite-rich bands alternating with weakly magnetic bands. The susceptibility normal to the banding is greatly reduced by self-demagnetisation, whereas the susceptibility parallel to the banding is unaffected by self-demagnetisation.

Although almost all rocks exhibit slightly anisotropic magnetic susceptibility, which can be interpreted in terms of petrofabric, the degree of anisotropy is generally insufficient to significantly influence the form of magnetic anomalies. Exceptions include banded iron formations and some rocks

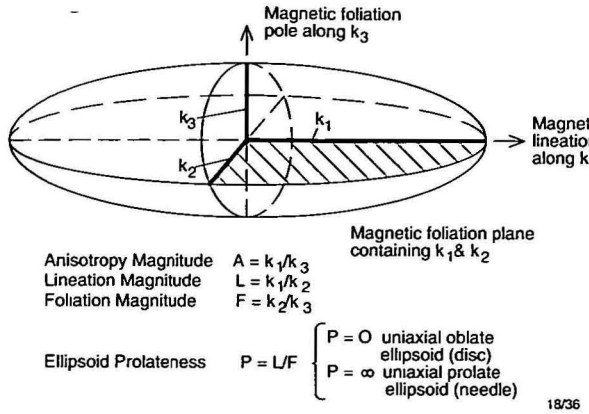

Figure 10. Relationship between the susceptibility ellipsoid and magnetic fabric elements.

and ores that contain pyrrhotite with a strong preferred orientation. In rocks with substantial magnetic anisotropy, susceptibility varies significantly with the field direction and, in general, magnetisation is not parallel to the applied field, because it tends to be deflected away from an axis of relatively low susceptibility towards an axis of higher susceptibility.

Acquisition of remanent magnetisation is also affected by anisotropy. The palaeomagnetic direction recorded by anisotropic rocks is deflected from the palaeofield direction. Thus palaeomagnetic results obtained from strongly anisotropic rocks are unreliable, unless they are corrected for anisotropy. Strong anisotropy can complicate magnetic interpretation in areas where remanence is important. If anisotropy effects are neglected, the inferred timing of remanence acquisition relative to folding can be misinterpreted (Clark & Schmidt 1994).

A recent book (Tarling & Hrouda 1993) is devoted the subject of magnetic anisotropy in rocks and readers are referred to this work for further information and a guide to the extensive literature on applications of magnetic anisotropy.

Properties of strongly magnetic rocks and ores

Magnetite-rich and monoclinic pyrrhotite-rich rocks and ores present particular difficulties for magnetic interpretation. Interpretation of structure and source geometry for these rocks is unreliable unless complicating factors are taken into account. These factors include:

- self-demagnetisation,
- anisotropy of susceptibility,
- Koenigsberger ratio,
- palaeofield direction during remanence acquisition,
- anisotropy of remanence acquisition,
- age of remanence with respect to deformation,
- perturbation of the local geomagnetic field direction by intense anomalies.

It should be noted that existing commercial modelling packages do not address these problems and are unsuitable for interpreting structures in these environments.

In Australia, types of mineralisation where these considerations are important include BIF-derived supergene-enriched iron ores, Tennant Creek-type discrete ironstone Au–Cu orebodies, BIF-hosted gold in Archaean greenstone belts, magnetite-rich Archaean VMS deposits, pyrrhotite-rich metasediments and sulphide ores in many areas, including the Pine Creek Inlier, the Cobar District and the Paterson Province, magnetite-rich ironstone-associated Cu–Au mineralisation, and BIF-associated Pb–Zn–Cu–Ag mineralisation of the east Mount Isa Inlier. The function of replaceable iron-rich lithology as chemical traps and the reducing power of magnetite are now recognised as important controls on mineralisation in the east Mount Isa Inlier, the Cullen Mineral Field of the Pine Creek Inlier, and other areas.

Rock magnetic research has concentrated on the properties of dilute dispersions of magnetic grains in rocks. The theoretical and experimental basis for understanding the magnetic properties of magnetite and pyrrhotite-rich rocks is, therefore, inadequate. In such rocks, the properties are strongly influenced by grain interactions, greatly modifying the magnetic behaviour.

The magnetic petrophysics and petrology of iron formations and ironstones is also a fertile area for research. Little is known about the magnetic properties of different facies of these rocks and the effects on them of alteration. The magnetic expression of transition from magnetite-facies to haematite-facies or sulphide-facies iron formations in mineralised environments is poorly known.

Clark & Schmidt (1994) have reviewed the magnetic properties of BIFs. Magnetite grains in BIFs are in the large multidomain size range. In most rocks, for which magnetite is an accessory mineral occurring as widely dispersed grains, large multidomain grains are associated with Koenigsberger ratios (Q values) less than unity, owing to inhomogeneous magnetisation and strong self-demagnetisation of such grains. When magnetite occurs in very high concentrations, however, interactions between grains reduce the effective self-demagnetising factors of the grains and enhance the specific susceptibility and, to an even greater extent, the specific remanence. Thus, the Koenigsberger ratio exhibited by BIFs can be substantial. Q values vary widely for BIFs, but predominantly fall in the range 1–2, with higher values occurring occasionally. Because remanence contributes substantially to total magnetisation, it should not be ignored in quantitative interpretation of magnetic signatures of BIFs.

The effective susceptibility of BIFs parallel to bedding exceeds the susceptibility normal to bedding, typically by a factor of 2–4. Bedding-parallel susceptibilities of magnetite-rich BIFs are typically 0.5–2.0 SI (0.05–0.16 G/Oe). Similarly, remanence is acquired more readily along layering than across it, leading to deflection of the remanence direction away from the palaeofield direction, towards the bedding plane. The anisotropy of remanence acquisition generally exceeds the susceptibility anisotropy and can produce large deflections of palaeomagnetic directions acquired in moderate to high (but not polar) palaeolatitudes. For this reason, remanence direction in BIFs usually lies fairly close to the bedding plane.

The strong anisotropy of BIFs means that the Q value of a BIF unit is sensitive to the orientation of the bedding with respect to the geomagnetic field. Remanence direction and the relative age of remanence and folding are best determined by palaeomagnetic study of fresh BIF samples (from mines or drill core), backed up by detailed modelling of magnetic anomalies over BIFs of known structure.

Magnetic properties of outcropping BIFs are usually greatly modified by weathering, which substantially decreases the bulk susceptibility, the degree of anisotropy and the remanence intensity. Deeper and more intense weathering of BIFs is assisted by faulting and may be associated with reduced magnetic response over intensely faulted zones. The magnetisation of haematite-rich supergene-enriched iron ores is much lower than that of their BIF precursors.

Much magnetic modelling ignores the effects of anisotropy and remanence and proceeds on the assumption of magnetisation parallel to the geomagnetic field. Dips of magnetic units are then interpreted from the shape of associated magnetic anomalies. This approach is inappropriate for interpretation of anomalies associated with BIFs, because anisotropy and remanence effects are demonstrably important and the direction of the resultant magnetisation may depart substantially from geomagnetic field direction. As an illustration, Figure 11 shows theoretical magnetic profiles over idealised fold structures, indicating the differences in anomalies produced by isotropic

induced magnetisation, anisotropic induced magnetisation (for A = 2.5), and anisotropic induced magnetisation plus pre-folding remanence (with intensity 1.5 times that of the isotropic induced magnetisation). The anisotropy and Koenigsberger ratio used are typical values for BIFs. Clearly, an interpretation of the magnetic signatures that ignores anisotropy and remanence will lead to serious errors, particularly in interpreted dips.

Magnetic petrology

Magnetic petrology integrates rock magnetism and conventional petrology to characterise the composition, abundance, microstructure and paragenesis of magnetic minerals, and to define the processes that create, alter and destroy magnetic minerals in rocks. By relating magnetic mineralogy, bulk magnetic properties and petrology to observed magnetic anomalies, an understanding of the geological factors that control magnetic signatures can be obtained, which can be used to improve geological interpretation of magnetic surveys.

Magnetic properties of rocks reflect, above all else, the partitioning of iron in the rock between strongly magnetic oxides and/or sulphides and weakly magnetic phases (silicates, carbonates etc.). This partitioning depends on chemical composition, oxidation ratio of the iron and petrogenetic conditions. Thus, a host of geological factors influence magnetic properties, and simplistic correlations between magnetic properties and lithotype are generally unreliable. Rules-of-thumb, such as 'susceptibilities go according to basic extrusive > basic intrusive > acid igneous > sedimentary' have so many exceptions that they are almost useless. It is also dangerous to extrapolate empirical correlations between mapped geology and magnetics in one area to another area, ignoring changes in depositional environment, metamorphic grade or structural setting.

A magnetic petrological classification that can provide a sound basis for geological interpretation of magnetics in a given province must rely on an understanding of the factors that control partitioning of iron. The most direct approach to this problem is to characterise the ferrous and ferric iron content of whole rocks and of all the minerals in the rocks, as a function of the geological variable being studied. This requires wet chemical determination of ferrous and ferric iron, petrographic determination of modal mineralogy and microprobe determinations of the mineral chemistry of each phase, to produce a complete inventory of iron in the sample. As yet, such studies are in their infancy, owing to the rarity of wet chemical analyses to determine whole rock ferrous and ferric iron and to difficulties in determining ferric/ferrous ratios in individual minerals, particularly hydrous silicates.

The data of Figures 8 & 9 are based on magnetic property measurements at the CSIRO Division of Exploration and Mining over the last 18 years and published studies and compilations. The systematic collection of petrophysical data by the geological surveys of Scandinavian countries, in particular, has greatly expanded the size and scope of the information available. It is evident from Figure 8 that each rock type exhibits a wide range of susceptibility and that the values are not generally diagnostic of lithology. Classical rock names are in fact much too broad to be useful for classification of magnetic properties. This is because the susceptibility of most rocks reflects the abundance of accessory minerals, particularly magnetite (sensu lato), which are ignored in petrological classification.

At a more refined level, however, there is significant geological information in basic magnetic properties, especially if the statistical characteristics of large collections are considered and if the measurements are supplemented by rock magnetic experiments to characterise the composition and microstructure of the magnetic minerals. The magnetic minerals in a meta-igneous rock, for example, are sensitive to its geological history, including the bulk composition and petrogenetic affinities of the magma, the degree of differentiation, conditions of emplacement, degree and type of hydrothermal alteration and conditions of metamorphism (temperature, pressure, fugacities of oxygen, water, sulphur, CO_2 etc.). Differences in magnetic properties can, therefore, reflect subtle variations in some or all of these influences. More detailed clasification schemes, based on the most important of these factors, may, therefore, allow more meaningful interpretation of magnetic surveys in terms of geology. In some cases, observed differences in magnetic anomaly patterns within single mapped units have indicated hitherto unsuspected heterogeneity, which has then been confirmed by remapping.

Bimodal susceptibility distributions reflect ferromagnetic and paramagnetic populations

The variation in magnetic properties for a given lithology is generally greater between geological provinces than within them, although large variations are also possible over smaller areas, even down to the outcrop scale. A notable feature of Figure 8 is that the susceptibilities of a number of rock types have distinctly bimodal distributions. More generally, bimodal susceptibility distribution represents distinct subpopulations within each rock type, for which ferromagnetic minerals are absent and present, respectively. Iron in the weakly magnetic subpopulation is incorporated into paramagnetic silicate minerals, predominantly as Fe^{2+}, whereas similar rocks that are moderately to strongly magnetic contain significant Fe^{3+}, which is incorporated into magnetite. Very highly oxidised rocks, however, tend to contain haematite rather than magnetite and are, therefore, also weakly magnetic. Puranen (1989) presents results from very large petrophysical sampling programs in Finland. His data show that all broad field names, such as 'granite', 'gabbro', 'mica schist', 'amphibolite' etc., exhibit distinctly bimodal susceptibility distributions.

Within each magnetic subpopulation, susceptibility tends to increase with basicity. The greater abundance of paramagnetic mafic minerals in rocks with lower SiO_2 increases the paramagnetic contribution to the susceptibility. This produces a small, but systematic difference, in the susceptibility of paramagnetic acid and basic rocks. The increasing sensitivity of modern magnetometers and the trend to more detailed magnetic surveys suggests that magnetic mapping may become useful even in very weakly magnetic terrains, where the rocks would hitherto have been classified as 'non-magnetic' on the basis of their apparent flat and featureless magnetic patterns in low-resolution surveys. More commonly, however, the observed magnetic signatures reflect variation in the abundance of ferromagnetic minerals.

When varietal mineralogy is incorporated into the rock classification, the bimodal susceptibility distribution tends to resolve into a paramagnetic subpopulation associated with particular varietal minerals and a ferromagnetic subpopulation associated with a distinct mineralogy. Bimodality often also reflects the fact that important geological factors, such as geochemical affinity, alteration and metamorphic grade, are not considered in the simple classification schemes used for most petrophysical summaries. A truly meaningful magnetic petrological classification scheme must include chemical and/or mineralogical data for protoliths, plus information on metamorphic grade and/or alteration.

Magnetic properties of igneous rocks

In the case of granitoids, bimodal susceptibility reflects the existence of two distinct categories, the magnetite-series and ilmenite-series granitoids of Ishihara (1977). Magnetite-series granitoids are relatively oxidised and correspond broadly to the I-type granitoids of Chappell & White (1974), whereas ilmenite-series granitoids are more reduced and are usually S-type. The new classifications, which have important petro-

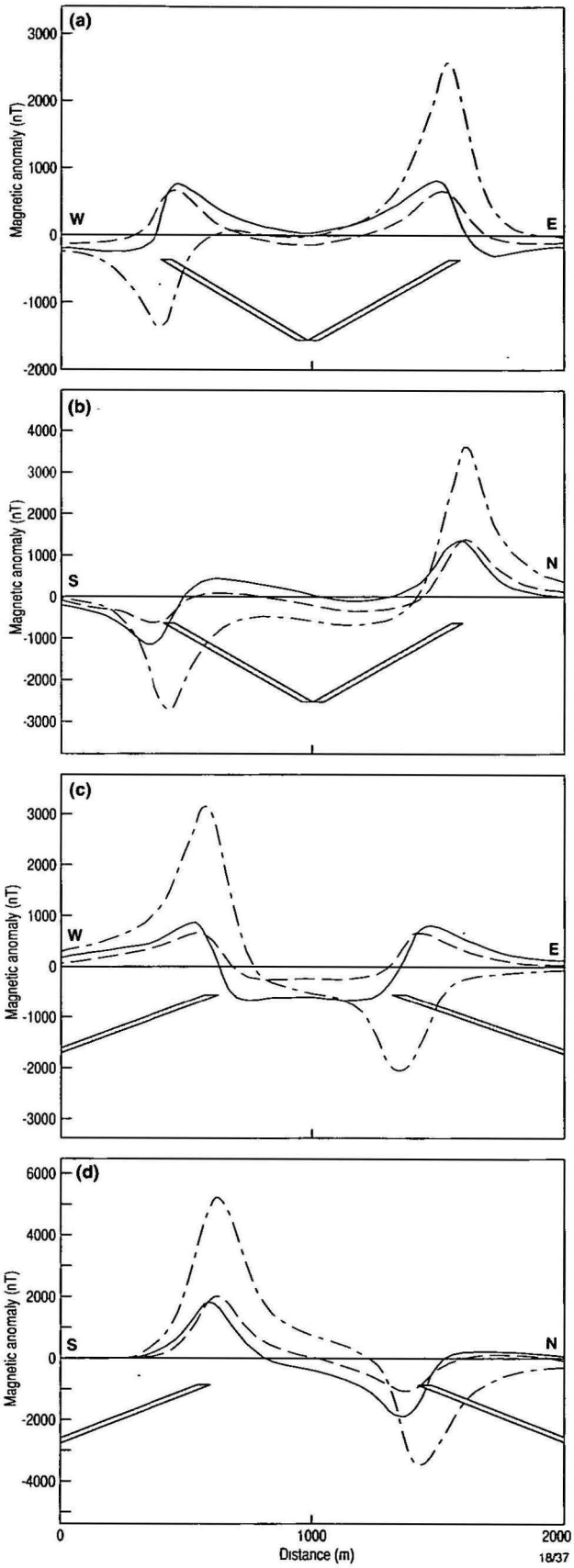

Figure 11. Magnetic anomalies of folded BIF units, showing the effects of anisotropy and pre-folding remanence on the total field anomalies. (a) E–W profiles over a N–S striking syncline, (b) N–S profiles over an E–W striking syncline, (c) E–W profiles over a N–S striking eroded anticline, (d) N–S profiles over an E–W striking eroded anticline. The regional geomagnetic field intensity is 54 000 nT, the field declination is 0° and the field inclination is –56°. Solid curves represent pure induced magnetisation with isotropic susceptibility (k = 0.754 SI = 0.06 G/Oe), dashed curves represent induced magnetisation with anisotropy (susceptibility parallel to bedding 0.942 SI = 0.075 G/Oe, A = 2.5), and dash–dot curves incorporate anisotropy and pre-folding remanent magnetisation (declination normal to strike, original inclination –10°, intensity 48.6 A/m = 0.0486 G). Because of the anisotropy, the Koenigsberger ratio depends on the field direction and bedding attitude, but it is about 1.5. After Clark & Schmidt (1994).

genetic and metallogenic implications, have led to the concept of mapping granitoid terrains using a hand-held susceptibility meter or a magnetometer, and provide a good example of the utility of categories based on magnetics.

Although broad rock names such as 'granodiorite' show only a weak correlation with magnetic properties, more detailed classifications that include varietal minerals are much more predictive. For example, hornblende–biotite granodiorites are predominantly ferromagnetic, with moderate susceptibility, whereas muscovite–biotite granodiorites are usually paramagnetic. Accessory minerals that occur commonly in ferromagnetic felsic granitoids include sphene, epidote, allanite, pyrite and haemoilmenite or Mn-rich ilmenite. The biotite is Fe^{3+} and Mg-rich and is generally brown, black or olive green.

Accessory minerals often associated with paramagnetic granitoids include cordierite, garnet or aluminosilicate (which are characteristic of S-type granites), reduced (low Fe^{3+}) ilmenite, pyrrhotite, and biotite that is Fe^{2+} and Al-rich, often with a 'foxy red' colour. Hornblende-bearing granitoid that is too reduced to contain magnetite is less common overall and tends to occur within specific provinces or 'basement terranes', for which the source material at depth is relatively reduced (Chappell et al. 1988). Susceptibility of felsic granitoid also correlates with feldspar colour (Blevin 1994). For granites with white plagioclase, relatively oxidised ferromagnetic granite generally has salmon pink K-feldspar, whereas reduced paramagnetic granite has white K-feldspar. There is a systematic increase in susceptibility with increasing pinkness of the K-feldspar. On the other hand, brick-red K-feldspar usually indicates hydrothermal alteration and is associated with low susceptibility. This simple relationship is disturbed if green plagioclase is present. The green colour reflects replacement of plagioclase by chlorite, sericite, albite, epidote and calcite. This alteration also tends to destroy magnetite. Granites with green plagioclase and pink K-feldspars exhibit variable susceptibility, reflecting destruction of some or all of the magnetite originally present in the granite.

There is a clear association between granite metallogeny and oxidation state, which translates into a correlation between magnetic susceptibility of granitoids and their associated mineralisation (Ishihara 1981; Blevin & Chappell 1992). In order of reducing susceptibility, Cu and Au are associated with magnetite-series, intermediate I-type granitoid suites; Mo, with more fractionated and oxidised magnetite-series I-type suites; and Sn, with paramagnetic, reduced, fractionated I- or S-type suites.

The overall tendency for magnetite content of ferromagnetic rocks to increase with basicity is somewhat obscured when igneous rocks from different provinces are compared. For consanguinous rocks, in particular, there is a general correlation between susceptibility and basicity. Andesites generally have similar, or slightly lower, susceptibility than related basalts. Rhyolites have a distinctly bimodal susceptibility distribution. Ferromagnetic rhyolites tend to be somewhat less magnetic than the more basic members of the series, and many rhyolites are paramagnetic (e.g. fayalite rhyolites, strongly peraluminous and strongly peralkaline rhyolites). Trachyandesites and trachytes generally have moderate to high susceptibility, comparable to or somewhat less than that of related alkali basalts, but corresponding phonolites are usually weakly magnetic. Within the ferromagnetic subpopulation of each

lithology, magnetic properties can also be related to geochemistry. For tholeiitic rocks in both oceanic and continental settings, iron and titanium-rich variants that are interpreted as related to hotspots have been found to have substantially higher susceptibility, reflecting greater modal titanomagnetite, than similar rocks with lower Fe and Ti contents (e.g. Anderson et al. 1975; de Boer & Snider 1979).

Granitic rocks and metamorphic rocks with secondary magnetite usually contain relatively coarse-grained multidomain magnetite, accounting for the generally low Q values of these rocks. On the other hand, young, rapidly chilled basaltic rocks (e.g. pillow lavas) exhibit very high Koenigsberger ratios, owing to the fine grain size of the titanomagnetites. In basaltic rocks the Q value of the primary thermoremanence is essentially a function of cooling rate, being highest for subaqueous chilled margins and small pillows and decreasing with distance from the margin. However, even thick doleritic sills and dykes are characterised by relatively high Q values, typically 1–10, provided the primary remanence has not been substantially modified by thermal or chemical overprints.

Plutonic rocks generally have low Koenigsberger ratios, owing to their coarse grain size, with the notable exception of some gabbroic to dioritic intrusives, for which the remanence is dominated by SD and PSD grains of magnetite (sensu lato). These efficient remanence carriers may be either fine (titano)magnetite inclusions in silicate grains or large, originally homogeneous, titaniferous magnetite grains that have undergone deuteric oxidation, which produces abundant oxyexsolution lamellae of ilmenite within relatively low-Ti magnetite. This subdivision of the magnetite grains by non-magnetic lamellae produces an effective grain size in the PSD range.

Ultramafic rocks (pyroxenites, hornblendites, serpentinised dunites etc.) in zoned Alaskan-type complexes are generally highly magnetic. The associated mafic and intermediate rocks (gabbro, diorite, monzonite) in these intrusions are also moderately to highly magnetic. Primary magnetite is the main magnetic mineral in these intrusive complexes. On the other hand, the primary spinel phase in unaltered komatiitic lavas (including spinifex textured peridotite, olivine orthocumulate and adcumulate (dunite) zones) and alpine-type peridotites is paramagnetic chromite and they are, therefore, weakly magnetic. However, komatiites are usually serpentinised, as are alpine-type peridotites. Serpentinisation usually creates substantial quantities of magnetite, accounting for the high susceptibility of serpentinised ultramafic rocks. This magnetite is generally multidomain, well-crystallised, almost pure Fe_3O_4, which is magnetically soft and carries relatively weak remanence ($Q < 1$). The NRM of serpentinites is often dominated by viscous remanence, subparallel to the present field. Large dunite bodies sometimes have a weakly magnetic, unserpentinised core within an envelope of highly magnetic serpentinite.

Magnetic properties of sedimentary rocks

'Clean' carbonates and clastic sediments have very low susceptibility. Some immature sandstones are magnetic because they contain significant quantities of detrital magnetite. Sediments deposited in the presence of metal-bearing solutions, associated with volcanic activity for example, may contain appreciable magnetite or, possibly, pyrrhotite and, therefore, be magnetic. Such sediments may be transitional to syngenetic massive mineralisation or to banded iron formation. Magnetite-rich banded iron formations are not only strongly magnetic, but characterised by high anisotropy of susceptibility. The susceptibility values for banded iron formation shown in Figure 8 are bulk susceptibilities, i.e. the average susceptibility along any three orthogonal directions.

Traditionally, aeromagnetic surveys over sedimentary basins were used primarily to determine depth to basement. In recent times it has become evident that modern high-resolution aeromagnetic surveys over sedimentary basins also provide considerable information about sedimentary lithology and structure. Little is known about the intrasedimentary sources responsible for the observed anomaly patterns. There is an urgent need for research into the magnetic petrophysics and petrology of intrasedimentary sources, directed at improving understanding of the geological significance of magnetic anomaly patterns. Gay (1992) has given examples of intrasedimentary anomalies associated with distributions of detrital magnetite. Reynolds et al. (1990a,b; 1994) have demonstrated that diagenetic monoclinic pyrrhotite and greigite are possible sources of low-amplitude, high-frequency anomalies, which in some cases may be associated with hydrocarbon seepage, over some sedimentary basins. There is, as yet, no definitive evidence of diagenetic magnetite produced by hydrocarbon seepage in quantities sufficient to produce observable anomalies (Reynolds et al. 1990b), but Machel & Burton (1991) have described chemical and microbial processes that could, in principle, produce authigenic magnetite and pyrrhotite, at the expense mainly of haematite, in the presence of hydrocarbons.

Effects of hydrothermal alteration

Studemeister (1983) pointed out that the redox state of iron in rocks is a useful indicator of hydrothermal alteration. Large volumes of fluid or high concentrations of exotic reactants, such as hydrogen or oxygen, are required to shift Fe^{3+}/Fe^{2+}. When reactions associated with large water/rock ratios occur, the change in redox state of the rocks produces large changes in magnetic properties, owing to the creation or destruction of ferromagnetic minerals.

Zeolite-grade hydrothermal alteration of mafic to silicic igneous rocks tends to decrease the susceptibility of these rocks according to the degree of development of zeolites (Emerson & Welsh 1987). Zeolite-rich rocks are generally paramagnetic, even when derived from strongly magnetic protoliths. Regional hydrothermal alteration of volcanic piles produces progressive demagnetisation from zeolite grade to greenschist grade. For example, primary titanomagnetite and ilmeno-magnetite in basalt progressively develops ferrirutile granules at ~150°C, with sphene replacing ilmenite lamellae by ~250°C, and polycrystalline titanohaematite replacing titanomagnetite above 300°C (Ade-Hall et al. 1971). However, contact metamorphism of hydrothermally altered, demagnetised igneous rocks, for instance by dyke injection, may produce secondary magnetite (Hall & Fisher 1987).

The available evidence suggests that both major types of alteration associated with epithermal systems, acid–sulphate and adularia–sericite alteration, tend to demagnetise volcanic rocks through replacement of magnetite by paramagnetic phases. Similarly, phyllic alteration and intense propylitic alteration associated with porphyry intrusions tend to destroy magnetite in the intrusion and in surrounding rocks. On the other hand, the potassic alteration zone associated with oxidised, magnetic felsic intrusions is often magnetite-rich. This is commonly observed for Au-rich porphyry copper systems (Sillitoe 1979). Early potassic (biotite-rich) alteration around the gold-mineralised Mount Leyshon complex (Queensland), which comprises intrusive breccias, porphyry plugs and dykes, produced abundant magnetite in metasedimentary and doleritic host rocks and is largely responsible for the Mount Leyshon magnetic anomaly (Sexton et al. 1995).

Serpentinisation of olivine-rich ultramafic rocks tends to produce abundant magnetite. At low grades, initial serpentinisation of olivine produces Fe-lizardite plus brucite. With further serpentinisation, the maximum iron content of lizardite is exceeded and magnetite is produced, along with lizardite, chrysotile and brucite. At higher grades, antigorite and magnetite are produced. For serpentinites, there is generally

an inverse relationship between density, which decreases with progressive serpentinisation, and susceptibility. Saad (1969) found that weakly serpentinised peridotites (~10%) are weakly magnetic (k ~100 μG/Oe = 126 × 10^{-5} SI), partially (~75%) serpentinised peridotites are moderately ferromagnetic (k ~500 μG/Oe = 6300 × 10^{-6} SI) and fully serpentinised peridotites are substantially more magnetic (k ~5000 μG/Oe = 63 000 × 10^{-6} SI).

Carbonate alteration of serpentinised ultramafics initially redistributes magnetite, without destroying it, and has little effect on susceptibility. Intense talc–carbonate alteration, however, consumes the magnetite, with iron entering magnesite as a siderite component, and demagnetises the rock.

Effects of metamorphism

Metamorphism has profound effects on magnetic properties. It follows that magnetic interpretation should take changes in metamorphic grade across the study area into account. Effects of metamorphism on magnetic properties have been discussed by McIntyre (1980), Grant (1985), Shive et al. (1988), Wasilewski & Warner (1988), Urquhart (1989), Frost (1991a,b), Olesen et al. (1991), Skilbrei et al. (1991) and Clark et al. (1992).

Fresh basalt and dolerite have moderate to high susceptibility. Burial metamorphism of igneous rocks to zeolite or prehnite–pumpellyite grade does not demagnetise them, in the absence of circulating hydrothermal fluids, but regional metamorphism to greenschist and lower to mid-amphibolite grades tends to demagnetise basic igneous rocks. In gabbro, the fine magnetic grains within silicates may be protected by their silicate hosts from metamorphic breakdown, so that gabbro may be somewhat less sensitive to low and medium-grade metamorphism than its extrusive and hypabyssal equivalents.

Where magnetite is an abundant cumulus phase, it appears to be much less prone to metamorphic breakdown than if it is present as a minor intercumulus mineral. Thus highly differentiated ferrogabbro and ferrodiorite, which contain abundant primary magnetite, remain strongly magnetic throughout medium to high-grade metamorphism. This probably reflects the fact that secondary metamorphic minerals become rapidly saturated in Fe^{3+} when magnetite starts to break down, ensuring that the rest of the magnetite remains stable during metamorphism. Felsic plutons seem to be more resistant to metamorphic destruction of magnetite in the greenschist and amphibolite facies than mafic rocks and felsic volcanic rocks.

Amphibolite-grade metamorphism overall produces heterogeneous magnetic properties with bimodal susceptibility, although dominated by weakly magnetic rocks. At this grade, magnetic mafic rocks are more common than magnetic silicic rocks. Chlorite and/or biotite-bearing amphibolite tends to be weakly magnetic, whereas hornblende-rich amphibolite may have much higher susceptibility.

Granulite-facies metamorphism of mafic protoliths frequently produces secondary magnetite and large increases in susceptibility. High-pressure granulite and eclogite are generally paramagnetic. Magnetite breakdown in these high pressure rocks generally occurs at 10–20 kb. The reactions occur at generally lower pressure for undersaturated basaltic rocks than for quartz tholeiite, for lower Mg/Fe ratios and for more reduced rocks.

These changes in properties reflect redistribution of ferric iron in metabasites during metamorphism. Ferric iron originally present in magnetite goes largely into haematite, epidote and chlorite during greenschist-grade metamorphism, then into biotite and amphibole in the amphibolite facies, into metamorphic magnetite in the granulite facies and, finally, into paramagnetic silicates such as garnet and clinopyroxene in the eclogite facies. The magnetite-in isograd reflects P-T-t conditions and appears to occur within lower granulite facies, above the orthopyroxene-in isograd for prograde metamorphism, followed by isobaric cooling (Olesen et al. 1991). For retrograde metamorphism or for isothermal decompression during rapid uplift the magnetite-in isograd lies within the upper amphibolite facies, above the biotite isograd (Skilbrei et al. 1991).

Decompression of high-pressure granulite during rapid uplift can produce fine-grained magnetite by breakdown of garnet and clinopyroxene. This magnetite may carry relatively strong and stable remanence. In general, however, metamorphic magnetite is relatively coarse-grained, well crystallised and fairly pure, i.e. it occurs as magnetically soft MD grains, which are associated with low Q values and unstable, predominantly viscous, remanence.

Prograde metamorphism of serpentinised ultramafics causes increasing substitution of Mg and Al into the magnetite, eventually shifting the composition into the paramagnetic field. Thus, metamorphism progressively demagnetises serpentinite, which becomes paramagnetic at granulite grade (Shive et al. 1988). Subsequent retrograde serpentinisation, if it occurs, can produce a magnetic rock again. Clark et al. (1992) noted a progressive decrease in magnetic anomaly amplitude associated with a major serpentinised ultramafic unit as metamorphic grade increases from prehnite–pumpellyite facies to upper amphibolite facies.

The iron content of sediments (generally higher for pelites than for psammites) and the Fe^{3+}/Fe^{3+} ratio, which reflects the redox conditions during deposition and diagenesis, have a major bearing on the capacity of sedimentary rocks to develop secondary magnetite during metamorphism (McIntyre 1980). Thus, magnetic patterns over metasedimentary rocks tend to reflect sedimentary facies variations, as well as metamorphic conditions. These patterns can be very useful for mapping, although the relationship between the magnetic marker units and conventional lithological units may be quite tenuous (McIntyre 1980).

Magnetite formation is favoured by high total iron and, therefore, tends to be associated with metapelites more frequently than metapsammites. Substantial chemical input by exhalative metal-bearing solutions, including iron, increases the potential for magnetite formation during subsequent metamorphism. Magnetite formation is favoured by intermediate redox state/oxidation ratio. Low oxidation states are associated with ilmenite in metasediments and very high oxidation states, with haematite. Very iron oxide-rich assemblages, for example BIFs, are self-buffered during metamorphism, preserving fine layering with magnetite- and haematite-rich bands.

Organic-rich sediments produce reduced graphitic metasediments, which are magnetite-free, but commonly contain pyrrhotite above greenschist grade. Red (haematite-bearing) sediments produce intermediate redox metasediments, which may be magnetite-bearing. Haematite goes to magnetite in the biotite or lower garnet zones for these rocks. The maximum ferromagnetic proportion in metasediments generally occurs at granulite grade.

Pyrrhotite is the main magnetic mineral in many metasedimentary rocks, particularly in mineralised areas. Clark & Tonkin (1994) discuss magnetic anomalies associated with monoclinic pyrrhotite in metasediments of the Cobar area, Australia. Remanent magnetisation and susceptibility anisotropy are often important in monoclinic pyrrhotite-bearing metasediments (Clark 1983b).

Conclusions

The aim of magnetic interpretation is to elicit *geological* information from magnetic survey data. There is a continuing need for magnetic petrophysical studies to constrain interpretation of magnetic surveys and for fundamental research in

magnetic petrology to improve understanding of the geological factors that create, alter and destroy magnetic minerals in rocks. A large-scale, systematic effort is required to create physical property databases, including comprehensive magnetic property data, classified according to magnetic petrological principles and integrated with geological and geochemical databases. New developments in 3D modelling, including inversion, and visualisation will assist efficient interpretation of large magnetic data sets. However, meaningful geological interpretation using these tools should allow incorporation of petrophysical information and magnetic petrological concepts. This paper notes some of the important ideas upon which such a research effort should be based.

References

Ade-Hall, J.M., Palmer, H.C. & Hubbard, T.P., 1971. The magnetic and opaque petrological response to regional hydrothermal alteration. Geophysical Journal of the Royal Astronomical Society, 24, 137–174.

Anderson, R.N., Clague, D.A., Klitgord, K.D., Marshall, M. & Hishimori, R.K., 1975. Magnetic and petrologic variations along the Galapagos Spreading Center and their relation to the Galapagos Melting Anomaly. Geological Society of America Bulletin, 86, 683–694.

Banerjee, S.K., 1991. Magnetic properties of Fe–Ti oxides. In: Lindsley, D.H. (editor), Oxide minerals: petrologic and magnetic significance. Reviews in Mineralogy, 25, 489–509.

Bleil, U. & Petersen, N., 1982. Magnetic properties of natural minerals. In: Angenheister, G. (editor), Physical properties of rocks. Landolt-Bornstein numerical data and functional relationships in science and technology, Group V: Geophysics and Space Research, Volume 1b, 305–365. Springer-Verlag, Berlin.

Blevin, P.L., 1994. Magnetic susceptibility of the Lachlan Fold Belt and New England Batholith granites. Australian Mineral Indutries Research Association, Project P147B, Final Report.

Blevin, P.L. & Chappell, B.W., 1992. The role of magma sources, oxidation states and fractionation in determining the granite metallogeny of eastern Australia. Transactions of the Royal Society of Edinburgh, Earth Sciences, 83, 305–316.

Buselli, G., 1982. The effect of near-surface superparamagnetic material on electromagnetic measurements. Geophysics, 47, 1315–1324.

Butler, R.F., 1992. Paleomagnetism: magnetic domains to geologic terranes. Blackwell, Boston.

Chappell, B.W. & White, A.J.R., 1974. Two contrasting granite types. Pacific Geology, 8, 173–174.

Chappell, B.W., White, A.J.R. & Hine, R., 1988. Granite provinces and basement terranes in the Lachlan Fold Belt, southeastern Australia. Australian Journal of Earth Sciences, 35, 505–521.

Clark, D.A., 1983a. Comments on magnetic petrophysics. Bulletin of the Australian Society of Exploration Geophysicists, 14, 40–62.

Clark, D.A., 1983b. Magnetic properties of pyrrhotite—applications to geology and geophysics. M.Sc. Thesis, University of Sydney, 256 pp.

Clark, D.A., 1984. Hysteresis properties of sized dispersed monoclinic pyrrhotite grains. Geophysical Research Letters, 11, 173–176.

Clark, D.A. & Emerson, D.W., 1991. Notes on rock magnetization characteristics in applied geophysical studies. Exploration Geophysics, 22, 547–555.

Clark, D.A. & Schmidt, P.W., 1994. Magnetic properties and magnetic signatures of BIFs of the Hamersley Basin and Yilgarn Block, Western Australia. In: Dentith, M.E., Frankombe, K.F., Ho, S.E., Shepherd, J.M., Groves, D.I. & Trench, A. (editors), Geophysical signatures of Western Australian mineral deposits. Geology and Geophysics Department (Key Centre) & UWA Extension, The University of Western Australia, Publication No. 26, 343–354.

Clark, D.A. & Tonkin, C., 1994. Magnetic anomalies due to pyrrhotite: examples from the Cobar area, N.S.W., Australia. Journal of Applied Geophysics, 32, 11–32.

Clark, D.A., French, D.H., Lackie, M.A. & Schmidt, P.W., 1992. Magnetic petrology: application of integrated rock magnetic and petrological techniques to geological interpretation of magnetic surveys. Exploration Geophysics, 23, 65–68.

Collinson, D.W., 1983. Methods in rock magnetism and palaeomagnetism. Chapman and Hall, London.

De Boer, J. & Snider, F.G., 1979. Magnetic and chemical variations of Mesozoic diabase dikes from eastern North America: evidence for a hotspot in the Carolinas? Geological Society of America Bulletin, 90, 185–198.

Dekkers, M.J., 1988. Magnetic properties of natural pyrrhotite. Part I: Behaviour of initial susceptibility and saturation- magnetization-related rock-magnetic parameters in a grain-size dependent framework. Physics of the Earth and Planetary Interiors, 52, 376–393.

Dekkers, M.J., 1989. Magnetic properties of natural pyrrhotite. II: High- and low-temperature behaviour of J_{rs} and TRM as a function of grain size. Physics of the Earth and Planetary Interiors, 57, 266–283.

Emerson, D.W. & Welsh, H.K., 1987. Some physical property characteristics of zeolitic rock—preliminary results. Exploration Geophysics, 18, 393–400.

Frantsesson, E.V., 1970. The petrology of the kimberlites (translated from the Russian by D.A. Brown). Australian National University, Department of Geology, Publication No. 150.

Frost, B.R., 1991a. Stability of oxide minerals in metamorphic rocks. In: Lindsley, D.H. (editor), Oxide minerals: petrologic and magnetic significance, Reviews in Mineralogy, 25, 469–487.

Frost, B.R., 1991b. Magnetic petrology: factors that control the occurrence of magnetite in crustal rocks. In: Lindsley, D.H. (editor), Oxide minerals: petrologic and magnetic significance, Reviews in Mineralogy, 25, 489–509.

Garanin, V.K., Kudryavtseya, G.P. & Lapin, A.V., 1978. Typical features of ilmenite from kimberlites, alkali-ultrabasic rocks and carbonatites. International Geology Review, 22, 1025–1050.

Gay, S.P., 1992. Epigenetic versus syngenetic magnetite as a cause of magnetic anomalies. Geophysics, 57, 60–68.

Grant. F.S., 1985. Aeromagnetics, geology and ore environments, I. Magnetite in igneous, sedimentary and metamorphic rocks: an overview. Geoexploration, 23, 303–333.

Hall, J.M. & Fisher, B.E., 1987. The characteristics and significance of secondary magnetite in a profile through the dike component of the Troodos, Cyprus, ophiolite. Canadian Journal of Earth Sciences, 24, 2141–2159.

Hoffman, V., 1992. Greigite (Fe_3S_4): magnetic properties and first domain observations. Physics of the Earth and Planetary Interiors, 70, 288–301.

Hoffman, V., Stanjek, H. & Murad, E., 1993?. Mineralogical, magnetic and Mossbauer data of smythite (Fe_9S_{11}).

Ishihara, S., 1977. The magnetite-series and ilmenite-series granitic rocks. Mining Geology, 27, 293–305.

Ishihara, S., 1981. The granitoid series and mineralization. Economic Geology, 75th Anniversary Volume, 458–484.

Kropacek, V., 1971. Distribution of the values of natural

remanent magnetization and magnetic susceptibility of some minerals. Studia Geophysica Geodaetica, 15, 340–352.

Kropacek, V. & Krs, M., 1971. Magnetism of natural pyrrhotite, haematite and ilmenite. Studia Geophysica et Geodaetica, 15, 161–172.

Krs, M., Krsova, M., Pruner, P., Zeman, A. & Jansa, J., 1990. A petromagnetic study of Miocene rocks bearing micro-organic material and the magnetic mineral greigite (Sokolov and Cheb basins, Czechoslovakia). Physics of the Earth and Planetary Interiors, 63, 98–112.

Krs, M., Novak, F., Krsova, M., Pruner, P., Kouklikova, L. & Jansa, J., 1992. Magnetic properties and metastability of greigite–smythite mineralization in brown-coal basins of the Krusne hory Piedmont, Bohemia. Physics of the Earth and Planetary Interiors, 70, 273–287.

Krs, M., Novak, F., Krsova, M., Pruner, P. & Jansa, J., 1993. Magnetic properties, selfreversal remanence and thermal alteration products of smythite.

Lowrie, W., 1990. Identification of ferromagnetic minerals in a rock by coercivity and unblocking temperature analyses. Geophysical Research Letters, 17, 159–162.

Machel, H.G. & Burton, E.A., 1991. Chemical and microbial processes causing anomalous magnetization in environments affected by hydrocarbon seepage. Geophysics, 56, 598–605.

McIntyre, J.I., 1980. Geological significance of magnetic patterns related to magnetite in sediments and metasediments—a review. Bulletin of the Australian Society of Exploration Geophysicists, 11, 19–33.

Nye, 1957. Physical properties of crystals. Oxford University Press, London.

Olesen, O., Henkel, H., Kaada, K. & Tveten, E., 1991. Petrophysical properties of a prograde amphibolite-granulite facies transition zone at Sigerfjord, Vesteralen, northern Norway. Tectonophysics, 192, 33–39.

O'Reilly, W., 1984. Rock and mineral magnetism. Blackie, Glasgow.

Parry, L.G., 1980. Shape related factors in the magnetization of immobilised magnetite particles. Physics of the Earth and Planetary Interiors, 22, 144–154.

Power, L.F. & Fine, H.A., 1976. The iron–sulphur system. Part I. The structure and physical properties of the compounds of the low-temperature phase fields. Minerals Science Engineering, 8, 106–128.

Puranen, R., 1989. Susceptibilities, iron and magnetite content of Precambrian rocks in Finland. Geological Survey of Finland, Report of Investigation 90.

Reynolds, R.L., Fishman, N.S., Wanty, R.B. & Goldhaber, M.B., 1990a. Iron sulfide minerals at Cement oil field, Oklahoma: implications for magnetic detection of oil fields. Geological Society of America, Bulletin, 102, 368–380.

Reynolds, R.L., Fishman, N.S. & Hudson, M.R., 1990b. Sources of aeromagnetic anomalies over Cement oil field (Oklahoma), Simpson oil field (Alaska), and the Wyoming–Idaho–Utah thrust belt. Geophysics, 56, 606–617.

Reynolds, R.L., Tuttle, M.L., Rice, C.A., Fishman; N.S., Karachewski, J.A. & Sherman, D.M., 1994. Magnetization and geochemistry of greigite-bearing Cretaceous strata, North Slope Basin, Alaska. American Journal of Science, 294, 485–528.

Ribbe, P.H. (editor), 1974. Sulfide mineralogy. Mineralogical Society of America, Short Course Notes, 1.

Roberts, A.P. & Turner, G.M., 1993. Diagenetic formation of ferrimagnetic iron sulphide minerals in rapidly deposited marine sediments, South Island, New Zealand. Earth and Planetary Science Letters, 115, 257–273.

Saad, A.H., 1969. Magnetic properties of ultramafic rocks from Red Mountain, California. Geophysics, 34, 974–987.

Schmidt, 1993. Palaeomagnetic cleaning strategies Physics of the Earth and Planetary Interiors, 76, 169–178.

Schwarz, E.J., 1974. Magnetic properties of pyrrhotite and their use in applied geology and geophysics. Geological Survey of Canada, Paper 74–59.

Schwarz, E.J. & Vaughn, D.J., 1972. Magnetic phase relations of pyrrhotite. Journal of Geomagnetism and Geoelectricity, 24, 441–458.

Sexton, M.A., Morrison, G.W., Orr, T.O.H., Foley, A.M. & Wormald, P.J., 1995. The Mt Leyshon magnetic anomaly. Exploration Geophysics, 26, 84–91.

Shive, P.N., Frost, B.R. & Peretti, A., 1988. The magnetic properties of metaperidotitic rocks as a function of metamorphic grade: implications for crustal magnetic anomalies. Journal of Geophysical Research, 93, 12,187–12,195.

Sillitoe, R.H., 1979. Some thoughts on gold-rich porphyry copper deposits. Mineralium Deposita, 14, 161–1744.

Skilbrei, J., Skyseth, T. & Olesen, O., 1991. Petrophysical data and opaque mineralogy of high grade and retrogressed lithologies: implications for interpretation of aeromagnetic anomalies in northern Vestraden, central Norway. Tectonophysics, 192, 21–31.

Snowball, I.F., 1991. Magnetic hysteresis properties of greigite (Fe_3S_4) and a new occurrence in Holocene sediments from Swedish Lappland. Physics of the Earth and Planetary Interiors, 68, 32–40.

Stacey, F.D. & Banerjee, S.K., 1974. The physical principles of rock magnetism. Elsevier, Amsterdam.

Studemeister, P.A., 1983. The redox state of iron: a powerful indicator of hydrothermal alteration. Geoscience Canada, 10, 189–194.

Tarling, D.H. & Hrouda, F., 1993. The magnetic anisotropy of rocks. Chapman and Hall, London.

Thompson, R. & Oldfield, F., 1986. Environmental magnetism. Allen and Unwin, London.

Thomson, G.F., Cornwell, J.D. & Collinson, D.W., 1991. Magnetic characteristics of some pyrrhotite-bearing rocks in the United Kingdom. Geoexploration, 28, 23–42.

Urquhart, W.E.S., 1989. Field examples of controls on magnetite content. Exploration Geophysics, 20, 93–97.

Vaughn, D.J. & Craig, J.R., 1978. Mineral chemistry of metal sulfides. Cambridge University Press.

Vaughn, D.J. & Lennie, A.R., 1991. The iron sulphide minerals: their chemistry and role in nature. Science Progress, 75, 371–388.

Ward, J.C., 1970. The structure and properties of some iron sulphides. Reviews of Pure and Applied Chemistry, 20, 175–206.

Wasilewski, P. & Warner, R.D., 1988. Magnetic petrology of deep crustal rocks—Ivrea Zone, Italy. Earth and Planetary Science Letters, 87, 347–361.

Worm, H.-U., 1991. Multidomain susceptibility and anomalously strong low field dependence of induced magnetization in pyrrhotite. Physics of the Earth and Planetary Interiors, 69, 112–118.

Worm, H.-U., Clark, D. & Dekkers, M.J., 1993. Magnetic susceptibility of pyrrhotite: grain size, field and frequency dependence. Geophysical Journal International, 114, 127–137.

Yakubovskaya, N.Y. & Ilyupin, I.P., 1982. Magnetic properties of picroilmenites from Siberian kimberlites (in Russian). Mineralogicheskiy Zhurnal, 4, 36–43.

AGSO Journal of Australian Geology & Geophysics, 17(2), 105–113

Quantitative methods for interpreting aeromagnetic data: a subjective review

P.J. Gunn[1]

Although rapid and relatively accurate graphical techniques exist for interpreting the depth to magnetic sources, these have now been largely supplanted by a wide range of computerised forward modelling routines capable of giving detailed estimates of source geometry as well as the source depth. Computer routines which have automated the depth estimation process also exist; however, these require considerable judgement on the part of the user, as they can give misleading results.

Introduction

The detail in total magnetic data, supplemented by the range of enhanced map and image products typically produced to display these data, normally provides an excellent basis for qualitative interpretations in which geological boundaries and lithologies are visually estimated. Interpretations of this type, which, in effect, produce outcrop or subcrop maps, are routine for areas where all magnetic units occur at or near the ground surface and when anomalies are relatively discrete. Where magnetic rocks occur at variable depth or beneath substantial non-magnetic cover, and where it is essential to know the depth to the magnetic sources, quantitative depth determinations are required. In some cases, specific details of geometry and magnetic properties of the magnetic sources are required and complete quantitative interpretation of magnetic anomalies must be undertaken. This paper reviews methods for determining depth and for performing quantitative interpretation of anomalies. Drawing on the author's experience, the discussion is restricted to those methods which, in the author's opinion, have proved themselves through usage and still have the potential to be widely applied.

Graphical depth determination

Applications of aeromagnetics to the detection and mapping of sediment thickness in sedimentary basins in pre-computer times were based on a range of graphical techniques which rely on the fact that deeper magnetic sources have broader anomalies than shallower sources. Various parameters defining this 'broadness' were measured and related to depth through simple empirical relationships or by the use of graphs.

These methods, and indeed virtually all quantitative interpretation methods, are based on the concept that magnetic sources can, in the majority of cases, be approximated by simple geometric sources. Some authors produced comprehensive atlases of model curves with which to match observed anomalies and thereby arrive at solutions of depth, width, attitude and magnetisation. The Parker Gay (1963) curves for the dipping dyke model, applicable to magnetic bodies with elongated plate-like geometry such as dykes, lava flows, magnetic sediments, basement uplifts and certain ore bodies, are a well-known example of such curves. Manual matching of anomalies to type curves is time consuming and is restricted to the anomaly types for which curves exist. Manual depth determination projects involving many anomalies are much simpler when based on more general models and less elaborate matching procedures. Some of the graphical methods that have been widely used are:

- ***The magnetic pole model*** incorporating point poles, single dipoles, and lines of magnetic dipole poles approximating, respectively, isolated magnetic sources with bottoms at much greater depth than their tops, the general case of isolated magnetic sources, and thin linear sheets of magnetic material. Smellie (1956) showed how to relate the width of such anomalies to the depth of their source (Fig. 1). The problem with such an approach is that wide sources cannot be approximated by the pole model and computed depths will be below the top of the magnetic source because the pole will appear inside the magnetic source.

- ***The prism and horizontal plate model*** developed by Vacquier et al. (1951). This proved much more useful than the pole model, as the prisms approximate a range of intrusive bodies of different width and the plates approximate intrusive sheets, lava flows, and basement uplifts. Vacquier et al. illustrated a series of model anomalies that facilitated an initial visual recognition of likely sources. They also produced simple empirical constants that vary with magnetic inclination, body width and strike and relate the depth of magnetic sources to the 'straight-slope'. This is the distance of the horizontal projection of the apparent straight portion of the steep side of the anomaly (Fig. 1). Despite being based on a visual artefact, the method proved very robust and produced realistic results with the initial delineation of the Gippsland, Bass, Torquay and Otway Basins being a classic example (Haematite Exploration 1965). Case history data suggest that the depth determinations are accurate to ± 15 per cent The weakness of the method is that it is not designed to interpret dipping magnetic bodies.

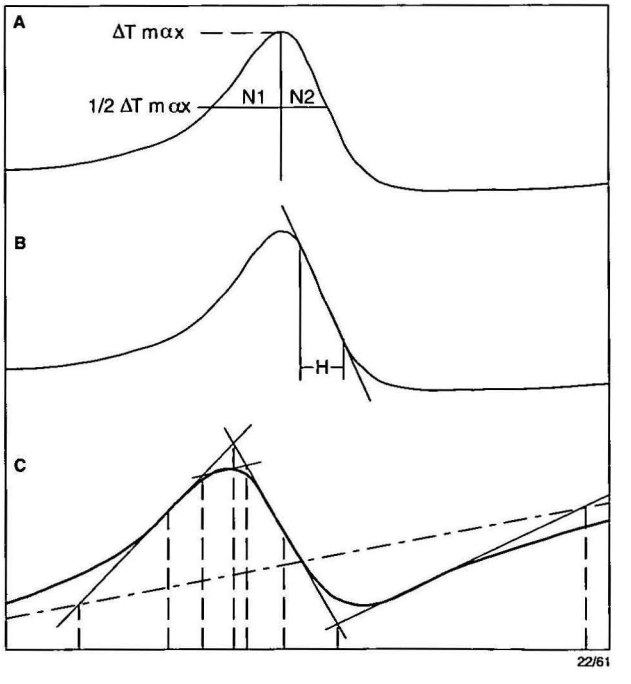

Figure 1. Illustration of parameters measured by graphical depth-determination methods. Depths were determined by relating the parameters to various sets of type curves. (A) the Smellie parameters (1956). (B) The Vacquier et al. (1951) 'straight-slope' parameter. (C) The Naudy (1970) 'ITI' parameters. The horizontal distances between the intersections of the tangents are the critical parameters.

[1] Australian Geological Survey Organisation, GPO Box 378, Canberra, ACT 2601

• ***The ITI (inflection tangents intersection) method*** of Naudy (1970) appears to be the most robust and realistic of all the graphical methods. This method is based on drawing a series of tangents at various inflection points on magnetic anomaly profiles, measuring the horizontal distances between their intersections (Fig. 1), and comparing these to intersections on type curves. As the horizontal distances define the shape of the anomaly, the method is a form of curve matching. Curves exist for vertical gradient and total magnetic intensity profiles and the models that can be interpreted include dipping magnetic sheets (the dipping dyke model), horizontal magnetic sheets, faults and contacts, and prismatic bodies with vertical sides. The method can give the dip of dyke-like bodies if a direction of magnetisation is known. A similar curve-fitting principle is used to estimate magnetisation of the source. The method is independent of linear regionals and the use of logarithmic type curves makes the technique independent of anomaly amplitudes. The method is not widely known because Naudy's original publication was in French and the use of the method was largely restricted to affiliates of Naudy's employer (Compagnie Generale de Geophysique).

The author has been involved with several interpretation projects based on the ITI method, the standard application of which is based on profile plots of total field and computed vertical gradient on 75 cm wide paper rolls. This enables large-scale representation and accurate interpretation of anomalies with amplitudes of the order of one nanotesla. Simultaneous plotting at smaller scales enables the interpretation of any high-amplitude anomalies. All anomalies in a survey area are interpreted on profile data. Subsequent inspection of anomaly trends allows corrections to be made for strike direction relative to the profile and for finite lengths of anomalies. The fact that depth estimates are produced for virtually all anomalies visible on the profile enables detailed contouring of the estimated depths to the magnetic sources. Case study data suggest that the results are accurate to ± 10 per cent. Reford & Butt (1983) reported on the successful ITI interpretation of results from a survey in the Timor Sea–Joseph Bonaparte Gulf area in 1965.

These graphical methods appear to have fallen into disuse, owing to a combination of the unwillingness of interpreters to spend time on them and the tendency to use the variety of automatic interpretation methods described below. It is not certain, however, that many, if any, of the recent interpretations of depths to magnetic sources have been made with the accuracy or detail possible with these graphical methods.

Modelling

The initial *raison d'etre* for graphical depth determination methods was the simple fact that exact modelling of anomalies in pre-computer days required time consuming and tedious manual computation of anomaly forms, using formulae or graticules. With the advent of computers and publication of a series of routines to allow modelling by trial and error, curve-matching processes have become routine. Probably the most significant of the computer modelling algorithms are:

• ***Computation of the magnetic field of a two-dimensional (infinite strike) body with an arbitrary polygonal shape*** (Talwani & Heirtzler 1964). This method calculates the effect of the polygon by summing the magnetic effect of a series of horizontal sheets with sloping edges that correspond to the sides of the polygon. Modelling with the routine is commonly referred to as 2D modelling. Won & Bevis (1987) have produced a faster version of this routine that can handle situations where the magnetic body can be partly above the point of observation and where the observation point can be inside the magnetic body.

• ***Computation of the magnetic effect of arbitrarily shaped three-dimensional bodies by approximating them to horizontal polygonal laminae*** (Talwani 1965). Good results can be produced with this routine (e.g. Gunn 1979), but the process of modifying the corners of the horizontal laminae to match a grid of observations, using a forward modelling process, can be very time consuming.

• ***Magnetic anomaly due to a dipping prism*** (Hjelt 1972). This routine calculates the magnetic effect of prismatic bodies with parallel sides for cases where the top and bottom of the body are horizontal.

• ***Magnetic effect of a body with polygonal cross-section and limited strike length*** (Shuey & Pasquale 1973; Cady 1980). This routine has a significant advantage over the Talwani & Heirtzler (1964) routine in that it enables cross-sections of bodies with finite strike lengths to be modelled with a single profile. The routine assumes that equal portions of strike length occur on either side of the profile being modelled, and that the body being modelled has the same strike cross-section along its complete strike length. Modelling with the routine is commonly referred to as 2.5D modelling.

• ***Magnetic anomaly of a finite-length right polygonal prism*** (Coggon 1976). This routine calculates the magnetic field of a body of arbitrary constant cross-section on a profile perpendicular to the body at any location along the length of the body. Modelling with this routine is commonly referred to as 2.75D modelling.

• ***Magnetic anomaly of a triaxial ellipsoid*** (Clark et al. 1986). This routine is extremely useful for modelling the response of a variety of ore bodies. It is capable of computing the effects of anisotropic susceptibility and demagnetisation. Demagnetisation is an effect whereby the magnetic effects of very magnetic bodies distort the ambient magnetic field such that the direction of the Earth's field changes and the computation of magnetic anomalies using simple induction relationship is no longer possible.

• ***Noddy, a modelling package specifically designed to simulate structural problems*** (Valenta et al. 1992; Jessel et al. 1993). Using this package it is possible to input a series of horizontal layers and then compute the magnetic effect on the stratigraphy after a specified sequence of folding, faulting and igneous intrusion. The routine is based on subdividing the undeformed magnetic units into small cubes. The magnetic effects of the original model and all deformed models are calculated by summing the magnetic effect on the cubes in their original or relocated positions. This package can give useful indications of the likely magnetic patterns in structurally complex areas.

• ***Computation of the magnetic effect of arbitrarily shaped magnetic bodies by approximating their surfaces to a series of triangular facets*** (Bott 1963; Lee 1980). These routines model virtually all situations; however, they depend upon having a routine that facilitates the translation of the shape of the body to the triangular facets. Lee's routine includes the possibility of correcting for the demagnetisation effect if no remanence is present. Lee also addresses the problem of defining the triangular facets.

These routines have been incorporated into various proprietary and commercially available packages of which the most advanced work interactively in Windows-type environments (Fig. 2). These packages allow the interpreter such options as definition of regionals, computation of residuals, multi-source models and inclusion of remanence, demagnetisation and anisotropy. The algorithm used for each modelling exercise depends upon whether the anomalies being interpreted are sufficiently elongated for a two-dimensional or quasi two-dimensional approximation to be used or whether a

three-dimensional model is required. The type of three-dimensional algorithm used depends on the form of the magnetic source and the detail required. Such routines have become basic interpretation tools; however, they can be time consuming to apply. They are suited to detailed analyses of single anomalies and clusters of anomalies and cannot be realistically applied to areal depth determination problems.

Inversion

A logical progression from interactive forward modelling was the development of automatic inversion routines that produce a geological model, the magnetic effects of which match an observed magnetic data set. Such inversion routines can either be linear or non-linear.

Linear inversion

Linear inversion techniques (Bott 1967; Safon et al. 1977) consist of subdividing the space below an observed magnetic field into a series of geometric bodies and then finding values of magnetisation for the shapes, such that the summed magnetic effects of all the bodies matches the observed magnetic field. This problem can be formulated as a set of simultaneous equations, in which the known values are the magnetic field at each observation point and the magnetic effect at each observation point, for each geometric body, for the case of unit magnetisation. The unknowns in the equation are the magnetisations of each body required to duplicate the observed field. The problem can be specified as having exactly the same number of bodies as observations, in which case an exact fit between observed and calculated fields will be obtained or there can be more observations than blocks, in which case a least squares solution will be required.

The geometric bodies can have any arrangement; however, most workers use a matrix-type grid of bodies with the objective of obtaining a clustered contiguous distribution of magnetisation values that can be related to a geological entity. In practice, a good fit between observed and calculated magnetic fields is obtained but unless the distribution of geometric bodies is heavily constrained to a probable solution, the magnetisation values bear no relationship, either spatially or numerically to reality. The cause of this problem appears to be related to the fact that truncated samples of magnetic fields are used as input to the problem and the solutions are consequently based on input values that do not necessarily give good representations of the true magnetic field. Linear inversion techniques based on solving simultaneous equations have not found widespread application to interpretation problems.

A variation of the linear inversion technique with wider application has been formulated by Bott (1967). He showed that if the geometric bodies have identical dimensions, and form a continuous layer at a constant depth, then a set of convolution coefficients can be calculated. When convolved with the observed magnetic field, the coefficients will produce the magnetisation of the blocks, provided a correct assumption is made for the direction of magnetisation in the blocks.

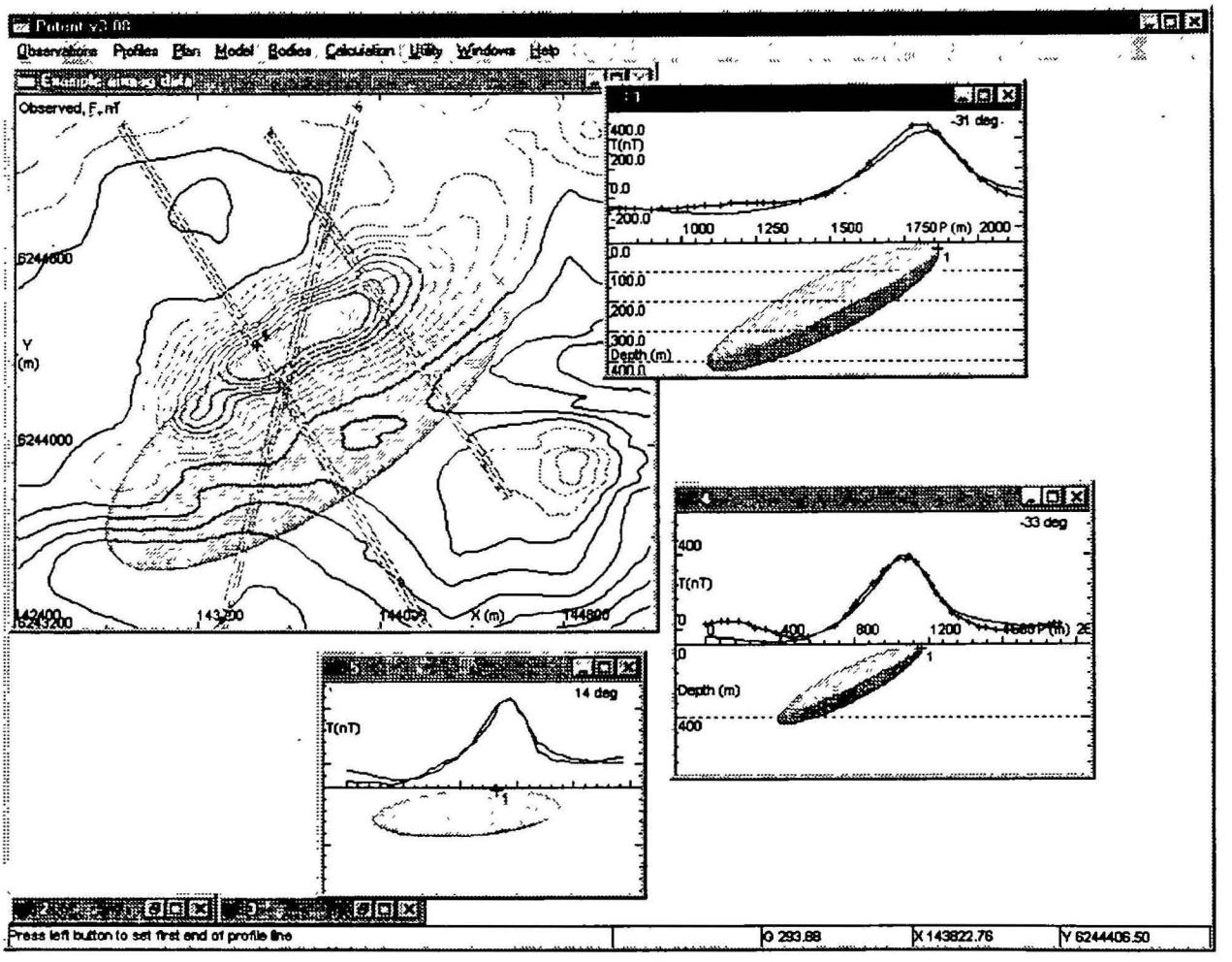

Figure 2. Sample output of an interactive Windows-based modelling package. In the example illustrated, the package was used to select profiles across an anomaly and produced matches at several locations between observed and calculated data using a triaxial ellipsoid model.

Linear inversion using convolution filters (or alternatively, fast Fourier transformation routines) can be used to transform maps or images of magnetic intensity into maps of susceptibility. Such processing, which appears to have moderate usage, allows easier mapping of lithologies than total magnetic intensity datasets. Gunn (1975a) gave the theory for designing such filters in the spectral domain, and (Gunn 1972a) an example of the application of the method to real data for a situation where the results have been verified by ground sampling.

Gunn (1975a) showed that when the relief on magnetic layers with constant magnetisation is relatively small, the relationship between the relief and the magnetic field it produces is almost linear. Gunn (1976) has demonstrated that accurate mappings of such relief can be obtained by the application of convolution filters (Fig. 3).

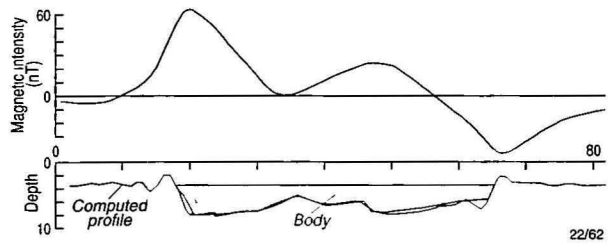

Figure 3. Direct mapping of the relief on a magnetic interface, using a convolution filter (after Gunn 1976). The magnetic profile was input to a filtering routine and the depth profile was output. A knowledge of the magnetisation of the magnetic body being mapped is necessary for the successful application of the routine.

Non-linear inversion

Non-linear inversion (Al Chalabi 1970; McGrath & Hood 1973; Gunn 1975b) attempts to obtain a match between observed and calculated magnetic fields by iteratively varying unknown parameters, such as the coordinates of model bodies and magnetisations. Using a trial and error method, variations that improve the fit between the observed field and calculated results based on the model are stored and used as a basis for new parameter estimates. Estimates that degrade the fit between the observed and calculated fields are discarded in favour of the previous estimate. Such routines consist of an algorithm to calculate the magnetic field of the model bodies plus an algorithm that varies the unknown parameters in such a way that convergence towards a fit between the observed and model fields is obtained. The 'fit' is commonly defined as the minimum of the sum of the squares of the differences between the observed and calculated fields.

Many sophisticated routines exist for estimating parameter variations that lead towards convergence; but a complete description of their characteristics is outside the scope of this paper. It is important to note, however, that the problem is not straightforward, as a simple progressive parameter variation based on successive improvements may not lead to the best fit. A 'local minimum' may be obtained in which both increases and decreases of a parameter value degrade the fit. The best fit or the 'global solution' may require a significantly different value of the parameter. Some non-linear inversion routines are capable of escaping from local mimima.

Non-linear inversion techniques have proved useful in certain well-constrained situations and their application can be much faster than interactive forward modelling. Some geophysicists combine the two techniques and use non-linear inversion to produce the final perfect fit to a solution initially obtained by interactive modelling.

In the author's experience, the main problems with non-linear inversion are that unless the problem is well constrained a solution will be obtained which, although giving a very good fit between the observed and calculated fields, is geologically unrealistic. Most non-linear inversion schemes allow the range of parameter variation to be constrained and it is thus possible to limit such problems. Another common problem involves eliminating secondary magnetic effects from the magnetic values used in the curve fitting. The occurrence of a noise bump or the effects of an adjacent anomaly will not be recognised as such by the matching process and the fit can thus become meaningless. Finally, the calculation of regionals is crucial. This can either be done by the interpreter or left to the routine. Either way, the estimated regional must be real or the interpretation will be unrealistic. Figure 4 gives an example of an interpretation based on a non-linear inversion technique where some of these problems were encountered.

Automatic depth-to-source estimations, using profile data

Several automated methods have been developed to estimate depths to magnetic sources using profile data. All assume that anomalies on the profiles are sufficiently elongated for a

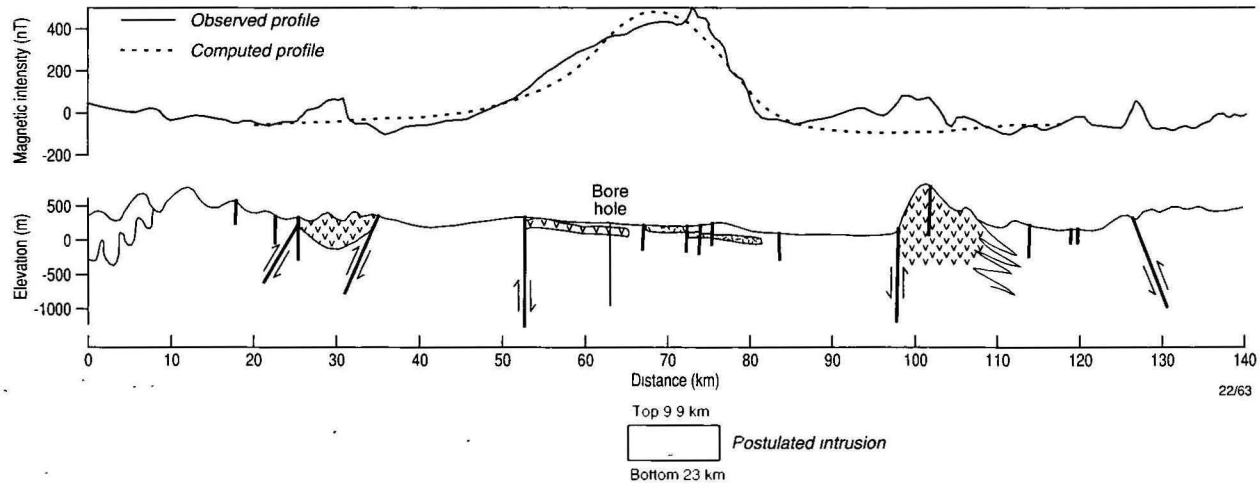

Figure 4. Example of non-linear inversion (after Gunn 1975b). The routine has iterated to find the best match in the least squares sense between an observed magnetic profile and a theoretical magnetic profile due to a prismatic body with a square cross-section. The routine automatically varied the dimensions, depth and magnetisation of the prism and the value of a constant background regional until no further significant improvement in the result could be obtained. The magnetic effects of more than one magnetic body are apparent on the profile. Portions of the profile containing magnetic effects due to shallow magnetic bodies were deleted from the curve-matching process.

two-dimensional assumption to be valid. The most widely used of these methods are:

• ***Werner deconvolution.*** Werner (1953) formulated the magnetic response of a thin dyke with an infinite length and an infinite depth in terms of a linear equation where two of the unknowns are the position and depth to the top of the thin dyke. 'Thin' in this context means that the width of the dyke does not influence the form of the anomaly and, for practical purposes, this applies to all dykes with a depth to their top greater than their width. Obviously, the depth to a thin dyke can be calculated from a set of four simultaneous equations incorporating four different samples of the magnetic field due to the thin dyke. Hartman et al. (1971) extended this idea and produced a more elaborate linear formulation which allows determination of a regional as well as the depth and position of the thin dyke. This elaboration allows the effects of regionals and interference between adjacent anomalies to be accounted for in the calculation of the depths and positions. Hartman et al. used this principle to produce an automatic routine which progressively samples magnetic field values along profiles and determines the depths and positions of all the thin dykes on the profile.

Obviously, not all dykes are thin, however; Hartman et al. realised that the anomaly for the horizontal and vertical gradients over the edges of thick dykes or contacts can be solved using the thin dyke formula and thus they were able to extend their method to these geometries. Horizontal thin sheets are interpreted in the same manner as dipping thin sheets. Different sample intervals are required to solve anomalies at different depths. The results are plotted as symbols on profiles, where the horizontal dimension gives the position and the vertical dimension, the depth. In practice, a scatter of determinations is obtained and virtually all anomalies are interpreted as both thin dykes and edges. Considerable skill appears to be required to use the results in a meaningful way. The concept, however, seems fundamentally sound. Jain (1974), using model data, has shown that the accuracy of the depth determinations is approximately 10 per cent.

• ***'Compudepth'.*** Compudepth is a proprietary method developed by Geometrics for which virtually no documentation is available apart from abstruse mathematical papers by O'Brien (1971, 1972). The method seems to be based on a spectral formulation of the analytic signal (Nabighian 1972). The presentation of the results is appealing, in that it shows a series of positions and depths (together with error bars) of the corners of magnetic sources. A match between the observed magnetic profile and a magnetic profile computed from the interpreted results is also presented. Such matches are generally good and indicate the validity of the results. The method appears to be capable of simultaneously mapping markers at different depths. The author has obtained geologically meaningful results with Compudepth on several projects (Gunn 1979), with some of the results being confirmed by drilling. This appears to be the only published case history supporting the method. However, in other instances the results appeared meaningless. It seems that successful application of the method requires some type of operator controlled tuning to produce optimum results.

• ***Phillips' autocorrelation method.*** Phillips (1979) bases an automatic interpretation method on the assumption that a two dimensional magnetic basement can be approximated by an assemblage of thin vertical or near vertical dykes. Autocorrelation functions of magnetic anomalies due to such dykes have a form that is independent of magnetic inclination and dip and which allows depth estimates to be algebraically calculated using combinations of autocorrelation values at various lags. Consistent depth estimates using a range of different lags are interpreted to indicate a valid depth estimate. Although several organisations, mainly located in the northern hemisphere, appear to be currently using this algorithm, very little published material relating to the routine has appeared in the public domain. Skilbrei (1991) reports using the method but does not include any clear examples of its application in his paper.

• ***Naudy curve-matching method.*** Naudy's (1971) automatic depth-determination routine for application to profile data is based on splitting anomalies into symmetric and asymmetric components, and matching the symmetrical component to the magnetic anomalies of standard simple geometrical forms, such as the dyke, contact and thin plate models. The anomaly that gives the best match is determined by the use of a similarity coefficient. The best match is indicated by minima in the similarity coefficient for a range of models with different depths and thicknesses. The position of the minimum in the similarity coefficient determines the location of the source and indicates the depth of the model. The output is a series of interpreted source depths and locations. Refinements to the method have been made by Shi & Boyd (1991, 1994), who used horizontal and vertical components of the magnetic field as well as the vertical gradient. Unfortunately, the process often produces simultaneous interpretations for all three basic models, but showing different depths. Similarity coefficient values may be output, but the true significance of these is often difficult to determine. The basic problem with the published routines is that the interpreter has no simple way of knowing the validity of any computed depth. This problem has been solved in a proprietary technique developed by Encom Technology Pty Ltd, who have incorporated a forward modelling routine into software based on the Naudy method. The modelling routine enables the checking of solutions and discarding of unrealistic depth estimates. The addition of an inversion routine allows initial depth estimates to be modified to obtain a perfect fit of the field due to the interpreted sources and the observed field (Fig. 5).

Even with the most accurate interpretations of profile data, corrections and correlations with map data must be made in order to obtain meaningful results. Correlation with contoured results is necessary to associate the depth determinations with specific magnetic anomalies. These correlations also enable the discarding of depths determined for short anomalies which do not approximate the infinite strike length assumption. Corrections can be made for cases where anomaly trends are not exactly perpendicular to the profiles.

The Euler depth determination method

A formulation of Euler's homogeneity relationship given by Reid et al. (1990) shows that:

$$(x - x_0)\,\delta T/\delta x + (y - y_0)\,\delta T/\delta y + (z - z_0)\,\delta T/\delta z = N(B - T)$$

where (x_0, y_0, z_0) is the position of the magnetic source whose total magnetic intensity field T is detected at (x,y,z). The total field has a regional value of B. N is a structural index which is equal to three for a point dipole and two for a vertical pipe. More complicated bodies, which are, in effect, assemblages of dipoles, have indices ranging from zero to three. An index of one appears to work for dykes and contacts approximated by lines of poles.

Reid et al. (1990) automated the solution of this linear equation for gridded data to produce solutions for the positions and depths of magnetic sources. By using field and computed derivative values at more points than necessary, they obtained an over-determined set of equations and were able to use least square inversion techniques to solve for the unknowns. The solutions are typically displayed as a series of circles, with the centre of the circle indicating the position of the source and the diameter of the circle indicating the source depth (Fig. 6). The method has proved useful for identifying source

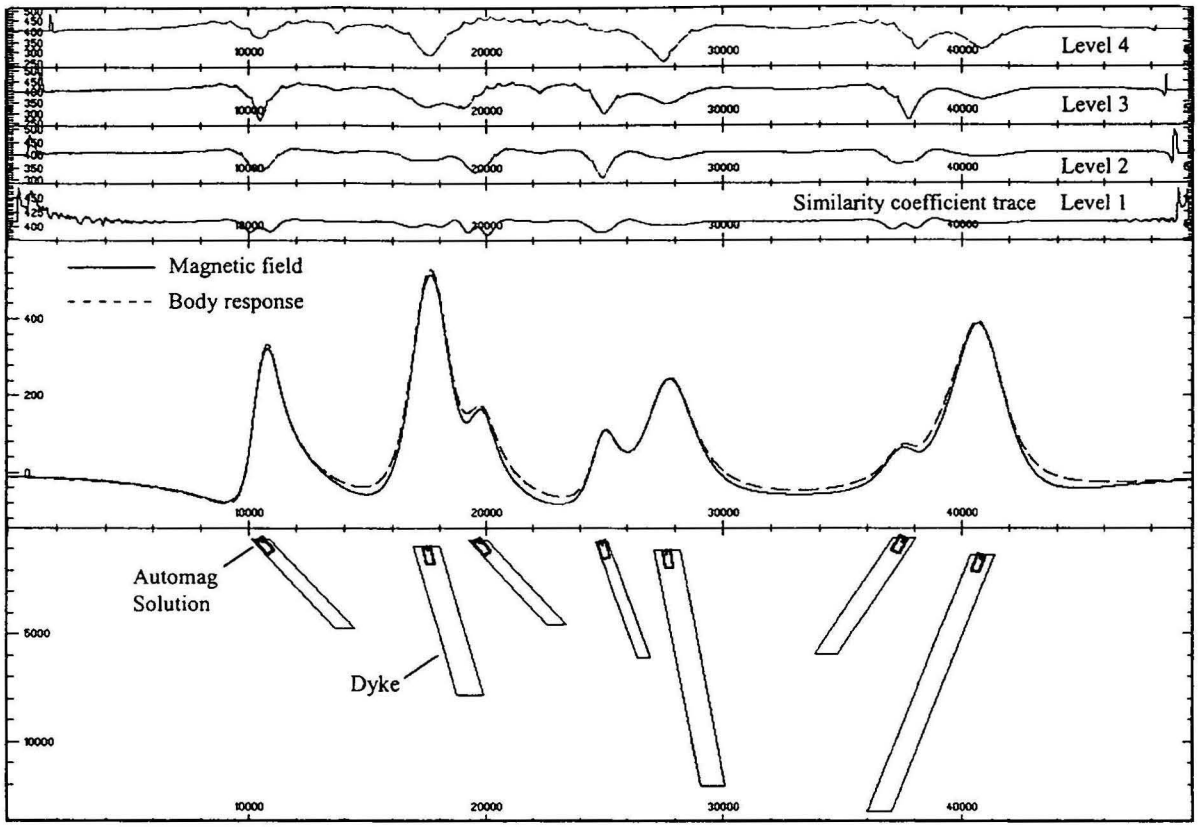

Figure 5. Example of the output of an automatic depth-determination routine based on a modification of the Naudy (1971) method. Initial depth estimates are indicated by minima in the similarity coefficients. The most realistic of these estimates are determined by forward modelling and an inversion routine adjusts the initial depth estimates to give a match of the observed field and the model field due to the interpreted bodies.

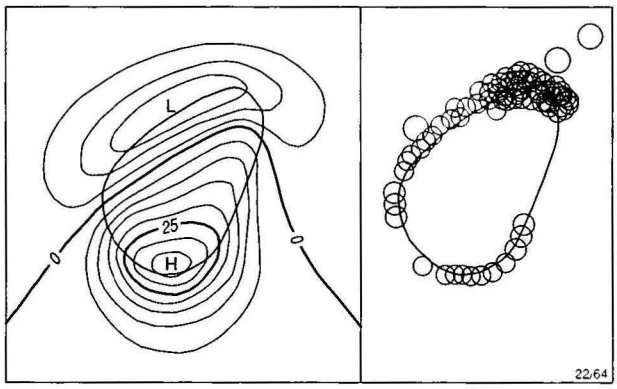

Figure 6. Example of the output of the Euler automatic depth routine (after Reid et al. 1990). The example shows results obtained using the model field over a sill-like body with an irregular outline. The correct structural index of 1 was used. Depth estimates were generally accurate to 13% although some spurious values not related to the body were obtained. Note that not all the body has been outlined.

positions and boundaries and for giving generalised indications of source depth.

From the examples presented by Reid et al. (1990), the method appears to be useful and since the publication of their paper it has been widely used. The author's experience, however, is that, although applications of the method appear to produce meaningful results, these are often difficult to correlate with the true depths and positions of magnetic sources when these are known from other information. Part of the problem in obtaining accurate depths using the Euler method may relate to the difficulty of computing accurate derivatives on which to base the depth estimates. Obviously, noise from shallow magnetic sources will corrupt the gradient estimates for deep magnetic sources, as will wide survey line spacings in areas of high-frequency magnetic anomalies.

The choice of the structural index is critical to obtaining meaningful results and the normal situation, where a survey area contains a range of sources with differing geometry, precludes a definitive processing of an area with a single structural index. Reid et al. (1990) advocated multiple processings with different indices, followed by judicious correlation with anomaly forms. This approach is only partly satisfactory. It may in fact be possible to compute the structural index of a source by formulating the problem to consider the field and its vertical gradient over the maximum of the field at various levels. At the maximum of the anomaly the horizontal derivatives are zero and the only unknowns are the depth, structural index, and the regional. Gunn (1972b) tested this approach on model data free of any regional and found that accurate structural indices were computed. The method was not pursued, because, at the time, the precision of the data required was not generally available. The precision of present-day data should, however, be sufficient, and the idea appears worthy of further investigation.

Analytic signal depth determinations

The analytic signal (Nabighian 1972, 1974, 1984; Roest et al. 1992) is a function related to magnetic fields by the derivatives; i.e.

$$\text{analytic signal, } |A(x,y)| = [\,(\delta T/\delta x)^2 + (\delta T/\delta y)^2 + (\delta T/\delta z)^2\,]^{1/2}$$

where T = magnetic intensity.

This function is extremely interesting in the context of interpretation, in that it is completely independent of the

direction of magnetisation and the direction of the Earth's magnetic field. This means that all bodies with the same geometry have the same analytic signal. Furthermore, as the peaks of analytic signal functions are symmetric and occur directly over the edges of wide bodies and directly over the centres of narrow bodies, interpretation of analytic signal maps and images should, in principle, provide simple, easily understood indications of magnetic source geometry. The half-widths of these peaks can be linearly related to depths, if the sources of the peaks are vertical magnetic contacts.

Roest et al. (1992) have applied the above properties to develop an automated interpretation system, which uses the anomaly peak property of the analytic signal to outline source geometry and the half-width property to obtain estimates of the depths to these sources. Examples presented by Roest et al. (1992) appear impressive; however, there is no way to determine the veracity of their results from their publication.

The analytic function certainly appears to be a worthwhile interpretation tool, but more case-history details are required before its general applicability can be assumed. The author has been involved in several projects where the analytic signal was calculated from map data. In general, sharp anomaly peaks were not obtained over anomaly edges and, instead, diffuse peaks were obtained, whose outlines were less clear than the original total magnetic intensity. Results published by Shuang Qin (1994) appear to support this observation. These deviations of the behaviour of the analytic signal from the ideal case can probably be ascribed to the fact that source geometry was more complicated than a vertical contact. The difficulty of accurately computing horizontal derivatives for small anomalies in directions perpendicular to flight-line directions may, however, have influenced the results. The author's experience with analytic signals computed on closely spaced profile data was more in accordance with the properties of the analytic signal expected from theory.

Analytic signal maps and images are useful as a type of reduction to the pole, as they are not subject to the instabilities that occur in transformations from low magnetic latitudes (McLeod et al. 1994); they also define source positions regardless of any remanence in the sources.

Spectral depth-determination methods

As well as having a form in the space domain, magnetic anomalies have a form in the frequency domain and, in theory, can be interpreted in the frequency domain. In practice, the spectra of single sources and multiple sources are much more complicated in the frequency domain than their space domain equivalents (e.g. Bhattacharyya 1966) and no routine interpretation is attempted with such representations.

The main attempts to use spectral data for depth estimates stem from a publication by Spector & Grant (1970) which was based on the unpublished thesis of Spector (1968).

Spector (1968) showed that for an ensemble of prismatic blocks with infinite depth extent the logarithmic radial energy spectrum of the total magnetic intensity consists of a straight line whose gradient is related to the average depth to the tops of the prisms. Furthermore, in the case of a double ensemble of prisms, two gradients would normally be obvious in the spectrum, with the steep gradient related to the deeper sources and the low gradient related to the shallow sources. It is important to realise, however, that the slope of spectra can only be used to calculate average depths when the sources are an ensemble of uncorrelated magnetic poles. Significant corrections for the average width of the prismatic bodies and their depth extent must be applied before any accurate depth estimation can be attempted for the spectra of ensembles of prismatic blocks. Examples given by Spector (1968) show that these corrections can modify depth estimates by the order of 50 per cent. Spector & Grant (1975) and Spector (1985) have published disclaimers, recommending that the method not be used for quantitative depth estimates. Despite this, publications regularly appear in the geophysical literature showing depth determinations based on logarithmic energy spectra with no mention of any refinement to the spectra by the width effect. In practical terms, it is very difficult to envisage how an average body width can ever be calculated in a terrane with elongated magnetic sources. The author has doubts that the approach can be used meaningfully for quantitative depth estimates other than in certain special situations.

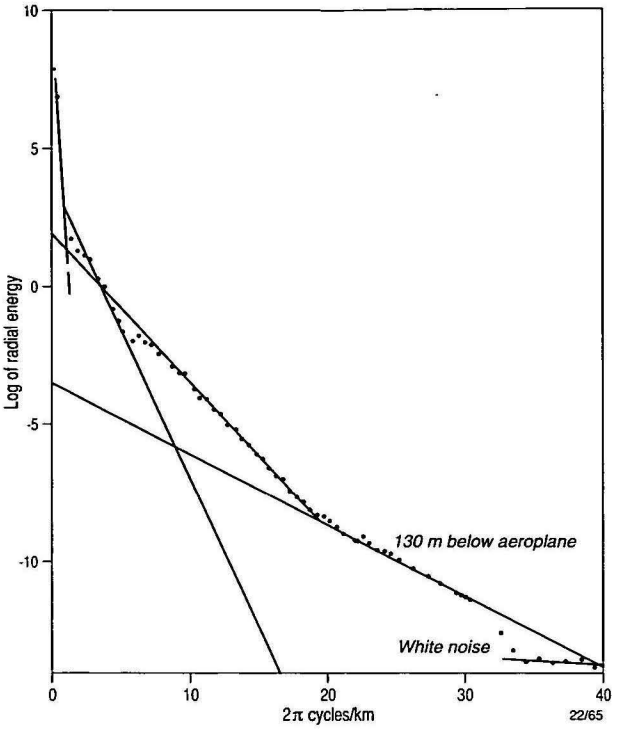

Figure 7. An example of a radially averaged logarithmic energy spectrum of a magnetic field. The spectrum shows straight-line segments, which correspond to 'ensembles' of magnetic bodies with the same average depth. It is not normally possible to calculate the depths of the layers using the gradient of the straight segments unless the average width of the anomalies in the ensemble is known. The shallowest layer is caused by surface culture and its gradient has been related to the flying height of the survey aircraft by assuming that the culture is approximated by a random distribution of magnetic poles.

The author has computed spectra of detailed aeromagnetic surveys over a sedimentary basin in a heavily populated area of France (Fig. 7). The shallowest linear segments of these spectra can be accurately related to the ground clearance of the surveys, because the magnetic effects of the dense culture in the area approximate a random distribution of magnetic poles. This case appears to be a special situation where the method can be used for the accurate determination of the depth to a magnetic layer.

Cross correlation

For a given digital waveform, the digital filter (subject to the constraint that the energy of its coefficients is unity) that gives the maximum output possible has an impulse response which is the reverse of the waveform being filtered. Such filters, discussed by Treitel & Robinson (1969), are called cross-correlation or matched filters and have application to the automatic interpretation of magnetic anomalies. Figure 8 shows an example from Gunn (1972b) where the anomaly due to a single dyke has been interpreted by a cross-correlation process that correctly gave a maximum correlation when the anomaly

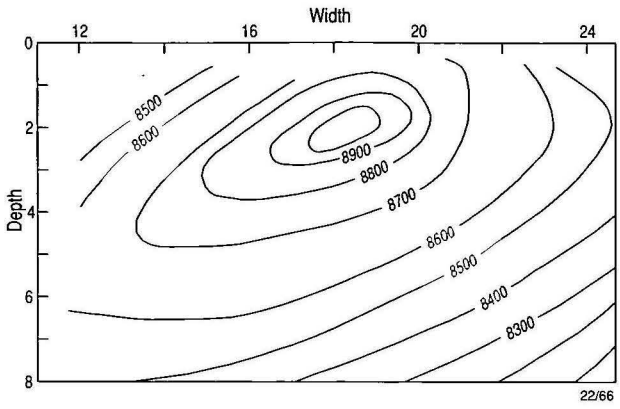

Figure 8. Interpretation of the depth and thickness of a vertical dyke using cross-correlation (after Gunn 1972b). The plot shows filter outputs obtained by convolving the magnetic field of a vertically magnetised vertical dyke, depth 2 units and width 18 units, with the normalised magnetic profiles of other vertical vertically magnetised dykes of various depths and widths. The maximum correlation was obtained for the model with the same depth and width as the dyke causing the anomaly being interpreted.

was convolved with its own waveform. This is the only work on this subject known to the author.

Conclusion

Software available for modelling anomalies can now easily handle virtually every situation. Interpretation, by a trial and error process, provides plausible combinations of body geometry and rock magnetic properties that give realistic explanations for the observed magnetic field. Efforts to automate this process do not appear to provide consistently reliable results. The reasoned judgement of geoscientists is still required to evaluate what is a reasonable solution and what is not.

No published method for automatically calculating 'depth to basement' appears consistently superior to the pre-computer methods used for this purpose. Depth-to-basement maps are probably inferior today compared to those of twenty years ago, owing to the reluctance of interpreters to individually examine every anomaly and to rely instead on 'shotgun' scatters of depth determinations produced by automatic routines. The association of a modelling solution–checking routine with the Naudy (1971) method, as described above, may be the solution to this problem.

References

Al Chalabi, M., 1970. Interpretation of two-dimensional magnetic profiles by non-linear optimisation. Bolletino Geofisica Teoretica et Applicata, 12, 3–20.

Bhattacharyya, B.K., 1966. Continuous spectrum of the total magnetic field anomaly due to a rectangular prismatic body. Geophysics, 31, 91–121.

Bott, M.H.P., 1963. Two methods applicable to computers for evaluating magnetic anomalies due to finite three dimensional bodies. Geophysical Prospecting, 11, 292–299.

Bott, M.H.P., 1967. Solution of the linear inverse problem in magnetic interpretation with application to oceanic magnetic anomalies. Geophysical Journal of the Royal Astronomical Society, 13, 313–323.

Cady, J.W., 1980. Calculation of gravity and magnetic anomalies of finite-length right polygonal prisms. Geophysics, 45, 1507–1512.

Clark, D.A., Saul, S.J. & Emerson, D.W., 1986. Magnetic and gravity anomalies of a triaxial ellipsoid. Exploration Geophysics, 17, 189–200.

Coggon, J.H., 1976. The magnetic and gravity anomalies of polyhedra. Geoexploration, 14, 93–105.

Gunn, P.J., 1972a. Application of Wiener filters to transformations of gravity and magnetic fields. Geophysical Prospecting, 10, 860–871.

Gunn, P.J., 1972b. Application of Wiener filters to transformations of gravity and magnetic data. Ph.D. Thesis, Durham University, U.K.(unpublished).

Gunn, P.J., 1975a. Linear transformations of gravity and magnetic fields, Geophysical Prospecting, 23, 300–312.

Gunn, P.J., 1975b. Interpretation of the Bathgate Magnetic Anomaly, Midland Valley, Scotland. Scottish Journal of Geology, 2, 263–267.

Gunn, P.J., 1976. Direct mapping of interfaces and thicknesses of layers using gravity and magnetic data. Geoexploration, 14, 75–80.

Gunn, P.J., 1979. Examples of computer based interpretation methods used as routine exploration aids. Bulletin of the Australian Society of Exploration Geophysicists. 10, 15–25.

Haematite Exploration Pty. Ltd., 1965. Bass Strait and Encounter Bay aeromagnetic survey 1960-61. BMR Petroleum Search Subsidy Act Publication No. 60.

Hartman, R.R., Teskey, D.J. & Friedberg, J., 1971. A system for rapid digital aeromagnetic interpretation. Geophysics, 36, 891–918.

Hjelt, S.E., 1972. Magnetostatic anomalies of a dipping prism. Geoexploration, 10, 239–254.

Jain, S., 1974. An automated method of direct interpretation of magnetic profiles. Geophysics, 41, 531–541.

Jessel, M.W., Valenta, R.K., Jung, G., Cull, J.P. & Geiro, A., 1993. Structural geophysics. Exploration Geophysics, 24, 599–602.

Lee, T.J., 1980. Rapid computation of magnetic anomalies with demagnetisation included, for arbitrary shaped bodies. Geophysical Journal of the Royal Astronomical Society, 60, 67–75.

McGrath, P. & Hood, P., 1973. An automatic least squares multi-model method of magnetic interpretation. Geophysics, 38, 349–358.

McLeod, I.N., Jones, K. & Ting Fan Dai, 1994. 3-D analytic signal in the interpretation of total magnetic field data at low magnetic latitudes. Exploration Geophysics, 24, 679–688.

Nabighian, M.N., 1972. The analytic signal of two dimensional magnetic bodies with polygonal cross-section: its properties and use for automated anomaly interpretation. Geophysics, 37, 507–517.

Nabighian, M.N., 1974. Additional comments on the analytic signal of two dimensional magnetic bodies with polygonal cross-section. Geophysics, 39, 85–92.

Nabighian, M.N., 1984. Towards a three-dimensional interpretation of potential field data via generalised Hilbert transforms: fundamental relations. Geophysics, 49, 780–786.

Naudy, H., 1970. Une methode d'analyse sur profiles aeromagnetiques. Geophysical Prospecting, 18, 56–63.

Naudy, H., 1971. Automatic determination of depth on aeromagnetic profiles. Geophysics 36, 717–722

O'Brien, D., 1971. An automated method for magnetic anomaly resolution and depth to source computation. Proceedings of the Symposium on Treatment and Interpretation of Aeromagnetic Data. Berkeley University, California.

O'Brien, D., 1972. Compudepth, a new method for depth to basement computation. Preprint of a paper presented at the Society of Exploration Geophysicists 42nd Annual Meeting, Anaheim, California, 29 November 1972.

Parker Gay, S., 1963. Standard curves for interpreting magnetic anomalies over long tabular bodies. Geophysics, 28, 161–200.

Phillips, J.D., 1979 ADEPT: A program to estimate depth to magnetic basement from sampled magnetic profiles. U.S. Geological Survey Open File Report 79-367.

Reford, M.S. & Butt G.R., 1983. Aeromagnetics in Australian petroleum exploration. Exploration Geophysics, 14, 113–130.

Reid, A.B., Allsop, J.M., Granser, H., Millet, A.J. & Somerton, I.W., 1990. Magnetic interpretations in three dimensions using Euler deconvolution Geophysics, 55, 80–91.

Roest W.R., Verhoef, V. & Pilkington, M., 1992. Magnetic interpretation using the 3-D analytic signal. Geophysics, 57, 116–125.

Safon, C., Vasseur, G. & Creu, M., 1977. Some application of linear programming to the inverse gravity problem. Geophysics, 42, 1215–1299.

Shi, Z., 1991. An improved Naudy-based technique for estimating depths on magnetic profiles. Exploration Geophysics, 22, 357–362.

Shi, Z. & Boyd, D., 1994. Automag—an automated method to estimate thickness of overburden from aeromagnetic profiles. Exploration Geophysics, 24, 789–794.

Shuey, R.T. & Pasquale, A.S., 1973. End corrections in magnetic interpretation. Geophysics, 38, 507–512.

Shuang Qin, 1994. An analytic signal approach to the interpretation of total field magnetic anomalies. Geophysical Prospecting, 42, 665–676.

Skilbrei, J.R., 1991 The interpretation of depth to the magnetic basement in the northern Barents Sea (south of Svalbard). Tectonophysics, 200, 127-141.

Smellie, D.W., 1956. Elementary approximations in aeromagnetic interpretation. Geophysics, 21, 1021–1040.

Spector, A., 1968. Spectral analysis of aeromagnetic data Ph. D. Thesis, University of Toronto, Canada.

Spector, A., 1985. Comment on "Statistical methods for interpreting aeromagnetic data by A. Spector and F.S. Grant". Geophysics, 50, 2278.

Spector, A. & Grant, F.S., 1970. Statistical models for interpreting aeromagnetic data. Geophysics, 35, 293–302.

Spector, A. & Grant, F.S., 1975. Comments on "Two-dimensional power spectral analysis of aeromagnetic fields". Geophysical Prospecting, 23, 391.

Talwani, M., 1965. Computation with the help of a digital computer of magnetic anomalies of arbitrary shape. Geophysics, 30, 797–717.

Talwani, M. & Heirtzler, D., 1964. Computation of magnetic anomalies caused by two-dimensional structures of arbitrary shape. In: Computers in the mineral industry. School of Earth Sciences, Stanford University.

Treitel, S. & Robinson, E.A., 1969. Optimum digital filters for signal to noise ratio enhancement. Geophysical Prospecting, 17, 248–293.

Vacquier, V., Steenland, N.C., Henderson, R.G. & Zeitz, 1951. Interpretation of aeromagnetic maps. Geological Society of America Memoir 47.

Valenta, R.K., Jessell, M.W., Jung, G. & Bartlett, J., 1992. Geophysical interpretation and modelling of three dimensional data in the Duchess area, Mount Isa, Australia. Exploration Geophysics, 23, 393–400.

Werner, S., 1953. Interpretation of magnetic anomalies of sheet-like bodies. Sveriges Geologiska Arsbok, 43, Stockholm.

Won, I.J. & Bevis, M.G., 1987. Computing the gravitational and magnetic anomalies due to a polygon: algorithms and Fortran subroutines. Geophysics, 52, 232–238.

AGSO Journal of Australian Geology & Geophysics, 17(2), 115–131

Regional magnetic and gravity responses of extensional sedimentary basins

P.J. Gunn[1]

The gravity and magnetic responses of extensional sedimentary basins vary with the stages of basin development. The major observed gravity responses are regional gravity highs, reflecting crustal thinning, and gravity lows, reflecting low-density sediment infill. Mafic bodies may develop beneath the area of maximum extension as a result of mantle depressurisation and crustal rupture. These may cause regional magnetic anomalies and add to gravity highs. The observed gravity field over a rifted area depends on the relative contributions of the sources of the gravity highs and lows. The observed regional magnetic field depends on the degree of development of mafic bodies.

Introduction

The aim of this paper is to review regional magnetic and gravity responses observed over extensional sedimentary basins and to demonstrate how these can be related to degrees of crustal extension and stages of basin evolution.

An 'extensional' sedimentary basin, in the context of this paper, is one formed as a result of a crustal extension process that may ultimately lead to crustal rupture and the generation of oceanic crust between two fragments of continental crust. An initial classic model for this widely studied phenomenon was proposed by Falvey (1974), who recognised the evolutionary nature of the process. Although numerous refinements have been published since, the current concepts of a 'pre-rift' stage of broad depression with limited faulting followed by a superimposed 'syn-rift' stage, involving a localised rift valley bound by major faults resulting from continued extension, and a final 'post-rift' phase, consisting of sediment accumulation over a subsiding rift or continental margin, accord with Falvey's basic model.

Much of the more recent work has concentrated on the extensional processes in the crust and how these control the structural, sedimentological and igneous development of basins. A major reference for such studies is the McKenzie (1978) model, which invokes plastic extension of the lithosphere and thinning of the crust. The McKenzie model explains the observed syn-rift and post-rift subsidence in most extensional basins. Kusnir & Ziegler (1992) refined the McKenzie (1978) model to include brittle extension in the upper crust and pure shear in a ductile lower crust and mantle, producing a model that also accords with many basins.

A markedly different model to explain crustal extension was proposed by Wernicke (1985), in which crustal extension is accommodated by a major, shallowly dipping shear plane that traverses the entire crustal section. The concepts of this 'crustal detachment' model, extensively reviewed by Lister et al. (1991), are more complicated than the McKenzie model, in that predicted features are asymmetrically distributed relative to the axis of extension. It is not the purpose of this paper to join the controversy over crustal extension models, however one should be aware of these models when proposing explanations for observed regional magnetic and gravity fields over extensional systems. While it is certainly possible that all the models apply to varying degrees in different areas, the examples presented below tend to support the McKenzie–Kusnir–Ziegler types of crustal extension model by virtue of the fact that the gravity and magnetic anomalies of most rift systems appear to be symmetrically distributed relative to the rift axes.

The economic importance of extensional basins to hydrocarbon and mineral exploration and the intense academic interest in extensional basins have engendered numerous studies of their structural, sedimentological and petrological characteristics. Seismic, gravity and magnetic surveys have complemented many of these studies. However, apart from one earlier work (Gunn 1984), studies of gravity and magnetic signatures of extensional basins have largely been on a case by case basis.

In relating gravity and magnetic anomalies to crustal extension and basin forming processes, this paper first considers the actual processes involved and then, by correlating the expected and observed gravity and magnetic responses for particular examples, deduces generalisations. Its assertion is, that by understanding the range of tectonic, structural, sedimentologic and magmatic events associated with the evolution of sedimentary basins, regional magnetic and gravity data can be meaningfully interpreted to provide significantly more information over extended terranes than has normally been the case.

Overview of the evolution of extensional sedimentary basins

Most authors describing the evolution of extensional basins have used an approach, similar to Falvey (1974), of describing and illustrating a series of stages corresponding to the evolution of the basin as extension progresses. The following sections describe characteristic stages in a manner which synthesises the work of Falvey (1974), Sheupach & Vail (1980), and others and the author's personal observations in a wide range of extensional basins.

Figure 1 illustrates the author's generalisation, as a series of cross-sections, of the stages of basin extension. Figure 2 gives a plan perspective of the same stages. It should be noted that basins undergo differential extension along their length and it is possible for an extensional basin to manifest several of the stages of extension simultaneously. Figures 3 and 4 give possible gravity and magnetic responses for these stages.

(i) Early extension or pre-rift stage

The first phenomenon of extensional basin formation seen in continental settings is crustal extension and thinning of the continental crust. Although the section illustrated (Fig. 1a) closely represents the Kusnir & Ziegler (1992) model, similar crustal geometry can be produced by the McKenzie (1978) and Wernicke (1985) models.

Despite the debate over the mechanism of the crustal extension, there are a number of features common to these models. These may include:

- ***Formation of a broad depression in the pre-existing basement surface.*** Relatively minor normal faults may cause depressions to develop on the basement surface. If these are in settings isolated from marine incursions, they will receive fluviatile and lacustrine sediments whose distribution may be influenced by that of the normal faults on the basement surface and by continued movement on these faults. A series of tilt blocks may be formed as extension continues. Processes presently occurring in the Lake Okavango area at the southern extremity of the East African Rift system appear to be due to the initial stages of extension (Le Fournier 1986). The area around Lake Bangweulu, which is north of Lake Okavango

[1] Australian Geological Survey Organisation, GPO Box 378, Canberra, ACT 2601

and which has undergone greater extension, contains a broad zone of tilted fault blocks (Le Fournier 1986). Such sediment assemblages are termed 'pre-rift'. The Lower Cretaceous Otway Group of the Otway Basin and Strezlecki Group of the Gippsland Basin appear to be examples of pre-rift sediments (Falvey 1974).

• ***Doming.*** The initial stages of crustal extension may be preceded by doming of the Earth's crust. Specific examples of such domes are given by Le Bas (1971) and Burke & Whiteman (1973) for the African continent, Logachev et al. (1978) for the Baikal Rift, Falvey (1974) for the Otway Basin of southeastern Australia, and Cloos (1939) for the Rhine and Red Sea Rifts. Such uplifts may be 1000 km across and of

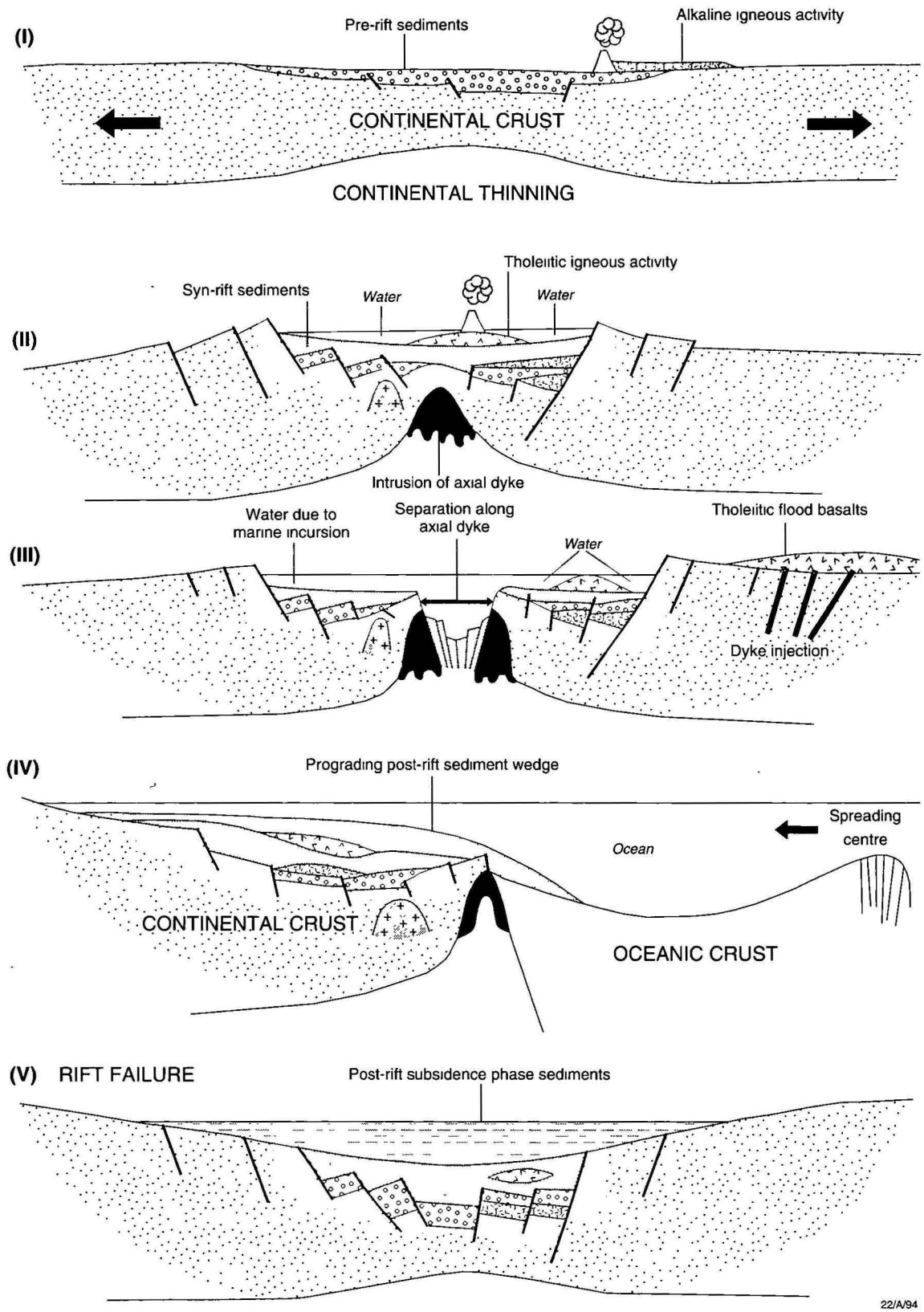

Figure 1. Stages of crustal extension (see text for an explanation of details).

the order of 3 km high. Seismic studies (e.g. Artmejev & Artyushkov 1971; Bridwell & Potzick 1981) suggest that these uplifts overlie cushions of low-velocity, low-density material underlying a thinned continental crust. Burke & Dewey (1973) considered that the cushions and doming result from heating and expansion of the mantle and lower crust by a plume-generated hot spot. Abnormally high heat-flow values recorded over areas of crustal extension (e.g. Bridwell & Potzick 1981) support this idea.

Jarvis (1984) quantitatively studied the uplift phenomenon by calculating the effects of thinning low-density crust and upwelling of hot mantle material. Basically, these phenomena cause competing effects, in that crustal thinning allows cooling of the mantle, which results in subsidence, and upwelling of hot mantle material causes expansion and uplift. Depending on which effect is dominant, uplift or subsidence will occur. The relative importance of the two effects depends primarily on the thickness of the crust and lithosphere.

The timing of these movements can vary relative to the initial crustal extension. Early doming can inhibit pre-rift sedimentation.

• ***Igneous activity.*** An effect of crustal extension and thinning is to move the lithosphere closer to the surface. When this happens, partial melting and the formation of magmas may result from decompression. Latin et al. (1990) list seven fundamental controls on the amount and composition of any partial melts produced. These are:

- temperature of the mantle,
- amount of extension,
- initial thickness of the lithosphere,
- composition of the asthenosphere,
- rate of extension,
- extent to which magmas interact with rocks they pass through, and
- nature of the magma extraction process.

White (1992) has noted that some extension systems are 'volcanic' and produce huge melt volumes, whereas others are 'non-volcanic' and have only a small igneous component. White's explanation for this is that if stretching is sufficiently rapid, so that the mantle does not cool by convective heat loss, then magma will be produced by decompression as the crust thins Slow stretching that allows cooling inhibits the melting process.

The igneous activity can manifest itself as extensive lava flows and volcanic centres, such as are associated with the East African Rift system (Williams 1978), or be restricted in nature, such as in the North Sea system of rifts (Latin et al. 1990) White (1992) gave examples to suggest that a result of magma production may be intrusion and underplating of the crust as well as extensive dyke injection into the crust.

The compilations of Le Bas (1971) and Burke & Whiteman (1973) show that domal uplifts are frequently associated with

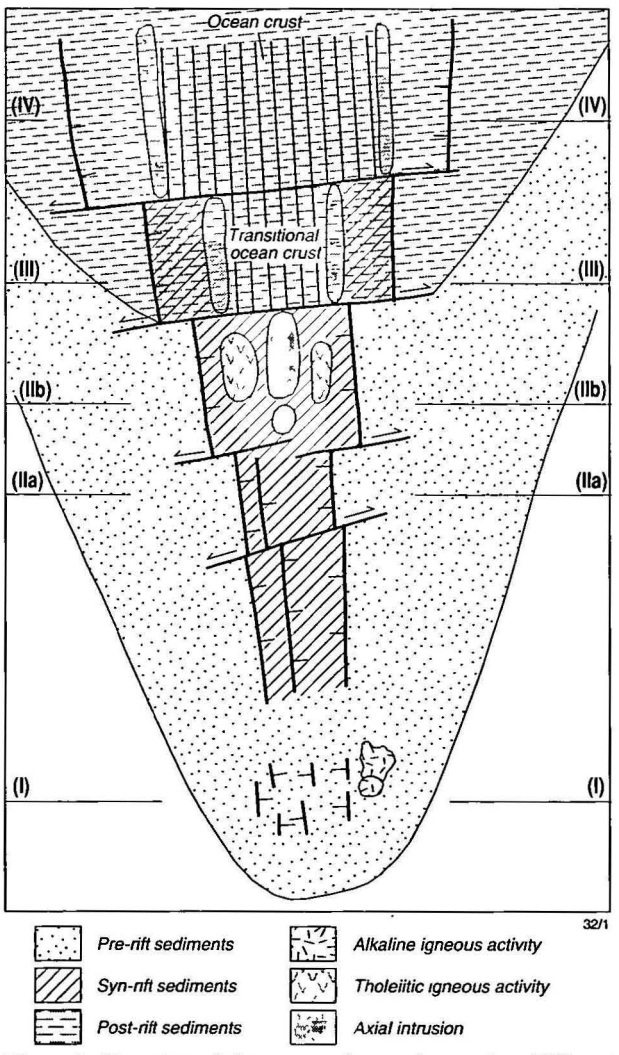

Figure 2. Plan view of the stages of crustal extension. Different degrees of extension are accommodated by transfer faults. This diagram assumes that that no significant strike-slip component occurs in the extension.

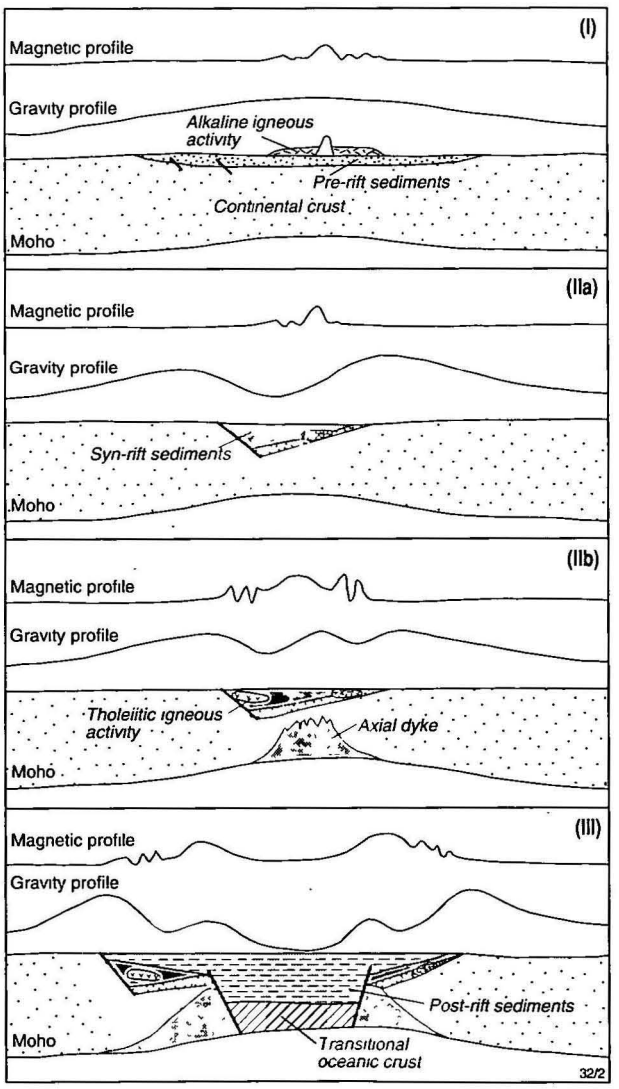

Figure 3. Magnetic and gravity expressions of the pre-rift and syn-rift stages. Sections correspond to sections shown in Figure 2.

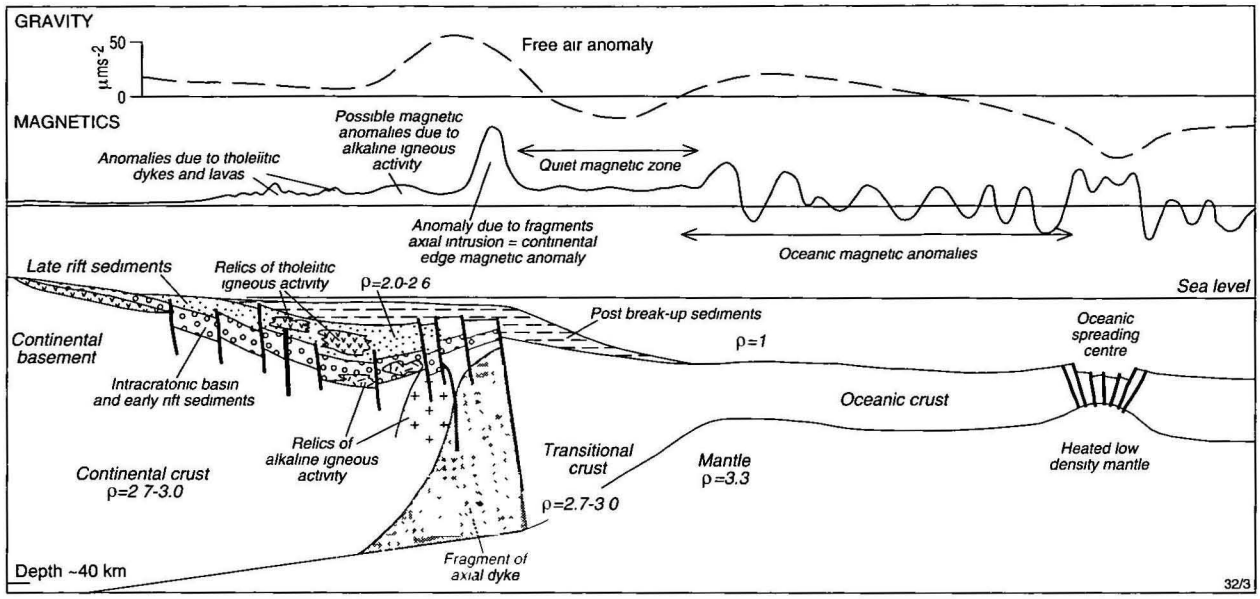

Figure 4. Idealised gravity and magnetic profiles over an 'Atlantic-type' continental margin where crustal splitting and sea-floor spreading have occurred.

alkaline igneous activity. Bott (1979) reviewed evidence showing that alkaline igneous activity can actually precede uplift. Magmatic activity associated with the earlier stages of crustal extension appears to have a tendency to be alkalic in nature.

Gravity and magnetic expressions of the pre-rift stage. The initial stages of crustal extension appear to be associated with broad gravity lows up to several hundred kilometres wide. Burke & Whiteman (1973) identified such situations in the Jos Plateau area (Ajakaiye 1970), the Cameroon Zone (Burke et al. 1971), Tibetsi (Louis 1970) and Ahaggar (Black & Girod 1970), all of which are located in Africa, in areas associated with Neogene uplift and alkali magmatism.

The areas of Lake Okavango and Lake Bangweulu at the southern extremity of the East African Rift system, where the initial stages of crustal extension are occurring, overlie gravity lows, albeit not as wide as the examples given above, and do not appear to be associated with uplift or marked igneous activity.

All the above gravity features are obvious on the gravity map of Africa (Fairhead 1986).

As described above, the broad gravity lows associated with the initial stages of extension appear to be due to elevated temperatures in the lithosphere where heating and expansion have reduced the density of the lithosphere. It is to be expected that they will disappear if the heat source in the lithosphere dissipates by convection or any other reason. This certainly appears to be the case, as such lows are not evident in the later stages of extension or in cases where extension has terminated. Low-density pre-rift sediment accumulation in the broad depressions caused by the earliest phase of extension will produce broad gravity lows, which will contribute to any more extensive lows caused by lithospheric heating.

The earliest stages of crustal extension do not appear to have any characteristic magnetic effects. However, as extension and crustal thinning progress, magma is likely to form and concentrate, initially as crustal underplating or as intrusive masses in the lower crust. The fact that alkaline igneous activity occurs in some early extension situations implies that these phenomena do occur early in the extension process. Alkaline intrusives will cause local gravity and magnetic anomalies, which will tend to be circular.

Gunn et al. (1995b) have identifed an extensive sheet of basic igneous material that was apparently extruded and/or intruded during the very earliest stages of extension of the Otway Basin in southeastern Australia. Modelling indicates that this lava flow/sill either forms a floor to the pre-rift section in the basin or occurs within the pre-rift section.

The effects of crustal thinning and accumulation of magma are also likely to produce observable effects. The Curie temperature, i.e. the temperature at which magnetite ceases to have a magnetic effect, is approximately 550°C and, on the basis of normal geothermal gradients, this is reached at depths of approximately 40 km (Sheriff 1988). This means that large masses of magnetite-bearing rocks should be detectable to this depth and that crustal underplating and the earliest stages of magma intrusion into the crust should be detectable with magnetic surveys.

Crustal thinning and magma underplating and intrusion do cause observable gravity and magnetic highs. However, the examples best described in the literature all appear to be associated with the syn-rift stage of extension and are described below in the context of syn-rift systems.

(ii) Syn-rift phase

The inevitable consequence of continued crustal extension is at least one major rupture in the upper, brittle crust. Typically, this produces a narrow fault-bound trough floored by the sediments accumulated during the pre-rift phase. These narrow troughs, which are of the order of 60 km wide, can be regarded as true rifts or grabens. They are often bound by a major fault on one side only, with the result that they have a half-graben geometry. Rift systems formed this way may occur along extensive branching linear zones; the East African Rift system is the classic modern-day example (Girdler 1972). The composite Central, Viking, Witch Ground and Moray Firth grabens of Jurassic age in the North Sea area (Ziegler 1990) are well-studied examples of older analogues. It is possible for such grabens to be confined between two major conjugate faults, but, more typically, rift polarity changes, whereby the major bounding fault on one side of the rift dies out and another develops along strike on the other side of the rift. Some workers (e.g. Rosendahl 1987) have envisaged these major faults as having concave traces and allowing differential extension by relay offsets with each other. Others (e.g. Gibbs 1987) have proposed that the bounding faults are relatively linear and that the mechanism that allows rift polarity to

change is the accommodation of differential extension by means of 'transfer faults' which trend at high angles relative to the trend of the rift system. Both fault systems, which allow differing degrees of extension along the rift system, may exist.

The consequences of development of a discrete rift system as a result of crustal extension are:

- ***A marked change in sedimentation.*** A marked unconformity at the top of the pre-rift section is induced by formation of the down-faulted trough, and the sediment input changes markedly from that of the pre-rift stage. The exact nature of the deposition varies according to factors such as provenance, sediment supply and whether a marine incursion happens. Common depositional systems include axial drainage along the rift floor and depositional fans prograding from the rift flanks. Shales may be deposited if water is deep enough. A transition from coarse-grained to fine-grained sedimentation may result from the progressive deepening of the central graben as extension progresses. Evaporites and carbonates may develop if climate and drainage are favourable.

- ***Change in structural style.*** Compared to the pre-rift stage, the structural style of the syn-rift stage is dominated by fewer and larger faults. The most significant of these are major bounding faults of the central graben, although other faults within the graben, which are generally reactivated faults that existed during the pre-rift stage, may have significant throws. The interior of the central graben normally consists of a series of tilted fault blocks, which continue to subside as extension continues. These may stabilise and become draped by syn-rift infill if extension slows and eventually stops. Faults of the syn-rift stage are sub-parallel to the axis of the central graben and are listric.

- ***Change in extension style.*** With the formation of central graben systems at the onset of the syn-rift phase, the manifestations of crustal extension change from the diffuse broad extension of the pre-rift phase to an extension focussed in the zones of the central grabens. The central grabens typically occur as branching systems, whose traces appear to reflect the combined effects of the direction of extension, the pre-existing grain of basement rocks, and the influence of any doming associated with the crustal extension. If doming occurred, 'triple junctions', comprising three radially oriented groups of grabens with 120° spacing between their axes may develop in response to the crustal stretching across the top of the zone (Burke & Dewey 1973).

With continued extension of the crust, the graben systems undergo differential extension along their length.

- ***Change in igneous activity.*** With increasing extension, the character of magma generated evolves from being alkalic towards that of tholeiitic mid-ocean ridge basalt and, as a result, becomes more magnetic. The ultimate product of crustal extension, if it continues, is crustal splitting and the generation of new oceanic crust at a new spreading centre. As a precursor to the development of a new spreading centre, mantle material must move to within approximately 7 km of the base of the crust, as this is the mean thickness of oceanic crust (Bott 1982).

Considerable seismic reflection and refraction data and gravity modelling support the concept of the upward movement of mantle material beneath rifted zones. What does not appear to be so clear from the literature is whether the upwelling material is entirely original mantle material or whether its upper portions are, in effect, an igneous intrusion of magma created from the mantle. Evidence detailed later in this paper suggests that many rifts are underlain by large magnetic bodies that can be considered to be masses of magma generated by crustal extension. As extension progresses, large diapiric igneous intrusions develop along the rift axis and these coalesce into what is, in effect, a large axial dyke of basic/ultrabasic material. Such dykes are a manifestation of the upwelling of mantle material and are the precursors of the systems that generate new oceanic crust. The intrusion of axial dykes may create an axial high on the floor of the rift (Schuepbach & Vail 1980; Vierbuchen et al. 1982). Evidence of this is best defined in seismic data which show isopach thinning over such highs.

Tholeiitic sills, dykes and volcanic flows may be emplaced within the syn-rift section as a result of the magma generation. This igneous activity tends to increase in intensity as the point of crustal rupture is approached, though the volume of igneous material varies considerably between rift systems.

Gravity and magnetic expression of the syn-rift phase. Generally, the gravity expression of the syn-rift stage of extension appears to result from the variable interaction of:

- a broad gravity low, several hundred kilometres wide, which is caused by heated low-density lithosphere—this effect disappears as the heat associated with the extension process dissipates,
- a broad gravity high due to crustal thinning,
- a narrow (approximately 60 km) gravity low due to low-density syn-rift sediments, and
- an axial gravity high due to the ascent of mantle material as a result of extreme crustal thinning and/or igneous intrusion into the crust.

The relative importance of these effects varies as crustal extension progresses (Fig. 3). Note that the combined effects of the broad gravity high resulting from crustal thinning and the gravity low from the low-density syn-rift sediments can result in two gravity highs flanking a gravity low. In any interpretation of gravity over rift systems it is important to realise that such gravity highs do not correspond directly to any excess mass The axial gravity high increases as extension increases and as basic magma and dense mantle material move closer to the surface. Rifts with differential extension along their lengths can have different gravity responses at different places.

The magnetic expression of syn-rift systems (Fig. 3) is not as well documented as gravity expression; however, there are enough examples for the conclusion to be made that magnetic anomalies associated with the extension arise from:

- crustal underplating by magma formed from decompression,
- axial intrusions developed along the axis of the rift as a precursor to crustal splitting; these initially develop as isolated circular intrusions, which eventually coalesce into a linear axial dyke; and
- dykes, sills and lava flows, which become more tholeiitic and more magnetic in character as extension progresses.

The East African Rift system probably provides the best example for study of the syn-rift stage of extension. It is an active extensional system that exhibits all the stages of extension, from the beginnings in southern Africa through progressively increasing degrees of syn-rift extension northwards to the Afar–Red Sea area. Here, the crust has split and oceanic crust has been generated. Most of the other well-studied syn-rift systems in the world are from failed rift systems, where extension has ceased and subsequent processes, such as subsidence and burial, have modified the original character.

The portion of the rift system in northern Tanzania and southern Kenya overlies a broad gravity low, several hundred kilometres wide, which Darracott et al. (1972) modelled as due to low-density lithosphere. This low-density effect is apparently related to the high heat flow observed in the area (Morgan 1982).

Gravity studies (Searle 1970; Khan & Mansfield 1971; Darracott et al. 1972; Fairhead 1976; Swain 1978, 1992) have shown that the graben portions of the rift system in East Africa correspond to narrow gravity lows caused by low-density syn-rift sediment infill. An axial gravity high can be noted in the centre of the narrow gravity low north of 4°S which

progressively increases northwards to the area of the Afar Triangle. There, it merges with a broad triangular gravity high, which is due to thinned continental crust increasingly intruded by mantle material towards the north, where extension is the greatest (Makris et al. 1975, 1991). The axial gravity high has been variably interpreted as due crustal thinning bringing dense mantle material closer to the surface, an igneous intrusion overlying the thinnest crust, or a sheeted dyke intrusion into the crust. It is probably due to a combination of all these factors. The northward increase in the amplitude of the axial anomaly can be taken as indicating greater crustal thinning and intrusion of the crust by magma.

Compilations of magnetic data over portions of the East African Rift system have been published by Wohlenberg (1975), but evidence for a magnetic expression due to an axial dyke is difficult to identify. The most probable reason for this is that the areas of Wohlenberg's compilations are located near the magnetic equator, where the inclination of the Earth's magnetic field is almost horizontal. Here, a north-striking linear feature, such as any axial dyke associated with the East African Rift system, will have only minor magnetic expression except near its ends (see the models of Vacquier et al. 1951 for verification of this assertion). Wohlenberg did, however, identify magnetic anomalies that appear to be associated with the axial dyke. It is not clear from his results if these are due to isolated anomalies aligned on the crest of the dyke or a semi-continuous anomaly. Figure 5 illustrates the gravity and magnetic features of the East African Rift in southern Kenya.

Many rift systems that have failed at the syn-rift stage illustrate similar features.

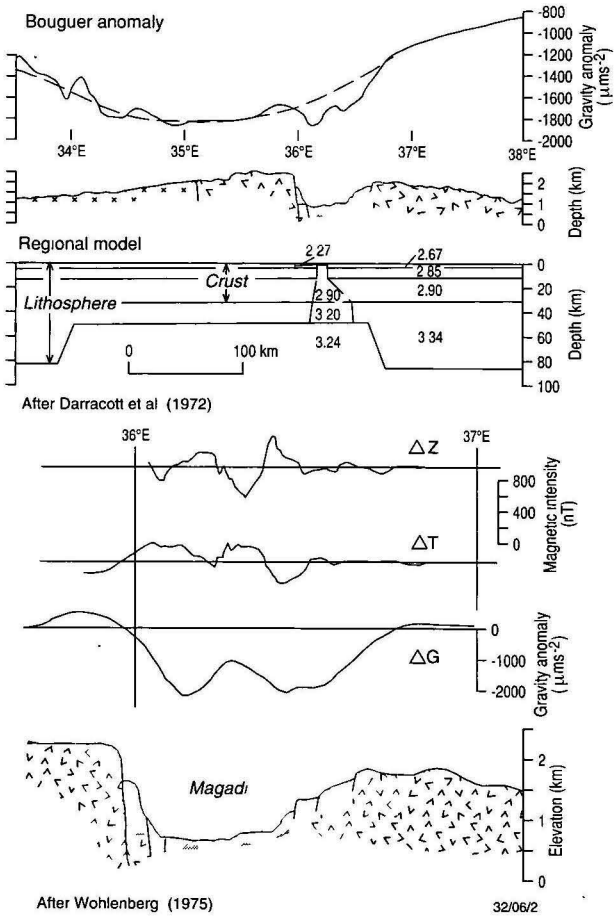

Figure 5. Gravity and magnetic profiles across the East African Rift, showing the broad regional gravity low due to the heated low-density mantle and upper crust, a gravity low over the rift due to low-density sediments in the rift, and a central gravity high within the gravity low over the rift due to an axial intrusion that appears to have a magnetic expression.

The Rhine Graben (Illes 1978) is part of a Tertiary continental rift system extending from the North Sea to the Gulf of Lyon. Although it does not seem to be extending at present, it appears to present an example of a preserved syn-rift system that has not been deformed. Werner & Kahle (1980a, b) presented a detailed analysis of the gravity field of the area, which consists of a broad gravity high with an amplitude of approximately 400 $\mu m.s^{-2}$ with a superimposed crestal axial low. They identified a localised gravity low, with amplitude up to 400 $\mu m.s^{-2}$, approximately 300 km long and 60 km wide, which they account for by the low-density sediment infill of the rift. Seismic studies listed by Werner & Kahler (1980a, b) show thinning of the crust to 25 km under the Rhine Graben. They produced a gravity model of the crust–mantle interface based on the crustal morphology defined by these seismic studies and showed that a regional gravity high of the order of 1000 $\mu m.s^{-2}$ is expected. They explained the gravity deficiency by the existence, beneath the Rhine Graben, of a deep-seated thermal anomaly, which they consider to have locally lowered the density of the lithosphere. The fact that the Rhine Graben occurs at the crest of a domal uplift (Cloos 1939) and overlies an area of elevated heat flow (Morgan 1982) suggests that the elevated heat-flow regime associated with the extension has not yet dissipated and is still influencing the regional gravity field.

The magnetic field of the Rhine Graben is less well studied than the gravity field. Edel et al. (1980, fig. 1) show an axial magnetic anomaly at least 80 km long in the vicinity of Strasbourg, which is the area of thinnest crust under the rift. Contour gradients indicate that this feature arises from a magnetic source approximately 6 km below the surface. This feature may be a magnetic axial dyke. Further north, as shown in magnetic data published by Campos Enriques et al. (1992), a major deep-seated magnetic anomaly occurs under the western side of the Rhine Graben. This could also be due to intrusion of a major dyke. Illes (1978) presented a map showing areas of uplift on the graben floor which show a close correlation with the positions of the major magnetic anomalies. High temperatures beneath the rift may raise the temperature in any underplated magma above the Curie point and thus preclude any magnetic response from this source.

The Oslo Rift (Neumann et al. 1992; Wessel & Husebye 1987) is a Permian rift in Norway that has been deeply eroded so that the igneous components of its floor have been exposed (Fig. 6). An intense alkalic igneous history has been revealed with stages progressing through widespread basalt magmatism in the pre-rift stage. A change to porphyry lavas with the onset of the syn-rift phase followed, with a progressive change from shield volcanism to central volcanoes and batholith intrusion. A regional gravity high over the rift (Ramberg 1976) is due to the combined effects of crustal and lithospheric thinning relative to adjacent shield areas and a 12 km thick high-density, high-velocity body in the lower crust under the rift axis and shoulders. Wessel & Husebye (1987) have interpreted the lower crustal feature as being due to dense cumulates and mantle-derived magmas. The deep magma accumulations are thought to have acted as source chambers for the lavas and magmas that reached the surface. A relatively rigid upper crust is thought to have forced the lateral spreading of these magmas. Regional magnetic data over the rift (Husebye & Ramberg 1978) show a major magnetic high with a deep-seated origin that correlates perfectly with the axis of the rift. This high is apparently produced by the magma chamber. Neumann et al. (1992) presented a detailed profile across this high and diagrammatically showed its relation to the magma chamber.

The Midland Valley of Scotland and Northern Ireland (Francis 1978; Cameron & Stephenson 1985) is a Devonian–

Carboniferous rift that failed at the syn-rift stage and which is comparatively well exposed as a result of later uplifts of the British Isles. McLean & Qureshi (1966) showed that the gravity field of the area is a broad high with a superimposed low. After correcting for the low density infill of rift, they defined a regional high, which they interpreted as indicating thinned crust under the rift. Seismic refraction results (Bamford 1978) which show high-velocity material at anomalously shallow depths beneath the Midland Valley seem to indicate crustal thinning or lower crustal transformations beneath the rift.

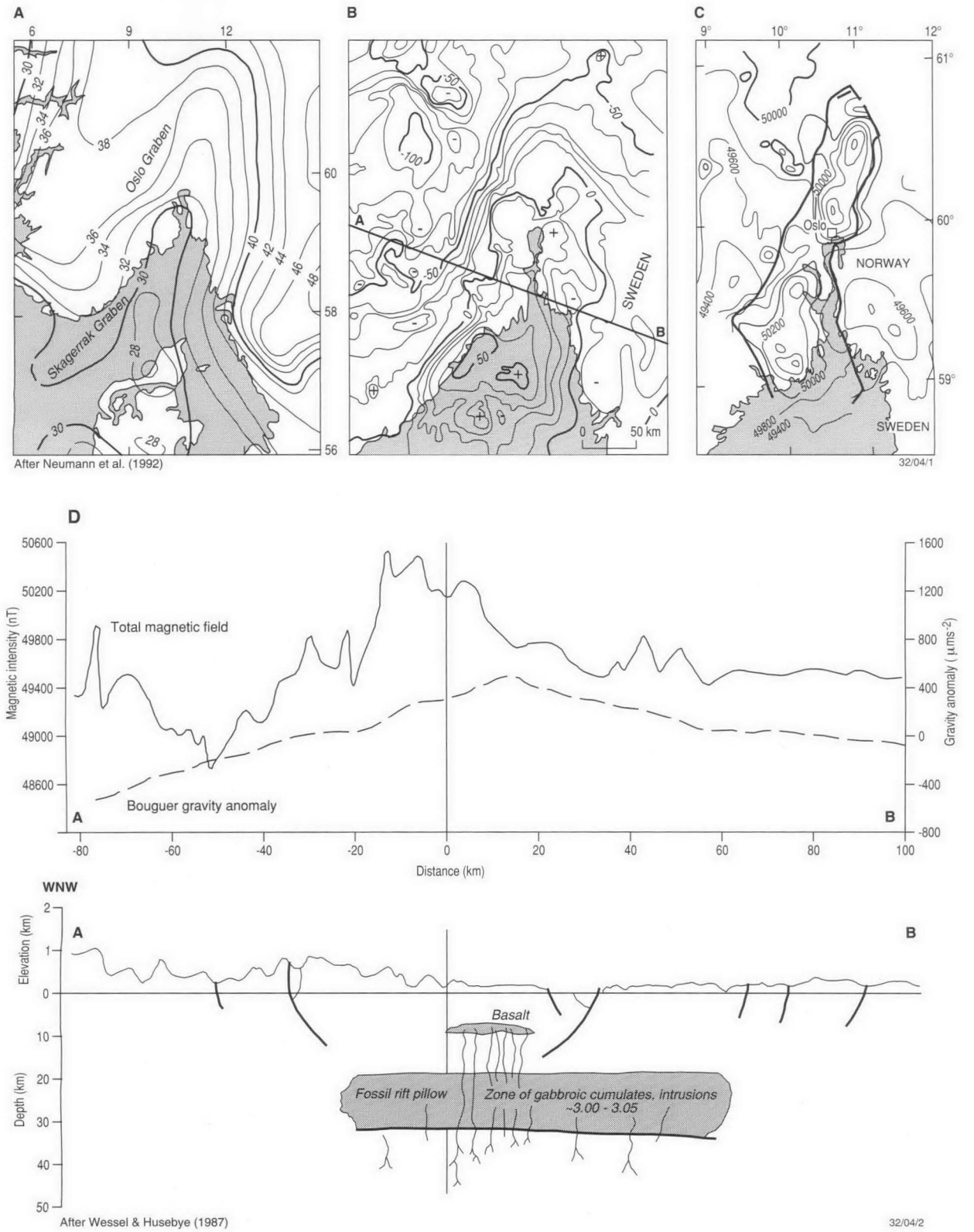

Figure 6. Regional magnetic and gravity fields of the Oslo Graben, showing a broad gravity high interpreted as being due to a combination of crustal thinning and a magma chamber in the lower crust. The magma chamber appears to be responsible for the large magnetic high that corresponds to the rift boundaries. (A) depth to Moho in km. (B) gravity field (units are 100 μms^{-2}). (C) magnetic field (units are nanoteslas). (D) detail and interpretation of Section AB.

The magnetic field of the Midland Valley, as mapped by regional surveys (IGS 1972), shows intense magnetic anomalies due to extensive Lower Carboniferous alkali dolerite lava flows and sills confined within the bounding faults of the rift. An Upper Carboniferous series of tholeiitic sills is confined within the rift and an associated series of dykes extends outside the rift. The evolution of magma type may reflect progressive crustal extension. Hall & Dagley (1970) filtered the aeromagnetic data in a manner that removed the effects of shallow sources to define the effects of deeper major features, and revealed that the Midland Valley overlies a major magnetic anomaly. This feature could be due to a magma chamber or crustal underplating by magma. The seismic refraction studies by Bamford (1978) revealed high-velocity material, which may be due to a magma chamber, approximately 10 km beneath the rift.

The magnetic anomaly map over the Midland Valley also shows three large circular magnetic anomalies. These correlate with localised gravity highs along a narrow linear gravity high on the axis of the rift, within the gravity low caused by the low-density sediments filling the rift (Davidson et al. 1984). The largest of the magnetic features, known as the Bathgate Magnetic High, was modelled by Gunn (1975), who interpreted it as due to an intrusive body approximately 11 km across with its top at 10 km deep. The axial gravity high may be due to the development of an intrusive axial dyke, and the magnetic anomalies to diapiric magma culminations along the axial dyke.

The Benue Trough of Nigeria (Benkhelil et al. 1988) is an elongate Mesozoic rift system with an axial basement ridge. All gravity profiles across the Benue Trough can be broken down into three main components:

- a regional gravity high, reflecting thinning of the continental crust,
- a superimposed negative anomaly due to the sediment infill in the trough, and
- an axial positive anomaly, which Freeth (1984) interpreted as due to the separation of the Earth's crust and the consequent intrusion of sheeted dykes.

Gravity and aeromagnetic interpretations by Ofoegbu & Onuoha (1990) and Ofoegbu (1984) support the concept that the axial basement high contains basic intrusions and is thus likely to be related to axial dyke intrusion induced by crustal extension. The axial high decreases northward, where the rift has been interpreted to have undergone less extension. The southern limit of the axial ridge correlates with a cluster of intrusions that have reached the surface. The intrusions of the Benue Trough manifest themselves as magnetic lows because they are located close to the magnetic equator, where magnetisation by induction results in magnetic lows.

Many Australian rift systems that failed at the syn-rift stage have gravity and magnetic signatures that accord with the above descriptions and the idealised profiles (Figs 3, 4).

Examples include:

- The Canning Basin of Australia (Purcell 1984), which contains a half-graben system known as the Fitzroy Trough.

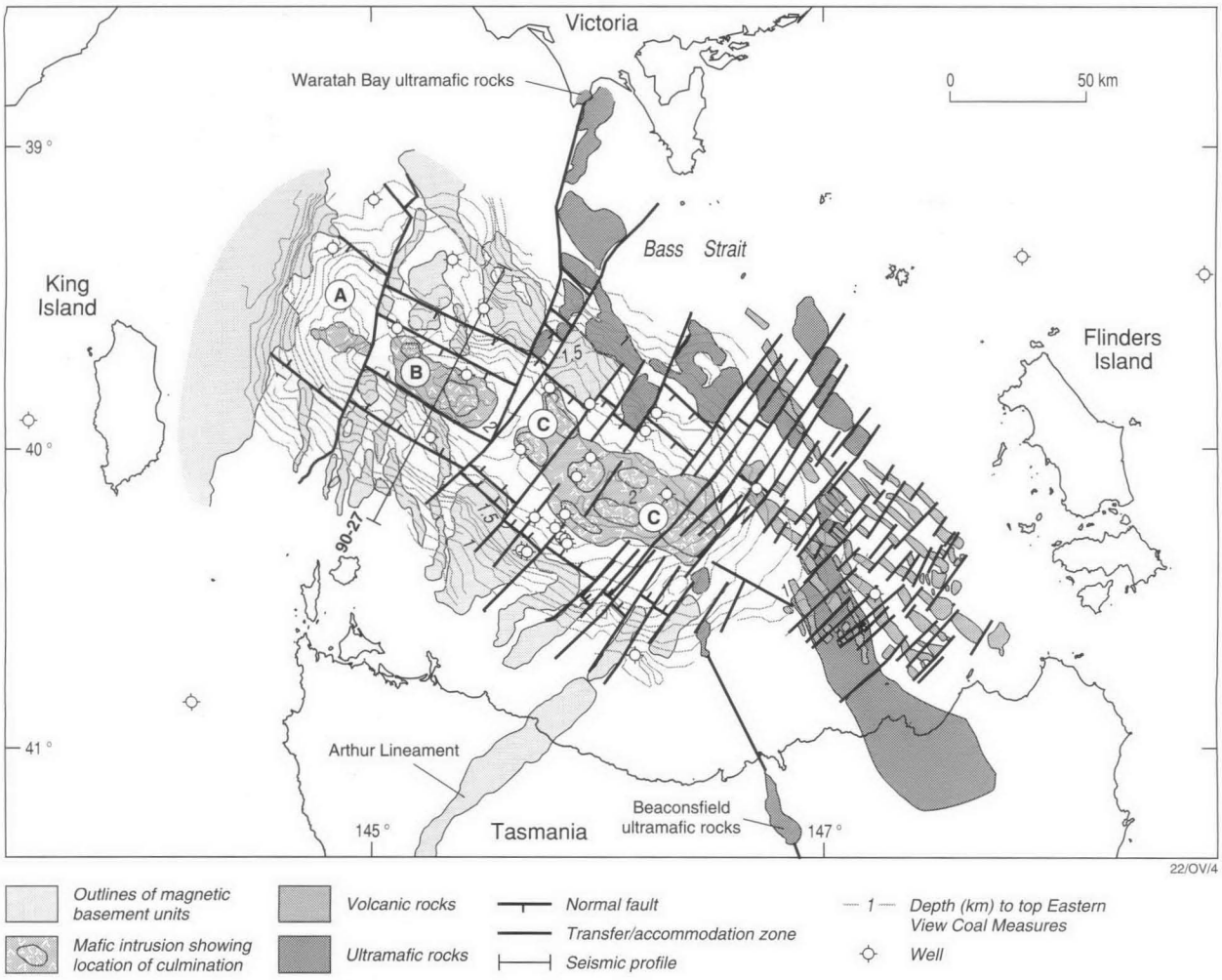

Figure 7. An interpretation of magnetic and gravity data over the Bass Basin of southeastern Australia which has identified major mafic bodies developing under an extensional basin (after Gunn et al. 1996). Three compartments (A, B and C) have been identified which under went different degrees of extension. The size of the mafic bodies correlates with the amount of extension of the compartments.

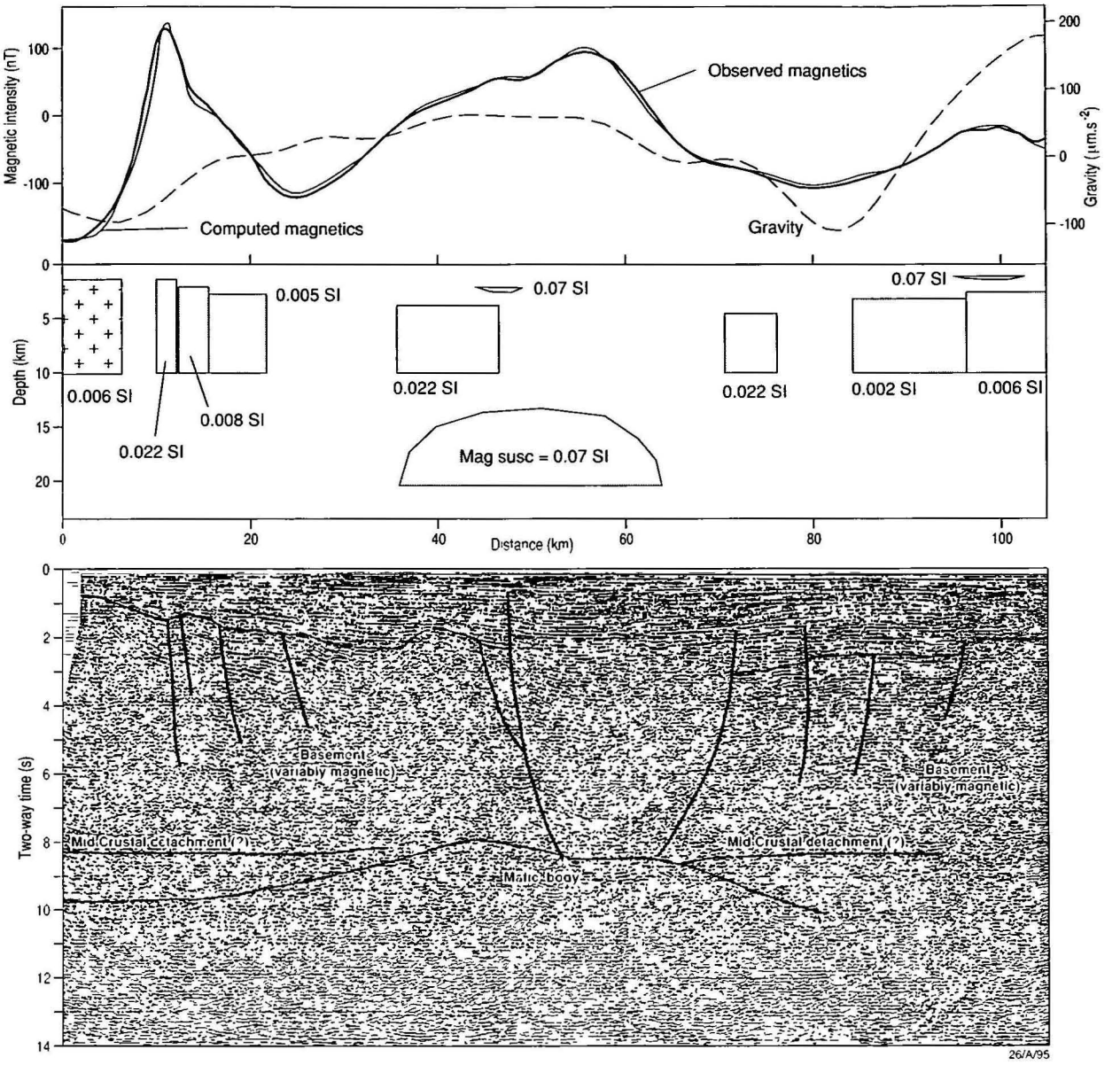

Figure 8. Modelling of gravity and magnetic data over the Bass Basin which has defined a major mafic body beneath the main basin depocentre. The form of this mafic body can be traced on 14 second reflection data (after Gunn et al. 1996).

The gravity expression of this area (Anfiloff 1984) shows a classical profile of a low over the low-density trough infill, flanked by positive 'shoulders' adjacent to the actual rift zone. The positive shoulders are probably due to thinned crust (cf. Fig. 3). Several major circular magnetic anomalies occur along the axis of the rift (Tucker et al. 1984 fig. 2). These may mark the beginnings of the development of an axial dyke.

- The Bass Basin between Tasmania and Victoria (Williamson et al. 1985), a failed Mesozoic extensional system, is underlain by large elongated oval magnetic intrusions about 10–15 km deep (Gunn et al. 1996). The intrusions can be interpreted as mafic bodies resulting from crustal extension. The gravity field over the basin (BMR 1992) shows a gravity low with central positive peaks. The gravity low can be explained by the low-density sediments in the basin and the central positives could be due to the intrusions underlying the basin. The intrusions, whose relative sizes correspond directly to degees of apparent crustal extension and basin development, are evident in 14 second seismic reflection data (Figs 7 & 8).
- The Bonaparte Basin of northwestern Australia, which contains a failed Devonian–Carboniferous rift, seems to have been preserved in a situation exhibiting all stages of rifting. These include the earliest stages of a pre-rift system through to a syn-rift system that has proceeded to crustal splitting (Gunn 1988). The gravity and magnetic responses of this rift are described below.

(iii) Rupture of the continental crust and insertion of oceanic crust

If extension progresses to the point where the continental crust ruptures, the split frequently appears to be along the axis of the rift axial dyke system (Sheupbach & Vail 1980). This results in the separation of the rift system into two, each half containing a fragment of the axial dyke.

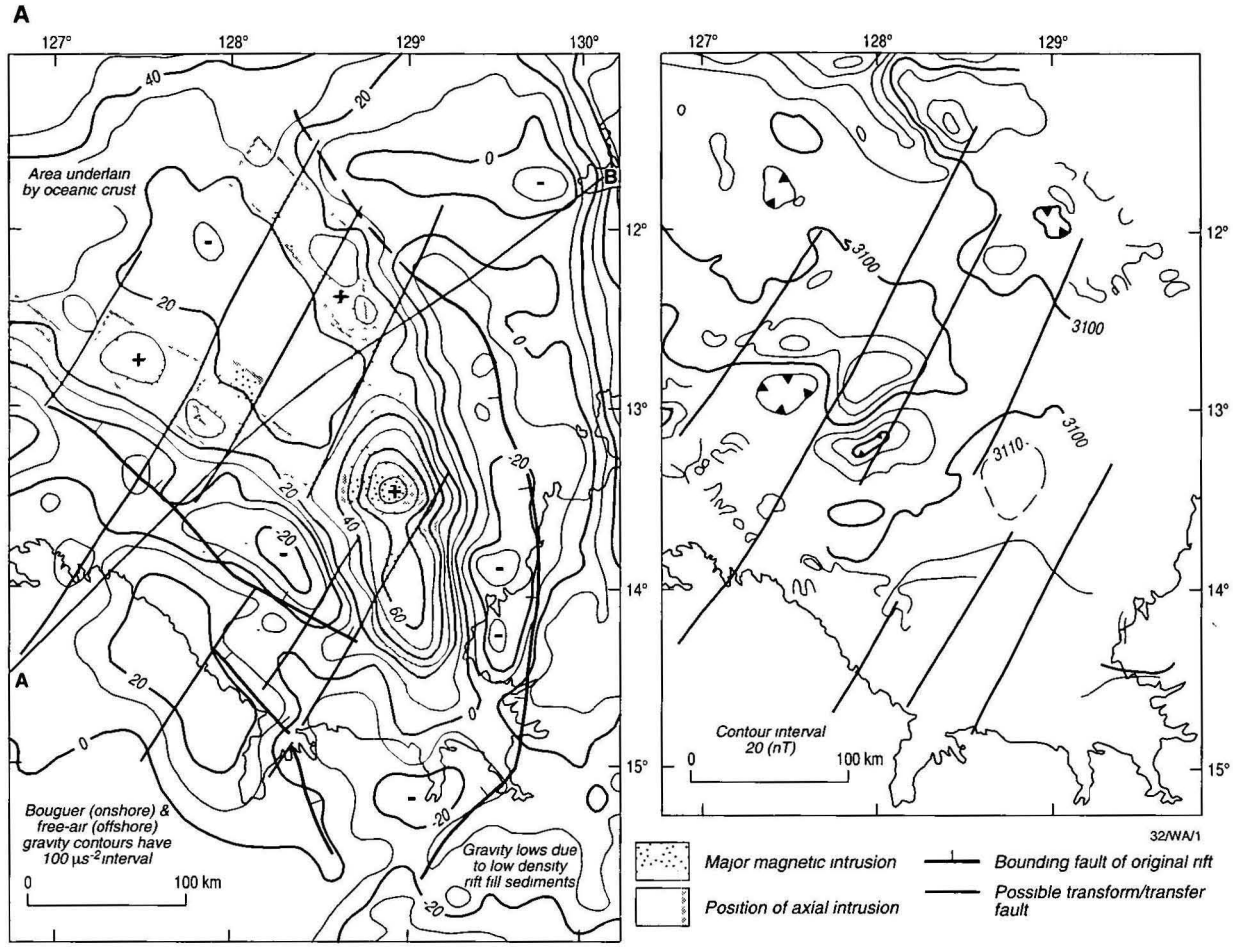

Figure 9A. Gravity and magnetic fields of the Joseph Bonaparte Gulf. An axial gravity high that increases in amplitude towards the northwest is evident. This has been interpreted as being due to progressively greater crustal extension in this direction accompanied by the development of an axial dyke. A limited amount of crustal splitting and generation of intermediate oceanic crust appears to have occurred at the northwestern limits of the area.

Crustal splitting may not occur on all arms of a rift system. Where multiple rift junctions occur, splitting is normally on two adjacent arms of the system, with the result that some rift arms may be left frozen without progressing to the crustal splitting stage. Such failed rifts are the aulacogens of Burke & Dewey (1973).

The best contemporary example of rupture of continental crust and transition to the initial stages of oceanic crust formation appears to be the Red Sea (Girdler 1991). Cochran (1988) described a transition from late-stage continental rifting at its northern end, through a transitional zone, to an area of oceanic crust and active spreading midway further to the south. In these areas, the outline of the Red Sea broadly corresponds to a downfaulted area approximately 100 kilometres wide. An axial depression with localised deeps appears to correspond to the area of maximum crustal extension and where the crust splits and oceanic crust eventual develops.

In analyses of magnetic data of the area, Cochran (1983) and Bonatti (1985) noted a series of isolated magnetic anomalies along the axial trough, increasing in magnitude southward and ultimately coalescing into a continuous magnetic ridge. These magnetic highs are interpreted as intrusions over local hot spots that eventually elongate and accrete into an axial intrusive dyke, which consists of magma produced by mantle differentiation. South of 19° in the region where oceanic crust is interpreted as having been emplaced, the axial trough widens and deepens. Linear magnetic anomalies are evident which have been identified as classical oceanic magnetic stripes caused by polarity reversals of magma created at an oceanic spreading centre.

The gravity field of the Red Sea (Cochran 1991; Makris et al. 1991) consists of a broad regional high due to crustal thinning under the Red Sea (known from seismic data). A gravity low, superimposed on this broad low, was explained by Cochran as being due to the low-density infill of the downfaulted area of the Red Sea. This is compounded by decreases in crustal density caused by the elevated heat flow in the area. Cochran's (1991) gravity modelling of a profile in the area of late-stage continental rifting identified a narrow dense body in the upper crust underlying the axial trough. This has been identified as being due to the intrusion of mafic material. Cochran's profile traverses an area where the axial trough is flanked by two large intrusions, which rise to higher levels than the dense material underlying the axial trough. These intrusions, which cause gravity and magnetic anomalies, have all the appearance of being fragments of an initial axial dyke that was split along its centre and subsequently intruded by oceanic crustal material.

Regions of differing extension about 60 km long have been noted along the length of the Red Sea. Transverse 'transfer fault' zones have been identified separating these areas.

The Joseph Bonaparte Gulf region in northwestern Australia is underlain by a failed Devonian–Carboniferous rift system that appears to contain elements showing transition from unruptured continental crust through to an area where some oceanic crust may have formed (Gunn 1988). Gunn's inter-

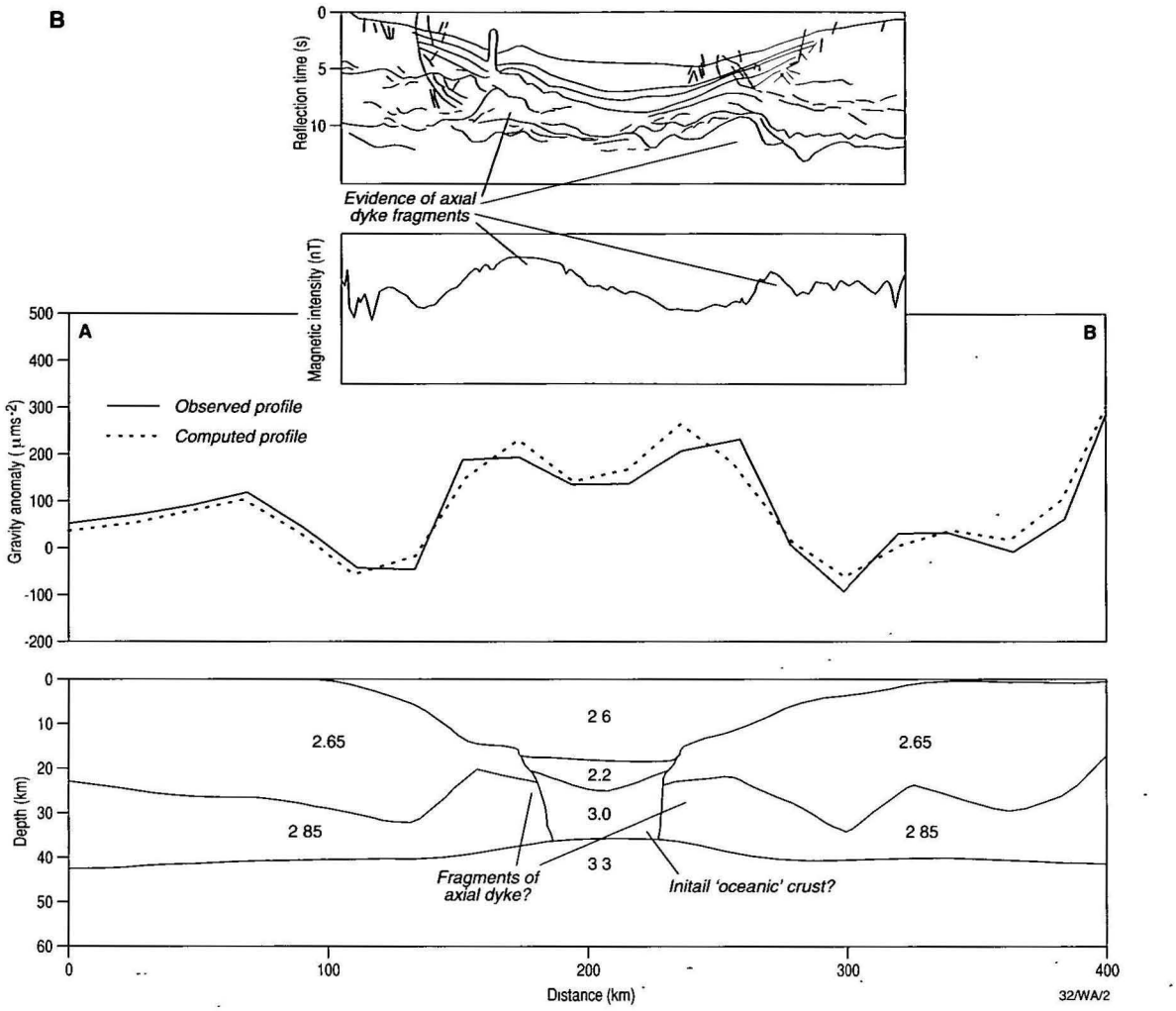

Figure 9B. Deep seismic reflection data along profile AB of Figure 9A. and modelling of gravity data supporting this concept of crustal splitting at the northern end of the Joseph Bonaparte Gulf. Magnetic highs that flank the area of postulated oceanic crust can be interpreted as due to fragments of axial dyke. The seismic data show evidence of these fragments. The gravity modelling is from Mory (1991) and the seismic interpretation is based on work by B. McConachie of the Australian Geological Survey Organisation.

pretation (Fig. 9), based on geological mapping and gravity, magnetic, seismic and drilling data, is that the area underwent differential extension with the degree of extension increasing northward. The gravity low at the southern end of the rift system is due to low-density sediment infill. Flanking gravity highs are 'shoulders' (cf. Fig. 3) reflecting thinned crust. The central gravity high, which increases in amplitude northward, is due to an axial dyke that gets progressively larger and shallower towards the north. Lows flanking this high are due to low-density sediments. Bifurcation of the axial gravity high is thought to indicate splitting of the axial dyke and the formation of oceanic crust between its fragments. Regional magnetic data support this interpretation (Fig. 9). Computer modelling of the gravity field in the area where crustal splitting is interpreted as having occurred is broadly consistent with the interpretation (Mory 1991). Deep (14 s) seismic reflection, gravity and magnetic data, recorded by the Australian Geological Survey Organisation during 1991 (Line 100/03) across the area where crustal splitting is interpreted to have occurred, indicate dense, magnetic diapiric features on either side of the area interpreted to be underlain by oceanic crust (McConachie 1996). These may be fragments of the axial dyke, as interpreted by Gunn (1988).

Studies, using aeromagnetic data, of the fracture pattern of the underlying basement have shown that the differential extension in the basin was accommodated by a series of northwesterly trending transfer faults (Fig. 9). The fracture patterns are demonstrated in data published by Gunn et al. (1995a) and in the aeromagnetic map of Australia (Tarlowski et al. 1997).

(iv) Sea-floor spreading and the development of continental margins

After the continental crust has split, a spreading centre may develop and oceanic crust form between the fragments of continental crust. As the continental fragments move further from the hot spreading centre, cooling of the continental crust causes contraction of the crust and mantle, resulting in subsidence of the continental margins. This subsidence may stimulate sediment progradation over the margin and further subsidence under the weight of sediment. The fragment of the axial dyke may be buried beneath sediment. If the axial dyke caused an uplift on the rift floor before crustal splitting, the uplift may be evident as a buried 'outer high' beneath the edge of the continental shelf.

Crustal splitting appears to occur roughly along the axis of the rift system. If the rift system is a half-graben, the fragments on either side of the split will differ. One side will contain the major bounding fault and a series of subsidiary tilted blocks, whereas the other will consist of what is effectively

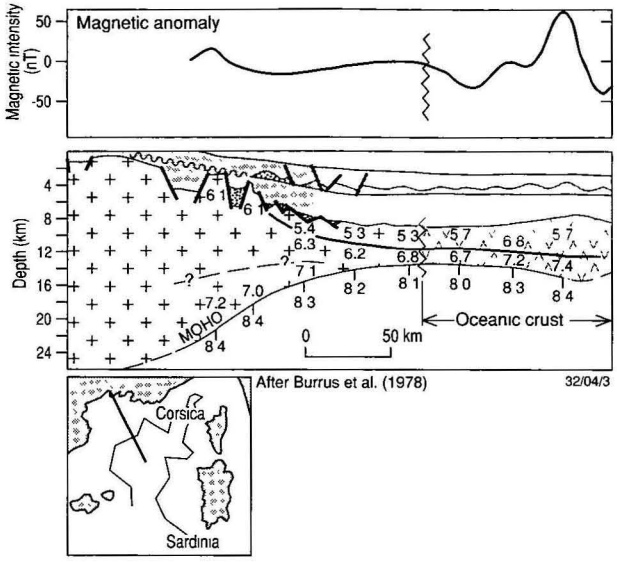

Figure 10. Correlations of seismic reflection and refraction results in the Gulf of Lyon in the Mediterranean showing a quiet magnetic zone over an area of transitional oceanic crust situated between an "outer high" magnetic anomaly on the seaward edge of the continental crust and magnetic anomalies over true oceanic crust.

a ramp containing a series of smaller faults. The splitting sometimes happens along one side of the rift system with the result that the complete floor of the rift is attached to one continental fragment. This seems to have happened along the east coast of Australia, where the eastern margin of Australia lacks any rift fragment and a complete rift floor appears to be attached to the western side of the Lord Howe Rise. Lister et al. (1991 fig. 18) illustrate a section across eastern Australia and the Lord Howe Rise that is consistent with this idea. Their figure shows igneous intrusions flanking the area of ocean crust. These are possibly fragments of the axial dyke and, if they are, they would have developed on the western side of the rift, where the splitting occurred.

The magnetic pattern of rifted margins changes from the magnetic response of the pre-existing basement on the landward side of the rift to a combined response of the basement plus the sedimentary and igneous rocks in the fragment of the rift system preserved on the margin The zone of crustal splitting is typically traced by a major linear magnetic anomaly caused by the fragment of the axial dyke split during crustal rupture.

The ultimate product of crustal splitting is an active mid-ocean spreading centre producing magnetic mid-ocean ridge-type basic magmas. These are symmetrically distributed on either side of the spreading centre as a result of the magma upwelling in a process resembling a convection cell. Characteristic oceanic magnetic lineations are produced symmetrically on either side of the spreading centre as reversals in the Earth's magnetic field cause reversals in the remanent magnetism of the magmas (Kearey & Vine 1990). Broad Bouguer gravity lows correlate with active oceanic spreading centres.

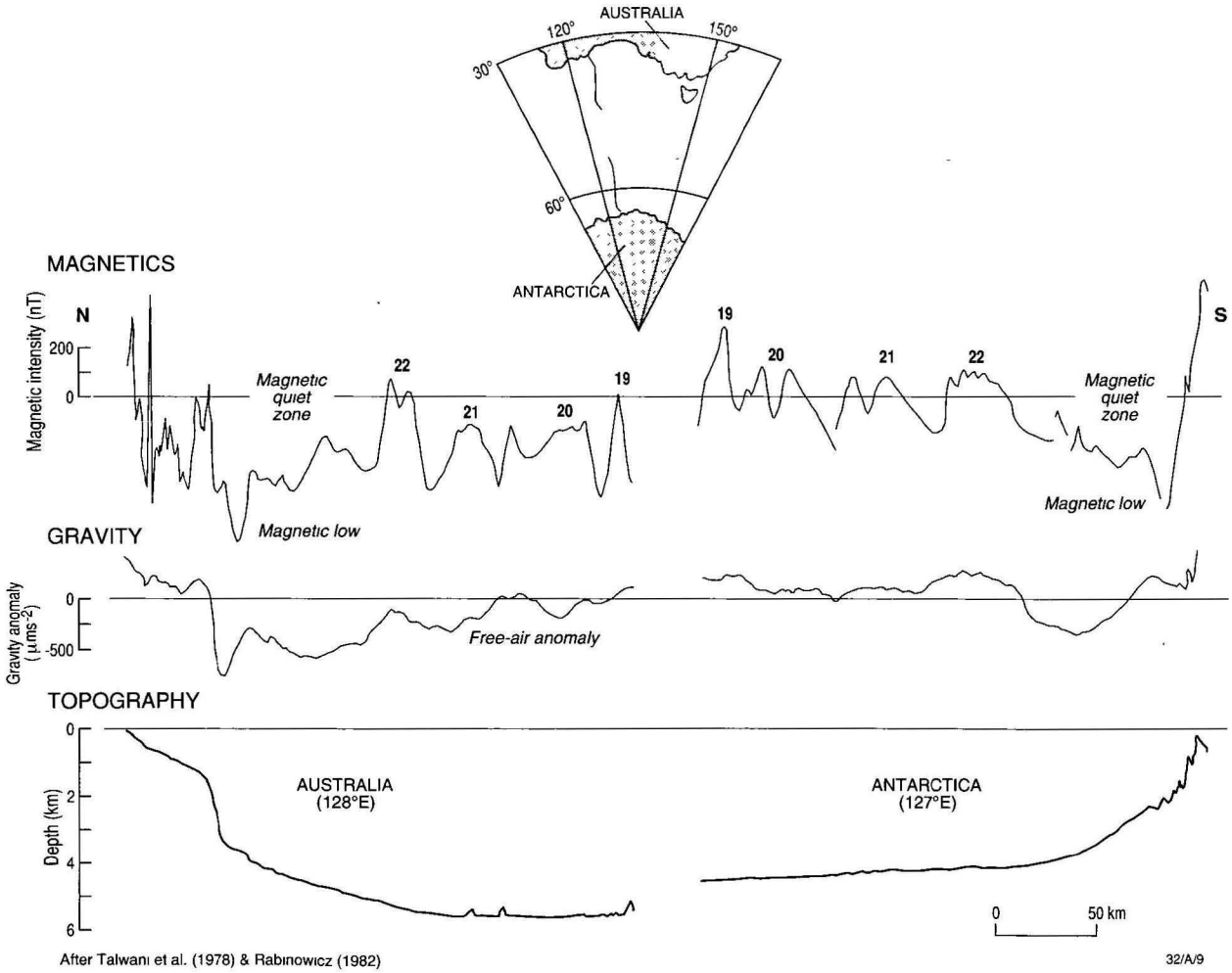

Figure 11. Gravity and magnetic profiles over the Australian and Antarctic continental margins. It should be noted that both margins have 'magnetic troughs'. These can be interpreted as being due to reversely magnetised fragments of axial dyke.

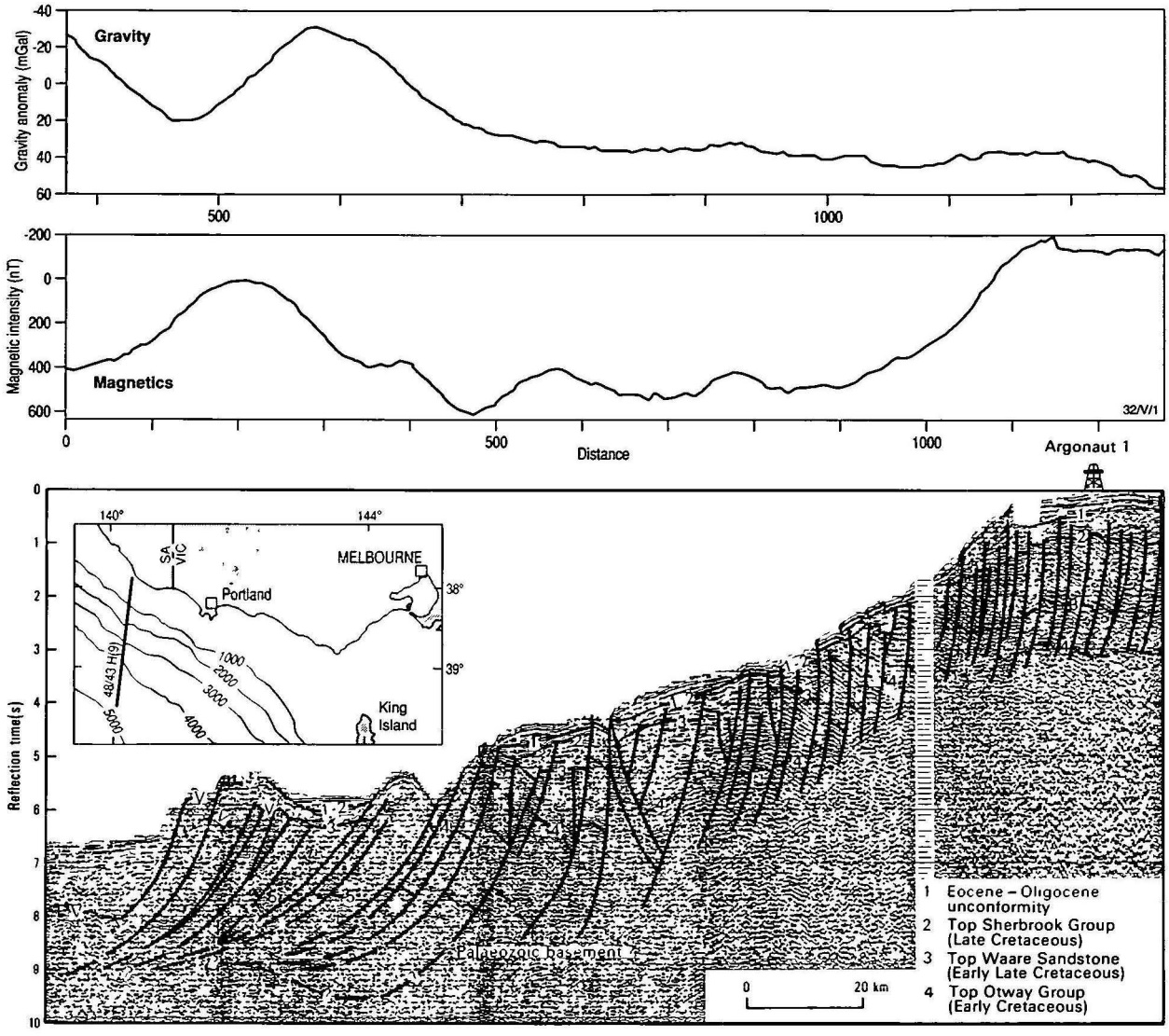

Figure 12. Profile over continental -oceanic boundary of Otway Basin in southeastern Australia. An outer high can be noted in the seismic reflection data (interpreted by Exon & Lee 1988) that is coincident with a magnetic high and a free air gravity high.

These have been interpreted by Talwani et al. (1965) to be due to low-density heated mantle and lower crustal material generating magmas at the spreading centres.

While it could be expected that the crust immediately seaward of the zone of crustal splitting would be normal oceanic crust, this does not appear to be the case. A 'magnetic quiet zone', typically up to several hundred kilometres metres wide, often occurs between the outer high magnetic anomaly and the oceanic crust containing the typical magnetic stripes of oceanic crust. Rabinowicz (1974), Talwani et al. (1978) Cochran (1983) and Burrus et al. (1987) gave examples of such quiet zones and, from their discussions of related data, these appear to correspond to areas of crust that is transitional between true continental crust and true oceanic crust. In some instances, magnetic quiet zones may correspond to a long constant polarity period that occurred in the Cretaceous, during which there were no magnetic field reversals (Harland et al., 1982).

A comprehensive world-wide study by Rabinowitz (1982) showed that distinct elongate belts of free air gravity anomalies are ubiquitous to passive continental margins (e.g. Fig. 8). They consist of a positive peak near the shelf break and an adjacent seaward gravity low. The positive gravity peak, which commonly correlates with a magnetic high, has been interpreted

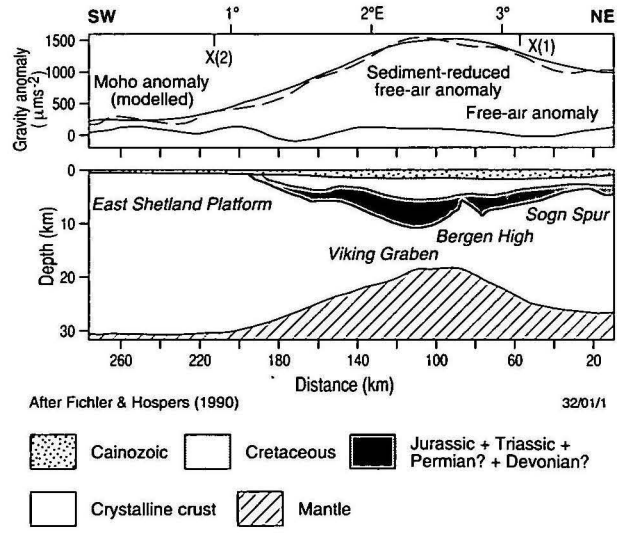

Figure 13. Gravity over the Viking Graben, North Sea. The absence of a significant gravity anomaly can be explained by the effect of low density post-rift sediments cancelling the effect of crustal thinning. The outlines of the sediment section and the base of the crust have been obtained from seismic data.

as being due to a dense intrusion into the upper crust. The seaward gravity low is probably due to the combined effects of a decrease in water depth and the transitional nature of the crust in this area, where the crust changes from 30–40 km of continental crust to approximately 7 km of oceanic crust.

The magnetic highs along the outer edge of continental shelves are generally recognised as marking an elevated edge of what can be regarded as magnetic oceanic crust. The elevated edge can be explained as a fragment of the axial dyke intrusion which developed immediately before continental rupture. Evidence for the splitting of the dyke into halves is provided by the fact that these continental edge magnetic anomalies can be recognised on the conjugate sides of oceans that have been created by spreading associated with rifting. Guenoc et al (1988) gave several examples from the Red Sea which appear to illustrate how a single axial dyke intrusion can be split down its axis with subsequent development of oceanic crust in a depressed area between the fragments.

Although the original junction between continental and oceanic crust is commonly marked by gravity and magnetic highs, these anomalies may be well landward of the shelf break as a result of sediment progradation widening the continental shelf (Fig. 4).

The eastern continental margin of the United States is marked by a linear positive magnetic anomaly several thousand kilometres long, known as the East Coast Magnetic Anomaly (Rabinowicz 1974, Behrendt & Klitgord 1980). This feature seems to be a continental margin magnetic anomaly.

Burrus et al. (1987) presented a correlation of crustal thickness and seismic velocity and a magnetic profile over a transition from continental crust to oceanic crust in the Gulf of Lyons in the Mediterranean (Fig. 10). Their section illustrates the magnetic high at the seaward edge of the continental crust, the magnetic quiet zone over the transitional crust, and the magnetic highs characteristic of oceanic crust.

The western part of the Galicia Bank (offshore Spain) is bordered, over a distance of about 125 km, by a ridge of peridotite (Malod et al. 1993), which was emplaced immediately before the opening of the North Atlantic in the area. The intrusions are also visible in seismic data, which indicate that they have domed overlying sediments. The peridotite intrusion, which is associated with a magnetic anomaly, appears to be the best documented example of the association of a continental margin magnetic anomaly, an 'outer high' and a fragment of axial dyke.

The southern margin of Australia, centred on the Great Australian Bight, contains a 'magnetic trough' that matches a similar magnetic trough on the conjugate Antarctic margin (Rabinowicz 1982: Talwani et al. 1978). These anomalies (Fig. 11) appear to be due to fragments of a reversely magnetised axial dyke.

The continental margin of southeastern Australia was produced by the separation of Australia and Antarctica (Falvey 1974). A profile of seismic reflection, gravity and magnetic data over the continental-oceanic crustal boundary on the southern margin of the Otway Basin (Fig. 12) shows all the features described above as being typically associated with continental margins produced by extensional pull-apart.

Gunn (1984) identified an elongate, narrow, positive magnetic anomaly, about 1000 km long, on the western margin of the Adelaide Geosyncline Proterozoic rift system in South Australia, as being due to an axial-dyke type intrusion. Gunn cited evidence to indicate that the source of this feature correlates with positive gravity anomalies, caused sediment doming and occurs on the junction between shelf sediments and a major depocentre. If an axial dyke was intruded and the crust separated beneath the Adelaide Geosyncline, the anomaly would be due to a fragment of the dyke. Alternatively, it could be due to an axial-dyke type intrusion along the western edge of the original rift system.

(v) Rift failure

Crustal extension may stop at any stage and fragments of the system as developed at that time may be preserved as 'failed rifts'. These failed rifts may be buried by sediments accumulating in depressions resulting from post-extension subsidence. Later erosion may expose early stages of the extension process and it is important to take account of this possibility when studying fossil extensional systems.

If extension ceases before crustal splitting occurs, the thermal anomaly associated with crustal thinning will dissipate and contraction will cause subsidence. A depression will develop over the failed rift system, which, providing enough sediment is being supplied, will develop as a 'post-rift' or 'sag phase' sequence. The load of the sediment will also contribute to the subsidence. Post-rift sequences typically have greater lateral extent than the syn-rift sequences they blanket.

The regional magnetic expression of the post-rift stage does not change from the earlier stages, because igneous activity stops with the cessation of extension and the subsequent cooling by conductive heat loss. An exception to this generalisation could happen if cooling lowered the temperature of deep magma accumulations below the Curie point, thereby causing them to have a magnetic response not present when their temperature was above the Curie point.

The gravity response of failed rifts covered by post-rift sections depends on the relative contributions of the gravity low caused by the low-density syn-rift and post-rift sediments and the gravity high caused by the thinned crust remaining under the zone of extension.

Fichler & Hospers (1990) made a detailed study of the gravity field over the North Sea failed Jurassic rift system, using detail obtained from seismic reflection data and deep seismic reflection profiling of the Moho configuration. Their study showed that the gravity effect of the classic post-rift section almost exactly cancels out the effect of crustal thinning. As a result, observed gravity values in the area give little indication of the underlying rift system (Fig. 13).

A different response is observed in Bonaparte Gulf, which as discussed above, contains a failed rift system that appears to show all the stages of rifting from rift initiation to crustal splitting. Sections by Gunn (1988) show the rift to be covered by a classic post-rift section that increases in thickness and extent towards the northern areas of the Gulf, where crustal extension reached its maximum. The gravity responses of the elements of the rift system can be observed despite a cover of low-density post-rift sediments (Fig. 7). At the northern extremity of the rifted area, however, where the thickness of post-rift sediments is greatest, the gravity low due to these sediments is becoming the dominant gravity response.

Conclusion

Gravity and magnetic anomalies associated with crustal extension and rifting vary according to the stage of extension, the degree of crustal thinning, the type of sediment filling any associated depocentre, and the intensity of any associated igneous activity. However, as is illustrated by the examples presented above, despite these complexities, it is possible to generalise the range of responses that can be expected to be associated with any of the stages of extension. It is essential to be aware of these responses before attempting any interpretation of gravity and magnetic data over extensional terranes. Virtually all the gravity and magnetic responses that the author has observed over known rift systems accord with the ideas presented in this paper.

References

Ajakaiye, D.E., 1970. Gravity measurements over the Nigerian Younger Granite Province. Nature, 225, 50–52.

Anfiloff, V., 1984. The gravity field of the Canning Basin. In: Purcell, P.G. (editor), The Canning Basin, W.A. Proceedings of the GSA/PESA Canning Basin Symposium, Perth, 1984, 287–298.

Artemjev, M.E. & Artyushyov, E.V., 1971. Structure and isostasy of the Baikal Rift and the mechanism of rifting. Journal of Geophysical Research, 76, 1197–1211.

Bamford, D., Nunn, K., Prodehl, C. & Jacob, B., 1978. LISB-IV Crustal structure in northern Britain. Geophysical Journal of the Royal Astronomical Society, 54, 43–60.

Behrendt, J.C. & Klitgord, K.D., 1980. High sensitivity aeromagnetic survey of the U.S. continental margin. Geophysics, 45, 1813–1846.

Benkhelil, J., Dainelli, P., Ponsard, J.F., Popoff, V. & Saugy, L., 1988. The Benue Trough: wrench related basin on the border of the equatorial Atlantic. In: Manspeizer, W. (editor), Triassic–Jurassic Rifting. Elsevier, 787–817.

Black, R. & Girod, M., 1970. Late Palaeozoic to recent igneous activity in Wast Africa and its relation to basement structure. In: Clifford, T.N. & Gass, I.G. (editors), African magmatism and tectonics. Oliver & Boyd, Edinburgh, 185–210.

BMR. 1992. Gravity anomaly map of Australia; scale 1:5 000 000. Bureau of Mineral Resources Geology & Geophysics, Canberra.

Bonatti, E., 1985. Punctiform initiation of seafloor spreading in the Red Sea during transition from a continental to an oceanic rift. Nature, 316, 33–37.

Bott, M.H.P., 1979. Subsidence mechanisms at passive continental margins. In: Watkins, J.S. (editor), Geological and geophysical investigations of continental margins. AAPG Memoir 29, 3–10.

Bott, M.H.P., 1982. The interior of the Earth, its structure, composition and evolution. Edward Arnold, London.

Bridwell, R.J. & Potzick, C., 1981. Thermal regimes, mantle diapirs and crustal stresses of continental rifts. In: Illes, J.H. (editor), Mechanism of graben formation. Elsevier, New York, 15–32.

Burke, K. & Dewey, J.F., 1973. Plume generated triple junctions. Journal of Geology, 81, 406–433.

Burke, K. & Whiteman, A.J., 1973. Uplift, rifting and breakup of Africa. In: Tarling, D.H. & Runcorn, K.S. (editors), Implications of continental drift to the earth sciences. Academic Press, London, 735–756.

Burke, K., Dessauvagie, T.F.J. & Whiteman, A.J., 1971. Opening of the Gulf of Guinea and geological history of the Benue depression and Niger delta. Nature Physical Science, 233, 51–55.

Burrus, J., Bessis, F. & Doligez, 1987. Heat flow, subsidence and crustal structure of the Gulf of Lions (NW Mediterranean): a quantitative discussion of the classic passive margin model. In: Beaumont, C. & Tankard A.J. (editors), Sedimentary basins and basin forming mechanisms. Canadian Society of Petroleum Geologists, Memoir 12, 1–16.

Cameron, I.B. & Stephenson, D., 1985. The Midland Valley of Scotland (3rd edition). British Geological Survey, Nottingham. 172pp.

Campos-Enriques, J.O., Hubral, P., Wenzel, F., Lueshen, E. & Meier, L., 1992. Gravity and magnetic constraints on deep and intermediate crustal structure and evolution models for the Rhine Graben. Tectonophysics, 206, 113–145.

Cloos, H., 1939. Hebung-Spaltung-Vulcanismus, Geolishe Rundschau, 30, 405–427.

Cochran, J.R., 1983. A model for the development of the Red Sea. AAPG Bulletin, 67, 41–69.

Cochran, J.R., 1991. Crustal structure and the mechanism of extension in the northern Red Sea: constraints from gravity anomalies. Tectonics, 10, 1018–1037.

Darracottt, B.W., Fairhead, J.D. & Girdler, R.W., 1972. Gravity and magnetic surveys in northern Tanzania and southern Kenya. Tectonophysics, 15, 131–141.

Davidson, K.A.S , Sola, M., Powell, D.W. & Hall, J., 1984. Geophysical model for the Midland Valley of Scotland. Transactions of the Royal Society of Edinburgh: Earth Sciences, 75, 175–181.

Edel, J.B., 1980. Contribution of magnetism and gravity to the knowledge of the Antepermian basement in the Rhine Graben. In: Advances in European geothermal research. Reidel, Boston, 89–98.

Exon, N. & Lee, C.S., 1988. Stratigraphy, depositional environments and petroleum maturation history of the Otway Basin and west Tasmanian margin. Bureau of Mineral Resources Geology & Geophysics, Yearbook 1988, 62–64.

Fairhead, J.D., 1976. The structure of the lithosphere beneath the eastern rift, East Africa deduced from gravity studies. Tectonophysics, 30, 269–298.

Fairhead, J.D., 1986. Geophysical controls on sedimentation. In: Frostich,L.E., Renaut. R.W., Reid, I., & Tiercelin, J.J. (editors), Sedimentation in East African rifts. Geological Society of London, Special Publication 25. 19–27.

Falvey, D.A., 1974. The development of continental margins in plate tectonic theory. APEA Journal, 14, 95–106.

Fichler, C. & Hospers, J., 1990. Gravity modelling in the Viking Graben area. In: Blundell, D.J. & Gibbs, A.D. (editors), Tectonic evolution of the North Sea rifts. Oxford Science Publications, 71–81.

Francis, E.H., 1978. The Midland Valley as a rift, seen in connection with the late Palaeozoic rift system. In: Neumann, E.R., & Ramberg, I.B. (editors), Tectonics and geophysics of continental rifts. Reidel, Boston, 132–147.

Freeth, S.J., 1984. How many rifts are there in West Africa? Earth and Planetary Science Letters, 67, 219–227.

Gibbs, A.D., 1987. Linked tectonics of the northern North Sea basins. In: Beaumont, C. & Tankard, A.J. (editors), Sedimentary basins and basin forming. Canadian Society of Petroleum Geologists, Memoir 12, 147–162.

Girdler, R.W. (editor), 1972. East African rifts. Elsevier, Amsterdam

Girdler, R.W., 1991. The Afro-Arabian rift system, an overview. Tectonophysics, 197, 139–153.

Guenoc, P., Paulot, G. & Coutelle, 1988. Surficial structures of the northern Red Sea axial valley from 23 degrees north to 28 degrees north in time and space evolution of new oceanic structures. Tectonophysics, 153, 1–23.

Gunn, P.J., 1975. Interpretation of the Bathgate magnetic anomaly. Scottish Journal of Geology, 2, 263–267.

Gunn, P.J., 1984. Recognition of ancient rift systems: examples from the Proterozoic of South Australia. Exploration Geophysics, 15, 85–97.

Gunn, P.J., 1988. Bonaparte Basin, evolution and structural framework. In: Purcell, P.G. & Purcell, R. (editors), The Northwest Shelf. Proceedings of the Petroleum Exploration Society of Australia Symposium, Perth, 1988, 275–286.

Gunn, P.J., Brodie, R.C., Mackey, T. & O'Brien, G.W., 1995a. Evolution and structuring of the Joseph Bonaparte Gulf as delineated by aeromagnetic data. Exploration Geophysics 26, 255–261.

Gunn, P.J., Mackey, T., Mitchell, J. & Cathro, D., 1995b. Evolution and structuring of the offshore Otway Basin as delineated by aeromagnetic data. Exploration Geophysics, 26, 262–268.

Gunn, P.J., Mitchell, J. & Meixner, A., 1996. Evolution and structuring of the Bass and Durroon Basins as delineated by aeromagnetic data. Australian Geological Survey Organisation, Record 1996/14.

Hall, D.H. & Dagley, P., 1970. Regional magnetic anomalies. Institute of Geological Sciences, Report 70/10.

Harland, W.B., Cox, A., V., Llewellyn, P.G., Picton, C.A.G., Smith, A.G. & Walters, R., 1982. A geologic time scale. Cambridge University Press, Cambridge.

Husebye, E.S. & Ramberg, I.B., 1978. Geophysical investigations. In: Dons, J.A. & Larsen, B.T. (editors), The Oslo palaeorift, A review and guide to Norges geologiske undersokelse. Inter-Union Commission on Geodynamics, Scientific Report 46, 41–55.

IGS, 1972. Aeromagnetic map of Great Britain, 1:625 000, Sheet 2. Institute of Geological Sciences, Nottingham.

Illes, J.H., 1978. Two stages of Rhine graben rifting. In: Neumann, E.R. & Ramberg, I.B., (editors), Petrology and geochemistry of continental rifts. Reidel, Boston, 63–72.

Jarvis, G.T., 1984. An extension model of graben subsidence—the first stage of basin evolution. Sedimentary Geology, 40, 13–31.

Kearey, P. & Vine, F.J., 1990. Global tectonics. Blackwell Scientific Publications, Oxford, 302 pp.

Khan, M.A. & Mansfield, J., 1971. Gravity measurements in the Gregory Rift. Nature Physical Sciences, 229, 72–75.

Kusnir, N.J. & Zeigler, P.A., 1992. The mechanics of continental extension and sedimentary basin formation: a simple pure-shear flexural cantilever model. Tectonophysics, 215, 117–131.

Latin, D.M., Dixon, J.E. & Fitton, J.G., 1990. Rift related magmatism in the North Sea Basin. In: Blundell, D.J. & Gibbs, A.D. (editors), Tectonic evolution of the North Sea rifts. Oxford Science Publications, 102–144.

Le Bas, M.J., 1971. Peralkaline vulcanism, crustal swelling and rifting. Nature Physical Sciences, 230, 85–87.

Le Fournier, J., 1986. Projet Georift. Bulletin Technique Elf Aquitaine, No. 117, 21–50.

Lister, G.S., Etheridge, M.A. & Symonds, P.A., 1991. Detachment models for the formation of passive continental margins. Tectonics, 10, 1038–1064.

Logachev, N.A., Rogozhina, V.A. Solonenko, V.P. & Zorin, Y.A., 1978. Deep structure and evolution of the Baikal rift zone. In: Neumann, E.R. & Ramberg, I.B. (editors), Petrology and geochemistry of continental rifts. Reidel, Boston, 49–62.

Louis, P., 1970. Contribution geophysique a la connaisance geologique du bassin du Lac Tchad. Memoir ORSTOM, 42, 311 pp.

Makris, J., Menzel, H., Zimmerman, J. & Gouin, P., 1975. Gravity field and crustal structure of north Ethopia. In: Pilger, A. & Rosler, A. (editors), Afar Depression in Ethopia, E. Schweisarbart'sche Verlagsbuchhandlung, Stuttgart, 135–144.

Makris, J., Henke, C.H., Egloff, F., & Akamaluk, I., 1991. The gravity field of the Red Sea and East Africa. Tectonophysics, 198, 1369–1381.

Malod, J.A., Murillas, J, Kornprobst, J. & Boillot, G., 1993. Oceanic lithosphere at the edge of a Cenozoic active continental margin (northwestern slope of Galicia Bank, Spain). Tectonophysics, 195–206.

McConachie, B.A., Bradshaw, M.T. & Bradshaw, J., 1996. Petroleum systems of the Petrel Sub basin—an integrated approach to basin analysis and identification of hydrocarbon exploration opportunities. APEA Journal, 36, 248–268.

McKenzie, D.P., 1978. Some remarks on the development of sedimentary basins. Earth and Planetary Science Letters, 40, 25–32.

McLean, A.C. & Qureshi, I., 1966. Regional gravity anomalies in the western Midland Valley of Scotland. Transactions of the Royal Society of Edinburgh. 66, 267–283.

Morgan, P., 1982. Heat flow in rift zones. In: Palmason, G. (editor), Continental and oceanic rifts. American Geophysical Union & Geological Society of America, Geodynamics Series, 8, 107–122.

Mory, A.J., 1991. Geology of the offshore Bonaparte Basin, northwestern Australia. Geological Survey of Western Australia, Report 29, 47 pp.

Neumann E, Olsen, K.H., Baldridge, W.S. & Sundvoll, 1992. The Oslo Rift: a review. Tectonophysics, 208, 1–18.

Ofoegbu, C.O., 1984. Interpretation of aeromagnetic anomalies over the lower and Middle Benue Trough of Middle Nigeria. Geophysical Journal of the Royal Astronomical Society, 79, 813–823.

Ofoegbu, C.O., & Onuoha, K.M., 1990. A review of geophysical investigations in the Benue Trough. In: Ofeogbu, C.O. (editor), The Benue Trough structure and evolution. Vieweg, 172–201.

Purcell, P.G. (editor), 1984. The Canning Basin, W.A. Proceedings of the GSA/PESA Canning Basin Symposium, Perth, 1984.

Rabinowicz, P.D., 1974. The boundary between oceanic & continental crust in the western North Atlantic. In: Burke, C.A. & Drake, C.L. (editors), The geology of continental margins. Springer–Verlag, Berlin, 67–84.

Rabinowitz, P.D., 1982. Gravity measurements bordering passive continental margins. In: Scrutton, R.A. (editor), Dynamics of passive margins. American Geophysical Union & Geological Society of America, Geodynamics Series, 6, 91–115.

Ramberg, I.B., 1976. Gravity interpretations of the Oslo Graben and associated rocks. Norges Geologiske Underskelse, Bulletin 325.

Rosendahl, B.R., 1987. Architecture of continental rifts with special reference to East Africa: Annual Review of Earth and Planetary Sciences, 15.

Searle, R.C., 1970. Evidence from gravity anomalies for thinning of the lithosphere beneath the rift valley in Kenya. Geophysical Journal of the Royal Astronomical Society, 21, 13–31.

Sheriff, R.E., 1988. Encyclopedic dictionary of exploration geophysics. Society of Exploration Geophysicists, Tulsa, Oklahoma, 323 pp.

Schuepbach, M.A. & Vail, P.R., 1980. Evolution of outer highs on divergent continental margins. In: Continental tectonics. National Academy of Sciences, Washington D.C., 50–62.

Swain, C.J., 1978. Gravity measurements in Kenya. Geophysical Journal of the Royal Astronomical Society, 53, 427–429.

Swain, C.J., 1992. The Kenya Rift axial gravity high: a reinterpretation. Tectonophysics, 204, 59–70.

Talwani, M., Le Pichon, X. & Ewing, M., 1965. Crustal structure of the mid-ocean ridges 2. Computed model from gravity and seismic refraction data. Journal of Geophysical Research, 70, 341–352.

Talwani, M., Mutter, J., Houtz, R. & Konig, M., 1978. The margin south of Australia—a continental margin palaeorift. In: Neumann, E.R. & Ramberg, I.B. (editors), Tectonics and geophysics of continental rifts. Reidel, Boston, 203–220.

Tarlowski, C., Gunn, P.J., & Mackey, T. 1997. Enhancements of the magnetic map of Australia. AGSO Journal of Australian Geology & Geophysics, 17(2)—this issue.

Tucker, D.H., Baccin, M. & Almond, R., 1984. Significance of airborne magnetic and gamma spectrometric data over the eastern margin of the Canning Basin. In: Purcell, P.G. (editor), The Canning Basin, W.A. Proceedings of the GSA/PESA Canning Basin Symposium, Perth, 1984, 299–318.

Vacquier, V., Steenland, N.C., Henderson, R.G. & Zeitz, 1951. Interpretation of aeromagnetic maps. Geological Society of America, Memoir 47.

Vierbuchen, R.C., George, R.P. & Vail, P.R., 1982. A thermomechanic model of rifting with implications for outer highs on passive continental margins. In: Watkins, J.S. & Drake, C.L. (editors), Continental margin geology. American Association of Petroleum Geologists, 765–778.

Werner, D. & Kahle, H., 1980a. A geophysical study of the Rhinegraben: I Kinematics and geothermics. Geophysical Journal of the Royal Astronomical Society, 62, 617–629.

Werner, D. & Kahle, H., 1980b. A geophysical study of the Rhinegraben. II Gravity anomalies and geothermal implications. Geophysical Journal of the Royal Astronomical Society, 62, 631–647.

Wernicke, B., 1985. Uniform-sense normal sense simple shear of the continental lithosphere. Canadian Journal of Earth Sciences, 22, 108–125.

Wessel, P. & Husebye, E.S., 1987. The Oslo Graben gravity high and taphrogenesis. Tectonophysics. 142,15–26.

White R.S., 1992. Magmatism during and after continental break-up. In: Storey, B.C., Alabaster, T. & Pankhurst, R.J. (editors), Magmatism and the causes of continental break-up. Geological Society, Special Publication 68, 1–16.

Williams, L.A.J., 1978. The volcanological development of the Kenya Rift. In: Neumann, E.R. & Ramberg, I.B. (editors), Tectonics and geophysics of continental rifts. Reidel, Boston, 101–131.

Williamson, P.E., Pigram, C.J., Colwell, J.B., Scherl, A.S., Lockwood, K.L. & Branson, J.C., 1985. Pre-Eocene stratigraphy, structure, and petroleum potential of the Bass Basin. APEA Journal, 25, 362–381.

Wohlenberg, J., 1975. Geophysikalshe aspecten der OstAfrikanische Grabenzone. Geologisches Jarbuch Reinhe E, (Geophysik) Heft 4, 82 pp.

Ziegler, P.A., 1990. Tectonic and palaeogeographic development of the North Sea rift system. In: Blundell, D.J. & Gibbs, A.D. (editors), Tectonic evolution of the North Sea rifts. Oxford Science Publications, 1–36.

AGSO Journal of Australian Geology & Geophysics, 17(2), 133–144

Application of aeromagnetic surveys to sedimentary basin studies

P.J. Gunn[1]

While aeromagnetic surveys have been mainly used in the past for mapping depth to magnetic basement of sedimentary basins and for delineating igneous units within the sedimentary section, the advent of high-resolution surveys flown close to the ground with close line spacing has revealed the existence of significant magnetic anomalies arising from sedimentary layers and their structure. As a result of these developments, aeromagnetic surveys now have greater relevance to sedimentary basin studies.

Introduction

The aim of this paper is to explain the types of aeromagnetic responses that arise from the various geological features associated with sedimentary basins and how these responses can be interpreted in the context of basin studies. The discussion is directed to petroleum exploration, but features relevant to mineral exploration are mentioned and, in any case, the generalities presented apply to virtually any study of sedimentary basins. In this paper, a sedimentary basin is any depression that has accumulated sediment, and no attempt has been made to distinguish between sedimentary basins of different origins and structuring.

All rock units are magnetic, but not all give rise to readily observable magnetic effects. The magnetic responses described here are those that may be expected to be detected with airborne surveying systems recording the magnetic field with a precision of ± 0.01 nT at a survey altitude of approximately 100 m above ground or sea level. Acquisition systems with such precision have become standard during the past five years, with the installation of optically pumped caesium and helium vapour magnetometers, improved compensation systems to remove the magnetic effects of survey aircraft, and the use of GPS navigation, which allows flight-line positioning to ±10 m or better. These improvements, combined with rapid digital sampling at intervals of about 8 m, survey lines at spacing of 500 m or less, and post-processing of data with microlevelling techniques, have resulted in data that can be contoured at 0.1 nT intervals. Horsfall (1996) and Luyendyk (1996) describe the acquisition and processing systems currently being used to produce such results.

While older aeromagnetic surveys over sedimentary basins, acquired with less rigorous parameters, were able to define the major magnetic features associated with sedimentary basins, data from this new generation of acquisition are able to map fine structural and sedimentary detail previously undetected. This detail is normally enhanced by a comprehensive range of data filtering and transformation routines complemented by imaging techniques (Milligan & Gunn 1997).

Overview

A diagrammatic overview of the types of rock units likely to cause magnetic responses in sedimentary basins is shown in Figures 1 and 2. Details of the magnetic responses of these units and their relevance to hydrocarbon exploration, together with specific examples, are elaborated in the following sections. Clark (1997) reviews the magnetic properties of rocks and minerals. His paper can be used as a basis for estimating the relative magnetic responses of the magnetic units illustrated.

Figure 1 shows three hypothetical basin cross-sections drawn to include geological features likely to give rise to magnetic responses in sedimentary basins. The sections are based on actual depth-converted regional seismic sections across the Bonaparte Gulf Basin of northwestern Australia (Gunn 1988)—extra geological units and structures have been added for the purposes of this paper. The Bonaparte Gulf Basin has been interpreted as a failed Devonian–Carboniferous rift that underwent differential extension (Gunn 1988), and the three sections cross areas of different extension. Figure 2, illustrating the areal distribution of the magnetic units, is also based on the Bonaparte Gulf Basin, with extra features added for the purpose of illustration.

From the figures it can be seen that superposition of magnetic units can occur and, consequently, any magnetic field observed over the sedimentary basin may include the combined effects of several magnetic markers.

The following sections describe specific examples of magnetic responses of the features illustrated in Figure 1.

Basement

The basement is the assemblage of rocks that underlies a sedimentary basin. If it contains numerous magnetic rock units, such as igneous intrusions or extrusives, magnetic sediments or magnetic metamorphic units, these can provide information on the morphology of the sedimentary basin and its structure.

If the magnetic units in the basement occur at the basement surface, then depth determinations for these will map the basin floor morphology. This approach has been used for several decades to locate sedimentary basins with economically significant thicknesses of sediment. The initial delineation of the Gippsland Basin (Haematite Exploration 1965) and the Bonaparte Basin (Reford & Butt 1983) are classic examples of the successful application of this technique.

The flight-line spacing of most of the older aeromagnetic surveys was of the order of several kilometres and while this was appropriate for proving the general shape of basins, closer spacing allows the definition of structures and features on the basement surface with direct relevance to hydrocarbon exploration.

Depth to basement, faults in the basement surface, and the relief of the basement surface have direct relevance to the depositional and structural history of the area. Many examples exist of positive basement blocks being directly related to hydrocarbon traps. Often they are overlain by sediments whose depositional isopachs and/or structure reflect the underlying basement structure. Such an example occurs in Joseph Bonaparte Gulf of northern Australia. Gunn et al. (1995a) have demonstrated that this area, which contains the remnants of a failed Devonian–Carboniferous rift, was originally underlain by an extensive subhorizontal sheet of Proterozoic sills and/or lava flows and that the present morphology of the sheet can be used to map transfer faults associated with Devonian–Carboniferous extension as well as a series of tilted blocks and horsts created by the extension (Fig. 3). Even though the magnetic data in this example are mapping structures at the base of the sedimentary section, correlations with seismic data show that the structures and their bounding faults are reflected in the overlying sediments.

'Basement grain' or the trend of basement faults and structure is frequently the main determinant of the primary

[1] Australian Geological Survey Organisation, GPO Box 378, Canberra, ACT 2601

fractures that develop to accommodate basin extension. For example, in the Viking Graben of the North Sea many transfer faults trend northeasterly, parallel to the grain of the underlying Caledonian basement. This feature is obvious in various structural maps compiled by Abbotts (1991) for the Viking Graben hydrocarbon fields. Transfer faults can be extremely difficult to recognise in seismic data, but the trends are often readily apparent in aeromagnetic data.

Basement structures may even contain hydrocarbon accumulations. The Clair Field in the West Shetlands area of the UK continental shelf (Coney et al. 1993) contains several billion barrels of oil in place, a large proportion of which is reservoired in a basement block of fractured Lewisian granite basement. The granite is magnetic and its form can be deduced from airborne data.

Granite can act as provenance for superior quality reservoir rocks. The author has noted situations in the North Sea where localised good high-porosity reservoir sandstones on the Viking

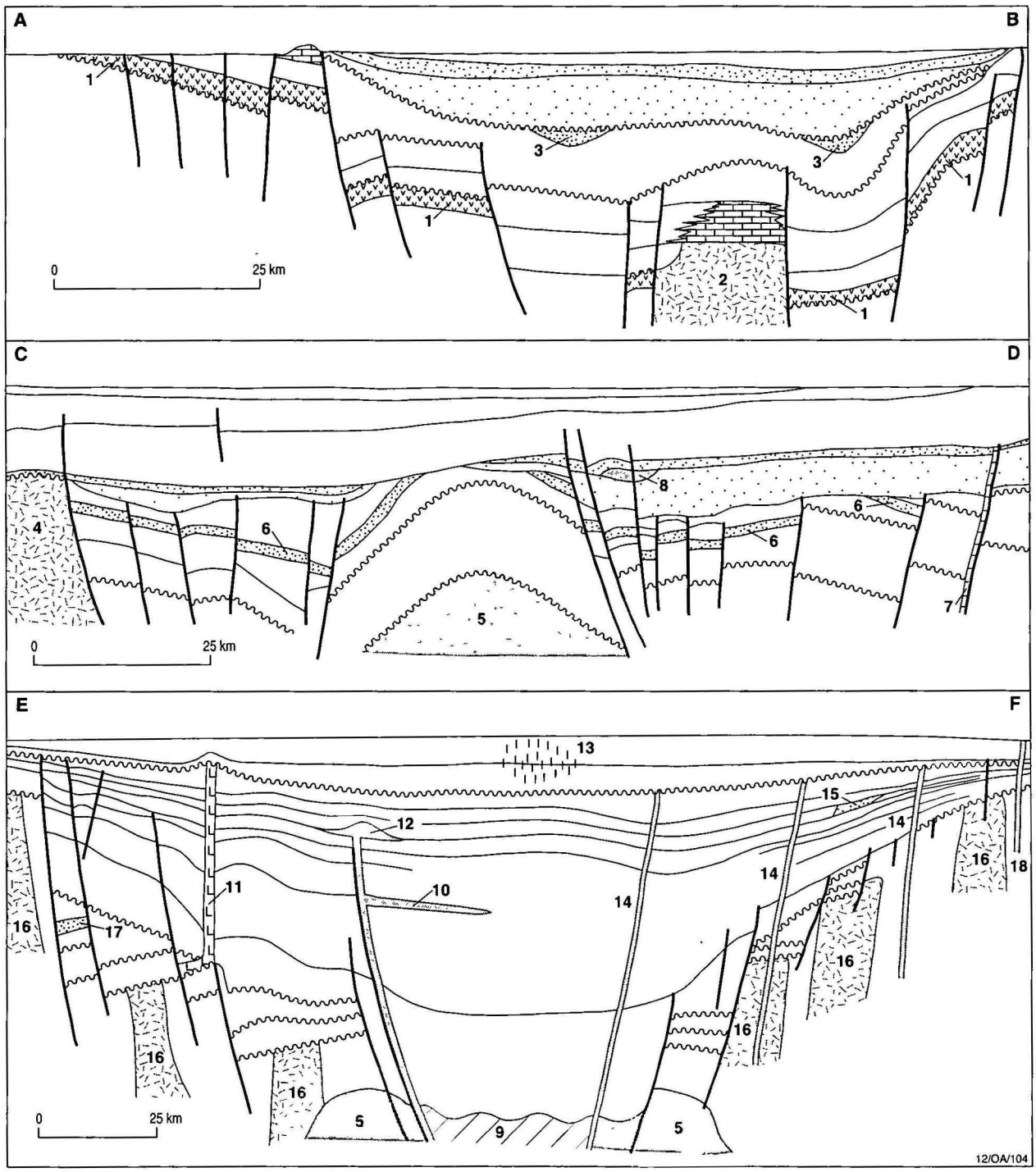

Figure 1. Basin cross-sections illustrating units and structures that can cause observable magnetic responses in a sedimentary basin. (1) Pre-existing flood basalts. (2) Magnetic basement high formed as a result of intrusion, erosion or structuring. (3) Detrital or chemically precipated magnetic minerals in palaeochannels. (4) Magnetic basement flanking the sedimentary basin. (5) Mid-basin crustal intrusion. (6) Magnetic sedimentary unit. (7) Magnetic minerals precipitated in a fault plane. (8) Intrasedimentary volcanics. (9) Oceanic crust. (10) Igneous sill. (11) Salt diapir. (12) Buried volcanic centre. (13) Diagenetic magnetite or pyrrhotite formed by hydrocarbon plumes. (14) Igneous dykes. (15) Detrital magnetic minerals in bar and fan systems. (16) Intrabasement magnetic bodies. (17) Magnetic massive sulphide gold–copper–silver–lead–zinc deposits. (18) Kimberlite and lamproite intrusions.

Graben of the North Sea have been derived from proximal granites next to the graben. Granites are commonly mappable with aeromagnetic data. However, identification with aeromagnetic data of basement lithology to predict the type of sediment in basins is rarely attempted, despite the potential of this approach.

Intrabasement intrusions and the possible generation of oceanic crust

The above discussion assumes that all intrusions associated with the basement subcrop at the basement surface and, consequently, depth determination of their tops will map the base of the sedimentary section. Obviously, this is not always the case and, to avoid errors of interpretation, every effort must be made to identify such basement features.

As well as features of the original basement that do not subcrop at the base of the sedimentary section, there may be intrabasement intrusions contemporaneous with or younger than the sediments overlying the basement. Such intrusions may be the result of crustal extension associated with the basin formation.

Gunn (1997b) reviews igneous intrusion processes associated with crustal extension, noting that a precursor to crustal splitting appears to be the intrusion of a series of major igneous bodies along the axis of the extension. These cause major magnetic anomalies, typically circular or elliptical and with apparent depths below the basin floor. Gunn cites examples of anomalies which may be of this type beneath the Bass and Canning Basins in Australia.

As basin extension progresses towards crustal rupture and generation of oceanic crust, the axial intrusions coalesce into a continuous axial dyke. If crustal splitting occurs, it apparently does so along the axis of the dyke or close to it, such that fragments of the dyke remain along the edges of the continental crust flanking oceanic crust. These fragments of the axial dyke cause linear 'continental margin magnetic anomalies', which may actually occur landward of the continental slope as a result of sediment progradation.

If oceanic crust is generated and preserved under sediments it may be expected to be distinguishable by the characteristic magnetic stripes caused by remanence of different polarity in the sea floor. In practice, the magnetic character of oceanic crust close to the continental–oceanic transition rarely exhibits such lineations; instead there is a 'quiet zone' up to several hundred kilometres wide. The quiet zone appears to be attenuated crust with a character intermediate between true continental crust and true oceanic crust.

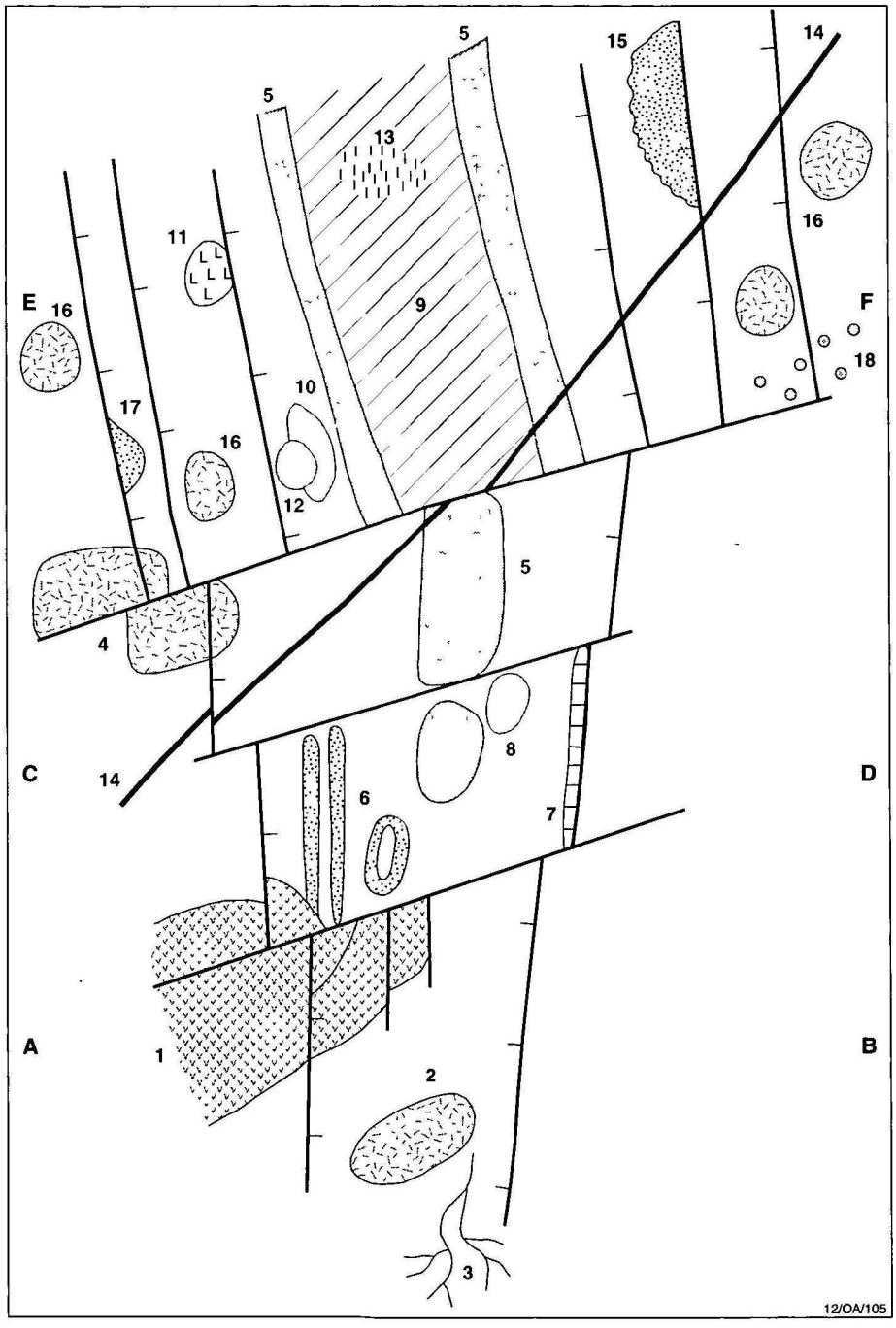

Figure 2. Types of areal distribution of units and structures that can cause observable magnetic responses in a sedimentary basin. The location of sections across this hypothetical basin, as illustrated in Figure 1, is indicated. See Figure 1 for an explanation of the various elements.

Sedimentary section

In general, magnetic anomalies caused by non-igneous sources within sediments are typically much weaker than those due to basement igneous and metamorphic rocks, which generally contain much greater concentrations of magnetic minerals.

Sedimentary layers may be magnetic if they contain enough magnetic minerals. However, they must have structural relief for them to give rise to a magnetic anomaly, as horizontal magnetic sheets only have anomalies at their edges. Small concentrations of magnetite in a sediment can produce an observable magnetic response.

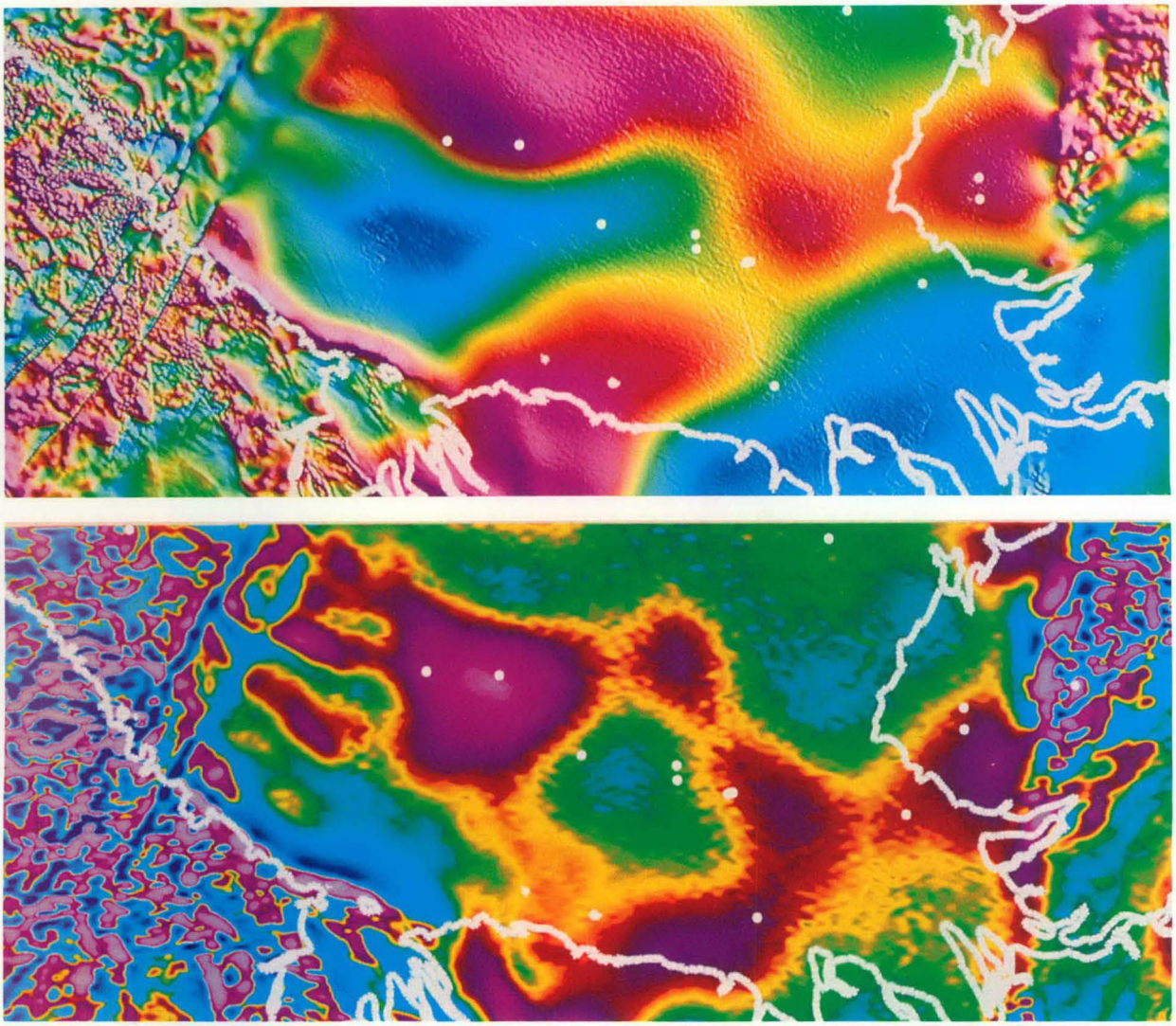

Figure 3. (A—top) Colour image of magnetic intensity of the southern portion of the Joseph Bonaparte Gulf in northwestern Australia. The red portions of the image are due to an extensive sheet of Proterozoic volcanics, whose present geometry reflects Palaeozoic structuring in the area. (B—bottom) Colour image of the vertical gradient of total magnetic intensity. This image resolves the detail in structure of the deep magnetic sheet. The high-frequency disturbances evident in the image are due to shallow magnetic markers (depicted in Fig. 3C), whose effects have been suppressed by filtering to emphasise the structure of the deeper unit. (C—top right) Interpretation of the above images (from Gunn et al. 1995a). The interpretation is consistent with seismic sections in the area. (D—bottom right) Grey-scale image that is the result of applying bandpass filtering to the data of Figure 3A. The image shows the distribution of magnetic minerals on or close to the sea floor. Palaeodrainage systems are evident. The narrow linear northwest-trending anomalies on the western margin of the gulf are due to submarine sand ridges.

Fishman et al. (1989) presented a detailed study of a Jurassic sandstone with a magnetic signature caused by detrital magnetite. Generally however, in sedimentary environments, detrital magnetite is rapidly oxidised to hematite, which is markedly less magnetic, although hematite can, in sufficient concentration, produce an observable magnetic effect.

Magnetic anomalies may be caused by disseminated pyrrhotite in shale and siltstone, such as occurs in turbidite sequences in the Cobar area of New South Wales (Clark & Tonkin 1994). Ilmenite may also give a weak magnetic response, and ancient beaches are known to contain enough of this mineral to give a weak but observable response (Mudge 1994). Maghemite, a weathering product with a similar susceptibility to magnetite and which is extremely stable under oxidising conditions, is often preserved in lateritic palaeoweathering surfaces and stream channels. Spectacular bifurcating magnetic anomalies in the Cobar area of New South Wales have such sources (Sheard et al. 1991). Figure 3 shows magnetic responses of palaeochannels defined by Gunn et al. (1995a) in the Joseph Bonaparte Gulf.

Aeromagnetic surveys over sedimentary basins, with close line spacing (~400 m) and sensitive instruments recording with noise envelopes no greater than ± 0.1 nT, almost invariably map coherent low-amplitude anomalies from sources within the sedimentary section. A series of examples published in *Preview* (1993) illustrate situations where aeromagnetic data appear to be mapping structure caused by folding and faulting as well as responses caused by intrasedimentary units. Figure 4, (from Gunn et al. 1995b) shows examples of the apparent delineation of channel systems, barrier bars, down-to-basin normal faults, transfer faults and reactivated basement faults in an area of the offshore Otway Basin. Cathro (1995), has confirmed many of Gunn et al.'s interpretations in the Otway Basin by correlating magnetic anomalies with seismic reflection responses (Figs 5, 6). Other examples of mapping magnetic intrasedimentary detail have been published for the Timor Sea

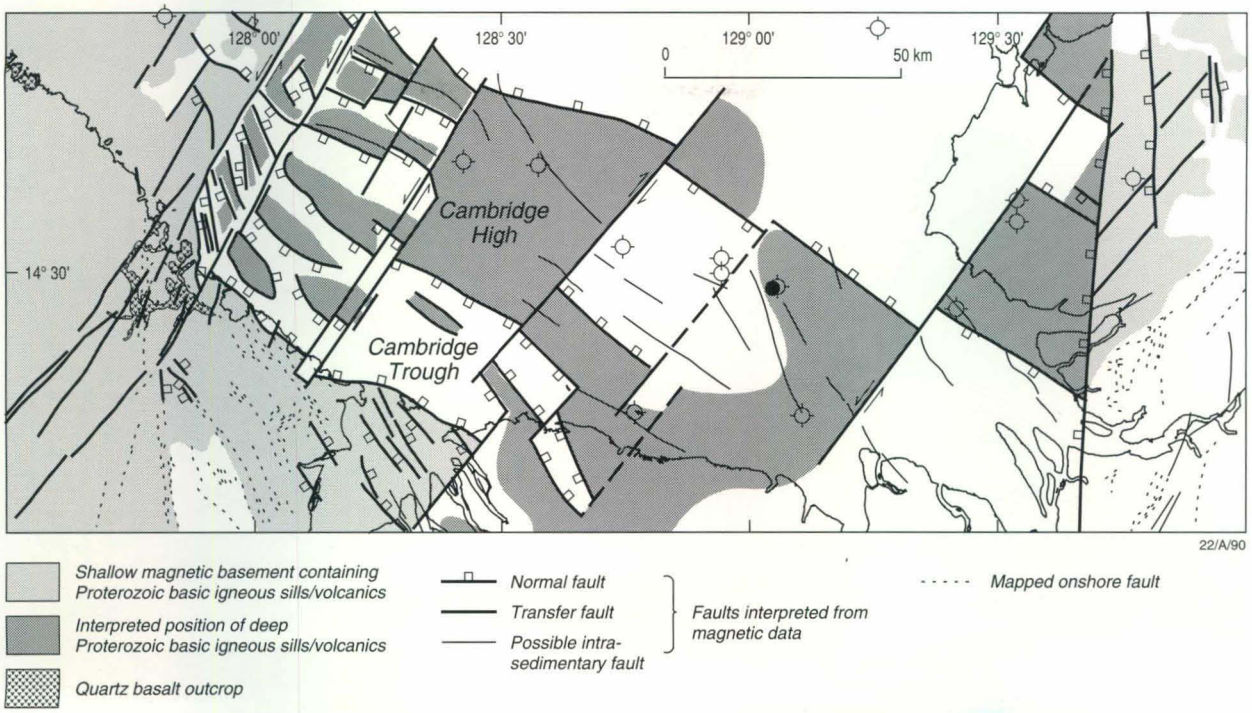

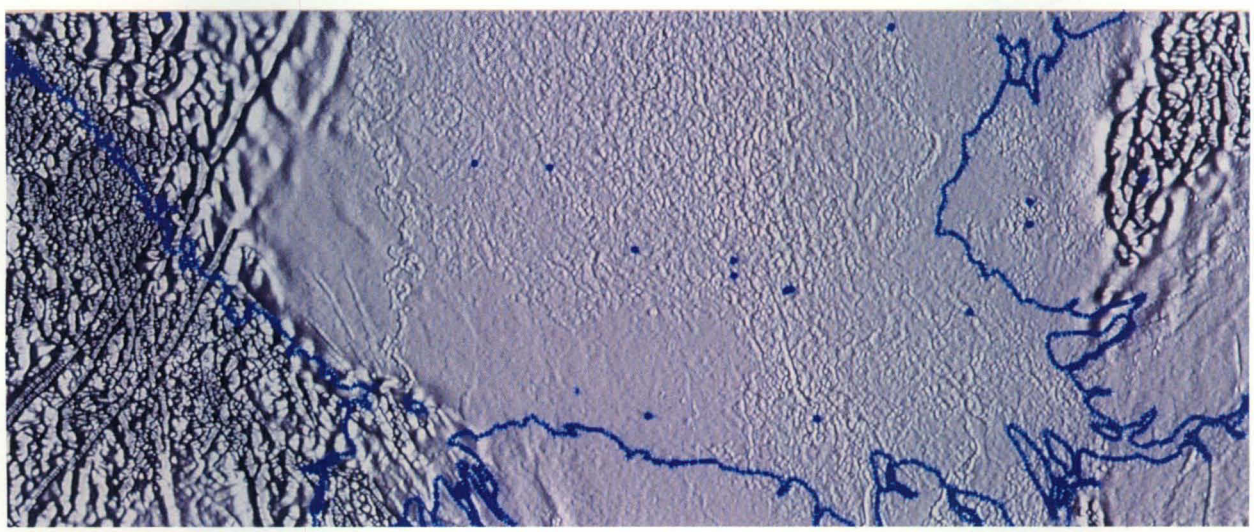

(Wellman & O'Brien 1991) and the Perth Basin (Heath et al. 1994).

In many of the above examples the true nature of the sources of the magnetic anomalies is unclear. For example, in many of the responses identified as arising from faulting this could either be due to dislocations of magnetic units or from the magnetic effects of magnetic minerals precipitated in fault planes. More research is required to understand the magnetic properties of sediments in relation to depth of burial, fluid migration and diagenetic changes. It is probable that the magnetic properties of sediments evolve in relation to basin development and that a knowledge of these relationships could allow details of thermal gradients, burial history, metamorphism, redox potentials, hydrocarbon maturation and fluid flowpaths to be estimated.

It should be noted that because of the weak and, therefore, subtle nature of the majority of the intrasedimentary responses, some form of data enhancement is normally required to clearly delineate such features relative to strong regional gradients and the more intense magnetic anomalies due to basement features, igneous intrusions and extrusions. Typical enhancement techniques are computation of vertical derivatives, matched filtering and various forms of bandpass filtering (Milligan & Gunn 1997).

Salt diapirs

Pure 'salt', comprising halite, gypsum and anhydrite, is diamagnetic, i.e. it has a negative magnetic susceptibility and, as a result, normally has a negative magnetic contrast relative to enclosing sediments. In such situations, high-sensitivity magnetic surveys map salt domes and salt ridges as magnetic lows. There are exceptions to this generalisation, such as the Paqualin salt diapir in the Timor Sea (Smith & Whitehead 1989), which has bands of diagenetic magnetite within zones of anhydrite and halite, resulting in a positive magnetic anomaly over the diapir.

Igneous units

In general, igneous rocks have a higher content of magnetic minerals, especially magnetite, than sediments and can be identified and mapped in sedimentary basins from magnetic data. Igneous features, such as intrusive plugs, dykes, sills,

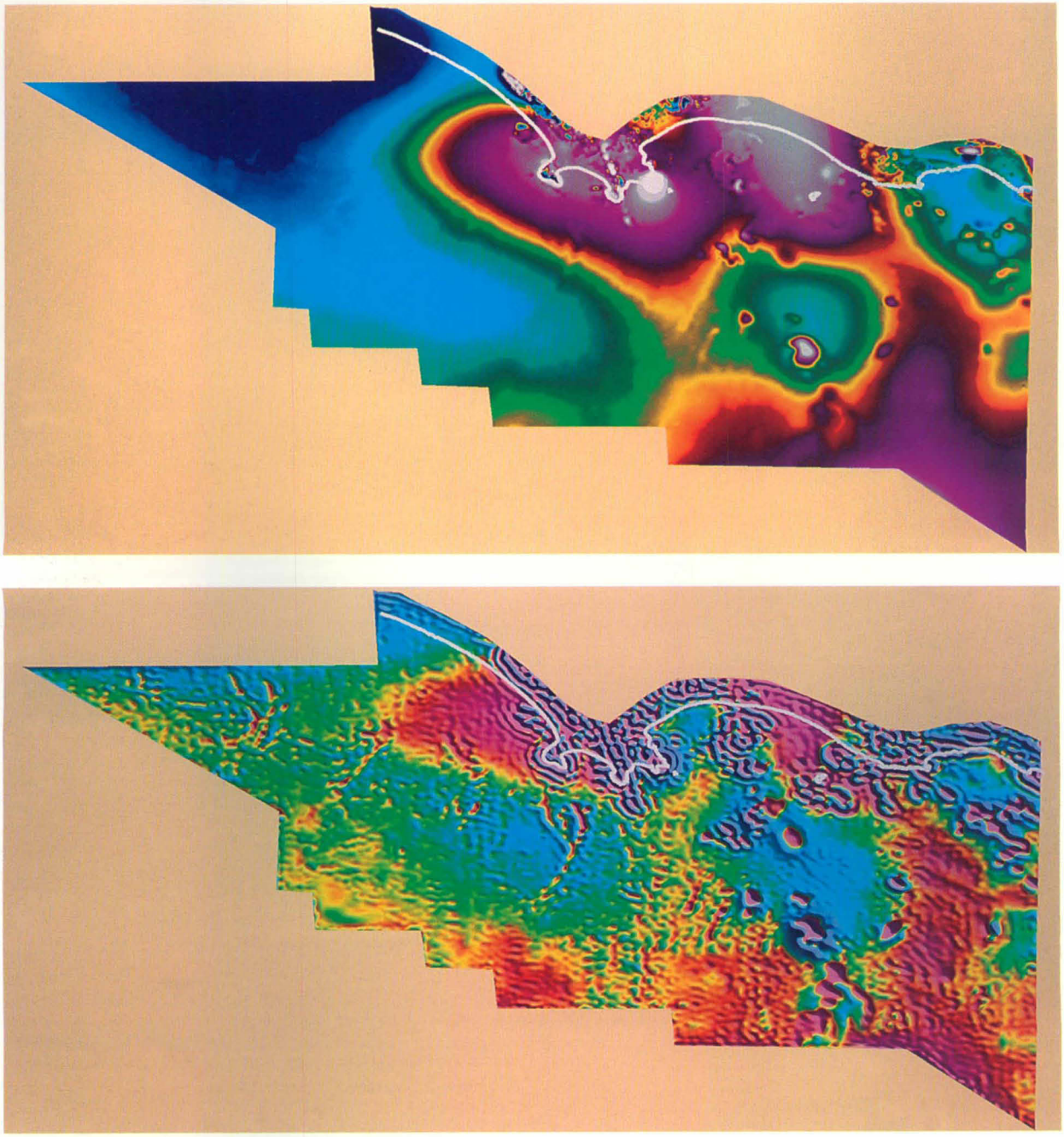

lava flows and volcanic centres, can occur at any stage of a basin's evolution and, therefore, be preserved at any level in the sedimentary section. Such features are significant in understanding the history of a basin and assessing its petroleum prospectivity.

Gunn et al. (1995b) have used aeromagnetic data to identify a phase of extrusion of basic igneous material during the earliest stage of extension of the Otway Basin in southeastern Australia. Structuring of the basin, postdating emplacement of this originally horizontal, contiguous magnetic sheet, is indicated by the magnetic effects of the present-day fragments of the sheet. Transfer-type extensional faults and down-to-basin normal faults can be recognised (Fig. 4).

Significant volcanic activity in the North Sea Jurassic rift system was restricted to outpourings of the Rattray volcanics in the vicinity of a triple junction (Latin et al. 1990). These are unconformably overlain by Middle Jurassic reservoir rocks, and definition of the present structure of the volcanics is of direct significance to exploration. Platt & Walker (1995) have given examples of magnetic data mapping these volcanics.

Late Tertiary to Recent volcanics and intrusives are prolific in the Otway Basin. Aeromagnetic data presented by Gunn et al. (1995b) clearly delineate these features (Fig. 4). Figure 7, from Cathro (1995), shows correlation of an igneous sill, evident on seismic data, and its magnetic expression.

Igneous intrusions can produce structural closure and, here, magnetic anomalies can be indicators of hydrocarbon traps, such as in the Canning Basin (Reeckman & Mebberson 1984), the Wilga Park gas discovery of the Gunnedah Basin (Hamilton et al. 1988), and the Omaha Oil Field in Illinois (Sparlin & Lewis 1994). They can also be important loci for reef development—e.g. the Sentry Bank reef in the Philippines (King & Morton 1987).

Intrusions are not always recognised as such on seismic sections and at various times have been mistaken for simple anticlinal domes, salt and shale diapirs, and carbonate reefs.

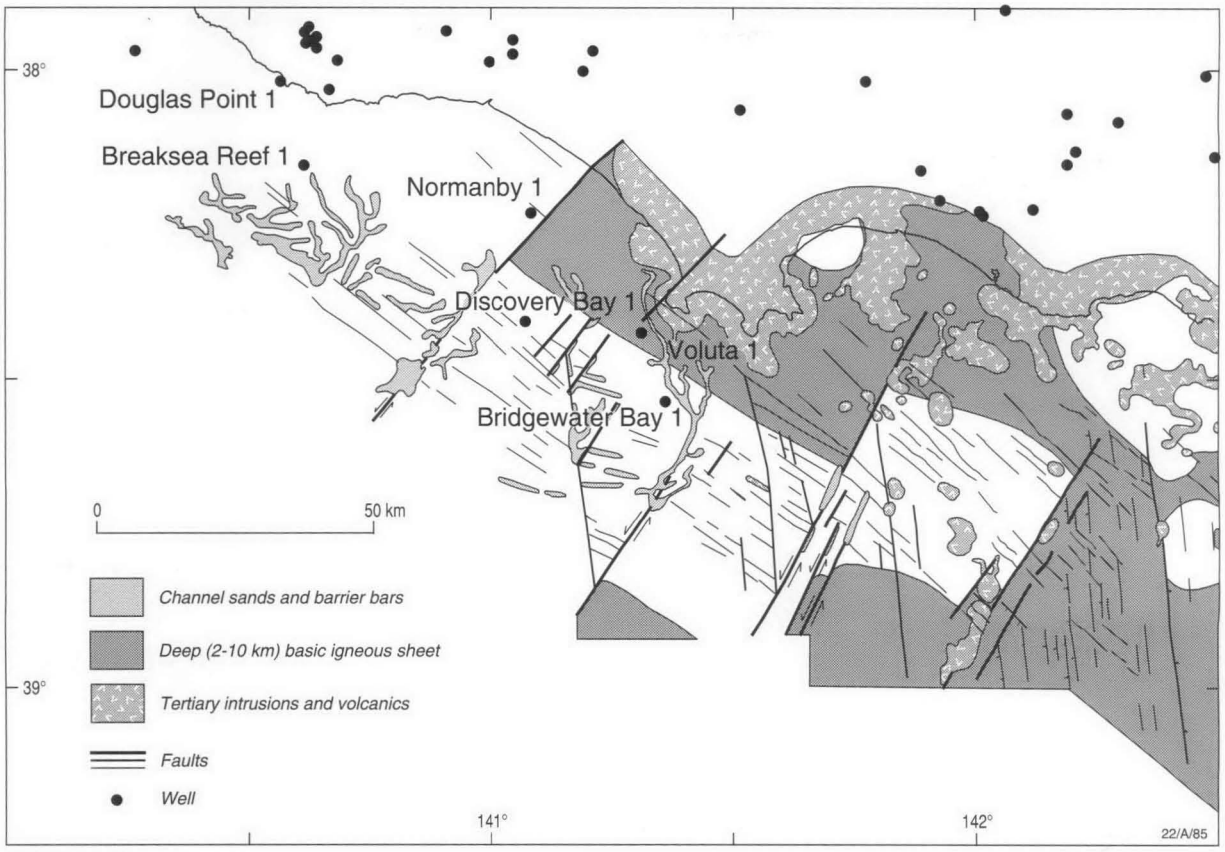

Figure 4. (A—top left) Non-illuminated colour image of total magnetic intensity of the offshore Otway Basin in southeastern Australia. Computer modelling indicates that the purple areas correspond to a sub-horizontal magnetic sheet, which can be interpreted as an extensive basic igneous event associated with the extension that initiated basin formation. The geometry of this sheet can be used to map the present day basin structure. (B—bottom left) Colour image of the vertical gradient of the above image. The vertical gradient resolves fine detail that has been interpreted to indicate volcanics, igneous intrusions, faults, channels and barrier bars. (C—above) Interpretation of the above images (after Gunn et al. 1995b).

Many dry holes have been unintentionally drilled on volcanic centres and intrusive plugs. The Tookoonooka–1 well in the Eromanga Basin of southwestern Queensland, for example, was drilled on a structural culmination, subsequently interpreted as overlying a Jurassic volcanic centre that significantly influenced Mesozoic sedimentation within a radius of 50 km (Young 1987). Jurassic volcanic rocks were not expected in this area, but could probably have been predicted from existing aeromagnetic data of the area, which show the anomaly of a classic plug-type intrusion at the location of Tookoonooka–1 (Fig. 8).

Seismic studies on the northeastern margin of the Joseph Bonaparte Gulf detected doming associated with high-amplitude seismic events within Triassic formations. Further seismic detailing associated with a marine magnetometer survey showed that the doming and high-amplitude responses are associated with igneous sills (Gunn 1987). This was the first indication of igneous activity this young in the area. The only way to avoid such surprises is to conduct magnetic surveys.

The thermal effects of igneous intrusions can cause maturation of hydrocarbon source material without associated changes in vitrinite reflectance (Reeckman & Mebberson 1984) and, thus, it is important to be aware of the existence of any igneous units that may cause such effects.

Kimberlite and lamproite diatremes may penetrate sedimentary sections and the magnetic expressions of many of these can be recognised as small sub-circular anomalies with amplitudes of the order of a few nanoteslas; e.g. a cluster of lamproite pipes on the Lennard Shelf of the Canning Basin (Jenke & Cowan 1994). Such intrusions, which are normally only a few hundred metres across, can often be distinguished from classical volcanic vents by their size and isolation; however, not all such features have magnetic responses.

Magnetic features related to hydrocarbons

Anomalous magnetisation may result from hydrocarbon seepage and the effects of this magnetisation may be detectable as a series of localised irregular high-frequency anomalies (Machel & Burton 1991; Henderson et al. 1984). Machel & Burton (1991) presented a comprehensive analysis of the geochemical, microbial, sedimentological and hydrogeological processes that control the formation of such magnetic mineralisation. The anomalous magnetisation is located in relatively reducing geochemical plumes. The magnetic minerals, magnetite and/or pyrrhotite, may be formed and hematite may be dissolved or replaced. Consequently, hydrocarbon seepage can result in positive or negative magnetic anomalies, or no anomalies at all, relative to the magnetisation of the country rock prior to the seepage. Machel & Burton's analysis identified a range of variables that influence the diagenetic changes affecting magnetic mineralisation. The interface between oxidising and reducing environments, which is normally the watertable, is characteristically the region where the most obvious transformations occur. This is frequently near the surface and, as a consequence, normally some distance above the hydrocarbon source. Previous watertable levels may have resulted in the formation of magnetic minerals below or above the present watertable.

While hydrocarbon seeps may migrate vertically and form magnetic minerals directly above hydrocarbon sources, lateral

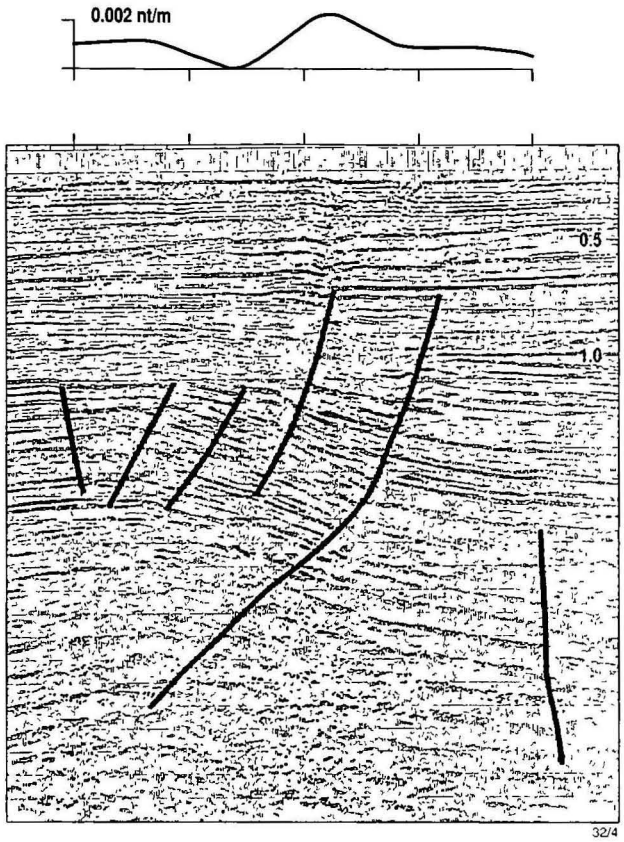

Figure 5. Correlation of magnetic and seismic responses of faults in the Otway Basin (after Cathro 1995).

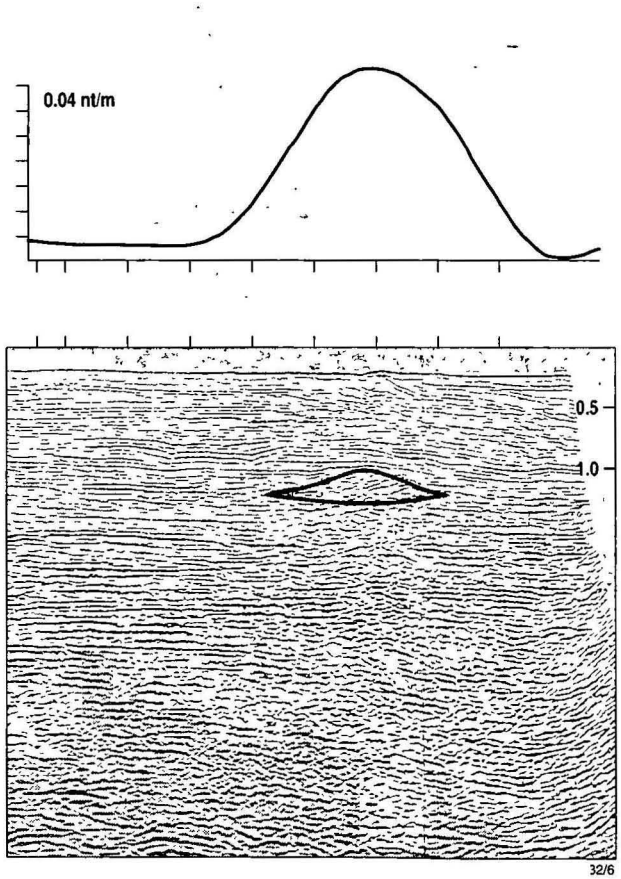

Figure 7. Correlation of magnetic and seismic responses of an igneous intrusion in the Otway Basin (after Cathro 1995).

groundwater flow may cause diagenetically formed magnetic minerals to be deposited away from the hydrocarbon accumulations from which the seeps originate. Figure 9 shows a correlation of high-frequency magnetic anomalies with hydrocarbon fields. These examples appear to indicate situations where vertical migration has occurred.

Magnetic features related to mineralisation

Isolated magnetic anomalies, generally circular or oval in plan and several hundred metres across, and with amplitude of tens to hundreds of nanoteslas, may arise from accumulations of magnetite and/or pyrrhotite, which may be associated with economic grades of copper, lead, zinc, silver and gold. Such deposits, e g the Abra deposit (Fig. 10) in the Bangemall Basin of Western Australia (Boddington 1990), which precipitate from mineral-bearing solutions, are frequently located within or adjacent to major faults. Gunn & Dentith (1997) reviewed the characteristics of such deposits, which are much more numerous than most people realise, and likely to occur at depth in many unexhumed sedimentary basins.

Conclusion

High-sensitivity aeromagnetic data are a valuable tool in studies of sedimentary basins. Current interpretation techniques concentrate on defining geometric attributes such as the depth and structure of magnetic units. The author is convinced it should be possible to extend the range of lithological and geochemical information that can be extracted from the data. Systematic studies relating the magnetic properties of sediments to their diagenetic history, depth of burial, and lateral facies changes are required if the interpretation methodology is to progress.

References

Abbotts, I.L., 1991. United Kingdom oil and gas fields, 25 years commemorative volume. Geological Society of London, Memoir 14.

Boddington, T.D.M., 1990. Abra lead–silver–copper–gold deposit. In: Hughes F.E. (editor), Geology and mineral resources of Australia and Papua New Guinea. Australasian Institute of Mining and Metallurgy, Monograph 14, 659–664.

Cathro, D., 1995 Correlation of marine seismic and high resolution airborne magnetic data: a case study in the western Otway Basin, offshore Victoria. Australian Geological Survey Organisation, Record 1995/53.

Clark, D.A., 1997. Magnetic petrophysics and magnetic petrology: aids to geological interpretation of magnetic surveys. AGSO Journal of Australian Geology & Geophysics, 17(2)—this issue.

Clark, D. A. & Tonkin, C., 1994. Magnetic anomalies due to pyrrhotite: examples from the Cobar area, N.S.W. Applied Geophysics, 32. 11–32.

Coney, D., Fyfe, T.B., Retail, P. & Smith, P.J., 1993. Clair appraisal: the benefits of a co-operative approach. In: Parker, J.R. (editor), Petroleum geology of northwest Europe: Proceedings of the 4th conference. Geological Society of London, 1409–1420.

Fishman, N.S., Reynolds, R.L., Hudson, M.R. & Nuccio, V.F., 1989. Source of anomalous magnetisation in area of hydrocarbon potential: petrologic evidence from Jurassic Preuss Sandstone, Wyoming–Idaho Thrust Belt. AAPG Bulletin, 73, 182–194.

Gunn, P.J., 1987. B87 Seismic Survey, Permit NT P28. Unpublished report for Elf Aquitaine Petroleum Australia Pty. Ltd.

Gunn, P.J., 1988. Bonaparte Basin: evolution and structural framework. In: Purcell P.G. & Purcell R.R. (editors), The North West Shelf, Australia. Proceedings of the

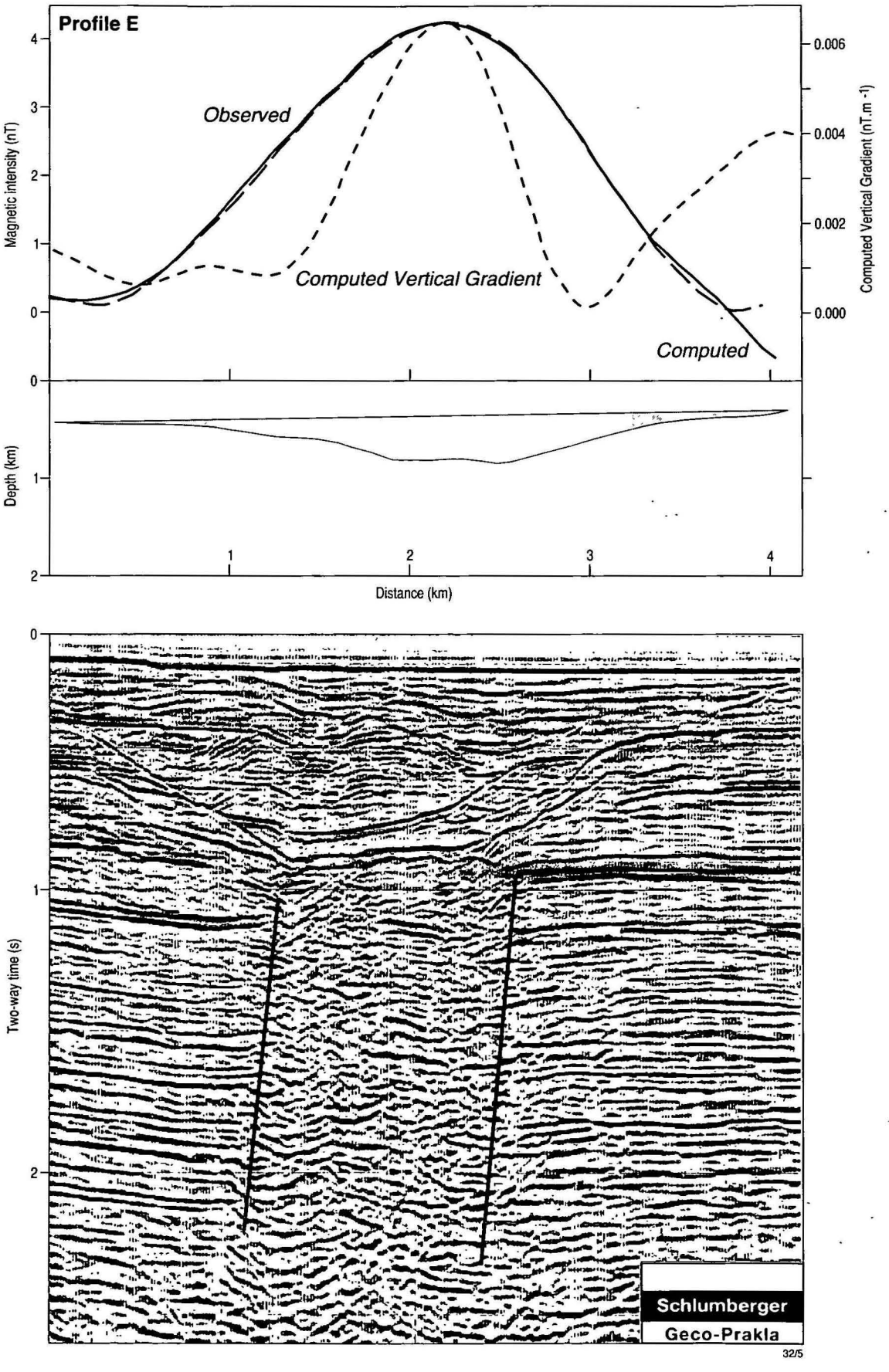

Figure 6. Correlation of magnetic and seismic responses of a channel in the Otway Basin (after Cathro 1995). Seismic data reproduced courtesy of Geco-Prakla.

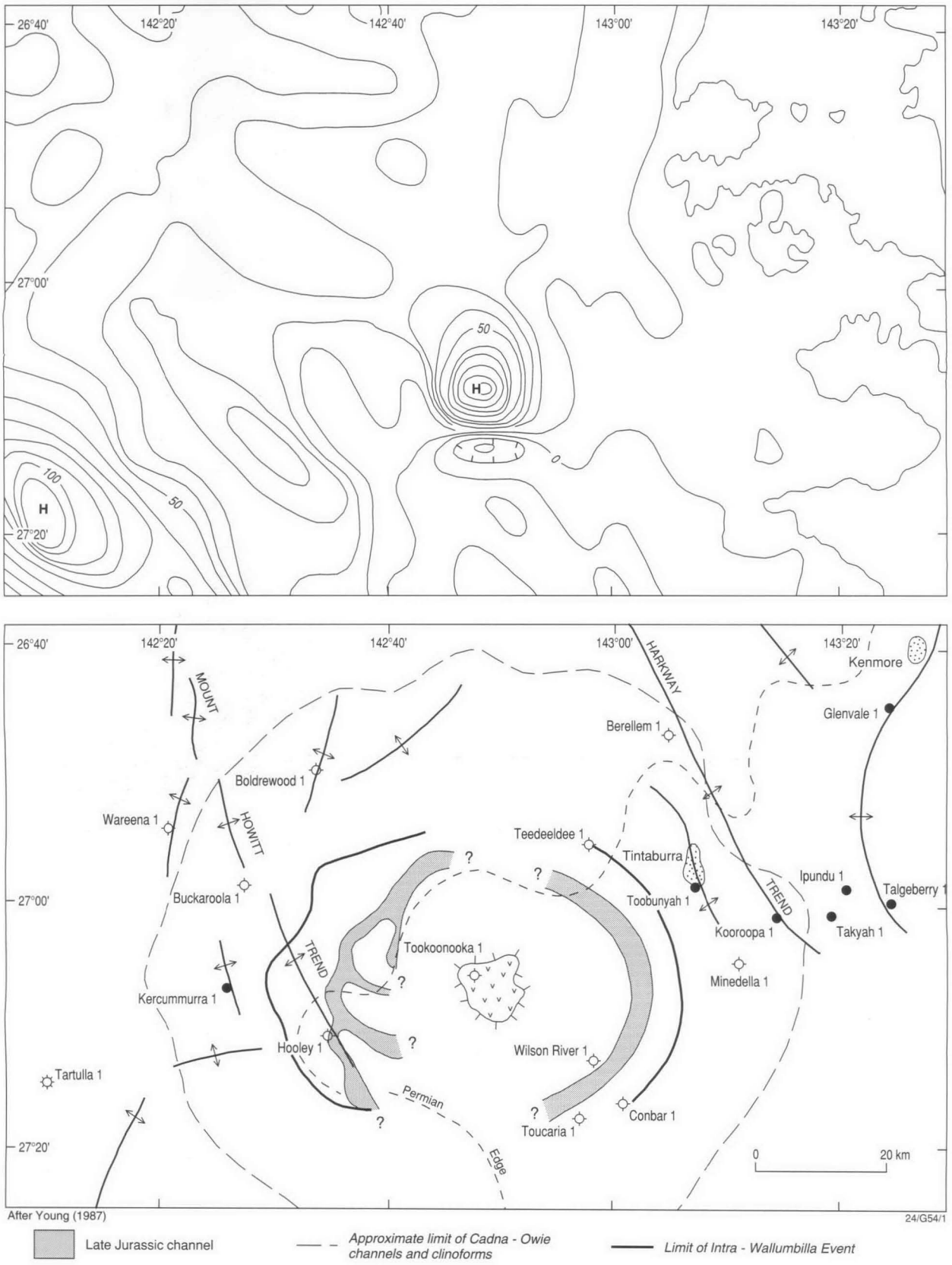

Figure 8. Sedimentary features related to the buried Tookoonooka volcanic complex (after Young 1987) and the magnetic response of the complex.

Figure 10 (facing page). Magnetic response of the Abra massive sulphide copper–lead–zinc deposit hosted by sediments of the intracontinental Bangemall Basin in Western Australia (after Boddington 1990).

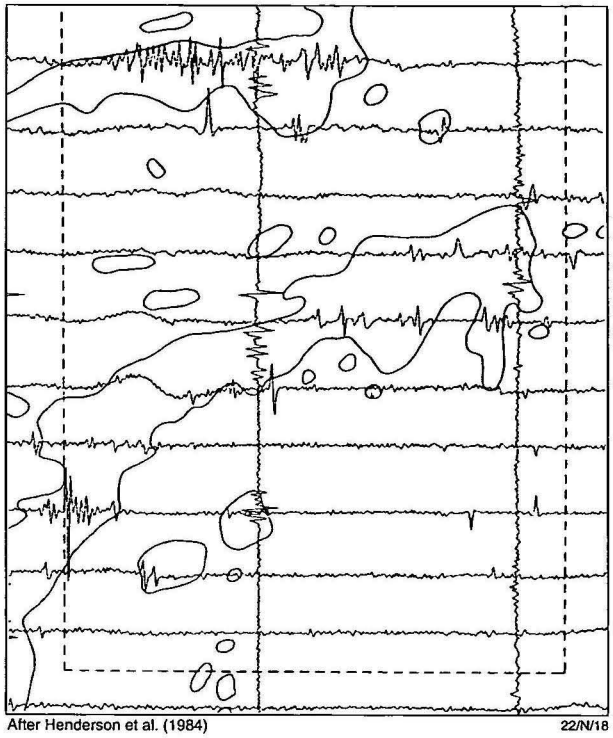

Figure 9. High frequency anomalies associated with hydrocarbon fields (after Henderson et al. 1984).

Petroleum Exploration Society of Australia symposium, Perth, 275–286.

Gunn, P. J., 1997a. Quantitative methods for interpreting aeromagnetic data: a subjective review. AGSO Journal of Australian Geology & Geophysics, 17(2)—this issue.

Gunn, P.J., 1997b. Regional gravity and magnetic responses of extensional sedimentary basins. AGSO Journal of Australian Geology & Geophysics, 17(2)—this issue.

Gunn, P.J. & Dentith, M., 1997. Magnetic responses of mineral deposits. AGSO Journal of Australian Geology & Geophysics, 17(2)—this issue.

Gunn, P.J., Brodie, R., Mackey, T. & O'Brien, G.W., 1995a. Evolution and structuring of the Joseph Bonaparte Gulf as delineated by aeromagnetic data. Exploration Geophysics 26, 255–261.

Gunn, P.J., Mackey, T., Mitchell, J. & Cathro, D., 1995b. Evolution and structuring of the offshore Otway Basin, Victoria as delineated by aeromagnetic data. Exploration Geophysics 26, 262–268.

Hamilton, D.S., Newton, C.B., Smyth, M., Gilbert, T.D., Russell, N., McMinn, A. & Etheridge, L.T., 1988. The petroleum potential of the Gunnedah Basin and overlying Surat Basin sequence, New South Wales. APEA Journal, 28, 218–241.

Haematite Exploration Pty. Ltd. 1965 Bass Strait and Encounter Bay aeromagnetic survey 1960-61. BMR Petroleum Search Subsidy Act Publication No. 60.

Heath, D.H., Clarke, V.S. & Bint, A.N., 1994. High resolution aeromagnetics clarifies structuring in the

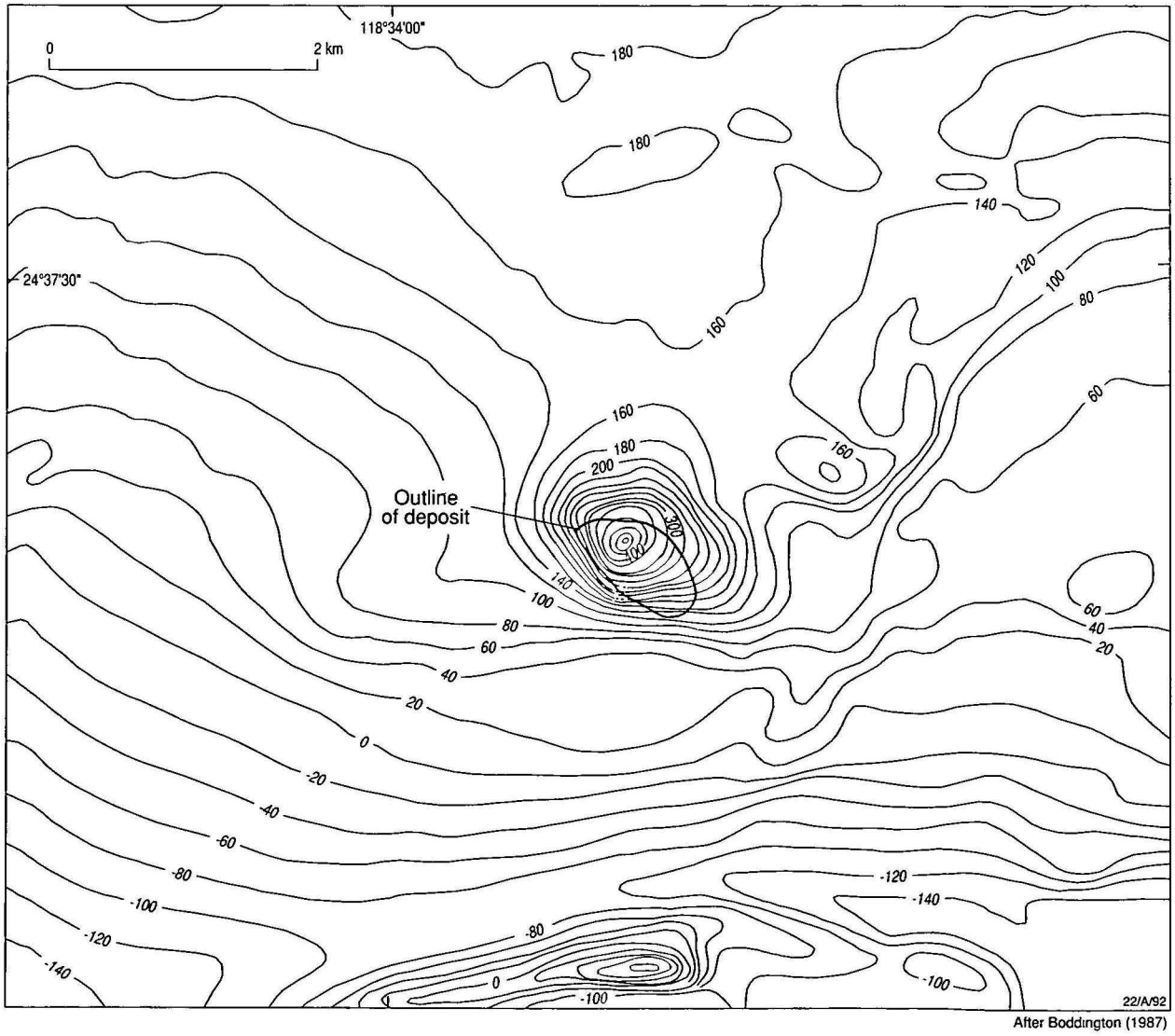

After Boddington (1987)

Vlaming Sub-Basin, Western Australia. Exploration Geophysics, 24, 535–542.
Henderson, R., Miyazaki, Y. & Wold, R., 1984. Direct indications of hydrocarbons from airborne magnetics. Exploration Geophysics, 15, 213–219.
Horsfall, K., 1997. Airborne geophysical data acquisition. AGSO Journal of Australian Geology & Geophysics, 17(2)—this issue.
Jenke, G. & Cowan, D.R., 1994. Geophysical signature of the Ellendale lamproite pipes, Western Australia. In: Dentith, M.C., Frankholme, Ho, Shepherd, S.E. Groves, D.J. & Tench, A. (editors), Geophysical signatures of West Australian mineral deposits, 402–414.
King, D. & Morton, D., 1987. Sentry Bank Reef—a case history. Exploration Geophysics, 18, 115–120.
Latin, D.M., Dixon, J.E. & Fitton, J.G., 1990. Rift related magmatism in the North Sea Basin. In: Blundell D.J. & Gibbs A.D.(editors), Tectonic evolution of the Red Sea rifts. Clarendon Press, Oxford, 145–157.
Luyendyk, A., 1997. Processing of airborne magnetic data. AGSO Journal of Australian Geology & Geophysics, 17(2)—this issue.
Machel, H.G. & Burton, E.A., 1991. Causes and spatial distribution of anomalous magnetisation in hydrocarbon seepage environments. AAPG Bulletin, 75, 1864–1876.
Milligan, P. & Gunn, P.J., 1997. Enhancements and presentation of airborne geophysical data. AGSO Journal of Australian Geology & Geophysics, 17(2)—this issue.
Mudge, S., 1994. Geophysical surveys of the Eneabba heavy-mineral sand field, Eneabba, Western Australia. In: Dentith, M.C., Frankholme, Ho, Shepherd, S.E. Groves, D.J. & Tench, A. (editors), Geophysical signatures of West Australian mineral deposits. 427–433.
Platt, N.H. & Walker, S., 1995. Integrated seismic, gravity and magnetic modelling: examples from the central North Sea. First Break, 13, 409–418.
Preview, 1993. New developments in the aeromagnetic technique for sedimentary basin exploration. Australian Society of Exploration Geophysicists, Preview, No. 42, 11–16.
Reeckman, S.A. & Mebberson, A.J., 1984. Igneous intrusions in the north-west Canning Basin and their impact on oil exploration. In: Purcell, P.G. (editor) The Canning Basin W.A., Proceedings of the GSA/Pesa Canning Basin Symposium, Perth, 1984, 389–400.
Reford, M.S. & Butt, G.R., 1983. Aeromagnetics in Australian petroleum exploration. Exploration Geophysics, 14, 113–130.
Sheard, N., Bishop, J.R. & Kissich, R.V., 1991. A practical approach to the filtering of airborne magnetic data in the Cobar region of N.S.W. Exploration Geophysics, 22, 353–356.
Smith, P. & Whitehead, M., 1989. Seismics, gravity and magnetics, a complementary study of the Paqualin structure, Timor Sea, Australia. Exploration Geophysics, 20, 25–29.
Sparlin, M.A. & Lewis, R.D., 1994. Interpretation of the magnetic anomaly over the Omaha Oil Field, Gallatin County, Illinois, Geophysics, 59, 1092–1099.
Wellman, P. & O'Brien, G.W., 1991. Vulcan Graben, Timor Sea: regional structure from a magnetic survey. Exploration Geophysics, 22, 433–438.
Young, I.F., 1987. Late Jurassic channels and associated fill, Eromanga Basin (ATP 259P), Queensland: a seismic stratigraphic study. Exploration Geophysics, 18, 238–242.

AGSO Journal of Australian Geology & Geophysics, 17(2), 145–158

Magnetic responses associated with mineral deposits

P.J. Gunn[1] & M.C. Dentith[2]

Systematic associations of magnetic minerals occur in many mineral deposits and, consequently, the probable presence of mineral deposits can be deduced from anomaly patterns in magnetic data. To be able to successfully apply such an approach an interpreter must understand the range of possibilities for the spatial distribution of magnetic minerals likely to occur in various types of mineral deposits and their host rocks.

Introduction

Significant concentrations of magnetic minerals occur in many mineral deposits and many mineral deposit types are associated with magnetic rock units. However, very few publications have addressed magnetic signatures of ore deposits and their host rocks other than on a deposit by deposit descriptive basis. The object of this paper, which considers mineral deposits in terms of their magnetic mineral associations and their known and expected magnetic responses, is to present an introduction to ways of using magnetic survey data to recognise favourable locations for orebodies and, where possible, to directly detect ore bodies. Ideas from previous works with similar objectives by McIntyre (1980), Webster (1984), Grant (1985), Hoover et al. (1991), Clark et al. (1992) and Gunn (1993) have been incorporated into the paper.

It is generally accepted that many economic mineral deposits have significant similarities in terms of mineral assemblages, geometry, host rocks, and structural and tectonic setting. This has led to the concept of 'deposit types' or 'ore deposit models', which groups deposits in terms of characteristics and origin. Reviews on the concept of ore deposit models have been published by Hodgson (1990), Roberts & Sheahan (1988), and Large (1992a). Cox & Singer (1986), Roberts & Sheahan (1988), Sawkins (1990), Solomon & Groves (1994), and others have produced comprehensive descriptive classifications of deposit types. Various specialist works exist for particular deposit types. The overview presented here of magnetic responses associated with mineral deposits is based on our subdivision of deposit types generalised from these works.

Magnetic minerals

A knowledge of the magnetic properties of minerals is fundamental to understanding the magnetic responses of mineral deposits. Clark (1997) has provided a comprehensive review of this subject in another paper in this volume, so the topic will not be elaborated here. As far as the relevance of magnetic properties to ore deposits is concerned, Clark's paper can be largely summarised by the following facts.

- Two types of magnetisation exist, viz.
  - induced magnetisation, which is proportional to the susceptibility of the material being magnetised and which has the same direction as the Earth's field;
  - remanent (permanent) magnetisation, which can have any direction.
- Induced magnetisation is far more common than remanent magnetisation. However, in certain cases remanent magnetisation can be orders of magnitude greater than induced magnetisation.
- All other factors being constant, the magnetic response of a magnetic body is directly proportional to the magnitude of its magnetisation.
- The magnetisation of a body can be directly related to the volume concentration of magnetic minerals in the body, and this relationship varies according to the magnetic mineral present.
- The only minerals that normally cause observable magnetic effects in the context of magnetic surveys related to mineral deposits are:
  - magnetite, the most magnetic mineral, which generally does not have significance remanence;
  - pyrrhotite, of which only the monoclinic form is magnetic and which frequently has remanent magnetisation an order of magnitude greater than its induced magnetisation—the susceptibility of pyrrhotite is approximately one-tenth the susceptibility of magnetite;
  - hematite, which can exhibit weak magnetic responses due to induced magnetisation and which sometimes has strong remanence;
  - ilmenite/titanohematite, which can give weak but observable magnetic responses;
  - maghemite, a weathering product, which can have strong magnetic responses.
- Pyrite, which is non magnetic, can be metamorphosed to pyrrhotite. This change tends to occur at upper greenschist–lower amphibolite grades. Pyrrhotite can be metamorphosed to magnetite.

Characteristics of magnetic responses

The form and amplitude of the magnetic response of a mineral deposit depend on many other variables in addition to the concentration of magnetic minerals present. Other key factors are the geometry and depth of the deposit, its orientation relative to magnetic north, and the inclination of the Earth's field at its location. These relationships are outside the scope of this paper, but are discussed in all basic texts on magnetic interpretation (e.g. Telford et al. 1990). The net result of these relationships is that there are no fixed anomaly forms that can be regarded as giving standard universal responses for mineral deposits. While this paper is able to describe the typical geometric distribution of magnetic minerals in a variety of mineral deposit types in their original undisturbed forms, the application of this knowledge to the detection of mineralisation requires an appreciation of how such magnetic accumulations will manifest themselves at different localities. The identification process must also account for any deformation, erosion, weathering, metamorphism or remobilisation that may have occurred during the deposit's history. Further complications can be caused by magnetic properties being anisotropic at both crystal grain and bedding scales, and the 'demagnetisation' factor, whereby the effects of extremely strongly magnetic bodies can locally alter the direction of the Earth's magnetic field and thereby influence their own magnetic anomaly. Competent interpreters of magnetic data should be familiar with such complexities.

Massive sulphide deposits

Many economic deposits occur as massive associations of sulphide minerals containing varying amounts of copper, zinc,

[1] Australian Geological Survey Organisation, GPO Box 378, Canberra, ACT 2601
[2] Department of Geology and Geophysics, The University of Western Australia, Nedlands, WA, 6009

lead, silver and gold. In many of these deposits the sulphide containing the economic mineral is a mass of pyrite and/or pyrrhotite making up 20–50 per cent of the weight of the deposit. Silica is the other main gangue mineral. Chalcopyrite, sphalerite and galena are the main economic minerals with gold and silver being generally subordinate in value. Magnetite may be present in the deposits and in some examples is the dominant gangue mineral. These deposits are referred to as massive sulphide deposits.

Various subdivisions exist for massive sulphide deposits in the published literature, of which by far the best known are the volcanic-hosted massive sulphides (Franklin et al. 1981; Lydon 1984, 1988; Large 1992b), which are hosted by volcanic rocks generally associated with marine sediments, such as shales and greywackes, in various plate-tectonic settings, such as mid-ocean-ridge ophiolites and convergent plate margin back-arc volcanic rifts, and in greenstone belts. Deposits with no obvious volcanic association, but of similar geometry, mineral associations and mineral zonings, occur in rift settings in shale/turbidite host rocks and diverse clastic assemblages identified as being deposited during the earliest (pre-rift) and latest (post-rift or sag phase) stages of rifting.

Disputes exist in the literature as to the relationship between deposits in the various settings. Some authors regard them simply as variations in a common mineralising process, according to tectonic setting and variables such as temperature, oxygen fugacity, salinity and concentration of mineralising solutions. Others invoke different origins for the varyious types. The controversy appears largely irrelevant to the study of the magnetic signatures of these bodies, because the same geometry and zoning of magnetic minerals, albeit with semi-systematic and semi-predictable variation, seem to be manifest in all massive sulphide deposits. The examples presented below support this assertion.

In recognising a common set of associations, it is instructive to use the widely recognised volcanic-hosted massive sulphide deposit type as a starting point. Figure 1, generalised from Lydon (1984) and Large (1992b), shows the idealised vertical cross-section of a volcanic-hosted mineral deposit. The deposit can have circular symmetry, but is commonly elongated in one horizontal direction. Many massive sulphide deposits occur adjacent to major faults, apparently the result of mineralising solutions ascending via the fault plane. Such deposits show the vertical zoning of Figure 1, but their form is equivalent to one side only of the model.

The notable features of typical massive sulphide deposits are:

- The economic minerals chalcopyrite, sphalerite and galena occur together with pyrite and/or pyrrhotite and/or magnetite as a massive tabular/mound-like mass in the upper central part of the deposit. Vertical zoning can occur, with chalcopyrite, magnetite and pyrrhotite tending to occur at the base of the massive sulphides, and sphalerite, galena and pyrite tending to occur in the upper part. The maximum horizontal dimension of the massive mineralisation appears to be of the order of 2000 m and the maximum thickness of the order of tens of metres. Massive sulphide deposits can be significantly smaller than these maximum dimensions.
- The massive sulphides are underlain by a stockwork of veins.
- Deposits are capped by a horizon consisting variably of pyrite, magnetite, pyrrhotite, hematite or silica-rich rocks. This 'ore equivalent horizon' may extend laterally for any distance up to tens of kilometres from the deposit.
- Not all the zones described above are always present.

The stockwork of veins is generally accepted to mark the 'chimney' by which mineralised solutions rose to where the

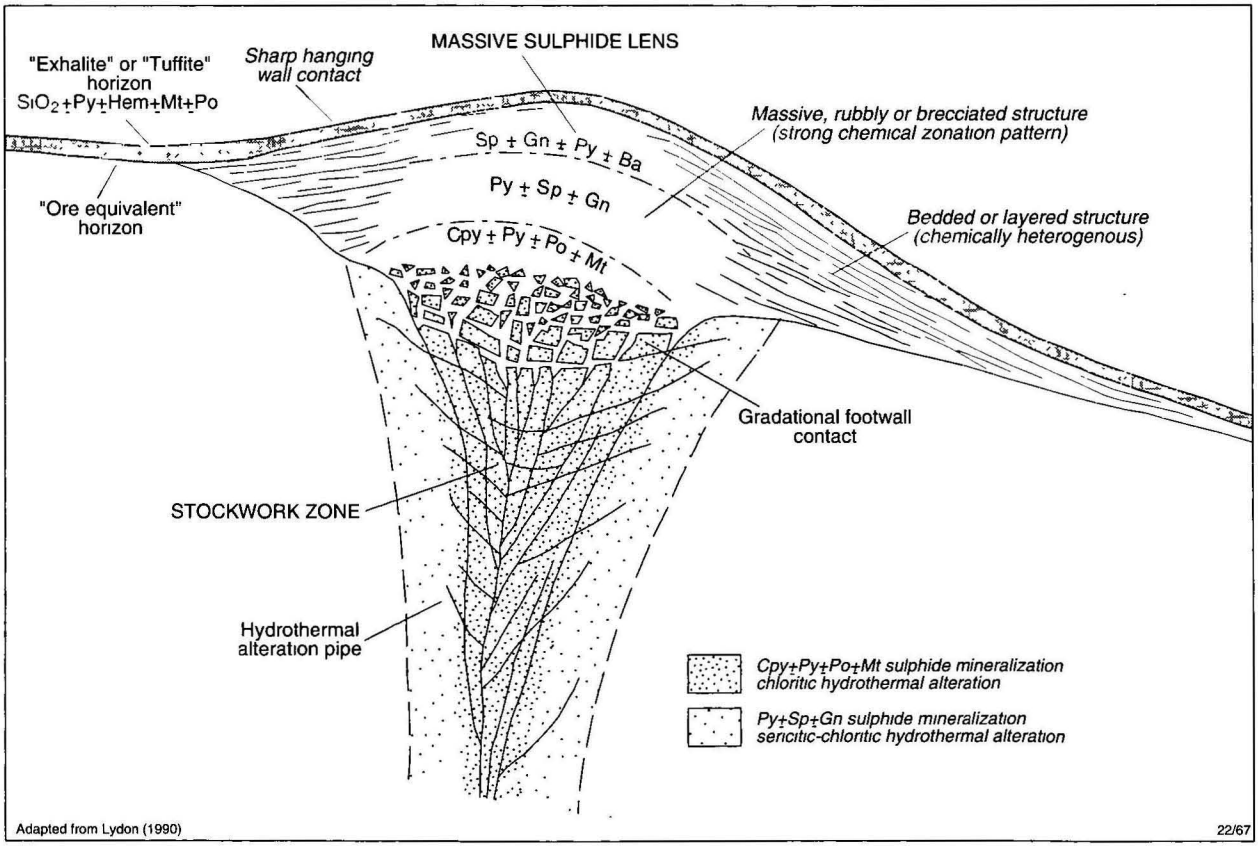

Figure 1. Idealised vertical cross-section of a massive sulphide deposit. Normally, the deposit would have circular symmetry in plan view. If the deposit has been localised by a fault, only one-half of the deposit as shown may occur. Not all the zones illustrated always occur in a single deposit.

massive sulphides were deposited (commonly regarded to be at or near the sea floor). The mineral zoning can be explained by phase diagrams relating the order of mineral precipitation to changes in temperature, oxygen fugacity and salinity as the mineralised solutions ascended. The laterally extensive horizon capping the deposit is variously regarded as a final pulse of an exhalative process associated with the deposit, a cap rock which has blocked vertical migration of mineralised solutions, or a pre-existing formation whose reactive properties have resulted in the precipitation of the massive sulphides from ascending mineralised solutions.

The magnetic response of this idealised model can be appreciated by considering the representations in Figure 2, which show, in diagrammatic form, simplified contours of magnetic fields over massive sulphide bodies with various distributions of magnetic minerals. Figure 2 assumes that the massive sulphides have been tilted on their sides and eroded to expose a plan of a vertical section through the original centre of the deposit and that the deposit is located at a magnetic pole, where there is no asymmetry due to the inclination of the Earth's magnetic field. Although many massive sulphide deposits do occur in situations where they have been tilted on their side, the geometry of the deposits in Figure 2 has been chosen primarily to illustrate that different parts of massive sulphide deposits may have different magnetic responses. If such deposits occur in other orientations, it should be remembered that magnetic responses of different parts of the deposit are likely to be superimposed. The models of Figure 2 assume that the magnetic effects of the lower numbered models are progressively incorporated into those of the higher numbered examples, although this is not always the case in nature.

Figure 2A shows zero response, as some massive sulphide bodies contain no magnetic minerals. The Teutonic Bore (Fritz & Sheehan 1984) and Woodlawn (Whiteley 1981) deposits appear to be examples.

Figure 2B shows a weak magnetic low. This can occur when mineralised solutions moving through the country rock destroy magnetic minerals adjacent to the deposit. Such processes can occur within and adjacent to the feeder pipe below the deposit. The Salt Creek deposit (Gunn & Chisholm 1984) appears to be an example.

Figure 2C shows the situation where magnetic materials such as magnetite or pyrrhotite occur within and/or at the top of the feeder pipe. The Orchan deposit (Hallof 1966; Large 1977) appears to be an example.

Figure 2D includes the responses of Figures 2B and 2C, but also includes the situation where the base of massive mineralisation has a layer of magnetic minerals. The Sullivan deposit of British Colombia (Ethier et al. 1976; Hamilton et al. 1982), which has a massive layer of monoclinic pyrrhotite beneath massive sphalerite and galena mineralisation in a pyrite gangue, accords with this situation.

Figure 2E is an extension of Figure 2D, where magnetic minerals occur throughout the deposit. The Abra deposit (Boddington 1990), which contains a magnetite gangue is an example

Deposits may also be capped by a laterally extensive horizon containing magnetic minerals which manifests itself as a magnetic ore equivalent horizon (Fig. 2E). The Hope and Gorob deposits of the Matchless Amphibolite Belt in Namibia (Campbell & Mason 1979; Breitkopf & Maiden 1988; Haussinger & Orkrush 1993) and deposits of the Namaqualand Metamorphic Complex in South Africa (Campbell & Mason 1979; Anhaeusser & Maske 1986) appear to be examples. The magnetite and pyrrhotite-rich Cu–Au and Pb–Zn deposits of the Cobar area of New South Wales area (Brooke 1975), which are associated with a magnetic disseminated pyrrhotite horizon (Clark & Tonkin 1994) may be deformed and

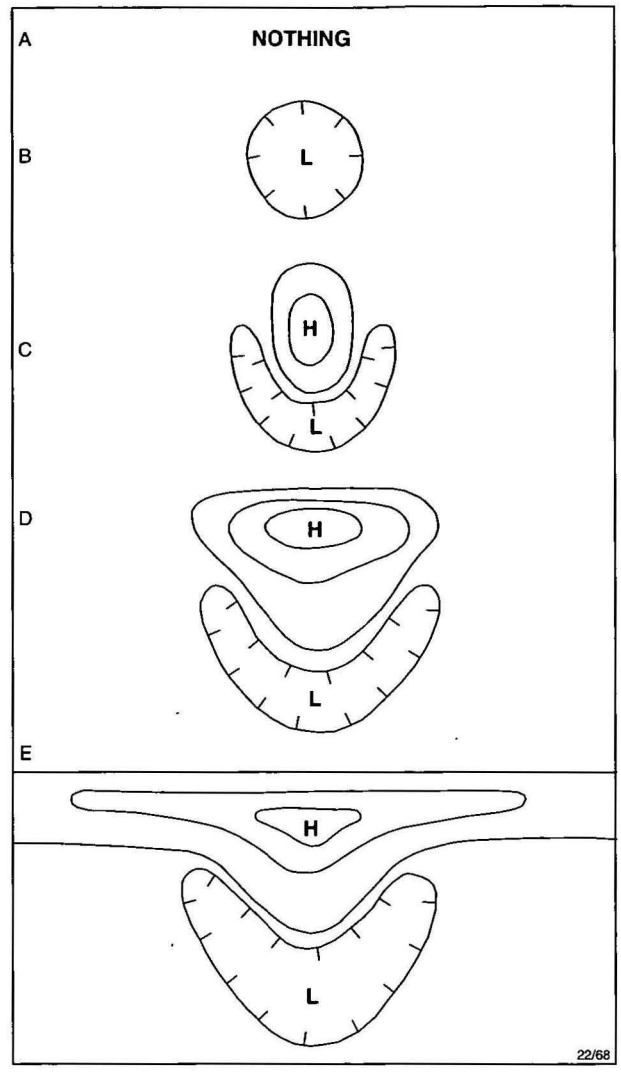

Figure 2. Idealised responses of massive sulphides. The associations with various types of mineral assemblages are given in the text of the paper.

remobilised variants of this type of deposit.

It must be remembered that the ability to detect such anomaly patterns will depend on the magnetic response of the adjacent host rocks.

Figure 3 illustrates the magnetic response of the Gurubang deposit (Aquitaine Australia Minerals 1977), approximately 20 km south of Cooma in New South Wales, in a Palaeozoic volcanic rift. The deposit, a sub-economic pyrrhotite-rich Cu–Zn deposit containing approximately 20 Mt of mineralisation, appears to display zoning consistent with Figure 1, in that the massive mineralisation is underlain by a zone of disseminated mineralisation and appears to be overlain by a magnetic pyrrhotite-rich 'ore equivalent horizon'. The magnetic response of the Gurubang deposit is similar to that illustrated in Figure 2E.

Figure 4 shows the magnetic response of the Rouez deposit, hosted by turbiditic sediments devoid of obvious igneous activity in a Proterozoic sequence in western France (Icart & Safa 1981; Sapin & Babu 1981; Lebouteiller 1981). The deposit contains approximately 100 Mt of sulphides containing Pb (6.3%), Zn (1.5%), Cu (0.6%), Ag (21 g/t) and Au (1.5 g/t). The dominant gangue is remanently magnetised pyrrhotite, which causes the magnetic response. The deposit is concordant with the local geology and occurs as several flat sheets which appear to be underlain by a feeder zone. A laterally equivalent

shale unit containing magnetic disseminated pyrrhotite appears to be an 'ore equivalent horizon'. The magnetic response of the Rouez deposit is also similar that illustrated in Figure 2e.

Magnetite-rich Cu–Au deposits of Tennant Creek

The Tennant Creek area of the Northern Territory of Australia contains numerous Cu–Au–Bi deposits. While these have many similarities to massive sulphide deposits, their characteristic differences, such as the subordinate occurrence of Fe sulphides to Fe oxides, vertical elongation as ellipsoid or tabular bodies, cross-cutting relation to host lithology and the presence of economic Bi grades, are sufficient for them to be regarded as a separate deposit type. Tonnages are typically smaller, with the largest deposit containing 7 Mt of ore.

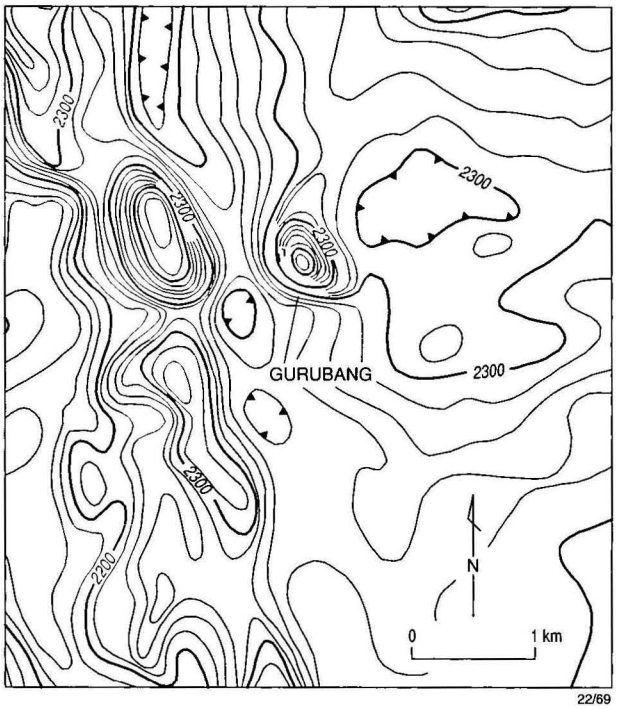

Figure 3. The magnetic response of the Gurubang deposit. The magnetic anomaly associated with the deposit is caused by remanently magnetised massive pyrhhotite. The low to the east of the deposit overlies a stringer zone and may be caused by destruction of magnetic minerals by alteration processes. The 'magnetic ridge' extending laterally from the deposit may be due to disseminated pyrrhotite in an 'ore equivalent horizon'.

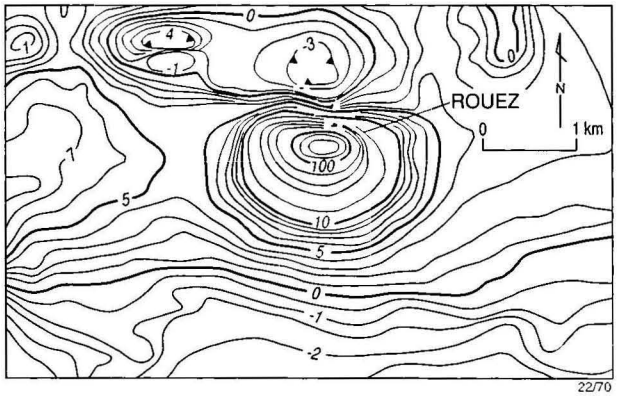

Figure 4. The magnetic response of the Rouez deposit. The main magnetic response is due to remanently magnetised massive pyrrhotite. The deposit is located on a laterally extensive magnetic ridge due to remanently magnetised disseminated pyrrhotite in a shale formation. The minor magnetic lows adjacent to the deposit could be due to destruction of the pyrhhotite by alteration processes.

The geology and geophysical responses of the deposits are well documented (Daly 1957; Gunn 1979; Farrar 1979; Hoschke 1985, 1991: Wederkind & Love 1990; Edwards et al. 1990; Hill 1990, Smith & Hall 1995) They are confined to a magnetite-rich unit of the local stratigraphy and appear to be localised by cross-cutting faults, often in fold hinges, near linear hematite shale lenses, which have many of the characteristics of 'ore equivalent horizons'. The mineralisation is significantly zoned.

The deposits have characteristic, easily recognisable, bull's-eye magnetic anomalies caused by high magnetic concentrations associated with the economic minerals (Figure 5). Magnetic data can be used to identify the extent of the favourable host stratigraphy, folds in the stratigraphy, the location of cross-cutting shears that may control the emplacement of the deposits, and the magnetic anomalies caused by magnetite associated with the economic minerals. Over 650 deposits with similar characteristics have been reported, but fewer than 200 of these contain significant economic mineralisation.

Porphyry copper deposits

The term porphyry copper deposit encompasses the Cu, Cu–Au and Cu–Mo deposits associated with intrusive stocks of generally felsic and porphyritic nature, emplaced above downgoing plates in island arc or Andean settings (Sawkins 1990). The mineralisation occurs as veins and disseminations in country rock above and adjacent to the upper portions of intrusions and in the upper parts of intrusions themselves. Systematic radial zoning of mineralisation and alteration has been identified in the majority of such deposits and a series of models for such zonings have been published (McMillan & Panteleyev 1980). Figure 6 shows a generalised representation of zoning in a porphyry ststem. As discussed by Clark et al. (1992), such intrusive systems have a semi-predictable magnetic response, albeit one related to the depth of erosion of the system. Figure 6 incorporates an idealised magnetic profile for a vertical inducing field (i.e. there is no distortion due to field inclination), reproduced from Clark et al. (1992), for the erosion level indicated in the figure.

Typically, such intrusive systems are emplaced in volcanics or are capped by volcanics associated with the intrusion. The volcanics, which are routinely inhomogeneous in nature, provide an erratic high-level magnetic response to the area. Destruction of magnetite in these volcanics by propylitic and phyllitic alteration can cause a smooth broad magnetic low over the vicinity of the intrusion. The felsic porphyry is generally, but not always, ferromagnetic in nature and, in such cases, a sharp localised magnetic high can occur in the centre of the magnetic low. This model produces a signature of porphyry copper deposits that is not directly related to the mineralisation, but rather to the ensemble of geology and processes associated with the formation of the mineralisation. Brant (1966) has published results of an aeromagnetic survey over the Bagdad porphry copper deposit in Arizona, which appears to fit this model.

Skarn deposits

Skarn deposits (Einaudi et al. 1981) consist of coarse-grained Ca–Fe–Mg–Mn silicates formed by replacement of carbonate rocks during regional or contact metamorphism and metasomatism. Skarn-hosted ore deposits, variably containing Sn, Fe, Cu, W, Zn, Pb and Ag, are commonly found at or near contacts between igneous plutons and sedimentary rocks. There are many variations between sub-classes of skarn deposits and this fact, combined with an apparent lack of definitive geophysical studies of such deposits, prevents more than a cursory overview of their magnetic signatures.

Emerson (1986) measured the magnetic properties of rock

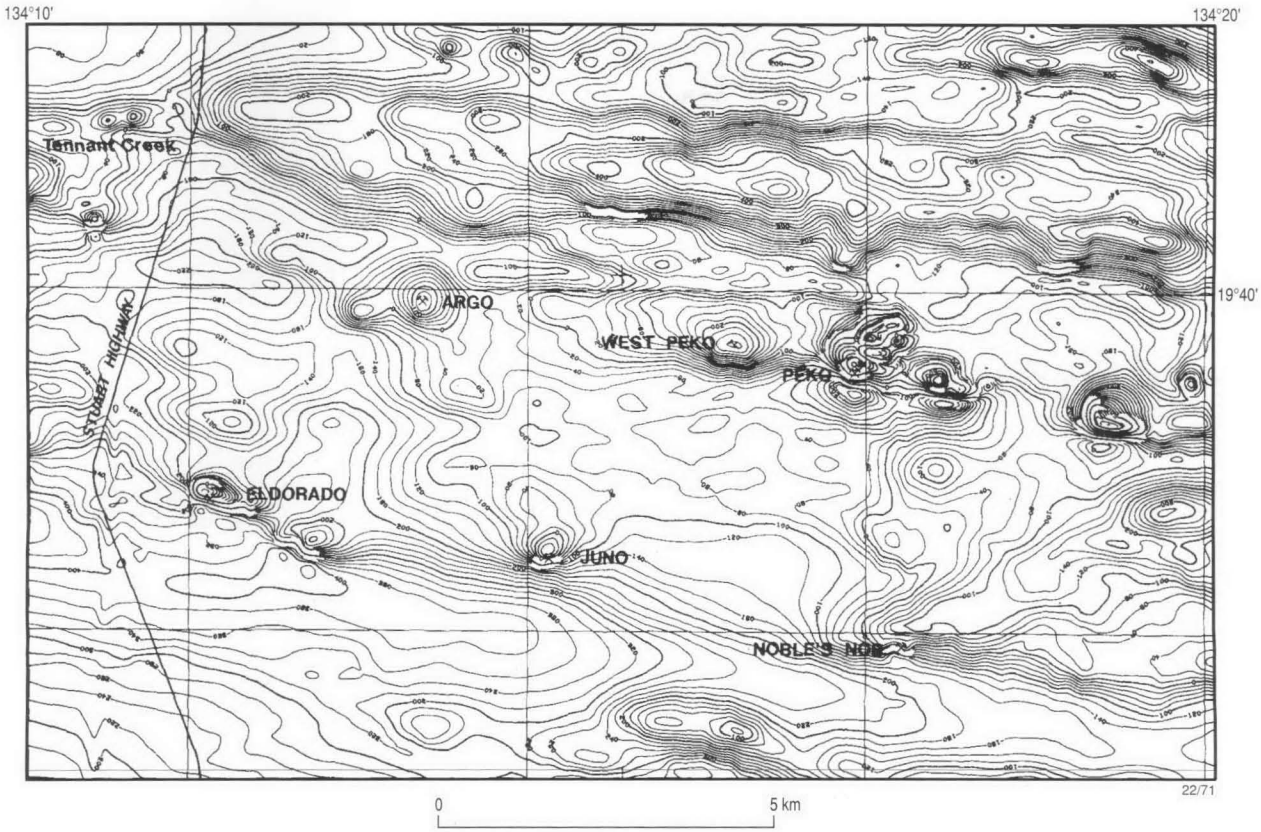

Figure 5. Magnetic responses of several Tennant Creek Cu–Au–Bi deposits (after Hoschke 1991). These manifest themselves as isolated 'bull's-eye' magnetic anomalies.

samples from the King Island W skarn deposit (Brown 1990), the Duckmaloi Bi–W skarn in New South Wales (Weber et al. 1978) and the Mount Moss Cu–Pb–Zn skarn in North Queensland (Manthorpe 1981) and concluded that the magnetisation is complex and variable and, while magnetics can aid skarn recognition, the technique cannot be relied upon for the recognition of skarn-hosted mineral deposits. Emerson did not specifically report on the magnetic responses of mineralised zones in these skarns.

Iron ores associated with igneous rocks include magmatic segregations, contact-metasomatic deposits and hydrothermal replacement deposits. Such deposits constitute only a small proportion of the world's iron production, but represent some of the best magnetic signatures, since they consist predominantly of magnetite. An example of such a deposit is the Marmora magnetite deposit, Ontario, described by Wahl & Lake (1957) as a contact replacement body in Palaeozoic limestones metamorphosed by a syenite intrusion. Metamorphism has altered the originally dolomitic limestone to a garnet, epidote or zoisite skarn. Magnetite occurs in the skarn as disseminated grains or as relatively pure masses. The mineralisation is blind, occurring at a depth of about 30 m. It was discovered through a prominent aeromagnetic anomaly (amplitude ~10 000 nT at a flight height of ~150 m). Two ground vertical magnetic intensity profiles were recorded across the ore body. One was carried out before stripping of the overburden, the second after stripping of around 30 m of cover. The former survey did not outline any zoning in the ore body, although Wahl & Lake stated that a first derivative of the data did. Differences in magnetisation were clear on the second survey and these were found to correlate closely with the grade of mineralisation.

Webster (1984) recognised a spatial association of tin deposits and the periphery of non-magnetic granites. These granites are usually identified with the ilmenite-series granitiods of Ishihara (1978), which have been linked with the S-type

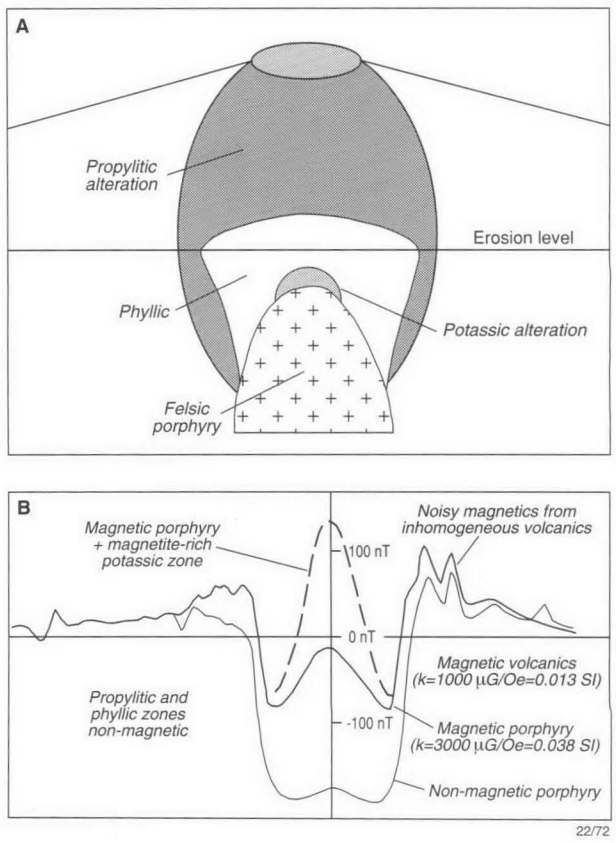

Figure 6. Idealised model for a porphyry copper deposit and associated magnetic responses (after Clarke et al. 1992). Note that the magnetic response of the system varies with depth of erosion.

granitoids of Chappell & White (1974). Tin deposits do not appear to be associated with magnetic granitoids (the magnetite type of Ishihara and the I type of Chappell & White). The tin deposits occur as cassiterite associated with sulphides and silicates in favourable carbonate horizons, breccias and veins. The primary deposits occur around cusps of ilmenite-series granitoids and frequently occur in magnetic aureoles associated with the granites. The aureoles could be due either to contact metamorphic effects or late stage mineralising fluids associated with the intrusions. Webster presented several examples from Tasmania (Cleveland, Renison, Mount Lindsay and Severn) and central New South Wales (Ardlethan and Tallenbung) to support his idea. Several of the Tasmanian deposits, viz. Renison, Mount Bischoff, Zeehan (Severn), Saint Dizier and Cleveland, are directly associated with magnetic anomalies apparently caused by associated pyrrhotite and sometimes magnetite. Large (1989) gave examples of these magnetic anomalies, which are sometimes isolated and clearly evident and sometimes partly obscured by other anomalies in the aureoles surrounding the granites.

The concepts of Webster (1984) appear capable of being generalised to allow the use of magnetics to identify:

- magnetic anomalies indicating the existence of granitic intrusions,
- whether the amplitudes of these anomalies indicate intrusions of the type likely to be associated with a particular type of skarn mineralisation,
- whether contact metamorphism and metasomatism are indicated by magnetic aureoles and,
- whether discrete anomalies likely to be directly associated with mineralisation are present.

Further work remains to be done in this field.

Placer mineral deposits

Placer deposits of minerals, notably gold, but also those of tin, platinum, heavy mineral sands, diamonds and various other minerals can be concentrated in palaeodrainage systems and on shorelines by virtue of having relatively high densities.

Often the channel systems hosting placer deposits are covered by later sediment or volcanics and, thereby, become difficult to delineate. Although the economic content of these channels does not give observable magnetic responses, there are several ways that magnetic data can be used to map the geometry of channels. These are:

- the channels may be eroded into a magnetic substratum, which can create a mappable anomalous response;
- detrital magnetite may be deposited on the floor of channels and the response of this magnetite may be mappable;
- channels may be filled by basalt flows, creating a magnetic anomaly which mirrors the channel geometry;
- maghemite may be formed in channel systems, producing a mappable magnetic pattern—spectacular magnetic images of palaeodrainage systems have been formed by this process in various parts of Australia, e.g. the Cobar area of New South Wales (Sheard et al. 1991).

The total magnetic intensity image of the Bendigo 1:250 000 map sheet (Denham 1997) includes several good examples of the mapping of palaeochannels by aeromagnetic data. These channels are extremely important in the context of gold exploration, as Bendigo has been a major producer of placer gold.

Magnetic data over the offshore area of the Joseph Bonaparte Gulf images a series of palaeochannels that apparently formed during a comparatively recent lowstand episode in the area (Gunn et al. 1995). It is unclear if detrital magnetite or maghemite is causing the anomalies. What is significant is that the clearly defined isolated channel in the west of the area is directly offshore from the mouth of the Ord River, which could be expected to drain erosion products from the diamondiferous Argyle lamproite pipe (Drew & Cowan 1994). This channel system could be prospective for alluvial diamonds

Mineral sand deposits, concentrated by gravity sorting along beaches, can contain heavy minerals such as rutile, zircon and monazite. The accumulations may be magnetically detectable if they also contain magnetite or ilmenite. Mudge (1994) reported that the mineral sand deposits of Eneabba in Western Australia, which are approximately 50 m below the ground surface and do not contain magnetite, have a weak magnetic response (less than 10 nT in ground survey data) due to their ilmenite content.

Carbonatite-associated mineralisation

Carbonatites (Bell 1989) are alkaline igneous rocks, typically intrusive, but also extrusive, which contain more than 50 per cent by volume of carbonate minerals. They contain exotic mineral assemblages, and a small percentage contain economic mineralisation. The Palabora carbonatite in South Africa contains 300 Mt of copper ore grading 0.69 per cent copper plus important economic grades of apatite and vermiculite, and the Kovodor Complex on the Kola Peninsula of Russia contains 700 Mt of iron ore reserves and 110 Mt of apatite (Sawkins 1990). These mineral concentrations of copper and iron, however, appear to be unique among carbonatites, and the main economic interest in carbonatites is that they are major sources of niobium, phosphate and rare-earth elements and significant sources of titanium, fluorite and vermiculite. Mariano (1989) gives a detailed review of economic mineralisation in carbonatites.

Intrusive carbonatites typically contain concentric zoning of carbonate rocks, which tend to occur in the cores of the intrusions, and alkalic rocks. Variable magnetite concentrations in these zones produce magnetic anomalies, often of the order of several thousand nanoteslas. In ideal circumstances, this magnetic zoning will be concentric, but shape variation in the carbonatite and variation in magnetite concentration may result in magnetic anomalies having oval, elliptical, crescent-shaped or horseshoe-shaped forms. The diameter of intrusive complexes may be of the order of several kilometres. The characteristic concentric zoning in the magnetic pattern, the intense anomaly

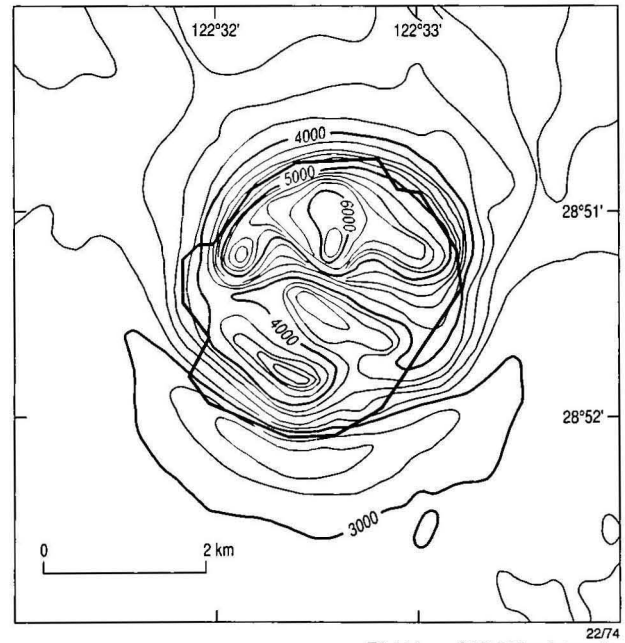

Figure 7. Magnetic response of the Mount Weld carbonatite (after Duncan & Willett 1990).

amplitudes and the tendency for carbonatites to occur in relative isolation allow the use of magnetic responses to target such intrusions. Carbonatites are enriched in uranium and thorium, and elevated radiometric count rates for these elements indicate the presence of a carbonatite rather than another type of concentrically zoned igneous intrusion.

Aeromagnetic surveys have been used successfully to discover carbonatites; approximately fifty were discovered in Ontario and adjacent parts of Quebec in the mid-1960s (Erdosh 1979). Erdosh described this carbonatite province, and gave examples of the deposits and their aeromagnetic responses. Several other examples of aeromagnetic responses have been published by the Ontario Department of Mines (1970).

Despite the widespread occurrence of carbonatites in various continents and their tendency to be geographically concentrated, there is a significant lack of reported carbonatite occurrences in Australia, the Mount Weld Carbonatite in the Archaean Yilgarn Craton (Willett et al. 1986; Duncan & Willett 1990) and the Cummins Range Carbonatite in northern Western Australia, at the junction of the Halls Creek and King Leopold Mobile Zones (Andrew 1990), being some of the few documented examples. These intrusions were discovered through the interpretation of regional aeromagnetic surveys. The Mount Weld Carbonatite has a circular plan and its detailed magnetic expression (Fig. 7) exhibits concentric zoning in accordance with the characteristics described above.

Diamonds

The known economic in-situ accumulations of diamonds occur in a small percentage of kimberlite and lamproite pipes and, although diamonds are known to occur in other igneous rocks and in rocks metamorphosed by high-pressure meteorite impacts, kimberlites and lamproites remain the prime objective of diamond explorers. The geology of these pipes, their mode of occurrence and their magnetic response are well documented, with MacNae (1979, 1995), Gurney (1989), Atkinson (1986), and Jaques (1994) providing sound introductions to these topics.

Kimberlite and lamproite pipes are emplaced as diatremes, originating at upper mantle levels, which rise to the surface with an explosive result that creates an ejecta-filled crater. Before any erosion occurs these craters are underlain by fresh intrusive material, which is approximately elliptical in plan and which tapers with depth. The maximum width of the pipes is of the order of several hundred metres, with examples of approximately 1500 m being known. The pipes can contain both magnetite and ilmenite and these minerals can give rise to observable magnetic responses. Kimberlite material can be serpentinised and this process can enhance the magnetic signature of the pipe. Not all kimberlites and lamproites are magnetic and clusters of intrusions can include magnetic, non-magnetic and reversely magnetised pipes in close proximity. Weathering of the upper parts of the systems can reduce any magnetic response.

Airborne magnetic surveys designed to detect kimberlite and lamproite pipes are typically flown along north–south flight-lines, 50–100 m above the ground with line spacing of the order of 200 m. A magnetic pipe will generally manifest itself as a circular or elliptical bull's-eye anomaly a few hundred metres across. Normally, no characteristic detail is resolvable in airborne anomalies; however, detailed ground magnetic surveys over such pipes frequently show concentric magnetic annuli, which reflect zoning of magnetic minerals in the intrusions (figure 1.16 of Atkinson 1986) The ease of detection of kimberlite and lamproite pipes with magnetic data depends on the magnetic response of the host lithology. A series of isolated, small circular anomalies is easy to detect in non-magnetic sedimentary terranes, but can be extremely hard to identify in areas covered by volcanics or surficial maghemite.

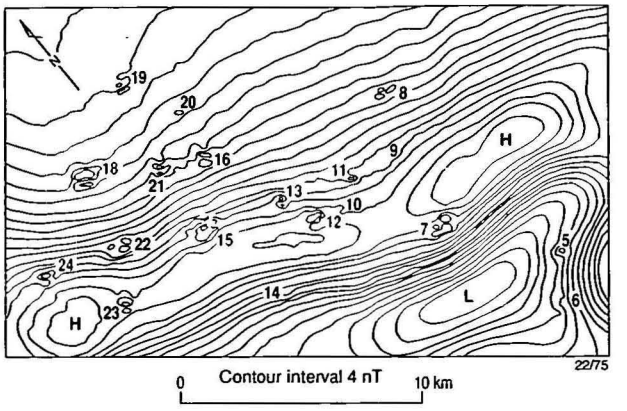

Figure 8. Magnetic responses of lamproites on the Lennard Shelf, Canning Basin, Australia (after Jenke 1983).

Compilations of the magnetic response of kimberlites and lamproites have been published by Gerryts (1970), Macnae (1979) and Atkinson (1986). Published Australian examples include descriptions of the non-economic Ellendale lamproite pipes by Jenke (1983) and Jenke & Cowan (1994). Magnetic contours clearly indicate these pipes relative to the non-magnetic sedimentary host rocks (Fig. 8). Drew & Cowan (1994) have published a description of the diamond-rich Argyle lamproite pipe and, while they conclude that the pipe is probably weakly magnetic, their actual survey results are equivocal as a result of topographic relief and relatively magnetic country rocks.

Chrome platinoids

Economic deposits of chromium, in the form of the mineral chromite, occur in ultramafic intrusions (Stowe 1987). These may be divided into two basic types, stratiform and podiform. The most famous examples of the former are the Bushveld Complex, South Africa and the Great Dyke, Zimbabwe. These layered intrusions are also host to economic platinum and magnetite mineralisation. In areas of poor exposure, magnetic surveys have been used to map the orientation of lithological layering in the Bushveld Complex and also to locate intrusive pipes (Buchanan 1988).

Podiform chromite deposits occur in peridotitic intrusions, often with an ophiolitic affiliation. Examples occur in the Urals, southwestern Europe and the Philippines. Describing deposits in the Urals, Klichnikov & Segalovich (1967) stated that direct search for chromite using the magnetic method is impossible, although zones of higher susceptibility due to serpentinite may occur adjacent to the ore zones. A relationship between magnesium chromite deposits and ultrabasic host rocks with a low iron content and, hence, reduced magnetic anomaly is also mentioned. Yungul (1956), in describing chromite deposits in Turkey, also mentioned that the strongest serpentinisation of the host rocks occurs near chromite bodies. However, the magnetic highs observed over the chromite bodies are attributed to remanent magnetisation of the chromite itself (Figure 9). Bosum (1970) reported on the magnetisation of chromite in deposits in Afghanistan, and also found remanent magnetisation to be important; Koenisberger ratios are generally greater than unity, with a maximum of nine.

Clearly, in exploration for chrome, magnetic surveying can play a role both in locating favourable host rocks and in identifying ore itself. However, mainly because of the magnetic nature of the local geological environment, magnetic data alone are not reliable and gravity data are normally also required.

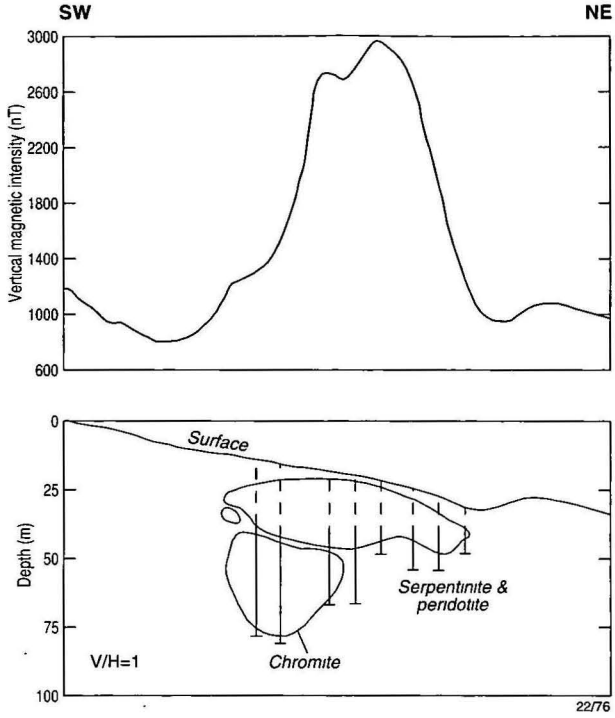

Figure 9. Geological cross-section and magnetic profile across a chromite body in the Guleman area, Turkey. The dashed part of the drill holes indicates the extrapolation to the surface of holes drilled after mining of the shallower ore body. Based on figures in Yungul (1956).

Gold

The low grades of economic gold mineralisation make direct detection using geophysical methods currently impossible (Doyle 1990). For this reason, the main use of magnetic data in exploration for gold is as a mapping tool in conjunction with other exploration methods, particularly geochemistry. The usual aims of such magnetic surveys are to:

- map particular stratigraphic horizons and lithologies which may be mineralised,
- identify structures that may be mineralised,
- detect the presence or absence of magnetic minerals caused by events which may be associated with processes creating gold deposits (e.g. alteration).

These approaches, which are not mutually exclusive, have been used to explore for gold mineralisation ranging in age from Archaean to Recent. As gold occurs in a wide range of geological environments, it is only possible in this review to cite a few examples of the application of magnetic techniques to gold exploration. Probably the best example is the use of high-resolution aeromagnetic data to map Archaean granitoid–greenstone terrains. Such surveys are particularly important in areas of poor outcrop, such as Western Australia (Isles et al. 1989).

In both the Yilgran Craton of Western Australia and the Abitibi region of Canada, gold deposits are spatially associated with large-scale structures defined by regional magnetic datasets (Read 1989; Groves et al. 1990). Once areas considered favourable to mineralisation have been located, surveys of increasing resolution are used to map at local and prospect scales. The value of the data is increased by the fact that gold mineralisation is often structurally controlled and is often found in iron-rich rocks (Groves et al. 1994), which tend to be relatively magnetic. For example, in the differentiated dolerite intrusion that hosts the world-class gold deposits of the Golden Mile at Kalgoorlie, Western Australia, the more magnetic phases of the intrusion are preferentially mineralised, especially where they are cut by faults.

Another example of the use of geophysics for geological mapping is the tracing of magnetic shale horizons in the West Rand Group of the Witwatersrand Basin, South Africa (Roux 1967). In favourable areas, these beds can be detected below several thousand metres of sediment. The gold itself occurs in conglomeratic horizons stratigraphically above these beds. However, the stratigraphic relationship between these units is fairly consistent and hence the location of the shales is a valuable indicator of the gold-bearing strata.

Magnetic anomalies associated with gold mineralisation itself may be due to either magnetite or pyrrhotite. The anomalies may be positive or negative depending on whether the process of mineralisation has deposited or destroyed these minerals. In the Yilgarn Craton the sulphides that may be associated with gold mineralisation depend on the local metamorphic grade. In greenschist facies deposits, pyrite or arsenopyrite are expected. However, at amphibolite facies either pyrite or pyrrhotite may be dominant (Groves et al. 1990). Dockery (1984) describes a positive anomaly due to disseminated pyrrhotite at the Lady Susan prospect in the Archaean of Western Australia.

Hydrothermal alteration associated with gold mineralisation may either create or destroy magnetite. Figure 10 shows a cross-section through the Archaean North Orchin gold deposit, south of Kalgoorlie, Western Australia. Mineralisation is controlled by a thrust, and the deposit is associated with a positive magnetic anomaly of several 100 nT, which has been interpreted as due to a magnetite-stable alteration halo (Williams 1994). Magnetic susceptibility data from drill core show the sub-surface distribution of susceptibility to be complex. Variations are partly due to a fine network of auriferous structures related to the main thrust.

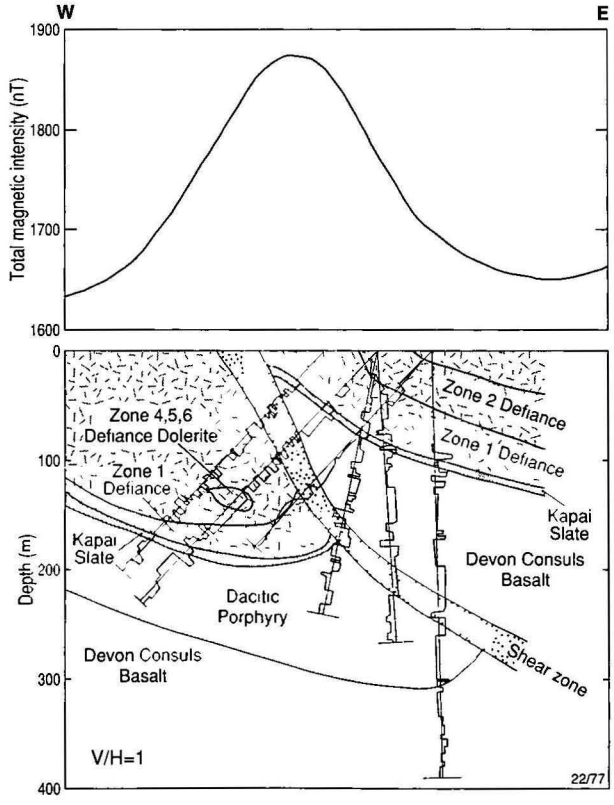

Figure 10. Geological cross-section and magnetic profle across the Orchin gold deposit, Western Australia. The magnetic anomaly is interpreted as due to a magnetite-stable alteration halo. Variations in magnetic susceptibility measured from diamond drill core are also shown. Based on figures in Williams (1994).

Irvine & Smith (1990) gave several examples of hydrothermal destruction of magnetite in the context of epithermal gold deposits. They correlated mineralising processes and zones of flat, smooth magnetic fields surrounding gold deposits.

Clearly, magnetic surveys have a role to play in exploration for gold, particularly when outcrop is poor. However, the responses due to mineralisation itself are diverse and not readily discriminated from anomalies due to other causes. A detailed knowledge of local geology thus appears to be a prerequisite for the successful application of magnetic surveys in gold exploration.

Iron ore

Exploration for iron ore based on its magnetic effects represents the earliest use of geophysics in mineral exploration. According to Espersen (1967), magnetic surveys to locate iron ore were carried out in Sweden as early as the middle of the seventeenth century.

The magnetic signature of iron deposits fundamentally depends on whether the mineralisation is in the form of magnetite or hematite. The majority of the world's iron production comes from ores in banded iron formation (BIF). Important occurrences of such ores are in the Pilbara region of Western Australia and the Lake Superior region of North America. Obviously, such a geological environment gives rise to extremely large and complex magnetic anomalies. The interpretation of data collected from such areas is complicated by the magnitude of the anomalies—which may be significant relative to the geomagnetic field where significant magnetite is present—the presence of strong remanent magnetisation, demagnetisation, and the markedly anisotropic nature of the magnetic properties of the BIFs (Clark & Schmidt 1994).

Kerr et al. (1994) describe the magnetic signatures of BIF-hosted iron ore deposits from the Pilbara region. Structural and stratigraphic control of the mineralisation is important here and the mapping of appropriate stratigraphic horizons and identification of suitable structures, such as faults and folds, are important aspects of the interpretation of magnetic data. The ores themselves form by supergene enrichment of BIF with magnetite being altered to hematite. The ore appears as zones of reduced magnetic intensity within the magnetic BIF horizons. However, this signature is not diagnostic and many similar but unmineralised 'lows' may occur. A similar approach to exploration and ore signature has been reported from Russia (Krutikhovskaya et al. 1967) and North America (Leney 1966).

Hematite iron ore containing approximately 60 per cent iron occurs as localised deposits in extensive quartz magnetite BIF containing approximately 30 per cent iron in the Middleback Ranges of South Australia (Owen & Whitehead 1965). Publications recording the magnetic properties and magnetic responses of these rocks include Taylor (1964), Webb (1966) and Gunn (1975). The hematite ore has a minor magnetic response; however, the BIF is strongly magnetic. Figure 11 shows computer modelling of magnetic profiles across the BIF, reproduced from Gunn (1967), indicating that weathering which converts magnetite to hematite can penetrate to depths of more than 100 m.

The Savage River deposit in northwestern Tasmania is a massive magnetite body that is generally thought to have a magmatic origin (Coleman 1975). The deposit is associated with a magnetic anomaly of more than 10 000 nT, and magnetic surveying, played a major role in the delineation of the deposit (Eadie 1970).

An example of an iron ore replacement deposit was given earlier in the section **Skarn deposits**.

Nickel deposits

Economic deposits of nickel are of two basic types, nickeliferous laterite and nickel sulphides (Knight 1975), and magnetic surveys play a key role in their exploration, for two reasons. Firstly, the deposits occur in association with basic to ultrabasic (meta)igneous rocks, and such rocks tend to have strong magnetic responses. Secondly, the presence of pyrrhotite and magnetite in many nickel sulphide deposits means that the mineralisation itself may be directly detectable by the magnetic method. Nickel-bearing laterites result from the weathering of basic and ultrabasic rocks and, obviously, these source rocks can be readily distinguished, using magnetic surveys, from other less-magnetic rocks.

During exploration, areas likely to contain nickel sulphides are first located with aeromagnetic data. Follow-up ground surveys are then usually required to better delineate prospective areas. An excellent example of the use of aeromagnetic data in this way is in exploration for the komatiitic peridotite-hosted deposits in the Archaean Yilgarn Craton of Western Australia. The geophysical expression of these deposits is described by Mutton (1987), Mutton & Willliams (1994), Pridmore et al. (1984) and Trench & Williams (1994). The deposits occur on or near the contact between komatiitic volcanics and underlying tholeiitic basalts. The sulphides occur in embayments in the contact between the two rock types, interpreted as troughs formed by thermal erosion during eruption of the ultramafics. Later deformation is often concentrated within these troughs. Since the stratigraphy is subvertical, magnetic surveys can be used to map the mafic–ultramafic contact and identify embayments. Subtle changes in thickness and geochemistry of the overlying ultramafics may also be detected.

Many occurrences of nickeliferous sulphides are associated with discrete magnetic anomalies (Dowsett 1967; McCall et al. 1995), some or all of which may be caused by the mineralisation itself. A detailed analysis of the source of magnetic anomalies associated with some Archaean nickel sulphide deposits in the Kambalda area, Western Australia, is described by McCall et al. (1995). Extensive studies of the magnetic properties of both ore and host rocks identified significant variation between individual deposits. The magnetisation of the ore and hanging-wall ultramafic units, the most likely causes of the magnetic anomalies, is affected by their metamorphic/ alteration history. Talc–carbonate alteration reduces the susceptibility of the ultramafics, owing to destruction of magnetite, whilst serpentinisation has the opposite effect. Temperature during metamorphism affects the mineralogy of the ores, with hexagonal pyrrhotite occurring in high-temperature areas. Modelling shows that a shallow magnetic ore body in an area of relatively unmagnetised ultramafics would produce a detectable magnetic anomaly. However, since the metamorphic/alteration environment varies significantly between deposits a few kilometres apart, it is not possible to confidently link any anomaly to previously undiscovered mineralisation.

Figure 12 shows cross-sections and corresponding magnetic profiles across deposits from the Thompson area of Manitoba, Canada. In the case of the Thompson ore body, Dowsett (1967) described pyrrhotite in the ore body as the major cause of the magnetic anomaly, but the nearby 'iron formation' is also a contributor. A peridotite body in the deeper part of the ore body is too deep to be a significant contributor. In contrast, the high-amplitude and longer wavelength magnetic anomaly associated with the Pipe ore body has a significant component originating in the peridotite body that hosts the ore. Also, the ore contains magnetite inclusions as well as pyrrhotite.

Despite the association of magnetic anomalies with many nickel sulphide ore bodies, magnetic data alone are unreliable for locating ore bodies and the use of other geophysical methods, particularly electromagnetics, is essential in target selection.

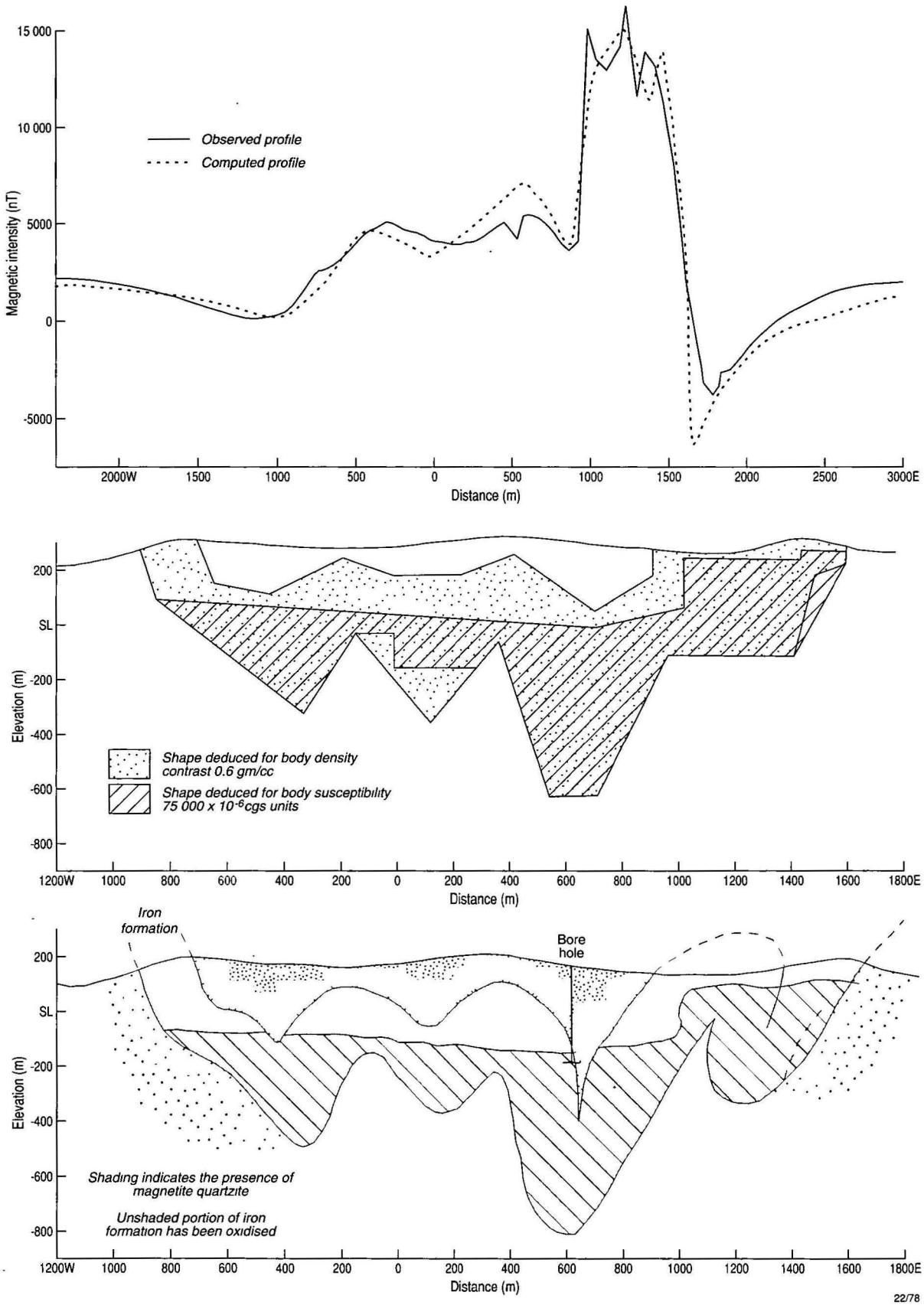

Figure 11. Interpreted magnetic profile over the Middleback Range iron formations, South Australia (after Gunn 1967) The interpretation has been based on detailed rock property measurements and subsequent correction of these values for demagnetisation. The computer program applied a terrain correction for portions of the magnetic mass above observation points. The interpretation indicated a folded layer of magnetite quartzite that has been extensively weathered in its upper levels to hematite. This interpretation is consistent with surface dips and the geometry of the iron formation indicated by gravity modelling.

Concluding remarks

It is apparent, from the examples described above, that the magnetic method can be used as a primary exploration tool for many mineral deposit types. It has not been possible here to exhaustively review studies already existing in the literature. To give a comprehensive coverage of the magnetic response of each of deposit type mentioned in this paper it would be necessary to devote at least a separate paper to each deposit type. What is obvious from the above review is that much more work relating magnetic distribution, magnetic responses and economic mineral accumulations is required. A thorough knowledge of the distribution of magnetic minerals in ore deposits and their host rocks is essential for the successful application of the magnetic method in exploration.

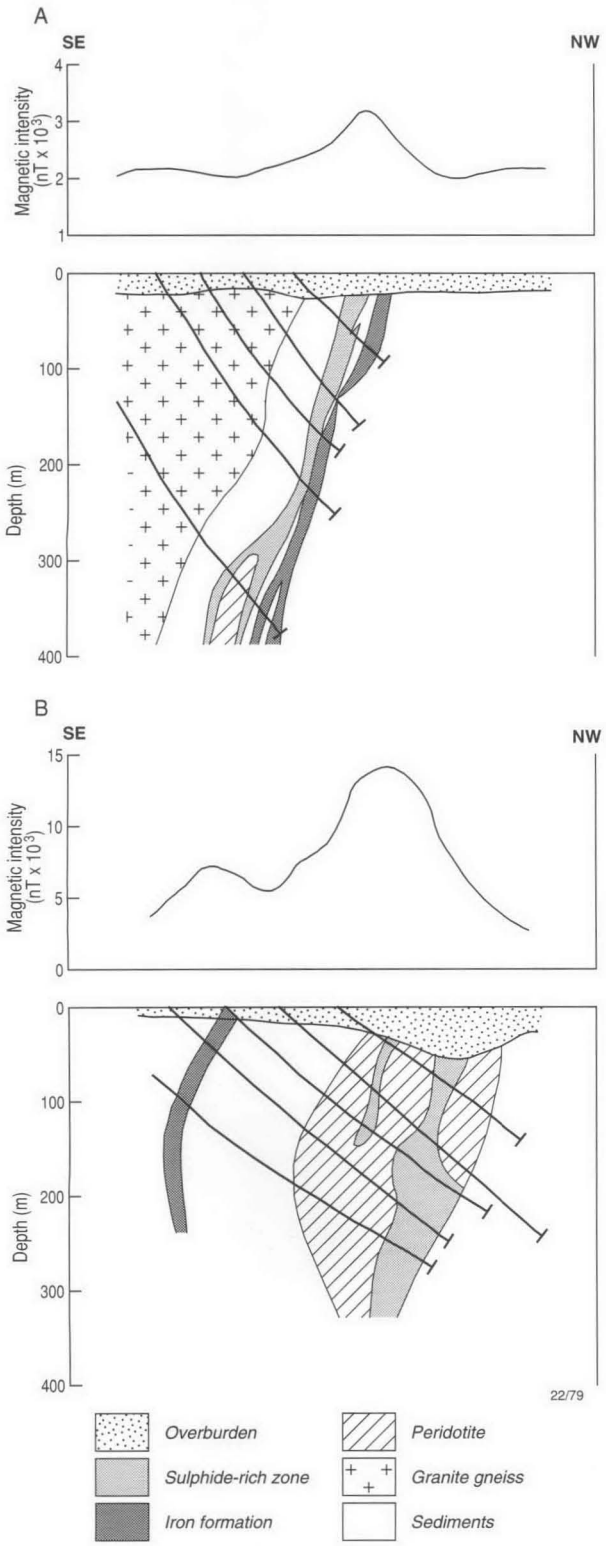

Figure 12. Geological cross-sections and magnetic profile across nickel sulphide deposits in the Thompson area, Manitoba. (A) Thompson mine, (B) Pipe mine. Note the difference in the scales of the magnetic profiles. Redrawn from Dowsett (1967)

Acknowledgements

Constructive comments on the manuscript by S. Webster and R. Haren were greatly appreciated.

References

Andrew, R.L., 1990. Cummins Range Carbonatite. In: Hughes, F.E. (editor), Geology of the mineral deposits of Australia and Papua New Guinea. Australasian Institute of Mining and Metallurgy, Monograph 14, 711–714.

Anhaeusser, C.R. & Maske, S. (editors), 1986. Mineral deposits of Southern Africa. Geological Society of South Africa, Johannesburg.

Aquitaine Australia Minerals Pty Ltd, 1977. Geological Survey of New South Wales, Open File Report for Permit EL786.

Atkinson, W.J., 1989. Diamond exploration philosophy, practice, and promises: a review. In: Ross, J. (editor), Kimberlites and related rocks. Geological Society of Australia, Special Publication 14, 1075–1107.

Bell, K. (editor), 1989, Carbonatites, genesis and evolution. Unwin Hyman, London, 618 pp.

Boddington, T.D.M., 1990. Abra lead–silver–copper–gold deposit. In: Hughes, F.E. (editor), Geology and mineral deposits of Australia and Papua New Guinea. Australasian Institute of Mining and Metallurgy, Monograph 14, 1195–1209.

Bosum, W., 1970. An example of chromite prospection by magnetics. Geophysical Prospecting 18, 637–653.

Brant, A.A., 1966. Geophysics in the exploration for Arizona porphyry coppers. In: Titley, S.R. & Hicks, C.L. (editors), Geology of the porphyry copper deposits: southwestern North America. University of Arizona Press, Tucson, 87–110.

Breitkopf, J.H. & Maiden, K.J., 1988. Tectonic setting of the Matchless Belt pyritic copper deposits, Namibia. Economic Geology, 83, 710–723.

Brooke, W.J.L., 1975. Cobar mining field. In: Knight, C.L. (editor), Economic geology of Australia and Papua New Guinea, Vol. 1, Metals. Australasian Institute of Mining and Metallurgy, Melbourne, 683–694.

Brown, S.G., 1990. King Island scheelite deposits. In:Hughes, F.E. (editor), Geology of the mineral deposits of Australia and Papua New Guinea. Australasian Institute of Mining and Metallurgy, Monograph 14, 1175–1194.

Buchanan, D.L., 1988. Platinum-group element exploration. Developments in Economic Geology 26, Elsevier, 178 pp.

Campbell, G. & Mason, R., 1979. The application of airborne and ground geophysical techniques to the search for magnetite quartzite associated base metal deposits in Southern Africa. In: Hood, P.J. (editor), Geophysics and geochemistry in the search for metallic ores: proceedings of Exploration 77, an international symposium, Ottawa, October 1977. Geological Survey of Canada, Economic Geology Report 31, 757–778.

Chappel, B.W. & White, A.J.R., 1974. Two contrasting granite types. Pacific Geology, 8, 173–180.

Clark, D.A., 1997. Magnetic properties of rocks and

minerals. AGSO Journal of Australian Geology & Geophysics, 17(2)—this issue.
Clark, D.A. & Schmidt, P.W., 1994. Magnetic properties and magnetic signatures of BIFs of the Hamersley Basin and Yilgarn Block, Western Australia. In: Dentith, M.C., et al. (editors), Geophysical signatures of Western Australian mineral deposits. Geology and Geophysics Department (Key Centre) and UWA Extension, University of Western Australia, Publication 26, Australian Society of Exploration Geophysicists, Special Publication 7, 343–354.
Clark, D.A. & Tonkin, C., 1994. Magnetic anomalies due to pyrrhotite: examples from the Cobar area, N.S.W., Australia. Applied Geophysics, 32, 11–32.
Clark, D.A., French, D.H., Lackie, M.A. & Schmidt, P.W., 1992. Magnetic petrology: application of integrated magnetic and petrological techniques to geological interpretation of magnetic surveys. Exploration Geophysics, 23, 65–68.
Coleman, R.J., 1975. Savage River magnetite deposits. In: Knight, C.L. (editor), Economic geology of Australia and Papua New Guinea, Vol. 1, Metals. Australasian Institute of Mining and Metallurgy, Melbourne, 598–604.
Cox, D.P. & Singer, D.A. (editors), 1986. Mineral deposit models. United States Geological Survey, Bulletin 1693.
Daly, J., 1957. Magnetic prospecting at Tennant Creek, Northern Territory 1935–37. Bureau of Mineral Resources, Australia, Report 114.
Denham, D., 1997. Applications and strategic importance in Australia of airborne geophysics. AGSO Journal of Australian Geology & Geophysics, 17(2)—this issue.
Dockery, B A. 1984 Geophysical case history of the Lady Susan gold deposit. In: Doyle, H.A. (editor), Geophysical exploration for Precambrian gold deposits. Geology Department and University Extension, University of Western Australia, Publication 10, 165–182.
Dowsett, J.S., 1967. Geophysical exploration methods for nickel. In: Morley, L.M. (editor), Mining and groundwater geophysics/1967. Department of Energy, Mines and Resources, Canada, Economic Geology Report 26, 310–321.
Doyle, H.A., 1990. Geophysical exploration for gold—a review. Geophysics 55, 134–146.
Drew, G.J. & Cowan, D.R., 1994. Geophysical signature of the Argyle lamproite pipe, Western Australia. In: Dentith, M.C., et al. (editors), 1994 Geophysical signatures of Western Australian mineral deposits. Geology and Geophysics Department (Key Centre) and UWA Extension, University of Western Australia, Publication 26 and Australian Society of Exploration Geophysicists, Special Publication 7, 393–414.
Duncan, R.K. & Willett, G.C., 1990. Mount Weld carbonatite. In: Hughes, F.E. (editor), Geology of the mineral deposits of Australia and Papua New Guinea. Australasian Institute of Mining and Metallurgy, Monograph 14, 591–597.
Eadie, E.N., 1970. Magnetic surveying of the Savage River and Long Plains iron deposits, north-west Tasmania. Bureau of Mineral Resources, Australia, Report 120.
Edwards, G.C., Booth, S.A. & Cozens, G.J., 1990. White Devil gold deposit. In: Hughes, F.E. (editor), Geology of the mineral deposits of Australia and Papua New Guinea Australasian Institute of Mining and Metallurgy, Monograph 14, 849–855.
Einaudi, M T., Mienert, L.D. & Newberry, R.J., 1981. Skarn deposits. In: Skinner, B.J. (editor), Economic Geology, Seventy-Fifth Anniversary Volume, 317–391.
Emerson, D.W., 1986. Physical properties of skarns. Exploration Geophysics 17, 201–212.
Erdosh, G. 1979. The Ontario carbonatite province and its phosphate potential. Economic Geology 74, 331–338
Espersen, J., 1967. Iron ore prospecting in Scandinavia and Finland. In: Morley, L.M. (editor), Mining and groundwater geophysics/1967. Department of Energy, Mines and Resources, Canada, Economic Geology Report 26, 381–388.
Ethier, K.G., Campbell, F.A., Both, R.A. & Krouse, H.R., 1976. Geological setting of the Sullivan orebody and estimates of temperature and pressure of metamorphism. Economic Geology, 71, 1570–1588.
Farrar, L.J.D., 1979. Some comments on detailed magnetic investigations of ellipsoidal bodies at Tennant Creek. Bulletin of the Australian Society of Exploration Geophysicists, 10, 26–33.
Franklin, J.M., Sangster, D.F. & Lydon, J.W., 1981. Volcanic associated massive sulphide deposits. In: Skinner, B.J. (editor), Economic Geology, Seventy-Fifth Anniversary Volume, 485–627.
Fritz, F.P. & Sheehan, G.M., 1984. The geophysical signature of the Teutonic Bore Cu–Zn–Ag massive sulphide deposit, Western Australia. Exploration Geophysics, 15, 127–142.
Gerryts, E., 1970. Diamond prospecting by geophysical methods: a review of current practice. In Morley L.M. (editor), Mining and groundwater geophysics/1967. Geological Survey of Canada, Economic Geology Report 26, 439–446.
Grant, F.S., 1985. Aeromagnetics, geology and ore environments. I, Magnetite in igneous, sedimentary and metamorphic rocks: an overview. II, Magnetite and ore environments. Geoexploration, 23, 305–365.
Groves, D.I., Knox-Robinson, C.M., Ho, S.E. & Rock, N.M.S., 1990. An overview of Archaean lode-gold deposits. In: Ho, S.E., et al. (editors), Gold deposits of the Yilgarn Craton, Western Australia: nature, genesis and exploration guides. Geology Department (Key Centre) and University Extension, University of Western Australia, Publication 20, 2–18.
Gunn, P.J., 1967. Gravitational and magnetic interpretation of the Middleback Range area, South Australia. Unpublished MSc thesis, University of Melbourne.
Gunn, P.J., 1975. Gravity and magnetic surveys over iron formations, Middleback Ranges South Australia. Australasian Institute of Mining and Metallurgy, Proceedings No. 255, 15–23.
Gunn, P.J., 1979. Examples of computer based interpretation methods used as routine exploration aids. Australian Society of Exploration Geophysicists, Bulletin, 10, 15–25.
Gunn, P.J., 1993. Magnetic signatures of gold, copper–lead–zinc–silver massive sulphide deposits in extensional sedimentary basins. Gunn Geophysics Pty Ltd, 182 pp.
Gunn, P.J. & Chisholm, J., 1984. Non-conductive volcanogenic massive sulphide mineralisation in the Pilbara area of Western Australia. Exploration Geophysics, 15, 143–153.
Gunn, P.J., Brodie, R.C., Mackey, T. & O'Brien, G.W., 1995. Evolution and structuring of the Joseph Bonaparte Gulf as delineated by aeromagnetic data. Exploration Geophysics, 26, 255–261.
Gurney, J.J., 1989. Diamonds. In: Ross, J. (editor), Kimberlites and related rocks. Geological Society of Australia, Special Publication 14, 935–965.
Hallof, P.G., 1966. Geophysical results from the Orchan Mines Ltd. property in the Mattagami area of Quebec. In: Hansen, D.A., et al. (editors), Society of Exploration Geophysicists' mining geophysics, Vol. 1, Case histories. Society of Exploration Geophysics, 157–171.
Hamilton, J.M., Bishop, D.T., Morris, H.C. & Owens,

O.E., 1982. Geology of the Sullivan orebody, Kimberly, B.C., Canada. In: Hutchinson R.W., Spence, C.D.& . Franklin, J.M. (editors), Precambrian sulphide deposits. Geologists Association of Canada, Special Paper 25, 597–665.

Haussinger, H. & Okrush, M., 1993. Geochemistry of premetamorphic hydrothermal alteration of metasedimentary rocks associated with the Gorob massive sulphide prospect, Damara Orogen, Namibia. Economic Geology, 88, 72–90.

Hill, J.H., 1990. TC-8 gold deposit. In: Hughes, F.E. (editor), Geology of the mineral deposits of Australia and Papua New Guinea. Australasian Institute of Mining and Metallurgy, Monograph 14, 857–869.

Hodgson, C.J., 1990. Uses (and abuses) of ore deposit models in mineral exploration. Geoscience Canada, 17, 59–69.

Hoover, D.B., Heran, W.D. & Hill, P.L. (editors), 1992. The geophysical expression of selected deposit models. United States Geological Survey, Open File Report 92-557.

Hoschke, T., 1985. A new drillhole magnetometer: preliminary results from Tennant Creek area. Exploration Geophysics, 16, 365–374.

Hoschke, T., 1991. Geophysical discovery and evaluation of the West Peko copper–gold deposit, Tennant Creek. Exploration Geophysics, 22, 485–496.

Icart, J.C. & Safa, P., 1981, Rouez: environment geologique et mineralisation. Chronique de la Recherche Miniere, No 458, 12–32.

Irvine,R.J. & Smith, M.J., 1990. Geophysical exploration for epithermal gold deposits. Journal of Geochemical Exploration, 36, 375–412.

Ishihara, S., 1978. Metallogenesis in the Japan island arc system. Journal of the Geological Society, 135, 389–406.

Isles, D., Harman, P.G. & Cunneen, J.P., 1989. The contribution of high resolution aeromagnetics to Archean gold exploration in the Kalgoorlie region, Western Australia. In: Keays, R.R., et al. (editors), The geology of gold deposits: the perspective in 1988. Economic Geology, Monograph 6, 389–397.

Jaques, A.L., 1994. Diamonds in Australia. In: Solomon, M. & Groves, D.I. (editors), The geology and origin of Australia's mineral deposits. Oxford University Press, 787–820.

Jenke, G., 1983. The role of geophysics in the discovery of the Ellendale and Fitzroy kimberlites. Proceedings, Third Biennial Conference of the Australian Society of Exploration Geophysicists, 66–72.

Jenke, G. & Cowan, D.R., 1994. Geophysical signature of the Ellendale lamproite pipes, Western Australia. In:Dentith, M.C., et al. (editors), Geophysical signatures of Western Australian mineral deposits. Geology and Geophysics Department (Key Centre) and UWA Extension, University of Western Australia, Publication 26 and Australian Society of Exploration Geophysicists, Special Publication 7, 403–414.

Kerr, T.L., O'Sullivan, A.P., Podmore, D.C., Turner, R., & Waters, P., 1994. Geophysics and iron ore exploration: examples from the Jimblebar and Shay Gap-Yarrie regions, Western Australia. In, Dentith, M.C., et al. (editors), Geophysical signatures of Western Australian mineral deposits. Geology and Geophysics Department (Key Centre) and UWA Extension, University of Western Australia, Publication 26 and Australian Society of Exploration Geophysicists, Special Publication 7, 355–368.

Klichnikov, V.A. & Segalovich, V.I., 1967. The application of geophysics to exploration for chromite and tungsten. In: Morley, L.M. (editor), Mining and groundwater geophysics/1967. Department of Energy, Mines and Resources, Canada, Economic Geology Report 26, 476–484.

Knight, C.L. (editor), 1975. Economic geology of Australia and Papua New Guinea, Vol. 1, Metals, Australasian Institute of Mining and Metallurgy, Melbourne, 1126 pp.

Krutikhovskaya, Z.A., Schmidt, N.G. & Kiselyov, M.I., 1967. Geophysical methods of prospecting and prognostic valuation of iron deposits in the USSR. In: Morley, L.M., (editor), Mining and groundwater geophysics/1967. Department of Energy, Mines and Resources, Canada, Economic Geology Report 26, 363–370.

Large, R.R., 1977. Chemical evolution and zonation of massive sulphide deposits in volcanic terranes. Economic Geology, 72, 549–572.

Large, R.R., 1989. Metallic mineral exploration models and case histories. In: Burrett, C.F. & Martin, E.L. (editors), Geology and mineral resources of Tasmania. Geological Society of Australia, Special Publication 15, 419–438.

Large, R.R., 1992a. Development of ore deposit models for exploration. Proceedings, Australasian Institute of Mining and Metallurgy, Annual Conference, Broken Hill, 175–179.

Large, R.R. (editor), 1992b. A special issue devoted to Australian volcanic-hosted massive sulphide (VHMS) deposits and their volcanic environment. Economic Geology, 87, 469–952.

Leboutieller, D., 1981. Rouez, les expressions geophysiques. Chroniques de la Recherche Miniere, No. 458, 33–49.

Leney, G.W., 1966. Field studies in iron ore geophysics. In: Hansen, D.A., et al. (editors), Society of Exploration Geophysicists' mining geophysics, Vol. I, Case histories. Society of Exploration Geophysicists, 391–417.

Lydon, J.W., 1984. Volcanogenetic massive sulphide deposits. Part 1, A descriptive model. Geoscience Canada, 11, 195–202.

Lydon, J.W., 1988. Ore deposit models, volcanogenetic massive sulphides. Part 2, Genetic models. Geoscience Canada, 15, 43–65.

Macnae, J.C., 1979. Kimberlites and exploration geophysics. Geophysics, 44, 1395–1416.

Macnae, J.C., 1995. Esoteric and mundane geophysics for diamondiferous pipe exploration. Exploration Geophysics, 26, 131–137.

Manthorpe, G.P., 1981. Structural and petrological investigation of the Mount Moss skarn, Ewan, north Queensland. B.Sc. Honours thesis, University of Queensland.

Mariano, A.N., 1989. Nature of economic mineralisation in carbonatites and related rocks. In: Bell, K. (editor), 1989. Carbonatites, genesis and evolution. Unwin Hyman, London, 149–176.

McCall, L.M., Dentith, M.C., Li, Z.X. & Trench, A., in press. The magnetic signature of komatiitic peridotite-hosted nickel sulphide deposits in the Widgiemooltha area, Western Australia. Exploration Geophysics, 26, 66–77..

McIntyre, J.I., 1980. Geological significance of magnetic patterns related to magnetite in sediments and metasediments—a review. Australian Society of Exploration Geophysicists, Bulletin, 11, 19–33.

Mudge, S.T., 1994. Geophysical surveys of the Eneabba heavy mineral sand field, Eneabba, Western Australia. In: Dentith, M.C., et al. (editors), 1994. Geophysical signatures of Western Australian mineral deposits. Geology and Geophysics Department (Key Centre) and UWA Extension, University of Western Australia, Publication 26 and Australian Society of Exploration Geophysicists, Special Publication 7, 428–431.

Mutton, A.J., 1987. Applications of downhole SIROTEM surveys in the Agnew Nickel Belt, W.A.. Exploration Geophysics 18, 295–303.

Mutton, A.J., & Williams, P.K., 1994. Geophysical response of the Rocky's Reward nickel sulphide deposit, Leinster, Western Australia. In: Dentith, M.C., et al. (editors), Geophysical signatures of Western Australian mineral deposits. Geology and Geophysics Department (Key Centre) and UWA Extension, University of Western Australia, Publication 26 and Australian Society of Exploration Geophysicists, Special Publication 7, 181–196.

Ontario Department of Mines, 1970. Aeromagnetic maps of carbonatite–alkalic complexes in Ontario. Preliminary Map No. P.452.

Owen, H.B. & Whitehead, S., 1965. Iron deposits of Iron Knob and the Middleback Ranges. In: McAndrew, J. (editor), Geology of Australian ore deposits. Proceedings, Eighth Commonwealth Mining and Metallurgical Congress, 301–308.

Pridmore, D.F., Coggon, J.H., Esdale, D.J. & Lindeman, F.W., 1984. Geophysical exploration for nickel sulphide deposits in the Yilgarn Block, Western Australia. In: Buchanan, D.L. & Jones, M.J. (editors), Sulphide deposits in mafic and ultramafic rocks. Institution of Mining and Metallurgy, London, 22–34.

Read, I., 1989. Geophysics in gold exploration—some examples. In: Garland, G.D. (editor). Proceedings of Exploration '87. Ontario Geological Survey, Special Volume 3, 473–485.

Roberts, R.G. & Sheahan, P.A. (editors), 1988. Ore deposit models. Geoscience Canada, Reprint Series 3, Geological Association of Canada, 194 pp.

Roux, A.T., 1967. The application of geophysics to gold exploration in South Africa. In: Morley, L.M. (editor), Mining and groundwater geophysics/1967. Department of Energy, Mines and Resources, Canada, Economic Geology Report 26, 425–438.

Sapin, S. & Babu, H., 1981. Le Gisement de Rouez: exploration et description. Chronique de la Recherche Mineriere, No. 458, 62–73.

Sawkins F.J., 1990. Metal deposits in relation to plate tectonics. Springer-Verlag, Berlin, 461 pp.

Sheard, N., Bishop, J.R. & Kissich, R.V., 1991. A practical approach to the filtering of airborne magnetic data in the Cobar region. Exploration Geophysics, 22, 353–356.

Smith, P. & Hall, D., 1995. Application of geophysics to the White Devil Gold Deposit, N.T. Exploration Geophysics, 26, 116–123.

Solomon, M. & Groves, D.I., 1994 The geology and origin of Australia's mineral deposits. Oxford University Press, 984 pp.

Stowe, C.W. (editor), 1987. Evolution of chromium ore fields. Van Nostrand Reinhold Company, 340 pp.

Taylor, C.P. 1964. Geophysical exploration for iron ore, Middleback Range area. Australasian Institute of Mining and Metallurgy Proceedings, No. 209, 19–41.

Telford, W.M., Geldart, L.P. & Sheriff, R.E., 1990. Applied geophysics. Cambridge University Press, 770 pp.

Trench, A., & Williams, P.K., 1994. Application of geophysics to nickel sulphide exploration in the Kambalda district, Western Australia. In: Dentith, M.C., et al. (editors), Geophysical signatures of Western Australian mineral deposits. Geology and Geophysics Department (Key Centre) and UWA Extension, The University of Western Australia, Publication 26 and Australian Society of Exploration Geophysicists, Special Publication 7, 169–180.

Wahl, W.G. & Lake, S., 1957. Airborne magnetometer survey discovers Marmora magnetite deposit. In: De Wet, J.P. (editor), Methods and case histories in mining geophysics. Proceedings, 6th Commonwealth Mining and Metallurgical Congress, 155–162.

Webb, J.E., 1966. The search for iron ore, Eyre Peninsula, South Australia. In: Hansen, D.A., et al. (editors), Society of Exploration Geophysicists' mining geophysics, Vol. I, Case histories. Society of Exploration Geophysicists, Tulsa, 379–390.

Weber, C.R., Paterson, I.B.L. & Townsend, D.J., 1978. Duckmaloi skarn. Geological Survey of New South Wales, Mineral Resources No. 43, 140–141.

Webster, S.S., 1984. A magnetic signature for tin deposits in south-east Australia. Exploration Geophysics, 15, 15–32.

Wederkind, M.R. & Love, R.J., 1990. Warrego gold–copper–bismuth deposit. In: Hughes, F.E. (editor), Geology of the mineral deposits of Australia and Papua New Guinea. Australasian Institute of Mining and Metallurgy, Monograph 14, 839–843.

Whiteley, R.J. (editor), 1981. Geophysical case history of the Woodlawn orebody, New South Wales, Australia. Pergamon Press, 588 pp.

Willett, G.C., Duncan, R.K. & Rankin, R.A., 1989. Geology and economic evaluation of the Mount Weld carbonatite, Laverton, Western Australia. In: Ross, J. (editor), Kimberlites and related rocks. Geological Society of Australia, Special Publication 14, 1215–1235.

Williams, P.K., 1994 Relationship between magnetic anomalism and epigenetic gold mineralisation in the Victory–Defiance area, Western Australia. In: Dentith, M.C., et al. (editors), Geophysical signatures of Western Australian Mineral deposits. Geology and Geophysics Department (Key Centre) and UWA Extension, The University of Western Australia, Publication 26, Australian Society of Exploration Geophysicists, Special Publication 7, 283–296.

Yungul, S., 1956. Prospecting for chromite with gravimeter and magnetometer over rugged topography in east Turkey. Geophysics, 21, 433–454.

AGSO Journal of Australian Geology & Geophysics, 17(2), 159–173

High-resolution geophysics in modern geological mapping

A.L. Jaques[1], P. Wellman[1], A. Whitaker[1] & D. Wyborn[1]

A modern geoscientific knowledge base developed through systematic mapping is a major component of sustainable development strategies, underpinning mineral resource assessment and exploration. High-resolution airborne magnetic and gamma-ray spectrometric surveys are fundamental to modern geoscientific mapping, providing cost-effective definition of structure and lithology in a diverse range of geological provinces and terrains. Magnetic (and gravity) data are particularly valuable in determining basement structure and continuity under cover. Gamma-ray spectrometric data provide geochemical (K, Th, U) maps that have proved valuable in mapping bedrock lithology and alteration, and for mapping regolith materials and activity, particularly in highly weathered (regolith-dominated) terrains.

More than 3 million line kilometres of new high-resolution airborne geophysics have been acquired by the Australian Commonwealth, State and Northern Territory geological surveys, since the commencement of the National Geoscience Mapping Accord, in support of geological mapping in a wide range of provinces. These new data, coupled with other modern mapping technologies, notably geographic information systems, provide a means of rapid, cost-effective geoscientific mapping and analysis in a wide diversity of geological environments and terrains. New geological maps and other thematic maps based on these geophysical data enable better definition of mineral potential and contribute directly to more effective and efficient exploration.

In all provinces, new high-resolution airborne magnetic and gamma-ray spectrometric data have resulted in better definition of both geological structure and lithological boundaries than indicated on previous maps. This paper shows, by examples, the usefulness of geophysical data over a wide range of mapping in support of the mineral industry.

Introduction

Exploration for Australia's onshore mineral and petroleum resources over the past four decades has relied heavily on the national geological and geophysical databases, principally the 1:250 000 geological map series and reconnaissance (1.6 km line spacing) airborne geophysical mapping undertaken by the Australian Geological Survey Organisation (AGSO), its predecessor, the Bureau of Mineral Resources, Geology and Geophysics (BMR), and the State and Northern Territory geological surveys. This period saw the discovery of major new mineral deposits, including several of world class—Kambalda (nickel), Alligator Rivers (uranium), Olympic Dam (copper–gold–uranium), Argyle (diamonds), Century (zinc–lead). The nominal gross value of the approximately 100 mineral deposits discovered in Australia over the past 30 years has been estimated at approximately $A195 billion (Blain 1992).

The national regional aeromagnetic and gravity (11 km station spacing) data provide an overview, enabling identification of major tectonic features and geological provinces, and a geophysical model or framework of the Australian continent (Denham 1997). Images of the gravity and magnetic anomalies (Morse et al. 1992; Tarlowski et al. 1992, 1997) have formed the basis of a crustal elements map of Australia, which defines the major tectonic domains forming the basement of the Australian continent (Shaw et al. 1995, 1996).

The National Geoscience Mapping Accord (NGMA) is a joint Commonwealth–State/Territory initiative, begun in 1990, which is producing, through multidisciplinary studies using modern technology, a new generation of geoscientific maps and data sets of strategically important regions of Australia. These will be the basis for a more comprehensive understanding of the geology of Australia and its mineral and petroleum resource potential. The new data sets will underpin resource exploration into the next century, and provide a basis for the development of sound land-management strategies.

The demand for faster updating of geological maps and more information on three-dimensional geological structure has coincided with major advances in mapping technologies, particularly in airborne geophysical mapping and geographic

Figure 1. Regional aeromagnetic data for part of the eastern Yilgarn Craton—black to white represents low to high magnetisation. Highly magnetised units, largely aligned north-northwest to north, outline structure in greenstone belts of low average magnetisation. Regions of granite and gneiss between the greenstones are of higher average magnetisation. Flight-line spacing 1500 m; grid-cell size approx. 500 m; image area 26°05′–32°5′S 120°–123°05′E.

[1] Australian Geological Survey Organisation, GPO Box 378, Canberra, ACT 2601

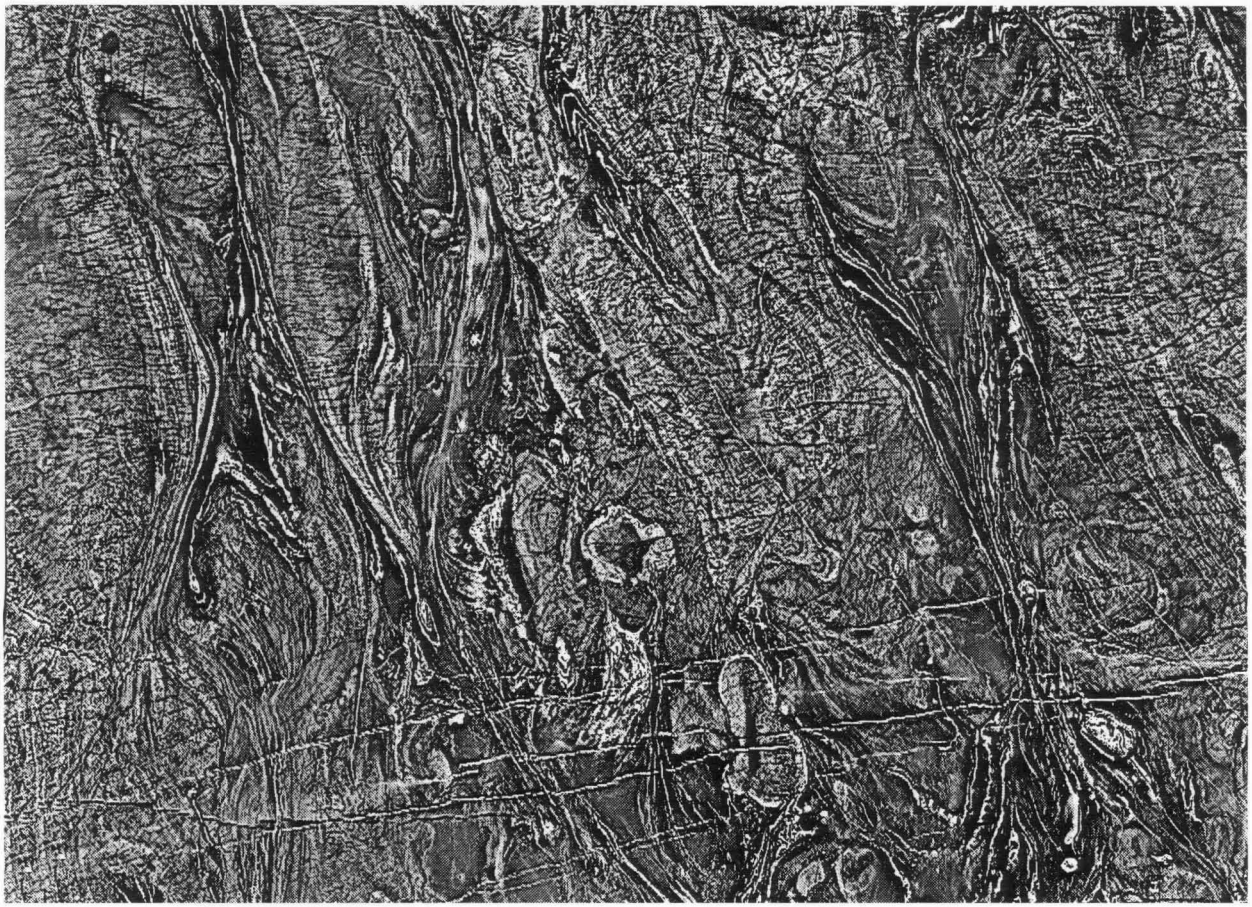

Figure 2. (A) 1st vertical derivative of 400 m flight-line spacing aeromagnetics for the northeastern Yilgarn Craton (northern part of Fig. 1). Although the original cell size of 90 m has been sub-sampled for this representation, the image shows considerably more structural detail of the greenstones (outlined in black) and banded gneiss than is evident in the regional data. Numerous lineaments (faults and dykes) are evident.

information systems (GIS), to revolutionise modern geological mapping. This paper describes the role played in geological mapping by regional geophysical data with flight-line spacing of 400 m or less, using examples from NGMA projects. Examples of prospect-level geophysical interpretation have been published by Smith (1985) and Dentith et al. (1994).

Modern geological mapping—an integrated approach

The first generation of systematic geological mapping of Australia was based on field traverses and aerial photography, and was rarely supported by gravity or airborne geophysical data. The new 'second generation' mapping uses a multidisciplinary approach with a heavy bias towards rapid non-invasive or remote-sensing methods. Mapping of mineral provinces is underpinned by high-resolution airborne magnetic and gamma-ray spectrometric data.

The value of an integrated approach to modern geological mapping, by the use of high-resolution airborne geophysical surveys, was recognised at the outset of the NGMA (e.g. Cook et al. 1989; Webster et al. 1989). In particular, it was recognised that magnetic data would provide more detailed structural and lithological information, and enable mapping in areas of poor outcrop or under cover. Mapping of the geology under cover was a major objective of the NGMA, recognising that only 17 per cent of Australia's hard-rock terrains crops out, the remainder being covered by younger basins or regolith. Mineral deposits discovered in the future are, therefore, likely to be under cover (blind) and their detection will rely heavily on geophysical methods (e.g. Skinner 1993; Woodall 1993), as recent major discoveries such as Olympic Dam, Cannington, and Earnest Henry have shown.

Second generation mapping under the NGMA encompasses both the preparation of geological maps based on high-resolution airborne geophysics and other remotely sensed data, and the development of new derivative and thematic map products based on geographic information systems. The integrated mapping approach also draws on gravity data and seismic reflection profiling to understand the crustal structure, precise geochronology for establishing time relationships of key geological units and events, regolith landform mapping, petrological and geochemical investigations, and metallogenic studies.

Important elements of the modern mapping approach can be summarised as:

- Compilation of existing information into databases.
- Digital capture of existing map data which meet modern standards, including geological and geophysical data sets;
- Acquisition of new remotely sensed data, especially high-resolution airborne magnetic and gamma-ray spectrometric data;
- Geological mapping to ground-check interpretations of geophysical and other remotely sensed data, to examine lithology and structural and stratigraphic relationships, to take samples for laboratory analysis, and to take field measurements of magnetic susceptibility and gamma-ray intensity;

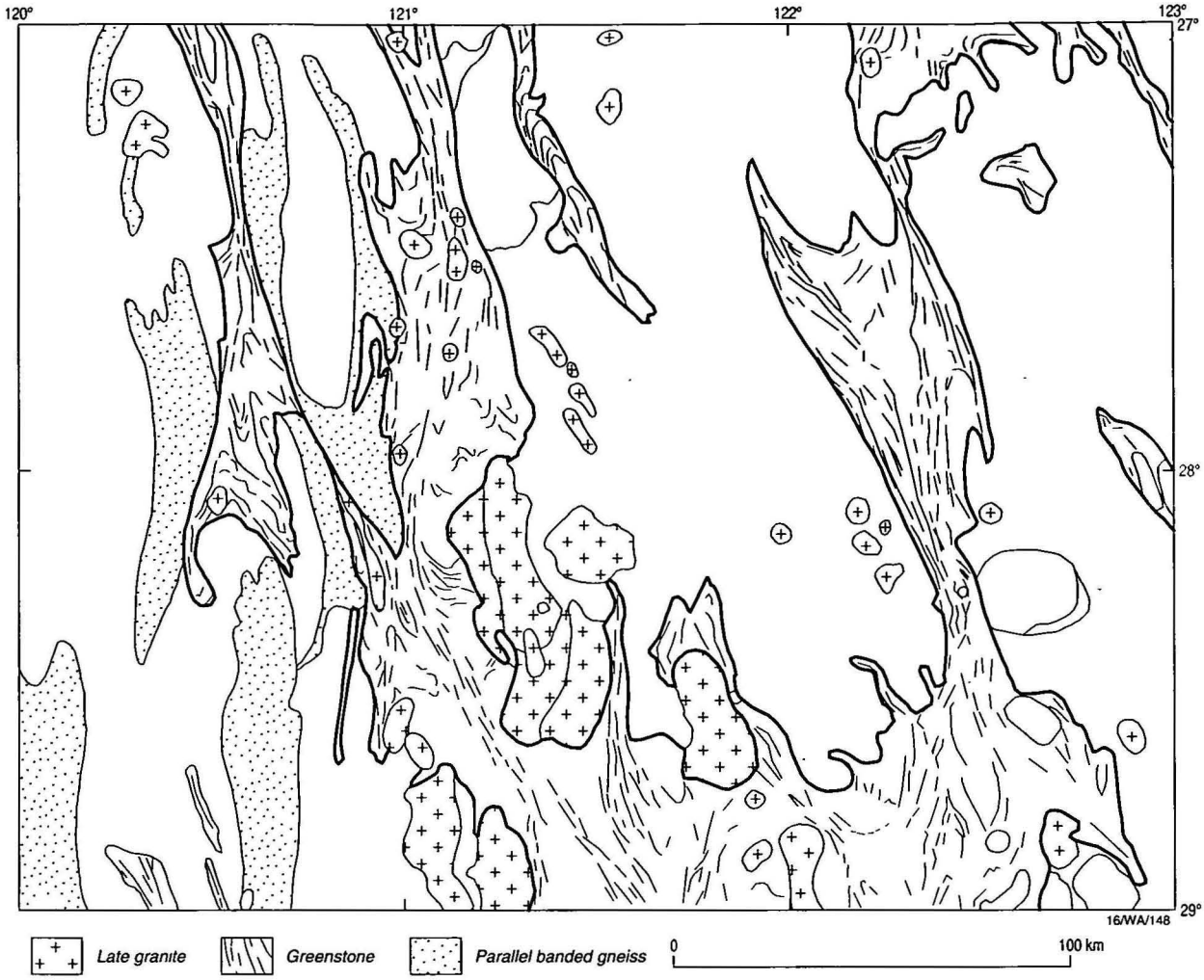

Figure 2. (B) Outlines of the greenstone belts, linearly banded gneiss and discrete granite intrusives for the area of (A).

- Laboratory studies, including petrology, rock geochemistry, palaeontology and geochronology, aimed at defining key parameters;
- Integration of remotely sensed data, geology, and supporting information in databases to form a GIS; and
- Development of standard and thematic maps and data sets.

Regional geophysical surveys as a basis for modern geological mapping

High-resolution airborne survey data

Boyd (1967) outlined the principles for the application of aeromagnetic surveys to geological mapping and noted the following unique qualities of aeromagnetic data: they comprise responses from magnetic minerals only; magnetic minerals are widely distributed in all terrains; and the data are unaffected by non-magnetic cover, including vegetation, water and surficial deposits. The ability to accurately map a single geological parameter in a uniform manner over a very large area makes aeromagnetics highly suited to structural and lithological mapping over a wide range of scales.

The potential of image-processed high-resolution airborne geophysical data for geological mapping and mineral exploration was recognised in the 1980s and effectively demonstrated in gold exploration in the Yilgarn province of Western Australia (e.g. Isles et al. 1989, 1990). Such surveys are now an integral part of most mineral exploration programs and form the basis of modern geological mapping, especially in basement terrains. Modern airborne magnetic and gamma-ray spectrometric surveys are flown at 50–400 m line spacing, and 40–80 m ground clearance. Sampling interval is commonly 7 m for magnetics, and data integration for spectrometry, 70 m. Instrumentation, global positioning satellite (GPS) navigation systems and image processing have advanced significantly in the past decade (e.g. Reeves 1992; papers in this issue).

The high sensitivity and small grid size of the resulting maps often enable mapping of features too subtle to be observed in outcrop or hand specimen. Consequently, high-resolution airborne geophysical surveys have been shown to be a cost-effective mapping tool in a diversity of terrains world-wide; this has been reaffirmed by our experience under the NGMA. In all provinces, including those where outcrop can be described as 'reasonable or fair', new high-resolution airborne magnetic and gamma-ray spectrometric data have resulted in far better definition of both geological structure and lithological boundaries than on previously published maps.

High-resolution gamma-ray spectrometry, flown simultaneously with magnetics, is a cost-effective mapping tool which provides a three-element—K, Th, U—chemical map of the ground surface. Gamma-rays have an effective penetration of up to 0.4 m, enabling mapping of bedrock and regolith in vegetated regions, unlike remotely sensed data such as Landsat Thematic Mapper and SPOT Image, whose effective penetration is limited to the top few microns and masked by vegetation cover.

Gamma-ray data have proved complementary to magnetic data in many terrains, enabling more precise location and, in some cases, redefinition of geological boundaries. They have

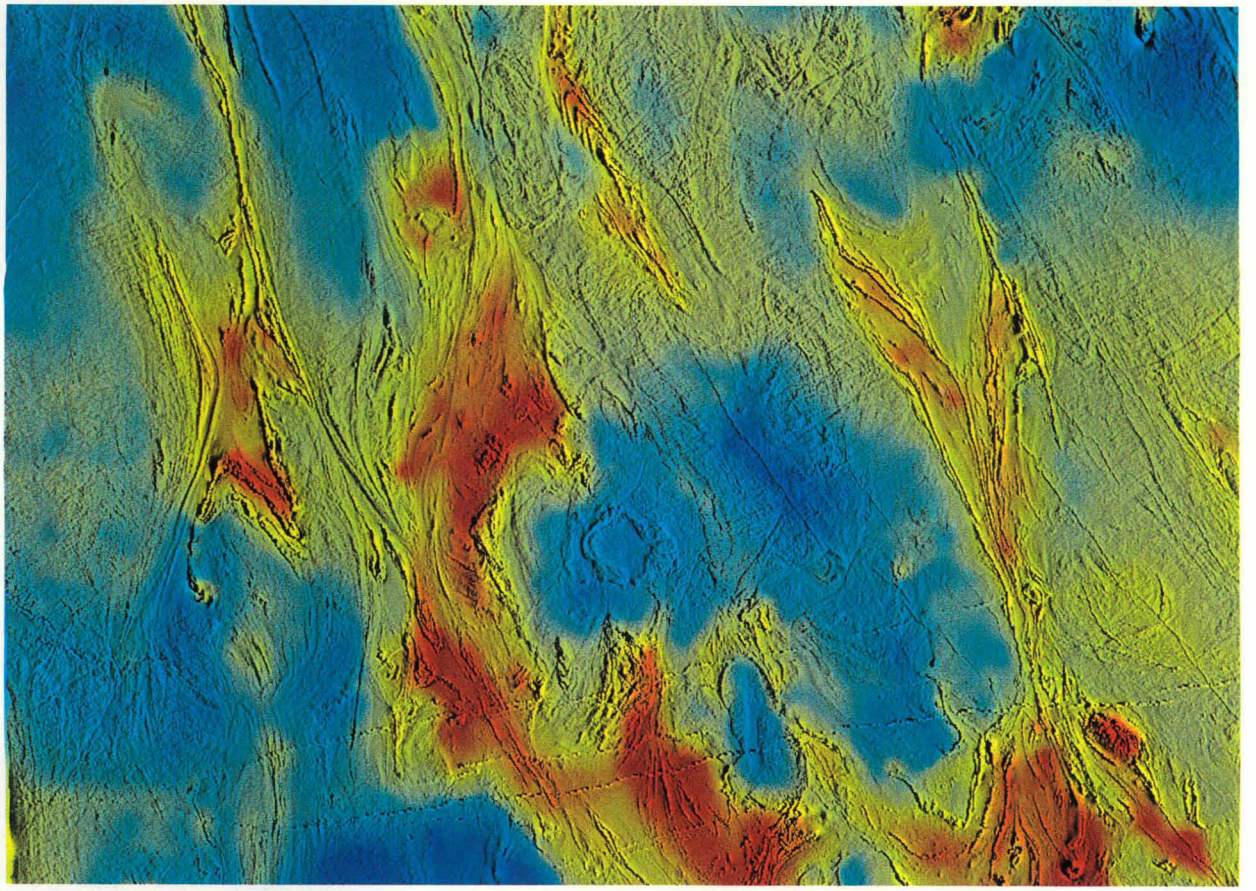

Figure 3. Combined image of 4 km spaced gravity data as hue (blue–gravity low to red–gravity high) and east gradient of the 400 m aeromagnetics as intensity for the same area as Figure 2. Granite correlates with low gravity (blue), mixed gneiss, migmatite and granite with intermediate gravity anomalies (lemon), and greenstone with high gravity (deep yellow–red). Very high gravity values are not evenly distributed throughout the greenstones and may represent local abundance of dense lithology, including basalt, dolerite and ultramafic rocks.

been found particularly useful for mapping basement in terrains with discontinuous outcrop or where basement is covered by thin soils or vegetation, including rainforest and mangroves. Gamma-ray data have proved valuable in mapping the stratigraphy and structure of non-magnetic rock units, such as sedimentary and low-grade metasedimentary sequences, and for recognising individual phases and zoning within units such as granitoid intrusions, which can frequently be mapped out on the basis of differing K, Th and U concentrations. One of the most significant recent applications of gamma-ray spectrometry is in the field of regolith-landform, soil, and land-resource mapping, where it has been used to map geomorphic activity, regolith types, land degradation, soil types and soil loss (Wilford et al. 1997; see below).

The importance of high-resolution airborne geophysics to the current generation of mapping is demonstrated by the fact that, since 1990, more than 3 million line km of high-resolution (500 m line spacing or closer) airborne geophysics have been acquired by AGSO and the State and Northern Territory geological surveys under the NGMA and other new mapping initiatives.

Gravity

Regional gravity data, from 2–4 km station spacing, have proved valuable in support of 1:250 000 scale geological mapping in regions with contrasting density. Gravity data are commonly used to delineate the position of boundaries at deeper levels than aeromagnetic data can, because they contain contributions from the whole crust/lithosphere and assist 3D modelling of crustal structure. Advanced processing and modelling software enable gridding and preparation of image maps, which can be interpreted in conjunction with other data sets and modelled to determine 3D structure (Murray 1997). The data have proved particularly useful in the Eastern Goldfields for defining the nature of granite–greenstone boundaries and boundaries between rocks that are similarly magnetised and, therefore, not resolved by aeromagnetic data. The gravity data show little variation in areas of overprinted structural deformation, in contrast to aeromagnetic data, which commonly show local lows attributed to the loss of magnetisation of the rocks.

Data processing and interpretation

The preferred parameters for acquisition and processing of high-resolution airborne geophysical data are now well defined (papers in this issue). Major advances in PC and work station processing power and reductions in cost of computer hardware, coupled with the development of advanced processing and imaging software (e.g. ER Mapper, Intrepid) have made image-processing and interpretation of geophysical data feasible at project and regional office level by field geologists.

Methods for display and presentation of geophysical data are reviewed by Milligan & Gunn (1997), and for interpretation of magnetic data by Gunn (1997) and gamma-ray spectrometric data by Dickson & Scott (1997).

Magnetic anomalies are normally displayed as a composite image with colour (hue and saturation) giving the long-wavelength information and shading (intensity) showing short-wave-

length anomalies. Other displays (grey-scale images, contours, and stacked profiles) are also prepared of anomalies or filtered versions of them.

Gravity, with a 4–10 km station spacing, is generally displayed as Bouguer anomaly contours or filtered gravity.

Gamma-ray spectrometric data are generally shown as composite colour images with intensity of potassium/thorium/uranium given as intensity of red/green/blue. Previous papers (e.g. Isles et al. 1990) have emphasised the value of multiple display to optimise the information and each set of independent data is shown both alone and in combination with others.

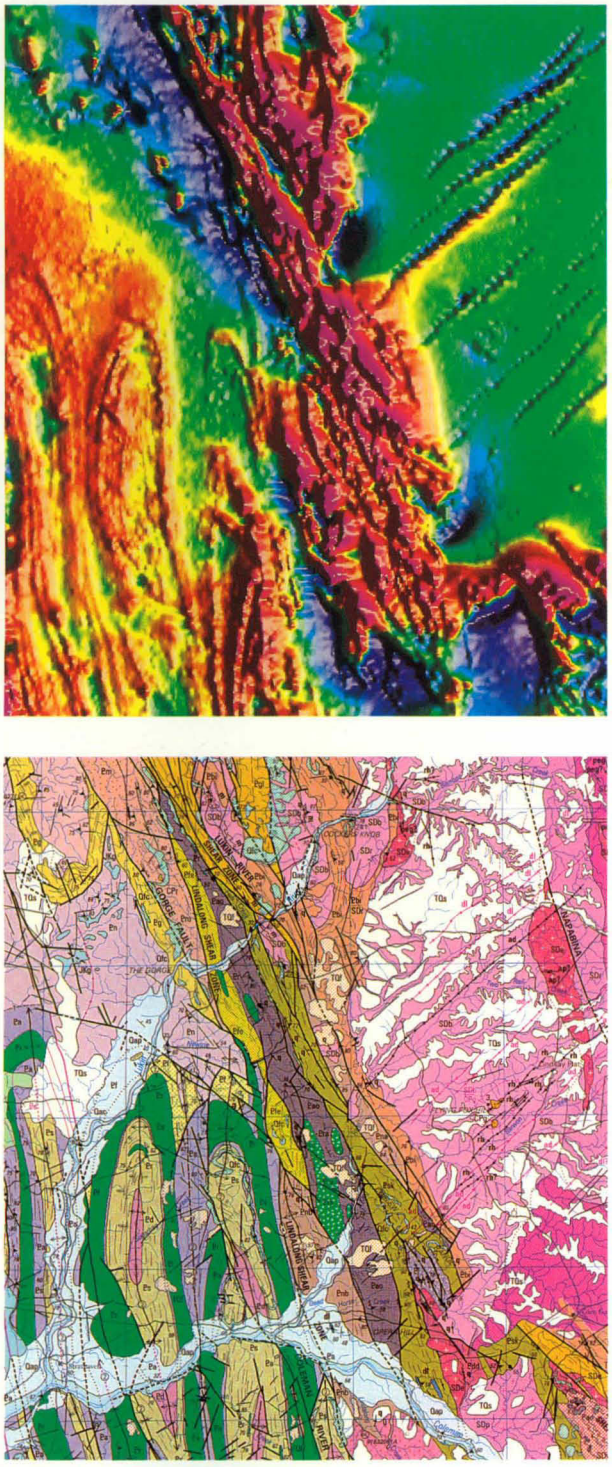

Figure 4. (A) Magnetic image of part of Ebagoola 1:250 000 Sheet area to show the difference in texture between low metamorphic grade sediments with fold patterns in the west, high metamorphic grade sediments with high magnetisation and fracture patterns in the centre and east, and low magnetisation granites cut by high magnetisation parallel dykes in the east–centre. (B) Basement geology of the same area.

The sophistication of modern software allows great flexibility with the ability to generate a wide range of filters and enhancements. For gamma-ray spectrometric data, images are normally prepared of a K/Th/U three-colour composite; sometimes they are displayed separately or as ratios. For magnetic data, the long and short wavelengths are shown separately on some displays. Most of the information relating to shallow sources is contained in the short-wavelength component; hence the grid values between lines should be an accurate interpolation of the data, and different displays of short-wavelength information should be employed (e.g. 1st, 2nd vertical derivative).

Data integration for mapping/interpretation

Data integration methods vary, depending mainly on the amount of geological information available, and the line spacing of the geophysical data sets. The following comments apply to the mapping of outcropping or shallow subcropping basement, not to the mapping of little-deformed sediments or regolith.

Where basement geology is well controlled by outcrops and aerial photography, magnetic and gamma-ray data are used to check and refine the geological mapping, and map variation within units in chemistry and magnetisation due to fracturing, chemical alteration or heating.

In areas of continuous or semi-continuous cover by regolith or basin sediment and poor geological control of basement (minor outcrops and drilling), geological mapping of basement depends critically on interpretation of magnetic anomalies, with some support from the gravity anomalies. The magnetic data can be considered to consist of two independent data sets, long and short-wavelength components. The boundary between geological units corresponds to steep gradients in the reduced-to-pole long-wavelength component, to a change in character/pattern in the short-wavelength component, and may correspond with a gravity gradient. Identification of rock type depends on the relative value of the gravity anomaly and long-wavelength magnetic anomaly, but most importantly on the texture of short-wavelength magnetic anomalies. Minor elongate features in short-wavelength magnetic anomalies can generally be separated into lithological bedding, faults/fractures, or dykes, using the criteria below.

Criteria	*Layering*	*Faults/fractures*	*Dykes*
Wave form	Complex	Simple	Simple
Apparent body width	Narrow to wide	Narrow to wide	Narrow
Continuity	Continuous/ segmented	Continuous	Continuous
Magnetisation	Normal or reverse	Often zero	Normal or reverse
Adjacent anomalies	Sub-parallel	Sub-parallel/or orthogonal	Sub-parallel
	Dissimilar	Similar	Similar

There is at present no standard for the graphic representation of geophysical interpretation. The two extreme practices are to map and classify the major anomalies in terms of anomaly characteristics, but without making a decision on what geological features they represent; and to map geophysics using only geological symbols, ignoring the anomalies that are not understood. 'Geomagnetic' maps represent an intermediate level of presentation where aeromagnetic features are depicted in terms of the established geology (Isles et al. 1990).

Two main features of magnetic anomaly maps are readily

identified—areas with uniform or characteristic magnetisation, and linear features forming discontinuities or trends. However, the source of magnetic anomalies is frequently not exposed and a direct relationship with lithology may be lacking. Complete magnetic interpretation needs an understanding of the geological significance of magnetic mineral bearing (mainly magnetite) rock units, including mineralogy, chemistry and metamorphic grade (e.g. McIntyre 1980; Grant 1985). Understanding magnetic properties through direct measurement of magnetic susceptibility in the field during mapping, supported by laboratory studies of magnetic petrophysics (Clark 1997), provides the basis for more effective use of aeromagnetic data as a geological mapping tool.

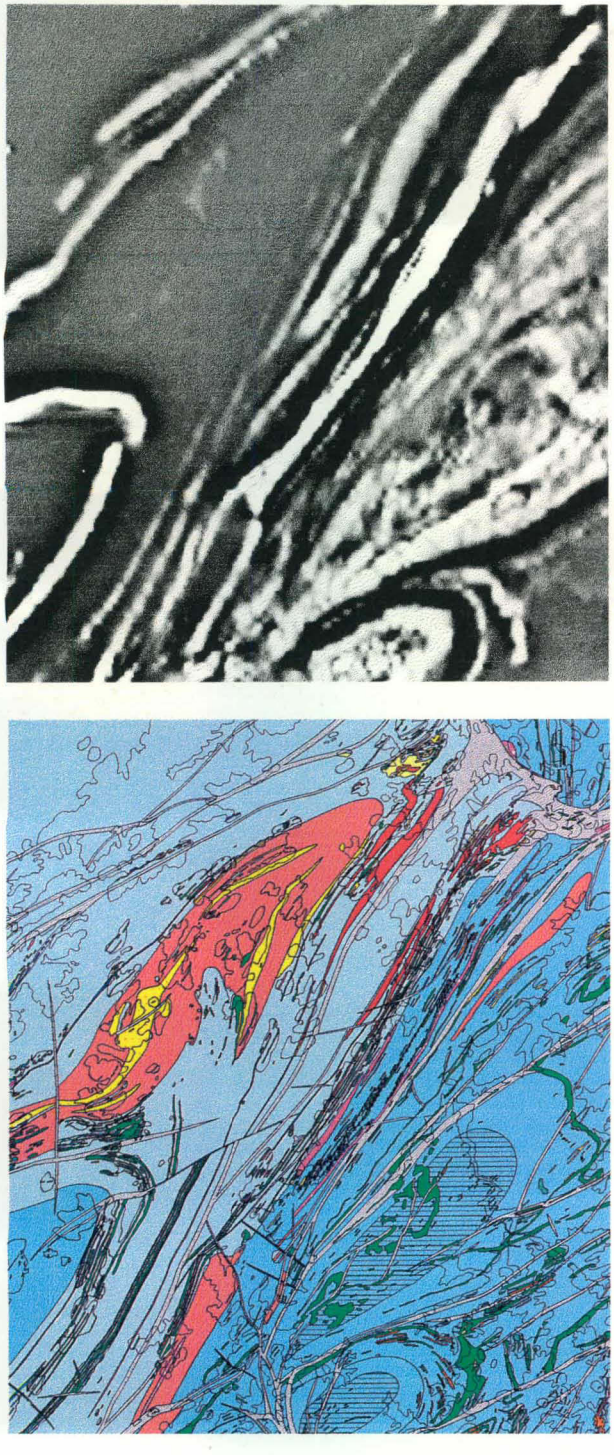

Figure 5. (A) 1st vertical derivative of magnetic data flown at 100 m line spacing and 60 m flight height for part of the Mount Gipps 1:25 000 Sheet, Broken Hill. The image shows the major structures, including NE-trending synform and antiforms defined by tight folds outlined by strongly magnetic units and NE-trending shear zones. (B) Preliminary solid geology interpretation, showing quartzofeldspathic gneisses in red, metasediments in blue, amphibolites in green, and shear zones in grey.

Visual interpretation is often subjective, so should be checked with computer-based modelling procedures. The location of body margins should be checked with the horizontal-gradient method (Cordell & Grauch 1985) or the second vertical derivative for gravity and magnetic bodies, and Euler deconvolution (Reid et al. 1990) and analytic signal (Roest 1992) for magnetic bodies. Folded magnetic horizons can be modelled in three dimensions to check the agreement between geology and magnetic anomalies (Jessell et al. 1993; Coggon & Lai 1993).

Interpretation detail is limited to the shortest anomaly wavelength. This normally approximates the flight-line spacing in areas of shallow or exposed basement (owing to gridding constraints), and about four times the depth of burial in areas of deep basement. Mapping of individual units is restricted by the pixel size of gridded, processed imagery, corresponding to approximately 90 m for magnetic and gamma-ray data flown with 400 m line spacing. The combination of comparatively coarsely spaced (400–500 m) airborne gamma-ray spectrometry with Landsat TM has proved useful in improving the resolution of the image and also for providing a topographic reference for the geophysical anomalies (Wilford et al. 1992).

Important boundaries are best mapped by a variety of techniques. The optimum boundary and its likely uncertainty can then be determined by comparison of the various boundary lines.

Mapping in Archaean greenstone belts

The Archaean Yilgarn Craton in Western Australia is characterised by poor outcrop (5–10%), deep weathering and extensive and complex regolith cover. Regional aeromagnetic images of the Eastern Goldfields (Fig. 1) show large areas of low to moderate average magnetisation, which correspond with granite and gneiss terrain, and elongate belts of lower average magnetisation, but containing highly magnetised units, which correlate with greenstone belts (Whitaker 1992, 1993b). The greenstone belts, which host most of the gold, nickel and base metal mineralisation in the craton, account for less than 30 per cent of the upper crust; the remainder being dominantly granitic.

Whitaker (1992, 1993a) and Williams & Whitaker (1993) recognised these domains in the regional magnetic and gravity data, and also some of the structures in the greenstone belts. However, the geology is only poorly resolved in the regional aeromagnetic images. In more detailed surveys (400 m flight-line spacing), structural differences between granite, gneiss and greenstone are more apparent (Fig. 2). Areas of granite show little compositional banding, with lineaments providing the most abundant anomalies. Areas attributed to gneiss show well-developed compositional banding and are classified into two main categories: small, widely distributed, contorted gneiss with little obvious directional control; and elongate, linearly banded gneiss commonly parallel to the major north-northwest to north-trending lineaments and to adjacent boundaries with greenstone. Boundaries between granite and gneiss are generally poorly defined. Bouguer gravity anomalies are higher over linearly banded gneiss than over adjacent large bodies of granite.

Of immediate economic interest is the definition of the extent of the greenstones beneath generally thin cover. The greenstones coincide with much higher Bouguer gravity anomalies than the adjacent granite and gneiss domains, but there are not enough gravity data to support detailed mapping.

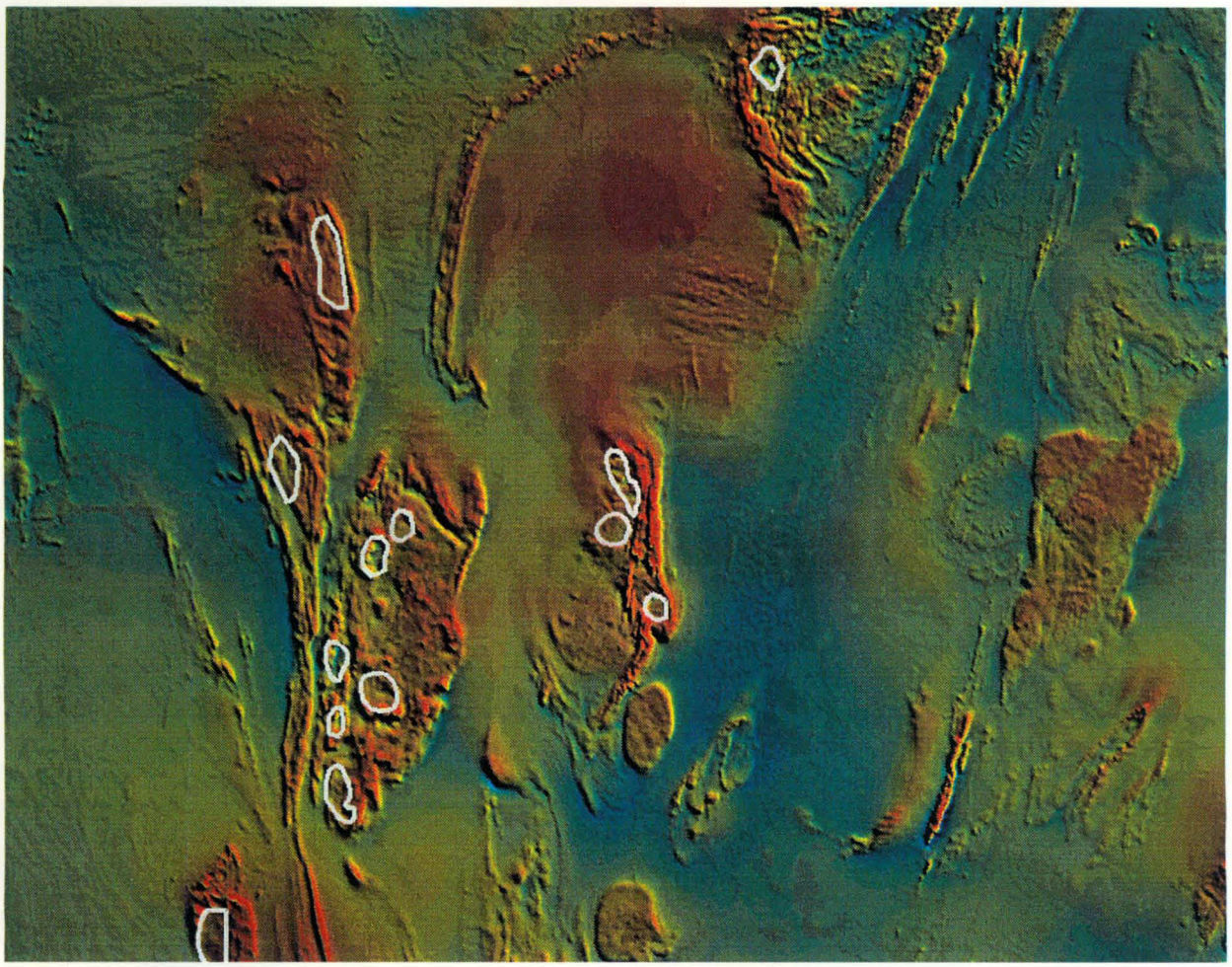

Figure 6. Magnetic image, Forbes 1:250 000 Sheet area, showing the strong magnetic signature of Ordovician oxidised igneous complexes. Possible volcanic centres of caldera-type are delineated (outlined in white) as potentially prospective for magmatic copper/gold deposits.

High-resolution aeromagnetic data have proved essential for defining the structure and continuity of the greenstone belts and have provided the basic data set for both mapping and exploration (e.g. Isles et al. 1990). The greenstone belts contain thin units of highly magnetised ultramafic and banded iron formation and moderately magnetised gabbro and amphibolite, which outline the internal structure (Fig. 2a, b). However, most rock types are poorly magnetised, including basalt, intermediate to acid volcanics, dolerite, and sediments. Long, narrow, poorly magnetised fault zones truncate lithological banding, and minor faults cause local dislocations. For solid geology maps, all available outcrop information must be integrated with the aeromagnetic interpretation, as average magnetisation identifies only a few rock types uniquely.

In and adjacent to the greenstone belts numerous circular to ovoid anomalies correspond to relatively late intrusions of granite. Pre, post and syn-deformation intrusion is indicated by the presence or absence of locally deformed greenstone around the stocks and from unusually elongated, lensoidal bodies of granite. Some granite is as poorly magnetised as the surrounding greenstone and difficult to discriminate in the aeromagnetic images. However, the larger bodies of granite may be identified by the gravity data, as they correspond with local gravity lows. Structurally controlled gold mineralisation is commonly associated with deformed granite–greenstone contacts and with some syn- and late-deformation intrusions. Thus, the location and nature of granite boundaries with adjacent greenstone are a useful exploration guide. Lithological contacts are poorly represented in the sparse basement outcrop, and most information on contact relationships is derived from interpretation of modern aeromagnetic data.

Combinations of images provide a convenient way of analysing spatial relationships between different data sets. Figure 3 displays gravity as hue (colour) with near-surface anomalies of the east gradient of the magnetics depicted by intensity. Interpretation of this image shows the close association of gravity lows (blue) with granite, and gravity highs (yellow-orange to red) with the greenstones. Very high gravity values are not uniformly distributed throughout the greenstone belts and may identify areas with abundant mafic and ultramafic rocks. Variable dip of granite–greenstone contacts is inferred from differences in position of the boundaries as determined from the two data sets. In some areas, lobes in granite contacts plunge under greenstone. Different thicknesses of granite are also inferred, with thin sheet-like structurally deformed bodies associated with only minor local gravity lows. Rare broad gravity gradients cut across the general trends of the greenstones, as mapped by the aeromagnetic data. These gradients may be associated with deep-seated faults, which, if that is the case, could have supplied mineralising fluids to adjacent or overlying greenstones.

The production of solid geology maps, which show the distribution and abundance of rock types and faults across the Yilgarn Craton, is an important step towards constraining tectonic models of the region. Integrated outcrop geology and geophysical images provide a useful intermediate product.

Figure 7. Gamma-ray spectrometric image (RGB=KThU) of the complex patterns of stratigraphy and structure of folded units of the Silurian–Devonian Hill End Trough north of Hill End. The Merrions Tuff is a widespread thin volcaniclastic unit with a red signature and a low gamma-response sub-unit (almost black) at its top. The unit is overlain by the yellowish-green Cunningham Formation, which is mainly shale and siltstone. The area covered by the image is 30 km wide.

Such maps provide a context for existing isotopic age data and geochemical studies, and assist the identification of complementary sample sites for ongoing studies. Results from these studies will aid assessment of proposed accretional terrane boundaries (e.g. the Keith–Kilkenny Lineament: Barley et al. 1989) and subdivisions of the craton and provinces. Some of these subdivisions (e.g. Norseman–Wiluna Belt of the Eastern Goldfields Province: Gee 1979) have been linked with enhanced prospectivity through their association with large historic mineral production. Maps of solid geology overlain with mineral deposits readily show empirical associations between mineralisation, structural setting, lithology and lineaments. However, the majority of known mineral deposits of the Yilgarn Craton occur in areas of outcrop, subcrop or in-situ regolith. Solid geology maps provide a means of reassessing areas with limited previous exploration success by placing known deposits in their full regional context, and a basis for exploring areas under cover.

Proterozoic terranes

High-resolution airborne geophysical data have proved essential for mapping structure and lithology in Proterozoic terranes such as the Arunta Inlier (Whiting 1986) and especially those with poor outcrop and deep weathering, such as Cape York and Arnhem Land. For example, fold patterns in metamorphic belts, faults and intrusive bodies are readily mapped and can be interpreted under cover, providing a much better understanding of the regional geology than was apparent from the earlier generation mapping.

In Cape York Peninsula, as part of the North Queensland NGMA project, regional magnetic and gravity data have been used to define the regional geological framework (Wellman 1992), and regional gravity and detailed magnetics (Fig. 4a) have been used to map the basement inlier and surrounding subcropping basement (Fig. 4b) (Wellman 1995). Siluro-Devonian granite, characterised by low density, low uniform magnetic intensity, and prominent dyke swarms, can be differentiated from Proterozoic metamorphic rocks characterised by high density, in which amphibolite and granulite-facies metamorphics (high magnetic intensity) can be distinguished from greenschist facies (low magnetic intensity). Wellman (1995) noted that magnetic intensity increased with metamorphic grade and that in greenschist and lower grade rocks depositional/lithological layering could be clearly mapped, whereas at higher grade a fracture pattern is prominent.

In the East Kimberley, enhanced composite K–Th–U gamma-ray spectrometric images have enabled more detailed lithological subdivision of geological units in the Halls Creek mobile zone. In several areas, recognition of key markers has enabled mapping of regional structural trends in Palaeoproterozoic trachytic volcanics (Brockman Formation and correlatives) rich in Nb, Th, U, and rare-earth elements (Shaw 1994).

In the Broken Hill Province, high-resolution (100 m line spacing, 60 m flight height) airborne geophysical data are the basis of a major Commonwealth–State program (the Broken Hill Exploration Initiative) to map and define the structure and stratigraphic relationships under cover. Detailed geological mapping at 1:25 000 scale by the New South Wales Department of Mineral Resources forms the basis of the interpretation. Figure 5a shows the first vertical derivative for part of the Mount Gipps 1:25 000 Sheet area, in which the fold structures of the Broken Hill synform and associated parallel antiforms of the Sundown, Broken Hill and Thackaringa Groups are clearly marked by the strongly magnetic units, particularly amphibolite, banded iron formations and magnetite-bearing pelitic and psammitic metasediments. Interpretation of the magnetic data with the outcrop lithological maps (Fig. 5b) defines the continuity of the geology beneath cover and the full extent of the shear zones marked by poorly magnetic mica schists.

Palaeozoic fold belts

In the Palaeozoic Lachlan Fold Belt new high-resolution (250–400 m line spacing) airborne geophysics has been used in an NGMA project focussed on rock and structural associations with known ore deposits in the Bathurst, Forbes, Narromine and Dubbo regions of central NSW. The main geological elements of the region are mafic Ordovician volcanics and associated clastic sediments, commonly with strong magnetic signatures overlain by and faulted against folded sedimentary sequences of Silurian–Devonian age. The sedimentary sequences contain felsic volcanic units, and the region is intruded by granites of similar age and other Carboniferous granite complexes. Some granites are strongly magnetic; others are non-magnetic. Airborne magnetic data have played a major role in mapping the extent of the Ordovician volcanic and plutonic rocks, which host significant gold and copper mineralisation. They have helped identify individual volcanic centres and, within these, zones of low magnetic intensity associated with hydrothermal alteration.

The extent of the Ordovician magmatism and the volcanic centres on the Forbes 1:250 000 Sheet area defined on the basis of the new magnetic data is shown in Figure 6 as a pseudo-colour image of the total magnetic intensity. The image defines:

- strongly magnetic Ordovician volcanic and intrusive units in the west and centre;

- poorly magnetic Silurian–Devonian sediments faulted against the Ordovician volcanics; and
- magnetic I-type granites of the Eugowra and Grenfell complexes in the east, and folded magnetic Late Devonian A-type volcanics in the southeast.

The recent discoveries of porphyry style gold–copper mineralisation coupled with the new mapping have highlighted the association of this style of mineralisation with large Ordovician intrusive complexes, and mapping with the new geophysics has extended the areas of Ordovician magmatism mapped in the field to areas under shallow to medium cover. Mapping with the magnetic and gamma-ray data has been supported by geochemical studies (including Nd isotopic measurements), which have shown that the Ordovician suite is potassic (shoshonitic) in character and ranges in composition from relatively mafic (< 50% SiO_2) to felsic (trachyte, > 60% SiO_2) and has a distinctive Nd isotopic signature (ε_{Nd} = + 6 to +8; Wyborn & Sun 1993). Thirteen possible Ordovician caldera-style volcanic centres have been highlighted in Figure 6, representing the sites of demagnetisation associated with hydrothermal alteration and potential mineralisation sourced from sub-volcanic intrusive complexes beneath. The extent of the magmatism and its associated mineralisation indicates that the Ordovician shoshonitic magmatism constitutes a significant metallogenic episode which brought gold into the Lachlan Fold Belt from the underlying lithosphere.

Gamma-ray spectrometry has proved invaluable in mapping the complex stratigraphy and structure of the Silurian–Devonian Hill End Trough. Figure 7 shows an RGB (K, Th, U) image of the complex patterns of folded units north of Hill End. The Merrions Tuff is a widespread thin volcaniclastic unit with red signature and a low gamma response sub-unit (almost black in Fig. 7) at its top. The unit is overlain by the *yellowish*-green Cunningham Formation, which is mainly shale and siltstone.

Applications

Volcanic geology

Magnetic data have proved essential in mapping large volcano-plutonic subsidence structures, not obvious from the surface or subcropping geology in the Red River 1:250 000 Sheet area, 50 km north of Georgetown, in Queensland (Wellman et al. 1994). Interest is in the economically important Carboniferous–Permian granites and felsic volcanics, and the mapping of major subsidence structures, 10–30 km across, which are the focus of the igneous activity. Subsidence structures are clear from surface geology where the igneous rocks change at the boundary of the subsidence structures, but they are not clear at the surface where granites or flat-lying volcanic sheets cross these boundaries. The magnetic intensity image (Fig. 8) is dominated by the anomalies associated with the subsidence structures. Some are due to bodies of relatively low magnetisation completely filling a subsidence structure, and others to strongly magnetic bodies intruded close to the margin of the subsidence structures. Support for the larger structures being subsidence structures comes from coincident local gravity lows. Without the magnetic image only some of the subsidence structure boundaries would be mapped from outcrop geology in the area of basement outcrop, and none of the subsidence structures would be correctly mapped in the area of Mesozoic cover.

Intrusive relationships, composition and zoning in igneous bodies

Magnetic data in particular are extremely useful for mapping oxidised I-type granites, where they record the complex crystallisation history of overlapping pluton emplacement. Painstakingly long field studies would be required to elucidate the history of these complex bodies, given outcrop. In poorly outcropping regions, their complexity would never be appreciated without magnetic data. A good example is the Early Devonian Yeoval Batholith from the central Lachlan Fold Belt south of Dubbo. The batholith is quite complicated (Fig. 9):

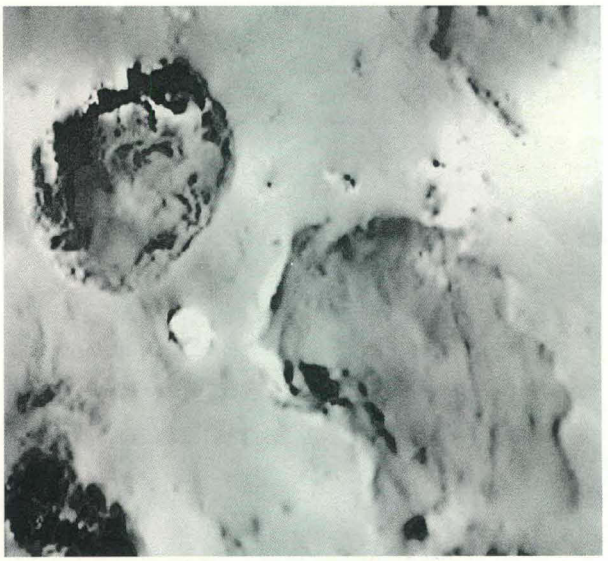

Figure 8. Magnetic anomalies due to subsidence structures. The image shows magnetic anomalies over part of the Red River 1:250 000 Sheet area. Subsidence structures are marked by elliptical bands of strong negative anomaly and/or elliptical areas of low irregular anomaly.

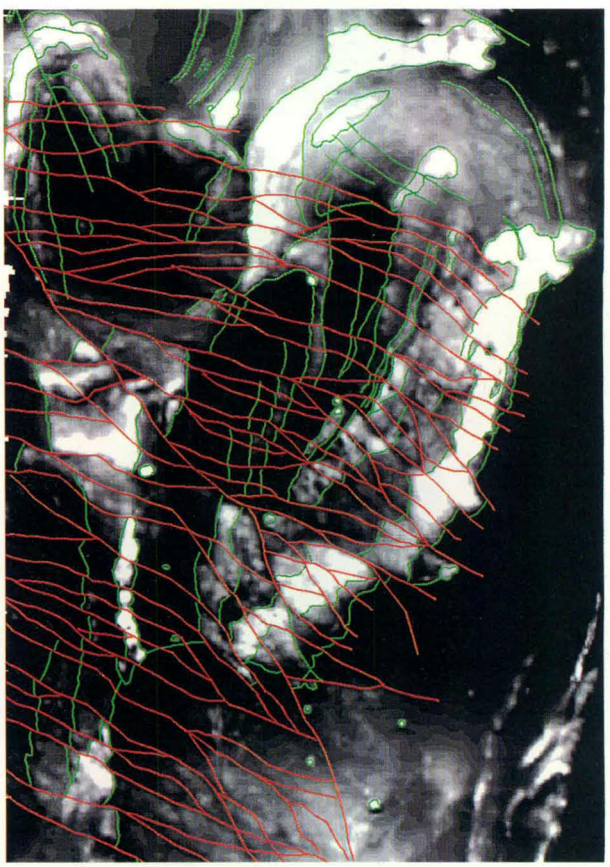

Figure 9. Strongly magnetic outer phases of the complicated Yeoval Batholith give way inwards to progressively more felsic and less magnetic inner phases, and the whole batholith has been cut by a complex series of WNW-trending right-lateral wrench faults.

strongly magnetic outer phases give way inwards to progressively more felsic and less magnetic inner phases, and the entire body has been cut by a complex series of west-north-west-trending right-lateral wrench faults. Mapping rocks of such complexity would be impossible in this area without magnetic data to control the field program. Potential mineralisation sites, associated with ultimate fluid saturation during fractional crystallisation, are much more likely to be targeted when the fractionation and structural histories are so well defined by the geophysical data.

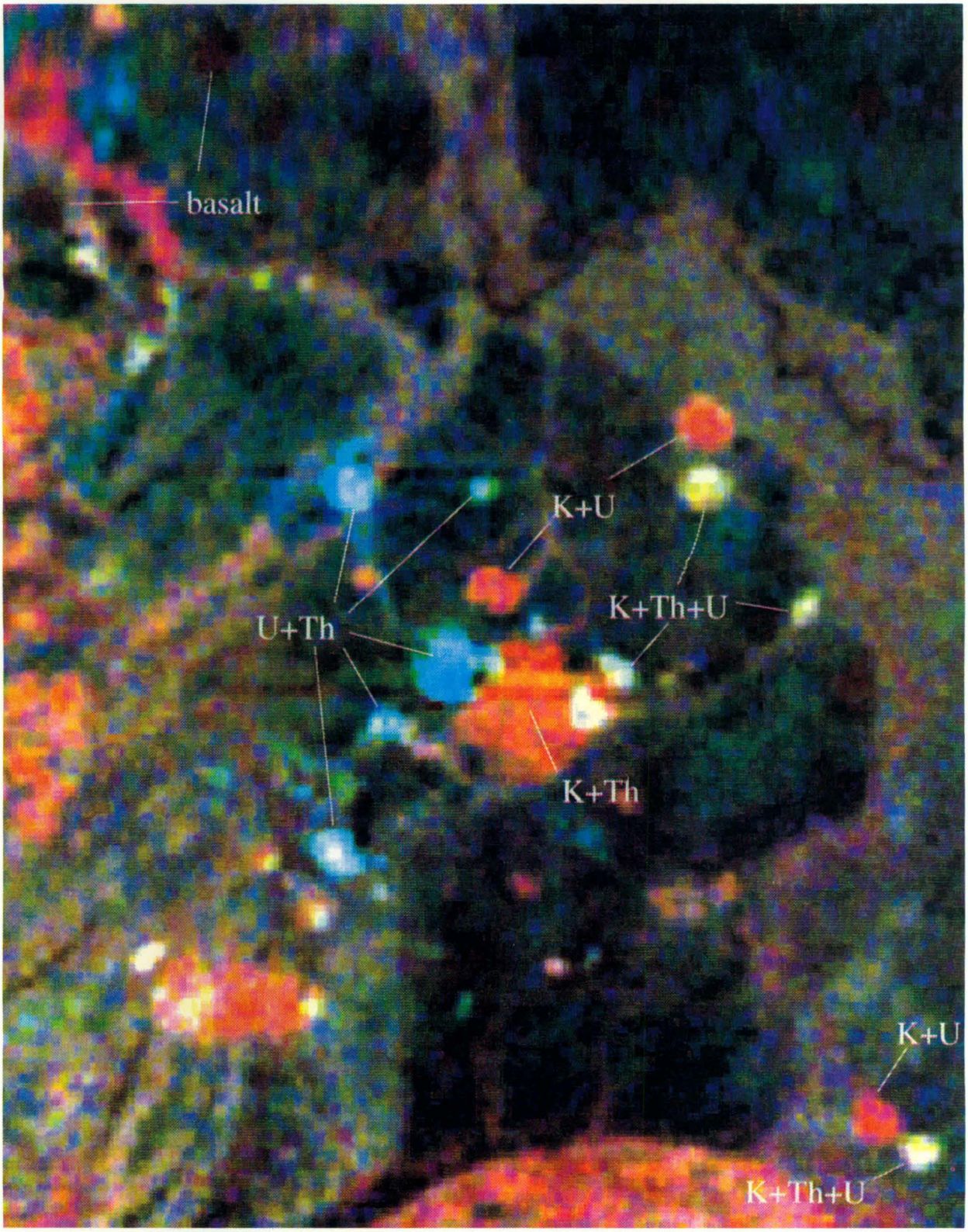

Figure 10. Gamma-ray image of an area south of Dubbo, showing the geochemically different signatures of a number of minor intrusions in the area. Some intrusions have dominant U+Th signatures, others dominant K+U or K+Th , and yet others are high in all three elements. The northern end of the Yeoval Batholith (Fig. 9) is shown at the bottom of the figure as a rounded red segment.

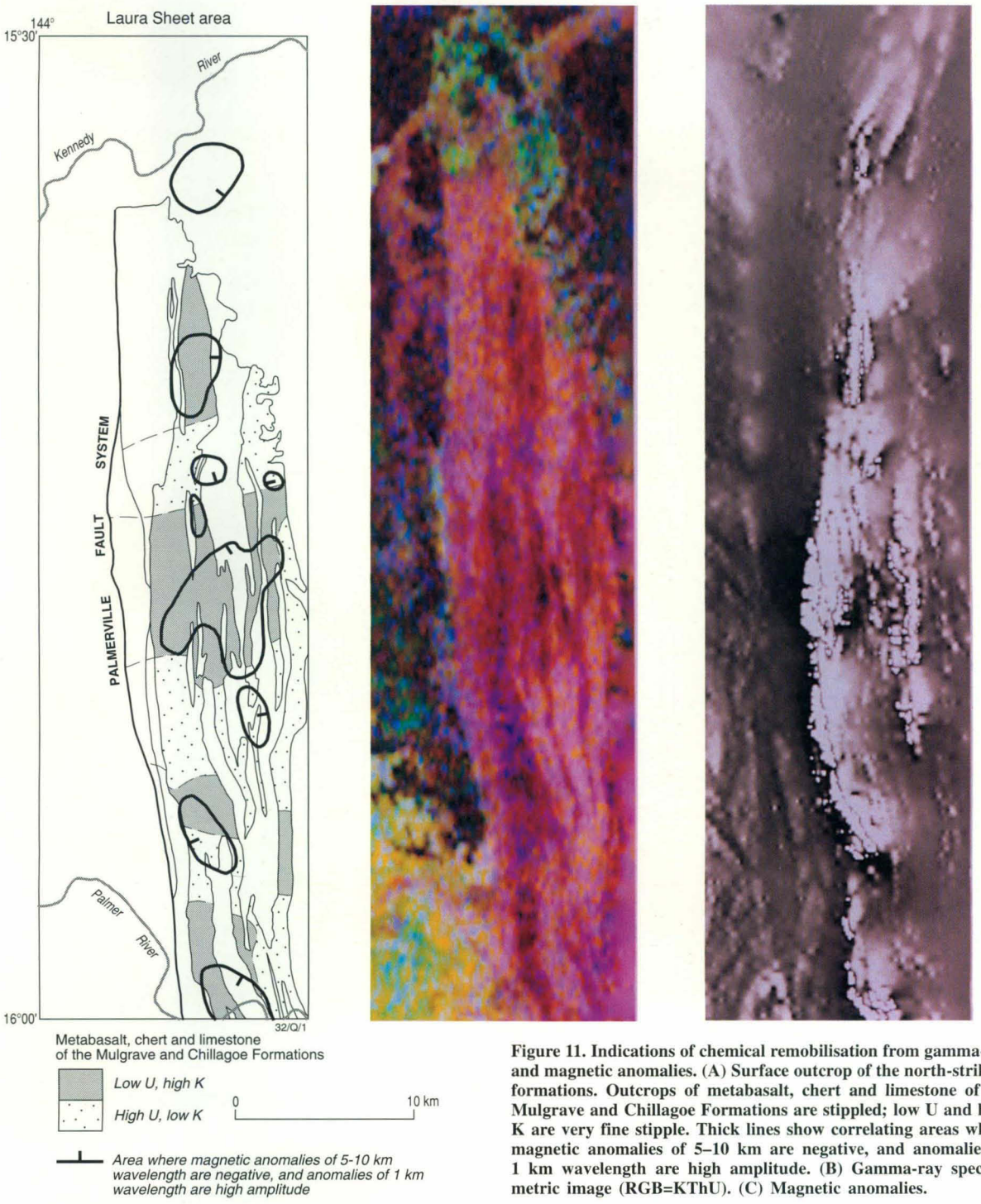

Figure 11. Indications of chemical remobilisation from gamma-ray and magnetic anomalies. (A) Surface outcrop of the north-striking formations. Outcrops of metabasalt, chert and limestone of the Mulgrave and Chillagoe Formations are stippled; low U and high K are very fine stipple. Thick lines show correlating areas where magnetic anomalies of 5–10 km are negative, and anomalies of 1 km wavelength are high amplitude. (B) Gamma-ray spectrometric image (RGB=KThU). (C) Magnetic anomalies.

Gamma-ray spectrometry is clearly a vital tool for distinguishing igneous rock bodies of different composition and degree of differentiation, as K, Th and U are critical elements involved in magmatic differentiation processes. A number of associated intrusive bodies south of Dubbo, of possible Mesozoic age and with alkaline affinity, are associated with the development of alteration and rare-metal mineralisation (Zr, Hf, Nb, Ta, light REE, Y). The gamma-ray image of the region (Fig. 10) shows that each intrusion has a different geochemical signature, the nature of which is yet to be investigated. Some have dominant U+Th signatures, others dominant K+U or K+Th, and some are high in all three elements. The northern end of the Yeoval Batholith (Fig. 9) is shown in the bottom of Figure 10 as a rounded segment with a high K signature.

Fluid flow

Magnetic and gamma-ray anomalies have the potential to map previous fluid flow through basement. Fluid flow may change the oxidation state of the rock and, hence, the rock magnetisation, and may transport elements, resulting in a change in the absolute amounts of U, Th and K in the rock. In the following example, geophysical anomalies disclose a superimposed pattern of large-scale changes (10 km wavelength) in chemistry which have been interpreted as the effects of hydrothermal systems within reactive lithologies (Wellman 1994).

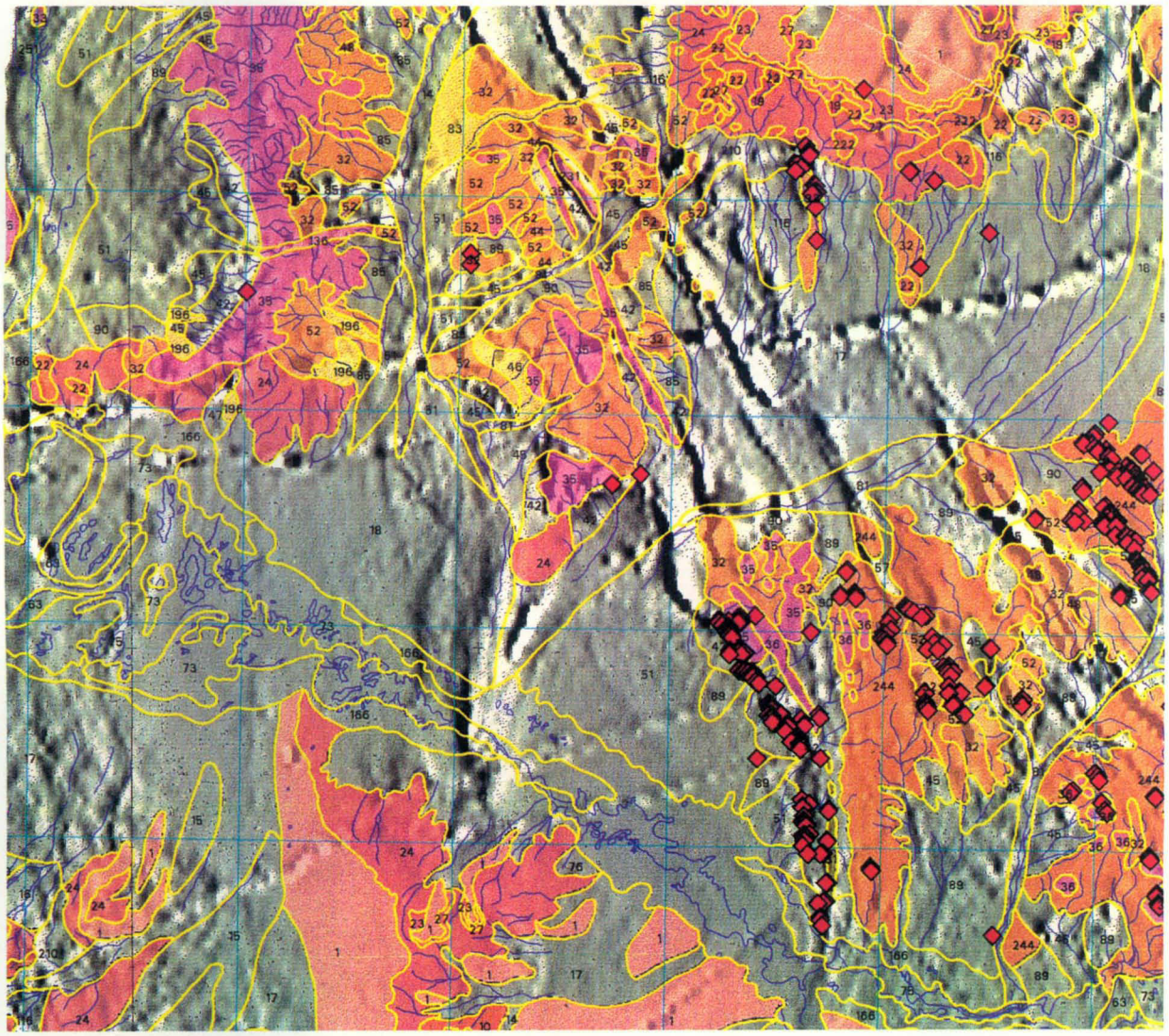

Figure 12. Thematic map of the Leonora 1:250 000 Sheet from the Eastern Goldfields of Western Australia, comprising in-situ regolith polygons (colour) and mineral deposit locations (red) draped over the east gradient of the aeromagnetics. The map shows that known mineralisation is largely confined to the in-situ regolith and that mineralised settings continue under cover.

Figure 11 shows the western margin of the Laura 1:100 000 Sheet area in north Queensland. East of the Palmerville Fault is an infaulted strip of Permian sedimentary rocks, and lower Palaeozoic Mulgrave and Chillagoe Formations forming north-striking, steeply dipping, semi-continuous bands. The spectrometric image shows relatively high concentrations of U, K and Th over one group of rocks (greywacke, greywacke/mudstone, and quartzose arenite); and low Th and high K or U over a second group of rocks (metabasalt, chert and limestone). Boundaries on the spectrometric image and on the geological map coincide closely, demonstrating the accuracy of the lithological mapping. On the spectrometric image, the second group of rocks can be divided along strike into areas of relatively high K, and areas of relatively high U. Variation along strike in K and U correlates roughly with along-strike variations in magnetic anomalies. Each area of relatively high K correlates with an area containing both high-amplitude magnetic anomalies of wavelength 1 km and a negative anomaly of wavelength 5–10 km. Each area of high U correlates with an area containing low-amplitude magnetic anomalies of wavelength 1 km and a positive anomaly of wavelength of 5–10 km. Hence, the spectrometric and magnetic images reflect both lithological layering and along-strike variation in properties, owing to chemical remobilisation by hydrothermal fluids. This example supports the use of regional geophysical data sets for mapping residues of chemical remobilisation.

Regolith mapping by gamma-ray spectrometry

Airborne gamma-ray spectrometric data are proving to be an important new tool for land-resource and land-degradation mapping because of their ability, unlike Landsat5 TM data, to penetrate vegetation cover to produce a chemical (K–Th–U) map of the surface (Wilford et al. 1997).

The image of the Ebagoola 1:250 000 Sheet area in north Queensland (Wilford et al. 1997) has been used to divide the regolith of the area into three types:

- deep in-situ slow-weathering regolith of the western and eastern plains shows black and greenish-blue on the image, owing to the surface accumulation of residual sand, Fe-oxides and resistate minerals (zircon);
- transported alluvial sediments give a braided river-deposit pattern, with a consistent colour which corresponds to the

mineralogy and geochemistry of the source rocks;
- in the central part of the image, mainly slowly eroding upland with thick in-situ regolith over bedrock, the image shows reddish colours over granite, and green/blue over metamorphic rocks.

Some of this non-alluvial sediment highland area is covered by quartzose sand, but field studies and the colour of the spectrometric image show that none of this regolith is transported.

Within the image, colour brightness is a measure of geomorphic activity: brighter colours correspond to areas of active erosion in the highlands and alluvial sediments derived from the eroded material, and the darker colours (including some greens) correspond to areas of very low erosional activity.

It is important to interpret the spectrometric data in the correct geomorphological and structural context. This can be done by merging the data with information of a higher spatial resolution. A composite image of three-colour spectrometric data with a hill-shaded high-frequency component highlights the texture of the spectrometric data. An image of spectrometric data combined with Landsat TM band 5 data has allowed definition of broad lithological units and structural domains, and information on the weathering and geomorphic history of the region (Wilford et al. 1992).

Integration, geographic information systems and thematic maps

Geographic information systems (GIS) are computer systems for managing and integrating spatial data—maps, digital images and geo-referenced data in tables. Modern GIS capitalise on advances made over the past decade in image processing, computing hardware (both processing power and data storage) and relational databases, to provide a unique environment for analysis of geological information by rapid digital integration of multiple data sets as layers in a map (e.g. Jaques 1993). GIS therefore play an important role in the new generation mapping: airborne geophysical and other data sets held as layers in the GIS may be integrated and combined with information in point form in databases to produce thematic maps at varying scales. For example, multiple layers of remotely sensed data (airborne geophysics, satellite data) can be combined with geological, geochemical, regolith, and mineral deposit data to produce an assessment of resource potential.

Thematic maps

Integration of spatial data by GIS enables development of new thematic map products of direct relevance to the minerals industry. These commonly include magnetic image maps, gamma-ray spectrometric image maps, tectonic elements, basement geology, mineral occurrence, metallogenic, alteration facies, metamorphic facies, mineralogy and mineral potential maps at various scales.

GIS can be used to generate mineral potential maps at province, region or prospect scale (e.g. Bonham-Carter et al 1990; Wyborn et al. 1994). Important layers for incorporation in GIS for mineral potential maps include geology (rock types, structure), geophysics (gravity, magnetic, and gamma-ray data), satellite images (Spot, Landsat TM), geochemistry and mineral deposit information. Many maps of mineral potential are most effectively presented using high-resolution airborne geophysics or geophysics plus Landsat TM data as a base, and can directly contribute to exploration strategies. An example is the overlay of in-situ regolith landform polygons and gold deposits on the east gradient of the magnetics from the Leonora region of the Eastern Goldfields (Fig. 12). The resulting mineral prospectivity map shows spatial relationships between the themes and the continuation of mineralised trends under cover.

Mapping mineral systems

GIS modelling generally involves combining specific map layers (commonly empirical associations) to generate a unique conditions map for a particular style of mineralisation. Other approaches involve statistical methods based on the location of known mineral deposits and various map layers. The 'weights of evidence' method (Bonham-Carter et al. 1990) uses Bayesian principles for combining multiple maps to produce new maps showing the probability of mineral occurrences and their associated uncertainty.

Successful mineral exploration, especially for world-class and new or unique deposits draws on both empirical and conceptual methods (e.g. Woodall 1994). Most mineral deposits are a spatially small part (less than 3 km^2) of a mineralising system resulting from the interaction of many geological factors, which can occur over a scale of tens of kilometres (district scale) or hundreds of kilometres (regional scale). Many of the essential elements or geological factors (e.g. faults, major folds, metamorphic grade, proximity to intrusions, host lithology, alteration halo, geochemical halo) can be defined within a GIS. Such deposits commonly have a regional and/or local magnetic and/or gamma-ray signature which can be directly mapped by high-resolution geophysics.

Therefore, if the geological factors essential for formation of a particular deposit type are understood and defined, a GIS can identify areas with potential for that type of deposit (Wyborn et al. 1994). This approach, i.e. a focus on the processes of ore formation, has advantages over statistical analytical methods in that it is not dependent on the existence of known mineral deposits in the region and is not limited to known types of mineral deposit.

AGSO has found this approach useful in mapping mineral potential in several important Proterozoic provinces, including the Mount Isa base-metal and Pine Creek gold–uranium provinces, where regional magnetic and gravity images have proved essential for defining the boundaries and structures of the basement (Wyborn et al. 1994).

Conclusions

High-resolution airborne magnetic and gamma-ray specrometric surveys, together with geographic information systems and modern computer data sets, are now seen as essential components of modern geological mapping. Under the National Geoscience Mapping Accord, Australian Commonwealth, State and Northern Territory governments are making a major commitment to the acquisition of high-resolution airborne geophysical surveys in Australia to underpin geological mapping aimed at sustaining resource exploration and development into the 21st century.

The usefulness of airborne geophysics, coupled with geological and petrological/geochemical investigations, in mapping metamorphic grade, petrological/geochemical zoning in igneous bodies, hydrothermal alteration, contact metamorphism, and regolith landforms has been clearly demonstrated. New thematic maps based on aeromagnetic and gamma-ray spectrometric surveys, coupled with ground-truthing and laboratory studies, will map metamorphic facies, redox fronts, regional alteration, and basement structure. Integration of these maps within geographic information systems will enable definition of mineral systems on a regional scale, and provide a basis for a much more comprehensive understanding of the geology and mineral and petroleum potential.

Acknowledgments

The authors gratefully acknowledge the assistance and advice of numerous AGSO colleagues, especially Peter Gunn for his encouragement to write this paper.

References

Barley, M.E., Eisenlohr, B.N.,Groves, D.I., Perring C.S. & Vearncombe, J.R., 1989. Late Archaean convergent margin tectonics and gold mineralisation: a new look at the Norseman–Wiluna Belt, Western Australia. Geology, 17, 826–829.

Blain, C., 1992. Is exploration becoming more cost effective? National Agricultural and Resources Outlook Conference, Minerals Exploration Symposium, 2, 23–29.

Bonham-Carter, G. F., Agterberg, F. P. & Wright, D. F., 1990. Weights of evidence modelling: a new approach to mapping mineral potential, Geological Survey of Canada, Paper 89-9, 171–183.

Boyd, D., 1967. The contribution of airborne magnetic surveys to geological mapping. In: L.W. Morley (editor), Mining and groundwater geophysics/1967. Department of Energy, Mines and Resources, Ottawa, Economic Geology Report 26, 213–227.

Clark, D.A., 1997. Magnetic petrophysics and magnetic petrology: aids to geological interpretation of magnetic surveys. AGSO Journal of Australian Geology & Geophysics, 17(2)—this issue.

Coggon, J. & Lai, J., 1993. 3-D magnetic model inversion for structure mapping. Exploration Geophysics, 24, 415–428.

Cooke, A., Pridmore, D.F., Hallberg, J.A., Isles, D.J. & Ross, J.R., 1989. Advances in geological mapping and interpretation through the high-resolution aeromagnetic method. In: Geoscience mapping towards the 21st century. 18th BMR Research Symposium, Canberra, 7–9 November 1989.

Cordell, L. & Grauch, V.J.S., 1985. Mapping basement magnetisation zones from aeromagnetic data in the San Juan basin, New Mexico. In: Hinze, W.J. (editor), The utility of regional gravity and magnetic anomaly maps. Society of Exploration Geophysicists, Tulsa, 181–197.

Denham, D., 1997. Airborne geophysics in Australia: the government contribution. AGSO Journal of Australian Geology & Geophysics, 17(2)—this issue.

Dentith, M.C., Francombe, K.F., Ho, S.E., Shepherd, J.M., Groves, D.I. & Trench, A. (editors), 1994. Geophysical signatures of Western Australian mineral deposits. Geology Key Centre & UWA Extension, University of Western Australia, Department of Geology and Geophysics, Publication 26; Australian Society of Exploration Geophysicists, Special Publication 7.

Dickson, B.L. & Scott, K.M., 1997. Interpretation aerial gamma-ray surveys—adding the geochemical factors. AGSO Journal of Australian Geology & Geophysics, 17(2)—this issue.

Gee, D.R., 1979. Structure and tectonic style of the Western Australian Shield. Tectonophysics, 58, 327–369.

Grant, F.S., 1985. Aeromagnetics, geology and ore environments: 1. Magnetite in igneous, sedimentary and metamorphic rocks: an overview. Geoexploration, 23, 303–333.

Gunn, P.J., 1997. Quantitative methods for interpreting aeromagnetic data: a subjective review. AGSO Journal of Australian Geology & Geophysics, 17(2)—this issue.

Isles, D.J., Harman, P.G. & Cunneen, J.P., 1989. The contribution of high resolution aeromagnetics to Archaean gold exploration in the region, Western Australia. Economic Geology, Monograph 6, 389–397.

Isles, D.J., Cook, A. & Hallberg, J.A., 1990. Aeromagnetic evaluation. In: Ho, S.E., Groves, D.I. & Bennett, J.M. (editors), Gold deposits of the Archaean Yilgarn Block Western Australia: nature, genesis and exploration guides. Geology Key Centre & University Extension, University of Western Australia, Department of Geology, Publication 20, 342–347.

Jaques, A.L., 1993. Second generation maps. GIS User, 5, 38–41.

Jessell, M.W., Valenta, R.K., Jung, G., Cull, J.P. & Geiro, A., 1993. Structural geophysics. Exploration Geophysics, 24, 599–602.

McIntyre, J.I., 1980. Geological significance of magnetic patterns related to magnetite in sediments and metasediments—a review. Australian Society of Exploration Geophysicists Bulletin, 11, 19–33.

Milligan, P.R. & Gunn, P.J., 1997. Enhancement and presentation of airborne geophysical data. AGSO Journal of Australian Geology & Geophysics, 17(2)—this issue.

Morse, M.P., Murray, A.S. & Williams, J.W., 1992. Gravity anomaly map of Australia. Bureau of Mineral Resources, Australia, 1:5 000 000 pixel map series, map numbers 21/A/52, 21/A/52-1.

Murray, A.S., 1997. Australian national gravity database. AGSO Journal of Australian Geology & Geophysics, 17(1)—in press

Reeves, C.V., 1992. New horizons for airborne geophysics mapping. Exploration Geophysics, 23, 273–280.

Reid, A.B., Allsop, J.M., Granser, H., Millett, A.J. & Somerton, I.W., 1990. Magnetic interpretation using Euler deconvolution. Geophysics, 55, 80–91.

Roest, W.R., 1992. Magnetic interpretation using the 3-D analytic signal. Geophysics, 57, 116–125.

Shaw, R.D., 1994. East Kimberly: geophysics. AGSO 93, Yearbook of the Australian Geological Survey Organisation. Australian Government Publishing Service, Canberra, 73–74.

Shaw, R.D., Wellman, P., Gunn, P., Whitaker, A.J. & Palfreyman, W.D., 1995. Australian crustal elements, based on distribution of geophysical domains; 1:5 000 000 scale map. Australian Geological Survey Organisation, Canberra.

Shaw, R.D., Wellman, P., Gunn, P., Whitaker, A., Tarlowski, C. & Morse, M., 1996. Guide to using the Australian crustal elements map. Australian Geological Survey Organisation, Record 1996/30.

Skinner, B.J., 1993. Finding mineral resources and the consequences of using them: major challenges in the 21st century. Australasian Institute of Mining and Metallurgy Centenary Conference, Adelaide, 30 March–4 April 1993, Australasian Institute of Mining and Metallurgy Publication 93/2, 1–8.

Smith, R.J., 1985. Geophysics in Australian mineral exploration. Geophysics, 50, 2637–2665.

Tarlowski, C., Simonis, F., Whitaker, A. & Milligan, P., 1992. The magnetic anomaly map of Australia. Exploration Geophysics, 23, 339–342.

Tarlowski, C., Gunn, P.J. & Mackey, T. 1997. Enhancements of the magnetic map of Australia. AGSO Journal of Australian Geology & Geophysics, 17(2)—this issue.

Webster, S.S., Woods, K.T. & Wyborn, D., 1989. Integrated geophysical/geological mapping interpretation: case histories from the Charters Towers region and elsewhere. In: Geoscience mapping towards the 21st century. 18th BMR Research Symposium, Canberra, 7–9 November 1989.

Wellman, P., 1992. A geological interpretation of the regional gravity and magnetic features of north Queensland. Exploration Geophysics, 23, 423–428.

Wellman, P., 1994. Mapping large-scale hydrothermal systems using coincident magnetic and gamma-ray spectrometric anomalies. AGSO Research Newsletter, 20, 16–17.

Wellman, P., 1995. Interpretation of regional magnetic and gravity data in Cape York Peninsula, Queensland. Australian Geological Survey Organisation, Record

1995/45.
Wellman, P., Mackenzie, D.E. & Bain, J.H.C., 1994. Permian Carboniferous magmatism in north Queensland, a new perspective. AGSO Research Newsletter, 20, 8–9.
Whitaker, A.J., 1992. Kalgoorlie magnetic and gravity interpretation, 1:1M scale map. Australian Geological Survey Organisation, Canberra.
Whitaker, A.J., 1993a. Regional geophysical constraints on tectonic models for the Eastern Goldfields Province. In: Williams P.R. & Haldane J.A.(compilers), Kalgoorlie 93, Extended Abstracts. Australian Geological Survey Organisation, Record 1993/54, 63–67.
Whitaker, A.J., 1993b. Esperance magnetic and gravity interpretation, 1:1M scale map, Australian Geological Survey Organisation, Canberra.
Whiting, T.H., 1986. Aeromagnetics as an aid to geological mapping—a case history from the Arunta Inlier, Northern Territory. Australian Journal of Earth Sciences, 33, 271–286.
Wilford, J.R., Pain, C.F. & Dohrenwend, J.C., 1992. Enhancement and integration of airborne gamma-ray spectrometric and Landsat imagery for regolith mapping—Cape York Peninsula. Exploration Geophysics, 23, 441–446.
Wilford, J.R., Bierwirth, P.N. & Craig, M.A.,1997. Application of airborne gamma-ray spectrometry in soil/regolith mapping and applied geomorphology. AGSO Journal of Australian Geology & Geophysics, 17(2)—this issue.
Williams, P,R. & Whitaker, A.J., 1993. Gneiss domes and extensional deformation in the highly mineralised Archaean Eastern Goldfields Province, Western Australia. Ore Geology Reviews, 8, 141–162.
Woodall, R., 1993. The third dimension: a geoscience challenge for the 21st century. Australasian Institute of Mining and Metallurgy Centenary Conference, Adelaide, 30 March–4 April 1993. Australasian Institute of Mining and Metallurgy Publication 93/2, 39–40.
Woodall, R., 1994. Empiricism and concept in successful mineral exploration. Australian Journal of Earth Sciences, 41, 1–10.
Wyborn, D. & Sun, S.S., 1993. Nd-isotopic fingerprinting of Cu/Au mineralisation in the Lachlan Fold Belt. AGSO Research News Letter, 19, 13–14.
Wyborn, L.A.I., Gallagher, R., Jaques, A.L., Jagodzinski, E.A., Thost, D. & Ahmad, M., 1994. Developing metallogenic geographic information systems: examples from Mount Isa, Kakadu and Pine Creek. In: Australian mining looks north—the challenges and choices. 1994 AusIMM Annual Conference, Darwin, 5–9 August 1994, technical program proceedings. Australasian Institute of Mining and Metallurgy Publication 5/94.

AGSO Journal of Australian Geology & Geophysics, 17(2), 175–185

Interpreting aeromagnetic data in areas of limited outcrop

P.J. Gunn[1], D. Maidment[1] & P.R. Milligan[1]

Interpretation of aeromagnetic data in areas of limited outcrop requires the use of all relevant data enhancement techniques for accurate positioning of geological boundaries and magnetic sources. Where no outcrop calibration exists, magnetic sources must be characterised by physical adjectives relating to their form, depth and relative magnetisation. The final stage of the interpretation process is to apply geological reasoning, in the context of the area being interpreted, to deduce the rock types causing the magnetic responses and the structural relationships of the lithological units.

Introduction

Despite the fact that geophysicists have been interpreting aeromagnetic maps since the 1940s and despite the impressive recent advances in the quality of the data sets collected and the software available for processing and presenting the results, interpretation methodologies applied to aeromagnetic data sets are still largely based on the individual approaches of different geophysicists.

The only notable effort to produce a standardised methodology for interpreting aeromagnetic data sets appears to be one described by Isles et al. (1989). Their approach is to identify outlines, trends and gradients of magnetic units in order to define a geological 'skeleton', which is subsequently fleshed out with geological boundaries, interpreted on the basis of known geology or inferred to produce a map resembling the solid geology. The confidence that can be placed on lithological identification depends on the amount of 'ground truthing' possible and the local knowledge of the interpreter. The technique works particularly well in areas such as partially exposed Archaean shields and Palaeozoic fold belts, which generally have steeply dipping sequences of geological units with sharp and well-defined boundaries at or near ground surface. Interpretation of these areas is also facilitated by the fact that the types of geology normally encountered have semi-predictable and recognisable magnetic responses. Modifications to this approach are required in more complex areas.

This paper describes a methodology evolved to interpret aeromagnetic data sets from areas of highly deformed metamorphic rocks with virtually no geological control. While the principles of the Isles et al. (1989) approach have been applied, it has been necessary to expand their techniques to deal with superposition of magnetic units, variable depth to magnetic sources, and extreme ranges of magnetisation in particular units. It has been necessary to develop methods of presentation, incorporating these variables and the representation of anomaly sources for situations where it has not been possible to give the anomaly sources a positive lithological identification. The Highland Rocks 1:250 000 map sheet in the Arunta Block of the Northern Territory is used to illustrate the methodology.

Geological setting and airborne geophysical survey coverage of Highland Rocks

The Highland Rocks 1:250 000 sheet area comprises parts of two major tectonic units; the Arunta Block and the Birrindudu Basin (Fig. 1). Geological information on the sheet area is scarce, the only detailed study being the 1:250 000 scale geological mapping done by the Bureau of Mineral Resources (Hodgson 1974). Page et al. (1976) discussed the geochronology of various rocks in The Granites-Tanami region; Blake (1978) and Blake et al. (1979) described the regional geology.

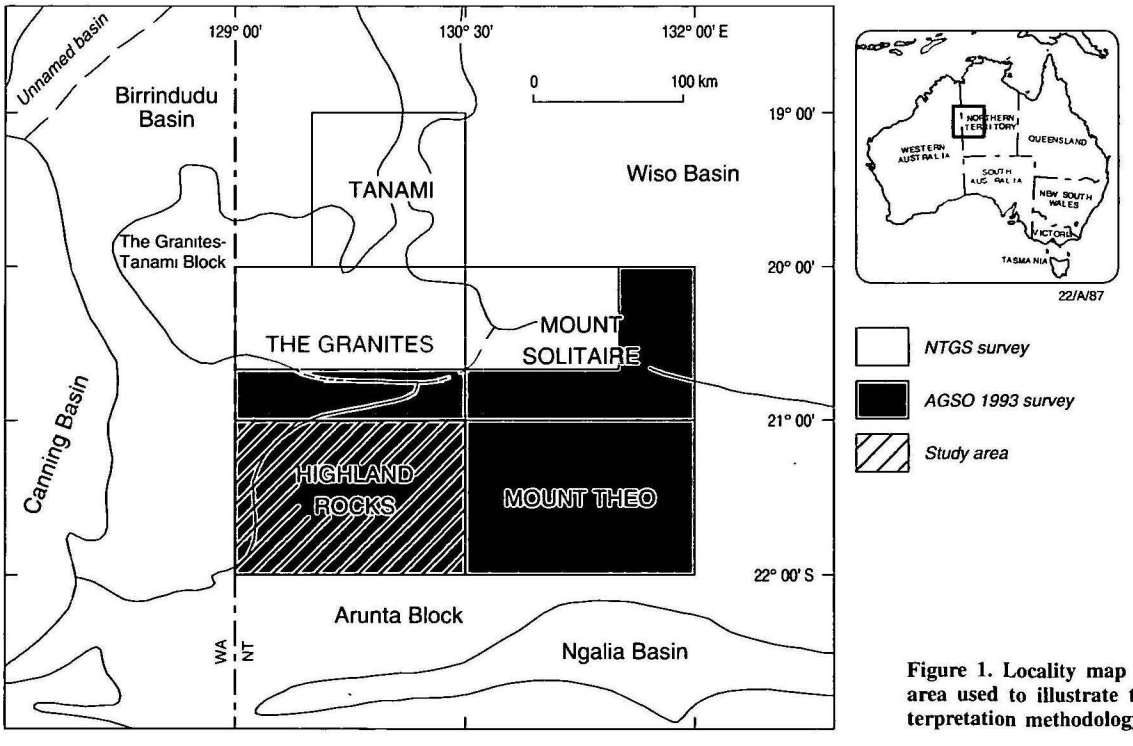

Figure 1. Locality map of the area used to illustrate the interpretation methodology.

[1] Australian Geological Survey Organisation, GPO Box 378, Canberra, ACT 2601

The oldest rocks in the area are highly deformed gneiss, schist, quartzite and granite of the Early Proterozoic Arunta Block, which occur as small isolated outcrops. Bedding, foliation and schistosity are steep to vertical and generally trend east–west (Hodgson 1974a,b). The regional structures and relationships between units are poorly understood, owing to extensive Cainozoic sand cover and laterisation of bedrock exposures. No meaningful stratigraphic correlation of outcrop data is possible.

In the west, Late Proterozoic sedimentary rocks of the Birrindudu Basin unconformably overlie Arunta Block metamorphics. The sediments belong to the Redcliff Pound Group and are predominantly arenites, which appear to have been folded into northeast to east-northeast-trending anticlines and synclines, which may also be faulted.

Isolated outcrops of folded and faulted terrestrial (?)Palaeozoic sedimentary rocks occur in the northwest and south, and there are also scattered outcrops of (?)Mesozoic sediments.

Aeromagnetic data have been collected over The Granites–Tanami area (Fig. 1) by the Australian Geological Survey Organisation (AGSO) and the Geological Survey of the Northern Territory. The AGSO portion of this coverage (Brodie 1994) comprised 111 710 line-km of data with 90 m nominal terrain clearance along north–south flight-lines spaced 500 m apart. East–west tielines were at 5000 m intervals. Navigation was by global positioning satellite (GPS). Magnetic data were recorded at 0.1 s intervals (approximately 7 m), and gamma-ray spectrometer data, every 1.0 s (approximately 67 m). The data were levelled and gridded to 100 m by AGSO.

Interpretation of the Highland Rocks data aimed at producing a regional interpretation at 1:250 000 scale; this being basically a constraint of the 500 m line spacing. It must be appreciated that with this line spacing it is difficult, without more information, to assign a geological cause to anomalous responses that only occur on one or two flight-lines. Not all such features have been recorded on the final interpretation map. It is AGSO's experience that data acquired on lines spaced at 500 m can be usefully imaged and displayed at 1:100 000 scale and that interpretations with such data should be done with 1:100 000 scale products. For areas such as Highland Rocks, where geological control is limited, a 1:250 000 interpretation map is considered consistent with this approach. We acknowledge that the data may warrant reworking at a larger scale by users who need more detailed information at specific localities.

Whiting (1986) interpreted a more detailed aeromagnetic survey (250 m line spacing, 80 m ground clearance) over an area of similar lithology at the eastern end of the Arunta Block. Whiting's study, which was able to use more extensive outcrop information and local geological knowledge than our study, and which incorporated detailed rock property measurements (Whiting 1988), resulted in a map where the interpreted units were identified as having specific lithologies. Whiting's study is an excellent example of how detailed correlation of outcrop geology and aeromagnetics can produce interpretation maps closely approximating the type of map that would be produced by geologists mapping in areas of good geological exposure. The interpretation process presented in this paper has not been able to avail itself of many geological correlations and, consequently, has been constrained to producing a map where many of the mapped units are described in terms of their magnetic character rather than specific lithology. Unfortunately, the area of Whiting's study was too far from Highland Rocks to allow direct correlation with his results.

Interpretation tools

The basic tools used to assist the interpretation of the Highland Rocks data set were:

- the INTREPID processing system—to filter and transform the original 100 m aeromagnetic grid into different representations of the data;
- the ER Mapper imaging system—to enhance and display data sets produced by INTREPID;
- a Novajet colour plotter—to produce large scale hardcopy output of the various images;
- the Arc/Info GIS system run on a Sun workstation—used to relate and overlay various layers of information, such as outcrop geology, magnetic data and versions of the interpretation. The interpretation was performed on screen in the Arc/Info system. Publication quality hardcopy results were produced directly from Arc/Info;
- the Encom Technology ModelVision potential field modelling package, which accepts ER Mapper grids.

Interpretation methodology

Interpretation methodology consisted of inspection of computer screen and hard-copy images, maps of the aeromagnetic data, and other relevant data to define:

- boundaries of magnetic units;
- structures dislocating or affecting the morphology of magnetic units;
- depth and attitude of magnetic units;
- any superposition of magnetic units;
- lithological units;
- chemical changes;
- a structural synthesis relating distribution of inferred lithologies and structure.

- ***Boundaries of magnetic units.*** Knowledge of the forms of anomalous responses due to different source geometry is fundamental to the estimatation of magnetic source boundaries. Compilations of theoretical anomalies due to plate-like bodies by Reford (1964) and for prismatic bodies by Vacquier et al. (1951), and various ad hoc modelling exercises using the ModelVision modelling package provide the necessary background knowledge in this regard. The inspection of such anomaly forms gives a basis for the positioning of source boundaries. As a general rule, boundaries are close to anomaly inflection points for sources with near vertical sides. An exception to this generalisation occurs with narrow sources whose width is less than their depth. In such situations, magnetic survey data cannot resolve the thickness of the source, only the position of the axis of the source unless additional information is available from mapping or modelling studies using rock-property data.

There are three types of source boundary.

- When a large discrete isolated magnetic anomaly occurs, it can be regarded as the response of a uniformly magnetised source and its boundary is traced where the edge of the source is estimated to be.
- For narrow anomalies, where the source thickness is less than the depth, the source can only be represented by a line.
- In many situations, concentrations of organised, semi-organised or random anomalies will occur which cover specific areas. Such anomalies can be due to:
  - an assemblage of magnetic and non-magnetic units,
  - faulted magnetic rock units,
  - folded magnetic rock units,
  - irregular weathering of magnetic units,
  - volcanic flows, where different flow portions have different magnetic properties, owing to variable chemical composition and cooling rate, and
  - combinations of the above.

Boundaries to such assemblages are drawn in such a way as to encompass all the anomalies that appear to be associated in character and spatial distribution. The boundaries then define

a 'magnetic unit' which, in most situations, will correspond to a geological unit, such as a particular lithology or lithological assemblage. Some interpreters refer to such assemblages as domains.

It is commonly possible to trace axes of individual magnetic anomalies within the defined unit. Sometimes these axes indicate fold or fault patterns. Some interpreters represent internal anomalies of geological units by lines described as 'trends within magnetic units'. This approach leaves open the question of the exact nature of the cause of the internal magnetic character. Other interpreters outline internal anomalies as if they are individual magnetic rock units. This approach can be more realistic, but the interpreter must be certain that the features being outlined do in fact correspond to discrete magnetic bodies. In terms of the Isles et al. (1989) methodology, individual anomaly axes and outlines of the internal magnetic rock units are the 'skeleton', and the boundary of the assemblage of anomaly axes and internal magnetic rock units is a geological 'unit'.

When interpreting the internal magnetic structure of magnetic domains it is important to assess whether the flight-line spacing in relation to the geological complexity of the area has allowed the gridding routine to produce a realistic representation of the anomaly distribution. If the flight lines are too widely spaced or orientated obliquely to the geological strike, the resultant contours and images will not correctly map magnetic detail and spurious anomalies will be apparent. In such situations it is difficult to map meaningful detail within magnetic units.

- ***Structures dislocating or affecting the morphology of magnetic units.*** Faulting can be recognised by:
  - offsets of apparently similar magnetic units,
  - sudden discontinuities of magnetic units,
  - an abrupt change in depth to magnetic sources,
  - a linear narrow magnetic low caused by weathering along a fault plane oxidising magnetic minerals to non-magnetic minerals (joints can have a similar magnetic expression),
  - a linear magnetic high, which may be discontinuous in nature, due to magnetic minerals precipitated in the fault plane.

Folding can be recognised by patterns of linear magnetic anomalies and the geometry of the larger magnetic sources in much the same way that folds can be recognised in outcropping geology.

- ***Depth and attitude of magnetic units.*** Depth and attitude (dips) can be estimated qualitatively by experienced interpreters familiar with typical anomalous responses of magnetic bodies. The depth of a magnetic source manifests itself as the sharpness of the resultant anomaly, with deeper sources causing broader anomalies. It is possible to roughly relate gradient of magnetic profiles or contour maps to depth of magnetic sources (Gunn 1997). Experienced interpreters can typically make such estimates visually with an accuracy of about 30 per cent. Depth can also be calculated by computer modelling.

Attitude of magnetic sources can be qualitatively estimated through a familiarity with anomaly forms and how they vary with dip. Such estimates can also be verified by computer modelling.

It is important to be able to distinguish between magnetic sources of effectively infinite depth and depth-limited sources such as horizontal lava flows or sills. Horizontal magnetic sources are generally surrounded by magnetic lows. Again, a familiarity with standard anomaly forms facilitates recognition

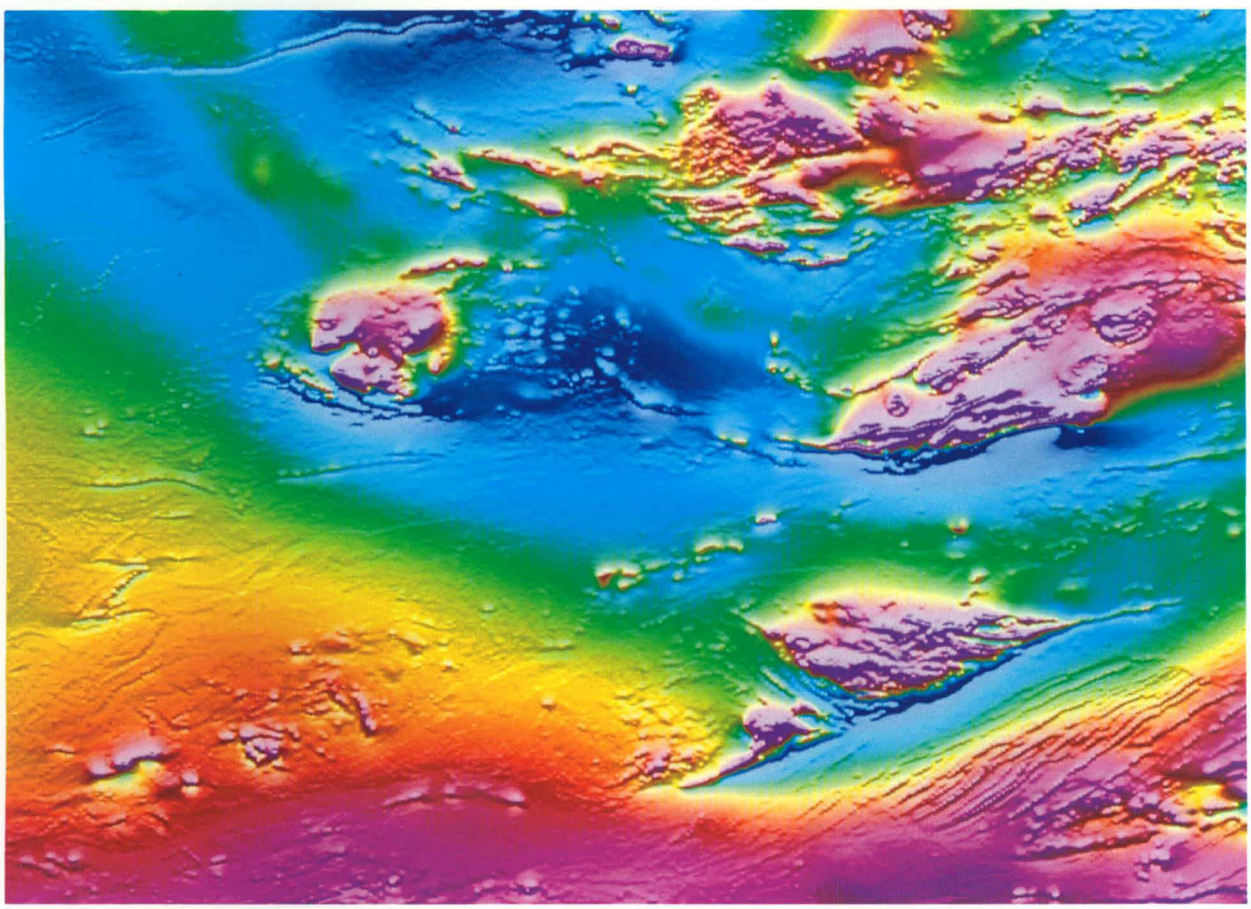

Figure 2. Total magnetic intensity colour image (red high–blue low) illuminated from the north.

of such bodies.

- ***Any superposition of magnetic units.*** It is possible for surveys to detect the magnetic effects of superimposed magnetic sources. It is important not to ascribe these responses to a single source. Depth estimates or the recognition of markedly different contour gradients should allow the identification of such situations.

- ***Lithological units.*** Lithological identification can be based on a combination of:
  - correlations with outcrop geology and drill hole data;
  - correlation with radiometric data—different radioelement concentrations can indicate particular lithologies (Dickson & Scott 1997);
  - correlation with gravity—gravity results indicate density;
  - amplitude of response can indicate possible lithology—for example, amplitudes of several thousand nanoteslas can indicate magnetite-rich ironstone. A basic knowledge of the different relative responses likely to arise from different rock units is required to be able to make plausible identifications. Such knowledge comes from experience; however, Clark (1997) provides a basis for this knowledge.

The outlines of magnetic units can suggest their lithology. For example, round or ovoid anomalies several kilometres across and which obviously cross-cut the local geology would suggest an intrusion. A magnetic high on all or part of the boundary of such a feature would suggest a magnetic aureole. Imagination, backed by a comprehensive geological training, is required to cover all possibilities.

The texture or character of magnetic units can also give clues to their origin. For example, lava flows generally exhibit a semi-random internal anomaly character, owing to the inhomogeneity of the magnetic properties of the flow.

- ***Chemical change.*** Discordant changes in magnetic intensity within a magnetic unit can indicate modification of magnetic properties by contact or regional metamorphism, alteration and weathering.

- ***Structural synthesis relating inferred lithology and structure.*** Finally, when all of the above facets of the interpretation have been assembled and considered, the interpreter must present the information as a useable product. Obviously, in areas of limited outcrop such interpretation products will be a compromise between what can be seen and what can be reasonably inferred. This distinction should be obvious to users of the interpretation product. It must be stressed again that a good understanding of fundamental geological concepts is required for an interpreter to be able to produce plausible interpretations.

The interpretation process is always iterative as no one image of data will show all relevant information. Different images and different data sets will contain relevant, albeit different, presentations of the total story. Our use of the various map, image and related data sets for the Highland Rocks interpretation is described below. Milligan & Gunn (1997) have described the algorithms used to produce the various displays and the advantages of the various products.

Total magnetic intensity contours

The basic AGSO products for all aeromagnetic surveys are line contour maps, which in the case of Highland Rocks were produced at 1:250 000 and 1:100 000 scales. The two different scales are necessary to appreciate the data in regional and detailed contexts. There is a tendency for interpreters to consider

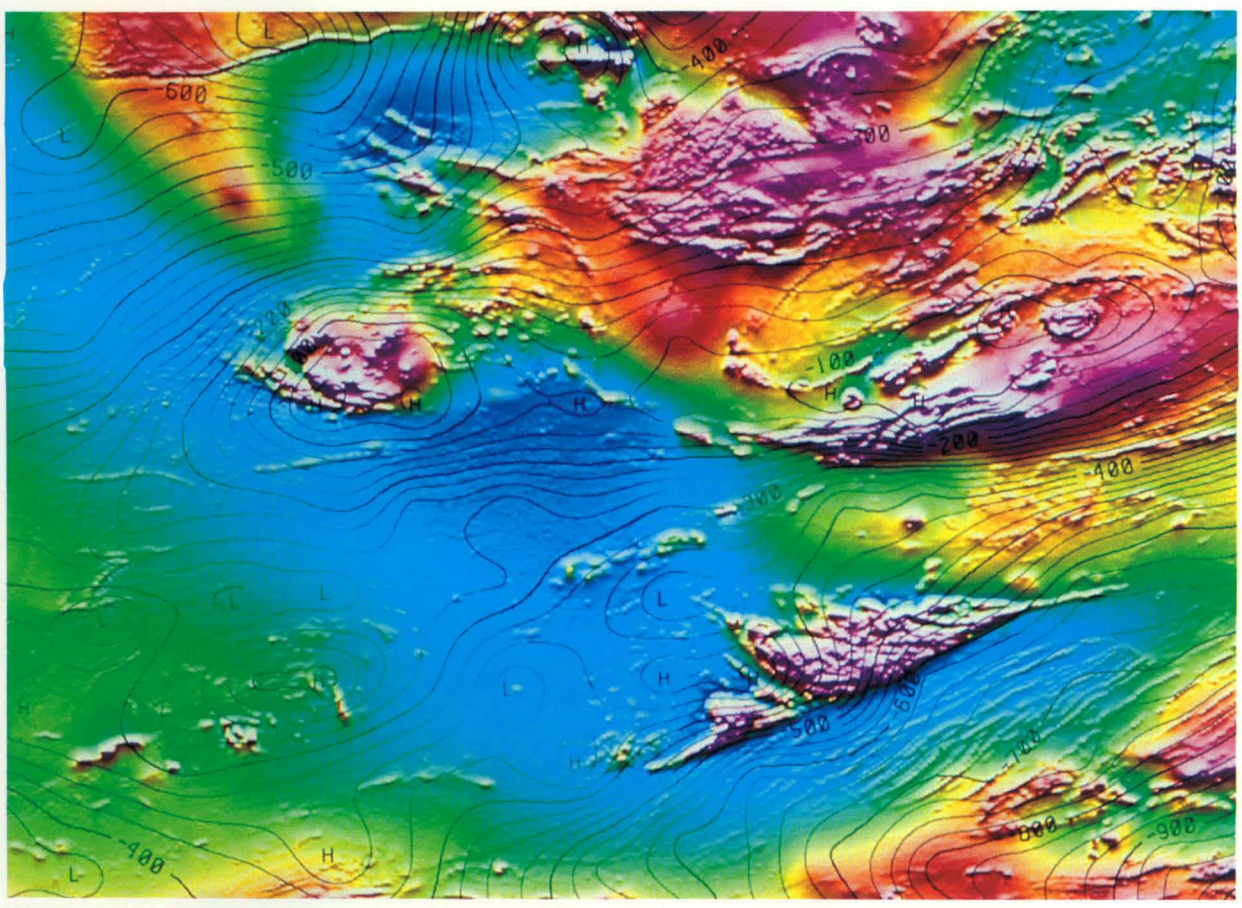

Figure 3. Colour image of reduction to pole of the total magnetic intensity (red high–blue low) with superimposed Bouguer gravity contours. Gravity contour interval is 25 m.s^{-2}. Image illuminated from the north.

that line contour maps are superseded by colour images. This is most definitely not the case and contours were essential to the interpretation. Line contour maps give a far superior representation of contour gradients than images and are thus more useful for the estimation of source outlines, depths and dips. Illuminated images can give a misleading indication of anomaly shapes and positions, because apparent anomaly shape depends on the colour palette used to display them.

It is also easier to extract amplitude values from line contour maps than images. Although colour contours were not used for this interpretation, we have become convinced, during other interpretation projects, that colour contours greatly facilitate interpretation by combining the advantages of contour representation with the instantaneous recognition of anomaly amplitudes. We have also found that the superposition of monochrome contours on a colour image of a magnetic data set is a valuable interpretation tool.

A further basic use of the line contour maps is to check the gridding and contouring process that has been applied to the line data. Superposition of flight lines on line contour maps allows an appreciation of whether artefacts are being generated by the processing.

Total magnetic intensity profiles

Normally, line profile data contain more information than gridded data by virtue of the fact that grid intervals are generally coarser than the sampling interval along the flight lines. This is certainly the case for the Highland Rocks data, which were originally recorded at a 7 m interval before being interpolated to a 100 m grid. This means that the gridded data are a smoothed representation of the profile data. It is even possible that aliasing could occur in the gridding process and misleading anomaly forms be generated. It is also possible that single anomalous peaks in contour maps and images are in reality multi-peaked anomalies. Profile data were checked to resolve these ambiguities—profile plots at different scales allow anomalies with different amplitudes to be studied.

Total magnetic intensity colour image (with northerly illumination)

The original image product of the Highland Rocks aeromagnetic data was a colour total magnetic intensity image with a northerly illumination, which created shadows on the southern side of anomalies (Fig. 2). This illumination gives the optimum display of the predominantly east–west strike of the study area. While the image is visually pleasing, it is only an intermediate product used for quality control, not the actual interpretation. This is because the inclination of the Earth's magnetic field in the study area is 50° and, consequently, the total field image, as recorded, shows extreme anomaly asymmetry. The asymmetry has been removed by the 'reduction to the pole' process described below.

Total magnetic intensity reduced to the pole

Basic interpretation of the aeromagnetic data set was performed on various images of the data set reduced to the pole. Where magnetisation of the rocks in an area is by induction, and no significant permanent magnetisation occurs in a direction other than that of the Earth's field, anomalies in reduced to the pole maps and images occur vertically above their sources. Such maps and images are thus significantly easier to interpret than original data sets in areas of significant magnetic inclination. Experience has shown that the assumption of induced magnetisation holds for most areas. When it does not, anomalies

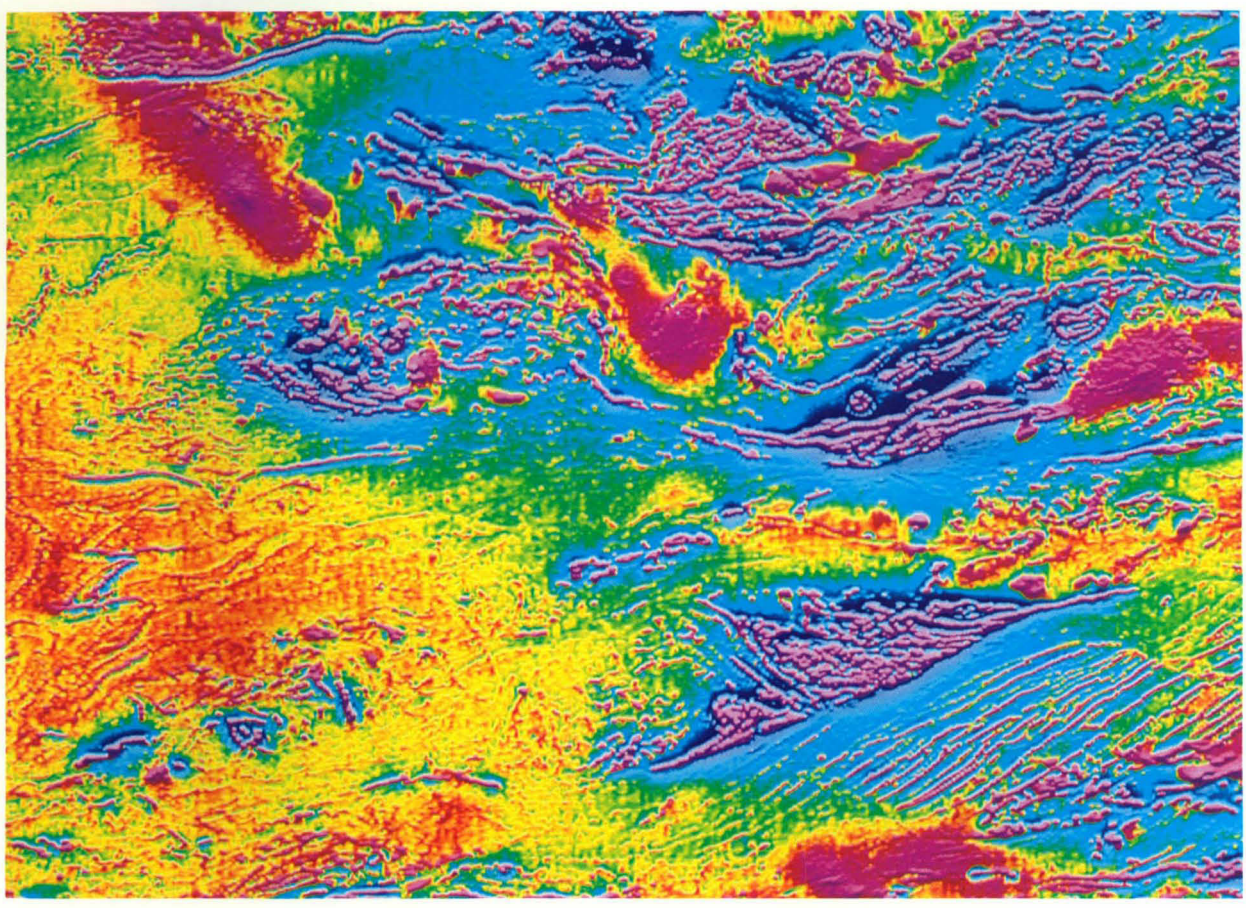

Figure 4. Colour image of the vertical gradient of the total magnetic intensity reduced to the pole, illuminated from the north (red high–blue low).

with a significant component of remanence manifest themselves after the reduction to the pole process with a smeared 'comet tail' (MacLeod et. al. 1993, fig. 2). No such smearing is obvious in the reduced to the pole images of Highland Rocks, so it is probable that no significant remanence is present.

The reduced to the pole representations of the total magnetic intensity produced for this interpretation were:

- reduced to the pole line contours. This map shows representations of field gradients, which are essential for determining magnetic source boundaries and for qualitative estimates of source geometry and depth.
- reduced to the pole colour amplitude image with no illumination. This image is a coloured representation of information in the line contour map and provides complementary information).
- reduced to the pole colour image with illumination from the north (Fig. 3). This image, which uses a rainbow colour scheme (blue low to magenta high), proved most useful for subdivision of the area into units of different magnetic intensity and character. It is most useful when overlain on the line contour reduced to the pole map. The northerly illumination enhances subtle magnetic features not obvious in the simple non-illuminated representations of the data. The image of Figure 3 has several limitations. The illumination process creates black shadows which obscure magnetic detail on the southern side of anomalies, and severely so when the anomalies are intense. The shadowing process also gives a misleading impression of exactly where anomaly boundaries and peaks occur, and this is an important reason why images should be used in conjunction with the line contour map of the same data.
- greyscale reduced to the pole image with northerly illumination. Many interpreters prefer greyscale images to colour images because they perceive that subtle magnetic features are more obvious in greyscale images. This appears to be so and greyscale images have a definite use in extracting fine detail in magnetically 'flat' areas. A major weakness of greyscale images is that they cannot realistically represent amplitude data.

Maps and images of the computed vertical gradient of the magnetic field reduced to the pole

Vertical gradients of magnetic fields represent magnetic fields in which regional effects and interference between adjacent anomalies have been suppressed. The computation of vertical gradients is analogous to the application of a high-pass filter. Versions of the vertical gradient of the total magnetic intensity reduced to the pole were indispensable for the interpretation of the Highland Rocks data set. The following maps and images of this type were produced:

- line contour map of the vertical gradient of the field reduced to the pole. As with the total magnetic intensity contours, this map is indispensable for the definition of true anomaly maxima and source edges as defined by contour gradients.
- colour image of the vertical gradient of the total magnetic intensity reduced to the pole illuminated from the north (Fig. 4). While this image provides an excellent definition of the fine detail of the study area combined with amplitude information, many of the narrow features appear simply as combinations of black and white features. While the image defines the existence of these features, it gives little indication of their amplitude. A further weakness is that the position of the transition of the black to the white portions of the image of the narrow linear features depends

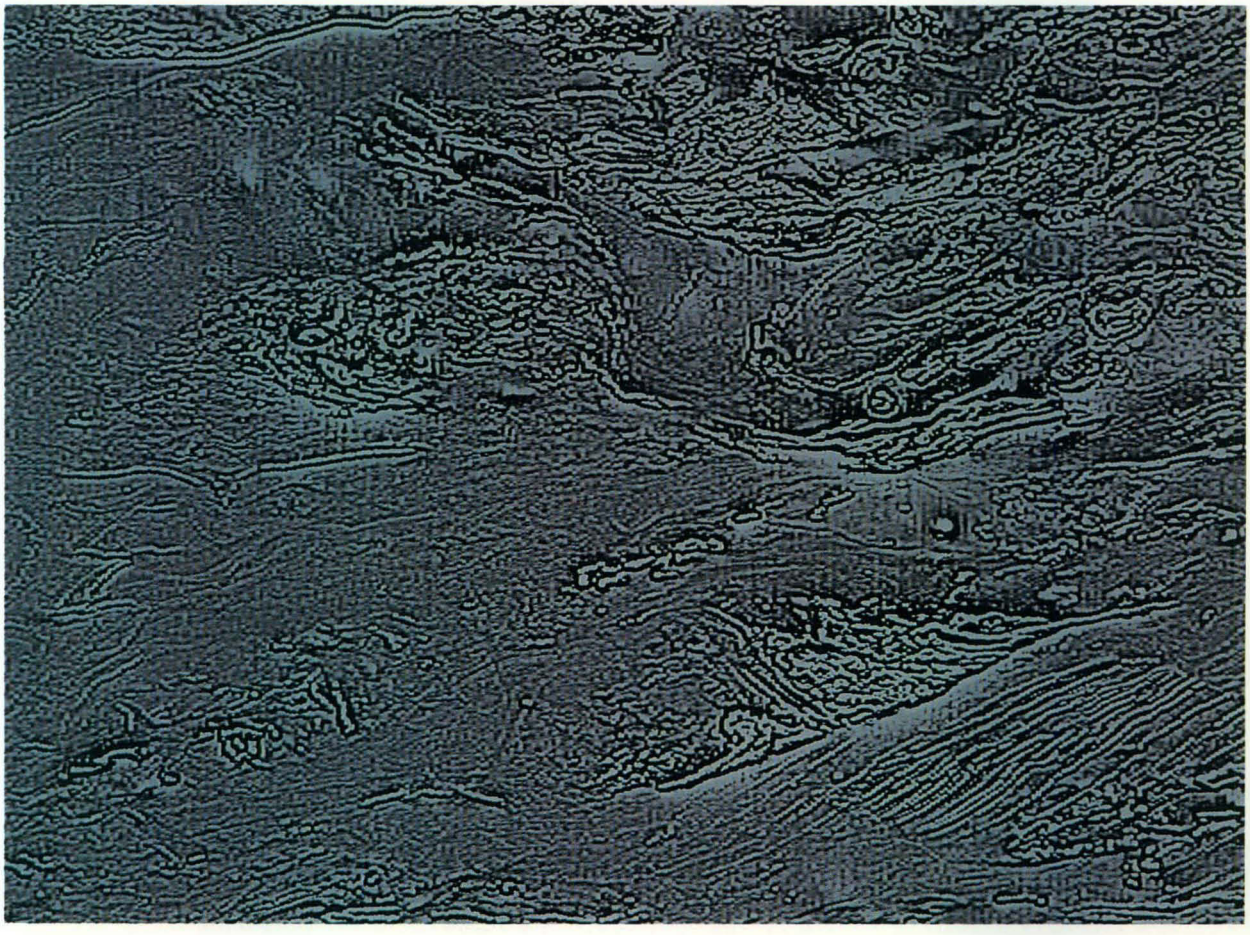

Figure 5. Greyscale image of the vertical gradient of the total magnetic intensity reduced to the pole.

on the direction of illumination and the azimuth of the illuminating 'sun'. Attempts to solve these problems by selectively displaying portions of the study area at larger scales, using greater dynamic colour ranges over the anomalies of interest, were not successful in practical terms. The only real solution was to use the line contour map in conjunction with the colour image. The vertical gradient image also enhances pixel features in linear anomalies trending at 45 to the flight lines. This results from a 'beading' effect produced by the interpolation routine when it encounters such anomalies. Most aeromagnetic gridding routines appear to have this defect, which degrades high-pass images of such data.

- greyscale image of the vertical gradient of the total magnetic intensity reduced to the pole (Fig. 5). This image provides a superior resolution of the subtle fine detail, but otherwise has the same problems as the colour version. Figures 6 and 7 show detail of the total magnetic intensity and vertical gradient images with superimposed contours. Such 'zooms' are essential to extract fine detail from the data.

Automatic gain control of computed vertical gradient of the magnetic field reduced to the pole

Automatic gain processing creates an image in which all anomalies are constrained to have approximately the same amplitude and weak features are, in principle, equally as evident as intense features. Although amplitude information is destroyed in such a process, the results are extremely useful for structural interpretations. The greyscale image, illuminated from the north, of the vertical gradient of the total magnetic intensity reduced to the pole (Fig. 8) helped greatly in the structural interpretation of Highland Rocks.

Digital elevation model (DEM)

A digital elevation image with a precision of ±4 m was produced for the study area by subtracting the survey plane ground clearance, as recorded by a radar altimeter, from the GPS-measured absolute height of the plane. This image (Fig. 9) was useful for correlating topography with magnetic features, which assisted interpretation. In particular, the DEM allowed the identification of magnetic anomalies due to sand dunes.

Radiometric and Landsat images

A complete spectrum of 256 channels of radiometric data was recorded over Highlands Rocks and these data together with Landsat MSS data were studied by Maidment (1994), who concluded that they map the regolith, but reveal little information about subsurface geology, owing to the extensive Cainozoic cover and pervasive weathering.

Gravity data

Gravity data from the AGSO regional coverage of the Australian continent exists over the study area. Even though the readings of these data are on an 11 km grid, contours of the gravity values were extremely useful in establishing the main structural units of the area. Figure 3 shows simplified gravity contours for the area superimposed on the total magnetic intensity.

Digital geology

Geological outlines, as recorded on published geological maps, were digitised and added to the Arc/Info GIS so they could be overlaid on the geophysical map and image products on a workstation screen in a way that assisted lithological identification and correlation with mapped structures.

Depth determinations and modelling

The Euler automatic depth routine (Reid et al. 1988) processes grids of data and provides estimates of depth to magnetic sources. The method has been used in the Highland Rocks area to identify and estimate depth for lines of magnetic poles. The model specification tunes the method for narrow linear anomalies, which are characteristic of much of Highlands Rocks. The routine also maps lineaments, although it does not detect all the fine subtle detail obvious in illuminated images. Our experience with the Euler method is that while it gives a general idea of depth, it cannot be relied upon to give accurate estimates in all cases.

Detailed depth and dip determinations were made with the ModelVision modelling package, which has the ability to select profiles in any direction between any points on the ER Mapper grid. Two and three-dimensional models were calculated where needed to solve particular structural problems.

For most situations visual estimates could be made using

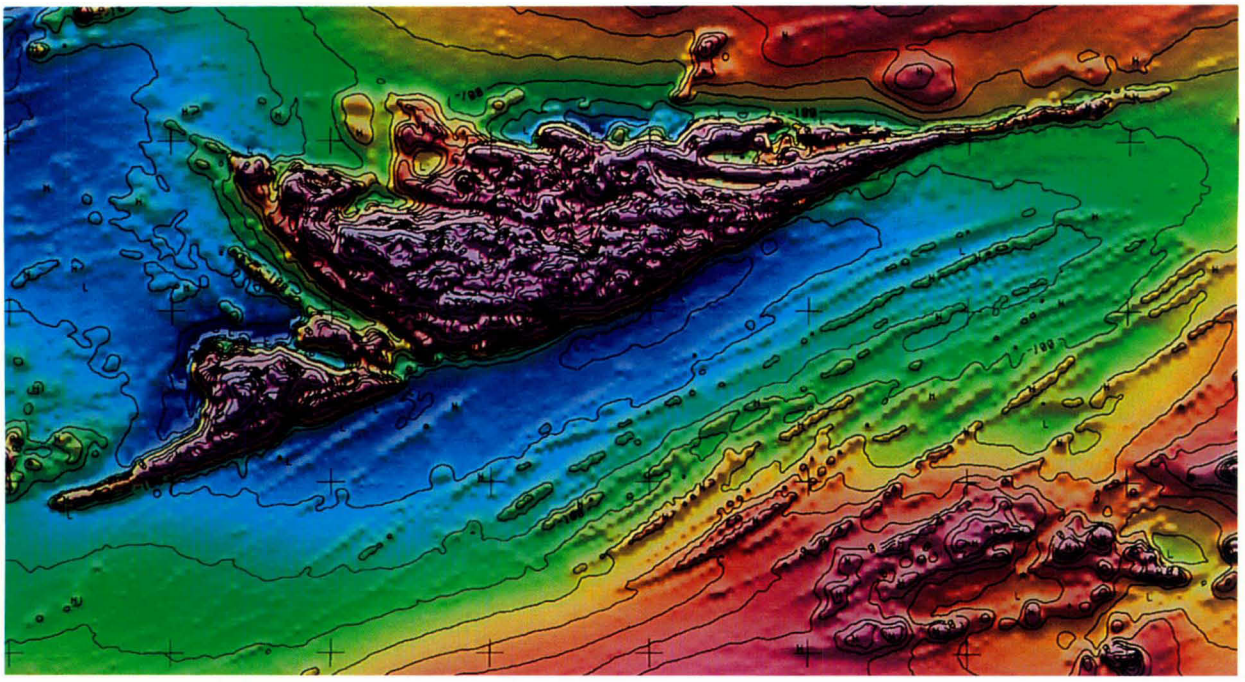

Figure 6. Detail of illuminated total magnetic intensity with superimposed contours.

contour map data to determine which magnetic sources were within a few hundred metres of the surface and which sources were 'deep'.

The Naudy automatic depth determination routine automatically determines depth to magnetic source, using profile data, and allows subsequent interactive modelling to verify depth estimates and calculate dips for the sources (Gunn 1997). This routine was not available for the Highland Rocks project,

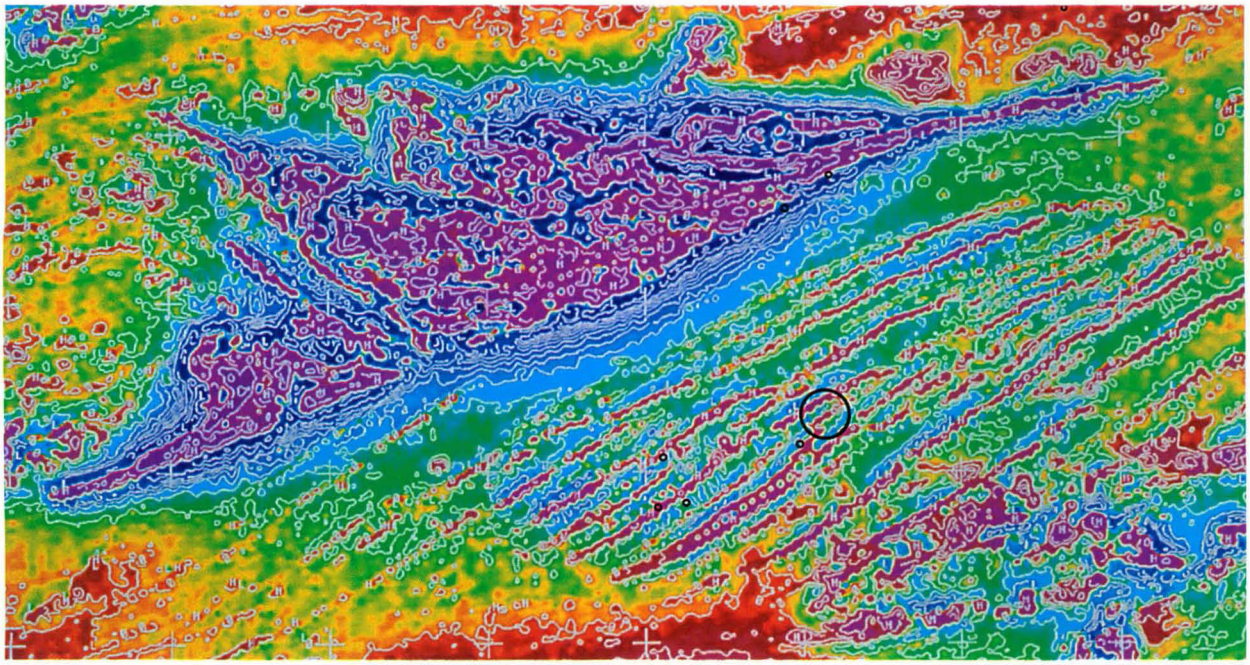

Figure 7. Detail of non-illuminated vertical gradient with superimposed contours.

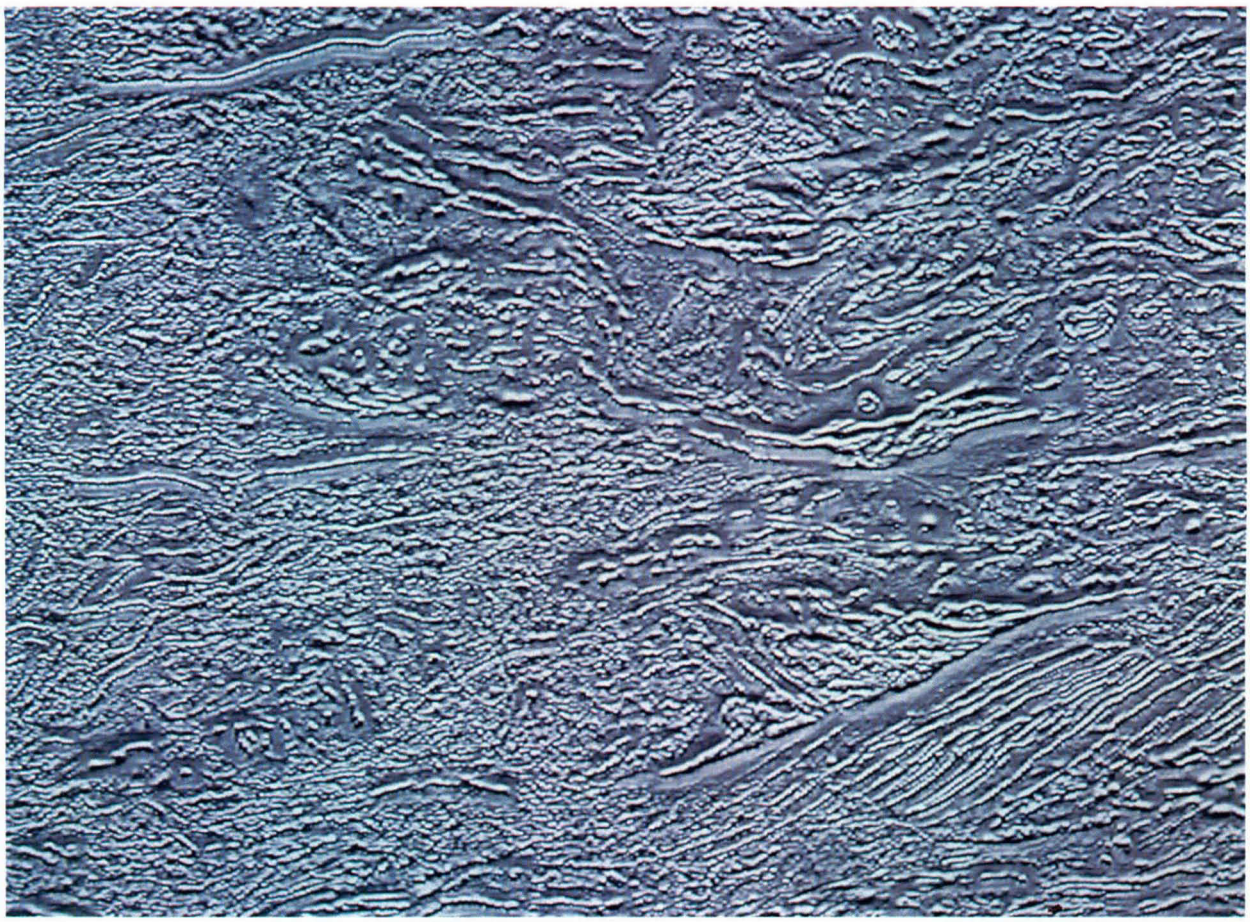

Figure 8. Greyscale automatic gain control of the vertical gradient of the total magnetic intensity reduced to the pole, illuminated from the north.

Figure 9. Digital elevation model of the study area.

but would have been ideal for detailed depth and dip determination.

Synthesis

The total field magnetic images of the area are dominated by several intense anomalies (Fig. 10), portions of which are at or close to the ground surface and other parts, according to their smooth contour gradients, several hundred metres below ground surface.

On the basis of correlation with limited outcrop information, these anomalies are identified as '*strongly magnetic metamorphics: outcropping or near surface*' and '*strongly magnetic metamorphics: buried*'. The boundaries of buried units are shown as dashed lines, as their positions are less definite. The irregular internal field of these units indicates faulting, folding or inhomogeneity. The internal detail is represented by lines denoting '*trend within magnetic unit*'. Although these strongly magnetic units are widely distributed across the study area, no basis exists for assuming that they are stratigraphically equivalent or that they are the same lithology, other than their similarity of magnetic character.

Anomalous zones may be further subdivided on the basis of magnetic intensity, and these are represented as '*moderately magnetic metamorphics: outcropping and near surface*' and '*moderately magnetic metamorphics: buried*'. The same comments apply to these units as apply to the strongly magnetic units. The remainder of the study area, with the exception of the extreme west and northwest, is occupied by '*weakly magnetic units*', which effectively have no background magnetic response.

Sub-circular features, whose forms suggest an intrusive origin, are described as '*moderately to strongly magnetic localised anomalies, possibly intrusive*'.

As well as these magnetic units, various linear magnetic features are obvious in the data. These are interpreted as:

- '*Prominent bedding trends*'—linear magnetic highs due to thin sheets of magnetic material. Possible sources include sheets of igneous material (lava flows and sills), magnetic sedimentary and metamorphic units and banded iron formations.
- '*Bedding trends*'—linear magnetic highs due to thin sheets of magnetic material causing anomalies of lesser amplitude than those causing the '*prominent bedding trends*'. The source of such anomalies could be weakly magnetic sedimentary or metamorphic units, or merely thinner occurrences of the types of features likely to cause the '*prominent bedding trends*'. A meandering palaeochannel has been mapped in this class in the northwest corner of the study area.
- '*Faults*'—interpreted on the basis of dislocations, offsets, terminations and alignments of magnetic units.
- '*Minor lineament*'—extremely weak magnetic lineaments which could be the expressions of jointing or faulting in weakly magnetic units.
- '*Weakly magnetic sediments Birrindudu Basin*'—deduced by drawing an envelope around the Proterozoic outcrops and the series of weak, frequently folded, linear magnetic units that appear related to the Birrindudu Basin.
- '*Weakly magnetic Palaeozoic sediments*'—deduced by drawing an envelope around the Palaeozoic outcrops and series of weak magnetic features, particularly evident in the colour vertical gradient image, that appear to be related to the Palaeozoic. These anomalies may be related to weathering of Palaeozoic rocks.

Many weak, narrow elongate magnetic anomalies correlate with sand dunes as mapped by the DEM. These features have not been recorded on the interpretation map.

The initial stage of the interpretation was the collation of all the above, obtained by inspection processes likely to

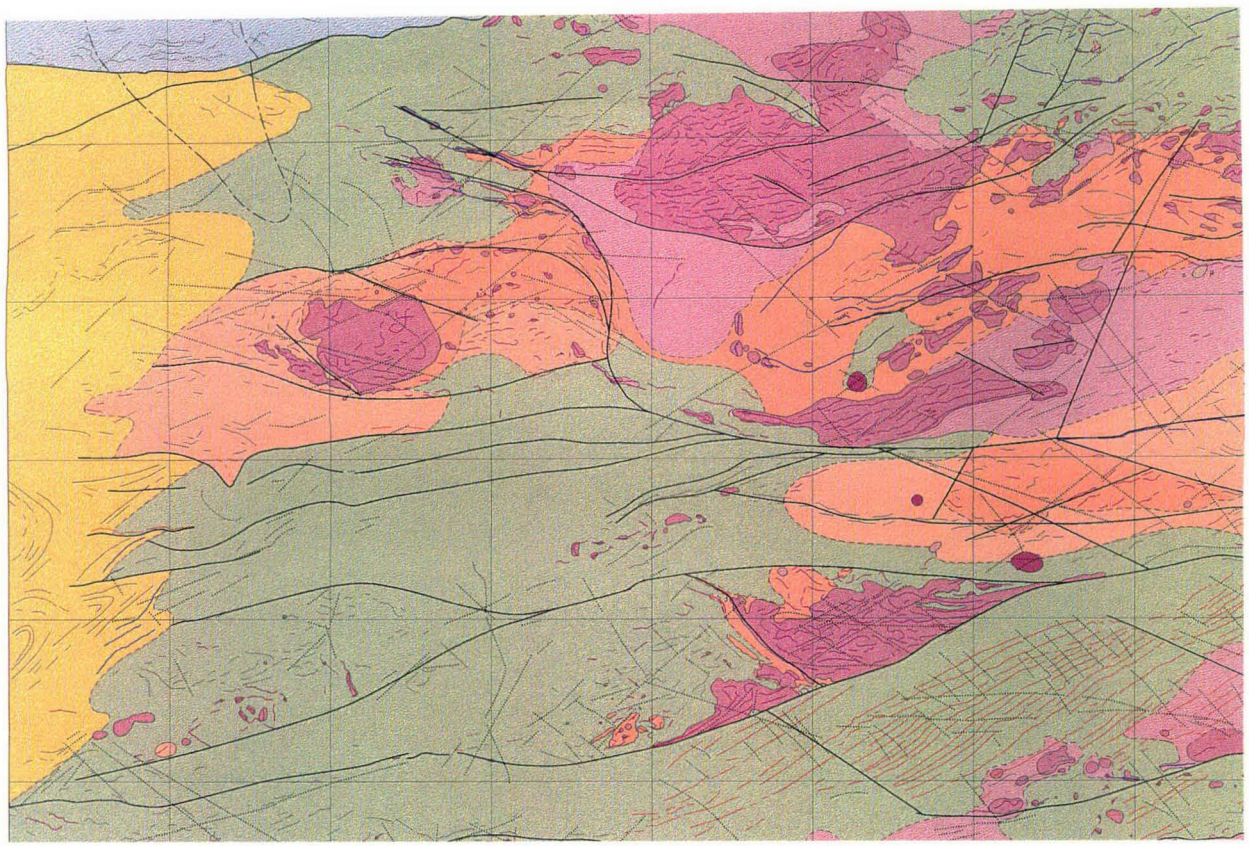

Figure 10. Interpretation map.

produce similar results with different interpreters, within Arc/Info. The second and final phase, which involved synthesising all available information to produce a geological interpretation, was more subjective and is more open to variation among different interpreters. A structural synthesis has interpreted the area as having undergone compression and overthrusting from the north. This concept is consistent with the general structural regime of the area. Its key is the identification of thrust faults which bound the thrust slices. The faults, many of which almost cross the sheet, are variously evident as sharp boundaries to units, linear anomalies from ironstones in the fault planes, weak narrow linear magnetic features, which may be due to accumulations of magnetic features in fault planes, or differences in magnetic properties of adjacent rock units. Computer modelling indicates that the thrusts have steep dips.

The gravity data, which are a key element in the thrust fault model, show a major east–west gravity high in the centre of the Highlands Rocks sheet. Culminations in this high correlate with the positions of intensely magnetic metamorphics. A steeper gradient on the southern side of this feature corresponds with a major zone of east–west faulting. The gravity high is interpreted as an imbricate thrust from the north which has emplaced dense, high-grade metamorphics against less dense, less magnetic metamorphics to the south. A gravity ridge in the southwest quadrant of the sheet, which correlates well with a zone of intense magnetic anomalies at its eastern end, but not at its western end, has been interpreted as a 'pop-up' slice of dense metamorphics, which is magnetic at one end and non-magnetic at its other end.

Conclusion

The interpretation methodology has produced a type of solid geology map which combines outlines of rock units that have been confidently identified by correlation with outcrop data and outlines of other units that have been geophysically mapped and which can, at this stage, only be described in general geophysical terms. This interpretation will provide a basis for further assessment of the area and as new information on local geology becomes available it will be possible to refine the interpretation by assigning specific lithologies to those units presently described in terms of their magnetic characteristics. For maximum use, such interpretation maps, when published at 1:250 000 scale, should show modelling locations, depth and dip determinations, and be accompanied by explanatory notes on the interpreted features.

References

Blake, D.H., 1978. The Proterozoic and Palaeozoic rocks of The Granites–Tanami region, Western Australia and the Northern Territory and interregional correlations. BMR Journal of Australian Geology & Geophysics, 3, 35–42.

Blake, D.H., Hodgson, I.M. & Muhling, P.C., 1979. Geology of The Granites–Tanami region. Bureau of Mineral Resources, Australia, Bulletin 197.

Brodie, R.C., 1994. The Granites area (The Granites(S), Highland Rocks, Mount Solitaire (S & E), Mount Theo) airborne geophysical survey 1993—operations report. Australian Geological Survey Organisation, Record 1994/23.

Clark, D.A., 1997. Magnetic petrophysics and magnetic petrology: aids to geologic interpretation of magnetic data. AGSO Journal of Australian Geology & Geophysics 17(2)—this issue.

Dickson, B.L. & Scott, K.M., 1997. Interpretation of aerial gamma-ray surveys—adding the geochemical factors. AGSO Journal of Australian Geology & Geophysics, 17(2)—this issue.

Gunn, P.J., 1997. Quantitative methods for interpreting aeromagnetic data: a subjective review. AGSO Journal of Australian Geology & Geophysics 17(2)—this issue.

Hodgson, I.M., 1974a. Geology of the Highland Rocks 1:250 000 Sheet area, Northern Territory. Bureau of Mineral Resources, Australia, Record 1974/120.

Hodgson, I.M., 1974b. Highland Rocks, Northern Territory, 1:250 000 Geological Series. Bureau of Mineral Resources, Australia, Explanatory Notes.

Isles, D.J., Harman, P.G. & Cunnen, J.P., 1989. The contribution of high resolution aeromagnetics to Archean gold exploration in the Kalgoorlie region, Western Australia. Economic Geology, Monograph 6, 389–397.

Maidment D.W., 1994. Preliminary regolith mapping of the Highland Rocks region using Landsat MSS and high resolution gamma-ray spectrometric imagery. Australian Geological Survey Organisation, Record 1994/38.

MacLeod, I.N., Jones, K. & Ting Fan Dai, 1993. 3-D analytic signal in the interpretation of total magnetic field data at low magnetic latitudes. Exploration Geophysics, 24, 679–688.

Milligan, P.R. & Gunn, P.J., 1997. Enhancements and presentation of airborne geophysical data. AGSO Journal of Australian Geology & Geophysics, 17(2)—this issue.

Page, R.W., Blake, D.H. & Mahon, M.W., 1976. Geochronology and related aspects of acid volcanics, associated granites, and other Proterozoic rocks in the Granites-Tanami region northwest Australia. BMR Journal of Australian Geology & Geophysics, 1, 1–13.

Reford, M.S., 1964. Magnetic anomalies over thin sheets. Geophysics, 29, 532–536.

Reid, A.B., Allsop, J.M., Granser, H., Millett, A.J. & Somerton I.W., 1990. Magnetic interpretation in three dimensions using Euler deconvolution. Geophysics, 55, 80–91.

Vacquier, V., Steenland, N.C., Henderson, R.G. & Zietz, I., 1951. Interpretation of aeromagnetic maps. Geological Society of America, Memoir 47.

Whiting, T.H., 1986. Aeromagnetics as an aid to geological mapping - a case history from the Arunta Inlier, Northern Territory. Australian Journal of Earth Sciences, 33, 271–286.

Whiting, T.H., 1988. Magnetic mineral petrogenesis, rock magnetism and aeromagnetic response in the Eastern Arunta Inlier. Northern Territory. Exploration Geophysics, 19. 377–383.

AGSO Journal of Australian Geology & Geophysics, 17(2), 187–200

Interpretation of aerial gamma-ray surveys—adding the geochemical factors

B.L. Dickson[1] & K.M. Scott[1]

Aerial gamma-ray surveying reflects the geochemical variations of potassium, uranium and thorium in the upper 30 cm of the Earth's surface. This thin layer is subject to the effects of weathering, which leads to loss of K in all rock types and, for felsic rocks, loss of U and Th as well. The extent of the loss depends on many factors, but is typically 20–30 per cent for all three radioelements. Intermediate and basic rocks show little change in radioelement concentrations during initial weathering, but pedogenesis can result in soils with 2–3 times the U and Th content of the parent rock. However, wide ranges in radioelement compositions occur for a given rock type and its weathered products. Mineralising processes can also affect radioelement contents. For example, K is increased in altered rocks at the Copper Hill and Goonumbla porphyry Cu deposits in central NSW. Thorium concentration shows both depletion and enrichment during hydrothermal alteration, as illustrated by the Au prospects at Bimurra, in northeast Queensland. Uranium is even more erratically affected by alteration and is generally not a useful indicator of alteration. Regolith processes can affect these alteration signatures. Highly weathered deposits may lose their K, particularly if hosted by K-feldspar, as at Goonumbla. Transported soils may disguise or change rock signatures often in unexpected ways—the Mt Leyshon Au deposit, in northeast Queensland, is seen in the aerial survey as a K-rich area because its signature is not contaminated by material weathered from late-Silurian dolerites. Detailed interpretation of aerial gamma-ray surveys for exploration purposes requires the delineation of the major geological units of the survey area, then examination of the subtle variations within the most prospective units, aided by other data sets (magnetics, Landsat TM) and field checking of the anomalous areas identified.

Introduction

While aerial gamma-ray surveys involve the physical measurement of gamma radiation, this is, in fact, a measure of the geochemical variation of potassium (K), uranium (U) and thorium (Th) in the upper 30 cm of the Earth's surface. Major variation in the three radioelements in the soil and exposed rock in this layer often allows broad lithological changes to be readily mapped, but minor variation in the gamma-ray response within units may be due to slight lithological changes, weathering and other regolith effects, or to mineralising events. A detailed interpretation of aerial gamma-ray data must take all these processes into account, particularly if the goal is to recognise the subtle radiometric signatures associated with mineralisation.

In this review the geochemistry of K, U & Th, their distribution in major rock types and the effect of weathering and pedogenesis are examined, along with the changes in radioelement distribution brought about by mineralising processes in a range of mineral deposits. Most of the work was completed under an AMIRA-sponsored project, P263 'Improving the interpretation of airborne gamma-ray surveys', conducted during 1988–1992, to investigate improved interpretation of aerial gamma-ray surveys, and has not been published previously. Areas and prospects discussed are indicated in Figure 1. More recent studies aimed at applying this knowledge and developing a methodology for detailed interpretation of aerial gamma-ray surveys are also briefly discussed.

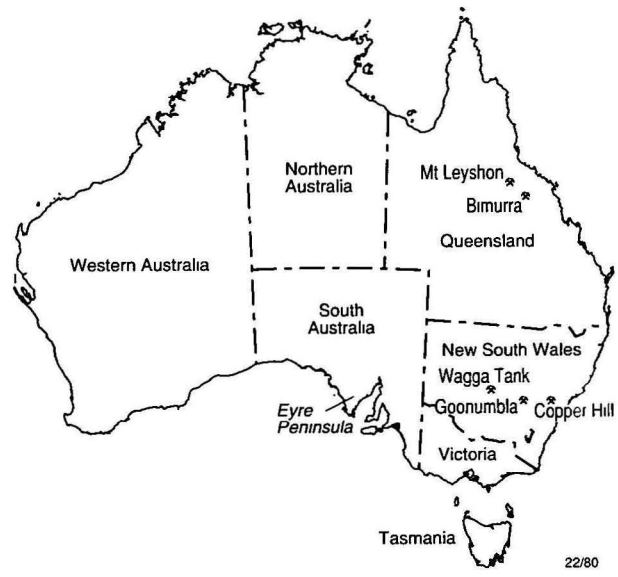

Figure 1. Location of deposits and other places discussed in this review.

Geochemistry of the radioelements (K, U & Th)

Potassium

Potassium is a major component of the Earth's crust (2.35%). It is an alkali element and shows a simple chemistry. The major hosts of K in rocks are potassic feldspars (principally orthoclase and microcline with ~13% K) and micas (biotite and muscovite with typically 8% K). Potassium is absent from mafic minerals. Consequently K is relatively high in felsic rocks (granites, etc), but low in mafic basalts and very low in dunites and peridotites (Fertl 1983). The weathering behaviour of the K-bearing minerals determines the radioelement contents of weathered rocks and soils. During weathering, the major K hosts will be destroyed in the order biotite–K-feldspar–muscovite. Potassium released during weathering can be taken up in the formation of K-bearing minerals such as illite or adsorbed in minor amounts into other clays, e.g. montmorillonite, under suitable conditions. The efficient uptake of K by clays is reflected in the low concentration of K in sea water (380 ppm).

Potassium is detected in a gamma-ray survey by measurement of the 1.46 MeV gamma-ray emitted by the decay of ^{40}K. This isotope constitutes 0.02 per cent of natural K and is, therefore, a direct measurement of the K content in the ground.

Uranium

Uranium is a minor component of the Earth's crust (~3 ppm). Its chemistry is dominated by two valence states U^{4+} and U^{6+}. The more reduced form, U^{4+}, is generally contained in insoluble minerals. Conversely, the oxidised form, U^{6+}, complexes with anions such as CO_3^{2-}, SO_4^{2-} and PO_4^{3-} to form many soluble species (Langmuir 1978). The mobility of U^{6+} is modified by adsorption to hydrous iron oxides, clay minerals and colloids and by reduction to insoluble U^{4+} minerals when waters encounter reducing environments (i.e. zones of carbonaceous material or pyrite).

Uranium may be present in rocks as the oxide and silicate minerals, uraninite and uranothorite; in major U-bearing minerals such as monazite, xenotime and zircon; as trace

[1] CSIRO Division of Exploration and Mining, PO Box 136, North Ryde, NSW 2113

amounts in other rock-forming minerals; or along grain boundaries, possibly as U oxides or silicates. Of the major U-bearing minerals, only zircon and monazite are stable during weathering. Uranium freed by the breakdown of minerals during weathering may be retained in authigenic iron oxides and clay minerals or precipitated under reducing conditions, forming uranium deposits in favourable circumstances.

Uranium is the parent of a decay series which ends in stable ^{206}Pb. If a decay series with a long-lived parent is left undisturbed for a period greater than 8 times the half-life of the longest lived daughter isotope, then each member of the decay series will be decaying at the same rate. For the U decay series this requires > 1.5 m.y. and at this time the series is said to be in radioactive equilibrium. Uranium itself does not emit gamma-rays during its decay and the most energetic gamma-rays emitted by its daughter isotopes come from ^{214}Bi which occurs late in the decay series. Thus, long periods are required for these gamma-rays to accurately indicate the U content of the ground. Between ^{238}U and ^{214}Bi, long-lived isotopes ^{230}Th ($t_{½}$=75 000 y.), ^{226}Ra ($t_{½}$=1600 y.) and ^{222}Rn ($t_{½}$=3.8 d.) all have different chemical and physical properties from uranium. The geochemistry of Th and Ra are discussed below. Radon (^{222}Rn) is an inert gas and may escape from rocks and soils after formation by decay of ^{226}Ra. Differential movement of U and its daughters may lead to separation of U and its gamma-emitting daughter ^{214}Bi, in which case the series is in a state of disequilibrium and U can no longer accurately determined by gamma-ray methods.

Thorium

Thorium is a minor component of the Earth's crust (~12 ppm), occurring only in valence state Th^{4+}. The solubility of Th complexes is generally low except in acid solutions (Langmuir & Herman 1980). However, organic compounds (e.g. humic acids) may enhance Th solubility in neutral pH conditions (Chopin 1988).

Thorium may be present in allanite, monazite, xenotime and zircon at levels >1000 ppm or as trace amounts in other rock-forming minerals. Major Th-bearing minerals (monazite and zircon) are stable during weathering and may accumulate in heavy mineral sand deposits. Thorium freed by the breakdown of minerals during weathering may be retained in Fe or Ti oxides–hydroxides and with clays. As with U, Th may also be transported adsorbed on colloidal clays and iron oxides.

Like U, Th does not emit gamma-rays during its decay, but is also the parent of a decay series which ends in stable ^{208}Pb. The most energetic gamma-rays emitted by daughter isotopes come from ^{208}Tl. Between ^{238}U and ^{208}Tl, major isotopes are ^{228}Ra ($t_{½}$=5.75 y.), ^{228}Th ($t_{½}$=1.91 y.) and ^{220}Rn ($t_{½}$=56 s). The short half-lives of the daughter isotopes in the Th decay series result in only ~40 years being required to establish equilibrium in the Th series and, generally, gamma activity is a good measure of Th content.

Radium

The geochemistry of Ra must also be considered, as Ra isotopes are long-lived members of both the U and Th decay series and Ra mobility can be a source of disequilibrium in both series. Radium is an alkali-earth metal and shows chemical behaviour similar to that of Ba. Radium can be mobilised in most groundwaters, particularly in those with very high salinity (Dickson 1990). Its mobility is restricted by co-precipitation with barium sulphates, Fe–Mn oxides or sulphates, or through adsorption by organic matter. Radium deposits around the margins of salt-lakes and near sandstone escarpments in swamps are a common form of disequilibrium in Australia. These rarely contain more than background amounts of U, but can have both ^{226}Ra and ^{228}Ra (Dickson et al. 1987).

Distribution of radioelements in rocks

The application of aerial gamma-ray surveying relies on the variable radioelement content of rocks. This section summarises the contents of many Australian rocks (Table 1). The data are based on laboratory gamma-ray measurements of rock and soil samples, using procedures described in Scott & Dickson (1990a). The laboratory gamma-ray method directly measures potassium (K), but derives the U and Th data from measurements of the radioactive daughters ^{226}Ra and ^{228}Ra, respectively, by sealing the sample and allowing time for ^{226}Ra–^{222}Rn equilibrium to be established. Unpublished results (Dickson) have confirmed that radiometric equilibrium between parent U and ^{226}Ra and between Th and ^{228}Ra does not occur to any large extent in unweathered rocks.

An examination of the average radioelement content for igneous rocks shows that there is a trend for increasing radioelement content with increasing Si content, i.e. felsic rocks have a higher radioelement content than ultrabasic and mafic rocks (Fig. 2). Thus, despite four orders of magnitude difference in concentration between K and U–Th, the elements show a sympathetic increase with increasing Si in the rocks. Generally, Th shows a much larger increase than U and ratios such as Th/U can be used to investigate the degree of differentiation within igneous suites. Rocks formed in the last stages of igneous emplacement (e.g. pegmatites and aplites), when temperatures were falling, no longer show this sympathetic behaviour, retaining high K values, but reduced U and Th content. These late-stage rocks occupy only small areas and are not often recognised in aerial surveys.

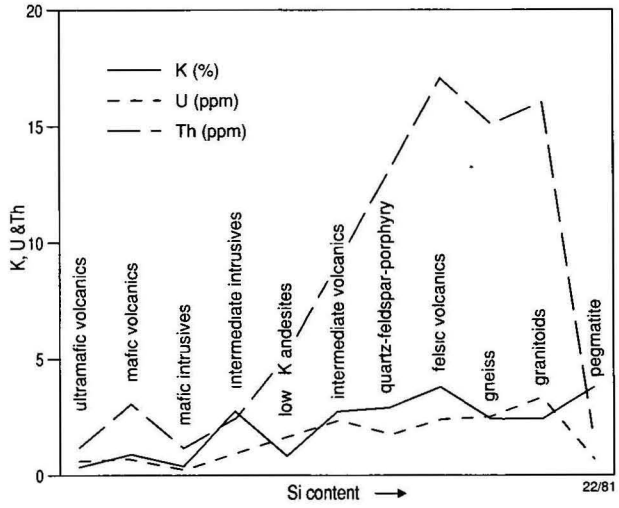

Figure 2. Variation in average K, U & Th content for igneous rocks with increasing acidity (Si content).

However, within any given rock type, there is a wide range of values (Table 1). These ranges were derived from average values for many individual units and are not raw data, which would give an even bigger spread. Because of the wide spread within each rock class, no global classification of rock type by radioelement content is possible. For example, a rock with an above-average radioelement content of 2.5% K, 3 ppm U and 15 ppm Th could be granite, felsic intrusive/extrusive, intermediate extrusive or shale. A rock with a low radioelement content (i.e. <1% K, <1 ppm U, <5 ppm Th) could be anything except felsic intrusive or shale. Nevertheless, within small regions, different rock types can often be identified on the basis of the relative concentration of radioelements.

Available data for metamorphic rocks (e.g. gneissic rocks derived from granite and amphibolites derived from dolerite) suggest that metamorphism does not affect radioelement content

Table 1. Radioelement content of Australian rocks and soils. Average value in brackets.

Rock type	*Rock*			*Soil*		
	K %	*U* ppm	*Th* ppm	*K* %	*U* ppm	*Th* ppm
Intrusives						
granitoids	0.3–4.5 (2.4)	0.4–7.8 (3.3)	2.3–45 (16)	0.4–3.9 (2.1)	0.5–7.8 (2.7)	2–37 (13)
gneissic rock	2.4–3.8 (2.4)	2.1–3.6 (2.5)	18–55 (15)	0.7–1.9 (1.3)	1.6–3.8 (2.2)	6–19 (12)
pegmatite	2.6–5.5 (3.7)	0.3–1 (0.7)	0.3–9.6 (2)			
aplites	0.6–4 (2.4)	1–8 (3.3)	3–20 (7)			
quartz–feldspar porphyry	1–5 (2.9)	1.3–2.9 (1.7)	6–14 (13)			
intermediate intrusives	0.7–5.6 (2.7)	0.1–1.2 (0.8)	0.8–6.1 (2.4)	0.7–3.4 (1.6)	1.5–2.3 (1.9)	2.9–8.4 (5.6)
mafic intrusives	0.1–0.8 (0.4)	0.0–1.1 (0.3)	0.0–3.1 (1.2)			
Extrusives						
felsic volcanics	2.0–4.4 (3.7)	1.4–13 (2.4)	13–28 (17)	1.8–3.2 (2.4)	1 3–2.4 (2.1)	10–18 (13)
intermediate volcanics	1.8–4.1 (2.7)	0.9–5 6 (2.3)	1.5–15. (9)	1.0–2.7 (1.9)	1.2–3.6 (2.1)	4–17 (10)
low-K andesites	0.7–0 9 (0.8)	1.0–2.5 (1.6)	3–8 (5)	0.8–1.5 (1.1)	1.2–1.5 (1.3)	4–6 (5)
mafic volcanics	0.3–1 3 (0 9)	0.3–1.3 (0.7)	2.0–5.0 (3.0)	0 2–1 4 (0 7)	0.6–2.5 (1.6)	3.3–13 (7.9)
ultramafic volcanics	0.2–0 9 (0.4)	0.3–0.9 (0.6)	0.0–4.0 (1 2)	0 6	2.0	6.
Sedimentary rocks						
Archaean shales	0.4–1.6 (0.9)	0.3–1.3 (0.9)	1–5 (2.7)	0.8	1.2	3
other shales	0.1–4.0 (2.6)	1.6–3.8 (2.6)	10–55 (19)	0.7–3.0 (1.5)	1.2–5 (2.3)	6–19 (13)
arenites	0 0–5.5 (1.8)	0.7–5.1 (2.3)	4–22 (12)	0.1–2.4 (1.3)	1.2–4.4 (2.1)	7–18 (11)
carbonates	0.0–0.5 (0.2)	0.4–2.9 (1.6)	0–2.9 (1.4)			

Sedimentary rocks generally have radioelement content reflecting the parent source rocks. Thus, immature sediments derived from granitic sources may be expected to have quite high radioelement content, but more mature sediments, composed primarily of quartz, should have very low values. However, experience shows that sandstone often has more phyllic interbands present and, hence, somewhat higher radioelement content than might be expected. This is reflected in the wide range of values given in Table 1.

Archaean shale from the Yilgarn area of Western Australia appears to have very much lower radioelement content than younger shale. Archaean shale contains an average 0 9% K, 0.9 ppm U and 2.7 ppm Th, whereas younger shale has 2.6% K, 2.6 ppm U and 19 ppm Th (Table 1). The common shale values quoted by Fertl (1983) are 2.7% K, 3.7 ppm U and 12 ppm Th, close to the values for Australian young shales and further suggesting that Archaean shale is quite distinct radiometrically.

Distribution of radioelements in soils

Although tables of radioelement content in common rock types are often quoted (e.g. Killeen 1979; Fertl 1983), data on soils derived from those rocks is very rare. When specific rock types (such as pegmatites, aplites, quartz-feldspar-porphyries and mafic intrusives) occur as narrow intrusions or in small areas, or are subject to faster weathering and erosion than the host country rock, it is difficult to find in-situ soils. Soils over such units may also be seriously contaminated by introduced material.

Because soil covers most of the Earth's surface, the relationship between the radioelements in surficial cover and underlying rock is of prime importance in using aerial gamma-ray surveys for geological mapping. This section reviews the effect of weathering on rocks and the radioelement content of many Australian soils.

As with rock samples, these results are based on laboratory gamma-ray measurements. With soils, there is potential for radiometric disequilibrium between parent U and ^{226}Ra to occur, given the disparity of the geochemistry between the two radioelements and intervening, long-lived isotope ^{230}Th. A study of U–^{226}Ra disequilibrium in Australian soils (Dickson 1995) found a wide spread in disequilibrium in Australian soils, although more were U-rich than ^{226}Ra-rich.

In addition to U–^{226}Ra disequilibrium, Rn loss could contribute significantly to lowering of the U signal measured during aerial surveys. The amount of Rn lost from soil depends on soil particle size, moisture content and the amount of handling of the sample. In-situ loss depends also on weather conditions (Schery et al. 1984). Laboratory measurement of Rn loss indicates typically around 20 per cent, but with a wide range up to 80 per cent (Greeman et al. 1990; Dickson unpublished results). Measurements of in-situ Rn loss by measurement of ^{226}Ra and ^{210}Pb (a daughter of ^{222}Rn) suggest losses greater than 25 per cent may occur in the top 50 cm of soil profiles (Graustein & Turekian 1990). In this summary, ^{226}Ra laboratory results are reported as U, but it must be borne in mind that aerial measurements are affected by disequilibrium in the U decay series.

Soils in situ over parent rocks

Granite shows a wide range of weathering behaviour, depending on its mineralogy and the weathering regime, climate, etc. Soils derived from granitoids generally lose around 20 per cent of their radioelement content during pedogenesis (Table 1). However, these results disguise far greater losses due to volume changes that accompany weathering. (Concentration, measured in weight units, does not always properly reflect the substantial losses that occur.) For example, for a soil profile over adamellite, density measurements indicate actual losses of 60 per cent of both K and Th with development of saprolite at a depth of

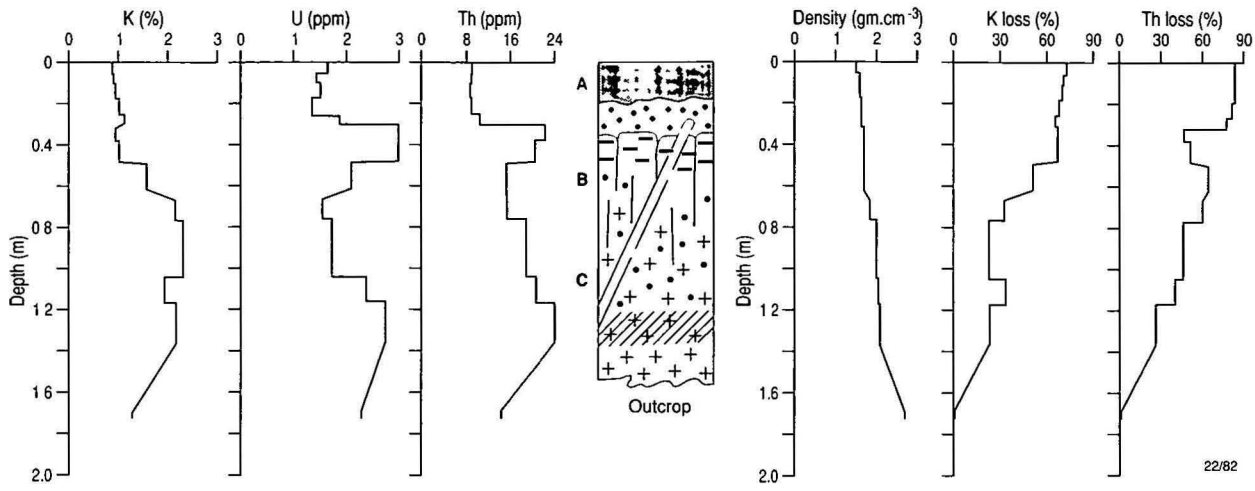

Figure 3. Distribution of K, U & Th in a soil profile over adamellite, Sutton, New South Wales, illustrating the effects of clay eluviation in the upper section of the profile.

0.5 m (Fig. 3). Unfortunately, density measurements are not generally available for weathering profiles.

The loss of K from granite is generally controlled by alteration of K-feldspar. Thus K content can increase during the early stages of weathering as a result of the removal of more easily weathered minerals (e.g. plagioclase, mafic minerals). Large K-feldspar phenocrysts are relatively resistant to weathering and can be present within residual soils, resulting in K enrichment. On the other hand, under lateritic weathering conditions, granitoid may be kaolinised, resulting in substantial loss of K, but apparent retention of 60–80 per cent of the U and Th.

The amount of U that can be mobilised from granitoid is determined by its host minerals. In many granites these are accessory minerals (zircon, sphene and monazite), which can contain up to 85 per cent of the total U. Only a minor part of the U in granite is in major rock-forming minerals, but a significant amount can be distributed along grain boundaries and microfractures. Mobilisation of U from or within granite appears to occur early in the weathering cycle. Its behaviour can be quite variable compared to K and Th, which behave more uniformly.

Studies on the weathering of ***intermediate intrusives*** found that there was no major change in radioelement content until pedogenesis, but there is generally an abrupt change in radioelement content at the saprolite–soil interface. This is illustrated for soil over diorite in central New South Wales (Fig. 4). This diorite is poorly distinguished from neighbouring basaltic rocks, which also increased in Th during pedogenesis. Samples were collected from the top of a hill, and the presence

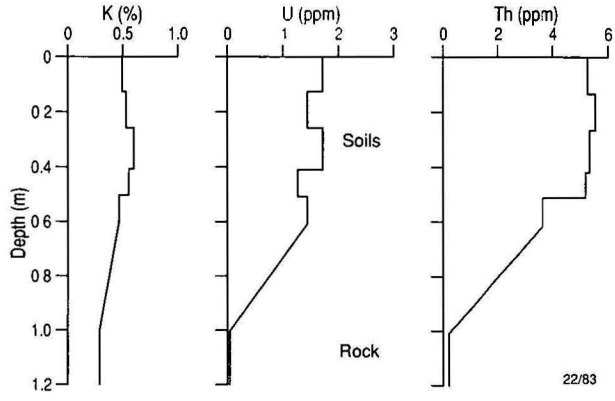

Figure 4. Distribution of K, U and Th in a soil profile over diorite, Blayney district, New South Wales.

of amphibole and epidote, minerals with low resistance to weathering, indicates that the soil is in situ. Increases in U and Th on passing from rock into soil are a feature of weathering of such rocks (Fig. 4), although the average values (Table 1) indicate increases by a factor of 2 are more common. These changes reflect loss of K-feldspar and retention of U and Th in either iron oxides and clays or in resistate minerals. Identification of intermediate intrusives in aerial gamma-ray surveys depends on the degree of K retention in soils, the effect of transported soils, and the radioelement content of adjacent units.

Dolerite tends to form dykes that weather readily, so that soils are often contaminated by transported material from adjacent, radioelement-rich rocks. However, studies of weathering rims on dolerite core-stones showed no change in radioelement content with weathering from fresh rock to saprolite. Thus, a complete profile would be expected to show a sharp change at the saprolite–soil interface, as observed with intermediate intrusives above.

Weathering of ***felsic volcanics*** generally produces soil showing loss of all three radioelements. Table 1 indicates that, as with granitoid, losses of 20–30 per cent are generally found. Soils over ***intermediate volcanics*** (including low-K andesites) had reduced K, but similar U and Th contents to their parent rocks.

Studies on the radioelement content of soils over ***mafic volcanics*** showed some remarkable changes. Weathering of Ordovician, Tertiary and recent basalts in eastern Australia was found to produce soils with major losses of K (up to 50%), but gains in U and Th (Table 1). Thus, these soils recorded average U and Th closer to those of soils derived from felsic rocks. These changes reflect loss of K from volcanic glass as it weathers and incorporation and concentration of U and Th into iron oxides during pedogenesis. A summary of results from studies of basalt weathering in southwest Victoria illustrates the changes (Fig. 5). The large increase in U and Th with weathering of mafic rocks has considerable effect on aerial gamma-ray surveying. Basalt flows in areas with little soil development can show clearly against radioelement-rich felsic rocks, but in an area of intensive weathering, the depletion of K and the concentration of U and Th can result in soils with radioelement signatures similar to that of weathered granite. In an area of basalt of various ages, different flows can be distinguished by the way their K and Th changes with weathering.

Soils over ***Archaean shale*** contain on average 0.8% K, 1.2 ppm U and 3 ppm Th, very close to the composition of unweathered shale (Table 1), indicating that pedogenesis does

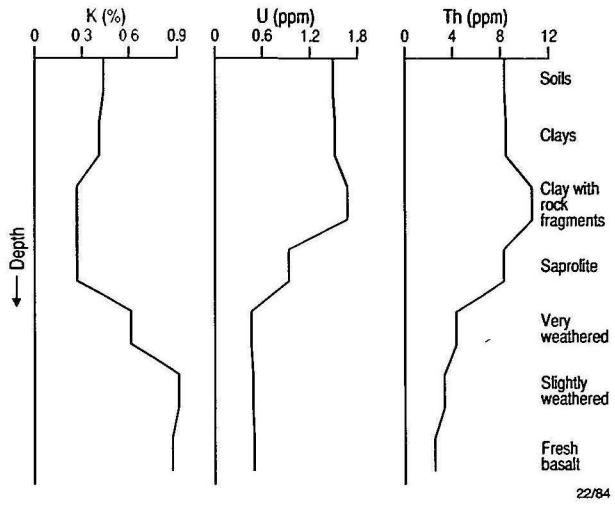

Figure 5. Variations in K, U & Th concentration during weathering of basalt.

not affect the radioelement composition. Soil over other ***shales*** contains 1.5% K, 2.3 ppm U and 13 ppm Th, suggesting that pedogenesis resulted in a large K loss, but retention of ~70% of the U and Th compared to the parent rock. In particular, lateritic weathering can result in almost complete K loss without affecting the other two radioelements, e.g. the radioelement content of a schist changed from 2.8% K, 2.8 ppm U, 18 ppm Th in fresh rock to 0.1% K, 2.4 ppm U, 16 ppm Th in lateritised rock. On the other hand, silicification can preserve shale units near the surface in weathering regimes, resulting in K and Th-rich areas that correspond to topographic highs. The retention of U and Th, but loss of K, can result in distinct aerial gamma-ray surveying signatures for argillic units.

Average radioelement content for soils over ***arenite*** is 1.3% K, 2.1 ppm U and 11 ppm Th, similar to that of the parent rocks (Table 1). Soils over radioelement-poor arenite, as over other radioelement-poor rocks, can show the effects of contamination by transported material. This results in higher radioelements values relative to underlying rock, although the effects of shaly interbands also need to be considered

Although no carbonate-derived soils have been analysed, these would be expected to be low in radioelements like their parent material.

Soils affected by other than in-situ weathering

Processes other than in-situ weathering can affect the radioelement content of soils. They include clay eluviation, colluvial and aeolian transport, and soil movement. All can affect the concentration of radioelements in the thin 30 cm layer measured during aerial surveying. This section examines these processes and considers how they may influence the interpretation of aerial surveys.

Sieve tests on soils have shown that U and Th are closely associated with the finest fractions of soils (Megumi & Mamuro 1977; Dickson & Scott 1991a). Consequently, clay and Fe-oxide translocation (eluviation) within the upper sections of a soil profile will result in redistribution of U and Th within the profile. An example of this is given in Figure 3, which shows a build up of U and Th in the top of the B horizon due to movement of clay material from the upper A horizon of the profile into fractures in the top of the B horizon.

Dust mantles and dune fields produced by aeolian processes are widespread in Australia. Introduced material, which may be derived from both local and distant sources, can enrich the radioelements in a soil, add a radioelement-poor dilutant or leave the radioelement content of the in-situ soil unchanged. Soils with a large aeolian fraction have been identified in central and southwestern New South Wales, large areas of South Australia—including much of the Eyre Peninsula, parts of southwestern Victoria and sections of the Yilgarn of Western Australia. This material can seriously affect the gamma-ray signature of an area by blanketing the underlying rock. The most recent major distribution of dust within Australia occurred during the arid period around 25 000 to 13 000 years BP (Bowler 1976). This was a major period of dune building in many areas around Australia.

An example of aeolian material enriching the radioelement content of a soil exists in central New South Wales. Aeolian material (known as parna) contains from 0.8–1.2% K (average 1%), 1.6–2.2 ppm U (av. 2 ppm) and 7.3–13 ppm Th (av. 10 ppm). Such material can effectively disguise local rocks, which have low U and Th of <1 and 3 ppm, respectively. The presence of such a soil may be indicated by uniform radiometric signatures over an extended area and/or a lack of correlation between the radioelement content of soil and adjacent outcrop or rock fragments contained in the soil.

Windblown sand dunes occur in southwestern Victoria and mask underlying volcanics. Quartz is commonly found in soils over basalt to the east of these dunes, although quartz is not a component of basalt. This probably reflects introduced material rather than authigenic quartz. The effect of such material depends on the amount introduced. Pure quartz dilutes, but does not affect the relative proportions of the radioelements. Quartz is also found in soils over basalt in eastern New South Wales and probably has a similar aeolian origin.

While there is no a priori method that can determine what, if any, useful geological information can be derived from a survey in areas subject to aeolian influence, useful information for exploration can still be extracted. For example, subtle variations of radioelements in an area subject to aeolian material can indicate areas of near-surface rocks or in situ soils, which may be further sampled to evaluate the underlying geology. Aerial gamma-ray surveys may also be used to determine variation in soil types in areas where outcrop is rare, as in southwestern Victoria and the western section of the Eyre Peninsula. An aerial survey gives almost total ground coverage, allowing definition of soil boundaries far more accurately than can otherwise be obtained. For exploration purposes, such soil information can be used in better evaluating soil geochemistry results or tracing back the origin of indicator minerals.

Local soil movement can distort the location of geological boundaries, especially where there is steep topography. In regional surveys it is probably not a significant problem, but if accurate boundary location is required in detailed surveys at the prospect scale, the interpreter must consider that soil creep could be occurring wherever boundaries are adjacent to slopes. This problem is probably most acute when soils from radioelement-rich rocks are transported across areas of radioelement-poor rocks.

Regolith related materials (calcrete, laterite, ferricrete, pisoliths, gossans)

Other regolith processes that can affect surface concentration of radioelements are chemical processes such as precipitation of Fe, carbonate or Si and extreme acid leaching due to sulphide weathering. In Australia, widespread development of ferricrete and calcretes has occurred during extensive periods of weathering. Such materials have their own radiometric signatures (Table 2).

Calcrete generally has low radioelement content with an average 0.3% K, 1.2 ppm U and 3.2 ppm Th (Table 2). Areas of calcrete, unless thin, can mask the signature of underlying rocks. In addition, incipient calcrete (i.e. nodules) present in soils can lower the radiometric content of soils. However,

Table 2. Radioelement content of regolith material. Average value in brackets.

Material	*No of samples*	*K %*	*U ppm*	*Th ppm*
Calcrete	26	0.0–1.0 (0.3)	0.6–2.4 (1.2)	0.7–7 (3.2)
Ferricrete	32	0.1–0.6 (0.4)	1.7–4.3 (2.7)	9–130 (24)
Pisoliths	71	0.0–4.4 (0 6)	1.7–5.0 (3.0)	7–100 (43)
Gossan	19	0–1.1 (0.4)	1 4–19 (6)	0.2–50 (12)

variations in the radioelement content of calcrete can sometimes give indications of the radioelements in underlying rock. Calcrete over rocks with low radioelements (basalt, carbonates) should have low radioelements, whereas calcrete formed over rocks with higher radioelements (e.g. siltstones, schists, gneiss) may have slightly higher Th. This was confirmed in an area near Cleve on the Eyre Peninsula, South Australia, where large areas with surficial or near-surface calcretes show variations in radiometric signature. Calcrete in an area showing higher K and Th than surrounding Quaternary sands was found to be forming over previously unrecognised in-situ rock.

Calcrete with U > Th occurs in isolated occurrences and indicates enrichment of pedogenic carbonate by groundwater-transported U. The relevance of this to localisation of other mineralisation is unknown. Calcrete can concentrate U from groundwater by precipitation with V to produce carnotite, leading to U deposits such as those in the Yilgarn Block (Carlisle 1983).

Iron-rich surface material (***ferricrete***) typically contains 0.4% K, 2.7 ppm U and 24 ppm Th (Table 2). Relative to underlying rocks, ferricrete concentrates Th and, to a lesser extent, U, but K is generally severely depleted. The extent of mobilisation and concentration of Th in ferricrete is illustrated by a sample of ferruginous material (Al-goethite and Fe-gibbsite deposited on quartz), collected from the Royal National Park, 30 km south of Sydney, which contained 130 ppm Th, whereas adjacent sandstone contained around 10 ppm Th.

Iron-rich ***pisoliths*** also show Th enrichment. Average values for Australian pisoliths are 0.6% K, 3.0 ppm U, and 43 ppm Th (Table 2). As with ferricrete, pisoliths are usually low in K relative to adjacent rock and may concentrate Th and, less often, U.

Gossans are more variable in their radioelement content than other ferruginous materials. Typical values are 0.4% K, 6 ppm U and 12 ppm Th (Table 2). In particular, gossans over felsic and sedimentary rocks appear to have elevated U (>3 ppm), whereas those over mafic and ultramafic rocks have low U (<3 ppm). Gossan with elevated (19 ppm) U, Cu, Pb, Zn, but negligible Th was found adjacent to a base-metal prospect in the Cobar area. Uranium-rich gossans (with anomalous Cu, Pb, Zn, As) were also found at Wagga Tank, south of Cobar, NSW, in a brecciated/faulted zone.

Extensive areas of Th-rich ferricrete and pisoliths can affect aerial surveys, but gossans do not generally cover large areas and would not be expected to significantly influence a regional aerial survey. Fragments of ferruginous material can concentrate in drainage channels, leading to Th-rich responses and, effectively, mapping drainage during aerial gamma-ray surveys. This results in the signature of underlying rock being obscured.

Summary

Superimposed on the variation of radioelement content within a rock class are weathering and other regolith effects. Consequently, whilst individual geological units can be recognised from an aerial survey, geological identity requires other information. Potassium is generally lost from all rock types during pedogenesis. Felsic rocks also show losses of U and Th with weathering, whereas intermediate, mafic and ultramafic rocks produce soils with relatively increased concentration of U and Th, the amount increasing with the basicity of the rock.

The average K and Th (but not U) contents for a rock relate well to averages for soil derived from that rock type. However, a study of the range of radioelement concentration (Table 2) shows that the difference in soils over the different rock-types for which significant data were gathered is small. There is no readily predictable relationship between soil radioelement content and parent rock. However, on a local scale and depending on rock type, soils can be good indicators of the underlying rocks.

Effect of mineralisation processes on radioelement distribution

This section reviews the variation in radioelements resulting from processes leading to various styles of economic mineralisation. Although many publications have appeared in recent years describing 'signatures' over various mineral deposits (for example, Dentith et al. 1994), very little work has been published on detailed evaluation of signatures and, in particular, how signatures are modified by weathering processes. Accordingly, most examples are taken from previously unpublished studies of a number of Australian deposits where combinations of subsurface, mine and surface rock, and surface soils were analysed for their radioelement content and mineralogy (Dickson & Scott 1991a).

Uranium & thorium deposits

The most direct application of aerial gamma-ray surveying to mineral exploration is in the search for U and Th deposits. Its use for U exploration has been widely reviewed (see, for example IAEA 1979; Ward 1981; Killeen 1979). The search for Th deposits in mineral beach sands is a similar application (de Meijer et al. 1994). In these applications, aerial gamma-ray surveys are used to look for elevated concentrations of the element and methods such as element ratios (e.g. Th/U) can be useful in defining subtle expressions of such deposits.

Granophile deposits

Mineral deposits of Sn, W and Mo are often associated with highly differentiated, late-stage granites. Tin, W, Mo, U and Th have complex chemical behaviour in magma, but tend to become concentrated in residual magma. Enriched parts of plutons may be indicated by high U and/or high Th, the U/Th ratio reflecting differences in oxidation states during the late-stage processes. Tin and W can be released to form Sn and W minerals during late-stage alteration, provided they are not incorporated into other secondary minerals. The Sn and W occurrences may form within the source granitic body or in the adjacent country rocks, but U and Th remain in the source granite (Yeates et al. 1982).

Aerial gamma-ray surveying is readily applied to exploration for granophile deposits, as many granites are well exposed and their derived soils generally reflect the radioelement content of the parent rock. The method may not identify mineralisation, but can target potentially mineralised systems. Examples of the application of aerial gamma-ray surveying include a study in the Lachlan Fold Belt, New South Wales by Yeates et al. (1982). They readily distinguished Sn–W granitoids from other granitoids by their high U content (>4–5 ppm) and often high U/Th. Similarly, studies in the Meguna Zone, Nova Scotia (Ford & O'Reilly 1985) found that mineral deposits of Sn, W, Mo and Cu were associated spatially with 'specialised' areas of granitic rocks. These areas were characterised by elevated U (amongst others) and depleted Th. Consequently, the U/Th ratio was a useful indicator of

such areas of specialisation and useful for targeting areas by aerial gamma-ray surveying.

Porphyry Cu–Au mineralisation

Potassium is commonly added to host rocks by mineralising hydrothermal solutions. It may be hosted by K-feldspar or muscovite and potential outcropping or subcropping mineralisation can be recognised by increases in K counts during radiometric surveying. Furthermore, because the chemistry of all three radioelements is different, hydrothermal alteration processes could also be expected to change the ratios of one radioelement to another although a priori changes are difficult to predict.

Many studies have described the variation of elevated K associated with alteration in porphyry Cu deposits. For example, Moxham et al. (1965) found that the K increase during alteration in porphyry Cu deposits in the southwest USA was of the order of 1.5% K and this was accompanied by an erratic U increase, but no Th increase. This could reflect the greater mobility of U compared to Th during hydrothermal alteration processes. Because Th is generally unaffected by alteration processes, the K/Th ratio gives a better indication of alteration than simply K. Similar results were found by Davis & Guilbert (1973).

The results described above do not, however, consider the effects of weathering. To examine how this may affect the signature of porphyry Cu deposits in aerial gamma-ray surveys, studies were made over two deposits in central New South Wales—one well exposed (Copper Hill) and the other extensively weathered (Goonumbla). As these studies have not been published previously, they will be discussed in some detail.

Copper Hill, New South Wales. The Copper Hill Cu–Au prospect occurs 3 km north of Molong in central New South Wales. A late Ordovician igneous complex, comprising quartz diorite and two stages of dacite, has intruded Ordovician andesites and basalts (Chivas & Nutter 1975). The earliest phase of dacite intrusion is highly fractured and variably altered to sericitic to chloritic assemblages. The best Cu–Au mineralisation occurs in this dacite in the chloritic alteration zone adjacent to sericitic alteration (Scott 1978).

The radioelement distribution of the rocks and in situ soils of the Copper Hill prospect was investigated, using analyses of samples from drill-holes and soil and rock samples from a 1 km E–W traverse over the prospect (Dickson & Scott 1989a). The K distribution across Copper Hill is illustrated in Figure 6. Potassium in altered dacite was found to be elevated (2.4–3% K) relative to Ordovician andesites and basalts (~0.6%) and unaltered dacite (~1.6%). Weathering of rocks and pedogenesis lowered the K concentration, but did not affect K relativities at any level of the weathering profile, because K is exclusively present as muscovite and soils are in situ. Uranium showed a narrow range of values (1–2 ppm) in all rocks and soils, whereas Th varied from 1 to 4 ppm in rocks and soils. It was concluded, and confirmed by a subsequent survey (which is unavailable for publication), that the Copper Hill complex was readily distinguished by its elevated K content.

Goonumbla, New South Wales. Porphyry Cu–Au mineralisation occurs at Goonumbla, 25 km north of Parkes, central New South Wales, at a number of prospects within a 30 km wide Silurian caldera (Heithersay et al. 1990). Mineralisation is specifically related to a number of vertical finger-like bodies of quartz monzonite which have intruded trachytes and K-rich andesites. Alteration ranges from potassic (with stockworks of quartz) to quartz sericite (phyllic) to propylitic. Because the intrusives are so narrow, potassic and phyllic alteration affect both the intrusive and adjacent intruded rocks. The three nearby deposits, E22, E26 and E27 are currently being mined as parts of the Northparkes mine.

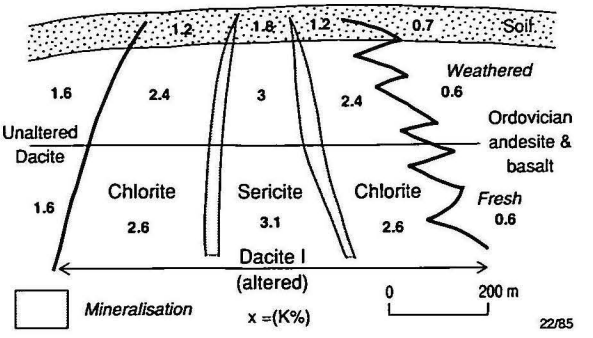

Figure 6. Summary of K concentration in rocks and soils of the Copper Hill complex (after Dickson & Scott 1991a).

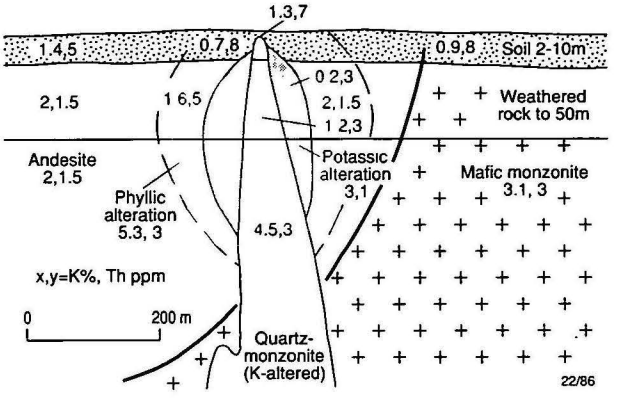

Figure 7. Summary of K and Th concentration in and around Northparkes mine, Goonumbla, New South Wales (after Dickson & Scott 1991a).

Rocks are weathered to depths of over 50 m and soils up to 10 m thick cover most of the area. Mineralised rocks do not crop out, but unaltered volcanics form low outcrops in the area. Since the onset of Miocene aridity, the Goonumbla area has been subject to continental aeolian and fluviatile deposition and some introduced components are generally present in soils.

Analyses of samples from drill holes and reconnaissance regional, outcrop and soil sampling shows that potassic-altered volcanics have K primarily hosted by orthoclase which is weathered out above 20 m, leading to a dramatic K decrease and U and Th increase (Scott & Dickson 1990a). Volcanics with phyllic alteration have high K (~5%), but, again, weathering rapidly decreases K (to ~1.6%), but doubles Th. Volcanics peripheral to mineralisation show less effects due to weathering.

The surface soil over the K-altered volcanics is at least partially introduced and has slightly higher K, U and Th than the underlying weathered rock. Soils over volcanics peripheral to mineralisation were found to be essentially derived in situ from the shallow underlying rock and showed a decrease in K and increase in U and Th relative to their parental rock.

A summary of the K and Th content of the rocks and soils of the E26 deposit, where phyllic alteration largely overlaps the potassic alteration, is shown in Figure 7. Uranium content is not shown, as rocks have consistently 1–3 ppm U.

Potassium is elevated in altered quartz monzonite relative to mafic monzonite. Potassic and phyllic alteration zones in volcanics are K-rich relative to unaltered volcanics. However, weathering of altered zones substantially reduces K in the potassic alteration zone relative to the phyllic and unaltered zones, i.e. a K-poor core develops. Thorium in andesite is less than in monzonite; it becomes slightly elevated during

alteration. The difference in Th between altered and unaltered rocks is maintained during weathering.

Soils of the area are Th rich and often contain a major component of introduced plagioclase-bearing material. As the K content of the introduced material is relatively low, underlying K-rich rocks can be reflected by the soils, particularly if the K is present as muscovite in soils, e.g. above phyllic alteration and unaltered volcanics. Soils with introduced material have around 8 ppm Th, i.e. much higher than rocks of the area.

This study found that weathering would have a profound effect on the aerial gamma-ray signature of the Goonumbla deposits, with a K-poor core being developed rather than the K-rich core seen if unweathered rocks were exposed. However, as the Goonumbla deposits are well covered by transported soils, no response was seen in the aerial surveys conducted over the prospect (Fig. 8). The survey shows areas of K (shown red) where unaltered volcanics crop out or come close to the surface, whereas transported soils are richer in Th

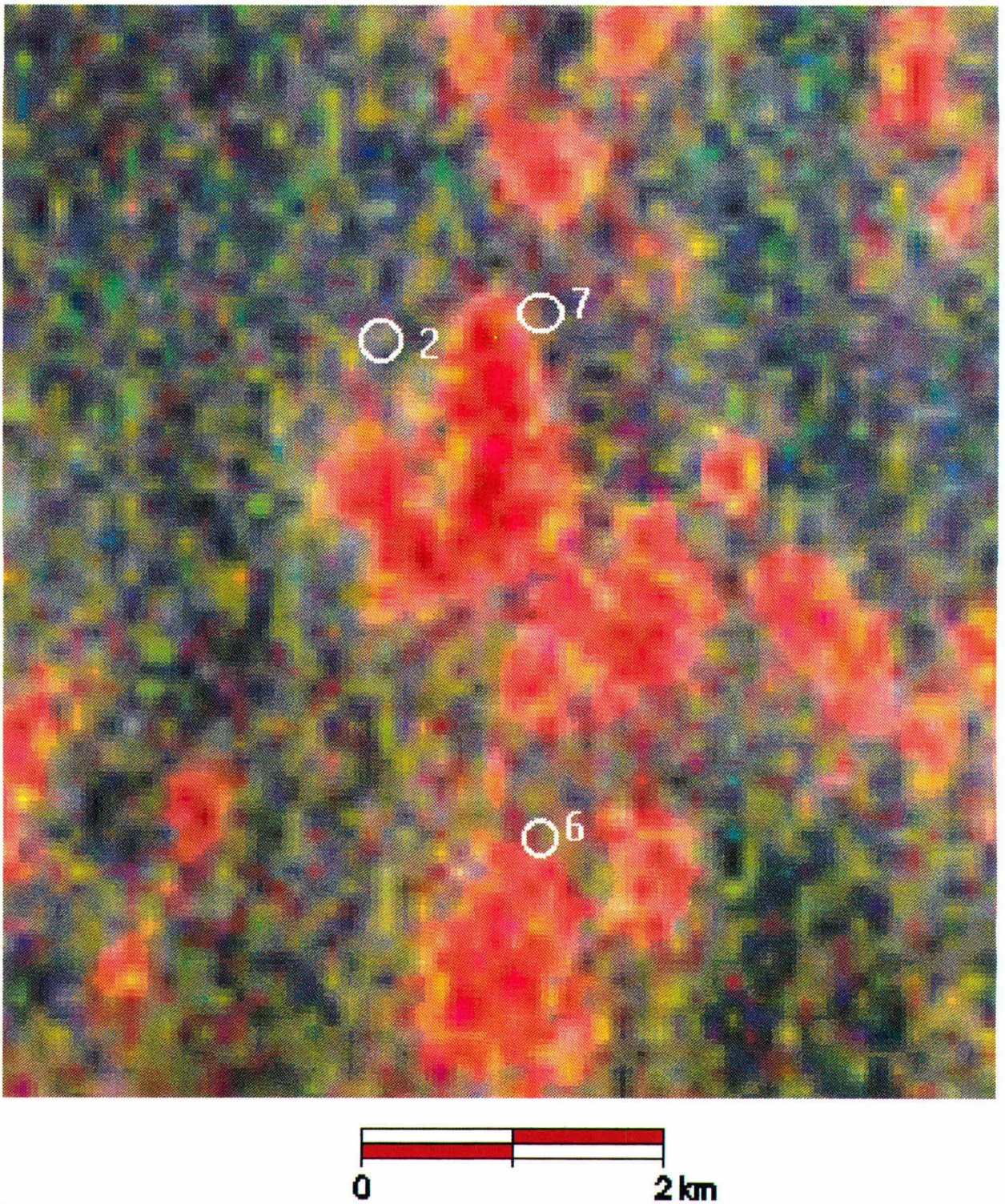

Figure 8. False colour image (K = red, U = blue, Th = green) of the area around the Northparkes mine, flown prior to commencement of mining by North Exploration. Location of the individual deposits (E22, E26 and E27) is indicated by circles. (Data published by permission R. Love, North Ltd)

(shown green). As predicted above, no K-rich signatures are seen in the area of the E22, E26 and E27 deposits.

Gold deposits

In a review of the application of aerial gamma-ray surveys to Au exploration in the literature up to 1988, Hoover & Pierce (1990) found 46 relevant references, half of which were in the Russian literature. The review showed that aerial gamma-ray surveying signatures of Au deposits were very variable with K being the most reliable pathfinder. Even where Au is within quartz veins, hydrothermal alteration of host rocks can give detectable haloes. Next to K, the most frequently cited radioelement indicator was Th depletion in altered rock. This is the so-called antagonism between K and Th (Ostrovskiy 1975) and refers to a coincident decrease in Th accompanying the increase in K with alteration. Other deposits show increases in both K and Th, which suggests that Th is mobilised in alteration systems, but that other variables control how this affects the final Th concentration. Increases and decreases in U are equally reported. Grebenchikov et al. (1977) identified five distinct radiometric signatures in five types of Au deposit in late Paleozoic volcanics, involving relative increases and decreases in all three radioelements. Clearly, no particular aerial survey signature exists for Au deposits, but the studies show that changes in all three radioelements can occur and may be detected in aerial gamma-ray surveys.

Since 1988, many more descriptions of the application of aerial gamma-ray surveying to Au exploration have appeared, although few have examined in detail the source of the observed signatures. To illustrate the potential indicators in aerial gamma-ray surveys and the problems encountered in detailed interpretation, detailed studies on two northeast Queensland deposits, the Mt Leyshon breccia-hosted Au deposit and the epithermal Au deposit at Bimurra (Fig. 1) are described below.

Breccia-hosted Au mineralisation—Mt Leyshon, Queensland. The Mt Leyshon Au deposit is 25 km south of Charters Towers in northeast Queensland. It occurs in a Permo-Carboniferous magmatic-associated breccia complex at the boundary of Cambrian Puddler Creek metasediments and Ordovician Fenian Granite (Paull et al. 1990). The mineralisation is sulphide-rich—Cu, Zn, Pb, Ag, Mo and Bi sulphides and sulphosalts accompanying pyrite. The breccia complex is extensively altered to sericitic and chloritic assemblages. Mineralisation at depth is associated with sericite–carbonate replacement of feldspars, whereas in outcrop the deposit is characterised by silicification and alunite development. Late stage (Silurian) doleritic dykes are extensively developed in the surrounding rocks, but not within the complex.

The distribution of radioelements in the rocks and soils of the Mt Leyshon complex was investigated, using analyses of outcrop and soil samples, collected before mining began, from a 3 km east–west traverse across the breccia complex (Dickson & Scott 1989b; Fig. 9).

The K content of outcropping rocks was found to decrease in the order Fenian Granite adjacent to mineralisation > background granite > eastern sericite + jarosite zone > other brecciated rocks (including ore zone) > dolerite. The U content (1–3 ppm) was highest in granite and lowest in dolerites. Low U values were found within the Au zone at Mt Leyshon proper, but high values (6–10 ppm) were found associated with surface gossan. The highest Th content occurs in the granite, with lower values associated with the altered and brecciated rocks. Relatively low Th values were found in the Au zone at Mt Leyshon proper.

Soils over the peripheral Fenian Granite were lower in radioelement content than the underlying rock. None of the three radioelements in the soils showed any correlation with the rock values. In contrast, there was a good correlation between radioelements in the fine (<4 mm) and coarse (>4 mm)

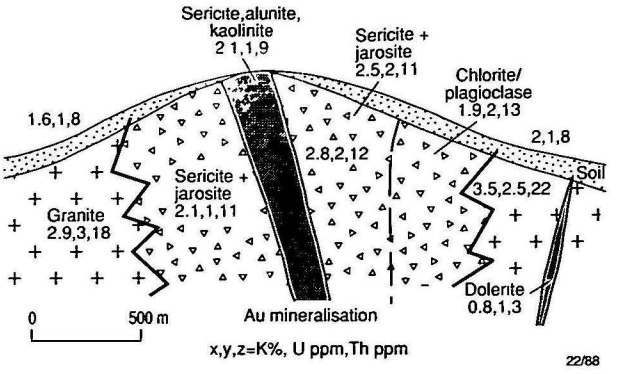

Figure 9. Summary of K, U & Th concentration in and around Mt. Leyshon Au deposit, northeast Queensland (after Dickson & Scott 1991a).

fractions of the soil. The lack of correlation between the radioelements in the soils and rocks suggests that the soils are at least partially derived from other sources. In addition, soils over the granite showed the presence of amphibole, a constituent of dolerite, but not granite. Thus, the likely source of much of the soils was considered to be the abundant and more readily weathered dolerites within the granite.

A consequence of the lowering of the K content of the granite soils by incorporation of substantial amounts of radioelement-poor material derived from weathering dolerites is that the areas of K-alteration associated with the Mt Leyshon complex are readily distinguished in the aerial gamma-ray survey of the area (Fig. 10). This signature is, however, due to weathering phenomena rather than the mineralisation processes. If the weathered rocks dominated the whole aerial survey image, the mineralised breccia might be expected to show as an area of low K.

Epithermal Au deposit—Bimurra, northeast Queenland. The Bimurra epithermal Au prospect, 130 km southeast of Charters Towers, is hosted in felsic–intermediate volcanic rocks. A description of the aerial survey of this area has been previously published (Irvine & Smith 1990).

The alteration system at Bimurra covers an area of 10 km^2 and occurs within the Devonian–Carboniferous rhyolitic–rhyodacitic tuffs and lavas of the Bimurra Volcanics (Wood et al. 1990). The prospect is partly covered by fluviatile sediments of the Tertiary Suttor Formation. The hydrothermal alteration at the prospect is reflected in most rock types by silicification and the development of potassic, phyllic and propylitic mineral assemblages.

A summary of the radioelement content of the rocks and soils of the Bimurra prospect (Fig. 11; Dickson & Scott 1991b), based on analyses of samples from detailed outcrop and soil sampling over the prospect, shows that major variation occurs in the K and Th content of the rocks of the area. Pervasive propylitic and phyllic alteration results in slightly lower K, but unaffected U and Th relative to more remote tuffs. Intense potassic alteration results in much higher K than unaltered tuffs, but such zones are often too small to be seen in an aerial gamma-ray survey and may also be confused with the similar signatures of radioelement-rich rhyolites in the area (4.4% K, 3 ppm U, 15 ppm Th).

The effect of silicification related to hydrothermal alteration depends on the extent of silicification. Moderate amounts result in decreased K but retention of Th, whereas massive silicification results in complete loss of all three radioelements. As intense silicification often occurs intimately associated with potassic alteration; such areas may be difficult to distinguish from unaltered rocks in an aerial survey. Zones of silicification are also hard to distinguish from the partly overlying K-poor, Th-rich sediments of the Suttor Formation,

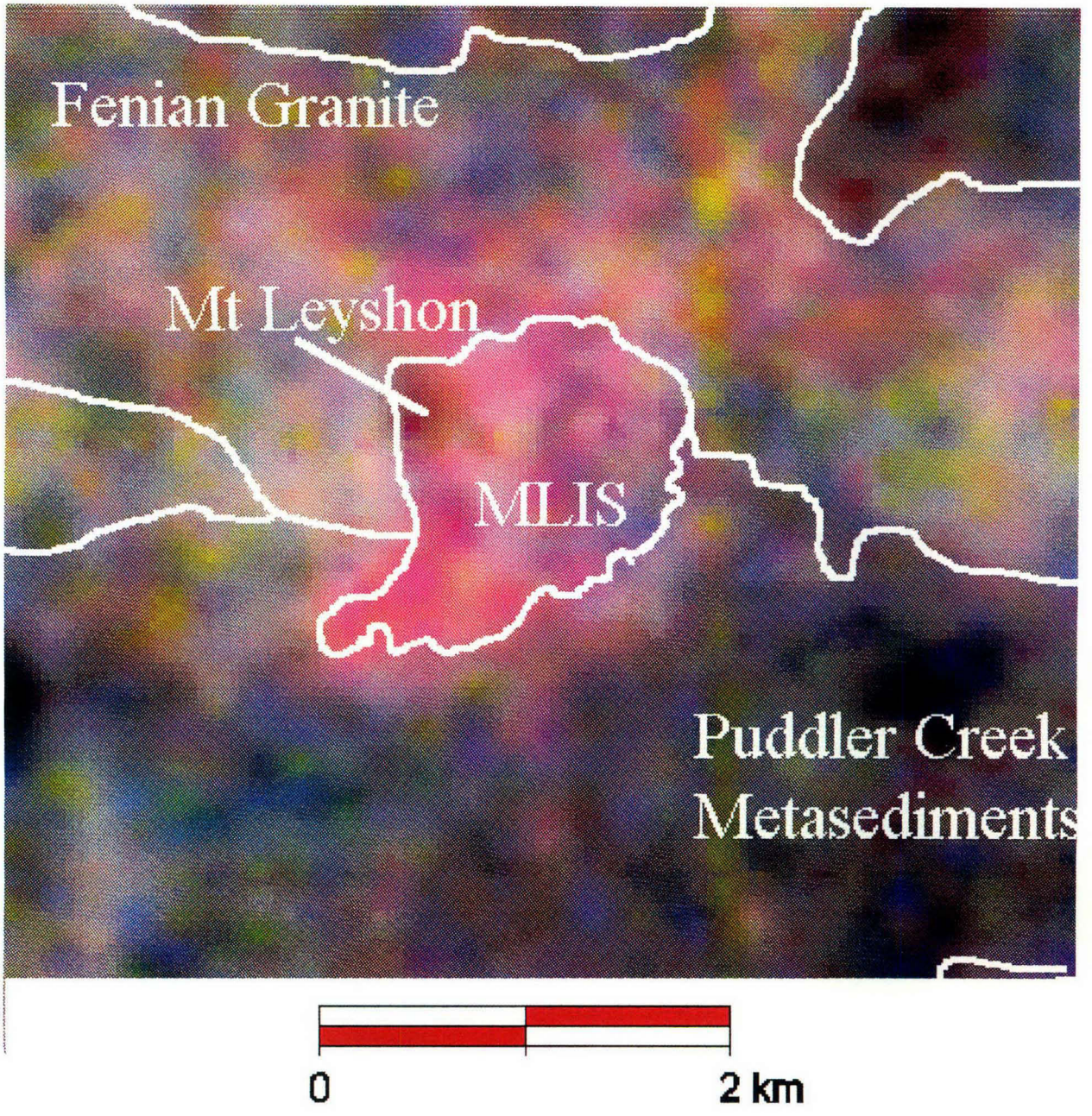

Figure 10. False colour image (K = red, U = blue, Th = green) of the area around the Mt Leyshon igneous suite (MLIS), flown by Esso Mining Ltd before present-day major mining (data published by permission of S. Beams, Terra Search Ltd).

which typically contains 0.5% K, 1 ppm U and 6 ppm Th.

Soils in the area are shallow (often <0.1 m) and immature and their radioelement content generally reflects that of their parental rocks. This is due to U and Th being mainly held in resistate minerals and K being largely present as relatively resistant mica.

The aerial survey images for K, U and Th over the Bimurra area are shown in Figure 12. The radioelement-rich rocks northwest of the prospect are the Mt Wyatt Formation. The low-radioelement zone in the northwest corner is a previously unmapped basalt plug of unknown age. The centre of the K image shows a strong zone of K depletion on the southern and eastern edge of the Mt Wyatt Formation (Fig. 12a). The deposit occurs within this zone, which represents silicificied rocks, but a substantial part of the low-K zone is also Tertiary sandstone of the Suttor Formation. Potassic alteration is not seen and the low K signature is not unique to areas of

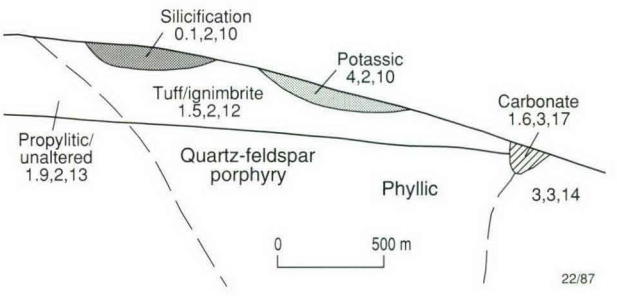

Figure 11. Summary of K, U & Th concentration in and around the Bimurra Au prospect, northeast Queensland (after Dickson & Scott 1991a).

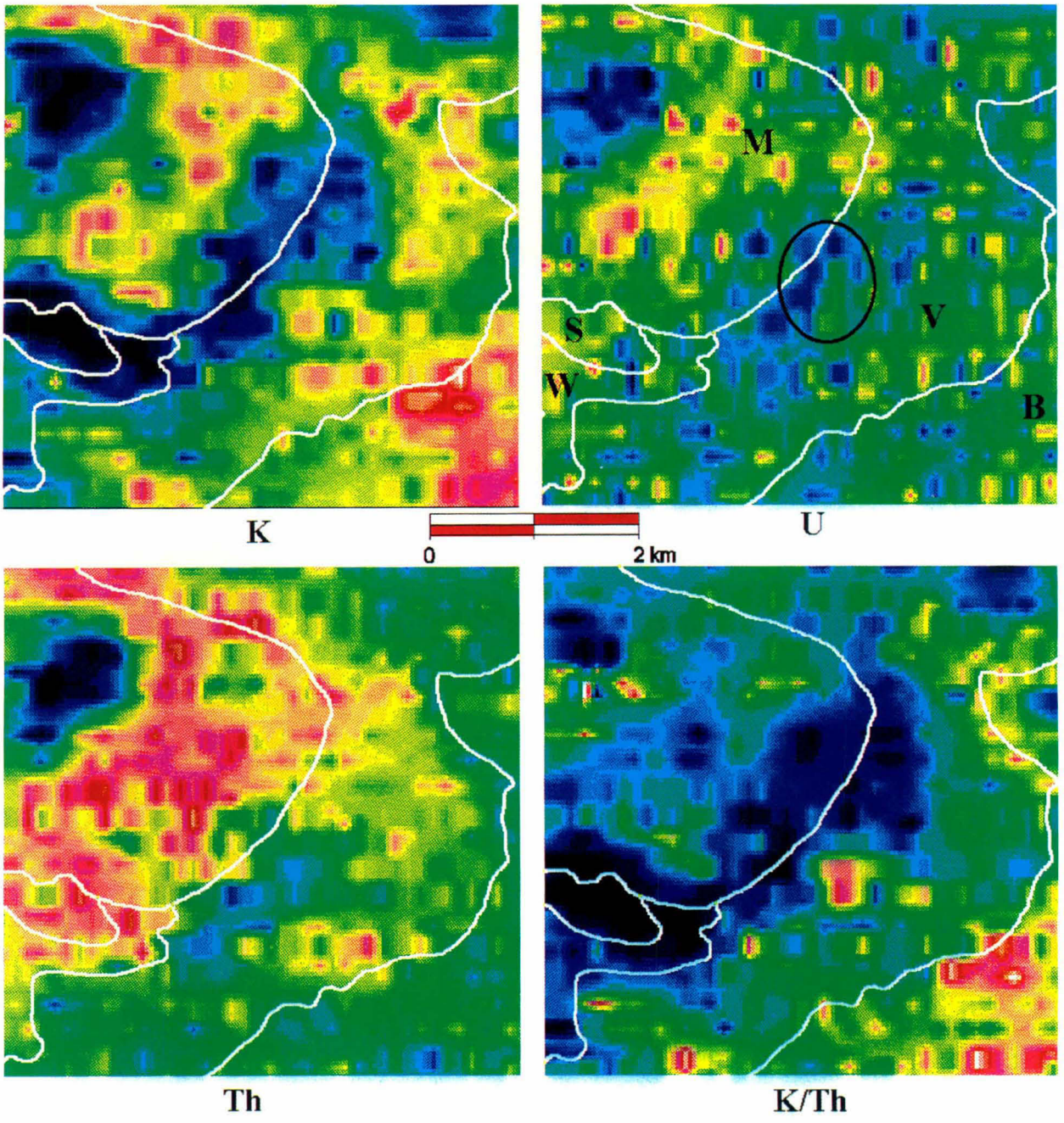

Figure 12. Images of K, U, Th and the K/Th ratio for the area around the Bimurra prospect, flown by BHP Ltd. Centre of the alteration area is indicated by black oval in U image. White outlines indicate geological mapping with M = Mt Wyatt Formation, V = Bimurra Volcanics, W = weathered Bimurra Volcanics, S = Suttor Formation and B = Bulgonunna Volcanics. (Data published by permission of D. Woods, Newcrest Mining Ltd).

alteration. Uranium and Th show some coincident depletion in the area of the deposit. Southwest of the deposit, there are K-rich rocks of the Bulgonunna Volcanics. Across the whole area, the K/Th ratio data best showed the area of high-K, depleted Th, although similar values were found over other areas of the Bimurra Volcanics and may reflect compositional variations in the volcanics. Thus a high K/Th ratio is not a unique alteration signature.

The study of this and other Au prospects in the area showed that locating areas of alteration in an aerial survey requires close examination on a small scale and is hampered by the similarity of signatures of different rock types, e.g. barren rhyolite has a K signature similar to K-alteration in trachyte. The ratios K/Th and K/U could be used to highlight potassic alteration zones, reflecting coincidentally increased K and lowered U or Th, but interpretation of such ratios has to take account of variable geology.

Stratabound polymetallic mineralisation

Mineralisation incorporating sulphides and exposed at the surface is subject to weathering that produces strong acidic conditions. Such conditions lead to development of gossan and can greatly affect the distribution of radioelements. A study of the distribution of radioelements in a stratabound polymetallic deposit at Wagga Tank, 130 km south of Cobar, illustrates the effect that weathering can have on sulphide-hosted mineralisation.

Deposits in the Cobar Field, western New South Wales, occur in a 65 km long belt which is zoned Cu–Au to Cu–Pb–Zn to Pb–Zn south to north. Cobar-type polymetallic deposits are

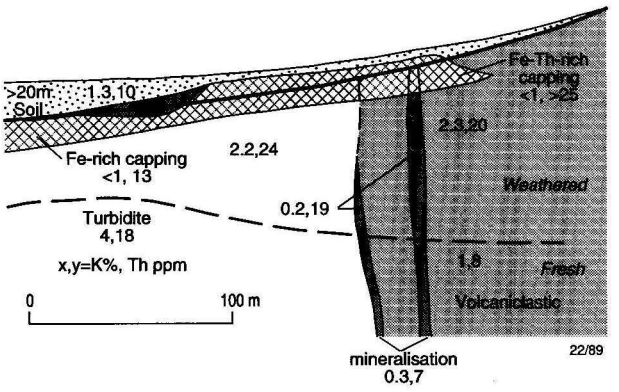

Figure 13. Summary of K and Th concentration in and around Wagga Tank polymetallic prospect, western New South Wales (after Dickson & Scott 1991a).

discordant to bedding, parallel to cleavage and adjacent to faults. The Wagga Tank polymetallic deposit is outside the Cobar Field proper, but has many similarities to Cobar-type deposits. The deposit occurs at the boundary of steeply dipping Devonian turbidites and volcaniclastics. Zn–Pb–Cu–Ag–Au mineralisation occurs within a zone of brecciation and alteration at the contact of the two rock types (Scott et al. 1991).

Weathering occurs to a depth of ~100 m and has resulted in the formation of a lateritic weathering profile characterised by surficial ferruginous enrichment. Under arid conditions, fluviatile material from the north and sheetwash from the east has covered the area to a depth of up to 30 m. Reworking of lateritic surficial material has distributed pisoliths and gossanous fragments through the soil profile above the deposit.

The radioelement distribution in the Wagga Tank deposit was determined from analyses of samples from diamond and percussion drill-hole samples and detailed surface soil samples collected in three traverses across the prospect (Fig. 13; Scott & Dickson 1990b). Potassium and Th are higher in the turbidites than in the volcaniclastic rocks. Weathering of rock depletes K, but raises Th in turbidites and raises both in volcaniclastics, i.e. weathering homogenises the radioelement content of the two rock types. An Fe-rich laterite capping formed during weathering has high Th close to mineralisation. Thorium in the laterite is present in all three Fe-oxide phases (maghemite, hematite, goethite). High-Th laterite was probably formed during acidic weathering over the deposit. Under more arid conditions (post-Miocene) some of this laterite was reworked and distributed through the overlying, transported soil. However, the uppermost soils over the deposit are dominated by feldspar-rich material, derived from granite to the north, and contain only insignificant amounts of Th-rich material. Thus, the Th-rich capping is not seen at the surface.

Uranium is approximately 3 ppm in rocks and approximately 2 ppm in surficial soils. Greater amounts were found in hematite related to weathered mineralisation close to faulting.

An aerial survey of the area showed primarily the different types of colluvium in the area and the Th-rich (possibly lateritic) areas. The Th-rich capping over the prospect, buried by transported soil, was not recognised.

Summary—radioelement signatures of mineralisation

Hydrothermal processes can result in changes to the radioelement content of the host rocks. Of the three radioelements, K is most often affected by such processes, Th less often and U very infrequently (U deposits excepted). Potassium is often increased during alteration, but weathering generally decreases the intensity of alteration signature. The effect of weathering depends on the host mineralogy of K, as K-feldspar and biotite are much less resistant to weathering than muscovite. Consequently, under intense weathering conditions, a K halo due to K-feldspar may be destroyed, but a halo related to muscovite can survive moderate weathering. Intense silicification accompanying epithermal mineralisation can result in decreased K, but weak to mild silicification may help preserve K-alteration from weathering.

Thorium may be mobilised during mineralisation processes, for example, being partly depleted in areas of K-alteration or intense silicification, but concentrated in Th-rich materials, such as laterite. It has been shown that some sulphide-rich, near-surface deposits may form ferruginous cappings.

The resolution of areas seen on the ground by aerial surveys is of the order of 200–300 m across. This defines the smallest halo that may be observed. Thus, a small, 100 m wide potassic zone, as found, for example, by ground sampling at Bimurra, will not be seen in the aerial survey. Experience has shown that deposits with signatures clearly seen in surveys are within alteration areas at least 1 km wide.

One of the complicating factors in extracting signatures of mineralisation from aerial surveys is the effect of changes of lithology. Often ground mapping is the only method to resolve the different rock types. The most complicating factor is transported soils, which obscure otherwise recognisable radioelement signatures.

The study of gamma-ray signatures of mineralisation is still in its infancy. Detailed studies of radioelement distribution within mineral deposits are rare and much evidence of signatures is anecdotal. Examples such as those at Mt Leyshon and Bimurra show that such evidence can be unreliable, as lithological and regolith variation may be mistaken for radiometric signatures. There is little in the way of systematic compilations of signatures of minerals deposits, although Hoover et al. (1992) have attempted to put together geophysical expressions (including radiometric signatures) for six styles of mineral deposits.

Applying the knowledge to interpretation of aerial gamma-ray surveys

This review has outlined the many changes that can occur to the signatures of rocks in aerial gamma-ray surveys due to weathering and mineralising processes. Aerial surveys measure the distribution of radioelements in only the upper 30 cm of the Earth's surface and although broad lithological variations are usually readily mapped, minor variations in the gamma-ray response within units, which may be indicators of mineralisation, are more difficult to evaluate. Approaches to this problem include:

- detailed image processing of aerial gamma-ray survey data to remove the effects of lithological variation and emphasise variation within geological units;
- modelling changes in radioelement content due to weathering and soil erosion across individual units and 'subtracting' these from the observed aerial gamma-ray data; and
- using other data sets, such as aerial magnetic survey data and Landsat TM data, processed to reveal the distribution of clay, iron oxides and vegetation in an integrated analysis of the aerial gamma-ray survey data.

Detailed image processing of aerial gamma-ray survey data is now standard practice. Preparation of a geological/regolith map overlay, to remove the effects due to lithological variation, is an essential step in the interpretation process. One procedure is to convert the overlay (in vector format) to a co-registered raster and use this to: (a) calculate the mean and standard deviation for K, U and Th within each geological unit; and (b) produce images with the mean subtracted and the residuals stretched over ± 3 standard deviations for display. This emphasises variations within each geological unit and also shows clearly any errors in location of geological boundaries. Major variation in the radioelements—both enrichments and

depletions—in prospective units would then be field checked. Other procedures can be used to produce the same result (Kovarch et al. 1994).

Modelling the changes in radioelement content due to weathering and soil erosion across individual units has become possible through digital elevation models (DEMs), which can be prepared from stereo SPOT images or aerial photography, or contour and drainage information digitised from topographical maps. These are now routine outputs of airborne geophysical surveys. This enables geomorphological processes, such as erosion and sedimentation, to be modelled, although available models for application to large areas are still under development. With the knowledge of how the radioelements in any given lithological unit may behave, a predicted surface distribution can be derived for them and subtracted from the aerial gamma-ray survey data. An example of an application of this procedure in searching for K alteration associated with Au mineralisation in basaltic rocks is given by Dickson et al. (in press). The procedure must still be considered experimental and is costly, particularly in deriving good quality DEMs, and is thus probably only applicable to areas of high potential for mineralisation.

The integrated analysis of aerial gamma-ray data with aerial magnetic survey data, Landsat TM and other data sets is a standard practice, although each data set is generally interpreted separately and the results then combined in an interpretative map. More detailed analysis is possible, particularly if we consider that Landsat TM data may be processed to reveal the distribution of clay and Fe oxides (Fraser et al. 1986), which have been shown to have an important role in retaining U and, more importantly, Th in weathered material. It should then be possible to combine the data of the land surface environment and knowledge of radioelement behaviour into a predictive model for radioelement concentration within prospective rock types, taking into account the varying landscape (via geomorphological modelling using DEMs). The predicted response would then be compared to the observed survey data and residuals examined for significant variation. This technique is still in the research stage, but an example of combining all these data sets, via regression analysis in the exploration for VMS-style base metals, is given by Dickson et al. (in press).

Conclusions

This review has illustrated the effects that weathering and mineralisation processes can have on gamma-ray surveying. The major points to be drawn from the data presented are:

- Rocks show a wide range of radioelement contents, but diversity within any lithology can be large enough to preclude automatic rock classification during interpretation of aerial gamma-ray surveys.
- Weathering of all rock types leads to loss of K and, for felsic rocks, loss of U and Th as well. The extent of the loss depends on many factors, but typical losses are 20–30 per cent for all three radioelements. Intermediate and basic rocks show little change in radioelement concentration during initial weathering, but pedogenesis can result in soils with 2–3 times the U and Th content of the parent rock. This can lead to confusion in signatures in some surveys, where soils from different lithological units can be similar in radioelement content.
- Mineralising processes can also affect radioelement content, with K the most affected. Potassium is increased in altered rock surrounding both base-metal and Au deposits. Thorium concentration can also be affected by alteration, but studies to date have shown both depletion and enrichment. Uranium is even more erratically affected by alteration and is generally not a useful indicator of alteration.
- Weathering can affect alteration signatures. Highly weathered deposits may lose their K, particularly if it is hosted by K-feldspar. Transported soils may disguise or change rock signatures in often unexpected ways.
- Detailed interpretation of aerial gamma-ray surveys requires a process of interpreting the survey into major geological units, then looking at the subtle variations within the most prospective units, aided by other data sets (magnetics, Landsat TM) and field checking any anomalous areas.

Acknowledgments

This review is based on studies made with colleagues in CSIRO Division of Exploration and Mining. We would like to thank the staff of Aberfoyle Resources, AMIRA, CRA Exploration, BHP Exploration, Billiton Australia, Geopeko, Geological Survey of Victoria, Placer Exploration, Stockdale Prospecting, and Western Mining Corporation for both their financial and material assistance during the original project. Subsequently, MIM Exploration and QMC Exploration have also assisted in the development of advanced techniques for interpreting gamma-ray surveys. Permission from Terra Search Pty Ltd, North Ltd and Newcrest Mining Ltd to publish radiometric images is gratefully acknowledged.

References

Bowler, J.M., 1976. Aridity in Australia: age, origins and expression in aeolian landforms and sediments. Earth-Science Reviews., 12, 279–310.

Carlisle, D., 1983.Concentration of uranium and vanadium in calcretes and gypcretes. In: Wilson, R.C.L. (editor.), Residual deposits: surface related weathering processes and materials. Geological Society of London. pp. 185–95.

Chivas, A.R. & Nutter, A.H., 1975. Copper Hill porphyry-copper prospect. In: Knight C.L. (editor), Economic geology of Australia and Papua New Guinea. Volume 1—Metals. Australasian Institute of Mining and Metallurgy, Monograph 5, 716–720.

Chopin G.R., 1988. Humics and radionuclide migration. Radiochima Acta, 44/45, 23–28.

Davis, J.D. & Guilbert, J.M., 1973. Distribution of the radioelements potassium, uranium and thorium in selected porphyry copper deposits. Economic Geology, 68, 145–60.

de Meijer, R.J., Tanczos, I.C. & Stapel, C., 1994. Radiometric techniques in heavy mineral exploration and exploitation. Exploration & Mining Geology, 3, 389–398.

Dentith, M.C., Frankcombe, K.F., Ho, S.E. & Shepherd, J.M., (editors), 1994. Geophysical signatures of Western Australian mineral deposits. Geology & Geophysics Department (Key Centre) & UWA Extension, University of Western Australia, Publication 26, and Australian Society of Exploration Geophysicists, Special Publication 7.

Dickson, B.L., 1990. Radium in groundwaters. Chapter 4-2—The environmental behaviour of radium. IAEA, Vienna, Technical Report Series, No. 310, 335–372.

Dickson, B.L., 1995. Uranium-series disequilibrium in Australian soils and its effect on aerial gamma-ray surveys. Journal of Geochemical Exploration, 54, 177–186.

Dickson, B.L. & Scott, K.M., 1989a. Radioelement distribution in rocks and soils at the Copper Hill Cu–Au deposit. CSIRO Division of Exploration Geoscience, Restricted Report 74R.

Dickson, B.L. & Scott, K.M., 1989b. Radioelement distribution in outcropping rocks across the Mt Leyshon gold deposit, N.E. QLD. CSIRO Division of Exploration Geoscience, Restricted Report 45R.

Dickson, B.L. & Scott, K.M., 1991a. Interpretation of aerial gamma-ray surveys. CSIRO Division of Exploration Geoscience, Restricted Report 301R.

Dickson, B.L. & Scott, K.M., 1991b. Radioelement distribution in rocks and soils in the Bimurra–Conway area, Drummond Basin, North Qld. CSIRO Division of Exploration Geoscience, Restricted Report 225R.

Dickson, B.L., Giblin, A.M. & Snelling, A.A., 1987. The source of radium in anomalous accumulations near sandstone escarpments, Australia. Applied Geochemistry, 2, 385–398.

Dickson, B.L., Fraser, S.J. & Kinsey-Henderson, A., in press. Interpreting aerial gamma-ray surveys utilizing geomorphological and weathering models. Journal of Geochemical Exploration.

Fertl, W.H., 1983. Gamma-ray spectral logging: a new evaluation frontier. World Oil, 79–91.

Ford, K.L. & O'Reilly, G.A., 1985. Airborne gamma-ray spectrometric surveys as an indicator of granophile element specialization and associated mineral deposits in the granitic rocks of the Meguma Zone of Nova Scotia, Canada. In: High heat production (HHP) granites, hydrothermal circulation and ore genesis. The Institution of Mining and Metallurgy, London, pp. 113–133.

Fraser, S. J., Gabell, A. R., Green, A. A. & Huntington, J. F., 1986. Targeting epithermal alteration and gossans in weathered and vegetated terrains using aircraft scanners: successful Australian case histories. Proceedings of the Fifth Thematic Conference, Remote Sensing for Exploration Geology, Reno, Nevada, 1, 63–84.

Graustein, W.C. & Turekian, K.K., 1990. Radon fluxes from soils to the atmosphere measured by ^{210}Pb–^{226}Ra disequilibrium in soils. Geophysical Research Letters, 17, 841–844.

Grebechikov, A.M., Khrust, A.R., Buchenkova, Ye.I., & Rusinova, O.V., 1977. Radioactive and alkaline elements in metasomatics of gold–silver deposits of Kazakhstan. International Geology Review, 19, 173–180.

Greeman, D.J., Rose, A.W. & Washington, J.W., 1990. Evaluation of radon precursors and radon production in major soil types for the NE U.S. Eos, April 24.

Heithersay, P.S., O'Neill, W.J., van der Helder, P. & Moore, C.R., 1990. Goonumbla porphyry copper district—Endeavour 26 North, Endeavour 22, and Endeavour 27 copper–gold deposits. In: Hughes, F.E. (editor), Geology of the mineral deposits of Australia and Papua New Guinea. Australasian Institute of Mining and Metallurgy, Monograph 14, 1385–1398.

Hoover, D.B. & Pierce, H.A., 1990. Annotated bibliography of gamma-ray methods applied to gold exploration. U.S. Geological Survey Open-file Report 90-203, 23pp.

Hoover, D.B., Heran, W.D. & Hill, P.L., 1992. The geophysical expression of selected mineral deposits. US Geological Survey Open File Report 92–557, 129pp.

IAEA, 1979. Gamma-ray surveys in uranium exploration, a manual. IAEA, Vienna, Technology Report Series, No. 186, 90 pp.

Irvine, R.J. & Smith, M.J., 1990. Geophysical exploration for epithermal gold deposits. Journal of Geochemical Exploration, 36, 375–412.

Killeen, P.G., 1979. Gamma-ray spectrometric methods in uranium exploration—application and interpretation. In: Hood, P.J. (editor), Geophysics and geochemistry in the search for metallic ores. Geological Survey of Canada, Economic Geology Report 31, 163–229.

Kovarch, A., Flood, P.G. & Tyne, E., 1994. Geographical information systems for regional scale geological analysis: the Manilla 1:250,000 map area, a case study. Proceedings of the 7th Australian Remote Sensing Conference, 1076–1083.

Langmuir, D., 1978. Uranium solution mineral equilibria at low temperatures with application to sedimentary ore deposits. Geochimica et Cosmochimica Acta, 42, 547–569.

Langmuir, D. & Herman, J.S. 1980. The mobility of thorium in natural waters at low temperatures. Geochimica et Cosmochimica Acta, 44, 1753–1766.

Megumi, K. & Mamuro, T., 1977. Concentrations of uranium series nuclides in soil particles in relation to their size. Journal of Geophysical Research, 82, 353–356.

Moxham, R.M., Foote, R.S. & Bunker, C.M., 1965. Gamma-ray spectrometer studies of hydrothermally altered rocks. Economic Geology, 6, 653–71.

Ostrovskiy, E. Ya., 1975. Antagonism of radioactive elements in wallrock alterations fields and its use in aerogamma spectrometric prospecting. International Geological Review, 17, 461–8.

Paull, P.G., Hodkinson, I., Morrison, G.W. & Teale, G.S., 1990. Mount Leyshon gold deposit. In: Hughes, F.E. (editor), Geology of the mineral deposits of Australia and Papua New Guinea. Australasian Institute of Mining & Metallurgy, Monograph 14, 1471–1481.

Schery, S.D., Gaeddert, D.H. & Wilkening, M.H., 1984. Factors affecting exhalation of radon from a gravelly sandy loam. Journal of Geophysical Research, 89, D5, 7229–7309.

Scott, K.M., 1978. Geochemical aspects of the alteration–mineralization at Copper Hill, New South Wales, Australia. Economic Geology, 73, 966–976.

Scott, K.M. & Dickson, B.L., 1990a. Radiometric characterization of surface expressions of the alteration associated with Cu–Au mineralization, Goonumbla, Central NSW. CSIRO Division of Exploration Geoscience, Restricted Report, 119R.

Scott, K.M. & Dickson, B.L., 1990b. Radioelements in weathered rocks and soils at the Wagga Tank polymetallic deposit Western NSW. CSIRO Division of Exploration Geoscience Restricted Report 91R.

Scott, K.M., Rabone, G. & Chaffee, M.A., 1991. Weathering and its effect upon geochemical dispersion at the polymetallic Wagga Tank deposit, NSW, Australia. Journal of Geochemical Exploration, 40, 413–426.

Ward, S.H. 1981. Gamma-ray spectrometry in geologic mapping and uranium exploration. Economic Geology, 75th Anniversary Volume, 840–849.

Wood, D.G., Porter, R.G. & White, N.C., 1990. Geological features of some Paleozoic epithermal gold occurrences in northeastern Queensland, Australia. Journal of Geochemical Exploration, 36, 413–443.

Yeates, A. N., Wyatt, B. W. & Tucker, D. H., 1982. Application of gamma-ray spectrometry to prospecting for tin and tungsten granites, particularly within the Lachlan Fold Belt, New South Wales. Economic Geology, 77, 25–1738.

AGSO Journal of Australian Geology & Geophysics, 17(2), 201–216

Application of airborne gamma-ray spectrometry in soil/regolith mapping and applied geomorphology

J.R. Wilford[1] P.N. Bierwirth[1] & M.A. Craig[1]

Gamma-ray spectrometric surveys are an important source of information for soil, regolith and geomorphological studies, as demonstrated by the interpretation of airborne surveys in Western Australia, central New South Wales and north Queensland. Gamma-rays emitted from the ground surface relate to the primary mineralogy and geochemistry of the bedrock, and the secondary weathered materials. Weathering modifies the distribution and concentration of radioelements from the original bedrock source. Once the radioelement response of bedrock and weathered materials is understood, the gamma-ray data can provide information on geomorphic processes and soil/regolith properties, including their mineralogy, texture, chemistry and style of weathering. This information can contribute significantly to an understanding of the weathering and geomorphic history of a region and, therefore, has the potential to be used in developing more effective land-management strategies and refining geochemical models in support of mineral exploration. Gamma-ray imagery is enhanced when combined with Landsat TM bands and digital elevation models (DEM). This synergy enables geochemical information derived from the gamma-ray data to be interpreted within a geomorphic framework. Draping gamma-ray images over DEMs as 3D landscape perspective views aids interpretation and allows the interpreter to visualise complex relationships between the gamma-ray response and landform features.

Introduction

Gamma-ray spectrometry

Airborne gamma-ray spectrometry is a passive remote-sensing technique. Gamma-rays are a form of high-energy short-wavelength electromagnetic radiation. They have no mass or electronic charge and are emitted at different energy levels or peaks that correspond to radioactive decay of particular radioisotopes. The relative abundance or concentration of these radioelements in soil and bedrock is estimated from the intensity of their emittance peaks. Airborne gamma-ray spectrometry measures the abundance of potassium (K), thorium (Th) and uranium (U) in rocks and weathered materials by detecting gamma-rays emitted from the natural isotopic radioactive decay of these elements. Measured K directly corresponds to the isotopic decay peak for ^{40}K. ^{40}K emits gamma-rays as it decays to ^{40}Ar. Measuring Th and U concentrations is more complex, since ^{232}Th and ^{238}U decay through a series of daughter nuclides until they reach stable Pb isotopes. Distinct emission peaks associated with ^{208}Tl and ^{214}Bi, are used to calculate the abundance of Th and U, respectively (Minty 1997). Consequently, U and Th are usually expressed in equivalent parts per million (eU and eTh), which indicates that their concentrations are inferred from daughter elements in their decay chain, whereas, because of its higher crustal abundance, K is typically expressed as a percentage (K%).

However, the estimation of U and Th in this manner assumes that the daughter products in the Th and U decay series are in equilibrium. In some cases the measured isotopes in the U and Th decay series (i.e. ^{208}Tl and ^{214}Bi) may not perfectly quantify the parent elements, because of disequilibrium in the decay chain. Disequilibrium occurs when one or more of the daughter products in the decay chain is removed or concentrated. For example, in some salt lakes and groundwater discharge sites, high eU and eTh values may be due to the accumulation of radium isotopes that are mobile in acid saline solutions (Dickson 1985). Disequilibrium should, therefore, be considered when interpreting gamma-ray data, particularly when correlating rock or regolith sample geochemistry with airborne gamma-ray responses.

The source of gamma-rays—bedrock vs regolith

Ninety per cent of gamma-rays emanate from the top 30–45 cm of dry rock or soil (Gregory & Horwood 1961). The intensity of gamma-rays emitted from the surface relates to the mineralogy and geochemistry of the bedrock and the nature of weathering. K has an estimated crustal abundance of 2.5 per cent. It occurs mainly in primary rock-forming minerals, such as K-feldspar and micas. The percentage of K is generally high in acid-felsic rocks and low in mafic rocks. In contrast, U and Th are relatively rare with an estimated crustal average of 3 ppm and 12 ppm, respectively. U is found at much higher levels in pegmatites, syenites, carbonatites, radioactive granites

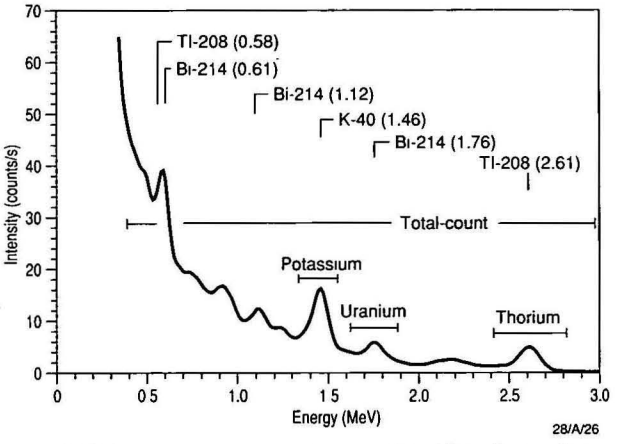

Figure 1. Airborne gamma-ray spectrum and position of potassium, thorium, uranium and total-count windows (modified from Foote 1968).

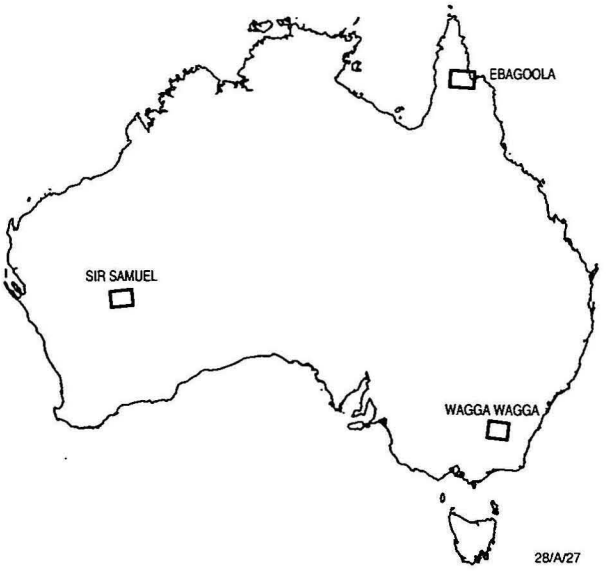

Figure 2. Location of the Ebagoola, Wagga Wagga and Sir Samuel study areas.

[1] Australian Geological Survey Organisation, GPO Box 378, Canberra, ACT 2601, Australia

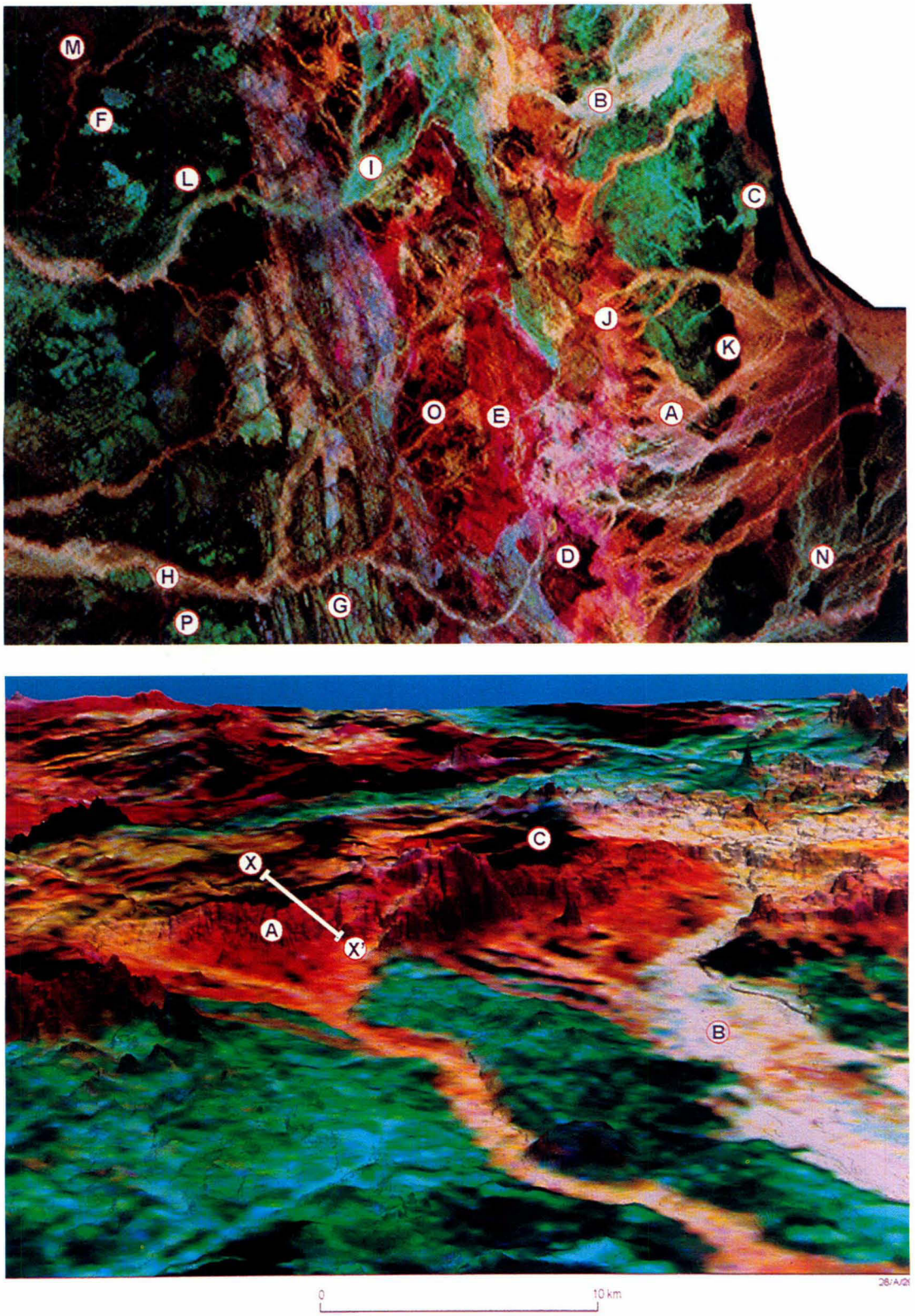

Figure 3. (a—above, upper) Three-band gamma-ray spectrometric image (K red, eTh green and eU blue) over the Ebagoola 1:250 000 map sheet area. A, alluvial sediments derived from granitic rocks; B, alluvial sediments derived from granitic and metamorphic rocks; C, alluvial sediments derived from metamorphic rocks; D, in-situ weathered residual quartz sands (sandy earths); E, lithosols over weathered granite (S-type); F. bauxitic and ferruginous plateaus; G, quartzite ridges; H, floodplain sediments; I, alluvial terrace sediments; J, eroding edge of the Great Escarpment; K, residual quartz sands over Mesozoic sandstones; L, lithosols over weathered siltstone; M, potassic and montmorillonite clays; N, former river channels; O, lithosols over weathered granite (I-type); and P, Fe duricrust. (b—above, lower) 3D perspective view of part of the Ebagoola gamma-ray image draped over a digital elevation model (DEM). The view is looking towards the southwest with Princess Charlotte Bay in the foreground. Features include active erosional edge of the Great Escarpment exposing granitic saprolite (A), active alluvial fan and floodplain sediments derived from the escarpment (B), and deep residual siliceous soils (C). For description of X–X^1 transect, refer to Figure 9. (c—opposite page) Landsat TM band 5 combined with RGB gamma-ray image over the northeastern corner of the Ebagoola 1:250 000 map sheet area. The Landsat image was edge-enhanced before being added to the gamma-ray imagery.

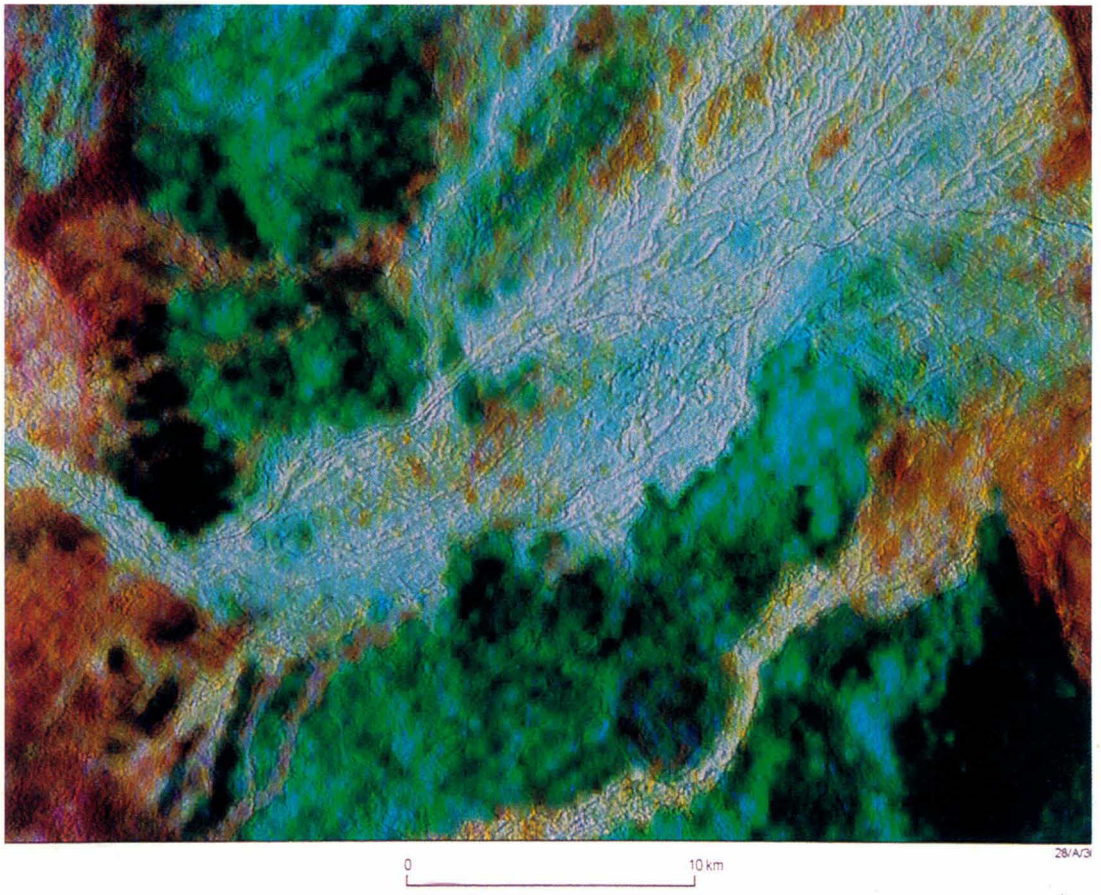

and some black shales. U and Th are found as traces in primary rock-forming minerals (e.g. feldspars), but are most common in accessory and resistate minerals (zircons, sphene, monazite, allanite, xenotime). The concentration of U and Th in igneous rocks generally increases with rock acidity (i.e. rocks with higher silica content).

During chemical and physical weathering, radioelements within rocks are released, redistributed and incorporated into the regolith* (including in-situ weathered and transported materials). In many cases, the radioelement characteristics of regolith materials differ markedly from their underlying source rocks. This is due to textural and geochemical reorganisation within the weathering profile. For example, some intensely weathered regolith materials typically show depletion of K, owing to leaching, and elevated U and Th values associated with clays and/or iron oxides in the upper part of the weathering profile (Koons et al. 1980; Dickson & Scott 1997).

* Regolith—a term used to describe all weathered material above fresh bedrock. Soil is interpreted as the uppermost part of a regolith profile. Regolith is used here to include soils and weathered rock (saprolite).

Attenuation of gamma-rays by water and vegetation

Water, as soil moisture or held within plant tissue, attenuates gamma-rays. However, the effects of soil moisture on gamma-ray emittance are complex. Gamma-ray intensity can increase or decrease, depending on soil moisture conditions (Minty 1997) —generally, a 20 per cent increase in soil moisture will result in a 20 per cent reduction of gamma-rays emitted at the soil surface. To avoid emittance variation due to changing soil moisture conditions, ground sampling and airborne measurements are best made when the ground is dry. Studies in the northern hemisphere have shown that the distribution of snow water equivalent cover can be mapped based on water-attenuation coefficients and repeated airborne measurements (Loijens & Grasty 1973; Carroll & Vose 1984).

Vegetation can attenuate gamma-rays reaching the aircraft, depending on the density of the cover. Gamma-rays are attenuated when the vegetation is dense and contains high volumes of woody material and water held in the tree canopy. However, in Australia, where vegetation consists mostly of open forest, woodlands, shrubs and heath lands, gamma-rays emanating from the soil or bedrock are largely unaffected by the vegetation cover. Even in well-vegetated country over parts of north Queensland, gamma-ray surveys effectively 'see through' the vegetation cover to map soil and bedrock types (Wilford 1992). Vegetation had little or no effects in the interpretation of airborne gamma-ray surveys for soil mapping in central New South Wales (Bierwirth 1996). Areas of dense vegetation (i.e. rainforest and pine forest) have the effect of subduing the gamma-ray response. In tropical environments, wetness indices derived from processed Landsat TM imagery have been used to correct airborne gamma-ray data for water and vegetation attenuation effects (Lavreau & Fernandez-Alonso 1991).

Plant tissue contains negligible traces of Th and U and, as a result, has little effect on the gamma-ray response. However, other studies show that the uptake of K by plants can contribute up to 15 per cent of the signal reaching the aircraft (Kogan et al. 1969). The effects of vegetation, both in terms of attenuation and contributions to the gamma-ray response, should, therefore, be considered when interpreting survey data.

Application of gamma-ray surveys to geological and regolith mapping

Airborne gamma-ray spectrometry has been used mainly as a tool for mineral exploration in locating U deposits and in lithological mapping (Darnley & Grasty 1971; Foote & Humphrey 1976; Galbraith & Saunders 1983; Tucker et al. 1984; Duval 1990; Graham & Bonham-Carter 1993). Although there has been some use of gamma-ray data for mapping

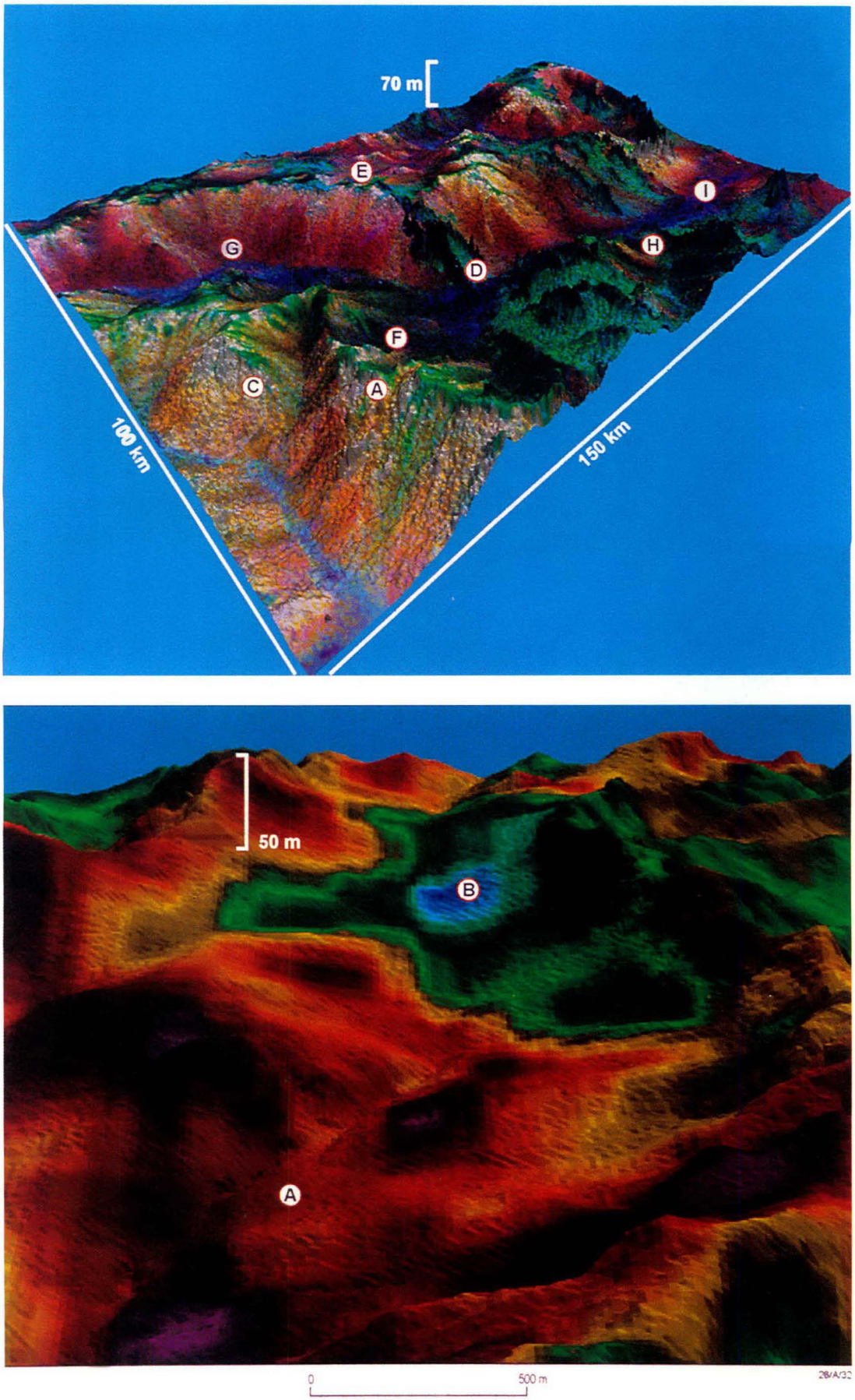

Figure 4. (a—top left) 3D perspective view of the Sir Samuel gamma-ray image draped over a digital elevation model (DEM). A variety of regolith materials can be distinguished and placed within a landscape context, including: A, silcrete forming a breakaway; B, ferricrete; C, granitic saprolite; D, ferricrete developed over greenstone rocks; E, aeolian sands derived from granitic source rocks; F, well-worked aeolian sands; G, sheet-flow fans derived from granite; H, Fe gravel lags; I, valley calcretes; (Image processing by M. Richardson, AGSO). (b—bottom left) 3D perspective of the K channel from the Wagga Wagga area draped over an elevation model.

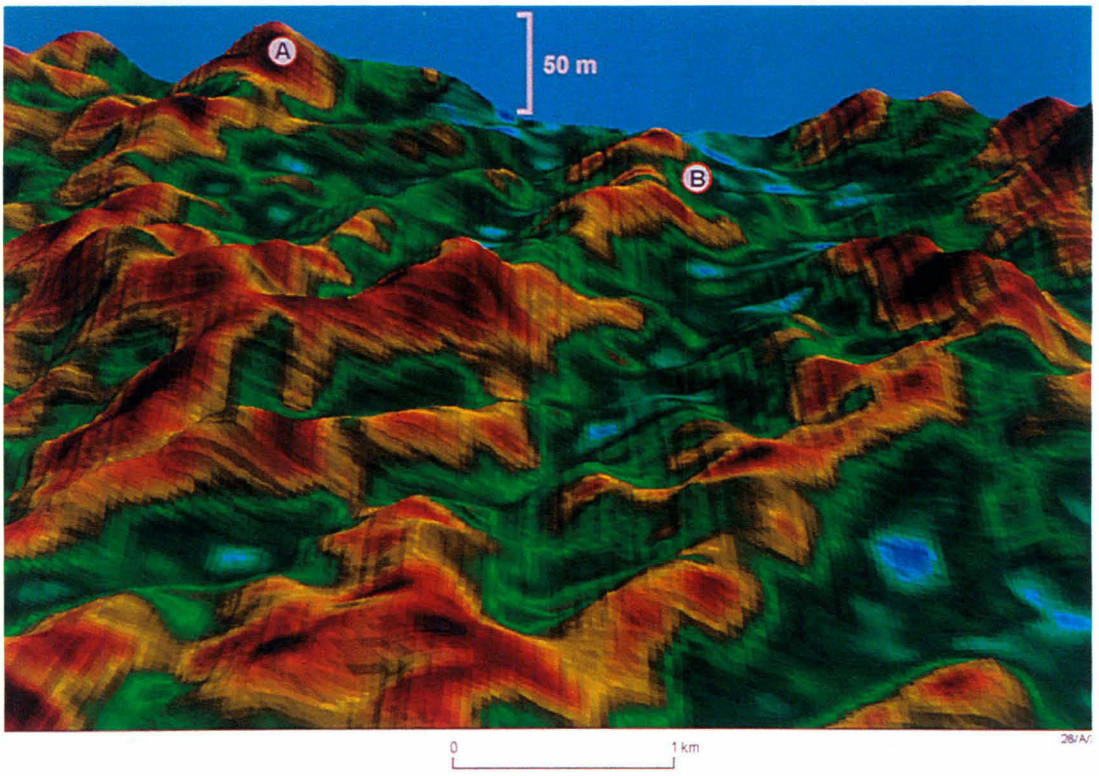

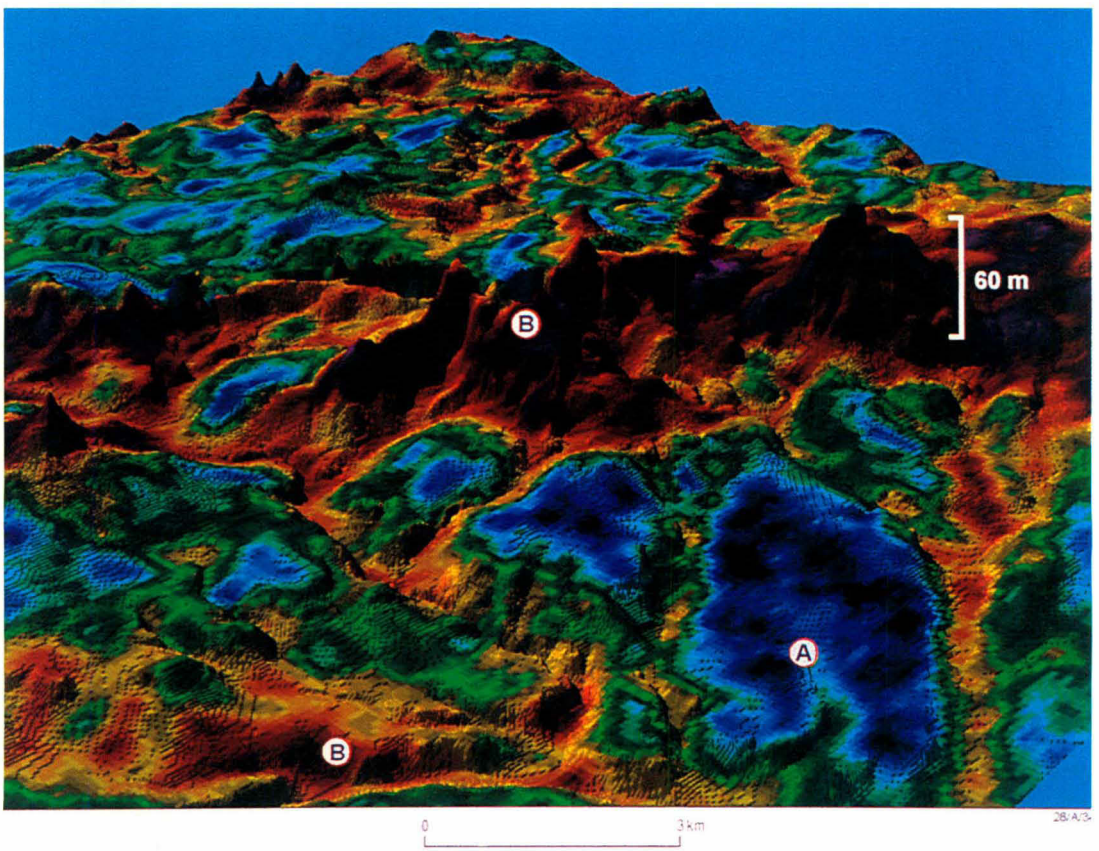

Partially weathered granites (A) are distinguished by their high K values, corresponding to K-feldspars and K-mica. Perched basins (B), consisting of highly weathered colluvial sands are distinguished by a low K response, owing to leaching of K from the weathering profile. (c—top right) 3D perspective of the K channel from the Wagga Wagga area draped over an elevation model (from Bierwirth 1996) . High potassium values over ridge tops (A, lithosols) and low values in the adjacent valleys (B, colluvial clayey earths) reflect soil catenas developed over weathered metasediments. The colluvial soils have developed on inactive footslopes where the K has been leached during pedogenesis. As the thickness of colluvium increases, the imaged K signal decreases, as a result of leaching and burial of the underlying bedrock. (d—bottom right) 3D perspective of the K channel from part of the Ebagoola area draped over an elevation model. Deeply weathered siliceous sands (A) over hill crests are distinguished by their low K values and are separated from (B) thinner soils forming on steeper slopes and along river channels which have incised into the bedrock, by higher K values. These soils form an extensive catena over granitic bedrock.

regolith types (Schwarzer et al. 1972), the main application of airborne surveys to date has been in geological mapping, which have been driven primarily by the interests of the mineral industry. As a result, gamma-ray responses of rock material are generally well understood. However, the response and distribution of radioelements in weathered materials is less well known. More recently, there has been a growing interest in, and use of, gamma-ray data in regolith and geomorphological studies (Dickson & Scott 1990; McDonald & Pettifer 1992; Wilford 1992; Cook et al. 1996). This paper discusses how airborne gamma-ray data can be used to map regolith materials and contribute to our understanding of geomorphic processes in the landscape.

High-resolution (100–400 m line spacing) airborne spectrometric data used in this study were acquired by the Australian Geological Survey Organisation (AGSO) as part of the National Geoscience Mapping Accord (NGMA) and the National Environmental Geoscience Mapping Accord (NEGMA) projects. These initiatives are producing a new generation of geological and environmental maps over strategically important areas of Australia. Airborne spectrometric data are a key contribution to the generation of these maps. Gamma-ray imagery together with other data sets, including Landsat TM, colour photography, and digital elevation models (DEMs), is being used to develop more effective and quicker geological and regolith mapping tools. The objective of this paper is to:

- briefly discuss processing and integration techniques to enhance airborne gamma-ray data for interpretation, and
- assess the use of airborne gamma-ray data for regolith mapping and application in applied geomorphology.

This evaluation of gamma-ray data for regolith mapping and applied geomorphology is based on three airborne surveys from different parts of Australia with diverse weathering and geomorphic settings.

Data acquisition and processing

Flight-line spacing for the airborne surveys was mainly 400 m, with one smaller area flown at 100 m spacing. Gamma-ray measurements were recorded at 70 m intervals along the flight-lines from a height of 100 m. The detector on the aircraft consists of sodium iodide (NaI) crystals. When subject to gamma-rays, the crystals emit visible light or 'scintillations', which are converted to a measurable electrical pulse (Grasty 1976). Four channels were measured, including total count, K, eTh and eU. These channels record gamma radiation in the following energy windows; 0.4–3.0 MeV for total count, 1.37–1.57 MeV for K, 2.41–2.81 MeV for eTh, and 1.66–1.86 MeV for eU. The total-count window measures a broad range of gamma-ray radiation, including the three windows used to measure K, eU and eTh (Fig. 1). Data collected in these channels are corrected for background cosmic and atmospheric radiation, variations in flight elevation and Compton scattering. A comprehensive description of the processing and correction procedures for airborne gamma-ray survey data is given by Minty (1997).

Data resolution and display

The resolution of airborne gamma-ray data depends on the flying height of the aircraft and the flight-line spacing of the survey. Low flying height and closely spaced flight-lines increase data resolution. As a general rule, surveys flown at 1.5 km, 400 m and 100 m line spacing are useful for 1:250 000, 1:100 000 and 1:50 000 mapping scales, respectively. Although survey data are flight-line intensive, with much higher sampling density along flight-lines than between flight-lines, much of this resolution is lost, owing to the unfocussed nature of gamma radiation. For example, 60 per cent of the radiation recorded by the spectrometer from a height of 100 m represents gamma-rays emitted from an area of about 120 m radius on the ground. Therefore, significant overlap between sample points along flight-lines occurs because of the large gamma-ray 'footprint' or field of view (Hansen 1992).

Gamma-rays are measured in counts per second for each radioelement. Most survey data are now calibrated into per cent K and parts per million (ppm) for Th and U. Gamma-ray data are displayed as images, flight-line profiles or contours. Image displays are the most widely used for interpretation, particularly for mapping, where spatial continuity is essential. Spatial patterns and textures are more difficult to interpret from contour and flight-line maps. Imaged data can also be readily enhanced, manipulated and integrated with other data sets, using geographic information systems (GIS) and image-processing software. However, interpretation based on flight-line profiles should not be overlooked, since they can show subtle changes in gamma radiation not seen in imaged renditions which have been smoothed to help interpolation between flight lines (Wilford 1992).

All gamma-ray data used in this study were gridded to either 50 or 80 m pixels, depending on the flight-line spacing of the survey, and geometrically corrected to the Australian Map Grid (AMG) before being displayed as images and integrated with other data sets.

Noise removal

The imagery often shows varying degrees of striping and/or background noise, particularly in the eU channel. Several techniques can be used to remove this noise, including conventional levelling using crossover ties, interchannel correlation methods, and micro-levelling procedures. These techniques are discussed by Minty (1997). In addition several image-processing and filtering procedures are available for reducing noise and improving image interpretability. These are outlined below:

Principle component analysis (PCA). This procedure statistically finds orthogonal axes of variance within the data (Richards 1986) and represents them as images. The first axis (PC1) maps material whose surface variance dominates the data. Progressive PC axes show less dominant variations and the last commonly shows and isolates the noise. Noise can then be removed from the data by rotating the PC axes, excluding the last noisy axis, back to the original channels.

Filtering. One way of reducing the visual effects of speckling in the image is to replace erroneous pixel values with the average value of surrounding pixels. This is done by applying moving box filters (Richards 1986). Spurious elongate artefacts in the imagery, often caused by poor height correction, can be removed by applying a rectangular box filter to each gridded channel.

PCA was deemed the most effective technique for removing noise in the channel data, since, unlike filtering, it maintains the spectral integrity of the data and does not involve spatial averaging or data degradation.

Image enhancement and integration

Pseudo-colour single-channel images and three-band composite images, with K in red, eTh in green and eU in blue, were found to be the most effective enhancement for distinguishing soil/regolith materials. Histogram stretching and band ratioing of the channels (eU/eTh, eU/K, eTh/K) were used to maximise contrast and highlight subtle features in the data. Single-channel and three-channel composite renditions preserve the integrity of the data, allowing relative concentrations of K, eTh and eU to be directly correlated with the geochemistry of soil/regolith materials.

Although clustered image displays, using unsupervised classification procedures, have been used successfully to highlight differences and similarities between geological units

and gamma-ray responses (Graham & Bonham-Carter 1993), similar techniques proved inadequate for separating regolith materials. Unsupervised classification algorithms were found to produce effective colour separation, but were difficult to interpret, owing to mixing of the gamma-ray channels. In addition, subtle gamma-ray responses and textural features were lost in classifying the data into similar spectral groups. Integration of the gamma-ray data with other complementary data sets was found to be the most effective enhancement technique.

Interpretation based on pseudo-coloured composite band and ratio images is further enhanced when combined with Landsat TM and digital elevation models (DEMs). Band 5 of Landsat TM was chosen to combine with gamma-ray imagery because it maximises landform features and subdues vegetation differences, which may be confusing in interpretation. A high band pass filter was used to enhance the high-frequency information in the TM band before adding it back to the gamma-ray image. The filtered image has the advantage of highlighting landform and structural edges, while removing areas of continuous tone which would otherwise distort the spectral characteristic of the gamma-ray image when the data sets are combined. The combined image (Fig. 3c) enables geochemical information derived from the gamma-ray responses to be interpreted within a geomorphic framework. The higher spatial resolution of the TM data also tends to sharpen the otherwise fuzzy gamma-ray image. In addition, adding back the high-frequency component of the total-count channel to the K, eTh and eU images was found to highlight edges associated with lithological and regolith boundaries.

Digital elevation models (DEMs) provide information on important geomorphic variables, including elevation, slope, aspect, convexity and relief. The accuracy of these variables largely depends on the spatial resolution of the DEM. The

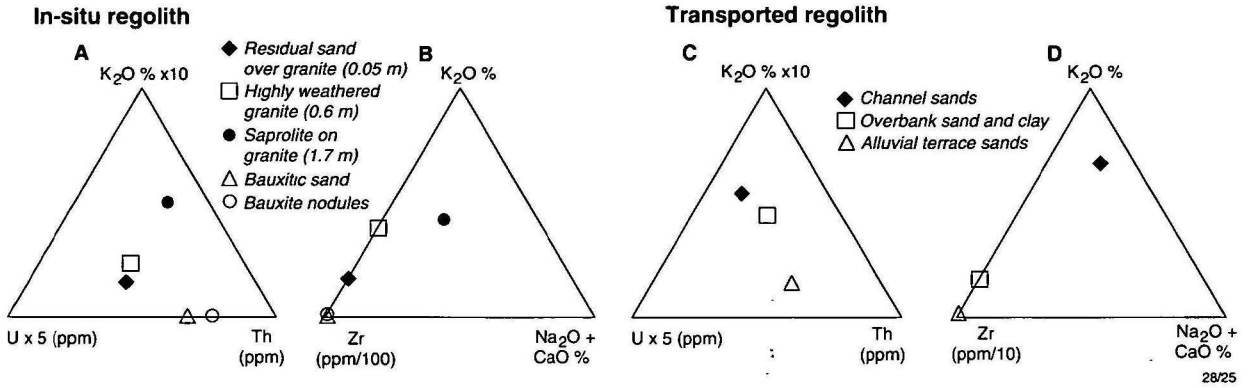

Figure 5. Ternary diagrams showing regolith geochemistry for K_2O, Th, U, Zr and Na_20 + CaO. A and B relate to in-situ weathering profiles on granite and bauxitic material. C and D relate to river channel, overbank and alluvial terrace sediments.

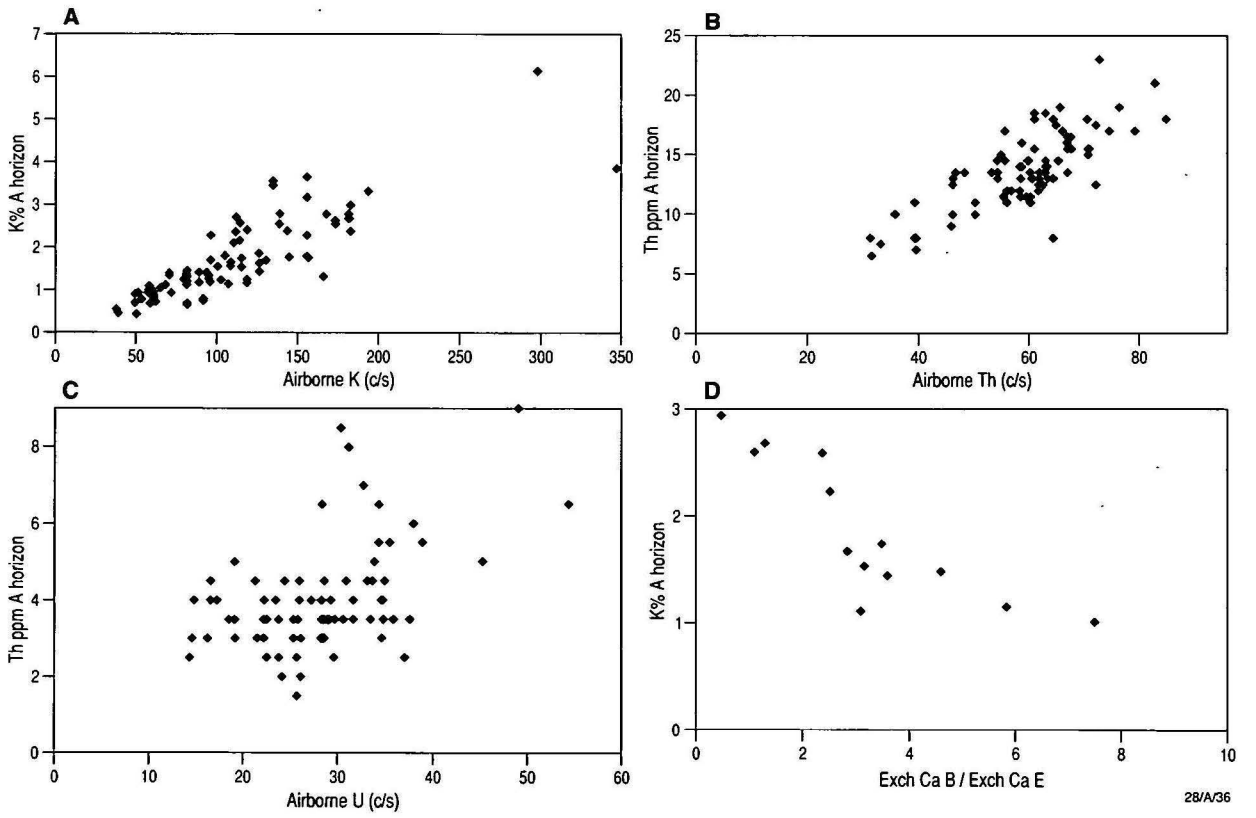

Figure 6. Scatter plots (a,b,c) showing the correlation between measured soil K, Th and U against aerial K, eTh and eU concentration over part of the Wagga Wagga region (from Bierwirth 1996). Evidence of leaching is shown in plot d, where site analyses of K in the upper A horizon are plotted against the ratio of exchangeable calcium in the upper B versus the bleached A2 (E Horizon).

variables have a controlling influence on geomorphic processes and distribution of soil/regolith materials. DEMs can be combined with the gamma-ray data as shaded relief images or as 3D perspective views, where the gamma-ray images are draped over the elevation model (Figs 3b, 4a–d). These displays facilitate the visualisation of complex relationships between the gamma-ray response and terrain morphology attributes.

Colour space transformations and pixel adding techniques are used to combine Landsat TM, DEM and gamma-ray images. Colour space manipulation is available on most image-processing platforms and is a common technique for merging multisensor data (e.g. Conradsen & Nilsson 1984; Welch & Ehlers 1987). Colour space transformations work by converting data sets into intensity, hue and saturation (IHS) components of colour. Once in IHS colour space, each of the colour parameters can be exchanged with other registered data sets before being converted back to the original RGB colour space coordinates for display. The IHS technique is used to combine Landsat TM band 5, artificial sun-angle illuminated DEM and total-count images with the K, Th and U channels by substituting these images as the intensity component of the gamma-ray channels. The result is an image which effectively shows the colours (or hue) of the gamma-ray data with the intensity of the colour modulated by either the Landsat, DEM or total-count image Figs 3c, 4a–d. The IHS technique, however, was found to distort to varying degrees the spectral characteristics of the original gamma-ray image. Another technique, which avoids this distortion problem, is a simple addition of proportions of each data set pixel-by-pixel. This method allows complete control over the percentage of each pixel added from each data set to the combined image (Wilford 1992).

Study areas

The study areas include the Ebagoola 1:250 000, Wagga Wagga 1:100 000 and Sir Samuel 1:250 000 map sheets (Fig. 2). Airborne gamma-ray surveys within these three areas provide a representative selection of different regolith materials, from deep chemical weathering and saprolite formation in Sir Samuel and parts of the Ebagoola region to generally less-weathered landscapes in Wagga Wagga study area. A summary of the climate, vegetation and geology of each area is given below.

Ebagoola

The Ebagoola study area has a warm monsoonal climate with distinct dry and wet seasons. Average annual rainfall is 1117 mm with 95 per cent falling in the wet season between November and April (Wagner 1989). Vegetation is mainly eucalyptus, open woodlands and forests. Land use is restricted to broad-scale cattle grazing, owing to the prolonged dry season. The geology of the Ebagoola study area can be divided into three main rock groups, comprising a central zone of Palaeozoic granites (granodiorite, muscovite–biotite and alkali-feldspar granites) and folded metamorphic rocks (phyllite, schist and gneiss) with gently dipping Mesozoic sediments (sandstones and siltstones) to the west and east (Blewett & Trail 1995).

Wagga Wagga

The Wagga Wagga study area has a temperate climate with average annual rainfall of 530 mm. Agricultural land use consists of wheat cropping, sheep grazing and dairy farming. Dryland salinity is an environmental problem in the area, owing to rising water tables caused by deforestation of the natural vegetation. The geology consists of Silurian granites intruding metamorphosed Ordovician slates and quartzites (Raymond 1992). In places, these rocks are unconformably overlain by Devonian sandstone. Large areas of Cainozoic alluvium and colluvium occur in valleys, floodplains and downslope from adjacent hills.

Sir Samuel

The Sir Samuel 1:250 000 area is semi-arid to arid with a mean annual rainfall of approximately 215 mm (Bunting & Williams 1979). Vegetation consists largely of mulga, blue bush, spinifex, mallee shrub and scattered trees (*Eucalyptus* spp.). Land use consists of broad-scale pastoral activities and mining. Rocks in the area are Archaean and include greenstone belts, consisting of metamorphosed sediments, volcanics and intrusives (Bunting & Williams 1979). The greenstone belts are separated by large areas of granite, including granodiorite, tonalite, monzonite and adamellite. These rocks are generally either exposed and deeply weathered (typically kaolinised to tens of metres below the surface) or covered by transported sediment.

Results—case studies

Interpretations of the three airborne surveys are firstly described in terms of gamma-ray response associated with in-situ and transported regolith material in the landscape. Then, selected examples from the surveys are used to illustrate how gamma-ray data can map areas of groundwater discharge and recharge and soil/regolith catenas and be used to assess weathering maturity and geomorphic processes in the landscape. Most of the examples are drawn from the Ebagoola study area. A comprehensive description and analysis of the airborne survey over the Wagga Wagga study area is given by Bierwirth (1996). The Wagga Wagga study involved a large number of ground spectrometer measurements, soil samples and XRF analyses. Interpretations in Ebagoola are based on limited laboratory and field spectrometric measurements, geochemical sampling and detailed field mapping (regolith). Major and minor elements for soil/regolith samples were determined using X-ray fluorescence (XRF); whereas X-ray diffraction (XRD) was used to identify minerals and clays. High specific gravity mineral concentrates were determined for some samples, using heavy liquids. Interpretation over the Sir Samuel area was largely based on field relationships and correlations with published regolith-landform maps (Craig & Churchward 1995).

Gamma-ray responses of in-situ soils/regolith

The gamma-ray responses of in-situ weathered regolith can be grouped according to the rock types being weathered. Where bedrock crops out or where soil/regolith materials are thin, the gamma-ray response directly relates to the primary rock minerals and geochemistry and, in places, secondary minerals associated with mineralisation (e.g. potassic alteration).

Regolith associated with metamorphic rocks

Regolith materials over metamorphic rocks in the Ebagoola study area are variable in nature and shallow. The variation reflects the lithological heterogeneity of the bedrock and landforms with moderate to high relief (>30 m). Areas of high relief are being actively eroded and regolith development is minimal, consisting mainly of lithosols overlying slightly weathered bedrock. The gamma-ray response from the partly weathered materials is essentially equivalent to the original bedrock response. Therefore, gamma-ray response over these landforms is directly related to bedrock geochemistry. Scree and lithosols on quartzite ridges have relatively high U values and are likely to reflect accessory resistant minerals, such as zircons, within the quartzites (area G, Fig. 3a) (Blewett & Trail 1995). Clayey earths on subdued topography between the quartzite ridges have formed by the weathering of schistose and phyllitic parent material. These soils are distinguished by moderately high K, eTh and eU values. The K element in the soils relates to potassic clays (illite) and micas. Th and U elements are likely to be associated with clays, Fe oxides and

Table 1. X-ray fluorescence (XRF), X-ray diffraction (XRD) and heavy-mineral separation for selected regolith samples over the Ebagoola area.

SAMPLE	SiO_2%	Al_2O_3%	FeO %	MgO %	CaO %	Na_2O %	K_2O %	Th ppm	U ppm	Zr ppm	XRD and heavy liquid separation
Bauxite nodules	55.24	27.26	4.83	0.07	0	0	0.03	41	2.5	869	*Kaolinite and quartz major, goethite and amorphous iron, zircons and rutile as trace*
Bauxitic sand	68.58	16.34	3.83	0.08	0.02	0	0.03	28	2.5	1243	*Quartz major, kaolinite, goethite and amorphous iron, zircon common - rutile as trace*
Clayey earth on schist	59.54	18.12	9.21	0.54	0.03	0.82	3.58	25	5.5	161	*Mica and kaolinite major, montmorillonite mixed layered clay and quartz trace*
Residual sand on sandstone	93.4	2.28	0.47	0.02	0.01	0	0.11	9	1.5	347	*Quartz major, amorphous iron - zircon and rutile as trace*
Residual sand on granite	92.53	3.74	0 98	0.03	0	0.01	0 51	13	4.5	204	*Quartz major, trace of amorphous iron, zircon and rutile*
Weathered saprolite	62 49	20.31	2.28	0.47	0	0.03	1.28	2.1	1.5	119	*Quartz major, minor kaolinite and K-feldspar*
Structured saprolite	65.92	16.38	4.73	0.81	0.23	1.03	2.41	17	3	262	*Quartz, kaolinite and K-feldspar major*
Shallow yellow earth on siltstone	61	7.4	24.19	0.03	0.04	0.01	0.09	9	2.5	208	*Quartz and kaolinite major, goethite and amorphous iron and zircon trace*
River channel sands	79 97	10.29	0.42	0.07	0.4	1.2	4.83	14	2	90	*Quartz major, K-feldspar, minor kaolinite and mixed layered clays*
Overbank - sand and clay	88.91	5.52	0.24	0.03	0.05	0.24	2.93	19	3.5	186	*Quartz major, minor K-feldspar, minor kaolinite and mixed layered clays*
Older alluvial terrace sands	95 59	1.22	0.31	0	0.02	0	0.46	16	5 5	399	*Quartz major - mica and zircon trace*

28/A/39

lithic fragments in the weathering profiles (Table 1).

In the Wagga Wagga study area, gamma-ray response varies over hilly landforms of metasedimentary rocks, according to soil depth and degree of leaching. On ridge tops, soils are very shallow with relatively fresh bedrock fragments exposed at the surface. These shallow soils are distinguished by their high K response (Fig. 4c), which corresponds to K-mica and illite associated with weathered rock fragments and minor clays. Soils downslope from the ridges are deeper and are distinguished by low K response. Soil–landform relationships of these soils are discussed later under the heading ***Soil/regolith catenas***.

Regolith associated with granitic rocks

Weathering profiles are developed on granitic bedrock in each study area. In Ebagoola, regolith on gently undulating rises consists of deep uniformly textured residual yellow to yellowish-orange massive sandy earths over granitic saprolite. These soils are low in all radioelements and appear black in the imagery (area D, Fig. 3a). They consist mostly of quartz sand that accumulated preferentially as other, more soluble, minerals were removed from the top of the weathering profile, either in solution or as fine grains. Apart from quartz, there are minor amounts of mica and kaolinite, and traces of resistate minerals, such as rutile and zircon (Table 1). Thinner sandy earth soils with a poorly developed quartz sand horizon are separated from the deeper residual soils by their higher K response. The gamma-ray response of these thinner soils reflects the chemical composition and mineralogy of the underlying granite, in particular the abundance of K-feldspar and mica in the near surface. S and I-type granites can be distinguished in areas of thin regolith cover by their gamma-ray response. S-type granite has generally higher K and eTh values

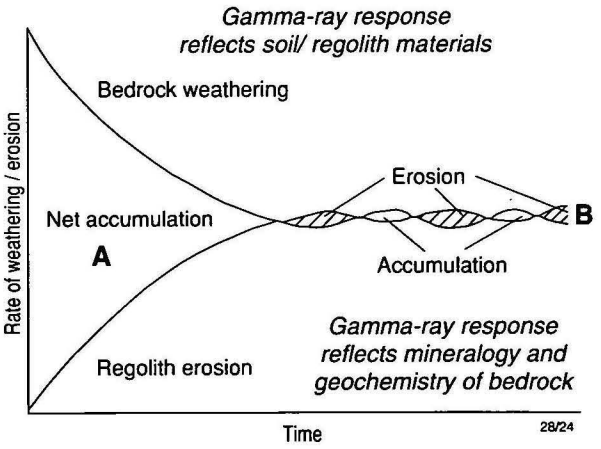

Figure 7. Diagrammatic representation of factors which affect the denudation balance in landscapes. Regolith or soil thickness at any one site will depend on the relative rates of regolith accumulation and erosion. A, weathering rates higher than erosion rates, resulting in regolith development; B, weathering and erosion rates are similar, resulting in thin permanently youthful regolith. In areas of active erosion, gamma-ray responses are likely to reflect geochemistry and mineralogy of the bedrock, whereas in areas of accumulation, the response is modified by pedogenesis (Figure modified from Crozier 1986)

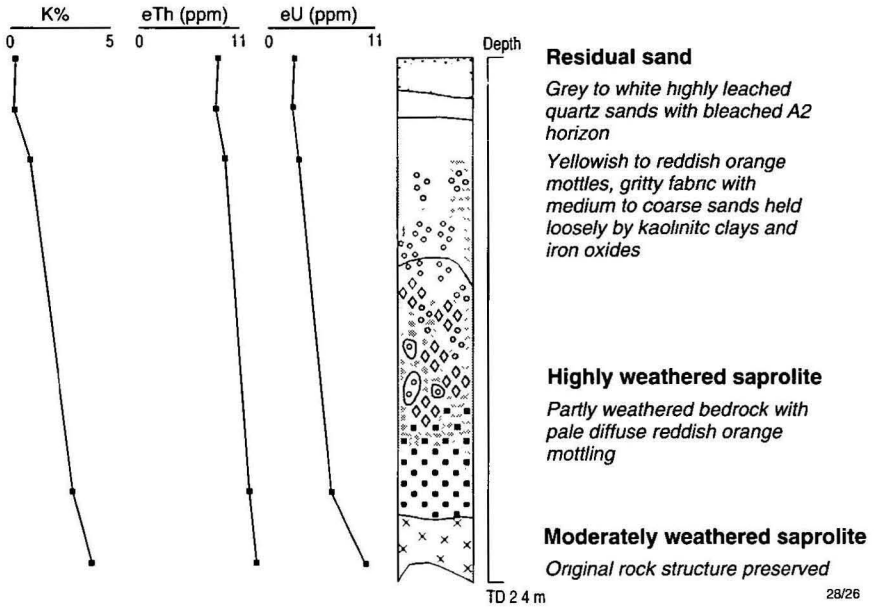

Figure 8. Highly leached, residual sandy weathering profile developed on granite in north Queensland (Ebagoola). K% and ppm equivalents of eTh and eU down the profile are measured by laboratory spectrometer.

than I-type granite (areas E & O, Fig. 3a).

In the Sir Samuel area, the gamma-ray response over granitic terrain varies, reflecting the degree of weathering and surface reworking by either aeolian or fluvial processes. Granitic saprolite is exposed in the Sir Samuel and Wagga Wagga study areas in areas of active erosion over hilly terrain. Here, the saprolite is distinguished by high K, eTh and eU responses, which reflect parent rock geochemistry and mineralogy. The freshest exposures in the Sir Samuel region are usually immediately downslope from breakaways (area C, Fig. 4a). Soil over the saprolite is typically thin with rock fragments at or near the surface. Geochemical analyses indicate that K is associated with K-feldspar in the coarse sand and gravel fraction of the soil (area A, Fig. 4a), whereas eTh and eU are likely to be associated with clays and lithic fragments.

Regolith associated with sedimentary rocks

In Ebagoola, regolith profiles developed on Mesozoic sandstone and siltstone consist, respectively, of deep, sandy red-yellow earths over highly weathered mottled bedrock, and shallower yellow earths over moderately weathered bedrock. The sandy earths give a low gamma-ray response for each radioelement (appear black in area K, Fig. 3a), owing largely to the accumulation of quartz sand, which is radioactively barren. The shallower, finer textured soils developed on siltstone give a higher eTh and eU response (area L, Fig. 3a), which reflects the geochemistry of the underlying bedrock. Gilgai or swelling clay soils (area M, Fig. 3a) developed on Mesozoic or more recent sediments are distinguished by higher K values, which are likely to be due to the presence of potassic clays (illite) and the absorption of K ions within the lattice of swelling clays (montmorillonite). In the Wagga Wagga area, low K, Th and U values characterise the gamma-ray response over weathered sandstone, reflecting the lack of radionuclides in the sandstone and abundance of silica sand, which is radioactively barren.

Ferruginous and siliceous duricrusts

Exposures in the Sir Samuel study area are generally poor and deeply weathered. In many places, saprolite is either covered by aeolian sands (see ***Gamma-ray response of transported soil/regolith***), cemented, or capped by silcrete and various ferruginous materials, including massive Fe duricrusts, ferricrete, ferruginous saprolite and iron-rich gravel lags. Typically, the radioelement characteristics of these weathered materials bear little resemblance to those of the underlying rocks. Silcrete and ferruginous crusts commonly form breakaways (area A, Fig. 4a) or mantles over undulating slopes and hill tops. Silcrete appears green and blue (area A, Fig. 4a), which indicates the lack of K and presence of Th and U. The high eTh and eU values are likely to relate to heavy-mineral grains (e.g. zircon) in the silcrete, or contamination by Th and U-rich groundwater during silcrete formation. Ferruginous material also appears green and blue, but typically has higher Th than silcrete. The high Th is likely to be associated with Fe oxides. However, some Fe duricrusts, particularly those developed over greenstone, are radiometrically barren (appear black in area D, Fig. 4a), which reflects the lack of the radioelements in the bedrock from which the Fe oxides have been sourced. In Ebagoola, unconsolidated ferruginous sands and, in places, cemented pisolitic Fe duricrusts are distinguished by their high Th values (areas P, Fig. 3a), which are likely to be due to Th associated with resistate minerals (e.g. zircon) and scavenging of Th by Fe oxides.

Gamma-ray response of transported soil/regolith

The gamma-ray response of transported regolith can be broadly divided and described in terms of alluvial, colluvial and aeolian material.

Alluvial material

Alluvial material includes sediment deposited by channel and overbank stream flow. In the Ebagoola study area, gamma-ray response is effective for mapping the distribution and provenance of alluvial sediment. River channel and alluvial fan sediments derived from granitic and metamorphic rocks are distinguished by high K, eTh and eU (area B, Fig. 3a). Sediment derived from metamorphic rocks is distinguished by low K and high eTh and eU, reflecting chemistry of the source rocks (area C, Fig. 3a). Sediment derived from granitic rocks is distinguished by high K and moderate to high eTh and eU (area A, Fig. 3a). In places, floodplain sediments are separated into channel and overbank deposits on the basis of their gamma-ray response. Channel sands are recognised by their

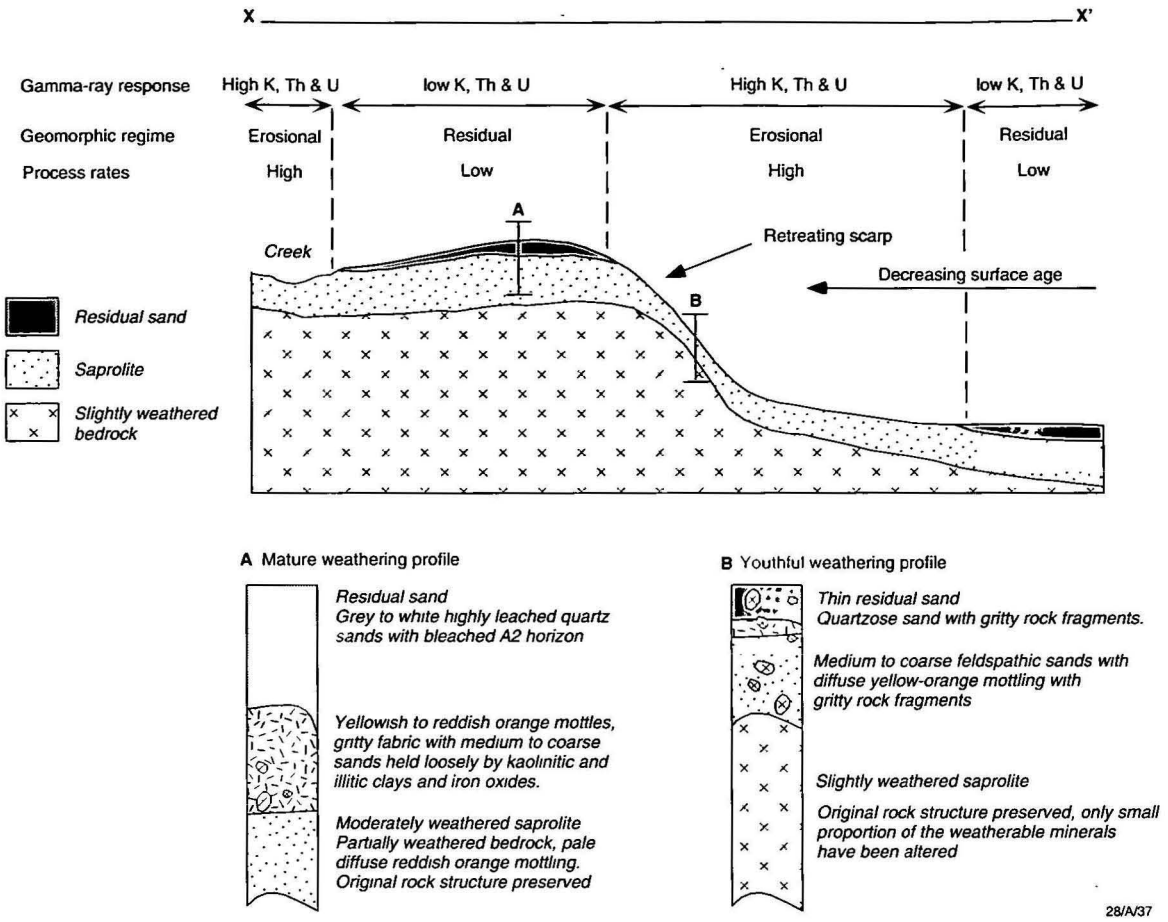

Figure 9. Relationship between gamma-ray response, soil/regolith type and geomorphic processes over the Great Escarpment in Ebagoola. Location of X–X^1 transect on the gamma-ray image shown on Figure 3b.

high K values and correspond to coarse-textured sediment rich in K-feldspar and mica. In contrast, soils developed on alluvial overbank sediment have lower K and relative high eTh and eU responses. Increased abundance of zircon in the overbank deposits (Table 1) may relate to higher eTh and eU responses. Adsorption of U and Th onto clay in the finer textured overbank sediment is also likely to contribute to higher eU and eTh responses. Differences in K concentration between channel and overbank sediment and implications for weathering development and depositional rates are discussed later under ***Weathering development and relative geomorphic activity***.

In the Wagga Wagga study area, river channel sediment derived from granitic bedrock is distinguished by high K values and relates to coarse-textured alluvial soils and sediment containing significant amounts of primary K-feldspar. Finer textured alluvial soils, where K and eTh are associated with clays, give a distinctive signature for floodplain sediment. Textural and possible age differences in the floodplain sediment can be distinguished on the basis of gamma-ray response. Variation in K and Th concentration is used to map areas of alkaline cracking clay, alluvial deposits of various ages and other non-cracking soils. Cracking clay and gilgai are indicated by low eTh response. This may be due to deposition of montmorillonite-rich clay with lower Th during a more arid period. More recent channels with greater amounts of illite and kaolinite clays have a higher Th response. Relatively more recent alluvial deposits are distinguished by elevated K and Th, which correlate with the amount of silt and clay particles in the sediment. Both K and Th are known to adsorb onto clay particles (Wedepohl 1969) and some K may be present in the silt and clay. This means that alluvial areas can be identified by radiometric signature and in some areas it may be used to predict surface grain size.

In the Sir Samuel study area, sediment derived from granitic sources is distinguished by high K, eTh and eU. However, many major river systems are delineated by a high eU response. The high eU may be associated with radium isotopes deposited from groundwater and saline lakes or U precipitated in calcrete, which tends to accumulate along valley floors.

Colluvial material

In the Wagga Wagga study area, active colluvial deposits derived from granitic rocks are distinguished by a high K response, associated with K-feldspars. They are separated from less active older deposits, which have low K signatures, owing to removal of soluble K-feldspar minerals from the weathering profile (Fig. 4b). The older colluvial deposits consist mostly of quartz sand within a clay matrix. The colluvial footslopes act as conduits for groundwater flow, with saline seepages occurring in creeks at the base of the footslopes. Highly weathered colluvial soils derived from the weathering metasedimentary rocks are also characterised by low K values. Detailed sampling of soil properties and radioelement concentrations (Bierwirth et al. 1996) indicate that loss of K on the colluvial footslopes is largely a result of leaching. Figure 6d, shows a leaching index (the ratio of exchangeable calcium in the upper B horizon versus the bleached A2 horizon) related to K in the A horizon of colluvial soils. As expected, K concentration in the soil inversely relates to degree of leaching. The same relationships were observed with K in the A2 and B horizons. Elsewhere, other studies have found that adsorption on clays and downslope surface transport dominate radioelement patterns (Martz & de Jong 1990). Soil chemistry and

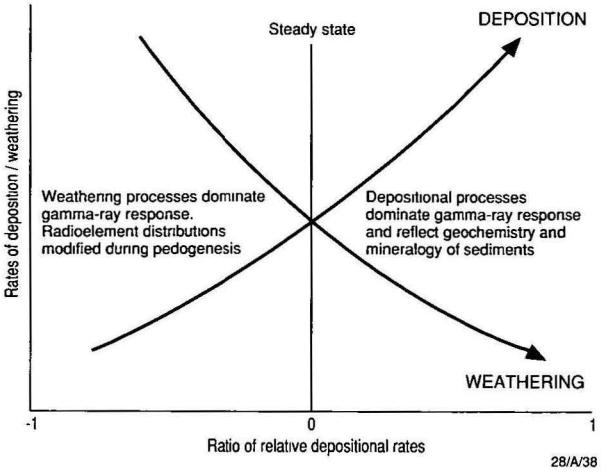

Figure 10. Relationship between gamma-ray response to relative rates of weathering and deposition. The steady state is where depositional and weathering processes have equal influence on the radioelement characteristics of the sediment.

radioelement concentrations (Fig. 6a, b) indicate that, despite the relatively coarse resolution of the airborne data (approx 100 m pixels), there is a good correlation between soil and airborne K and eTh measurements. This suggests that certain field site attributes or soil relationships based on geochemical trends (e.g. degree of leaching) can be extrapolated using gamma-ray signatures. Airborne eU values, however, are poorly correlated with soil measurements (Fig. 6c). In the Sir Samuel region, active colluvial fans derived from granitic rocks show high K responses, reflecting the abundance of coarse K-feldspar grains (area G Fig. 4a). Less active colluvial fans typically have subdued K response.

Aeolian material

A large proportion of the Sir Samuel study area is covered by sandplain or aeolian reworked sheet-flow fans, which consist of hummocky dunes and sand sheets. Well-worked quartzose aeolian sand is characterised by low radioelement response (black hues, area F, Fig. 4a) and can be separated from feldspathic sand, which has a high K signature. The feldspathic sand is sourced from and found adjacent to weathered granite.

Extensive areas of the Riverine Plain, including parts of Wagga Wagga study area, are covered by wind blown parna. Parna consists of clay and silt-size aggregates and was deposited during drier periods in the Quaternary (Butler 1956). Areas interpreted as parna on field sample data (Bierwirth 1996) are associated with high eTh response. However, since parna and older alluvial deposits have similar gamma-ray signatures, they are not easily separated. Further complications arise where the parna is weathered to various degrees or partly mixed with other material, as a result of bioturbation and fluvial reworking. Isolating the Th response associated with parna material is difficult and depends largely on the background radioelement patterns.

Groundwater recharge and discharge

In the Ebagoola and Wagga Wagga study areas, highly porous quartzose soils, developed in situ over granite, are readily distinguished from heavy-textured soils, which typically exhibit much higher K and/or Th/U responses (areas D & M, Fig. 3a). The sandy soils are potential groundwater recharge zones. Discharge zones sometimes have observable gamma-ray signatures. Salt lakes and freshwater springs often concentrate U series elements (Dickson et al. 1987), including dissolved Ra and sometimes U itself. In the Wagga Wagga study area, no evidence has been found for soil accumulation of Ra or U. However, evidence suggests that airborne eU anomalies associated with discharge sites (Bierwirth 1996) could be due to radon gas exsolving from groundwater.

Soil/regolith catenas

Catenas describe a sequence of soils developed from similar parent material, but having different characteristics, owing to variation in slope and drainage. Catenas are recognised on gamma-ray imagery over granitic rocks in the Ebagoola study area and shaly lithology in the Wagga Wagga study area. In Ebagoola, they consist of deep uniformly textured sandy (quartzose) earths, which grade at depth into highly weathered saprolite, and shallow sandy earths and red-yellow podzolic soils, which grade at depth into moderately to slightly weathered saprolite. The distribution of these regolith types reflects different rates of erosion and accumulation on different slopes. Uniformly textured soils occur over flat hill tops and are characterised by low K, Th and U values (area A, Fig. 4d), whereas shallower soils are associated with steeper slopes (area B, Fig. 4d) and are distinguished by their high K response. In the Wagga Wagga study area, the hill tops have thin and poorly developed soils, which consist largely of lithosols. Downslope and adjacent to these hills, the soils are deeper and finer textured, and have formed on colluvium derived from weathered sediments upslope. These soils form a catena over many square kilometres of terrain underlain by Ordovician metasediments and are easily mapped using the K channel draped over a DEM. High K values delineate areas of thin soil cover and low values correspond to deeper colluvial soils (Fig. 4c).

Weathering development and relative geomorphic activity

Bedrock-dominated landforms

The development of a weathering profile in bedrock-dominated landforms depends on the balance between the rate of bedrock weathering and the rate at which weathered material is removed (Fig. 7). The most stable parts of a landscape are where the rate of weathering exceeds the rate of erosion. Deep weathering profiles develop and are preserved in stable areas with low relief and where rates of erosion are relatively low.

Stable landscapes in the Ebagoola study area tend to have either low values for K, eTh and eU, which correlate with residual quartz sand, or low K and relatively high eTh and eU, associated with accumulation of oxides and resistate minerals. Strongly leached aluminous and ferruginous bauxitic soils developed on highly weathered Tertiary plateaus are delineated by low Th and U gamma-ray values (area F, Fig. 3a). A representative bauxite profile from top to bottom comprises a residual sandy (quartz) A horizon (10–70 cm), a zone of unconsolidated bauxitic/iron pisolites and nodules supported in a sandy matrix (1.2+ m), and a pallid zone, consisting mainly of kaolinitic clay with very little iron. The top of the profile is very low in soluble cations and consists mainly of iron and aluminium oxides, kaolinite, quartz and resistant minerals (Table 1). Soil geochemistry of bauxitic sand and nodules has shown them to be relatively high in Th, U and Zr, and low in K, Na and Ca (Fig. 5a,b). Low K has resulted from either intense leaching of K-bearing minerals in the weathering profile or low initial K concentration in the underlying bedrock. High Th and U are likely to correspond to the surface concentration of resistate minerals (e.g. zircon up to 1200 ppm, Table 1) and scavenging by Fe oxides.

In the Ebagoola study area depletion of K over granitic landforms, owing to leaching, is used to separate completely weathered saprolite on stable landforms from thinner, partly weathered saprolite on steeper, actively eroding slopes (Wilford 1995). Geochemical and radionuclide trends down the com-

pletely weathered profile are shown in Figure 8. This profile type has developed on stable landforms with low mean slopes and comprises residual sand overlying highly weathered mottled saprolite and structured saprolite. Residual sand forms from deep chemical weathering, resulting in the loss of soluble mineral constituents (K_2O, CaO, Na_2O) and concentration of resistant quartz and accessory minerals, such as zircon and monazite, in the upper part of the weathering profile (Fig. 5a,b). Residual quartz sand without accessory minerals is low in K, eTh and eU, and appears black in the image (area D, Fig. 3a; area C, Fig. 3b). In contrast, thinner, partly weathered profiles that form on steeper, actively eroding slopes are distinguished by their higher K response, reflecting the presence of alkali-feldspar and mica derived from the partly weathered granite. Conversely, on stable landforms, where weathering exceeds erosion, K decreases in concentration as K-bearing minerals are progressively leached from the weathering profile. These relationships are clearly illustrated in a 3D perspective view (Fig. 3b), where the edge of a major erosional scarp separates an area with high geomorphic activity and youthful weathering profiles from one with low geomorphic activity and mature weathering profiles. An explanation of the relationships between gamma-ray response, soil/regolith type and geomorphic processes in relation to the perspective image (Fig. 3b) is shown diagrammatically in Figure 9. Denudation balance in landscapes (or the relative rates of regolith formation versus rates of erosion) can be determined using airborne surveys. Gamma-ray response over an actively eroding landscape is likely to reflect the mineralogy and geochemistry of the bedrock, whereas that over stable landforms is likely to reflect soil/regolith materials (Fig. 7).

However, not all low K or high Th and U values in the gamma-ray image are associated with highly weathered substrates, because different bedrock types can give similar responses. Interpreting the degree of weathering and inferring process rates from gamma-ray responses requires an understanding of the radioelement characteristics of bedrock and weathered material. Therefore, care should be taken when using such relationships, because other regions may differ, depending on their bedrock type and weathering history.

Depositional landforms

Gamma-ray imagery can be used to show the degree of weathering and relative depositional activity in fluvial environments. Recently deposited channel sand sourced from mixed granitic and metamorphic provinces has high K, eTh and eU values (white hues, area B, Fig. 3a,b). The radioelement response from this sand closely reflects the chemistry of the bedrock from which it was derived. This suggests that erosion, transportation and deposition of the sediment is relatively rapid, with little time for weathering to modify the radioelement composition of the original bedrock source.

In contrast, older perched alluvial terrace and overbank sediments, also derived from granitic and metamorphic rocks, have lower K and relatively higher eTh and eU values (blue/green hues, area I, Fig. 3a). These differences probably reflect textural and compositional differences between the coarser channel sand and finer overbank sediment, and modification of the radioelements by pedogenesis and leaching. Compared with the channel sediment, the overbank and terrace sediments show relatively lower concentrations of readily soluble mineral constituents (CaO, NaO, K_2O; Fig. 5c,d) and a increase in resistant minerals, such as zircon. Of the soluble mineral constituents, K is detectable by airborne spectrometry and the low K concentration in the terrace sediment is likely to partly relate to surface leaching of K. The low K concentration may indicate a less active depositional regime with sufficient time for weathering to modify the distribution and/or concentration of radioelements in the sediment before deposition. Similar associations have been used in the Ebagoola study area (Wilford 1992) to distinguish palaeochannels and former river channels on the preferential loss of K and relative concentration of resistate minerals, indicated by higher eTh and eU responses (area N, Fig. 3a).

The gamma-ray response in active depositional regimes is likely to reflect the geochemistry and mineralogy of the bedrock from which sediment is derived, whereas the gamma-ray response in less active depositional systems is likely to reflect weathering processes. This is only true, however, where the concentration of radioelements in sediment is responsive to weathering processes (Fig. 10).

Discussion

Gamma-ray response over the three study areas shows broad correlation with rock units. However, variation within units corresponds mainly to the regolith, including in-situ and transported material. The source of gamma-rays emanating from the ground surface can be described as primary or secondary. Primary sources relate to the geochemistry and mineralogy of bedrock; secondary sources, to modification of radioelement distribution by weathering and pedogenesis. The latter is complex: some of the factors affecting the gamma-ray response over a single lithology are shown in Figure 11.

During weathering, radioelements are released from primary mineral constituents and incorporated into clay, iron oxides, groundwater and organic matter. K is geochemically mobile and soluble under most weathering conditions. During weathering it is lost from primary minerals, such as K-feldspar and mica, in solution and/or adsorbed onto clay minerals, such as illite, montmorillonite and, to a lesser, extent kaolinite. U and Th are typically much less mobile than K. U is leached and released from soluble minerals under oxidising conditions and precipitates in reducing conditions (Hansen 1992). Surface concentrations of eU can be associated with resistate minerals such as zircon and monazite, clay or ^{226}Ra exsolved from groundwater. Th can be highly mobile when combined with organic complexes in groundwater and soils (Dickson 1991). Th is also associated with resistate minerals and tends to be concentrated in residual regolith profiles. Both U and Th released during weathering are readily adsorbed onto clay minerals and are co-precipitated with Fe oxides in soils (Dickson & Scott 1990).

Although these secondary sources of gamma-rays relate to a variety of different materials and processes, some general trends do emerge. Typically, Th and U are associated with silt/clay fractions and sesquioxides in soils and tend to concentrate in highly weathered profiles relative to K. K is typically high in slightly weathered regolith (depending on bedrock composition) and low in highly weathered regolith, owing to leaching. The relative mobility of major mineral constituents released during weathering and their gamma-ray response are shown in the sequence below.

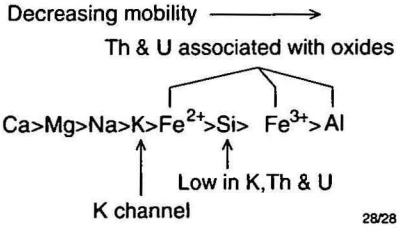

The sequence is generalised and ordering may change with to environmental conditions. As primary minerals weather, cations (e.g. K^+ Na^+ Ca^{+2}) are either incorporated into clay minerals (i.e. smectite & illite) or lost in solution. Further weathering leads to the development of kaolinitic clays and accumulation of silica, iron and aluminium oxides. The lack

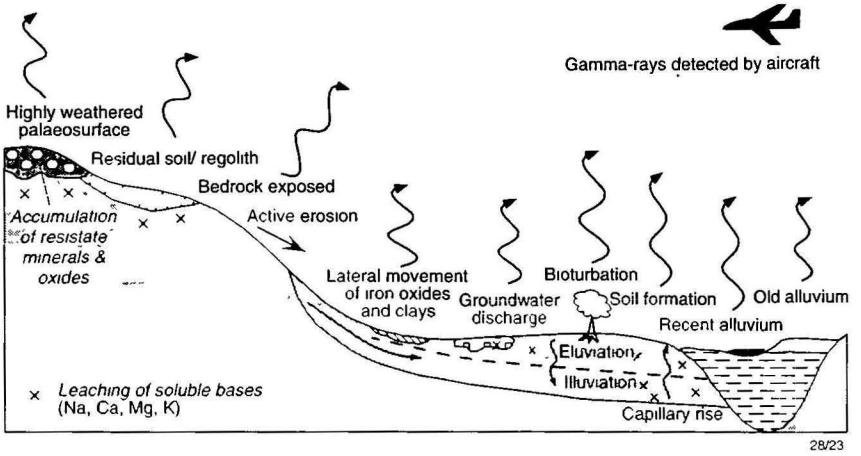

Figure 11. Diagrammatic sketch of factors affecting gamma-ray response over the same bedrock type. Gamma-rays will reflect the primary mineralogy and geochemistry of the bedrock, the nature of secondary weathering materials, groundwater dynamics and geomorphic processes in the landscape. Pedogenesis is important in modifying the distribution of radioelements at the surface.

of radioelements in quartz can be used in places to indirectly map highly siliceous soils.

The K channel and K/eTh & K/eU ratio channels can be used in places to assess the degree to which the source materials of regolith are weathered or leached—since K response is associated with easily weathered minerals, whereas Th and U are typically associated with residual clay, oxides and accessory minerals (previous weathering sequence diagram). For example, high and low K/eTh & K/eU ratio values over potassic rocks in the Ebagoola study area are likely to be associated with slightly weathered and highly leached soils, respectively. These highly leached soils also have a very low exchangeable cations and organic matter content (Isbell & Gillman 1973) and high porosity and permeability. In places, highly leached low-relief landforms in the Ebagoola study area, delineated by low K response, correlate well with moderately acidic soils (Biggs & Philip 1995). These acid soils are likely to have developed through the removal of basic cations and replacement by acidic ions (H^+ or Al^{+3}) during weathering. Studies from Wagga Wagga (Bierwirth 1996) indicate that in some areas airborne K images can be used to map soil acidity Soil samples in stable landforms (i.e. areas where pedogenic processes dominate) showed a positive correlation between K and pH. This highlights the potential use of airborne surveys in indirectly mapping and assessing the nutrient status, pH and water-holding capacity of certain soils. Gamma-ray surveys have the potential to extend certain soil or regolith site-attribute information spatially and map it as continuous variables across the landscape. Airborne measurements record total concentration of radioelements at the surface and, therefore, measured K does not equate to exchangeable K in soils or availability to plants.

General geochemical trends in surface regolith samples were reflected in the airborne measurements. K and, to a lesser extent, Th correlated reasonably well with aerial measurements. However, U soil measurements generally correlate poorly with estimated aerial concentration. This poor correlation is largely due to the occurrence of radon, a decay product in the U decay chain and not the parent U. The lack of correlation may also be explained by the low count rates and high noise content of the U channel in the airborne data. Correlations are likely to be highest over homogenous regolith material and where Th and U are in equilibrium with their radioactive daughter isotopes.

The gamma-ray response of regolith material from each of the study areas varied according to differences in lithology, weathering and geomorphic history. Radioelement response over actively eroding landforms is likely to be closely correlated to bedrock geochemistry and mineralogy. However, in more stable landforms, where regolith materials are accumulating, weathering can result in radioelement response showing a marked disparity from the underlying bedrock signatures. If the gamma-ray responses of the bedrock and regolith are known, then areas of regolith accumulation associated with low geomorphic process rates can be separated from bedrock areas associated with relatively high process rates. These relationships can then be used to assess the denudation balance in the landscapes or the relative rates of regolith formation and erosion.

The relative depositional activity of alluvial sediments and the provenance from which the sediments are derived can be distinguished Active depositional environments have similar gamma-ray signatures to their source rocks, indicating relatively rapid erosion, transportation and deposition, with minimal modification by weathering. Gamma-ray responses in less-active depositional environments often differ from their source rock responses, owing to removal of radionuclides by pedogenic processes. This information has the potential to be used in improving the interpretation of stream-sediment geochemistry for mineral exploration.

Gamma-ray data provide complementary geochemical information for land-system mapping, which, to date, has been largely based on interpretation of aerial photographs. The land-system approach uses landforms as a surrogate for mapping soil and regolith types. In many cases, the gamma-ray data can be used to extend or further subdivide landscape units, particularly in areas of poor landform expression. Modelling gamma-ray data with ancillary data sets has been used successfully in predicting soil/regolith attributes (Wilford & Butrovski 1996; Gessler, P.E. 1996). In addition, vegetation often has little effect on the gamma-ray response, unlike surface scanners such as SPOT and Landsat TM, where vegetation patterns can have a confusing effect in identifying soil and regolith boundaries. However, a limitation of airborne gamma-ray spectrometry for detailed terrain evaluation compared with SPOT, Landsat and, in particular, aerial photography is its comparatively poor spatial resolution. For example, over 20 per cent of the gamma-ray signal will be derived from a ground radius of greater than 300 m for a survey flown at a height of 100 m (Minty 1997). For this reason, the interpretability of gamma-ray imagery is enhanced by combining it with data sets of higher spatial resolution. Integrating gamma-ray imagery with Landsat TM and digital elevation models enables the distribution of radioelements to be interpreted in a landscape context. The integrated images allow for accurate geographic positioning and, as such, are useful for field interpretation. Three-dimensional perspective views allow the gamma-ray response relating to regolith, catenas and geomorphic processes to be visualised and separated from lithological responses.

Conclusions

A gamma-ray image is a geochemical map showing the distribution of radioelements K, eTh and eU in rocks and regolith. Gamma-ray response from regolith material relates to present-day and past weathering and geomorphic processes in the landscape. Once the gamma-ray response and relationships between bedrock and regolith are understood, gamma-ray data can provide information on regolith properties, including mineralogy and chemistry. From this, inferences can be made about the style of weathering, degree of leaching, pH, texture, nutrient status, and thickness of regolith material, and relative geomorphic process rates. Gamma-ray data often provide a more direct remote-sensing tool for soil mapping than surface scanners (e.g. Landsat), which rely on vegetation surrogates to map soil types.

In areas of bedrock terrain, gamma-ray response correlates broadly with major geological units. Variation within these units can correspond to lithological variation and different styles of in-situ weathering, which reflect underlying lithology, time and geomorphic processes. Gamma-ray response from transported sediment will reflect the bedrock source, texture and style of weathering, which is, in part, controlled by the rates of erosion, transport and deposition in the catchment. Radiometric models developed to explain relationships between gamma-ray response and regolith material in one region may not be transferable to another, because of differences in bedrock lithology, geochemical environment and weathering history. In bedrock terrains, gamma-ray relationships and responses are often specific to major lithological types and, therefore, interpretation is best made within these major groups. Similarly, interpretation in depositional landforms is best made within major river catchments, since relationships between gamma-ray response and regolith material are likely to change with the type of lithology being eroded and the rate of erosion within catchments.

There are limitations in using airborne gamma-ray data. Not all regolith types can be distinguished by their gamma-ray response. Different regoliths can have similar responses, whereas other materials are radioactively barren with no distinguishable gamma-ray signature. Variation in the intensity of the gamma-ray signal, reflecting changes in soil moisture, is likely to be difficult to separate from regolith response. Furthermore, small-scale surface features, particularly, those located between flight lines, are likely to be undetected, because of the relatively poor spatial resolution of the survey data. Gamma-ray data should, therefore, not be used in isolation in any comprehensive terrain analysis or evaluation, but together with all other available information.

However, despite these limitations, airborne gamma-ray surveys provide information on surface geochemistry, distribution of common primary and secondary minerals, different styles of weathering and geomorphic processes in the landscape. Airborne gamma-ray data are, therefore, invaluable for mapping regolith (including soils) and in mineral exploration. The significance of airborne gamma-surveys for regolith mapping is likely to increase as we improve our understanding of the behaviour and distribution of radioelements in weathering profiles. Airborne gamma-ray data can assist in land-degradation and salinity studies by delineating areas of active erosion and areas of groundwater discharge and recharge. The use of airborne gamma-ray surveys in mineral exploration will be more effective when the responses due to weathering and geomorphic processes are understood, allowing subtle variations in lithology or changes through mineralisation to be resolved.

Airborne gamma-ray data have the potential to complement and accelerate presently used land-system approaches for mapping regolith and soils. The effectiveness of using gamma-ray data for mapping regolith will increase when they are combined and modelled with other complementary data sets, particularly terrain attributes, such as slope and relief.

References

Bierwirth, P.N., 1996. Investigation of airborne gamma-ray images as a rapid mapping tool for soil and land degradation—Wagga Wagga, NSW. Australian Geological Survey Organisation, Record 1996/22.

Bierwirth, P.N., Gessler, P. & McKane, D., 1996. Empirical investigations of airborne gamma-ray images as an indicator of soil properties—Wagga Wagga, N.S.W. Proceedings of the 8th Australasian Remote Sensing Conference, Canberra, 1996.

Biggs, A.J.W. & Philip, S.R., 1995. Soils of Cape York Peninsula. Queensland Department of Primary Industries, Mareeba, Land Resources Bulletin QV95001.

Blewett, R.S. & Trail., D.S., 1995 Ebagoola, Queensland (SD/54-12), 1:250 000 Geological Series Commentary. Australian Geological Survey Organisation, Canberra.

Bunting, J.A. & Williams, S.J., 1979. Explanatory notes on the Sir Samuel geological sheet. Geological Survey of Western Australia, Perth.

Butler, B.E., 1956. Parna an aeolian clay. Australian Journal of Science, 18, 145–151.

Carroll, T.R. & Vose, G.D., 1984. Airborne snow water equivalents over a forested region using terrestrial gamma radiation, Proceedings of 41st Annual Eastern Snow Conference, New Carrolton, Maryland, 6–8 June.

Conradson, K. & Nilsson, G., 1984. Application of integrated Landsat, geochemical and geophysical data in mineral exploration. Proceedings of the Third Thematic Conference on Remote Sensing for Exploration Geology, Colorado Springs, Colorado, 499–511.

Cook, S.E., Corner, R.J., Groves, R.J. & Grealish, G., 1996. Application of airborne gamma radiometric data for soil mapping. Australian Journal of Soil Research, 43/1, 183–194.

Craig, M.A. & Churchward, H.M., 1995. Sir Samuel regolith-landforms (1:250 000). Australian Geological Survey Organisation, Canberra.

Crozier, M.J., 1986. Landslides: causes consequences and environment. Croom Helm, London, p. 138.

Darnley, A.G. & Grasty, R.L., 1971. Mapping from the air by gamma-ray spectrometery. Proceedings of the 3rd International Geochemical Symposium, Toronto, Ontario, Canadian Institute of Mining and Metallurgy, Special Volume 11, 485–500.

Dickson, B.L., 1985. Radium isotopes in saline seepages, south-western Yilgarn, Western Australia. Geochimica et Cosmochimica Acta, 49, 361–368.

Dickson, B.L., 1991. Thorium migration: evidence from the geological record. Environmental Radioactivity Workshop, Tahiti, Sept 2–6 1991.

Dickson, B.L. & Scott, K.M., 1990. Radioelement distributions in weathered granitoids and aeolian soils in NSW. AMIRA P263: Improving the interpretation of airborne gamma-ray surveys. CSIRO Division of Exploration Geoscience. May 1990, Unpublished report.

Dickson, B.L. & Scott, K M , 1997. Interpretation of aerial gamma-ray surveys —adding the geochemical factors. AGSO Journal of Australian Geology & Geophysics, 17(2)—this issue.

Dickson, B.L., Giblin, A.M. & Snelling, A.A., 1987. The source of radium in anomalous accumulations near sandstone escarpments, Australia. Applied Geochemistry, 2, 385–398.

Duval, J.S., 1990. Modern aerial gamma-ray spectrometry and regional potassium map of the conterminous United States. Journal of Geochemical Exploration, 39, 249–253.

Foote, R.S. & Humphrey, N.B., 1976. Airborne radiometric techniques and applications to U exploration. In: Exploration for U ore deposits. International Atomic Energy Agency, Vienna, 17–34.

Foote, R.S., 1968. Improvement in airborne gamma radiation data analyses for anomalous radiation by removal of environmental and pedologic radiation changes. In: Symposium on the use of nuclear techniques in the prospecting and development of mineral resources. International Atomic Energy Meeting, Buenos Aires.

Galbraith, J.H. & Saunders, D.F., 1983. Rock classification by characteristics of aerial gamma-ray measurments. Journal of Geochemical Exploration, 18, 49–73.

Gessler, P.E., 1996. Statistical soil-landscape modelling of environmental management. PhD Thesis, Australian National University.

Graham D.F. & Bonham-Carter, G.F., 1993. Airborne radiometric data: a tool for reconnaissance geological mapping using a GIS. Photogrammetric Engineering & Remote Sensing, 59(8), 1243–1249.

Grasty, R.L., 1976. Applications of gamma radiation in remote sensing, ecological studies, analysis and synthesis, In: Schanda, E. (editor), Remote sensing for environmental sciences. Springer-Verlag, Berlin, New York, 18, 257–275.

Gregory, A.F. & Horwood, J.L., 1961. A laboratory study of gamma-ray spectra at the surface of rocks. Department of Energy, Mines & Resources, Ottawa, Mines Branch Research Report R85.

Hansen, D.A., 1992. In: Blaricom, R.V. (compiler), Practical geophysics II for exploration geologists. Northwest Mining Association, USA.

Isbell, R.F. & Gillman, G.P., 1973. Studies on some deep sandy soils in Cape York Peninsula, North Queensland—morphologial and chemical characteristics. Australian Journal of Experimental Agriculture and Animal Husbandry, 13, 81–87.

Kogan, R.M., Nazarov, I.M. & Fridman, S.D., 1969. Gamma-ray spectrometry of natural environments and formations. Israel Program for Scientific Translations, Jerusalem.

Koons, R.D., Helmke., P.A. & Jackson, M.L., 1980. Association of trace elements with iron oxides during rock weathering. Soil Science Society of America, Journal, 44, 155–159.

Lavreau, J., & Fernandez-Alonso, M., 1991. Correcting airborne radiometric data for water/vegetation screening using Landsat Thematic Mapper imagery. 8th Thematic Conference on Geologic Remote Sensing, Denver, Colorado, April 29–May 2.

Loijens, H.S., & Grasty, R.L., 1973. Airborne measurments of snow water equivalent using natural gamma radiation over southern Ontario, 1972–73. Ontario Science Series No. 34, Inland Waters Directorate, Water Resources Branch, Ottawa.

Martz, L.W. & de Jong, E., 1990. Natural radionuclides in the soil of a small agricultural basin in the Canadian prairies and their association with topography, soil properties and erosion. Catena, 17, 85–96.

McDonald, P.A. & Pettifer, G.R., 1992. The application of airborne radiometric classification techniques to salinity studies in Western Victoria. Geological Society of Australia, Abstracts, 32, 305.

Minty, B.R.S., 1996. The fundamentals of airborne gamma-ray spectrometry. AGSO Journal of Australian Geology & Geophysics, 17(2)—this issue.

Raymond, O. L., 1992. The geology of Wagga Wagga and the Kyeamba valley—1:100 000 scale preliminary edition. Australian Geological Survey Organisation, Canberra.

Richards, J. A., 1986. Remote sensing digital image analysis: an introduction. Springer-Verlag. Berlin.

Schwarzer, T. F., Cook, B.G. & Adams, J.A.S., 1972. Low altitude gamma-spectrometric surveys from helicopters in Puerto Rico as an example of the remote sensing of thorium, uranium and potassium in rocks and soils. Remote Sensing Environment , 2, 83–94.

Tucker, D.H., Bacchin, M. & Almond, R., 1984. Significance of airborne magnetic and gamma spectrometric anomalies over the eastern margin of the Canning Basin. In: Purcell, P.G. (editor), The Canning Basin, W.A. Proceedings of Geological Society of Australia/Petroleum Exploration Society of Australia Symposium, Perth, 1984.

Wagner, C., 1989. Cape York Peninsula resource analysis. Premier's Department Report Queensland. Connell Wagner Pty Ltd.

Wedepohl, K. H.(editor), 1969. Handbook of Geochemistry, vol II-5, Springer Verlag, Berlin.

Welch, R. & Ehlers, W., 1987. Merging multi-resolution SPOT HRV and Landsat TM data, Photogrammetric Engineering and Remote Sensing, 53(3), 301–303.

Wilford, J.R., 1992. Regolith mapping using integrated Landsat TM imagery and high resolution gamma-ray spectrometric imagery—Cape York Peninsula. Bureau of Mineral Resources, Australia, Record 1992/78.

Wilford, J.R., 1995. Airborne gamma-ray spectrometry as a tool for assessing relative landscape activity and weathering development of regolith, including soils. AGSO Research Newsletter, no. 22, 12–14.

Wilford, J.R. & Butrovski, D., 1996. Use and modelling of airborne gamma-ray spectrometry in soil/regolith mapping and applied geomorphology. Proceedings of the 8th Australasian Remote Sensing Conference, Canberra, 26–29 March.

AGSO
AUSTRALIAN GEOLOGICAL SURVEY ORGANISATION

AGSO Journal of Australian Geology & Geophysics

Volume 17, Number 2

CONTENTS

Thematic issue: Airborne magnetic and radiometric surveys
Guest associate editor: Peter Gunn

AGSO JUBILEE 1946-96